

RESEARCH ADMINISTRATION

N72-70963

NASA-TMX 67563

U.S. AIR FORCE
NATIONAL AERONAUTICS
AND SPACE ADMINISTRATION

JOINT CONFERENCE
ON
LIFTING MANNED HYPERVELOCITY
AND REENTRY VEHICLES

April 11 - 14, 1960

A COMPILATION OF THE PAPERS PRESENTED

PART I

CLASSIFICATION CHANGE

April 11-12, 1960

By authority of *NSA Memo dtd 2-24-72*
Changed by *M-RJdc* Date *2-28-72*

LANGLEY RESEARCH CENTER
Langley Field, Virginia

15/ by H. Maine

CLASSIFIED DOCUMENT - TITLE UNCLASSIFIED

This material contains information affecting the National Defense of the United States within the meaning of the espionage laws, Title 18, U.S.C., Secs. 793 and 794, the transmission or revelation of which in any manner to an unauthorized person is prohibited by law.

U.S. AIR FORCE -
NATIONAL AERONAUTICS AND SPACE ADMINISTRATION

JOINT CONFERENCE
ON
LIFTING MANNED HYPERVELOCITY
AND REENTRY VEHICLES
April 11-14, 1960

A Compilation of the Papers Presented

Part I
April 11-12, 1960

Langley Research Center
Langley Field, Virginia

TABLE OF CONTENTS

	Page
INTRODUCTION	vii
LIST OF CONFEREES	ix

TECHNICAL PAPERS PRESENTED

April 11, 1960

I. GENERAL REENTRY CONSIDERATIONS

SESSION CHAIRMAN: Russell G. Robinson

1. Motion and Heating During Atmosphere Reentry of Space Vehicles . . . by Thomas J. Wong, Glen Goodwin, and Robert Slye . . .	1
2. Modulated Entry . . . by Frederick C. Grant	19
3. Introductory Considerations of Manned Reentry Orbital Vehicles . . . by Eugene S. Love	39

II. AERODYNAMICS AND HEAT TRANSFER

SESSION CHAIRMAN: Laurence K. Loftin

4. Investigation of the Flow Over Simple Bodies at Mach Numbers of the Order of 20 . . . by Arthur Henderson, Jr.	55
5. Measurements of Radiation From Air and Carbon Dioxide . . . by T. N. Canning, H. E. Bailey, W. R. Leak, and W. A. Page	73
6. Radiative Heat Transfer at Parabolic Entry Velocity . . . by Kenneth K. Yoshikawa, Bradford H. Wick, and John T. Howe	81
7. The Aerodynamic Characteristics of Some Lifting Bodies . . . by David H. Dennis and George G. Edwards	103

- [REDACTED]
8. Convective Heat Transfer to a Blunt Lifting Body
 . . . by John O. Reller, Jr., and H. Lee Seegmiller *T.M. X-378* 121
 9. The Aerodynamic-Force and Heat-Transfer Characteristics of
 Lifting Reentry Bodies . . . by William O. Armstrong,
 P. Calvin Stainback, and Charles H. McLellan *T.M. D-439* 141
 10. Flow Fields, Pressure Distributions, and Heat Transfer for
 Delta Wings at Hypersonic Speeds . . . by Mitchel H. Bertram, *T.M. X-376*
 William V. Feller, and James C. Dunavant . . . 163
 11. Research on Blunt-Faced Reentry Configurations at Angles of *T.M. X-315*
 Attack Between 60° and 90° . . . by William H. Phillips 187
 12. The Effect of the Bow Shock Wave on the Stability of Blunt-
 Nosed Slender Bodies . . . by Alvin Seiff *T.M. X-377*
 and Ellis Whiting . . . 201
 13. Flexible Gliders . . . by Robert T. Taylor, Joseph H. Judd,
 and Donald E. Hewes . . . 215

April 12

III. GUIDANCE, CONTROL, COMMUNICATIONS, AND PILOTING PROBLEMS

SESSION CHAIRMAN: Clinton E. Brown

14. A Guidance Technique for the Approach to an Atmospheric
 Reentry . . . by Alan L. Friedlander
 and David P. Harry III . . . 223
15. An Exploratory Investigation of Some Midcourse Guidance
 Systems for the Return From the Moon
 . . . by G. Allan Smith . . . 231
16. Navigation and Guidance During Satellite Entry
 . . . by John M. Eggleston . . . 251
17. An Investigation of the Errors of an Inertial Guidance System
 During Satellite Reentry . . . by John S. White . . . 263
18. Centrifuge Study of Pilot Tolerance to Acceleration and the
 Effects of Acceleration on Pilot Performance
 . . . by Brent Y. Creer, Capt. Harald A. Smedal, USN (MC),
 and Rodney C. Wingrove . . . 273

19. A Study of Longitudinal Control Problems at Low and Negative Damping and Stability, With Emphasis on Effects of Motion Cues . . . by Melvin Sadoff, Norman M. McFadden, and Donovan R. Heinle 295
20. Review of Techniques Applicable to the Recovery of Lifting Hypervelocity Vehicles . . . by Joseph Weil and Gene J. Matranga 313 *TN X-33A*
21. Low-Speed Flight Characteristics of Reentry Vehicles of the Glide-Landing Type . . . by John W. Paulson, Robert E. Shanks, and Joseph L. Johnson 329 *TN X-331*
22. Radio Transmission Through the Plasma Sheath Around a Lifting Reentry Vehicle . . . by Macon C. Ellis, Jr., and Paul W. Huber 345 *TN D-507*

IV. DYNAMIC LOADS, STRUCTURES, AND MATERIALS

SESSION CHAIRMAN: Richard Heldenfels

23. Aeroelastic Research at High Speeds . . . by A. Gerald Rainey 367 *TN X-326*
24. Experimental Hypersonic Flutter Trends and Piston-Theory Comparisons . . . by Richard P. White, Jr., and Dale E. Cooley 381
25. Wind-Induced Oscillations of Missiles in the Launch Position . . . by Donald A. Buell and George B. McCullough 395
26. Dynamic Response Studies of Launch Vehicles . . . by Harry L. Runyan, Homer G. Morgan, and H. B. Tolefson 407
27. Flutter Research on Skin Panels . . . by Eldon E. Kordes, Weimer J. Tuovila, and Lawrence D. Guy *TN D-451* 421
28. Noise Considerations for Manned Reentry Vehicles . . . by David A. Hilton, William H. Mayes, and Harvey H. Hubbard 439 *TN D-450*
29. Some Landing Studies Pertinent to Glider-Reentry Vehicles . . . by John C. Houbolt and Sidney A. Batterson 453 *TN D-448*

~~CONFIDENTIAL~~

TN D-483	30. Landing Energy Dissipation for Manned Reentry Vehicles . . . by Lloyd J. Fisher, Jr.	475
	31. Structures for Reentry Heating . . . by Roger A. Anderson and Robert T. Swann . T.M. X-3/3	491
	32. Ablation for Manned Reentry Vehicles . . . by Leonard Roberts	511
	33. Ablative Properties of Materials . . . by Raymond C. Savin and Hermilo Gloria	529
	34. A Method of Correlating Ablating Materials . . . by Bernard Rashis and Andrew J. Chapman III	537
TN X-312	35. Research on Radiation Heat Shields for Bodies and Leading Edges . . . by Melvin S. Anderson, Donald H. Trussell, and C. W. Stroud	549
	36. Materials for Application to Manned Reentry Vehicles . . . by Eldon E. Mathauser	559
	37. Experimental Study of a Hot Structure for a Reentry Vehicle . . . by Richard A. Pride, Dick M. Royster, and Bobbie F. Helms . T.M. X-3/4	571
	38. Structural Considerations of Inflatable Reentry Vehicles . . . by Robert W. Leonard, George W. Brooks, and Harvey G. McComb, Jr. T.N. D-487	583

~~CONFIDENTIAL~~



INTRODUCTION

This document is Part I of a compilation of papers presented at a USAF/NASA Conference on Lifting Manned Hypervelocity and Reentry Vehicles held at the Langley Research Center on April 11-14, 1960. This conference was held jointly by the U.S. Air Force and the National Aeronautics and Space Administration to provide industry and government agencies the most recent results of research and development activities relating to manned hypervelocity and reentry vehicles which have lifting capability and ability to maneuver in the atmosphere. The papers were presented by the Air Force, NASA, and the Dyna-Soar contractor, Boeing Airplane Company.

1

2

3

4

5

LIST OF CONFEREES

The following were registered at the Joint Conference on Lifting Manned Hypervelocity and Reentry Vehicles, Langley Field, Virginia, April 11-12, 1960.

ABBEY, Capt. George W.	Wright Air Development Div.
ABBOTT, Ira H.	NASA - Headquarters
ABRAHAMS, Robert P.	Kearfott Co., Inc.
AIKEN, William S., Jr.	Office of Commander of Tactical Air Command
ALBERI, Americo	Republic Aviation Corp.
ALDERSON, Ross C.	Minneapolis-Honeywell Regulator Co.
ALEXANDER, Grover L.	Wright Air Development Div.
ALLEN, William	NASA - Headquarters
ANDERSON, Harvey L.	Wright Air Development Div.
ANDERSON, Melvin S.	NASA - Langley Research Center
ANDERSON, Roger A.	NASA - Langley Research Center
ARCIDIACONO, Thomas	Fairchild Engine and Airplane Corp.
ARMSTRONG, William O.	NASA - Langley Research Center
ATWELL, Col. Lawrence A.	Office of Director of Personnel Procurement and Training
BADERTSCHER, Robert F.	Battelle Memorial Institute
BADGER, Frank S., Jr.	Haynes Stellite Co.
BAILEY, Capt. Cecil	ARDC, Liaison Office, Langley Field
BAILEY, Harry E.	NASA - Ames Research Center
BAKER, Thomas F.	NASA - Flight Research Center
BAKER, William W.	Wright Air Development Div.
BATTERSON, Sidney A.	NASA - Langley Research Center
BEALS, Vaughn L.	North American Aviation, Inc.
BEAVER, Wallace W.	The Brush Beryllium Co.
BECKER, John V.	NASA - Langley Research Center
BECKWITH, Ivan E.	NASA - Langley Research Center
BELL, Marion W. J.	North American Aviation, Inc.
BELSLEY, Steven E.	NASA - Ames Research Center
BENDER, Eugene H.	Office of Defense, Research and Engineering
BERESFORD, Thomas E.	Northrop Corp., Radioplane Div.
BERLOT, Robert R.	G. M. Giannini and Co., Inc.
BERTRAM, Mitchel H.	NASA - Langley Research Center
BICKNELL, Prof. Joseph	Massachusetts Institute of Technology
BIKLE, Paul F.	NASA - Flight Research Center
BIRD, King D.	Cornell Aeronautical Laboratory

BLAND, William M.
BOBCO, Richard P.
BOGLE, Robert W.
BOND, Aleck C.
BOOTH, Lt. Col. Raymond W. W.

BOUSHEY, Brig. Gen. H. A.

BOYKIN, James A., Jr.
BRAITHWAITE, W. M.
BRAUN, Gerhard W.
BRAUN, Max Thomas
BRAY, Richard S.
BREBNER, George G.
BREUHAUS, Waldemar O.
BRIDGE, Charles S.
BRODSKY, Robert F.
BROOKS, George W.
BROWN, Clinton E.
BUELL, Donald
BUNN, Lloyd T.
BUSEMANN, Dr. Adolf

CAMPBELL, Robert Leon
CAMPBELL, William F.
CANGELOSI, John I.
CARR, Robert E.
CARTER, Cecil V.
CARTER, James W.
CHAMBERLIN, James A.
CHAPIN, William T.
CHAPLICK, Robert G.
CHAPMAN, Andrew J. III
CHAPMAN, Philip W.
CHARAK, Mason T.
CHILDERS, Milford G.
CLAIR, Jack E.

CLARK, Charles C.
CLOSE, Robert R.
CLOSE, William H.
COHEN, Nathaniel B.
COLEMAN, John R.
COMPTON, William A.
CONCHA, Joseph I.
COOLEY, Dale E.

NASA - Space Task Group
Northrop Corp., Nortronics Div.
Curtiss-Wright Corp.
NASA - Space Task Group
Office of the Director of Research
and Development, DCS/Development
Asst. for Advanced Technology,
DCS/Development
Wright Air Development Div.
NASA - Lewis Research Center
Air Force Missile Development Center
Boeing Airplane Co.
NASA - Ames Research Center
British Joint Services Mission
Cornell Aeronautical Laboratory
Litton Industries
Aerojet-General Corp.
NASA - Langley Research Center
NASA - Langley Research Center
NASA - Ames Research Center
E. I. du Pont de Nemours & Co., Inc.
NASA - Langley Research Center

Boeing Airplane Co.
Canadian Joint Staff
Republic Aviation Corp.
North American Aviation, Inc.
Chance Vought Aircraft, Inc.
Redstone Arsenal
NASA - Space Task Group
General Electric Co.
NASA - Goddard Space Flight Center
NASA - Langley Research Center
American Bosch Arma Corp.
NASA - Headquarters
Lockheed Aircraft Corp.
Ford Instrument Co., Div. of Sperry-
Rand Corp.
International Nickel Co., Inc.
Bendix Aviation Corp.
NASA - Langley Research Center
NASA - Langley Research Center
Northrop Corp., Radioplane Div.
Solar Aircraft Co.
Air Technical Intelligence Center
Wright Air Development Div.

CORNOG, Robert
COUGHLIN, Kenneth J.
CRAMER, Granville R.
CREEL, R. L.
CREER, Brent Y.
CRONVICH, Lester L.
CROWELL, William E.
CZARNECKI, Edwin Gregory

DACEY, Leonard N.
DAGGITT, Maj. William E.

DAHM, Werner K.
DAIGLE, Furnand F.
DAUM, Fred L.
DAVIS, Maj. Gen. Leighton
DAVIS, Dr. Thomas
DAVISON, Gordon N.
DEGEN, Max
DE LONG, William B.
DIEDERICH, Franklin W.
DIGGES, Kennerley H.
DOBRZANSKI, Janusz S.
DOMIZI, Dario
DONELY, Philip
DONLAN, Charles J.
DONNELL, William F.
DUNNEN, Earl Martin
DOUGLASS, William M.
DRAKE, Hubert M.
DRALEY, Eugene C.
DRATCH, Joseph E.
DUNAVANT, James C.
DUNCAN, Lt. Comdr. Robert C.

EAKINS, Lt. Col. William W.
EDWARDS, George G.
EGGLESTON, John M.
ELLIS, Macon C.
ERICKSON, Myles D.
EVANS, A. J.
EVANS, Porter H., Jr.
EVANS, William
EVANS, William L.
EZRA, Arthur A. H.

Ramo-Wooldridge
The Martin Co.
Thiokol Chemical Corp.
Bureau of Naval Weapons
NASA - Ames Research Center
Applied Physics Laboratory - J. H. U.
Cornell Aeronautical Laboratory
Boeing Airplane Co.

Operations Analysis Office (AFCOA)
Director of Operational Requirements,
DCS/Operations
Redstone Arsenal
Radio Corp. of America
Wright Air Development Div.
AFDDC, The Pentagon
Analytic Services, Inc.
Boeing Airplane Co.
The Raytheon Co.
E. I. du Pont de Nemours & Co., Inc.
Avco Manufacturing Corp.
Wright Air Development Div.
Hughes Aircraft Co.
National Carbon Co.
NASA - Langley Research Center
NASA - Space Task Group
Texas Instruments, Inc.
Boeing Airplane Co.
Douglas Aircraft Co., Inc.
NASA - Flight Research Center
NASA - Langley Research Center
Avco Manufacturing Corp.
NASA - Langley Research Center
Office of Chief of Naval Operations

AF Cambridge Research Center
NASA - Ames Research Center
NASA - Langley Research Center
NASA - Langley Research Center
NASA - Ames Research Center
NASA - Headquarters
Walter Kidde & Co., Inc.
Republic Aviation Corp.
Convair
The Martin Co.

FAGET, Maxime A.
FALK, James B.
FEDZIUK, Henry A.
FEIGEN, Morris
FELLER, William V.
FELT, Morris E., Jr.
FERER, Lt. Col. Benjamin H.

FIKES, Joseph E.
FINK, Martin R.
FINSTON, Prof. Morton
FLATHERS, Arthur E.
FLATZ, John S.
FLYNN, Warren A.
FOWELL, Leonard R.
FORREST, Clarence
FOWLER, Robert M.

FOWLER, Roy G.
FRANK, Robert G.
FRIEDLANDER, A. F.
FRIEND, Carl F.
FULLING, Roger W.

GARRICK, I. E.
GAY, Lt. Clarence C., Jr.
GESSOW, Alfred
GIESEMAN, Maj. Earl R., Jr.

GILDEA, David J.
GILKEY, Kenneth J.
GILMER, William N.
GILRUTH, Robert R.
GLODECK, Edward
GLOVER, Col. Walter P.
GOETT, Harry J.
GOLDBAUM, George C.
GOLDIE, John Harrison
GOODWIN, Glen
GORANSON, R. Fabian
GOTTSCHALL, Richard C.
GRANT, Frederick C.
GREENE, Lawrence P.
GREGORY, Lt. Phillip C.
GRIERSON, Lt. Col. Walter H.
GRIMES, David L.

NASA - Space Task Group
McDonnell Aircraft Corp.
NASA - Langley Research Center
Space Technology Laboratories, Inc.
NASA - Langley Research Center
The Martin Co.
Asst. for Advanced Technology,
DCS/Development
Army Ordnance Missile Command
United Aircraft Corp.
Massachusetts Institute of Technology
General Electric Co.
Wright Air Development Div.
Temco Aircraft Corp.
Northrop Corp., Norair Div.
Bell Aircraft Corp.
Metals Research Laboratory, Union
Carbide Metals Co.
Convair
General Electric Co.
NASA - Lewis Research Center
Ryan Aeronautical Co.
E. I. du Pont de Nemours & Co., Inc.

NASA - Langley Research Center
Wright Air Development Div.
NASA - Headquarters
Office of the Director of Research
and Development, DCS/Development
North American Aviation, Inc.
Wright Air Development Div.
Experiment, Inc.
NASA - Space Task Group
Boeing Airplane Co.
Wright Air Development Div.
NASA - Goddard Space Flight Center
Douglas Aircraft Co., Inc.
Boeing Airplane Co.
NASA - Ames Research Center
NASA - Headquarters
Bendix Aviation Corp.
NASA - Langley Research Center
North American Aviation, Inc.
Wright Air Development Div.
AMC Aeronautical Systems Center
Narmco Industries, Inc.

GROSS, Stanley H.
GUY, Lawrence D.
GUYTON, Robert D.

Airborne Instrument Laboratory
NASA - Langley Research Center
Wright Air Development Div.

HAGUE, John R.
HALE, Capt. Roy E.
HALL, Edward N.
HALL, Dr. Gordon J.
HAMLIN, Benson
HAMMOCK, David M.
HANE, Lt. Col. John R.

General Electric Co.
ARDC, Andrews AFB
United Aircraft Corp.
Cornell Aeronautical Laboratory
Boeing Airplane Co.
Redstone Arsenal
Office of Director of Personnel
Procurement and Training

HANLEY, Gerald M.
HARGIS, Calvin B.
HARRIS, Ralph J.
HARRIS, T. Aubrey
HARTWIG, Frederic W.
HAVEL, Charles J.
HAYES, Lt. Thomas C.
HAYNES, Robert Miller
HEDGEPEETH, John M.
HELDENFELS, Richard R.
HELMS, Bobbie F.
HENDERSHOTT, William B.
HENDERSON, Arthur, Jr.
HENSEL, Rudolph W.
HEPLER, Andrew Karl
HERMANN, Dr. Rudolph
HERTLER, Eugene G.
HESS, George K., Jr.
HEWES, Donald E.
HIBBERT, Col. Richard B.
HILDEBRAND, Robert B.
HINDERS, Urban A.
HODGE, John M.
HOFFMAN, Dr. Horace E.
HOLLEMAN, Euclid C.
HOUBOLT, John C.
HUBBARD, Harvey H.
HUBER, Paul W.
HUFFINGTON, James E.
HUNTINGTON, Robert C.
HUNTZICKER, John H.

Convair
Wright Air Development Div.
Naval Air Material Center
NASA - Langley Research Center
Space Technology Laboratories, Inc.
Kelsey-Hayes Co.
Wright Air Development Div.
Boeing Airplane Co.
NASA - Langley Research Center
NASA - Langley Research Center
NASA - Langley Research Center
Naval Air Development Center
NASA - Langley Research Center
Arnold Engineering Development Center
Boeing Airplane Co.
Univ. of Minnesota
Chrysler Corp.
Bendix Aviation Corp.
NASA - Langley Research Center
Office of Asst. Chief of Staff, USAF
Boeing Airplane Co.
Wright Air Development Div.
U. S. Steel Corp.
Office of Chief of Naval Research
NASA - Flight Research Center
NASA - Langley Research Center
NASA - Langley Research Center
NASA - Langley Research Center
Boeing Airplane Co.
Motorola, Inc.
The RAND Corp.

INGRAM, T. Sgt. Jesse C.
ISENBERG, Dr. Joel S.

Wright Air Development Div.
Flight Science Laboratory

JACOBSEN, Charles A.
JAFJE, David
JAMES, Maj. Harold L.

JAYNES, Col. Roy A.

JOHNS, Frank R.
JOHNSON, Caldwell C., Jr.
JOHNSON, James H.
JOHNSON, J. Malcolm
JOHNSON, Joseph L., Jr.
JONES, David J., Jr.
JONES, Dewey I.
JORDAN, Gareth H.
JORDAN, Peter F.
JUNTILLA, Harry W.

KAPLAN, Abner
KAUFMAN, Capt. William C.
KEARNEY, Lt. Comdr. Stuart D.
KEHLET, Alan B.
KIRK, Robert L.
KLEINHESSELINK, Glenn J.
KLEPINGER, Richard H.
KLIMA, Otto, Jr.
KNAPP, Russell H.
KOCH, Charles J.
KOHLMASE, Charles E., Jr.
KORDES, Eldon E.
KORYCINSKI, Peter F.
KOSTOCH, Francis R.
KRUSOS, James N.
KULLAS, Albert J.

LAMAR, William E.
LAMPROS, Alexander F.
LANGE, Roy H.
LARRABEE, Prof. E. E.
LASSEN, Herbert A.
LAU, Conrad A.
LAWLER, Edward D.
LEBOVITS, Morris
LEDBETTER, Girvis Erwin
LEE, Alan Hilman
LEFLER, Emery D.
LEONARD, Robert W.

McDonnell Aircraft Corp.
American Machine and Foundry Corp.
Office of Director of Development
Planning, Strategic Air Div.
Office of Director of Systems
Management, WADD
Naval Air Development Center
NASA - Space Task Group
North American Aviation, Inc.
North American Aviation, Inc.
NASA - Langley Research Center
Convair
Wright Air Development Div.
NASA - Flight Research Center
The Martin Co.
Air Defense Command, Ent AFB

Space Technology Laboratories, Inc.
Wright Air Development Div.
Office of Chief of Naval Research
NASA - Space Task Group
Litton Industries
General Motors Corp.
Wright Air Development Div.
General Electric Co.
Boeing Airplane Co.
The Martin Co.
NASA - Jet Propulsion Laboratory
NASA - Langley Research Center
NASA - Langley Research Center
North American Aviation, Inc.
Aeronca Manufacturing Corp.
The Martin Co.

Wright Air Development Div.
Pacific Missile Range
Lockheed Aircraft Corp.
Massachusetts Institute of Technology
Space Technology Laboratories, Inc.
Chance Vought Aircraft, Inc.
Naval Air Development Center
Solar Aircraft Co.
Boeing Airplane Co.
Boeing Airplane Co.
Wright Air Development Div.
NASA - Langley Research Center

LESKO, James Stephen
LEVIN, Ellis
LEVIN, Kenneth
LEVINE, Philip
LINDLEY, Charles A.
LITTELL, Robert E.
LIU, Dr. Tung-Sheng
LOFTIN, Laurence K., Jr.
LOFTUS, Lt. Joseph P.
LOHSE, Edward
LONG, Joseph E.
LOVE, Eugene S.
LOW, George M.
LOWELL, Herman H.
LU, Hoshen R.
LUIDENS, R. W.
LUKESH, John S.
LYNCH, Robert A.
LYON, Frank J.

MAC ALLISTER, Leonard C.
MAC MORRIS, David
MADDEN, Robert T.
MARSHALL, Edmund V.
MARTIN, Richard E.
MARTZ, Ronald B.
MASON, Dr. John L.

MASON, Leroy John
MASON, Col. Regnald H.

MATHAUSER, Eldon E.
MATHEWS, Charles W.
MAYES, William H.
McCOMB, Harvey G., Jr.
McKENZIE, Lt. Col. M. A.
McLELLAN, Charles H.
McMAHON, Howard H.
MEAD, Merrill H.
MELLEN, David L.
MELNIK, R.
MERCER, Jack R.
MEYER, Rudolph
MILLER, Bernard P.
MILTON, John F.
MOORE, Col. Walter L.

Boeing Airplane Co.
Boeing Airplane Co.
Bell Aircraft Corp.
Avco Manufacturing Corp.
Marquardt Aircraft Co.
NASA - Headquarters
Wright Air Development Div.
NASA - Langley Research Center
Wright Air Development Div.
Burroughs Corp.
Office of Scientific Research, ARDC
NASA - Langley Research Center
NASA - Headquarters
NASA - Goddard Space Flight Center
Republic Aviation Corp.
NASA - Lewis Research Center
Northrop Corp., Nortronics Div.
Convair
North American Aviation, Inc.

Ballistic Research Laboratories
Sundstrand Aviation
Goodyear Aircraft Corp.
Chance Vought Aircraft, Inc.
Convair
Wright Air Development Div.
The Garrett Corp., AiResearch
Mfg. Div.
Boeing Airplane Co.
Asst. Chief of Staff for Guided
Missiles, USAF
NASA - Langley Research Center
NASA - Space Task Group
NASA - Langley Research Center
NASA - Langley Research Center
Wright Air Development Div.
NASA - Langley Research Center
Canadian Joint Staff
NASA - Ames Research Center
Minneapolis-Honeywell Regulator Co.
Grumman Aircraft Engineering Corp.
United Aircraft Corp.
Grumman Aircraft Engineering Corp.
Radio Corp. of America
Boeing Airplane Co.
Wright Air Development Div.

MORAN, William R.
MORGAN, Homer G.
MOSSMAN, Emmet A.
MULHERN, John J.
MUNTER, Paul L.
MUSE, Thomas C.

MUZZEY, Benjamin C.

NAGEL, Adelbert Leslie
NAY, Harvey O.
NELSON, Melvin A.
NELSON, R. L.
NESTINGEN, Irvin M.
NEVINS, James L.
NEWMAN, Lt. Col. J. C.
NICHOLS, Mark R.
NIELSEN, Jack N.
NING, Ted C.
NORTH, Warren J.

OCHS, Capt. Edward J., Jr.
OVERALL, John W.

PAGLIANETE, Francis J.
PARKINSON, John B.
PASCHALL, Lt. Col. Benjamin F.
PAUL, Robert H.
PAULSON, John W.
PEARSON, E. O.
PECK, Robert F.
PELLINI, William S.
PENN, Col. William W.
PENTECOST, Joseph L.
PERRINE, Calvin H., Jr.
PETERSON, Homer C.
PHILLIPS, Richard L.
PHILLIPS, Warren L.
PHILLIPS, William H.
PIERCE, Roger J.
PILAND, Robert O.
PITTMAN, W. D.
PLASCOTT, Roland H.
POSTLE, Robert
PRATT, George L.

IBM
NASA - Langley Research Center
The Martin Co.
Naval Air Development Center
Republic Aviation Corp.
Office of the Director of Defense,
Research and Engineering
Boeing Airplane Co.

Boeing Airplane Co.
Hughes Tool Co.
Boeing Airplane Co.
Lockheed Aircraft Corp.
Convair
Massachusetts Institute of Technology
AFDAP, Headquarters, USAF
NASA - Langley Research Center
VIDYA, Inc.
Wright Air Development Div.
NASA - Headquarters

Wright Air Development Div.
Lockheed Aircraft Corp.

Bureau of Naval Weapons
NASA - Langley Research Center
Wright Air Development Div.
North American Aviation, Inc.
NASA - Langley Research Center
NASA - Headquarters
General Electric Co.
Naval Research Laboratory
ARDC, Andrews AFB
Aeronca Manufacturing Corp.
The Martin Co.
M. I. T. Lincoln Laboratories
Bendix Aviation Corp.
Hughes Aircraft Co.
NASA - Langley Research Center
Collins Radio Co.
NASA - Space Task Group
McDonnell Aircraft Corp.
British Joint Services Mission
Bell Aircraft Corp.
Arnold Engineering Development
Center

PRESS, Harry
PRIDE, Richard A.
PURSER, Paul E.
PUTNAM, Dale W.

RABER, Christopher L.
RAINEY, A. Gerald
RAINEY, Robert W.
RARING, Richard
RASHIS, Bernard
RAYBURN, Leo
REDELSHEIMER, S. M.
REESE, Bruce A.
REESE, David E., Jr.
RELLER, John O., Jr.
RHODE, R. V.
RICHARDSON, Francis H.
RICLES, Robert
RIEDINGER, Louis A.
RITCHEY, Wallace M., Jr.
ROBERTS, Leonard
ROBINSON, Russell G.
ROCHEN, Herb
RODRIGUEZ, Edward
ROETHE, Floyd A.
ROSS, Robert S.
ROTELLI, R. L.
ROYSTER, Dick M.
RUNYAN, Harry L.
RUTH, Laverne M.

RUTKOWSKI, Joseph
RYKEN, John

SADOFF, Melvin
SAILOR, J. Douglas
SALYERS, E. L.
SANDO, Robert M.
SANDORF, Prof. Paul E.
SANIAL, Thomas
SAUER, John G.
SAVIN, Raymond C.
SCHAEFER, J. W.
SCHLIE, Lt. Col. Walter

SCHMIDT, Craig M.

NASA - Headquarters
NASA - Langley Research Center
NASA - Space Task Group
Boeing Airplane Co.

General Electric Co.
NASA - Langley Research Center
NASA - Langley Research Center
NASA - Headquarters
NASA - Langley Research Center
The Raytheon Co.
McDonnell Aircraft Corp.
Purdue Research Foundation
NASA - Ames Research Center
NASA - Ames Research Center
NASA - Headquarters
Air Force Flight Test Center
Republic Aviation Corp.
Lockheed Aircraft Corp.
Wright Air Development Div.
NASA - Langley Research Center
NASA - Ames Research Center
NASA - Headquarters
Litton Industries
Librascope, Inc.
Goodyear Aircraft Corp.
Boeing Airplane Co.
NASA - Langley Research Center
NASA - Langley Research Center
Office of Defense Research and
Engineering, Department of Defense
Bendix Aviation Corp.
Bell Aircraft Corp.

NASA - Ames Research Center
Lockheed Aircraft Corp.
McDonnell Aircraft Corp.
Westinghouse Electric Corp.
Massachusetts Institute of Technology
Grumman Aircraft Engineering Corp.
Universal-Cyclops Steel Corp.
NASA - Ames Research Center
NASA - Lewis Research Center
Office of Director of Operational
Requirements, DCS/Operations
Bell Aircraft Corp.

SCHMITT, Thomas J.
SCHNEIDER, William C.

SCHREIBER, Leonard H.
SCHUBERTH, Edward R.
SCHWICHTENBERG, Dr. A. H.

SCIDMORE, Don L.
SCOVILLE, Maj. Curtis L.
SEAGER, Donald B.
SEATON, Charles H.
SEIFF, Alvin
SHANKS, Robert E.
SHOEMAKER, John R.
SHORTAL, Joseph A.
SIVELLS, James C.
SKAVDAHL, Howard
SMITH, Charles G.
SMITH, G. Allan
SMITH, James C., Jr.
SMITH, Turner L.
SNODGRESS, Richard B.
SODERBERG, Laurence R.
SOEHNGEN, Erich E.
SOLLENBERGER, Comdr. Robert L.
SOULÉ, Hartley A.
SPIELBERG, Irving N.
SPURR, Harold G.
STAINBACK, P. Calvin
STALK, Maj. George

STALZER, Lt. Charles E.
STAUBACH, Richard L.

STEINMETZ, H. F.
STEVENS, John E.
STEVENS, Victor I., Jr.
STEWART, John D.
STITT, L. E.
STOECKER, Lawrence R.
STREETT, Capt. James K.
STROUD, C. W.
SVIMONOFF, Maj. Constantence
SWANN, Robert T.
SWOFFORD, Maj. Gen. R. P., Jr.
SYVERTSON, C. A.

Bureau of Naval Weapons
Office of Chief, Bureau of Naval
Weapons
Convair
Lockheed Aircraft Corp.
Lovelace Foundation for Medical
Education and Research
Boeing Airplane Co.
ARDC, Andrews AFB
Lockheed Aircraft Corp.
Aeronutronic Systems, Inc.
NASA - Ames Research Center
NASA - Langley Research Center
Goodyear Aircraft Corp.
NASA - Langley Research Center
Arnold Engineering Development Center
The RAND Corp.
Boeing Airplane Co.
NASA - Ames Research Center
Chrysler Corp.
Ballistic Research Laboratories
NASA - Headquarters
The Martin Co.
Wright Air Development Div.
U.S. Naval Air Test Center
NASA - Langley Research Center
Space Technology Laboratories, Inc.
British Joint Services Mission
NASA - Langley Research Center
Office of Chief, Defense Atomic
Support Agency
Pacific Missile Range
Pratt & Whitney Aircraft Div.,
United Aircraft Corp.
McDonnell Aircraft Corp.
Chance Vought Aircraft, Inc.
NASA - Ames Research Center
General Electric Co.
NASA - Lewis Research Center
Beech Aircraft Corp.
Wright Air Development Div.
NASA - Langley Research Center
Wright Air Development Div.
NASA - Langley Research Center
Air University
NASA - Ames Research Center

TEMPLE, Jack L.
THOMAS, Richard E.
THOMPSON, Floyd L.
THOMPSON, Jim Rogers
THOMPSON, Kenneth O.
THRALL, Edward W., Jr.
TOLEFSON, Harold B.
TORDA, Thor P.
TRIBBET, Louis W.

TRIMPI, Robert L.
TRUEBLOOD, Joseph R.
TRUSSELL, Donald H.
TRUSZYNSKI, Gerald M.
TUOVILA, Weimar J.
TURETZKY, Arthur A.
TUSCH, Carl W.

UIMANN, Edward
URBANIK, John

VAGLIO-LAURIN, Dr. Roberto

VALE, Robert E.
VALENTINE, H. H.
VAN BUITEN, Robert D.
VANTINE, Harry, Jr.
VAS, Prof. Erwin E.
VELTON, Edward Jon

WALDRON, Howard F.
WALKER, Harold J.
WARNER, Donald D.
WARREN, Walter
WATSON, Robert
WENTSCH, Robert E.
WERNER, Jerard Ben
WESESKY, John L.
WESTERBACK, Ivar
WHITE, John S.
WHITE, Richard P., Jr.
WICK, Bradford H.
WILBUR, Stafford W.
WILLIAMS, Harry E.
WILLIAMS, Walter C.

Boeing Airplane Co.
Ohio State Univ.
NASA - Langley Research Center
Lockheed Aircraft Corp.
Univ. of Minnesota
Douglas Aircraft Co.
NASA - Langley Research Center
Armour Research Foundation
Office of Director of Development
Planning, DCS/Development
NASA - Langley Research Center
ARDC, Andrews AFB
NASA - Langley Research Center
NASA - Flight Research Center
NASA - Langley Research Center
American Machine and Foundry Co.
ARDC, Liaison Office, Moffett Field

General Electric Co.
Republic Aviation Corp.

Polytechnic Institute of Brooklyn,
Aerodynamics Laboratory
NASA - Space Task Group
NASA - Lewis Research Center
National Academy of Sciences
Naval Air Development Center
Princeton Univ.
Convair

Canadian Joint Staff
NASA - Flight Research Center
Northrop Corp., Norair Div.
General Electric Co.
Grumman Aircraft Engineering Corp.
Ramo-Woolridge
Lockheed Aircraft Corp.
Air Force Flight Test Center
Sperry Gyroscope Co.
NASA - Ames Research Center
Cornell Aeronautical Laboratory
NASA - Ames Research Center
NASA - Headquarters
NASA - Jet Propulsion Laboratory
NASA - Space Task Group

[REDACTED]

WILLIAMS, Maj. Wayland W.
WILSON, Herbert A., Jr.
WISEMAN, Homer E.
WISNIEWSKI, R. J.
WOLKO, Howard S.
WOOD, Clotaire

Strategic Air Command, Offutt AFB
NASA - Langley Research Center
Strategic Air Command, Offutt AFB
NASA - Lewis Research Center
Office of Scientific Research, ARDC
NASA - Headquarters



MOTION AND HEATING DURING ATMOSPHERE

REENTRY OF SPACE VEHICLES

By Thomas J. Wong, Glen Goodwin, and Robert Slye
Ames Research Center


SUMMARY

The results of an analysis of the motion and heating during atmospheric reentry of manned space vehicles has shown the following:

1. Flight-corridor depths which allow reentry in a single pass decrease rapidly as the reentry speed increases if the maximum deceleration is limited to $10g$.
2. Use of aerodynamic lift can result in a three- to fivefold increase in corridor depth over that available to a ballistic vehicle for the same deceleration limits.
3. Use of aerodynamic lift to widen these reentry corridors causes a heating penalty which becomes severe for values of the lift-drag ratio greater than unity for constant lift-drag entry.
4. In the region of most intense convective heating the inviscid flow is generally in chemical equilibrium but the boundary-layer flows are out of equilibrium. Heating rates for the nonequilibrium boundary layer are generally lower than for the corresponding equilibrium case.
5. Radiative heating from the hot gas trapped between the shock wave and the body stagnation region may be as severe as the convective heating and unfortunately occurs at approximately the same time in the flight.

INTRODUCTION

Reentry into the earth's atmosphere at circular satellite speed has been studied extensively in recent years. However, as space voyages become more ambitious and atmosphere reentry is made from flights in the vicinity of the near planets or the moon, the reentry speed will be in excess of circular satellite speed. It has been found by a number of



investigators that as the reentry speeds increase, the manned vehicle must be guided through relatively narrow corridors in order to enter in a single pass or to avoid excessive deceleration and heating (refs. 1 and 2).

It is the purpose of this paper to discuss these reentry corridors, to show how they may be widened by aerodynamic forces, and to assess the heating penalties paid for this aerodynamic widening. In addition to the main objective, the various modes of aerodynamic heating to the reentry vehicle will be discussed.

SYMBOLS

A	vehicle reference area, sq ft
C_D	vehicle drag coefficient
C_{D0}	drag coefficient at zero lift
$C_{D_{MAX}}$	maximum drag coefficient
C_L	vehicle lift coefficient
$C_{L_{MAX}}$	maximum lift coefficient
C_Q	coefficient in total-heat equation
C_q	coefficient in heating-rate equation
G_{MAX}	maximum resultant deceleration, g units
g	earth's gravity acceleration, 32.2 ft/sec ²
L/D	vehicle lift-drag ratio
$(L/D)_{MAX}$	maximum vehicle lift-drag ratio
Q_s	stagnation-point heat absorbed, Btu/sq ft
\dot{q}_s	stagnation-point heating rate, Btu/(sq ft)(sec)
R	nose radius, ft

Re	Reynolds number
r_0	earth's radius, ft
S	surface area, sq ft
V_E	reentry velocity, ft/sec
\bar{V}_E	entrance velocity ratio, $\frac{V_E}{\sqrt{gr_0}}$
\bar{V}_X	exit velocity ratio or final velocity ratio in total-heat equation
W	vehicle weight, lb
Δy_p	corridor depth, miles
α	angle of attack, deg

REENTRY CORRIDORS

Figure 1 illustrates what is meant by a reentry corridor. A space vehicle approaching the earth is on a flight path which is a conic section until it encounters the earth's atmosphere, where the flight path will depart from the conic shape because of aerodynamic forces. The overshoot boundary is defined as the path at which the vehicle just encounters enough atmospheric drag to slow down sufficiently to enter in a single pass. Flight paths above this overshoot boundary result in a multiple pass reentry. The lower or undershoot boundary is determined by deceleration limits, usually taken as $10g$ for manned reentry vehicles. The corridor boundaries, however, may be further limited by heating considerations.

It is convenient to define the corridor depth as the difference in conic perigee altitude between the overshoot and the undershoot boundary. Conic perigee is the perigee the vehicle would experience in the absence of an atmosphere on the earth. For shallow reentries of the type discussed, the difference between the corridor depth defined in this way and the actual depth at the outer edge of the atmosphere is small.

Effect of Reentry Speed

The depths of these reentry corridors are functions of three parameters: $W/C_D A$, L/D , and the entrance speed. The effect of entrance speed on corridor depth is shown in figure 2.

In figure 2 is plotted the corridor depth for nonlifting vehicles in miles as a function of \bar{V}_E , the ratio of reentry speed to satellite speed. This curve was calculated by assuming a $10g$ maximum deceleration at the undershoot boundary. Note the very rapid narrowing of the corridor depth as the entrance speed increases. For example, at a speed 10 percent greater than local satellite speed the corridor depth is roughly 26 miles; at escape speed, the corridor has narrowed to 7 miles; and at an entrance speed of 1.6 times satellite speed, the corridor depth is somewhat less than 3 miles. These very narrow corridor depths, therefore, appear to place rather strenuous requirements on guidance system accuracy and any aerodynamic widening of these corridors which can be achieved should be extremely helpful.

For return trips from the vicinity of the moon the resulting reentry speed will be approximately escape speed or a speed ratio equal to $\sqrt{2}$ with respect to satellite speed. Therefore, the main part of this paper will be restricted to this reentry speed.

Effect of Deceleration Limits

The effect on the corridor depth of relaxing the restriction on maximum deceleration is shown in figure 3. On this figure is plotted corridor depth in miles as a function of the maximum deceleration in g units for a nonlifting vehicle. At the overshoot boundary the deceleration encountered for reentry is approximately $8g$ and corresponds to a zero corridor depth; as the deceleration is increased to $10g$ the corridor depth has opened up to about 7 miles. If a deceleration of $20g$ can be tolerated by the vehicle and its occupants, the corridor depth is increased to 20 miles. This curve was calculated by assuming that $W/C_D A$ of the vehicle was constant during the reentry. Substantial corridor widening can be obtained if the vehicle has a variable $W/C_D A$. For nonlifting vehicles, the flight corridor can be widened only by relaxing deceleration limits or by changing the $W/C_D A$ of the vehicle in flight.

Effect of Lift

The next point to be considered is the widening of these corridors by the use of aerodynamic lift, and this effect is shown in figure 4. Corridor depth in miles is shown as a function of the lift-drag ratio of the vehicle. The corridors shown are for reentries in which L/D is held constant at least until the flight path becomes horizontal. First, consider the lower region, which is the corridor depth for nonlifting vehicles. This corridor is the 7-mile corridor for a nonlifting vehicle experiencing a maximum deceleration of $10g$. The middle shaded region represents the corridor widening brought about by lowering of the undershoot boundary through the use of positive lift. For values of the lift-drag ratio up to approximately unity, considerable widening is evident. However, at high values of the lift-drag ratio, the increase in corridor depth becomes relatively small. High values of the lift-drag ratio are ineffective simply because the resultant deceleration has been limited to $10g$. If a higher maximum deceleration can be tolerated, the rising trend of this curve persists to higher values of the lift-drag ratio.

The corridor depth increase resulting from raising the overshoot boundary is shown by the upper shaded region. This results from using negative lifts to deflect the vehicle flight path downward into the denser atmosphere so that sufficient drag can be encountered to permit entry in a single pass. Note that the use of negative lift to raise the overshoot boundary is not as effective as was the use of positive lift to lower the undershoot boundary. This results from the exponential nature of the atmospheric density variation with altitude. Above certain altitudes the vehicle is unable to produce sufficiently high forces to deflect its flight path. It may now be seen that the use of lift has increased these boundaries from 7 miles for the nonlifting vehicles, for the $10g$ maximum deceleration, to 37 miles at an L/D of $1/2$ and 50 miles at an L/D of unity.

For values of the lift-drag ratio greater than $1/2$, multiple-pass entry will result if this lift-drag ratio is held constant throughout the entire reentry. However, in reference 3 it is shown that the beneficial effects of high lift-drag ratio may be realized and the vehicle kept in the atmosphere if the lift is decreased after the vehicle flight path has become horizontal.

It seems, then, that the use of aerodynamic lift can considerably widen the entrance corridors. The question now raised is what penalty is paid in terms of aerodynamic heating for this beneficial effect. Before discussing the aerodynamic heating, it is of interest to review the domains of fluid mechanics wherein maximum convective heating occurs for these vehicles and to examine their flight path with the objective

of determining whether any new mode of heat transfer appears as the flight speeds are increased above satellite speed.

AERODYNAMIC HEATING IN CORRIDOR

Convective Heating

The flight paths of representative vehicles entering the earth's atmosphere at escape speed are shown in figure 5. The flight paths of three representative vehicles flying at undershoot boundary ($L/D = 1/2$), overshoot boundary ($L/D = -1/2$), and in a nonlifting 10g maximum deceleration path are shown. Examination of a large number of vehicle paths has indicated that the region of maximum convective heating lies within an altitude band of from 150,000 to 250,000 feet and over a narrow speed range. The region of maximum heating is shown by the shaded area and the characteristics of the flow in the region will now be examined. A curve representing flight at a constant Reynolds number of 10^6 based upon a 10-foot length is also shown on the chart. Flight paths above this line have Reynolds numbers of less than 10^6 , and flight paths lying below this line have Reynolds numbers greater than 10^6 .

Notice that the region of severe convective heating occurs at Reynolds numbers in the vicinity of 10^6 and, therefore, it is expected that the flow over these bodies may be laminar. Also shown in figure 5 by the horizontal line labeled "mean-free path 5/1000 foot" is the region where rarefaction effects would be expected to become appreciable. It can be seen that in the region of most intense convective heating the flow is well within the continuum regime.

It is of interest to examine the flow in the region of most intense convective heating to determine whether the flow is in chemical equilibrium and also whether any new modes of heating are present which would add to the already severe convective heating. These states of flow are shown in figure 6 in terms of altitude as a function of velocity with the region of maximum heating from the previous figure indicated as the shaded rectangle. The solid line on the upper portion of the chart divides the regions of equilibrium and nonequilibrium inviscid flow. Flight at velocities and altitudes below this line results in flows which are in chemical equilibrium at the boundary-layer edge for bodies having nose radii larger than 1 foot. It appears, therefore, that the inviscid flow will be substantially in chemical equilibrium during the regions of most intense convective heating.

The situation is somewhat different, however, with respect to the flow in the boundary layer. The state of the flow in the boundary layer

is shown by the lower solid curve. Flight at altitudes and velocities below this second curve result in flows which are in chemical equilibrium. Notice, however, that a large portion of the region of intense convective heating is in a region where the flow in the boundary layer is out of equilibrium. Admittedly, the boundary between equilibrium and nonequilibrium is broad. The line shown in figure 6 was chosen where the convective heating has been decreased 30 percent below its equilibrium value by nonequilibrium effects. Generally, nonequilibrium flows in the boundary layer tend to reduce the convective heat transfer below the equilibrium values for noncatalytic walls. This results from the fact that energy is contained within the gas which would normally be available for transfer to the body. Present estimates indicate reactions at the wall will be small, as ablation is very effective in reducing the number of atoms which diffuse to and strike the wall. In addition, walls which are kept reasonably cold in order to survive are covered with a layer of cold gas through which only a few atoms survive in their trip towards the surface of the body. Chung at Ames Research Center has recently developed theoretical methods which allow prediction of these heating rates over shaped blunt bodies for nonequilibrium flow conditions.

Radiative Heating

Also shown in figure 6 by the solid black area is the region of maximum radiative heating. This is the heating which arises from the radiation from the hot gases trapped between the bow shock wave and the body surface. In the solid black region the radiative heating is of magnitude equal to that of the convective heating. The exact magnitude depends upon the nose radius of the body and on the correctness of measured air radiation rates. The general mechanism of radiation heating will not be discussed here except to say that the radiation heating can be as important as the convective heating, and unfortunately occurs at nearly the same time in the flight.

To sum up, then, it can be seen from figure 6 that the inviscid flow over most of these reentry bodies will be in equilibrium but that the flow in the boundary layer may not be. The net result of nonequilibrium flow in a boundary layer is to reduce heat transfer to the wall for the case of an ablating wall, which appears to be the one of most practical engineering importance. Radiative heating will be severe and will occur roughly at the same time in the flight as the maximum convective heating.

Heating at Corridor Boundaries

There is a fundamental difference between the heating rates encountered during an overshoot boundary and an undershoot boundary. Typical heating rates for a vehicle having a lift-drag ratio of 1/2 and W/C_{DAR} of 56 are shown in figure 7. In this figure are plotted the stagnation-point heating rates as a function of time for the overshoot-boundary flight and for flight at the undershoot boundary. Notice that the heating rate has a very high maximum at the undershoot boundary. The heating rate then drops to a low value and has a second maximum which occurs as the vehicle approaches satellite speed, after which time the heating rate is fairly low. Along the overshoot boundary the heating rates are reasonably low, but persist for fairly long periods of time. Two conditions must be dealt with by the thermal protection system: high rates existing for a short time along the undershoot boundary, and low heating rates persisting for a very long time along the overshoot boundary. In other words, the thermal protection system must be able to cope with both high heating rates for short periods and low heating rates of long duration where the total amount of heat being taken aboard the vehicle becomes quite large.

It is possible to estimate these heating rates by means of the following relatively simple relations taken from reference 1. The peak value of the heating rate is

$$\dot{q}_s = \frac{19 (C_q \bar{V}_E)^2 \sqrt{\frac{W}{C_{DAR}}} \sqrt{G_{MAX}}}{[1 + (L/D)^2]^{1/4}} \quad (1)$$

The constant C_q has been determined from machine computations and has a value varying from unity to approximately 0.6, depending upon the flight path. The heat absorbed between $\bar{V}_E = 1.4$ and $\bar{V}_X = 1$ is,

$$Q_s = \frac{8,800 [1 + (L/D)^2]^{1/4} \sqrt{\frac{W}{C_{DAR}}}}{C_Q \sqrt{G_{MAX}}} \quad (2)$$

The term C_Q has also been determined from machine computations and varies from unity to about 0.8, depending upon the flight path. The lift-drag ratio, which enters into these equations directly, can be seen to reduce the heating rate, as it occurs in the denominator of the upper equation, and to increase the total heat absorbed. If the vehicle lift-drag ratio were independent of the drag coefficient, estimation of the heating rates for various vehicles under various flight

conditions would be very simple. However, these two quantities are interrelated and, in order to assess the heating penalties for widening the corridors by the use of aerodynamic lift, a family of vehicles will be considered.

To illustrate this point and to demonstrate why certain modes of operation are more desirable than others from the heating standpoint, the characteristics of a set of bodies have been determined. The assumptions and the bodies used are shown in figure 8. As shown by the plan and side elevations, the bodies considered have flat-bottom delta wings with 75° of sweep. The nose diameter was taken equal to the body thickness. The drag and lift coefficients were determined from the simple Newtonian relationships shown. The minimum value of drag coefficient C_{D_0} was assumed to be the sum of the nose drag and wing leading-edge drag. The skin-friction drag was neglected in this simplified analysis. Maximum drag coefficient was taken to be 1.7 and a vehicle weight of 6,000 pounds was assumed. Figure 9 shows the calculated W/C_{DA} as a function of the lift-drag ratio for two modes of operation: $(L/D)_{MAX}$ and C_{LMAX} . As expected, W/C_{DA} increased as the vehicle became thinner and was able to produce a higher value of the lift-drag ratio. Of course, flight at C_{LMAX} did not result in a change in W/C_{DA} .

The maximum heating rate at the undershoot boundary was calculated from equation (1) for a vehicle nose diameter equal to the body thickness. In figure 10 is shown the maximum heat-transfer rate for the stagnation region of the nose as a function of the lift-drag ratio. For vehicles operating at $(L/D)_{MAX}$, W/C_{DA} , and hence heating rate, increases with lift-drag ratio. For operation at C_{LMAX} the heating rates increase only slightly as the lift-drag ratio increases. This increase reflects the smaller nose diameter of the thinner bodies. The main point evident from this figure is that if high constant lift-drag ratio is to be used to widen the flight corridors, then high heating rates are to be expected.

The maximum heating rate at the stagnation point of a body is not the sole parameter used to judge the attractiveness of a particular design. One other quantity of interest is the total heat taken aboard as the vehicle is decelerated from escape speed to satellite speed, and this is shown in figure 11. Notice that as the lift-drag ratio increases, the total heat taken aboard the vehicle increases, and for the case of operation at $(L/D)_{MAX}$, this increase in total heat is significant. The final point of this study is to show the interdependence of these two parameters and to indicate the order of the heating penalty for widening reentry corridors.

Heating rate and heat absorbed at the stagnation point as functions of corridor depth are shown in figure 12. These quantities were obtained from equations (1) and (2). The corresponding corridor depths were taken from figure 4. The curves in this figure are for operation at $(L/D)_{MAX}$; heating rates are shown by the solid curve and total heat by the dashed curve. It can be seen that the heating rate and total heat absorbed begin to increase rather sharply above corridor depths of about 50 miles. This increase corresponds to operation at a value of $(L/D)_{MAX}$ of unity and for a constant value of the lift-drag ratio during the reentry. Operation at maximum lift coefficient, which was shown earlier not to yield severe heating penalties, is not shown in this figure because the corridor depths corresponding to this mode of operation cannot be determined from the assumption that L/D and $W/C_D A$ for the vehicle were constant during the reentry. This is the basic assumption used in this paper. However, these results as summed up in figure 12 certainly indicate that if lift-drag ratios sensibly above unity are used, a relatively large heating penalty will result.

SUMMARY OF RESULTS

The results of this analysis, which was made with the assumption that the lift-drag ratio and the vehicle $W/C_D A$ were constant during the reentry, have indicated that the corridor depths through which a vehicle must be guided to avoid excessive decelerations and still make an entry in a single pass are very narrow. It is indicated that the use of aerodynamic lift can widen these corridors three- to fivefold. In addition to the widening of the corridors a vehicle capable of producing a reasonable lift-drag ratio has the advantage of being able to produce fairly sizable amounts of lateral range. The analysis of a simple family of bodies has indicated that rather severe heating penalties are paid for corridor widening for lift-drag ratios above unity. In addition to these general conditions, a survey of the modes of heat transfer in this new regime of flight speeds and altitudes has indicated that the flow over the bodies in the inviscid region between the boundary layer and the shock wave may be expected to be in chemical equilibrium; the flow will probably be laminar over at least reasonably sized bodies. Continuum flow can also be expected. It has been determined that the flow in the boundary layer may be out of equilibrium, but the net effect of this phenomenon on the heat-transfer rate for noncatalytic walls appears to be a lessening of the severity of the heating problem. An examination of the radiant energy received by the body from the hot gases contained between the shock wave and the body surface has indicated that a new mode of heating is present here which was not present for decaying satellite or ICBM reentry. Radiant heating may be as

severe as the convective heating for large bodies and unfortunately occurs at the same time in the flight.

REFERENCES

1. Chapman, Dean R.: An Analysis of the Corridor and Guidance Requirements for Supercircular Entry Into Planetary Atmospheres. NASA TR R-55, 1960.
2. Wong, Thomas J., and Slye, Robert E.: The Effect of Lift on Corridor Width and Guidance Requirements for the Return Lunar Flight. (Prospective NASA paper.)
3. Lees, Lester, Hartwig, Frederic W., and Cohen, Clarence B.: The Use of Aerodynamic Lift During Entry Into the Earth's Atmosphere. GM-TR-0165-00519, Space Tech. Labs., Inc., Nov. 20, 1958.

STAT

CONIC PERIGEE

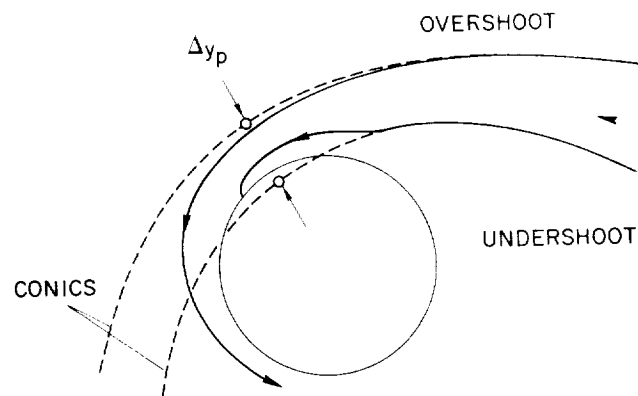


Figure 1

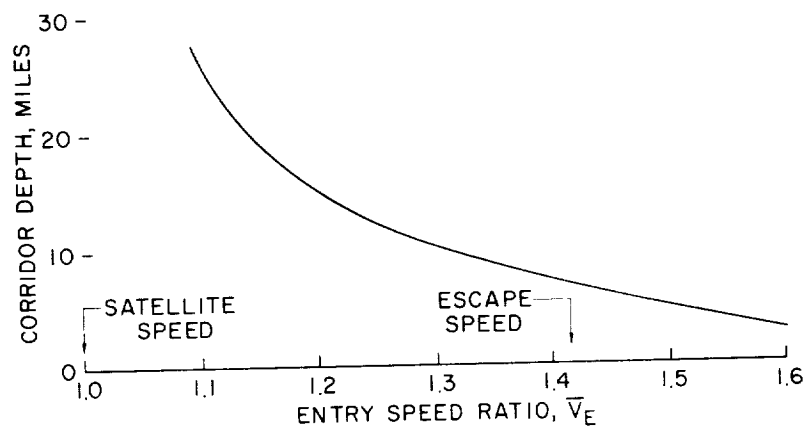
EFFECT OF ENTRY SPEED UPON CORRIDOR DEPTH
NONLIFTING VEHICLE, $G_{MAX}=10$ 

Figure 2

STAT

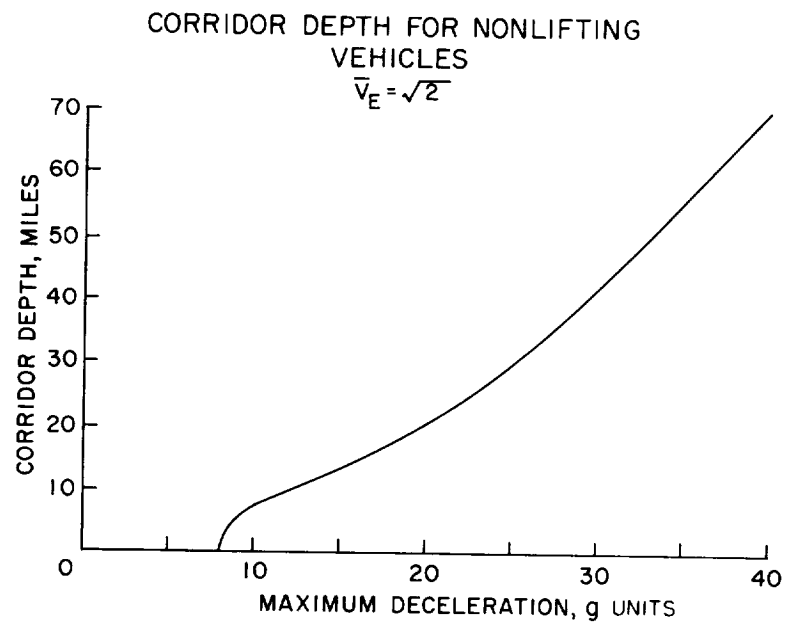


Figure 3

CORRIDOR DEPTHS FOR LIFTING VEHICLES
 $\bar{V}_E = \sqrt{2}$; $G_{MAX} = 10$

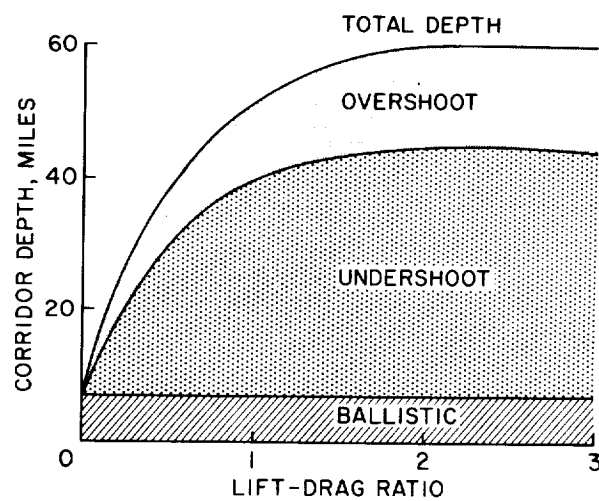


Figure 4

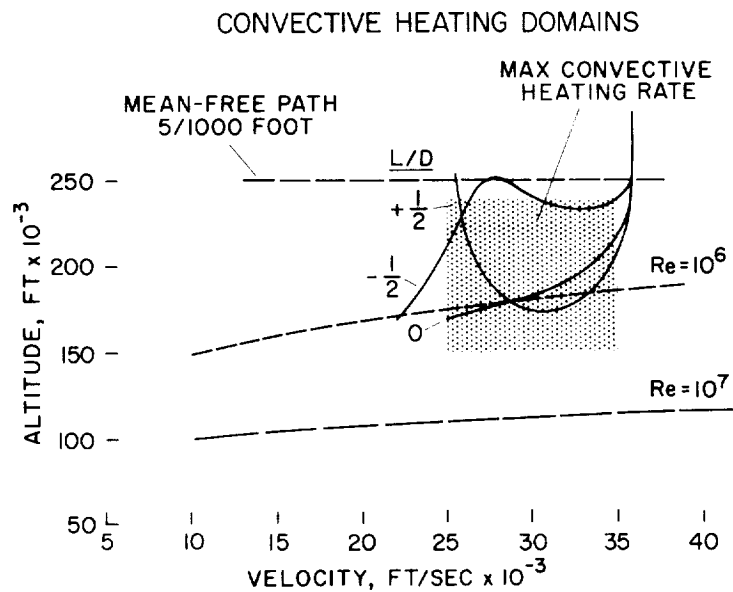


Figure 5

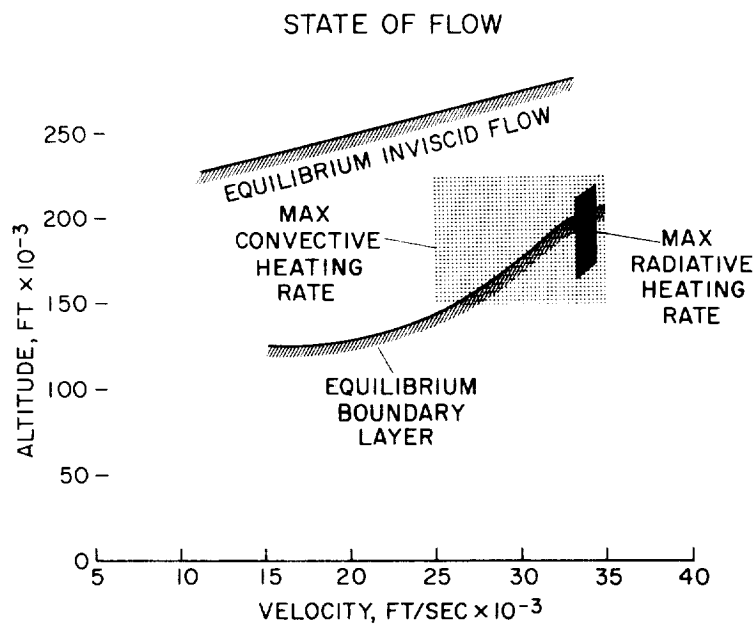


Figure 6

HEATING HISTORIES

$$L/D = \pm \frac{1}{2}, \bar{V}_E = \sqrt{2}, \frac{W}{C_D A R} = 56$$

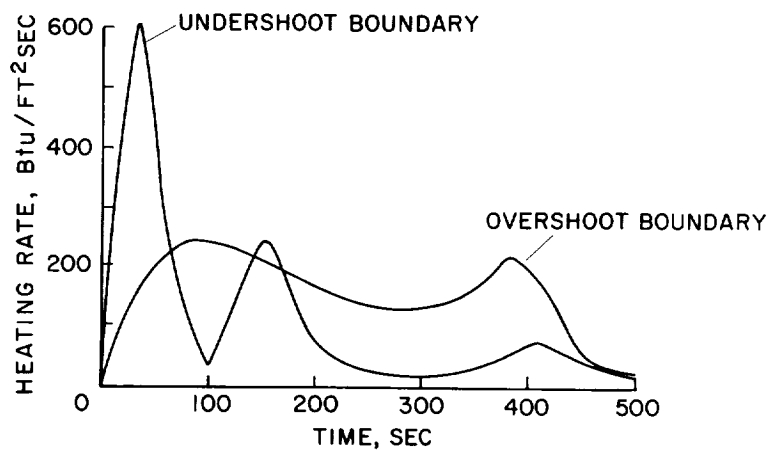
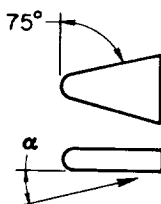


Figure 7

LIFTING BODIES USED IN ANALYSIS



$$C_D = C_{D_0} + (C_{D_{MAX}} - C_{D_0}) \sin^3 \alpha$$

$$C_L = (C_{D_{MAX}} - C_{D_0}) \sin^2 \alpha \cos \alpha$$

C_{D_0} = NOSE DRAG + LEADING EDGE DRAG

$C_{D_{MAX}} = 1.7$

$W = 6000 \text{ LB}$

$L/D = 1, 2, 3, 4$

Figure 8

VEHICLE PARAMETERS

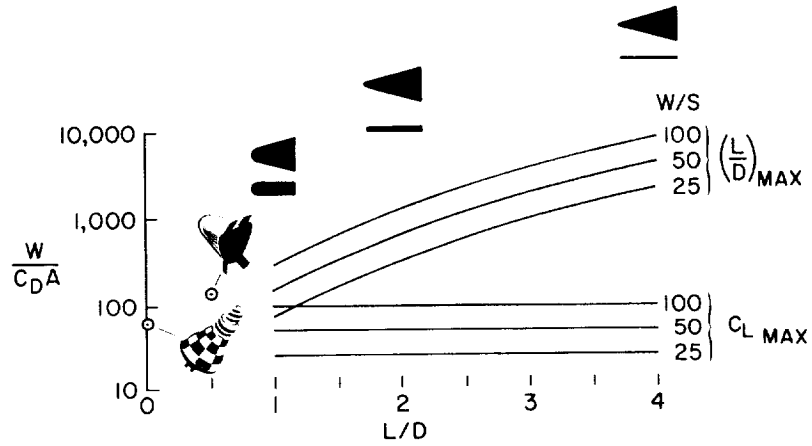


Figure 9

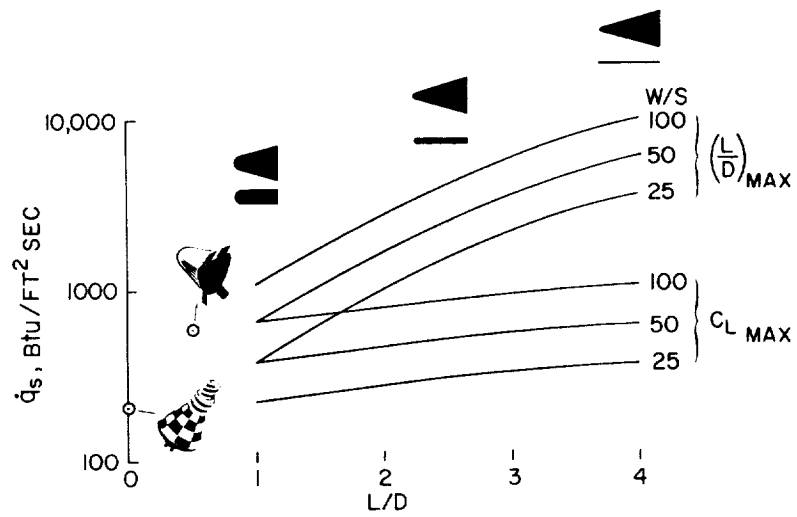
STAGNATION POINT HEATING RATE
UNDERSHOOT BOUNDARY, $G_{MAX} = 10$ 

Figure 10

HEAT ABSORBED BETWEEN ESCAPE AND
SATELLITE SPEED
UNDERSHOOT BOUNDARY, $G_{MAX}=10$

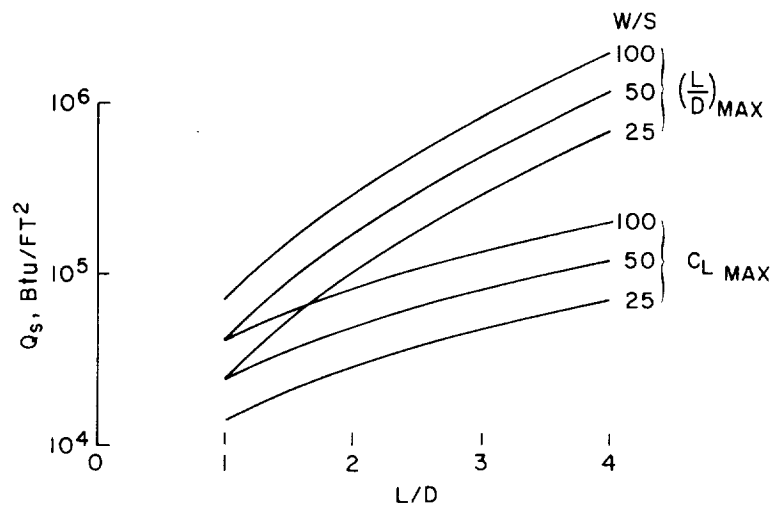


Figure 11

STAGNATION POINT HEATING
UNDERSHOOT BOUNDARY, $G_{MAX}=10$, $W/S=100$ LB

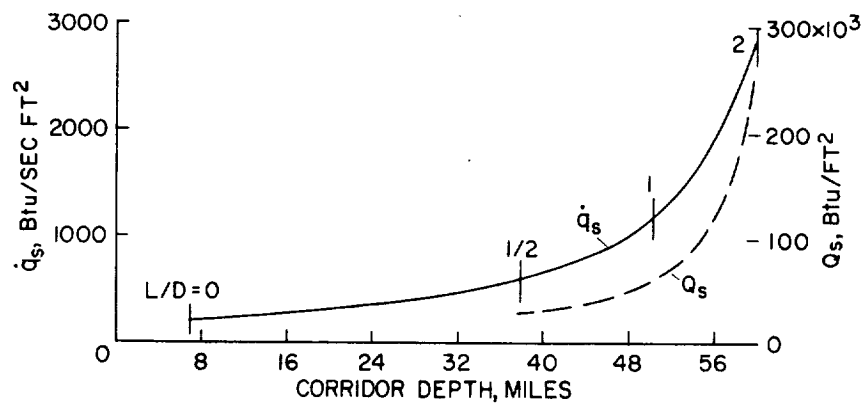


Figure 12

~~SECRET~~

~~SECRET~~

|

MODULATED ENTRY

By Frederick C. Grant
Langley Research Center

SUMMARY

The technique of modulation, or variable coefficients, is discussed and the analytical formulation is reviewed. Representative numerical results of the use of modulation are shown for the lifting and nonlifting cases. These results include the effects of modulation on peak acceleration, entry corridor, and heat absorption. Results are given for entry at satellite speed and escape speed. The indications are that coefficient modulation on a vehicle with good lifting capability offers the possibility of sizable loading reductions or, alternatively, wider corridors; thus, steep entries become practical from the loading standpoint. The amount of steepness depends on the acceptable heating penalty. The price of sizable fractions of the possible gains does not appear to be excessive.

INTRODUCTION

For low entry angles, provision of a small L/D is helpful in the reduction of peak loadings. At the higher entry angles, defined arbitrarily as those greater than 6° , even high L/D will not keep the peak loadings below some nominal limit such as $10g$. For super-circular entry a g limitation defines a corridor width. To stay within a g limit at steep entry angles, the technique of modulation, or variable coefficients, must be introduced. In this paper numerical results will be shown only for entry at satellite and escape speed; however, the indicated trends are independent of the velocity.

In entry from escape speed, as in lunar return, the ability to withstand steep entry provides a margin for error in the guidance problem; however, at satellite speeds large retro-rockets are needed to achieve steep entry angles. From a practical standpoint there are certain military purposes, emergency conditions, and abort conditions for which it is possible that steep entry will be required at satellite speeds.

SYMBOLS

C_D	drag coefficient
C_L	lift coefficient
C_R	resultant-force coefficient
D	drag
g	acceleration due to gravity
h	altitude
$K = \frac{V_0^2}{2g\beta^{-1}}$	
L	lift
Q	total heat absorbed
r_B	ballistic modulation ratio
r_L	lifting modulation ratio
r_0	radius from center of earth to atmospheric entry point
V	velocity
x	horizontal distance
α	angle of attack
β^{-1}	atmospheric scale height, $-\frac{dh}{d \log_e \rho}$
γ	flight-path angle with local horizontal, positive up
Γ	minimum acceleration index
λ	parameter (ref. 1)
ρ	air density

Subscripts:

MAX	maximum
MIN	minimum
Mod	modulated
o	initial conditions
Opt	optimum
pe	perigee
Unmod	unmodulated
1	start of modulation
2	end of modulation

A dot over a symbol indicates a derivative with respect to time.
Bar over symbol indicates values for $(L/D)_{MAX}$.

DISCUSSION

The modulation principle is illustrated in figure 1 which shows a loading history with and without modulation for a lifting vehicle. The resultant aerodynamic force in units of the vehicle weight is plotted against the corresponding times. In the upper right corner, the corresponding trajectories are sketched. For the unmodulated case, the loading rises to a sharp peak just before the bottom of the pull-up at which point the curve has been ended (corresponds to the upper trajectory in the sketch). For the modulated case, at some point in the entry the loading is not allowed to increase further and is held constant by continuous reduction of the resultant-force coefficient (corresponds to the lower trajectory in the sketch). Deeper penetrations of the atmosphere always occur in modulated pull-ups. If the proper point for start of the modulation has been selected, the vehicle will have nearly zero lift coefficient as it levels out. If the modulation is started too soon, the vehicle will not have leveled out sufficiently as the lift coefficient approaches zero. Higher loadings will be experienced subsequently than were maintained during the modulation period. For late starts of the modulation and consequent higher loading levels, the lift coefficient will not have approached zero at the bottom of the pull-up and the full capability of the vehicle will not be realized. For the

case shown, the shaded area next to the unmodulated curve may be loosely regarded as an impulse which is shifted to later times and lower loading levels for the modulated case. For precision, components of the impulse must be considered. The basic idea, however, is to replace a large force acting for a short time by a smaller force acting for a longer time to make essentially the same change in velocity. The modulation scheme indicated in figure 1 is that used in references 1 and 2.

The following simple relation governs the air loading:

$$\frac{\text{Resultant force}}{\text{Weight}} \propto C_R \rho V^2$$

As indicated in figure 1 the rise in ρV^2 during entry is combated during the modulation period by the decrease in C_R . The following two cases can be distinguished:

Ballistic:

$$C_R = C_D$$

Lifting:

$$C_R = \sqrt{C_D^2 + C_L^2}$$

In the ballistic case the drag coefficient is reduced during modulation. In the more complicated lifting case both lift and drag coefficients are changed simultaneously according to whatever functional relation exists between them.

The nature of the difference between the two cases can be visualized more concretely in terms of force polars. Force polars for the two cases are sketched in figure 2 along with the physical means necessary to attain the polars. In the ballistic case an axisymmetric vehicle is visualized as decreasing its frontal area from a large value to a small value. The corresponding polar is part of the C_D axis. In the lifting case a winged vehicle is visualized as changing attitude from an angle of attack of 90° to an angle of attack of 0° while the force coefficients trace out a loop in the C_D, C_L plane. This is the extreme range of lift modulation; the optimum range lies, as will be shown, between maximum lift coefficient and minimum drag coefficient.

In the ballistic case a geometry modulation is needed; in the lifting case an attitude modulation is needed. Other cases can be imagined in which both geometry and attitude modulation occur simultaneously and thus

trace out paths intermediate to the two shown. It can be shown (refs. 3 and 4) that the g -alleviation capability for the lifting case depends strongly on a single parameter, the maximum lift coefficient in units of the minimum drag coefficient. For the ballistic case, the alleviation depends on the ratio of maximum drag coefficient to minimum drag coefficient. (See ref. 1.) For unit minimum drag coefficient the parameters appropriate to the two cases are marked on the polars as r_B , the ballistic modulation ratio, and r_L , the lifting modulation ratio.

In the analysis of reference 2, the modulation was effectively restricted to the portion of the polar on the low-drag side of maximum lift-drag ratio (between the two lowest dots). This restriction leads to an underestimation of the possible g alleviation and an overestimation of the heat load associated with a given g level.

ANALYTICAL FORMULATION

Isolation of the two modulation parameters is made possible by the separation of the modulation problem into two limiting cases with appropriate analytic assumptions. (See fig. 3.) Formulas derived with these assumptions are presented in appendix A. In the ballistic case variations in the flight-path angle are presumed to be unimportant whereas the velocity changes are considered to be significant. In the lifting case the complementary assumptions are made; that is, changes in velocity are ignored whereas changes in flight-path angle are considered to be important. In physical terms, the assumptions correspond to separation of the two possible operations on the velocity vector, changes of magnitude and changes of direction. On course, these assumptions do not apply to the portions of the trajectories beyond peak g which are indicated in figure 3 as dashed lines.

The assumption of constant velocity in the lifting case is conservative in the sense that it leads to an underestimation of the g alleviation. Neglect of the actual velocity decrease means that in the real lifting case higher lift coefficients can be used at the same altitudes for the same loading limit. A lower loading limit than is indicated by the analysis is thus possible in the real case.

The ballistic case has been analyzed in reference 1 and the principal result is indicated in figure 4. Plotted vertically is the peak resultant force in units of the peak resultant force for no modulation. The sole parameter on which the g alleviation depends is the modulation ratio r_B , the ratio of maximum drag to minimum drag. A region of rapid initial gains is followed by one in which diminishing returns have set in. The alleviation ratio always decreases but always at a slower rate. The ballistic case is completely solved in terms of the ballistic

modulation ratio. In the lifting case, a different modulation ratio, maximum lift coefficient to minimum drag coefficient, plays the leading role.

The analysis of the lifting case (refs. 2 to 4) is complicated by the simultaneous appearance of lift and drag coefficients. The principal result of the analysis is shown in figure 5. The vehicle is presumed to enter the atmosphere at some specified lift and drag coefficients indicated as point 1 on the schematic polar at the upper left. At some point in the trajectory, shown at the right, the resultant force is held constant and the coefficients are varied through the bottom of the pull-up (point 2) and trace a portion of the drag polar from points 1 to 2. For this type of entry, the loading that is held during the modulation along arc 1,2 is found to vary inversely with a function Γ . (See fig. 5.) The integral term of this function is the more important and is a simple line integral along the polar. Since the peak loading is minimum for maximum Γ , it is of interest to know the proper choice of points 1 and 2 which yields maximum Γ for any given polar. By differentiation of the Γ function, the maximum value of Γ is found to occur for modulation between maximum lift coefficient and minimum drag coefficient.

The optimum polar with which to connect specified maximum lift and minimum drag points is indicated in figure 6 and is derived as follows: Since the endpoints are specified, it is a question of maximizing the integral term (fig. 6) of the function Γ . Since the integration is with respect to C_R , the largest possible C_L at every C_R value is required. Lines of constant C_R are circles centered on the origin, one of which is indicated in the figure. The dashed curve (fig. 6) represents a realistic polar between points 1 and 2. For maximum C_L at a given C_R , the dashed curve must be pushed as far clockwise as possible along the lines of constant C_R . This movement forces the dashed curve into coincidence with the right-angle polar between points 1 and 2 (drawn as a solid line). For the right-angle polar, Γ is a simple logarithmic function only of the ratio of maximum lift coefficient to minimum drag coefficient. The values of Γ for real polars will be somewhat less than the values for right-angle polars between the same maximum lift and minimum drag points. However, the previously mentioned conservative nature of the constant-velocity assumption leads in many cases to better loading estimates when the right-angle polar is substituted for the actual polar.

For a family of vehicles with Newtonian drag polars, the results of the lifting analysis are shown in figure 7. The base loading is, in this case, that experienced in entry at the corner of the optimum polar. (See appendix B.) Although the analysis yields results in terms of the

lift modulation parameter, in this figure the corresponding $(L/D)_{MAX}$ of the vehicle has been used. Since vehicles of increasing $(L/D)_{MAX}$ have increasing lift-modulation parameters, the trend of the curves is the same on either basis. As in the ballistic case, diminishing returns appear at the higher parameter values, but appreciable gains are evident for $(L/D)_{MAX}$ values as low as unity. The ratios plotted in figure 7 are independent of the velocity and entry angle to the order of approximation of the analysis.

NUMERICAL RESULTS

Figure 8 shows some concrete examples of the acceleration levels to be expected for steep entry at satellite speed with and without modulation. (See appendix A.) The entry-angle range is between 6° and 12° . On the left are shown the unmodulated g levels for the ballistic case, $L/D = 0$, and for a pure lifting case, $L/D = \infty$. Curves for the higher finite L/D values cluster in the neighborhood of the $L/D = \infty$ curve. With a nominal limit of $10g$ only the lifting vehicle at the low end of the range is acceptable. In the modulated case it is necessary to put limitations on the modulation capability. For example, in the ballistic case, an indefinitely large modulation capability means indefinitely low peak loadings. A vehicle which had and used such a capability would strike the earth just as if the earth had no atmosphere. Similar considerations preclude an infinite modulation ratio in the lifting case. For the ballistic case, then, a 50-to-1 drag-modulation capability was assumed as a representative high value. For the lifting case an L/D of 2 was specified as representing a high lift capability. On the basis of $10g$ being permissible, the ballistic vehicle is acceptable through most of the range and the lifting vehicle is satisfactory through the entire range. For escape speed the absolute values of the loadings are different, but the relative magnitudes are about the same.

Until now nothing has been said about the effect of modulation on entry corridor width or on the heating penalties associated with modulated entry. Figure 9 deals with these considerations. (See appendix C.) The vertical scale is Chapman's entry corridor width in miles for a $10g$ entry at escape velocity; the horizontal scale is the $(L/D)_{MAX}$ of a family of vehicles with Newtonian drag polars. Two modes of operation are indicated by solid lines: full modulation from maximum lift coefficient and no modulation from maximum lift-drag ratio. Rather spectacular gains in corridor width are evident for the higher L/D , at least in terms of the $L/D = 0$ value which is about 7 miles. Some idea of the relative heating penalties is indicated for a vehicle with the high L/D of 2.8. This represents a difficult case. Vehicles of lower $(L/D)_{MAX}$ will have easier heating problems.

Trajectories corresponding to the four modes of operation of the high L/D vehicle are indicated in figure 10. The dashed portions of the trajectories indicate the portions corresponding to the modulation period. Note that all the pull-ups are completed within a minute. The reference total heat is that absorbed down to the bottom of the pull-up for entry at maximum lift coefficient without modulation. Figure 10 shows this to be the highest altitude lowest heating pull-up and figure 9 shows it to have the narrowest corridor. Entry at $(L/D)_{MAX}$ without modulation yields a wider corridor but 2.8 times as much heat absorption. Passing to full modulation yields the widest corridor, the deepest penetration, and 6.1 times as much heat absorbed. The remaining trajectory corresponds to partial utilization of the vehicle capability. For this case more than 100 miles of corridor can be maintained for 1.7 times as much heat absorption as in the narrow-corridor low-heating pull-up at maximum lift coefficient without modulation. In terms of weight, this means about 70 percent more ablative material is required. In general, the question comes down to a trade-off between corridor width and heating penalties and can be settled only by a systems study of the mission. Since modulation from maximum lift coefficient is more favorable from both the heat absorption and loading standpoints, it is merely a question of how far to modulate.

Results for drag modulation on a ballistic vehicle are not shown in figure 9 since the gains are small. At $r_B = 21$, calculations have shown the ballistic vehicle to gain in corridor width from 7 to 30 miles while heat absorption rises about 60 percent. The unit of heat absorption is, of course, different from that used in the lifting example just discussed.

In figure 10, the peak heating rates in the pull-ups range from about 500 Btu/ft²-sec in the pull-up at $(C_L)_{MAX}$ without modulation to about 2,800 Btu/ft²-sec in the pull-up with full modulation. All the heating values shown in figures 9 and 10 refer to the stagnation point of a 1-foot-radius sphere at which point the heating rate is presumed to vary as $\rho^{1/2} V^{3.15}$.

CONCLUDING REMARKS

In conclusion, it may be said that coefficient modulation on a vehicle with good lifting capability offers the possibility of sizable loading reductions or, alternatively, wider corridors so that steep entries become practical from the loading standpoint. The amount of steepness depends on the heating penalty that is acceptable; however, the price of sizable fractions of the total possible gains does not appear to be excessive.

L
1
0
4
9

L

APPENDIX A

FORMULAS DERIVED BY USE OF ANALYTIC ASSUMPTIONS

The analytic assumptions indicated in figure 3 have allowed a number of simple peak loading formulas to be derived. These formulas are:¹

Unmodulated ballistic (ref. 5):

$$\frac{\text{Resultant force}}{\text{Weight}} = - \frac{\sin \gamma_0}{e} K$$

Unmodulated lifting (ref. 2):

$$\frac{\text{Resultant force}}{\text{Weight}} = 2(1 - \cos \gamma_0) \sqrt{1 + \left(\frac{D}{L}\right)^2} K$$

Modulated ballistic (ref. 1):

$$\frac{\text{Resultant force}}{\text{Weight}} = - \frac{\sin \gamma_0}{e} \lambda e^{1-\lambda} K$$

$$r_B = \lambda e^{\frac{1}{\lambda} - 1}$$

Modulated lifting (ref. 3):

$$\frac{\text{Resultant force}}{\text{Weight}} = \frac{2(1 - \cos \gamma_0)K}{\Gamma}$$

$$\Gamma = \sinh^{-1} r_L \quad (\text{for ideal polars})$$

(A1a)

(A1b)

The additional assumption that the net force due to gravity and coordinate acceleration is a small fraction of the aerodynamic force is implied by these formulas. Details are given in the indicated references.

¹Differences of notation from that of the references have been introduced. In the case of reference 2 a factor accounting for velocity decrement has been suppressed to conform with the constant-velocity assumption.

The quantity K is the ratio of the initial kinetic energy to that acquired in a free fall at constant g through the scale height β^{-1} ; that is,

$$K = \frac{V_0^2}{2g\beta^{-1}}$$

The formulas (A1) above have been used to plot figure 8. In figure 8 the parameter values assumed are: $V_0 = 25,900$ fps; $\beta^{-1} = 23,300$ ft; and $g = 32.2$ fps.

L
1
0
4
9

APPENDIX B

DETAILS OF CALCULATIONS OF ALLEVIATION FUNCTION

IN LIFTING CASE

For attitude modulation on a vehicle with an ideal polar (fig. 6) the minimum peak loading has been shown to be (ref. 3)

$$\left(\frac{\text{Resultant force}}{\text{Weight}} \right)_{\text{Mod}} = \frac{V_o^2}{2g\beta^{-1}} \frac{2(1 - \cos \gamma_o)}{\Gamma_{\text{Opt}}} \quad (\text{B1a})$$

where

$$\Gamma_{\text{Opt}} = \sinh^{-1} r_L \quad (\text{B1b})$$

The corresponding peak loading for entry without modulation (at the corner of the ideal polar) is (from appendix A)

$$\left(\frac{\text{Resultant force}}{\text{Weight}} \right)_{\text{Unmod}} = \frac{V_o^2}{2g\beta^{-1}} \frac{2(1 - \cos \gamma_o)}{\frac{r_L}{\sqrt{1 + r_L^2}}} \quad (\text{B2})$$

The alleviation ratio shown in figure 7 is the quotient of equations (B1) and (B2); that is,

$$\frac{\text{Modulated resultant force}}{\text{Unmodulated resultant force}} = \frac{r_L}{\sqrt{1 + r_L^2} \sinh^{-1} r_L} \quad (\text{B3})$$

The Newtonian drag polars of reference 6 have been used to provide the relation between r_L and $(L/D)_{\text{MAX}}$ which is implicit in figure 7. These polars may be written in the form

$$\left. \begin{aligned} C_L &= C_{D\text{MAX}} \left(1 - \frac{1}{r_B} \right) \sin^2 \alpha \cos \alpha \\ C_D &= C_{D\text{MAX}} \left[\frac{1}{r_B} + \left(1 - \frac{1}{r_B} \right) \sin^3 \alpha \right] \end{aligned} \right\} \quad (\text{B4a})$$

The angle for maximum lift coefficient is $\tan^{-1}\sqrt{2}$ and that for maximum lift-drag ratio $\bar{\alpha}$ is defined by the relation

$$\left(\frac{L}{D}\right)_{\text{MAX}} = \frac{1 + 3 \cos 2\bar{\alpha}}{3 \sin 2\bar{\alpha}} \quad (\text{B4b})$$

The corresponding ratio r_B of maximum drag to minimum drag on the polar is found from the relation

$$\frac{2}{r_B - 1} = \frac{3 \sin \bar{\alpha} - \sin 3\bar{\alpha}}{1 + 3 \cos 2\bar{\alpha}} \quad (\text{B4c})$$

The relation between r_B and r_L for the polars (B4a) is

$$r_L = \frac{2\sqrt{3}}{9}(r_B - 1) \quad (\text{B4d})$$

Eliminating r_B between equations (B4c) and (B4d) yields r_L as a function of $\bar{\alpha}$ and hence through equation (B4b), of $(L/D)_{\text{MAX}}$.

Although figure 7 shows a correct trend, proper use of the numerical values requires that the basis of the figure be clearly understood. The Γ values used in figure 7 are those corresponding to optimum polars between the maximum lift and minimum drag points of the polars given in eq. (B4a). Also, the unmodulated peak loading (the unit loading) is that experienced in an entry for which $L/D = r_L$. Thus, at the higher L/D values, the reference loading is essentially that experienced without modulation at infinite L/D . The ratios of figure 7 can be scaled to whatever values of Γ and $\left(\frac{\text{Resultant force}}{\text{Weight}}\right)_{\text{Unmod}}$ are appropriate by the relations

$$\left. \begin{aligned} \left(\frac{\text{Resultant force}}{\text{Weight}}\right)_{\text{Mod}} &\propto \frac{1}{\Gamma} \\ \left(\frac{\text{Resultant force}}{\text{Weight}}\right)_{\text{Unmod}} &\propto \sqrt{1 + \left(\frac{D}{L}\right)^2} \end{aligned} \right\} \quad (\text{B5})$$

APPENDIX C

DETAILS OF CALCULATIONS OF CORRIDOR WIDTH

The curves and points of figure 9 correspond either to numerical integrations or to formulas such as those used to construct figure 8. To avoid confusion, the construction of figure 9 requires explanation.

The conic perigee point for the undershoot boundary was determined in all cases by the relation:

$$(r_o - r_{pe})_{undershoot} = r_o \sin^2(\gamma_o)_{MAX} \quad (C1)$$

which holds for parabolic orbits. The values of $(\gamma_o)_{MAX}$ corresponding to a given load limit (log in fig. 9) were determined either by the formulas of appendix A or by numerical integrations.

The overshoot boundary was defined as the altitude at which C_{LMAX} in inverted flight yields 1 g unit of aerodynamic lift. This definition is consistent with the assumption of constant velocity. The actual overshoot boundary is somewhat higher.

The values of stagnation-point relative heat shown in figure 9 and the corresponding corridor widths were all obtained by numerical integration in the ARDC atmosphere (ref. 7) for the $L/D = 2.8$ vehicle of references 3 and 4. For this vehicle $(r_o - r_{pe})_{overshoot} \approx (0.10)10^6$ feet. The initial conditions were $V_o = 36,500$ feet per second at $h_o = 350,000$ feet. The curve marked unmodulated was faired to agree with the machine computations for this vehicle. Results from references 6 and 8 lie slightly below this curve. The trajectories of figure 10 were obtained in the same numerical integration which yielded the heating values.

The curve marked "full modulation" is based on the alleviation function indicated in figure 7 and explained in appendix B.

REFERENCES

1. Phillips, Richard L., and Cohen, Clarence B.: Use of Drag Modulation to Reduce Deceleration Loads During Atmospheric Entry. ARS Jour., vol. 29, no. 6, June 1959, pp. 414-422.
2. Lees, Lester, Hartwig, Frederic W., and Cohen, Clarence B.: The Use of Aerodynamic Lift During Entry Into the Earth's Atmosphere. GM-TR-0165-00519, Space Tech. Labs., Inc., Nov. 20, 1958.
3. Grant, Frederick C.: Importance of the Variation of Drag With Lift in Minimization of Satellite Entry Acceleration. NASA TN D-120, 1959.
4. Grant, Frederick C.: Analysis of Low-Acceleration Lifting Entry From Escape Speed. NASA TN D-249, 1960.
5. Allen, H. Julian, and Eggers, A. J., Jr.: A Study of the Motion and Aerodynamic Heating of Ballistic Missiles Entering the Earth's Atmosphere at High Supersonic Speeds. NACA Rep. 1381, 1958. (Supersedes NACA TN 4047.)
6. Chapman, Dean R.: An Analysis of the Corridor and Guidance Requirements for Supercircular Entry Into Planetary Atmospheres. NASA TR R-55, 1959.
7. Minzner, R. A., and Ripley, W. S.: The ARDC Model Atmosphere, 1956. Air Force Surveys in Geophysics No. 86 (AFCRC TN-56-204), Geophysics Res. Dir., AF Cambridge Res. Center (Bedford, Mass.), Dec. 1956. (Available as ASTIA Doc. 110233.)
8. Chapman, Dean R.: An Approximate Analytical Method for Studying Entry Into Planetary Atmospheres. NACA TN 4276, 1958.

MODULATION PRINCIPLE

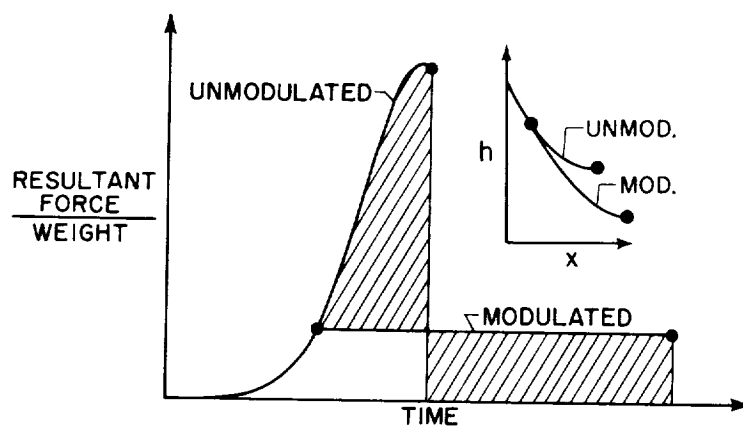


Figure 1

GEOMETRY AND ATTITUDE MODULATION

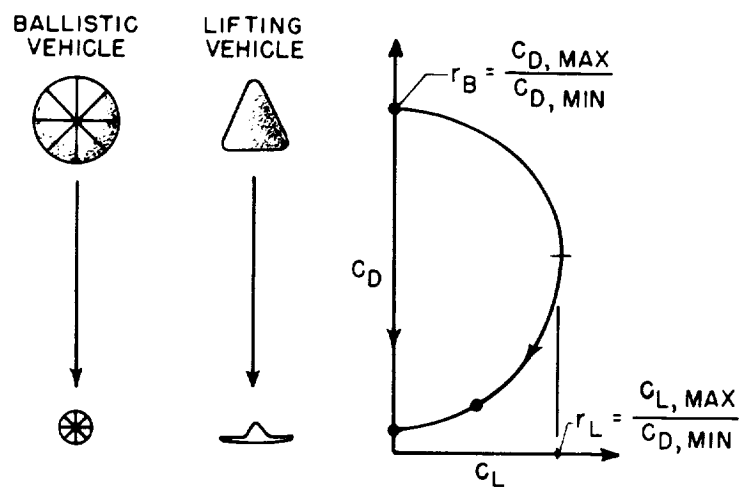


Figure 2

ANALYTIC ASSUMPTIONS

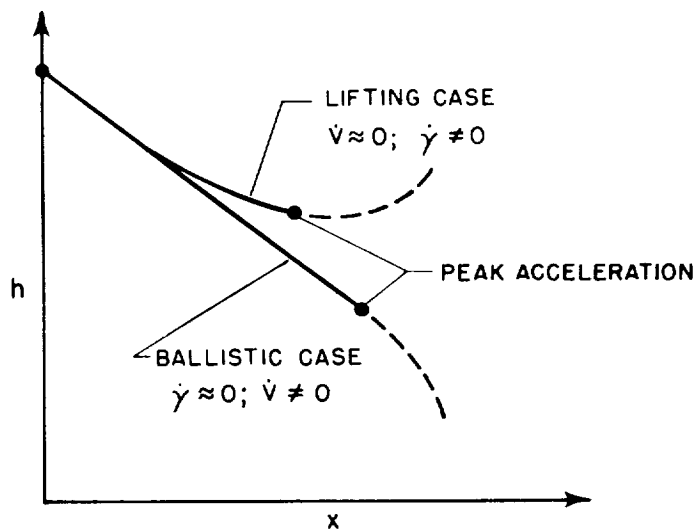


Figure 3

BALLISTIC-CASE GEOMETRY MODULATION

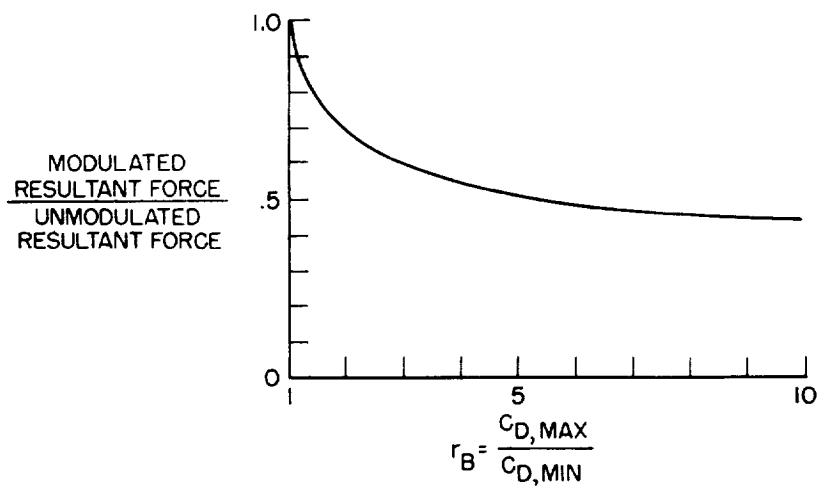


Figure 4

LIFTING-CASE ANALYTICAL RESULTS

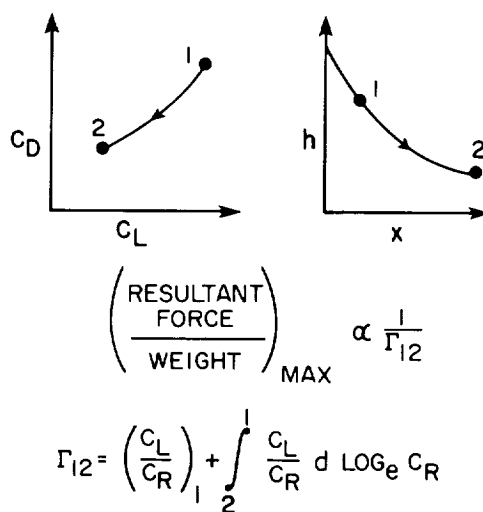


Figure 5

LIFTING-CASE OPTIMUM POLAR

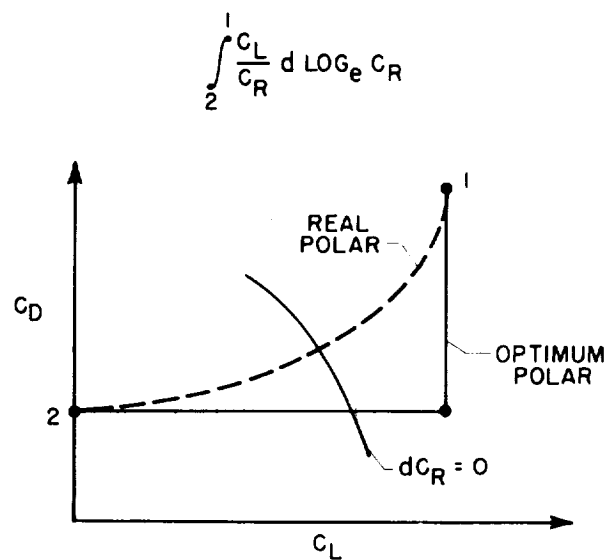


Figure 6

LIFTING-CASE ATTITUDE MODULATION

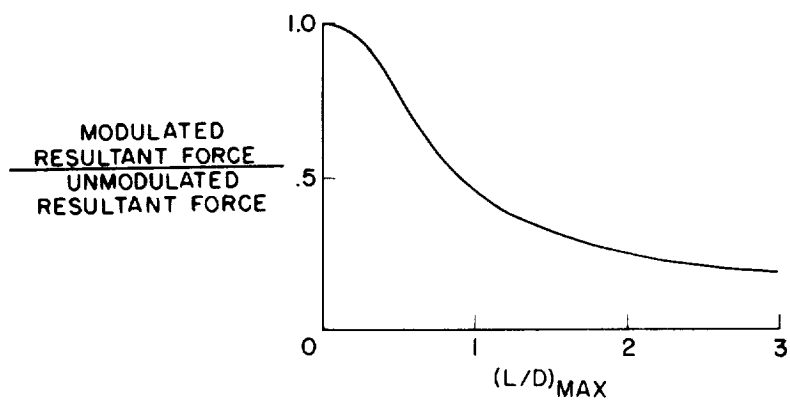


Figure 7

PEAK ACCELERATIONS

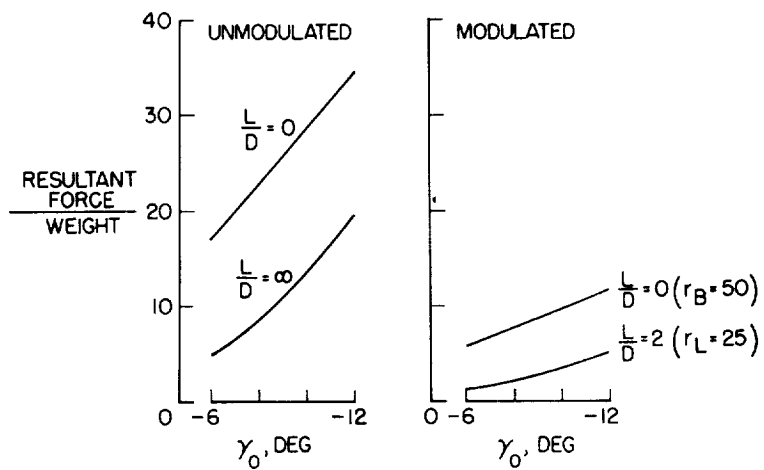


Figure 8

EFFECT OF MODULATION ON CORRIDOR WIDTH

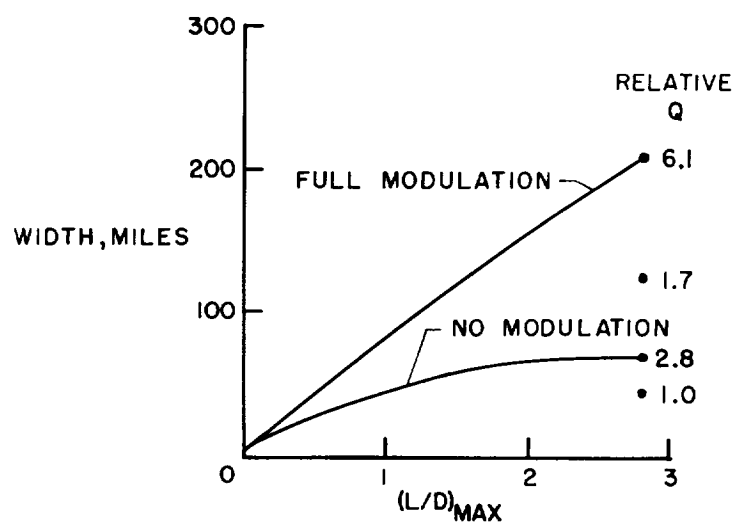


Figure 9

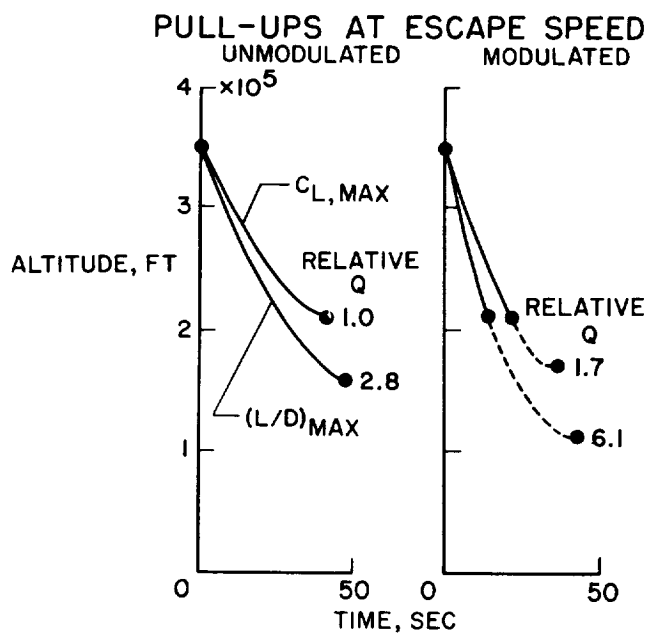


Figure 10

•

•

•

•

•

•

•

•

•

•

•

INTRODUCTORY CONSIDERATIONS OF MANNED REENTRY

ORBITAL VEHICLES

By Eugene S. Love
Langley Research Center

3

INTRODUCTION

Most of the papers to be presented in this and the next few sessions of the conference will treat either specific problem areas of manned reentry vehicles or problems peculiar to specific vehicle types. Prior to this focusing of attention, this paper will review broadly some of the characteristics and operational features of these vehicles with the thought that such a review may be helpful in maintaining a better perspective of the interplay of problems and capabilities. In the course of this review, some of the problem areas that will be dealt with in subsequent papers will be pointed out.

SYMBOLS

W	gross weight
S	planform area for lifting vehicles, frontal area for ballistic vehicles
L/D	ratio of lift to drag
T_w	temperature of wall
C_L	lift coefficient
γ	entry angle
Q_0	heat load for $L/D = 0$ and $\gamma = 0$
Q	heat load
\bar{R}_{lat}	ratio of maximum lateral range at \bar{V}_0 to maximum lateral range at $\bar{V}_0 = 0.927$

CONFIDENTIAL

G deceleration referenced to gravitational acceleration
 ϕ bank angle
 \bar{V}_0 ratio of velocity at start of turn to satellite velocity
 x_0, y_0 dimensions of accessible landing area for $\gamma \approx 0^\circ$
 x, y dimensions of accessible landing area for $\gamma > 0^\circ$
Subscript:
max maximum value

DISCUSSION

At the outset it is sobering to look at the wide range of shapes, sizes, lift-drag ratios, and other items that are encompassed by currently proposed reentry vehicles. The variety of these configurations is illustrated in figure 1, where several vehicle types are sketched and oriented about the figure so as to define in a general way their wing-loading and maximum lift-drag ratios at hypersonic speeds. These vehicles may be divided into two classes: those that land horizontally - on the right, and those that land vertically - on the left. As an aid in the discussions that follow, a brief description of these vehicles will be given first, along with a few particulars of operation. Unless otherwise specified, the case of fixed L/D and small entry angle is inferred.

At the lower left in figure 1 for zero lift-drag ratio is shown a vehicle of the Mercury capsule type. It has a face-loading of about 75 lb/sq ft. Maximum equilibrium face temperatures are near 3,100° F, but the configuration has an ablating shield, which maintains a considerably lower temperature through a combined ablating and charring process that will be discussed in a subsequent paper.

If some lifting capability is given to the rigid ballistic capsule type, there evolves the lifting capsule or lifting body with an associated decrease in face or wing loading. Some lifting-body types with low L/D are illustrated near $(L/D)_{\max}$ of 0.5 and wing loadings of the order of 55 or 60 lb/sq ft. Maximum equilibrium temperatures not far removed from the nose of such vehicles would range around 3,300° F, for which a combination of absorption and radiation is indicated as a possible solution to the heating problem. It should be noted here that

CONFIDENTIAL

the temperatures that are quoted for the lifting vehicles are representative of those experienced in middle-of-the-corridor reentry. Both round- and flat-bottom versions of the low L/D lifting body are shown; each has merits; and with regard to shape and other aspects, at least two of the papers to be presented subsequently will be devoted primarily to lifting-body types. In this connection the lifting-body types may be considered to encompass the lower central portion of the figure up to values of $(L/D)_{\max}$ near 1.5. Note that with increasing $(L/D)_{\max}$ the shape change is basically that of enlarging and slenderizing the vehicle so that the vehicle becomes more wing-like. If wing loadings near 50 lb/sq ft or so are desired, and at the same time the lifting-body concept is carried to higher $(L/D)_{\max}$, the vehicle contains more volume than is needed for a given payload, at the expense of size and weight; this trend begins to show up near $(L/D)_{\max}$ of 1.5. The result is that in arriving at vehicles having $(L/D)_{\max}$ of the order of 2 or greater and wing loadings of the order of 30, the vehicles tend to be similar whether the approach comes from the direction of the low L/D lifting bodies or from the direction of high L/D wing-body combinations. A representative vehicle in this category is shown at the right. Leading-edge temperatures range around 2,500° F for this vehicle and can be handled through radiation. A combination of radiation and absorption could be used for the high L/D lifting-body type, which has temperatures near 3,100° F some distance from the nose.

Next, consider some lightly loaded types shown at the top of figure 1. At the top left with a face-loading near 1.5 lb/sq ft is depicted a vehicle of the variable-drag type originally proposed by Allen and Eggers of the Ames Research Center as a means for controlling deceleration and trajectory. The particular vehicle shown here is patterned after the AVCO design and consists of a basic capsule and drag brake - shown open in this sketch - that is capable of achieving about 20 to 1 drag variation. The drag brake is a lightweight, foldable structure having an umbrella-like design. The vehicle is radiation cooled, and temperatures on the foldable structure would not exceed about 1,200° F.

At the top right is shown a lifting vehicle also with wing loading of about 1.5 lb/sq ft. The vehicle shown is of the inflatable type and is characterized by its thick wing and blimp-like features with the capsule almost entirely buried within the thick wing. There are several lightly loaded lifting vehicle schemes that differ markedly in design; however, since most of these have similar wing loadings and values of $(L/D)_{\max}$ near 1 as shown for this configuration, they are regarded herein as constituting a single class. A paper on these vehicles is included in this volume. This class of vehicles experience leading-edge temperatures near 1,500° F and will handle their heating problems primarily

through radiation. These vehicles as well as the variable-drag vehicle rely on the perfection of lightweight materials and coverings. High temperature membranous materials and impregnated metallic cloth appear to offer solutions. A subsequent discussion will be devoted to the structural aspects of such materials.

From these brief descriptions of the vehicles, the landing characteristics are, for the most part, obvious but will be amplified briefly. The lightly loaded variable-drag type uses no parachute and impacts at a velocity of about 50 fps. To lessen this jolt, the use of crushable and shock-absorbing structure is envisioned; this approach is also involved in the landing of the Mercury capsule and the low L/D lifting bodies, but these vehicles use parachutes as well, so that their impact velocities are reduced to about 30 fps. A subsequent paper will treat some aspects of shock-absorbing structures.

The two vehicles shown in figure 1 at the far right (ordinate center) will land conventionally on landing gear or skids. The lightly loaded lifting vehicles have no special gear, and with their low rates of descent and landing speeds simply glide to sort of a skidding, belly landing. Results of free-flight studies of entry vehicles at landing and approach speeds are covered in one of the subsequent papers.

A few words about peak decelerations may be of interest. For small entry angles and fixed L/D , peak decelerations experienced by the vehicles may be correlated with L/D . The nonlifting types at the left in figure 1 would experience a peak deceleration of about $8g$; however, the variable-drag type could reduce this to about $4g$ through drag modulation. Vehicles with L/D near 0.5 would experience deceleration of about $2g$, and vehicles with L/D of about 1 and greater would experience decelerations no greater than $1g$.

A broad look at figure 1 conveys the correct impression that many lifting reentry vehicles have basically a more or less delta planform. For this reason the characteristics of blunt leading-edge delta wings have received considerable study and will be the subject of two or three conference papers.

A few remarks about maneuverability appear in order because of its reflection upon the environment encountered during reentry and the flexibility of operation. To illustrate, note that figure 1 categorizes the vehicles according to $(L/D)_{\max}$. If a vehicle had a wide angle-of-attack capability, it would obviously have the capacity of significantly varying L/D ; for example, the vehicles to the far right, if provided with sufficient trim-and-control capability and stability, could reduce their L/D considerably to L/D near 0.5 by going to angles of attack near maximum lift (about 55°) and to L/D of essentially zero by

providing 90° angle-of-attack capability. Some of the subsequent papers will treat the aerodynamic and operational problems of such vehicles at moderate and high angles of attack. The problems of wing-like vehicles at very high angles of attack are in some respects similar to those of basically nonlifting types oriented to produce small lift (for example, the Mercury capsule with the horizontal axis at small negative inclination). A matter to be considered, however, is that wide flexibility of operation is not achieved without change in the heating and the peak decelerations.

Because of space limitations in figure 1, the relative size of the vehicles is not given too accurately, although the trends shown are correct. The Mercury capsule is the smallest and the lightly loaded vehicles are the largest, in particular the lifting type which is considerably larger than shown in relation to the other vehicles.

The general magnitude and relation of vehicle size to other vehicle properties such as wing-loading, unit structural weight, payload and gross weight are indicated in figure 2. These results are for a fixed payload capability of 2,000 pounds; however, the results are general in that the planform area for other payloads is in direct proportion. By payload is meant all weight except structural weight. The planform area is shown as a function of the average unit structural weight. This unit is frequently used in vehicle studies to avoid involvement of structural details and is particularly suitable for the purpose of this review, in that structural details will be given special attention in subsequent papers. This unit is merely the ratio of the structural weight of the vehicle to the wetted area, where the structural weight includes heat shield, insulation, and load-bearing structure. Spotted along the abscissa for reference are some basic structure types, ranging from the membrane and woven mesh types that would be common to the lightly loaded vehicles (such as shown at the top of fig. 1) to the rigid metallic type (such as represented by the vehicles to the far right in fig. 1). Each of the three hatched bands shown in figure 2 corresponds to a fixed wing loading. The values shown have been selected somewhat arbitrarily; however, a value of 1.5 lb/sq ft would be representative of the lightly loaded vehicles, while a value of 30 lb/sq ft would be representative of the winged rigid metallic types. The value of 70 lb/sq ft would be representative of a highly compact vehicle (Mercury face loading is about 75 lb/sq ft), and it is currently doubtful that manned reentry vehicles will have wing loadings much in excess of this value. The width of each wing-loading band is associated with the shape variation of vehicles; the widths shown encompass all shapes of current interest in that ratios of wetted area to planform area from 6 to 2 are represented.

Across figure 2 is shown a hazy band separating very roughly the area of currently feasible vehicles from the doubtful area. For wing-loadings of the order of 1.5 to 3 lb/sq ft, this band can be determined

with fair reliability by the state of the art in such things as thermal limitations on materials, fabrication techniques, aided by specific vehicle studies. The same is true for wing loadings of 25 to 75 lb/sq ft. However, there are less reliable guides to indicate how this dividing band should go (or whether it should be continuous) in the intervening range of wing loadings, although the few studies in this region tend to be in agreement with the fairing shown; the band is shown dashed for this range to indicate this further uncertainty. The right end of this band is stopped by the wavy line to indicate that in this region the volume of the vehicle has reached a minimum value for the particular payload. In this regard a value of 15 lb/cu ft of internal volume has been used as a guide. Slightly higher and slightly lower values are indicated from vehicle studies; the value for the Mercury capsule is about 13 lb/cu ft.

Several conclusions are evident from figure 2. First, for any wing loading the current state of the art confines vehicle design to an area in which the size and weight of vehicles are highly sensitive to the interplay of unit structural weight and shape. Second, for a fixed payload, the planform area of the lightly loaded vehicles may easily be more than an order of magnitude greater than the metallic types. Third, for a fixed payload, the gross weight of the lightly loaded vehicles and the metallic vehicles will be of the same general magnitude. To illustrate these latter conclusions in more detail, two points are shown that represent the results of rather detailed vehicle studies, one with wing loading of 1.5 lb/sq ft and the other with wing loading of 30 lb/sq ft. The lightly loaded vehicle (an inflatable type) was estimated to have a planform area of about 2,700 sq ft and a gross weight of about 4,000 pounds; the other vehicle (a rigid metallic type) was estimated to have a planform area of about 140 sq ft and a gross weight of approximately 4,200 pounds. In addition, the values of $(L/D)_{\max}$ were estimated to be about 1 for the vehicle with a wing loading of 1.5 lb/sq ft and about 2 for the vehicle with a wing loading of 30 lb/sq ft. With rare exceptions, gross weight for a fixed payload increases with $(L/D)_{\max}$. Consequently, for a given payload and $(L/D)_{\max}$ it seems unlikely within the present state of the art that lightly loaded vehicles will have any weight advantage over the more heavily loaded types; in fact they may be heavier.

As a final comment on the lightly loaded vehicles, they have the attractive feature of being foldable and stowable in compact packages atop boosters. However, this compactness is in relation to their large inflated or erected size. For a given payload and $(L/D)_{\max}$, the more detailed studies indicate that the size of the package containing the foldable vehicle is little different from the size of the rigid metallic vehicle.

Some operational considerations are next considered. One of the important aspects of reentry-vehicle operation is the range and maneuverability after reentry has been initiated. This requirement generally determines the $(L/D)_{\max}$ that is needed, although other requirements, such as conventional landing capability, may indirectly be the determining factor. Moreover, because of the trend for gross weight to increase with $(L/D)_{\max}$, there may be reason to compromise $(L/D)_{\max}$ somewhat, provided the aforementioned requirements are not infringed upon too heavily. With these factors in mind, a review of the effect of L/D on one of these requirements seems appropriate; namely, range capability after entry. Calculations have been made to determine the maximum accessible landing areas as a function of L/D for the optimum turn and bank angle. Accessible landing area is meant to describe an area within which the vehicle could maneuver to a landing at any point. The peripheries of these areas are shown in figure 3. The initial conditions for these calculations are shown at the top. The velocity ratio \bar{V}_0 at the start of the turn was 0.927; this represents about a 2,000 fps velocity loss to permit the astronaut to acquire the information necessary to make a decision to turn and to acquaint himself with his entry conditions. A shallow entry is assumed, $\gamma \approx 0^\circ$, and the maximum bank angle is taken as 60° . Results are not shown beyond $L/D = 2.5$, since this L/D is about the maximum known requirement for any reentry mission; furthermore, the preceding paper showed that little was to be gained in g-alleviation by use of modulated entry beyond (L/D) 's of this magnitude.

The familiar crab-shaped pattern that characterizes these accessible landing areas is immediately evident, as is the well-known growth of accessible landing area with L/D - the maximum longitudinal range increasing in direct proportion to L/D , and the maximum lateral range increasing as the square of the L/D at low L/D 's, and as L/D to the 1.8 power for L/D 's greater than about 0.5. Thus, in going from, say, an $(L/D)_{\max}$ capability of 0.5 to 2.5 there is a fivefold gain in maximum longitudinal range and about a twentyfold gain in maximum lateral range. One way to view the superposed areas shown in this figure is to regard them as corresponding to vehicles having the same minimum L/D capability but an increasing maximum L/D capability. When so considered the chart shows solely the effect of increasing $(L/D)_{\max}$ in that the retro maneuver for all vehicles is made at the same point in orbit.

One additional word is in order about the vehicles with zero or small L/D . For the conditions of these calculations the zero L/D vehicle has no maneuver capability and, therefore, has no accessible landing area. However, the lightly loaded variable-drag vehicle can, during the last portion of its final orbit before entry, make use of

drag modulation to alter its landing point in a longitudinal direction. Furthermore, it is of course possible for any vehicle, including the nonlifting types, to generate side force by suitable orientation and thereby to have lateral maneuver capability. Mode of operation and other factors can have significant effects on range capability during low L/D operation, as will be evident from the results given in a subsequent paper.

It is also of interest to examine the reduction in accessible landing area that takes place after entry as a function of the velocity at the start of the turn. This performance feature reflects on the delay that can be permitted in the decision to turn after entry has been initiated and on the handling of emergency situations, and has possible military implications. Figure 4 considers some aspects of this feature. First consider the illustrative sketch of accessible landing areas shown on the right. Let the largest landing area be that accessible to a vehicle beginning its turn at $\bar{V}_0 = 0.93$. By comparison, if the vehicle does not turn but proceeds down range in the entry and starts the turn when the velocity has decayed to $\bar{V}_0 = 0.75$, the accessible landing area has reduced considerably; and, if turning is delayed until $\bar{V}_0 = 0.50$, the accessible landing area is only a small fraction of that available with early turning. Of course, the maximum longitudinal range is, as shown, unaffected in these considerations. The most important features (in addition to the reduction in the size of the accessible landing area) are the displacement of this area down range and, in particular, the maximum lateral range capability. The variation of the latter with \bar{V}_0 is given by the curve on the left where the maximum lateral range is given in a normalized form \bar{R}_{lat} which is the ratio of the maximum lateral range at any \bar{V}_0 to that for $\bar{V}_0 = 0.927$. This form has been found to be essentially independent of L/D at least for L/D between 0.5 and 3. This result can be used with figure 3 to get some idea about this effect in terms of actual range. For example, consider a vehicle with $(L/D)_{max}$ of about 1. If the turn were started at $\bar{V}_0 = 0.927$, the maximum lateral range would be about 500 nautical miles; however, if the turn were delayed until $\bar{V}_0 = 0.5$, this would be reduced to about 100 miles.

Thus far consideration has been given only to entry angles near zero. In this respect, past studies of orbital entry vehicles have focused largely on shallow entries because of the temperature limitations of radiation cooled structures, or, for nonlifting vehicles such as Mercury, because of g-limitations. Shallow entries have a number of undesirable features associated with the very small initial aerodynamic forces and small initial rates of deceleration. For example, during the first half of the time period of a shallow entry of a lifting vehicle,

it is not possible to effect any large changes in the flight path, yet the heating rates are high in spite of the low aerodynamic forces. Most of the undesirable features of shallow entries can be avoided by use of steep entries. In the case of the lunar mission, only entry angles steeper than about 4.5° are permissible if multiple passes are to be avoided. Increasing attention must therefore be given to the performance and to the aerothermal and structural problems in steep entries.

First, consider the degree to which steeper entries affect the accessible landing area of lifting vehicles. In contrast to the shallow entry, the steep entry immediately reaches a region of high dynamic pressure in which large maneuvering forces are available. Rapid deceleration occurs so that the vehicle, in leaving the pullup that places it in the glide regime, encounters a resulting velocity-altitude relation that permits significant maneuvering. Thus, steep entries are not necessarily accompanied by serious reductions in lateral-range capability.

Figure 5 illustrates how increasing entry angle alters the accessible landing area. In the sketch at the top of this figure the maximum longitudinal and lateral dimensions of the accessible area for $\gamma \approx 0^\circ$ are designated x_0 and y_0 , respectively. The reduction in these dimensions that takes place with increasing entry angle and decreasing $(L/D)_{\max}$ is shown at the lower left and right. It is apparent that lateral range, (plotted as y/y_0 on the right) is considerably less sensitive to entry angle than longitudinal range x/x_0 . Thus the steeper entry angles tend to circularize the accessible area as shown in the sketch at the top, where the area for a -6° entry is compared qualitatively with the area for the grazing entry. (This superposition of accessible areas merely infers that the retro maneuver for the steeper entry is performed at a later time in orbit.) The small reduction in lateral range capability for moderate entry angles is of particular importance in that these steeper entries can be employed with little or no increase in the number of orbits that a vehicle in an inclined orbit would be required to make before it could reenter and reach a given landing point.

The previous paper has pointed out that properly maneuvered lifting vehicles are inherently capable of steep entry without excessive decelerations. The principal deterrent to the steep entry is thus the occurrence of peak heat rates beyond the current capability of radiation-cooled structures. For example, leading-edge equilibrium temperatures in the range of $3,300^\circ\text{F}$ to $4,500^\circ\text{F}$ are required for an entry angle in the vicinity of -8° , depending on vehicle design. Hoped-for developments in nonmetallic materials and structures may ultimately permit radiation-cooled designs with this capability. However, at present the only alternative is to prevent the occurrence of these excessive temperatures

in a structure capable of heat absorption. In the remaining discussion, the heating requirements imposed on such a structure will be considered.

Figure 6 shows typical trajectories for a steep entry angle, about 60° in this example. In the upper trajectory the vehicle enters in the attitude indicated by the small sketch of a winged vehicle and executes a maximum lift pullup. This type of pullup gives the minimum heat load and minimum heat rate in the pullup. The pullup is followed by a variable-lift push-over - shown by the dashed part of the curve - and thence into the steady glide path. The variable-lift part of the maneuver may alternatively be started ahead of peak acceleration for the purpose of G-modulation (shown by the lower dashed curve on this same trajectory). As indicated by the scale near the top of the slide, the major fraction of the heat load in this type of entry is dealt with by radiation cooling in the steady glide portion. The problems of the low L/D lifting body vehicle (sketched at the lower right), also in a pullup-glide entry, are similar to those of the winged vehicle except that the fraction of the heat load that can be disposed of by radiation is less because of the characteristically higher wing loading and higher heat rate. A representative value of the glide parameter for this vehicle is about 175 as contrasted with about 50 for the winged vehicle.

This pullup-glide maneuver permits minimum G, a maximum degree of range control after entry has been initiated, and minimum structural change to the shallow-entry radiation-cooled glider. The principal structural change consists primarily of the addition of heat-absorbing material in the leading-edge region to accept the heat load generated during the pullup. The aerodynamic problems here are essentially the same as in the shallow entry since the same vehicle shape, attitudes, and velocities are involved. Obviously, there is concern here with the hypersonic real-gas characteristics of lifting configurations in the high-lift attitude. The problems in these areas are discussed in subsequent papers.

The lower trajectory in figure 6 is an alternative handling of steep entry, which minimizes the convective heat load of the vehicle, the entry time, and the entry range. In this trajectory only enough lift is used to keep the maximum G at the design limit, and the vehicle operates in the high-drag region of the force polar. Prior to landing, a transition to the normal low-drag attitude may be made if the vehicle is equipped with the necessary trimming and stabilizing devices. This type of entry involves problems of stability, control, and heat transfer in the high-drag low-lift attitude, and will receive attention in one or two other conference papers. Note by the scale at the top that a large fraction of the heat load in this type of entry will be dealt with by radiation plus absorption, but bear in mind that the total heat load is minimized.

The thermostructural problems of these two types of steep entry are illustrated in more detail in figures 7 and 8. Figure 7 illustrates the minimum-lift entry and figure 8 the pullup-glide entry. These results were calculated for a flat-bottomed 70° swept-wing vehicle having a leading-edge diameter of 1 foot, an L/D of 1 in pullup and glide, an $(L/D)_{\max}$ of 2.5 in modulated entry, a wing loading of 25 lb/sq ft, and a gross weight of 10,000 pounds. The trends shown are typical of flat-bottomed vehicles in general and are not restricted to the particular vehicle used in these illustrations. In each figure shown the relative total heat load that would have to be absorbed, and the duration of this period of heat absorption, as a function of entry angle. Note that the heat load is normalized with respect to Q_0 , the heat load for $L/D = 0$ and $\gamma = 0$.

Consider first the minimum-lift entry, on which there has been placed an arbitrary restriction of 10 G. For a low-temperature structure the relative total heat load that would have to be absorbed remains low up to an entry angle of about -7° . For the purpose of providing a quantitative feel for an approximate upper limit on weights involved to cope with these heat loads, the vehicle has been assumed to employ a material with an effective heat capacity of 1,000 Btu/lb. In this case, about 10 percent of the vehicle weight would be heat-absorbing material at an entry angle of -7° and about 25 percent at an entry angle of -9° . Obviously, the use of more effective materials would reduce these weights in direct proportion to the increased heat capacity of the materials. Later papers will deal with materials having higher heat capacity.

If a more logical approach is taken and a high-temperature structure such as an internally cooled molybdenum structure capable of radiation cooling at a nominal temperature of $2,500^\circ$ F is employed, the net heat absorption requirement is reduced to small values, as shown by the lower curve, and the associated weight penalties would amount to only a percent or so of vehicle weight.

The times involved in heat absorption in these minimum-lift entries are shown to be very short, of the order of 2 minutes for the steeper entries. These short times favor the use of externally applied ablation materials, as will be discussed in subsequent papers. A possible difficulty in the absorption of the heat load in this type of entry lies in the fact that the entire forward-facing surface must be capable of heat absorption; however, the quantities involved per unit of surface area are small.

Consider next the pullup-glide entry (fig. 8). A quick comparison with the minimum-lift entry is possible since the scales are the same. The cold-wall heat loads and times involved in heat absorption are notably larger than for the minimum-lift entry. In general, it is not practical

CONFIDENTIAL

to attempt to provide absorption for the entire cold-wall heat load. However, with the hot-wall condition ($2,500^{\circ}\text{F}$), heat absorption is restricted to the pullup phase only, and the weight penalties are again quite small, including the case of modulated entry. With the same conservative assumptions as before, there would be at most some 3 percent or so of vehicle weight in absorption material. In view of the very short time of the pullup heat pulse, about 1 minute, the possibility of using ablation materials is very good. Furthermore, the area to be protected in this case is restricted to the leading-edge region, in contrast to the minimum lift entry. The magnitudes of the decelerations are also indicated on the heat-load curves in figure 8. The curves are shown dashed beyond a G_{max} of 10. Note that in the modulated case G_{max} is 6 at $\gamma = -12^{\circ}$.

In closing, it is worth noting that the surface requiring heat capacity tends to increase with: (a) departures from a flat plate, (b) increases in wing loading, and (c) increases in entry velocity. With regard to the increase in entry velocity, the same configuration used in these calculations for the pullup-glide type of entry from an orbital mission would require heat capacity over the entire lower surface in a middle-of-the-corridor return from a lunar mission. The heat loads involved in the lunar mission would be of the order of 3 to 4 times those shown for the orbital mission. The lunar mission problem, however, is otherwise similar in character to the steep-entry orbital case, and the same type of radiation-plus-absorption structural approach appears feasible.

CONFIDENTIAL

ORBITAL MANNED REENTRY VEHICLES

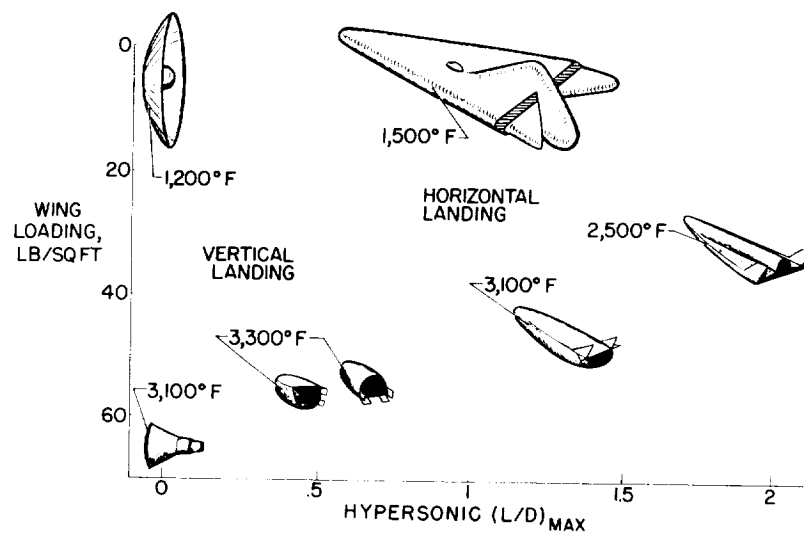


Figure 1

VEHICLE PROPERTIES AND CURRENT STATUS

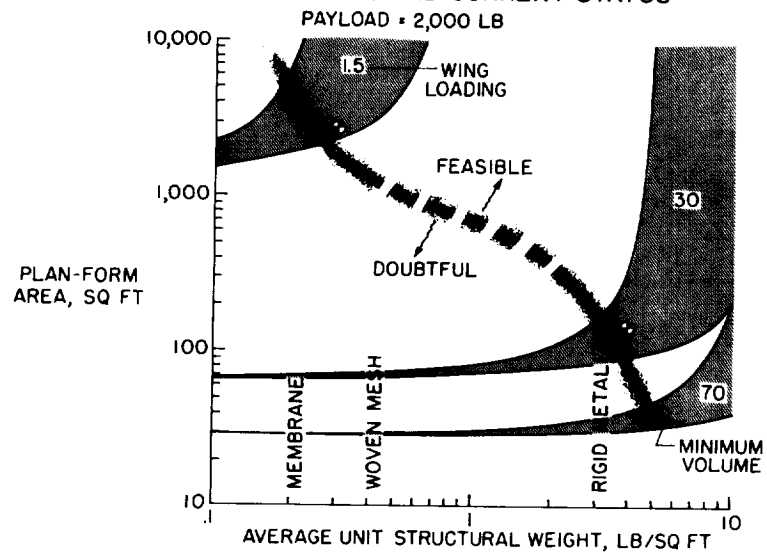


Figure 2

EFFECT OF L/D ON ACCESSIBLE LANDING AREA $\bar{V}_0 = 0.927$; $\gamma \approx 0^\circ$; $\phi_{\text{MAX}} = 60^\circ$ LATERAL RANGE, NAUT. MILES

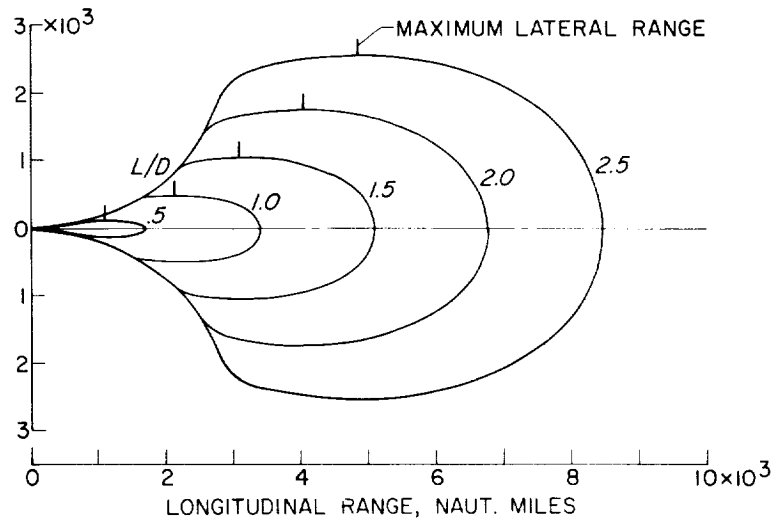


Figure 3

EFFECT OF VELOCITY AT START OF TURN ON MAXIMUM LATERAL RANGE $\gamma \approx 0$

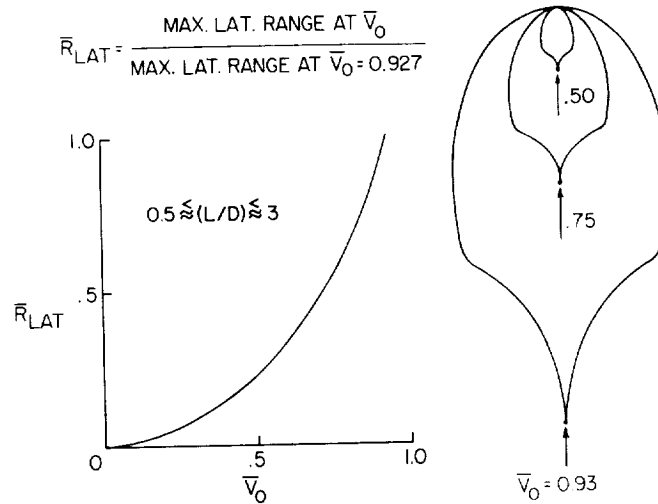


Figure 4

EFFECT OF ENTRY ANGLE ON ACCESSIBLE LANDING AREA

$$0.93 \lesssim \bar{V}_0 \leq 1; (L/D)_{\text{MIN}} = 0$$

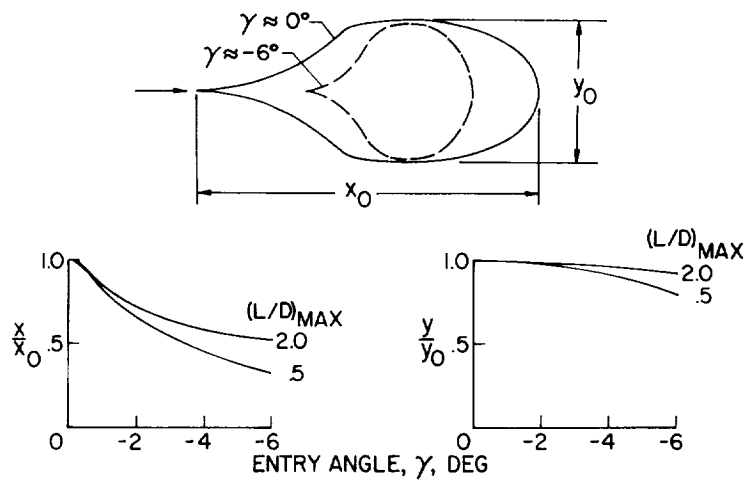


Figure 5

STEEP REENTRIES

$$\gamma \approx -6^\circ$$

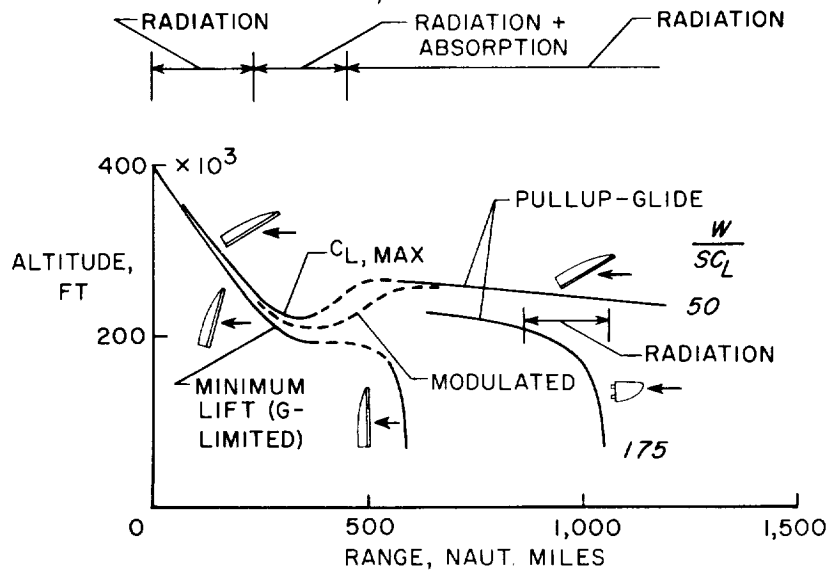


Figure 6

MINIMUM-LIFT REENTRIES FOR $G_{MAX} = 10$

HEAT LOAD

DURATION OF HEAT PULSE

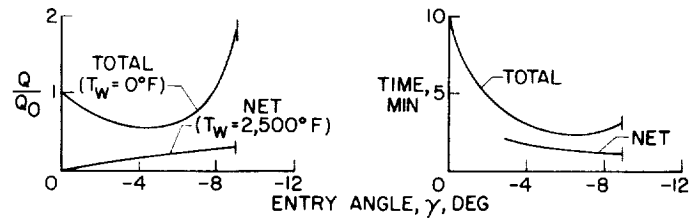


Figure 7

PULLUP-GLIDE REENTRIES FOR $L/D = 1$

HEAT LOAD

DURATION OF HEAT PULSE

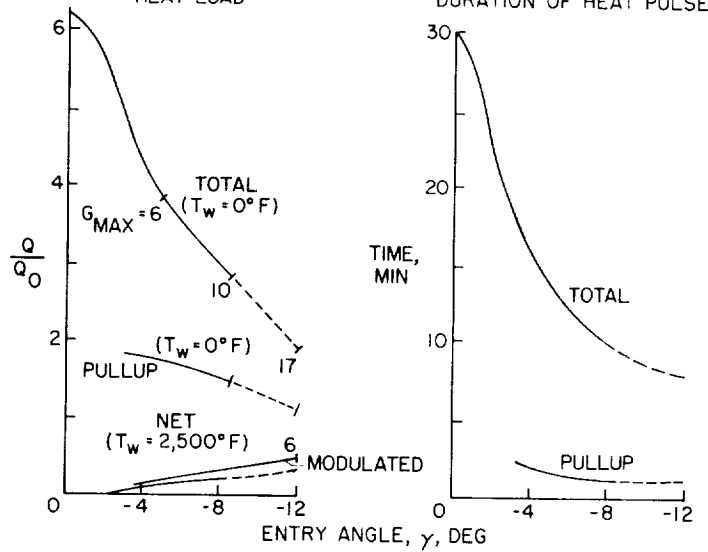


Figure 8

INVESTIGATION OF THE FLOW OVER SIMPLE BODIES AT
MACH NUMBERS OF THE ORDER OF 20

By Arthur Henderson, Jr.
Langley Research Center

SUMMARY

It is shown that adequate means are available for calculating inviscid direct and induced pressures on simple axisymmetric bodies at zero angle of attack. The extent to which viscous effects can alter these predictions is indicated.

It is also shown that inviscid induced pressures can significantly affect the stability of blunt, two-dimensional flat wings at low angles of attack. However, at high angles of attack, the inviscid induced pressure effects are negligible.

INTRODUCTION

The flow phenomenon encountered by vehicles in the reentry Mach number range is very complex. The extreme heating, loading, and stability problems which the designer must cope with are in many cases incompletely understood. In the preliminary evaluation of the design of a reentry vehicle, the ability to predict pressure distributions is of fundamental importance in understanding all these aspects of the reentry problem. Thus, the present paper is concerned with assessing the adequacy of currently available methods of predicting pressures on blunt noses and in the induced-pressure region behind blunt noses on the simple axisymmetric and two-dimensional types of configurations which will form components of complete reentry vehicles. Most of the experimental work has been performed in a perfect fluid in order to simplify the understanding of the basic fluid dynamics of high Mach number flight.

SYMBOLS

b	surface distance from nose stagnation point to nose-cylinder juncture
c	chord length
$C_{D,n}$	nose drag coefficient
C_{m,l_e}	pitching moment about leading edge
C_N	normal-force coefficient
d	maximum body diameter
M_∞	free-stream Mach number
$M_{\infty,n}$	free-stream Mach number at nose
$M' = \frac{dM_\infty}{d(x/t)}$	
p	static pressure
p_∞	free-stream static pressure
$p_{\infty,n}$	free-stream static pressure at nose
$p_{\infty,l}$	free-stream static pressure at orifice location in tunnel when model is absent
p_{MAX}	maximum static pressure on model
R_d	Reynolds number based on maximum body diameter
s	surface distance measured from stagnation point
t	plate thickness
x	streamwise surface distance measured from model nose-cylinder juncture

x_{cp}	center-of-pressure location, measured from model nose
α	angle of attack
γ	ratio of specific heats
ρ_{∞}	free-stream density
ρ_s	density behind normal shock

DATA REDUCTION

Much of the data in the present paper was obtained in the 2-inch helium tunnel at the Langley Research Center. This tunnel utilizes a conical nozzle. The flow in conical nozzles deviates from the desired flow in that there is a longitudinal pressure and Mach number gradient, and a lateral conical flow-angularity distribution. This deviation from the desired state raises a question of interpretation of the data.

A series of characteristics calculations was therefore performed in the Langley 11-Inch Hypersonic Tunnel Section on the two-dimensional sonic-wedge—slab illustrated in figure 1 in order to obtain a first-order picture of the effects of conical flow.

The pressure distributions shown in figure 1 were obtained by using

$$M_{\infty} = M_{\infty,n} + M' \frac{x}{t} \quad (1)$$

where M_{∞} is the free-stream Mach number, $M_{\infty,n}$ is the free-stream Mach number at the nose, and $M' = \frac{dM_{\infty}}{d(x/t)}$. Pressure distributions were calculated for a constant free-stream Mach number ($M' = 0$) and for conical flow with various values of M' . Figure 1 shows the results for $M' = 0$ and $M' = 0.05$ only. The pressures for $M' = 0.05$ were normalized three different ways as shown and compared with the $M' = 0$ case.

The normalizing methods are:

Method 1 utilizes $p/p_{\infty,n}$

where p is the calculated body static pressure and $p_{\infty,n}$ is the free-stream static pressure at the nose.

Method 2 utilizes $p/p_{\infty,l}$

where $p_{\infty,l}$ is the local free-stream static pressure that would exist at the point in the flow where p is calculated if the body were not present.

Method 3 utilizes
$$\frac{p + (p_{\infty,n} - p_{\infty,l})}{p_{\infty,n}}$$

This is the so-called "buoyancy-correction" method (ref. 1) which has been used successfully at supersonic speeds to correct the pressure drag of bodies which were tested in flow with a slight longitudinal pressure gradient.

Of the three, the buoyancy-correction method most closely represents the pressure distribution that exists for uniform flow. This method has therefore been used to normalize the data obtained in conical flow. However, the data are presented as p/p_{∞} .

The adequacy of the buoyancy-correction method in radial flow decreases with increasing x/t and with increasing M' ; therefore, it must be used with caution. However, for flow with Mach number gradient but zero flow angularity, the buoyancy-correction method gives good results to the highest M' investigated ($M' = 0.2$).

OUTGASSING EFFECTS

The pressure distributions to be presented were obtained by using metal tubing with short lengths of plastic tubing in the pressure-measuring circuit. The plastic tubing was used only where necessary, was kept as short as possible, and was carefully selected to insure that it had negligible porosity. The entire system of model, metal and plastic tubing, and manometer was thoroughly outgassed prior to obtaining data. These precautions were necessary because of the low pressures encountered.

Figure 2 illustrates the effect that outgassing and porosity can have on pressure measurements. The tests were performed on a hemisphere-cylinder model in the Langley 11-inch hypersonic tunnel (ref. 2). The figure presents two sets of induced-pressure-distribution measurements. Both sets were obtained on the same model with identical flow conditions in the tunnel. The higher of the two sets of data was obtained with about 3 feet of plastic tubing exposed to the atmosphere in the pressure-measuring circuit. No attempt was made to outgas the system before obtaining data. The other set of data was obtained after the plastic tubing was replaced by metal tubing (with short plastic jumpers) which was then thoroughly outgassed before data were obtained. It can be seen that the results are in error by a factor of about 2 at $x/d \approx 8$ because of outgassing and porosity effects in the plastic tubing.

RESULTS

Blunt-Nose Pressures

It has been well established that modified Newtonian flow theory gives good predictions of the pressure distribution on blunt bodies at Mach numbers above about 3, from the stagnation point back to the region where the angle between the free-stream flow direction and the tangent to the body surface is on the order of 30° or less, depending on the Mach number, as long as the body curvature is not so large that centrifugal-force effects must be accounted for. In the region of the nose-cylinder juncture, where entropy and vorticity effects enter the picture, Newtonian theory fails. In an attempt to eliminate this deficiency, Lees suggested modifying the theory by matching the two-dimensional Prandtl-Meyer solution to the Newtonian at the point on the body where both the body pressure and the slope of the body pressure with surface distance were the same (refs. 3 and 4). In this form, the theory predicts that the shoulder pressure will be identical on different bodies which are tested at the same Mach number.

Figure 3 shows the pressure distribution on two noses with a fineness ratio of 1. The body shapes are of the form

$$x \propto r^n \quad (2)$$

where x and r are Cartesian coordinates, x in the streamwise direction. In the figure, the exponents for the bodies with moderate and large bluntness are $n = 2$ and $n = 6$, respectively. It is seen that both bodies do have essentially the same shoulder pressure. The forebody

pressures are predicted fairly well by the modified Newtonian-Prandtl-Meyer theory except near the shoulder, where the lower pressure downstream of the corner expansion probably alleviates the nose pressure somewhat through the boundary layer. The agreement between theory and experiment in the region of high curvature on the $n = 6$ body is noteworthy since no centrifugal-force corrections were included. The modified blast-wave theory (ref. 5) closely predicts the pressures in the initial induced-pressure region. However, the pressures for the body with the lower nose drag ($n = 2$) are seen to decrease more with surface distance than the pressure for the $n = 6$ nose, which is in accord with the blast-wave prediction to be discussed later.

It has been pointed out in the literature that the details of the flow in the nose region of blunt bodies are affected by the shape of the sonic line (see for instance, refs. 6, 7, and 8). The sonic-line shape for a given body shape depends strongly on the density ratio across the shock. Figure 4 compares the pressure distributions on a hemisphere-cylinder obtained at hypersonic speeds by using test mediums with different density ratios across the shock. The circles represent data obtained in helium at $M_\infty = 19$ and $\rho_s/\rho_\infty \approx 4$, while the hatched areas represent data obtained in dissociated air in the AEDC Hotshot I tunnel (ref. 9) at $M_\infty = 15.6$ and $\rho_s/\rho_\infty \approx 10$. The type of sonic-line shape generated by these two flows is as illustrated. An examination of the data reveals that any differences which may exist are certainly small, even in the neighborhood of the sonic point on the body ($p/p_{MAX} \approx 0.5$). Thus, the effect of sonic-line shape as well as effective specific-heat ratio is seen to be unimportant as far as blunt-nose-forebody pressure-ratio distributions are concerned, at least for the hemisphere nose. The theory in figure 4 is again modified Newtonian-Prandtl-Meyer and modified blast-wave.

The experimental shoulder pressure obtained in helium is seen to be higher than the theory, whereas the shoulder pressure on the models shown in figure 3 was well predicted by the theory. The value of R_d was the same for both sets of helium data. The difference in results can possibly be attributed to a shape effect; that is, the hemisphere has continuous curvature while the n -powered bodies have a finite expansion at the shoulder.

The pressure at the nose-cylinder juncture of blunt-nosed bodies is affected by a variation of Reynolds number as well as geometry; this is illustrated in figure 5 for the hemisphere-cylinder. (See ref. 2.) The figure shows the variation of p/p_{MAX} with R_d for various values of x/d . Clearly, the effects of Reynolds number can be appreciable at and close to the shoulder. The point labeled "theory" at $R_d = \infty$ is the

inviscid modified Newtonian-Prandtl-Meyer value. Except possibly at very low Reynolds numbers, the effects of Reynolds number become negligible beyond $x/d = 0.5$. This does not imply that there are no boundary-layer effects farther downstream; rather the boundary-layer effects that do exist are essentially unaffected by a variation in Reynolds number beyond $x/d = 0.5$.

It is of interest to note that the experimental points are a composite of results from the 2-inch helium tunnel and the 11-inch constant Mach number helium tunnel.

Induced Pressures

The blast-wave analogy (see refs. 3 and 10 to 13, for example) furnishes the designer with a rapid means of estimating blunt-nose induced body pressures. However, its adequacy from the standpoint of accuracy has been seriously questioned. (See, for instance, ref. 14.) This section of the paper is devoted to assessing the usefulness of the blast-wave theory.

Figure 6 presents the results of a series of exact characteristics calculations which were made to determine the inviscid induced pressures on cylinders behind various nose shapes at Mach numbers from 6.9 to 40 in both air and helium. The calculated values have been plotted by using the blast-wave parameter and it is seen that all the results fall within a narrow band (except values closer than about 2 to 4 diameters behind the shoulder, which have been neglected). Thus, within the range of variables covered, the blast-wave theory furnishes a triple correlation parameter; that is, all the calculated pressures beyond a few body diameters from the shoulder fall within a narrow band for a wide range of Mach numbers and nose-drag coefficients, and for two values of specific-heat ratio. These theoretical results indicate that the blast-wave theory furnishes an excellent correlating parameter whose usefulness extends over a much wider range of nose drags than the assumptions upon which blast-wave theory are based would appear to warrant. Also, inherent in the nose-drag dependence is the implication that induced pressures are independent of nose shape. Thus, the models shown in figure 7 were designed to check experimentally the range of validity of the nose-shape-independence concept, and to check the extent to which induced pressures could be correlated by nose drag. There were six pairs of models. Each pair consists of two cylindrical rods with different nose shapes but the same nose drag. The nose-drag coefficients vary from 0.2 to 1.2. Pressures were obtained at x/d locations from 0.02 to 20 at $M_\infty = 21$ in helium. Figure 8 presents the results for the $C_{D,n} = 0.2$ and 1.2 bodies; these are typical of all the results.

It can be seen that except at $x/d = 0.02$, the induced-pressure distribution is essentially independent of nose shape, at least for $0.2 \leq C_{D,n} \leq 1.2$.

Figure 9 presents all the pressure data obtained on the models of figure 7 plotted against the blast-wave parameter $\frac{x/d}{M_\infty^2 \sqrt{C_{D,n}}}$. As indicated in the figure, good correlation is obtained for x/d equal to or greater than 2.5.

Although blast-wave theory correlates induced pressures well and predicts the induced-pressure dependence on nose drag and independence of nose shape, the blast-wave theory is not capable of predicting absolute induced-pressure values, as illustrated in figure 10 for a hemisphere-cylinder (ref. 2). Because of the assumptions upon which the theory is based, the theory cannot give good results near the shoulder nor far downstream. However, blast-wave theory can be modified so that the end-point conditions (that is, the pressure at the shoulder and the pressure at an infinite distance downstream) are taken into account (ref. 5). If the Newtonian-Prandtl-Meyer prediction is used for the shoulder pressure and the value obtained from characteristics calculations is used for the far downstream pressure, the resulting modified blast-wave theory gives the lower curve in figure 10. This curve gives a good prediction of trend but is clearly too low. It should be borne in mind, however, that the end points by which the theory was modified were obtained from inviscid predictions.

It has been demonstrated earlier in the paper that the shoulder pressure varies with geometry and Reynolds number. If viscous and geometry effects are included by using the experimentally determined end points to modify the blast-wave theory, the short dashed line is obtained; it is seen to fit the measured pressure distribution. Thus, blast-wave theory can apparently be modified to predict accurately the induced-pressure distributions if some means can be found to determine the shoulder pressure and the asymptotic downstream pressure for any combination of geometry and Reynolds number. At present, no such method exists; work in this area is needed. Until a satisfactory method of modifying blast-wave theory can be found, empirical equations can be determined from the correlation plots. When x/d is measured from the shoulder, as in this paper, the correlation plots yield equations which do not apply near the shoulder. Better correlation can be obtained near the shoulder if x/d is measured from the nose; however, the correlation far downstream then becomes less satisfactory.

Two-Dimensional Induced-Pressure Effects

The large induced pressures that can occur at reentry Mach numbers may have considerable effect upon the stability of a vehicle. The magnitude of these effects and the conditions under which they may or may not be important are illustrated in figures 11 and 12. The normal-force coefficient, pitching-moment coefficient about the leading edge, and center-of-pressure location are plotted against chord-thickness ratio for a flat slab with a blunt leading edge at 5° to 20° angle of attack at $M_\infty = 20$ in perfect air.

The nose shape was varied with α so that both wedges had sonic velocity and the apex of the wedges lay on the center line of the slab. Although this is not a realistic configuration, it allowed the pressure distributions (which were integrated to obtain C_N and $C_{m,le}$) from reference 13 to be used. These pressure distributions were obtained by the method of characteristics and include the inviscid induced-pressure effects. The values of C_N , $C_{m,le}$, and x_{cp}/c which were derived by using these pressure distributions are compared with values of the same parameters derived by using pressure distributions determined from the tangent-wedge approximation. Of importance is the difference between these two sets of curves. It is seen that induced-pressure effects on all three parameters investigated can be large in the low angle-of-attack range. However, at 20° the contribution of the induced effects is negligible.

CONCLUDING REMARKS

The designer has adequate means at his disposal for calculating the inviscid direct and induced pressures on simple axisymmetric bodies at zero angle of attack. Viscous effects can modify these results however, particularly near the shoulder on noses and in the induced-pressure region. Additional research is needed to determine the magnitude of viscous effects for any combination of geometry and Reynolds number. Until a satisfactory means of predicting viscous effects is found, empirical equations based on the blast-wave correlating parameter can be used in the induced-pressure region.

REFERENCES

1. Love, Eugene S., Coletti, Donald E., and Bromm, August F., Jr.: Investigation of the Variation With Reynolds Number of the Base, Wave, and Skin-Friction Drag of a Parabolic Body of Revolution (NACA RM-10) at Mach Numbers of 1.62, 1.93, and 2.41 in the Langley 9-Inch Supersonic Tunnel. NACA RM L52H21, 1952.
2. Mueller, James N., Close, William H., and Henderson, Arthur, Jr.: An Investigation of Induced-Pressure Phenomena on Axially Symmetric, Flow-Alined, Cylindrical Models Equipped With Different Nose Shapes at Free-Stream Mach Numbers From 15.6 to 21 in Helium. NASA TN TN D-373, 1960.
3. Lees, Lester, and Kubota, Toshi: Inviscid Hypersonic Flow Over Blunt-Nosed Slender Bodies. Jour. Aero. Sci., vol. 24, no. 3, Mar. 1957, pp. 195-202.
4. Wagner, Richard D., Jr.: Some Aspects of the Modified Newtonian and Prandtl-Meyer-Expansion Method for Axisymmetric Blunt Bodies at Zero Angle of Attack. Jour. Aero/Space Sci. (Readers' Forum), vol. 26, no. 12, Dec. 1959, pp. 851-852.
5. Love, E. S.: Prediction of Inviscid Induced Pressures From Round Leading Edge Blunting at Hypersonic Speeds. ARS Jour. (Tech. Notes), vol. 29, no. 10, pt. 1, Oct. 1959, pp. 792-794.
6. Hayes, Wallace D., and Probstein, Ronald F.: Hypersonic Flow Theory. Academic Press, Inc. (New York), 1959.
7. Traugott, Stephen C.: Shock Generated Vorticity and Sonic Line Slope on the Surface of Blunt Bodies in Supersonic and Hypersonic Flight. RR-14, The Martin Co., Feb. 1959.
8. Van Dyke, Milton D., and Gordon, Helen D.: Supersonic Flow Past a Family of Blunt Axisymmetric Bodies. NASA TR R-1, 1959.
9. Boison, J. Christopher: Experimental Investigation of the Hemisphere-Cylinder at Hypervelocities in Air. AEDC-TR-58-20, ASTIA Doc. No.: AD-204392, Arnold Eng. Dev. Center, Nov. 1958.
10. Cheng, H. K., and Pallone, A. J.: Inviscid Leading-Edge Effect in Hypersonic Flow. Jour. Aero. Sci. (Readers' Forum), vol. 23, no. 7, July 1956, pp. 700-702.

11. Bertram, M. H., and Baradell, D. L.: A Note on the Sonic-Wedge Leading-Edge Approximation in Hypersonic Flow. Jour. Aero. Sci. (Readers' Forum), vol. 24, no. 8, Aug. 1957, pp. 627-629.
12. Henderson, Arthur, Jr., and Johnston, Patrick J.: Fluid-Dynamic Properties of Some Simple Sharp- and Blunt-Nosed Shapes at Mach Numbers from 16 to 24 in Helium Flow. NASA MEMO 5-8-59L, 1959.
13. Bertram, Mitchel H., and Henderson, Arthur, Jr.: Effects of Boundary-Layer Displacement and Leading-Edge Bluntness on Pressure Distribution, Skin Friction, and Heat Transfer of Bodies at Hypersonic Speeds. NACA TN 4301, 1958.
14. Bogdonoff, Seymour M., and Vas, Irwin E.: A Study of Hypersonic Wings and Controls. Paper No. 59-112, Inst. Aero. Sci., June 16-19, 1959.

DATA-REDUCTION METHODS ON A BLUNTED TWO-DIMENSIONAL FLAT PLATE IN CONICAL FLOW

$$M_{\infty,n}=20; M'=0.05; \gamma=5/3$$

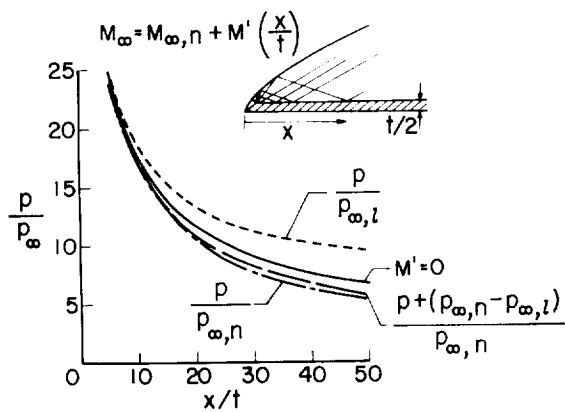


Figure 1

EFFECT OF TUBING ON HEMISPHERE-CYLINDER INDUCED PRESSURE MEASUREMENT

$$M = 16.6; \gamma = 5/3$$

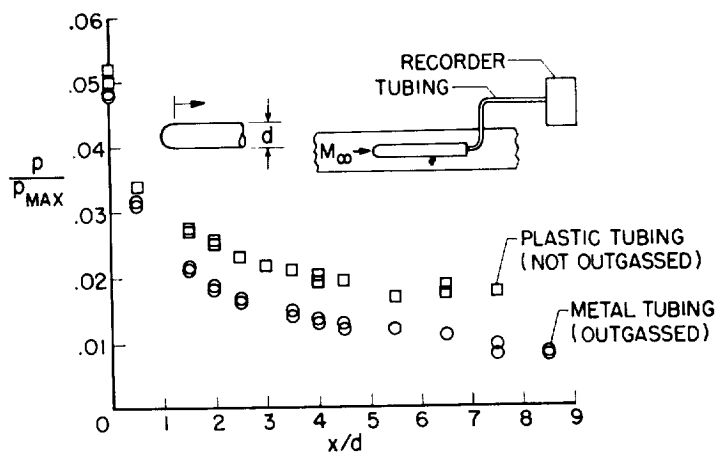


Figure 2

BLUNT-BODY PRESSURE DISTRIBUTIONS

$$M_\infty = 19; R_d = 0.32 \times 10^6; \gamma = 5/3$$

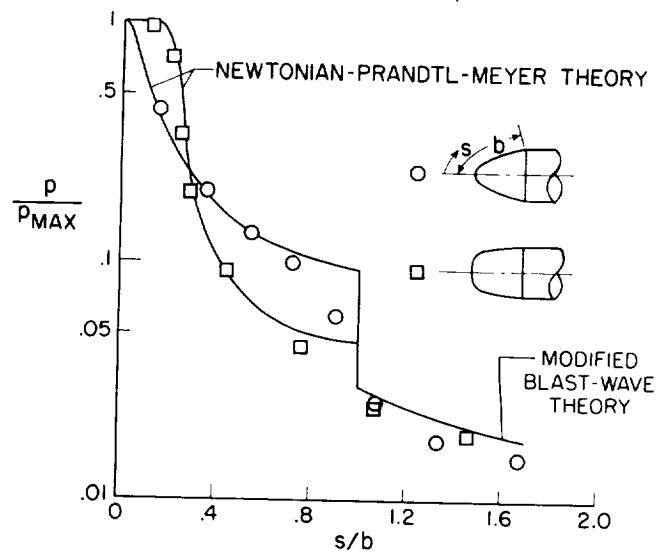


Figure 3

PRESSURE DISTRIBUTIONS ON HEMISPHERE-CYLINDER

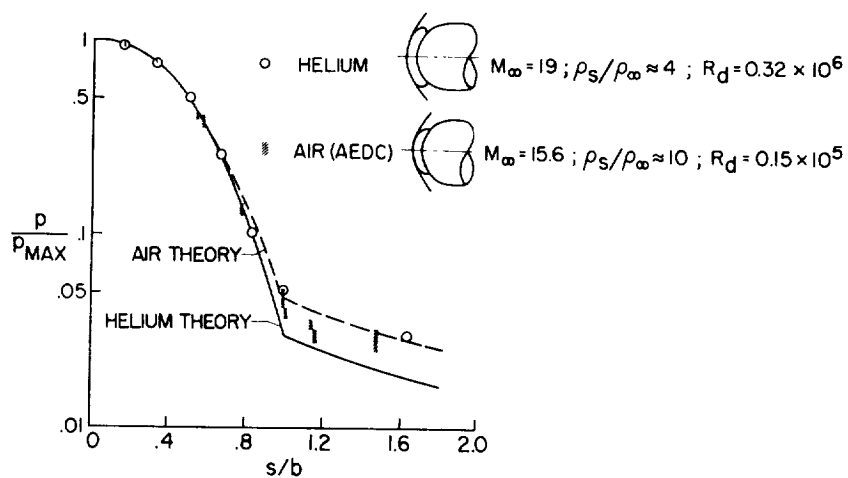


Figure 4

EFFECT OF REYNOLDS NUMBER ON INDUCED PRESSURES ON HEMISPHERE-CYLINDER

$$15.6 \leq M_\infty \leq 21; \gamma = 5/3$$

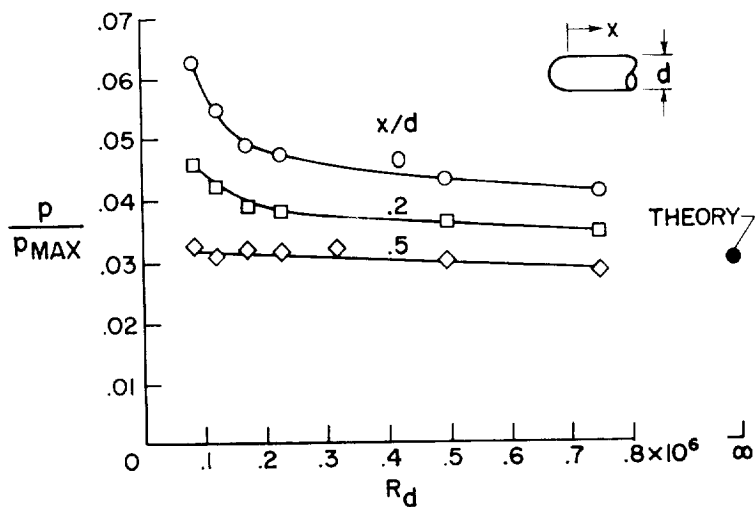


Figure 5

CORRELATION OF THEORETICAL INDUCED PRESSURES BY BLAST-WAVE PARAMETER

$$6.9 \leq M_\infty \leq 40; 0.04 \leq C_{D,n} \leq 1.37; 7/5 \leq \gamma \leq 5/3$$

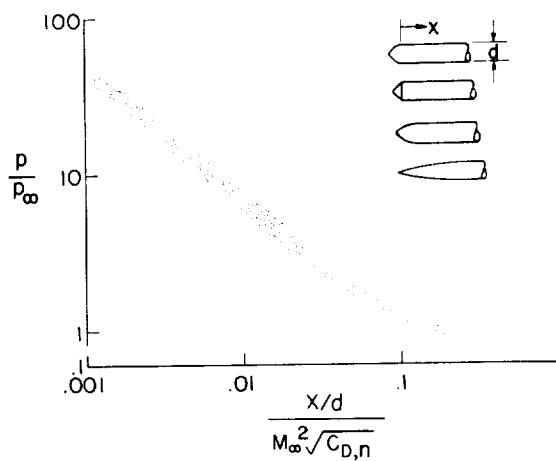


Figure 6

MODELS USED IN INVESTIGATION OF NOSE-SHAPE-INDEPENDENCE CONCEPT

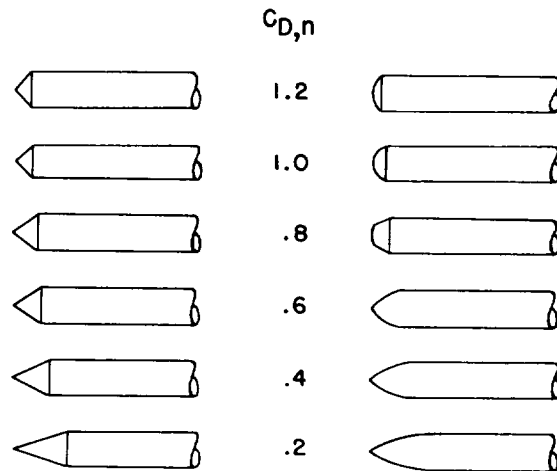


Figure 7

INDUCED PRESSURES, NOSE-SHAPE-INDEPENDENCE CONCEPT $M_\infty = 21$, $\gamma = 5/3$

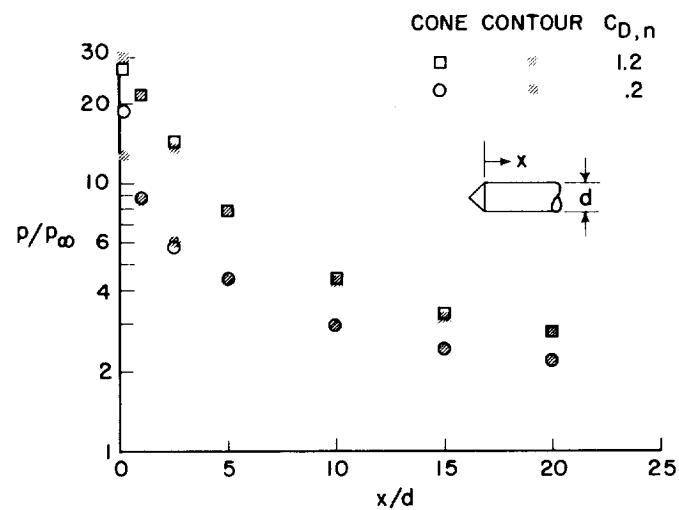


Figure 8

EXPERIMENTAL INDUCED PRESSURES

$$0.2 \leq C_{D,n} \leq 1.2; M_\infty = 21; \gamma = 5/3$$

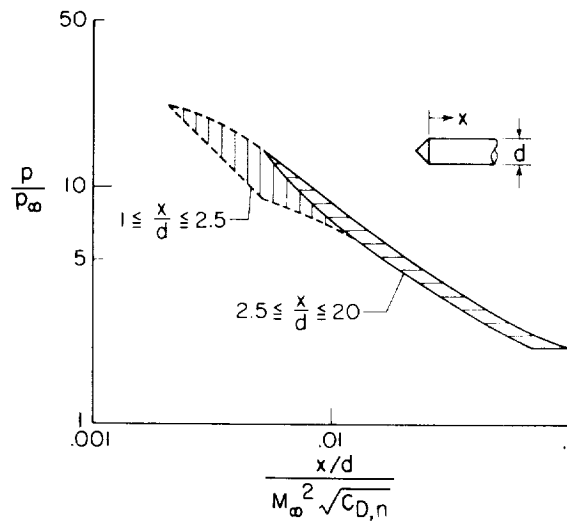


Figure 9

INDUCED PRESSURES ON HEMISPHERE-CYLINDERS

$$M_\infty = 21; \gamma = 5/3$$

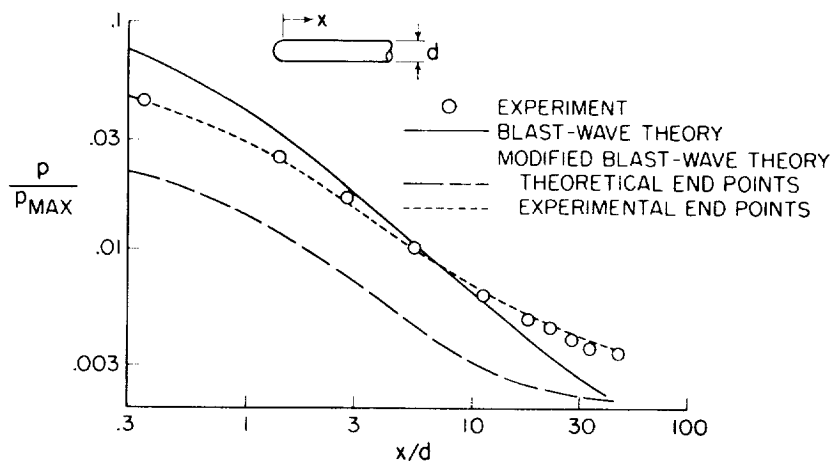


Figure 10

EFFECT OF INDUCED PRESSURE ON TWO-DIMENSIONAL FORCE AND MOMENT CHARACTERISTICS

$$M_\infty = 20; \gamma = 7/5$$

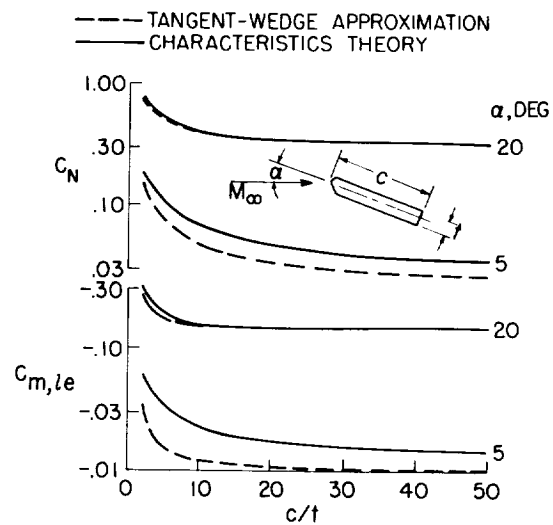


Figure 11

EFFECT OF INDUCED PRESSURE ON TWO-DIMENSIONAL CENTER-OF-PRESSURE LOCATION

$$M_\infty = 20, \gamma = 7/5$$

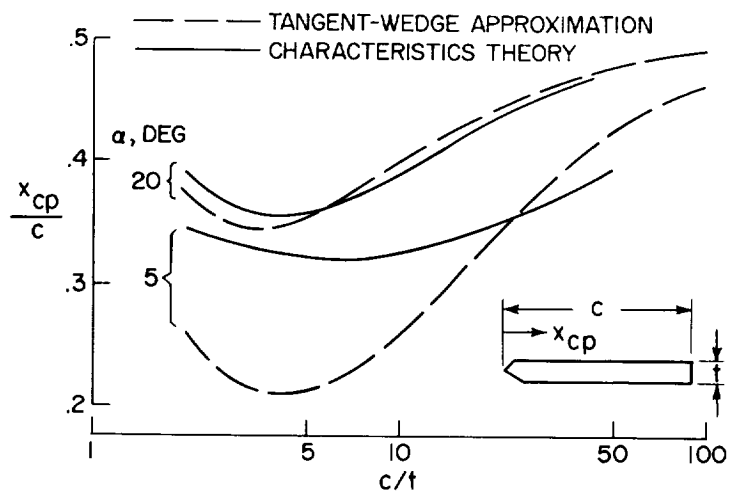


Figure 12

12/12/2020

12/12/2020

12/12/2020

MEASUREMENTS OF RADIATION FROM AIR AND CARBON DIOXIDE

By T. N. Canning, H. E. Bailey, W. R. Leak,
and W. A. Page
Ames Research Center

INTRODUCTION

Before the radiant heat flux experienced by a space vehicle during reentry can be calculated, it is necessary to know how much energy the hot gas in the shock layer will radiate. A semiempirical theory, based on tests with air in a shock tube, has been developed by Kivel and Bailey (ref. 1). Reported herein is an independent set of measurements of the radiation from the shock layer made in a ballistic range. In addition, some measurements have been made in carbon dioxide to obtain an idea of the radiant heat flux to be expected for entry into the Venusian atmosphere.

TESTS

The data presented are measurements of the total radiation from the hot gas caps of models fired from high-speed guns. The experimental set-up is illustrated in figure 1. The radiation sensors were photomultipliers, which were positioned to view the flight path from the side at 90° and 17° . The models were $1/4$ inch in diameter and of two different types. The first type of model was a flat-faced model that had a copper cap on the nose to prevent ablation. The second type of model had a spherical nose and was made of polyethylene. A typical oscilloscope record is also shown.

To reduce the data to $\text{BTU}/\text{sec-ft}^2$, it is necessary to estimate the volume of the hot gas cap. These estimates of the effective radiating volume include the effects of shock-wave shape and standoff distance as well as the expansion of the flow as it progresses radially outward from the stagnation point. Additional effects considered in the reduction of the data are: (1) the expected spectral distribution of the radiation as reported in reference 1, (2) the spectral response of the photomultiplier, and (3) the diffraction of the light in passing through the first slit.

RESULTS

It should be emphasized at the outset that the measurements are rough and preliminary. The measured values are consequently believed to be correct only to within a factor of 2 or 3. The results of the tests in air are summarized in figure 2 where the total radiation per unit volume is plotted as a function of velocity. All data were obtained on models fired into air at less than atmospheric pressure. The measured radiation has been corrected to standard density by multiplying by the ratio of standard density to the computed density in the shock layer. This correction, which in some cases is as large as 35 percent, is justified for small density changes since the radiation is proportional to the number of particles radiating.

The theoretical results for equilibrium flow predicted in reference 1 are also shown in figure 2. All data points lie above the theoretical curve. For velocities above 15,000 ft/sec the agreement is fair. However, at velocities below 15,000 ft/sec the observed radiation exceeds the predicted value by a factor as large as thirty. This discrepancy may be due to the relatively slow rate of oxygen dissociation and the slow rate of excitation of molecular vibrations which result in a gas temperature temporarily higher than the equilibrium value. A crude estimate of the radiation in this nonequilibrium case may be obtained by computing the equilibrium radiation expected from the gas at the temperature predicted behind the shock wave for $\gamma = 1.4$. These values are shown in figure 2 as the curve labeled ideal gas temperature.

That a portion of the shock layer may indeed be out of equilibrium at the lower speeds is shown in figure 3. Here the variation of radiation relaxation time with velocity is shown according to Camac and others (ref. 2). In addition, the time required for a particle to flow from the shock wave to the stagnation point is shown for both the flat-faced and the spherical-nose models. At velocities below 14,000 ft/sec the entire shock layer may be out of equilibrium for the spherical-nose models. Most of the shock layer is in equilibrium on the flat-faced models, especially at the higher velocities.

In addition to the tests in air which were just discussed, some of the flat, copper-faced models were fired into carbon dioxide at a pressure of 1/10 atmosphere. The carbon dioxide contained about 2 percent to 5 percent air as a contaminant. This gives approximately the correct composition for the atmosphere of Venus as presently predicted. It was initially believed that the radiation in carbon dioxide might be many times stronger than the radiation in air. This belief was based on the relatively high emissivity of carbon dioxide observed in furnaces

(ref. 3). Actually, at the temperatures encountered in the shock layer, the carbon dioxide will dissociate into carbon monoxide, atomic oxygen, and molecular oxygen. In figure 4 the mole fractions of dissociation products are shown as a function of velocity for flight through carbon dioxide at a pressure of 1/10 atmosphere. These calculations assume thermodynamic equilibrium behind the shock wave. The breakup of the carbon dioxide begins at a velocity of 8,000 ft/sec and is virtually complete when a velocity of 20,000 ft/sec is reached. Consequently, if the radiation from the shock layer in carbon dioxide is to be computed, it is necessary to know the emissivities of carbon dioxide, carbon monoxide, and oxygen. At higher temperatures the emissivity of the carbon dioxide decreases with increasing temperature, whereas the emissivities of carbon monoxide and oxygen increase with increasing temperature. This suggests that a very rough estimation of the radiation may be obtained by using the emissivity of carbon dioxide up to a velocity of 8,000 ft/sec, where dissociation commences, and then assuming a constant value for the emissivity at higher velocities. Figure 5 shows the measured values of the radiation in carbon dioxide. In addition, the radiation predicted on the basis of the emissivity variation indicated in the inset of figure 5 is plotted. Two curves are given, the first uses the equilibrium temperature and the second uses the ideal gas temperature for $\gamma = 1.3$. The measured values lie between these two curves. At this point it should be mentioned that the estimation of the emissivity for carbon dioxide is very approximate and does not rest on as firm ground as does the estimation of the emissivity of air.

In figure 6 the measured values of the radiation in air and in carbon dioxide are compared. The radiation from the carbon dioxide is only slightly larger than from the air, instead of being much larger as initially expected. This measured difference, however, applies only for the velocity and density ranges covered by the tests. It is quite possible that at higher speeds or different densities the results would be radically different.

CONCLUSIONS

From the results obtained it may be concluded that:

1. The measured radiation in air agrees well with the radiation predicted on the basis of shock-tube results as long as the fluid in the shock layer is in equilibrium.
2. The radiation may be much greater if the fluid is not in equilibrium.
3. The radiation in carbon dioxide is only slightly larger than the radiation in air at least in the velocity and density range covered by these tests.

REFERENCES

1. Kivel, B., and Bailey, K.: Tables of Radiation From High Temperature Air. Res. Rep. 21 (Contracts AF 04(645)-18 and AF 49(638-61)), AVCO Res. Lab., Dec. 1957.
2. Camac, M., Camm, J., Keck, J., and Petty, C.: Relaxation Phenomena in Air Between 3000 and 8000° K. Res. Rep. 22 (Contract AF 04(645)-18), AVCO Res. Lab., Mar. 1958.
3. McAdams, William H.: Heat Transmission. Third ed., McGraw-Hill Book Co., Inc., 1954.

EXPERIMENTAL SETUP

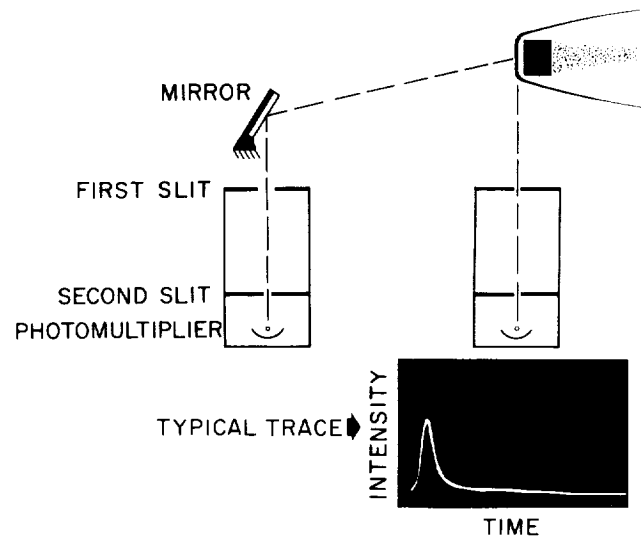


Figure 1

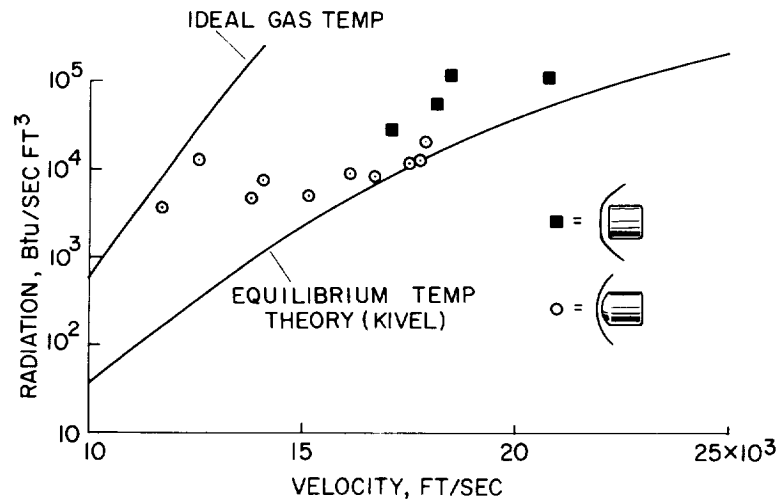
RADIATION IN AIR
ADJUSTED TO ATMOSPHERIC DENSITY IN SHOCK LAYER

Figure 2

RADIATION RELAXATION TIME AND FLOW TIME
THROUGH SHOCK LAYER
ADJUSTED TO ATMOSPHERIC DENSITY IN SHOCK LAYER

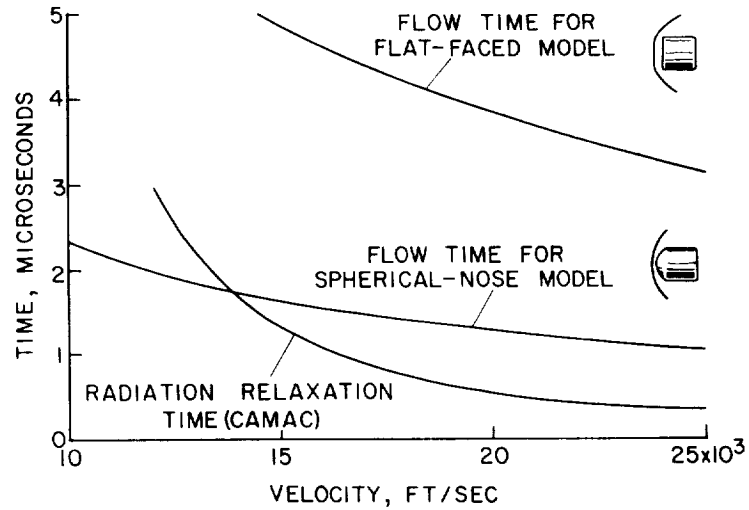


Figure 3

EQUILIBRIUM COMPOSITION OF CO₂ BEHIND A NORMAL
SHOCK WAVE
RANGE PRESSURE EQUALS 1/10 ATMOSPHERE

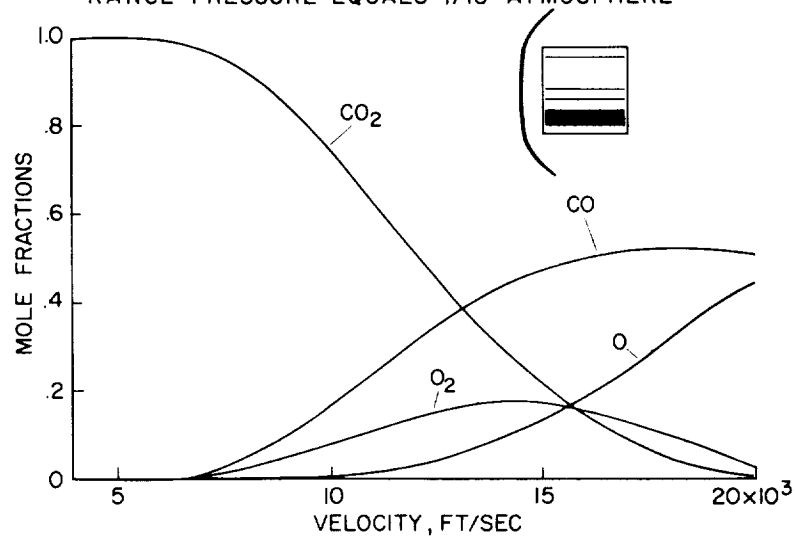


Figure 4

RADIATION IN CARBON DIOXIDE ADJUSTED TO ATMOSPHERIC DENSITY IN SHOCK LAYER

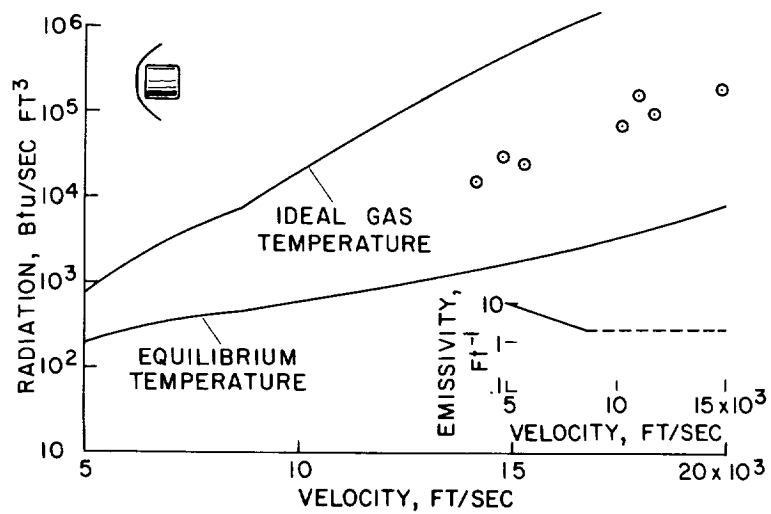


Figure 5

COMPARISON OF RADIATION IN AIR AND IN CO₂ ADJUSTED TO ATMOSPHERIC DENSITY IN SHOCK LAYER

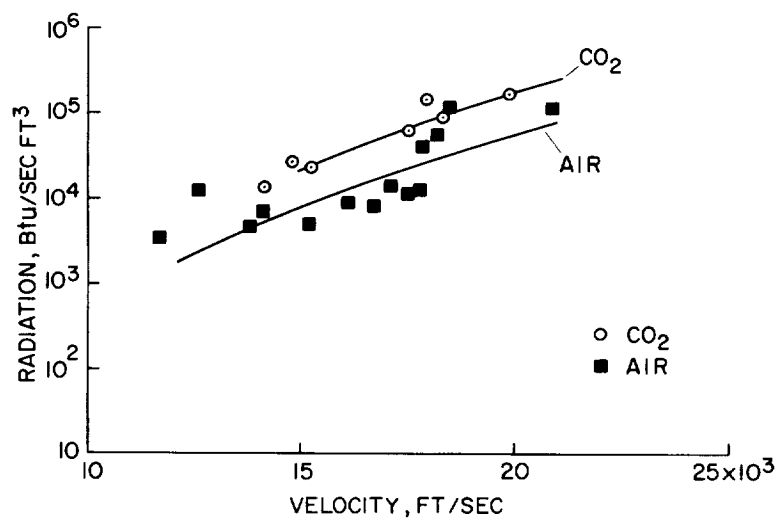


Figure 6

~~CONFIDENTIAL~~

~~CONFIDENTIAL~~

|

RADIATIVE HEAT TRANSFER AT PARABOLIC ENTRY VELOCITY

By Kenneth K. Yoshikawa, Bradford H. Wick,
and John T. Howe
Ames Research Center

INTRODUCTION

This paper has a twofold purpose: (1) to provide an assessment of the importance of radiative heating in the design of manned vehicles entering the earth's atmosphere at parabolic velocity and (2) to present a brief summary of the results of an exploratory analysis of the process of shielding a vehicle nose from radiation by injecting an absorbing gas into the boundary-layer air.

COMPARISON OF MAGNITUDE OF RADIATIVE AND CONVECTIVE HEAT TRANSFER

In making the assessment of the importance of the radiative heat transfer, the available data on the emissivity of high-temperature air was applied to calculate the stagnation point radiative heating for a number of parabolic entry vehicles and entry conditions. Corresponding values of convective heating were also determined. The geometry and flow equation used for calculating the stagnation point radiative heating rates are shown in figure 1. The shaded portion of the gas cap radiates to the stagnation point. The transfer of heat is, in detail, a complicated process. For our purposes, however, certain assumptions could be made which lead to the simple equation shown for the radiative heating rate at the stagnation point. The factor δ in the equation is the shock standoff distance, and the factor E_t is the total energy being radiated per unit time from each unit volume. The factor of $1/2$ is to account for the fact that only one-half the total energy leaves each side of a thin shock layer.

Appendix A summarizes (1) the assumptions upon which the equation is based, (2) the procedures and information used in applying the equation, and (3) the limitations and probable accuracy of the estimates. Also given in appendix A are the stagnation point radiative heating rates for a wide range of velocities and altitudes and a comparison of the rates with the corresponding stagnation point laminar convective heating rates. Appendix B defines the symbols used in this paper. As indicated in

appendix A, the accuracy of the radiative heating estimates are limited by uncertainties as to the accuracy and applicability of the values of E_t used. The particular values of E_t used are for air in equilibrium behind the shock wave. As noted in appendix A, the use of equilibrium values of E_t appears to be satisfactory for a number of parabolic velocity entry vehicles and entry conditions. A factor of uncertainty of 2 appears to be a possibility for the equilibrium values of E_t .

There is a distinct possibility, however, of nonequilibrium radiation for some vehicles, depending upon their geometry and weight. In this event, the radiation rates could be at least an order of magnitude higher than those for equilibrium conditions. Granting that there are these uncertainties connected with the radiative heating estimates, it is believed, however, that they are useful in two respects. The estimates can be used to provide a qualitative answer as to the importance of radiative heat transfer for parabolic velocity entries and, also, provide a good indication of the vehicle parameters which influence the radiative heat transfer.

The radiative and convective heating rate estimates for parabolic entry velocity were for the single-pass undershoot type of entry limited to a maximum deceleration of $10g$. (For a further description of the undershoot type of entry, see ref. 1.) Some of the estimates for zero-lift entries are given in figure 2. The maximum radiative heating rate is plotted in Btu/sec-sq ft as a function of nose radius in feet. The dashed curve is for spheres of varying radii, and the solid curve is for a blunt body consisting of a cylinder with nose shapes of varying radii. The nose shapes were derived by progressively blunting a 45° half-angle cone until finally the nose was only a spherical segment. Both heating-rate curves are for zero lift-drag ratio, parabolic entry velocity, and a vehicle loading of 100 lb/sq ft. Also shown in the figure is a simple equation for the maximum radiative heating rate. The equation was empirically derived from the heating-rate estimates for a number of zero-lift entries. (Limitations to the use of this equation are given in appendix A.) The equation shows that the radiative rate varies directly with the vehicle nose radius and roughly is the square of W/A and $1/C_D$. The maximum radiative heating rate curve for the spheres illustrates the linear relationship between heating rate and R that exists when the other two factors are constant. The blunt-body curve illustrates the effect of a coupling between nose radius and C_D for the case of a practical vehicle of a given weight and area. In this case an increase in nose radius causes an increase in C_D . Consequently, the apparent effect of nose radius is much less than that for the spheres. Maximum convective heating rates for the two cases are shown in figure 3. These are for equilibrium laminar boundary-layer conditions. Also shown in the figure is the simple equation for maximum convective heating rate. A comparison of the equations for the

two types of heating shows that they are functions of the same vehicle factors. However, the factors have a more powerful influence in the case of radiative heating.

It is also of interest to compare the maximum radiative and convective rates for the blunt-body case. To make this comparison easier, the blunt-body curves have been transposed to figure 4. The radiative rate ranges from a small fraction of the convective for a 2-foot radius to nearly equal to the convective for a 10-foot radius. The change with nose radius is due more to the reduction in convective heating than to the increase in radiative heating.

Next to be considered are the time histories of the heating rates and the heat absorbed at the stagnation point during the complete entry. The pertinent features of the time histories can be briefly stated. The radiative and convective rates peaked at nearly the same time and the period of the radiative heating was about $1/3$ of that for the convective. The radiative and convective heat absorbed at the stagnation point during the complete heating periods is shown in figure 5. Here the heat absorbed in Btu/sq ft is plotted as a function of nose radius for the blunt-body case. The trends of these curves are found to be similar to the heating-rate curves. The ratio of radiative heat to convective heat for a given nose radius is less than the corresponding ratio for the heating rates. This is because of the fact that the period of the radiative heating was shorter than that for the convective heating.

Another factor of importance in assessing the radiative heating contribution is the total heat absorbed during entry. In order to provide values of total heat absorbed, it was necessary to make some approximations in the case of radiative heating. It was found that for the 2-foot-radius nose, the total radiative heat absorbed was less than 5 percent of the convective, and in the case of the 10-foot-radius nose the total radiative heat was about 25 percent of the convective. This increase in percentage in going from the 2-foot to the 10-foot radius was almost entirely because of a change in total radiative heat absorbed.

In considering the effect of L/D on stagnation point radiative heating rates, one should account for the interrelationship of L/D and the pertinent vehicle parameters; namely, nose radius R , weight-to-area ratio W/A , and drag coefficient C_D . It is not possible to select completely typical variations of the vehicle parameters with L/D . Further, there is a question of whether W/A and R should vary with L/D . In the case of C_D , there is no question that C_D should decrease with increasing L/D , but only a question of how C_D should decrease. The particular variation chosen was that given by Newtonian hypersonic flow for a flat wing at high angles of attack. The stagnation point radiative heating rates for lifting entry conditions are shown in

figure 6. Maximum radiative heating rate per unit nose radius is plotted as a function of L/D for three selected values of weight-to-area ratio. The heating rate scale is logarithmic. The results are for L/D held constant during entry until zero flight-path angle is reached. Further, the entries are the single-pass undershoot type limited to a maximum deceleration of $10g$. With deceleration held constant with increasing L/D , a broadening of the entry corridor is obtained. For constant W/A , there is an order of magnitude increase in the radiative heating rate per unit nose radius in going from $L/D = 0.5$ to $L/D = 2.0$. This increase is due to the fact that the higher L/D vehicle initially plunges deeper into the atmosphere, as a consequence of its lower drag coefficient and somewhat higher entry angle. Now a valid objection can be raised that the effect of L/D should not be compared at constant W/A . A reduction in W/A with increasing L/D undoubtedly would be more realistic. In fact, a low value of W/A appears to be essential if high stagnation point radiative rates are to be avoided at the higher values of L/D .

These radiative rates for the lifting-entry case are compared in figure 7 with the corresponding convective rates. The ratio of the radiative-heating rate to the convective rate per unit radius is plotted as a function of L/D for the previously selected values of W/A . A logarithmic ordinate scale is used. It is noted that the ratio increases by about an order of magnitude when L/D is increased from 0.5 to 2.0 at constant W/A . Again note the desirability of low W/A for the higher L/D values.

In addition to examining the stagnation point heating rates for lifting-entry vehicles, one should also examine heating rates at other points on the vehicles and the total heat absorbed by the heat shield. This is particularly necessary for high angle-of-attack entries. Unfortunately, such information is yet to be obtained.

Now consider these results from the standpoint of the design of heat-protection systems for parabolic-entry vehicles. It is apparent from the heating-rate estimates that heat-protection systems will be needed which are effective against both radiative and convective heating. A statement cannot be made, at this time, as to the complexity and weight penalty due to uncertainties in the radiative heating estimates and a lack of adequate information as to the reaction of heat-shield materials to combined radiative and convective heating. Of particular concern is the reaction of ablative materials which look very promising for protection against convective heating during parabolic entries. A point that needs to be mentioned about subliming ablative materials is that they are not likely to have as high an effective heat of ablation for radiative heating as they have for convective heating. The high effective heat of ablation in the case of convective heating is largely due to the heat-blocking effect of the vaporized materials. In the case of

radiative heating, a heat blocking is not likely to occur unless the vaporized materials prove to be strongly absorbing.

USE OF GAS INJECTION TO REDUCE RADIATIVE HEAT TRANSFER

The interest in the ablative type of heat shield stems, of course, from its attractiveness from the standpoints of weight and simplicity. In the event, however, that ablative materials cannot be found which will hold up when exposed to radiative heating, more complicated heat-protection systems will be required. One possible system involves the injection of a highly absorbing gas into the boundary layer. This gas could be blown through the vehicle wall or ablated from the surface. An exploratory analysis of this process has been made by Howe (ref. 2). The method of analysis and the results are briefly introduced and outlined in the following discussion.

It is well known that transpiration of a gas through the vehicle wall into the boundary layer can greatly diminish the convective heating at the surface. The possibility exists that the radiative heat transfer to the vehicle can also be diminished if the gas injected into the boundary layer is opaque to radiation. Of course the absorption of radiation by the opaque gas would raise the temperature gradient of the boundary layer at the wall and therefore increase the convective heat transferred to the vehicle; the question is, could a net saving of heat transfer be achieved by injection of the opaque gas, and what absorption properties need this gas have in order to be effective.

It is not a simple matter to answer these questions in an exact sense. In general, the treatment of a radiation field within a binary compressible boundary layer involves solving nonlinear, coupled, partial differential-integral equations.

An exploratory analysis has been made in which simplifying assumptions make the problem more tractable. If the results of this analysis are positive, one would be encouraged to investigate further experimentally or theoretically.

Figure 8 shows a sketch of the physical model analyzed and lists the equations used. The radiant energy incident on the boundary layer is assumed to be directed normal to the vehicle surface and it is assumed that no scattering occurs. The vehicle surface is at a temperature much lower than that of the shock layer. The bulk of the opaque gas is in the cold regions of the boundary layer and radiation emitted by this "gray" gas can be neglected in comparison with the radiation absorbed.

The laminar compressible boundary layer is treated as an inert binary mixture of air and the opaque gas. The partial differential equations to be solved are the usual continuity, momentum, and diffusion equations, a modified energy equation (to include the divergence of the radiation flux), and the absorption law (in which I is the local intensity of radiation, y is the direction outward normal to the wall, ρ_f is the local density of the foreign absorbing gas, and k is the absorption coefficient).

These partial differential equations are transformed to a set of ordinary differential equations by making the usual boundary-layer stagnation-region assumptions, resulting in a set of nonlinear coupled ordinary differential equations which must be solved in a certain sequence by numerical methods. The usual boundary conditions are employed. Some of the results of the analysis follow.

Figure 9 shows the ratio of intensity of radiation striking the wall to that incident at the outer edge of the boundary layer as a function of C for two different rates of blowing at the wall. The term $-F_{\text{wall}}$ is the usual boundary-layer parameter proportional to the blowing rate by the relationship (in the axisymmetric stagnation region)

$$(\rho v)_{\text{wall}} = -F_{\text{wall}} \sqrt{\beta \rho_e \mu_e}$$

where $(\rho v)_{\text{wall}}$ is the product of mixture density and velocity normal to the wall at the wall and β , ρ_e , and μ_e are velocity gradient parallel to the wall, density, and viscosity coefficient at the outer edge of the boundary layer, respectively. As shown in the figure, the abscissa C is linearly related to the absorption coefficient k . It is seen that the fraction of the incident radiation which strikes the wall diminishes exponentially with increasing absorption coefficient, and diminishes with increasing blowing rate. For $C = 1$ and $-F_{\text{wall}} = 1$, 93 percent of the incident radiation is absorbed by the opaque gas. At first glance, this appears to be very advantageous. However, before forming an opinion, one should first assess what $C = 1$ means in terms of actual gas absorption coefficients. Furthermore, how does the total (radiative and convective) heat-transfer rate with injection of an absorbing gas compare with that of injection of a nonabsorbing gas?

In relating $C = 1$ to actual gas absorption coefficients, it is pointed out that the required value of the absorption coefficient k is dependent on the flight condition because of the relationship with C . For a flight speed of 34,000 ft/sec at 175,000-foot altitude and a body nose radius of 1 to 10 feet, the required k is of the order of 10^5 to 10^7 sq ft/slug for values of C from 0.1 to 1.5. Little is known of

the absorption coefficient properties of even ordinary gases. It appears that carbon dioxide has an absorption coefficient of the order of 10 sq ft/slug at ordinary pressures and temperatures up to 1,600° C. The coefficient for water vapor is roughly an order of magnitude higher than that of carbon dioxide; therefore, the gas to be blown into the boundary layer should be 3 to 5 orders of magnitude better than water vapor in this regard.

Assuming that this strongly absorbing gas is injected into the boundary layer, the radiation absorbed by the gas increases the temperature gradient and, therefore, the convective heat-transfer rate at the vehicle surface. The question which remains to be answered is whether or not a net saving of heat transfer is achieved by blowing an opaque gas. Figure 10 shows the ratio of total rate of heat transferred to the wall with injection of an absorbing gas to that with injection of a transparent gas as a function of the dimensionless absorption coefficient C . The dimensionless incident radiation intensity I_e is proportional to the actual intensity. The symbol j_e is the sum of enthalpy and kinetic energy exterior to the boundary layer. It is seen that there is an overall saving in heat transfer (by as much as 68 percent) and that it increases for increasing values of absorption coefficient and increasing values of incident radiation flux.

CONCLUDING REMARKS

Briefly, the results of this exploratory analysis indicate two things. First, the opaque gas must have a very high absorption coefficient in order to be effective. Second, a net saving of heat transfer can be achieved by blowing an opaque gas into the boundary layer to absorb radiation incident on the vehicle. Efforts to find gases with high absorption coefficients are worthwhile and necessary. Additional theoretical and experimental work is warranted to extend and verify the results of this approximate analysis.

The assessment of the radiative heating problems can be summarized as follows. On the basis of available knowledge of the radiation from high-temperature air, it is concluded that radiative heat transfer will be important in the design of parabolic entry vehicles. The vehicle parameters influencing the radiative-heating rates were determined and found to be the same as those for convective-heating rates. These were nose radius, vehicle weight-to-area ratio, and drag coefficient. Their effect was greater in the case of radiative heating, and nose radius had an opposite effect. Conclusions cannot be drawn at present as to the influence of radiative heat transfer on vehicle shape, and heat-protection-system complexity and weight because of uncertainties as to

~~CONFIDENTIAL~~

the radiant energy emitted from shock heated air and a lack of information on the reaction of heat-shield materials to combined radiative and convective heating.

~~CONFIDENTIAL~~

APPENDIX A

SUMMARY OF RADIATIVE HEATING ESTIMATES

Basic Radiative Heating Rate Equation (Fig. 1)

In deriving the equation shown in figure 1, the following four assumptions were made: (1) the radiation intensity is uniform within the gas-cap volume radiating to the stagnation point, (2) radiation is not absorbed within the volume, (3) the stagnation point absorbs all of the incident radiation without any reemission, and (4) the shock standoff distance δ is small compared to the nose radius R . The third assumption is equivalent to assuming that the stagnation point is a black body which is cold relative to the air in the gas cap. With these assumptions the radiative-heating rate can be expressed by the following equation:

$$\dot{q}_r = \frac{E_t}{4\pi} \int_0^\tau \frac{\cos \theta}{r^2} d\tau$$

where r is the radius vector between an elemental gas volume and the stagnation point, θ is the angle between the free-stream velocity and the radius vector, and τ is the gas-cap volume radiating to the stagnation point. The equation reduces to the simple equation shown in figure 1 which is repeated here

$$\dot{q}_r = \frac{\delta E_t}{2}$$

This equation applies to the radiation from a plane shock layer to a plane wall. With the fourth assumption (i.e., δ is small compared to R), it is valid for the radiation from a spherical segment shock layer to the stagnation point of a spherical nose (i.e., the geometry shown in fig. 1). If the fourth assumption is not made, then the radiative heating rate for the geometry shown in figure 1 can be expressed as

$$\dot{q}_r = k_s \frac{\delta E_t}{2}$$

The factor k_s , termed the shape factor, thus is the ratio of the stagnation point heating rate of a spherical nose to the heating rate per unit area of a plane wall.

Procedures and Data Used in Applying Basic Radiative Heating Rate Equation

In applying the equation to a particular entry trajectory it is necessary to determine the relation between velocity and altitude and the associated values of atmospheric and gas-cap densities and temperatures. With this information, values of δ and E_t can then be determined. The trajectory calculations were made by the use of Chapman's approximate analytical method of studying entry motion (ref. 1). In determining the densities and temperatures of the shock-heated air, the assumption was made that the heated air was in equilibrium. The equilibrium values of densities and temperatures at the required velocity and altitude conditions were obtained from reference 3. Shock standoff distances were evaluated by the following expression which was derived by Hayes (ref. 4):

$$\delta/R = \frac{\rho_1/\rho_2}{1 + \sqrt{2 \rho_1/\rho_2}}$$

where ρ_1 is the atmospheric density and ρ_2 is the equilibrium shock-layer density. The values of E_t for equilibrium conditions were obtained from charts of $E_t/2$ which were presented in reference 5.

Accuracy and Limitations of the Radiative Heating Estimates

In determining the accuracy and limitations of the estimates there are four principal questions that need to be answered. These are

(1) For what conditions is it valid to assume that equilibrium conditions exist in the gas cap?

(2) For what conditions is it valid to assume that the radiation intensity is uniform and that no absorption of radiation occurs within the gas cap?

(3) What is the probable accuracy of the values of E_t used?

(4) What is the probable accuracy of the estimates of the shock standoff distances?

Figure 11 is useful in considering these questions. The figure is a velocity-altitude map on which important regions have been indicated. In the upper right of the figure, portions of the velocity-altitude variations for two representative parabolic velocity entries are shown. The region of stagnation-point maximum radiative heating rates for single-pass, 10-g undershoot entries at parabolic velocity is also indicated; for these entries, the maximum radiative heating rate occurred at approximately 34,000 feet per second. The altitude-velocity boundary labeled "Radiative relaxation distance = Shock standoff distance, $R = 1$ foot" is useful in considering the validity of the assumption that the shock-heated air is in equilibrium. This boundary was based on an extrapolation of radiative relaxation rate data obtained from shock-tube measurements (ref. 6) at conditions corresponding to lower velocities and altitudes than those for parabolic velocity entries. In view of the extrapolation required, the boundary is very approximate at velocities near parabolic entry. For a nose radius other than 1 foot, a boundary can be determined roughly by the relation $\rho_1 R = \text{Constant}$. The boundary is useful in the following way. If the maximum radiative rate predicted on the assumption of equilibrium conditions occurs at an altitude that is either at or above the boundary, then the equilibrium assumption is invalid, since nonequilibrium conditions exist throughout the shock layer except near the wall. At some lower altitude, equilibrium will be reached at a short enough distance behind the shock front for nonequilibrium radiation effects to be unimportant. At the present time, not enough is known about nonequilibrium radiation to permit this lower boundary to be defined. The second question, regarding the validity of the assumption of uniform radiation intensity and no absorption within the gas cap, is answered by comparing the altitude of the maximum radiative heating rate for a given entry trajectory with the altitude below which radiation decay and absorption become important. A larger radius is the more critical in this case; hence the boundary is shown for the largest nose radius considered, a 10-foot radius. If the altitude for the maximum radiative heating rate, based on the assumption of uniform radiation and no absorption, lies above this boundary, then the assumption is valid. This boundary where radiation decay and absorption become important is based on the results of an unpublished analysis by Dean R. Chapman and Kenneth K. Yoshikawa of the Ames Research Center. By examining the question as to the probable accuracy of the equilibrium values of E_t used, it can be seen from figure 11 that the region of maximum radiative heating rates for the parabolic entries considered is well outside the region covered by AVCO shock-tube measurements. Thus,

as mentioned in the main part of the paper, values of E_t determined by theoretical extrapolations were used. (It should be mentioned that, even for the region denoted as AVCO air radiation data, the values of E_t were based on theory as modified by a limited number of measurements spread over the designated region.) There is considerable uncertainty as to the accuracy of these extrapolated values of E_t ; the present best guess is a factor of uncertainty of 2. In the case of the values of shock standoff distances, no experimental check of the values given by Hayes' relation (ref. 4) has been obtained at conditions approaching those for parabolic entry velocities. Comparison of predicted and measured values at lower velocities, however, has indicated agreement within 10 percent.

Radiative Heating Rate Values for a Range of Velocities and Altitudes

Presented in figure 12 are values of stagnation point radiative heating rates for a wide range of velocities and altitudes. The values were estimated by use of the procedures and data previously described and are subject to the limitations and uncertainties just described. In figure 13, these radiative heating rates are compared with the corresponding equilibrium laminar convective heating rates. The convective heating rates were calculated by the method given in reference 2.

Maximum Radiative and Convective Heating Rates for Specific Parabolic Velocity Entries

The empirical equations for maximum radiative and convective heating rates which were given in figures 2 and 3, respectively, have certain restrictions as to their application. They apply only to single-pass, nonlifting, parabolic-velocity entries which are limited to a maximum deceleration of $10g$.

APPENDIX B

SYMBOLS

Heating-Rate Estimates

A	vehicle reference area, sq ft
C_D	vehicle drag coefficient based on A
E_t	total energy radiated per unit time per unit volume in gas cap, Btu/sec-cu ft
k_s	shape factor (see appendix A)
\dot{q}	stagnation point heating rate, Btu/sec-sq ft
R	vehicle nose radius, ft
r	radius vector from unit volume in gas cap to stagnation point, ft
\bar{V}	ratio of entry velocity to satellite velocity
W	vehicle weight, lb
δ	shock standoff distance, ft
θ	angle between radius vector r and flight-velocity vector, deg
ρ	mass density of air, slugs/cu ft
τ	volume of gas cap radiating to stagnation point, cu ft

Subscripts:

r	radiative
c	convective
1	ahead of shock wave
2	behind shock wave

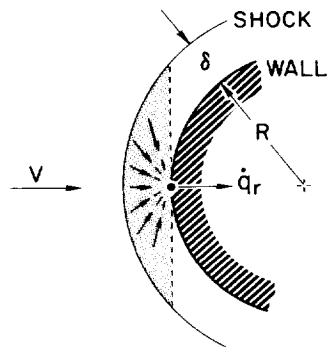
Radiation Shielding Analysis

C	dimensionless absorption coefficient, $k\sqrt{\frac{\rho_e\mu_e}{2\beta}}$
F	blowing rate parameter, $-F_{\text{wall}} = \frac{(\rho v)_{\text{wall}}}{\sqrt{\beta\rho_e\mu_e}}$
I	intensity of radiation in y-direction, ft-lb/sec-sq ft
j	enthalpy plus kinetic energy per unit mass, sq ft/sec ²
k	absorption coefficient, sq ft/slug
l	dimensionless intensity of radiation, $l_e = I_e j_e \sqrt{2\rho_e\mu_e\beta}$
\dot{q}	stagnation-point heating rate, Btu/sec-sq ft
v	velocity of gas in y-direction, ft/sec
y	coordinate normal to the wall, ft
β	velocity gradient parallel to wall at outer edge of boundary layer, 1/sec
μ	coefficient of viscosity of air, lb-sec/sq ft
Subscripts:	
e	outer edge of boundary layer
f	foreign gas
wall	properties evaluated at wall

REFERENCES

1. Chapman, Dean R.: An Analysis of the Corridor and Guidance Requirements for Supercircular Entry Into Planetary Atmospheres. NASA TR R-55, 1960.
2. Howe, John T.: Radiation Shielding of the Stagnation Region by Transpiration of Opaque Gas. (Prospective NASA paper.)
3. Hochstim, Adolf R.: Gas Properties Behind Shocks at Hypersonic Velocities. I. Normal Shocks in Air. Rep. No. ZPh(GP)-002, CONVAIR, Jan. 30, 1957.
4. Hayes, Wallace D.: Some Aspects of Hypersonic Flow. The Ramo-Wooldridge Corp., Jan. 4, 1955.
5. Kivel, B., and Bailey, K.: Tables of Radiation From High Temperature Air. Res. Rep. 21 (Contracts AF 04(645)-18 and AF 49(638)-61), AVCO Res. Lab., Dec. 1957.
6. Camac, M., Camm, J., Keck, J., and Petty, C.: Relaxation Phenomena in Air Between 3,000 and 8,000° K. Res. Rep. 22 (Contract AF 04(645)-18), AVCO Res. Lab., Mar. 1958.

GEOMETRY AND EQUATION FOR RADIATIVE HEATING



RADIATIVE HEATING RATE:

$$\dot{q}_r = \left(\frac{\delta E_t}{2} \right)$$

WHERE:

δ = SHOCK STANDOFF, FT

E_t = TOTAL RADIATION ENERGY RATE PER UNIT VOL, Btu/SEC-FT³

Figure 1

STAGNATION POINT MAXIMUM RADIATIVE HEATING RATES $L/D=0, \bar{V}=\sqrt{2}, W/A=100$

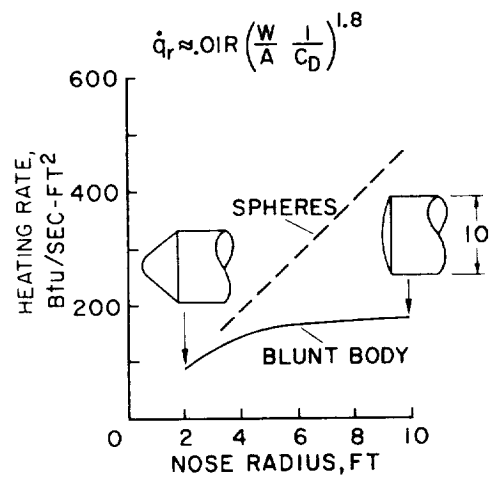


Figure 2

STAGNATION POINT MAXIMUM CONVECTIVE HEATING RATES

$$L/D=0, \bar{V}=\sqrt{2}, W/A=100$$

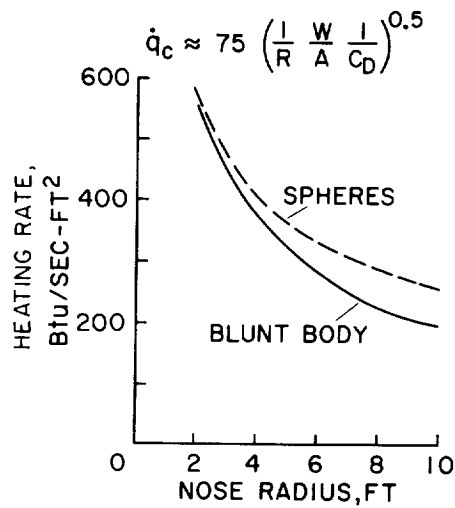


Figure 3

STAGNATION POINT MAXIMUM HEATING RATES FOR BLUNT BODY

$$L/D=0, \bar{V}=\sqrt{2}, W/A=100$$

$$\dot{q}_c \approx 75 \left(\frac{1}{R} \frac{W}{A} \frac{1}{C_D} \right)^{0.5}$$

$$\dot{q}_r \approx .01 R \left(\frac{W}{A} \frac{1}{C_D} \right)^{1.8}$$

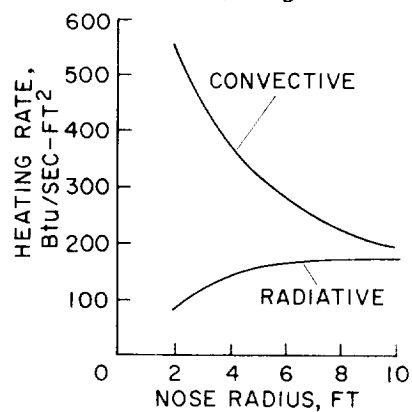


Figure 4

STAGNATION POINT HEAT FOR BLUNT BODY $L/D=0$, $\bar{V}=\sqrt{2}$, $W/A=100$

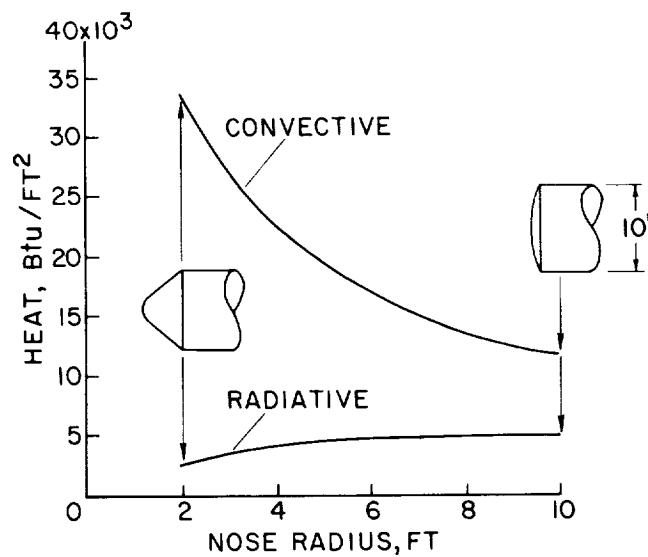


Figure 5

STAGNATION POINT MAXIMUM RADIATIVE HEATING RATES FOR LIFTING ENTRY

$$\bar{V} = \sqrt{2}$$

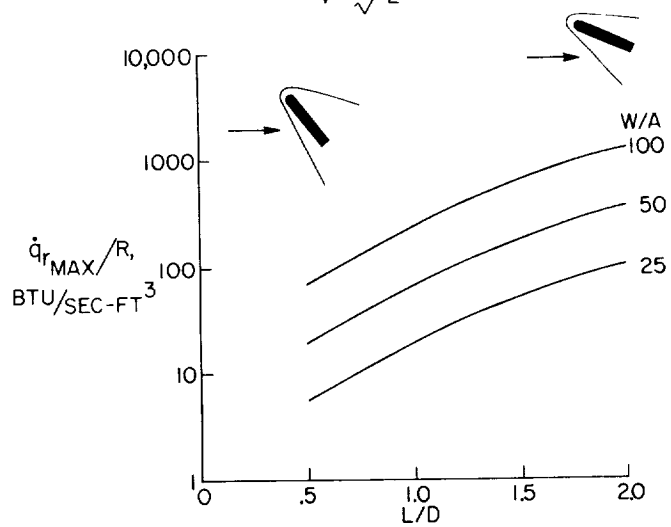


Figure 6

RATIO OF MAXIMUM RADIATIVE-TO-CONVECTIVE HEATING RATES FOR LIFTING ENTRY

$$\bar{V} = \sqrt{2}$$

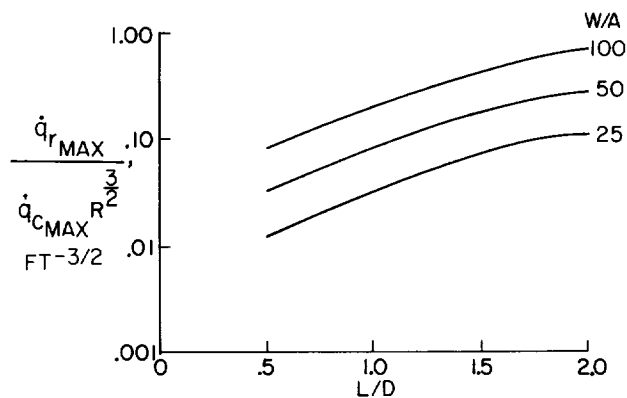


Figure 7

PHYSICAL MODEL AND EQUATIONS FOR RADIATION SHIELDING

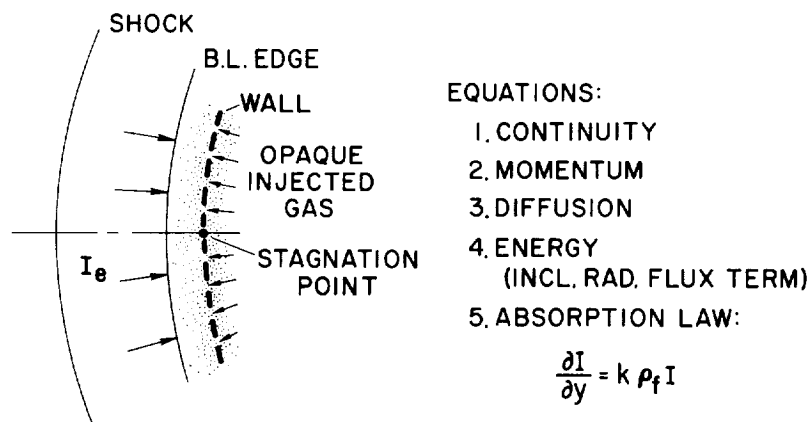


Figure 8

RADIATIVE ABSORPTION IN BOUNDARY LAYER

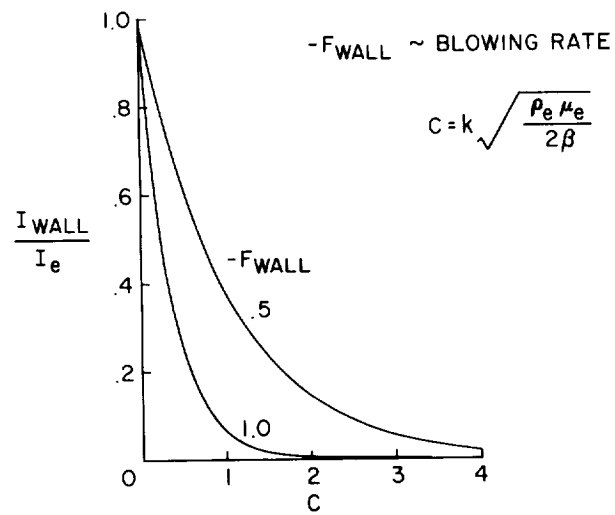


Figure 9

TOTAL RATE OF HEAT TRANSFER COMPARISON

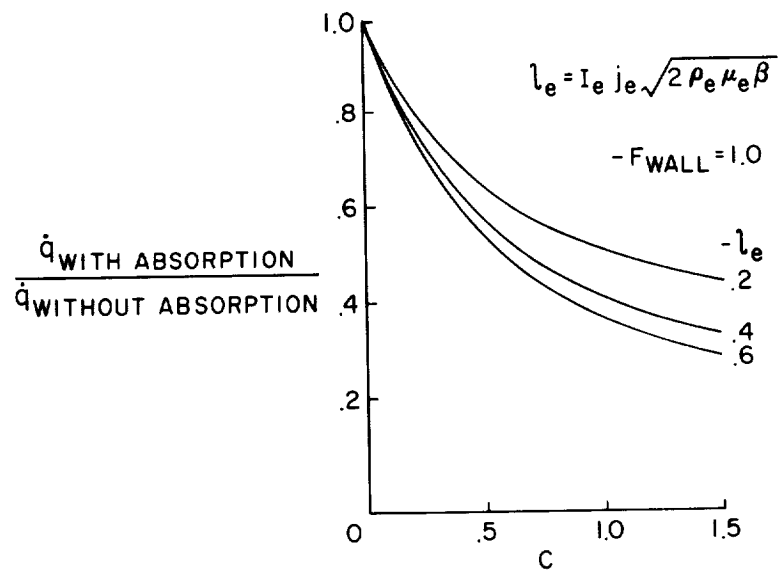


Figure 10

IMPORTANT VELOCITY-ALTITUDE REGIONS

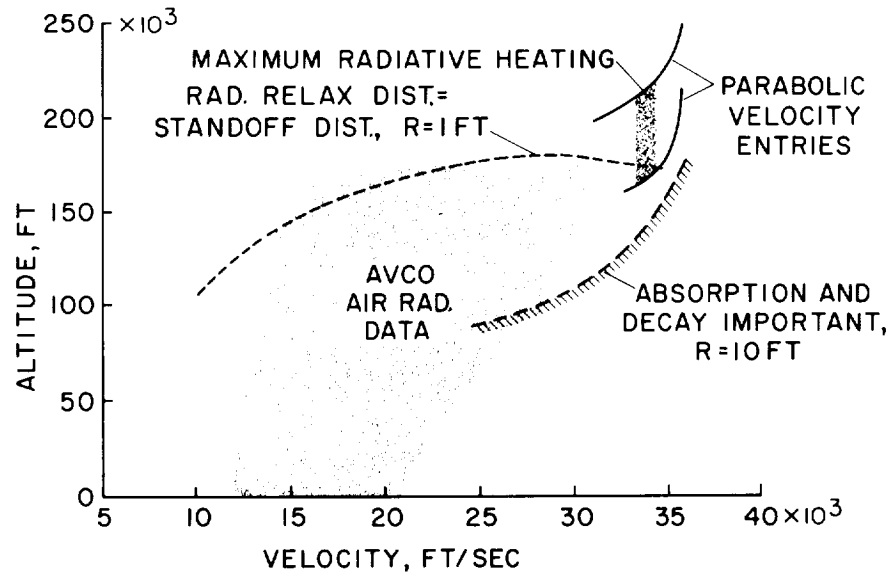


Figure 11

RADIATIVE HEATING

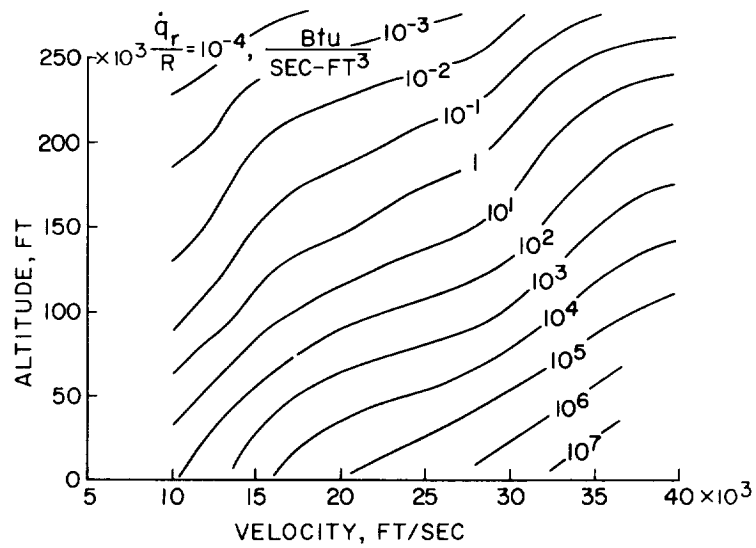


Figure 12

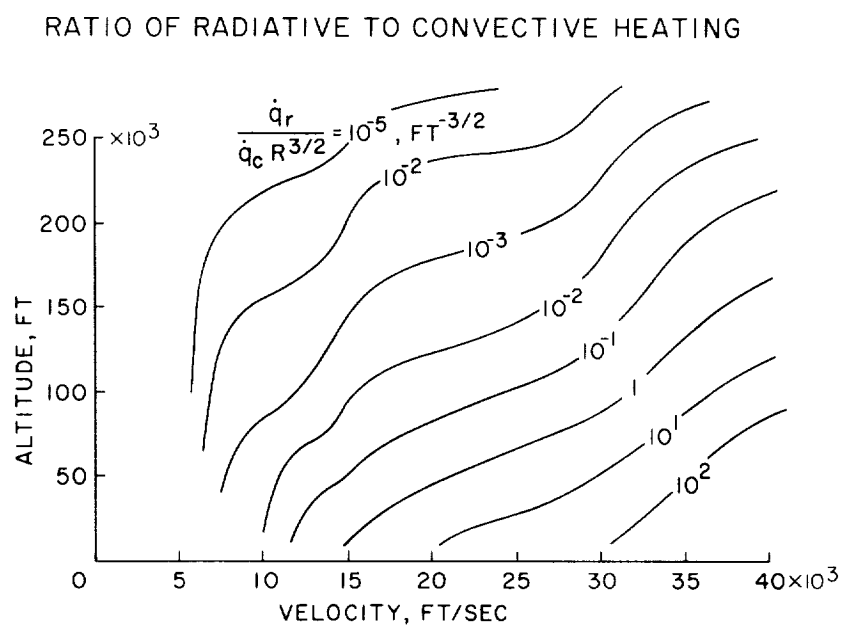


Figure 13

THE AERODYNAMIC CHARACTERISTICS OF SOME LIFTING BODIES

By David H. Dennis and George G. Edwards
Ames Research Center

SUMMARY

Lifting bodies having low fineness ratio and hypersonic lift-drag ratios of about 0.5 are discussed briefly. Results of a recent investigation of relatively slender blunt half-cones show hypersonic maximum lift-drag ratios of about 1.5. It is demonstrated that a blunt half-cone with a half-cone angle of 13° can be modified to form an entry vehicle having the capability of a conventional landing while retaining a hypersonic lift-drag ratio of about 1.5. Some preliminary static stability and control results are presented.

INTRODUCTION

Studies of vehicles suitable for entry into the earth's atmosphere have covered a wide range of configurations including nonlifting and lifting bodies and a variety of winged shapes. This paper presents some of the work performed at Ames Research Center on the lifting-body portion of the spectrum of possible entry vehicles. To be discussed are bodies consisting of portions of blunt cones. The first two bodies, to be discussed only briefly, have lift-drag ratios of about 0.5 and have, therefore, rather limited maneuvering capability during entry. The third configuration, a relatively slender, blunt half-cone, has considerably greater maneuverability due to its lift-drag ratio of about 1.5 at hypersonic speeds. The aerodynamic characteristics of this basic half-cone shape are shown. Modifications made to provide for adequate subsonic characteristics and for control throughout the speed range are described and test results are presented.

SYMBOLS

C_L	lift coefficient
C_l	rolling-moment coefficient
C_m	pitching-moment coefficient
$C_{m,0}$	pitching-moment coefficient at $C_L = 0$
C_n	yawing-moment coefficient
C_{l_β}	effective dihedral parameter
C_{m_α}	static longitudinal stability parameter
C_{n_β}	static directional stability parameter
L/D	lift-drag ratio
$(L/D)_{\max}$	maximum lift-drag ratio
l	body length
M	Mach number
R	Reynolds number
α	angle of attack, deg
δ	deflection of control surface, deg
δ_E	elevon deflection, deg
δ_Y	yaw-flap deflection, deg

DISCUSSION

Bodies Having Low Lift-Drag Ratios

Results for a body having a low lift-drag ratio were presented in reference 1. The body shape tested and some of the measured

aerodynamic characteristics are reviewed briefly in figures 1 and 2. Figure 1 shows a three-view sketch of the body, which is essentially a blunt 30° half-cone with four low-aspect-ratio flaps for control. The aerodynamic characteristics of this particular configuration have been determined over a wide speed range from tests in several wind tunnels. Some of the measured and estimated aerodynamic characteristics are shown in figure 2. At the left of figure 2 is the variation with Mach number of maximum trimmed lift-drag ratio. The experimentally determined lift-drag ratio is slightly more than 0.5 at the higher Mach numbers. This value agrees well with the theoretical value of 0.56 for $M = \infty$ that was calculated with the use of impact theory. Also shown (fig. 2) as functions of Mach number are the experimentally determined static longitudinal- and lateral-directional stability derivatives along with estimated values of these characteristics from impact theory. The particular points to be observed are as follows: First, the configuration was statically stable about the pitch and yaw axes and had positive dihedral effect; second, the stability levels were relatively insensitive to variations of angle of attack near the attitude for $(L/D)_{\max}$ or to variations of Mach number at the higher supersonic speeds; and, third, the performance and stability at high speeds were well predicted in this case with the use of simple impact-theory calculations.

Studies have continued on other lifting bodies having lift-drag ratios of about 0.5 at hypersonic speeds. An investigation has been initiated recently on another cone-segment-type body. The particular shape, shown in figure 3, is approximately one-sixth of a blunt cone. The cone half-angle is 58° and, at the attitude where the estimated value of L/D is 0.5, the cone axis is aligned with the stream. With the high incidence angle of the conical surface, this body would experience higher heating rates over a relatively smaller surface than the 30° half-cone. Thus, this shape would be more attractive for use with ablation-type thermal protection.

Initial experimental results obtained with the cone-segment body of the type presented in figure 3 show that the measured value of L/D at the design attitude agrees with the estimated value of 0.5. The body is longitudinally stable about its center of volume but it is considerably out of trim in the present configuration. Also, as in the case of most lifting configurations operating at high angles of attack, this shape has the disadvantage of having a negative lift-curve slope. Further analysis and testing will be required to establish the desirability of employing body shapes of this type.

Returning again to the blunt half-cone shapes, the generally favorable aerodynamic properties of the 30° blunt half-cone indicated that study of other bodies of this type might prove to be of interest.

Since a lift-drag ratio of 0.5 at hypersonic speeds provides for relatively limited maneuverability, it was desired that further study be directed toward bodies having higher lift-drag ratios.

Basic Body Having High Lift-Drag Ratio

One approach to obtaining higher values of L/D that was studied briefly was the addition of a small wing to the top surface of the 30° half-cone. Lift-drag ratio at hypersonic speeds was increased by this means to a value of about 0.9. Another approach for increasing L/D , by increasing body slenderness, was more extensively investigated both analytically and experimentally for half-cone angles in the range from 10° to 20° . Of the more slender half-cone shapes, one was selected for the detailed study to be discussed herein. This configuration, shown in figure 4, has a half-cone angle of 13° . According to estimates, the value of L/D for this shape at infinite Mach number is about 1.5 and is 1.25 to 1.33 at Mach numbers from 3 to 5. This lift-drag ratio is sufficient to provide for lateral ranges during entry from satellite orbit of about 1,000 nautical miles, or about 5 times that available to a vehicle with a value of L/D of 0.5. With this lateral range, incidentally, it is possible to return to a launch point after one circumnavigation of the earth for most orbits attained by launching in the continental United States.

The longitudinal characteristics of this shape were measured at supersonic speeds and results obtained at a test Mach number of 5 are presented in figure 5. The circled data points, as well as the dashed lines indicating the estimated variations of lift-drag ratio and pitching-moment coefficient with lift coefficient, are for the basic 13° blunt half-cone. The theory used was a combination of impact theory on the nose and on the conical surface and shock-expansion theory over the top surface. The base drag was obtained from the assumption that the base-pressure coefficient was 0.7 of the vacuum-pressure coefficient. As in the case of the 30° half-cone, the relatively simple analytical methods provide a fairly good estimate of lift-drag ratio and of the variation of C_m with C_L , at least at the Mach numbers of these tests. However, the body trims near $C_L = 0$ rather than near $(L/D)_{\max}$ as estimated. Trim nearer $(L/D)_{\max}$ can be achieved by modification of the lower afterportion of the conical surface as shown on the sketch at the top of figure 5 and by the triangular data points. The stability is essentially unchanged but the trim point is at a lift-drag ratio of approximately 1.2. The lower-surface modification increased the value of $(L/D)_{\max}$ slightly.

Forces and moments on this body were also measured at low speeds to determine if such a body shape would be flyable at subsonic speeds

at the conclusion of an entry maneuver. Figure 6 shows the measured variations of pitching-moment coefficient and lift-drag ratio with lift coefficient at a Mach number of 0.25. It may be seen that the body is neutrally stable and has a maximum lift-drag ratio of only 1.7. The low lift-drag ratio is due to the large base area (47 percent of the planform area) and to the poor pressure recovery at the base.

Modified Body Having High Lift-Drag Ratio

In order to improve the rather poor subsonic characteristics just described, an investigation of the flow characteristics and the effects of body modifications was conducted in the Ames 12-foot pressure tunnel. Much of this program pertained to boattailing the body in an effort to reduce the base area, to improve the lifting characteristics of the upper surface, and to promote a positive $C_{m,0}$. Some typical body shapes and test results are presented in figures 7 and 8. Figure 7 shows three lifting bodies: the blunt half-cone, one of the boattailed bodies, and a vehicle with the same boattailed body with canopy, vertical surfaces, elevons, and a trailing-edge flap. The large influence of modifying the rear portion of the body on the lift-drag ratios can be seen in figure 8. Base area was reduced from 47 percent to 17 percent of the planform area and the improved flow increased the base-pressure coefficient from -0.24 to about 0. The configuration with canopy and stabilizing surfaces shows even higher lift-drag ratios than the modified body alone. This effect has been attributed to a favorable end-plate effect due to adding the vertical surfaces and to the increased aspect ratio due to adding elevons. Note that the pitching-moment curve for the complete configuration is nearly linear and, for these data, shows trim at a lift coefficient of 0.55.

Some effects of variations in canopy shape were also determined during the course of the investigation at subsonic speeds. The original spherical canopy is shown in figure 9 and a faired canopy is shown in figure 10. It was anticipated that the faired canopy might improve the lift as well as provide additional volume; however, the results were quite adverse. The faired canopy interfered with the strong vortex flows that originate at the leading edges of the upper surface so that at some angle of attack, the vortices were diverted outward to impinge on the vertical surfaces and roll controls. The resulting moment characteristics were nonlinear and the lift-drag ratio was reduced. It appears, then, that the canopy should not extend to the leading edges of the top surfaces of the body.

The body modifications and the addition of stabilizing fins and elevons resulted in relatively good subsonic stability and performance characteristics, and conventional landing capability is indicated. To

study means for providing for control of this type of configuration throughout the speed range, the afterportion of the study configuration was modified further to include pitch and yaw flaps in addition to the elevons which are primarily for roll control. These modifications are illustrated in figures 11 and 12. Figure 11 shows the configuration just discussed, without elevons; the revised configuration is shown in figure 12. An objective was to provide controls which would have a minimum of cross coupling. The sides of the body were flattened and faired into the vertical stabilizer surface to provide for the yaw controls. Similarly, the bottom was flattened and a pair of pitch controls was provided. These modifications affected only the rear one-third of the body and the resulting body lines were not as conducive to good pressure recovery at the base as those of the original model. The base area of the revised configuration is 22 percent of the planform area compared with 17 percent for the previous configuration. Most of this increase is represented in increased base area of the vertical surfaces and elevons which were thickened to relieve the heating problems at their leading edges.

Figure 13 shows the revised configuration with simulated landing gear. Typical preliminary results obtained on this model are presented in figure 14. Pitching-moment coefficient and lift-drag ratio as functions of lift coefficient are shown. It is evident that the landing gear had little effect. The modifications increased minimum drag considerably and the revised configuration does not exhibit the high lift-drag ratios at low lift coefficients that were characteristic of the earlier model. However, the lift-drag ratios are about the same as before at the higher lift coefficients, and the pitch characteristics remain good. For example, the lift-drag ratio is 3.2 at a trimmed lift coefficient of 0.6 with a static margin of 9.5 percent (the center of gravity at 55 percent of the body length). With the development of improved low L/D landing techniques (see, e.g., refs. 2 and 3), it is felt that a vehicle such as this would be capable of performing a conventional landing.

Some of the characteristics of this revised vehicle at supersonic speeds are shown in figure 15. Variations of α , C_m , and L/D with C_L are shown for a test Mach number of 5. The lift curve may be seen to be very nearly linear. The vehicle is stable about the center of gravity at 55 percent of the length and is trimmed near maximum lift-drag ratio for the control settings indicated (lower flaps deflected 15° and elevons deflected -15°). The maximum lift-drag ratio, about 1.3, is essentially unchanged from that of the original 13° half-cone.

Figure 16 shows the variations with Mach number of the static longitudinal- and lateral-directional stability derivatives. It can be seen that the configuration was statically stable about the pitch

[REDACTED]

and yaw axes throughout most of the test range and had positive dihedral effect. Two probable areas of difficulty to be noted are the nearly neutral pitch and yaw stability at a Mach number of about 0.9 and the high dihedral effect. This latter characteristic indicates the probability of a Dutch roll problem.

Measurements were made at transonic and supersonic speeds of the effectiveness of the pitch and yaw flaps and of the elevons. The measured moment-coefficient increments resulting from control deflections are shown in figures 17 and 18. Pitching-moment increments due to deflection of the lower pitch flaps and due to deflection of the elevons are shown in figure 17. It may be seen at the top of figure 17 that the pitch flaps provide large nose-down moments at subsonic and transonic speeds. At supersonic speeds the controls become relatively powerful when the deflection becomes positive relative to the stream. (The deflection angle is measured relative to the surface of the body.) The effectiveness of the elevons as pitch controls may be seen to decrease with increasing Mach number as is the case for any planar control of this type. The indicated reversal at transonic speeds for an elevon deflection of 10° results from the effects of the pressure disturbance from the control on the top afterpart of the body. Yawing-moment and rolling-moment increments due to deflection of one yaw flap and differential deflection of the elevons are shown in figure 18. Again, the controls provide large moments in the subsonic and transonic speed ranges and their effectiveness decreases with increasing Mach number. (The elevon deflections for the data shown are $+20^\circ$ and -20° relative to a nominal position of -10° relative to the cone axis.) Only minor cross-coupling problems have been indicated in the test results obtained.

CONCLUDING REMARKS

The studies, thus far, of the half-cone type of lifting body have shown that, within limitations, this class of body shapes is useful for atmosphere entry requiring maneuvering capabilities. In the case of the low-fineness-ratio shapes, controllable flight through the transonic speed range would be difficult to achieve and the final landing would, of necessity, probably be by parachute or other auxiliary device. For the higher-fineness-ratio shapes, controllable flight throughout the speed range appears feasible and, with development, the capability of conventional landing is probably attainable.

[REDACTED]

REFERENCES

1. Eggers, Alfred J., Jr., and Wong, Thomas J.: Re-Entry and Recovery of Near-Earth Satellites, With Particular Attention to a Manned Vehicle. NASA MEMO 10-2-58A, 1958.
2. Bray, Richard S., Drinkwater, Fred J., III, and White, Maurice D.: A Flight Study of a Power-Off Landing Technique Applicable to Re-Entry Vehicles. (Prospective NASA paper.)
3. Weil, Joseph, and Matranga, Gene J.: Review of Techniques Applicable to the Recovery of Lifting Hypervelocity Vehicles. (Prospective NASA paper.)

BLUNT 30° HALF-CONE LIFTING BODY

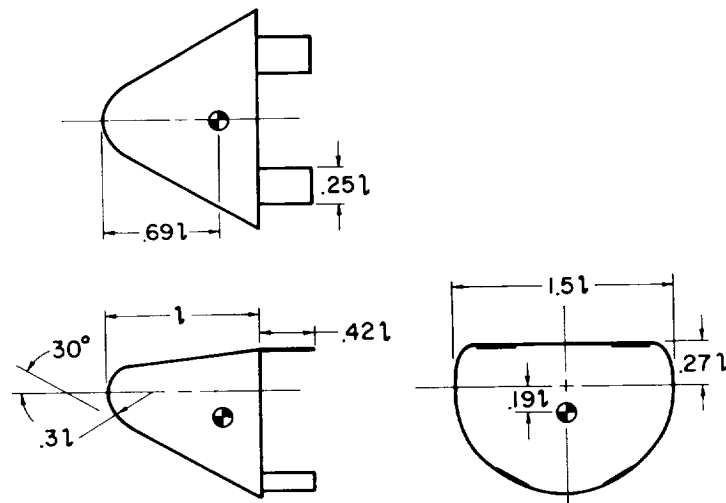


Figure 1

PERFORMANCE AND STATIC STABILITY OF 30° BLUNT HALF-CONE

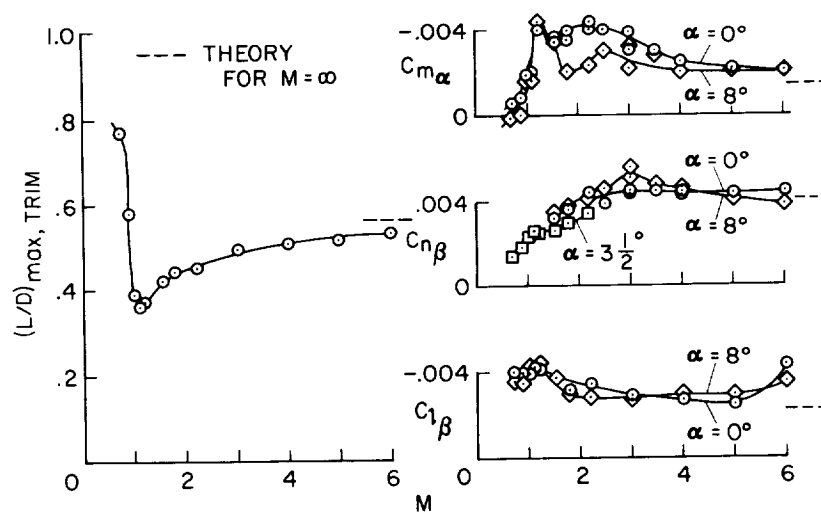


Figure 2

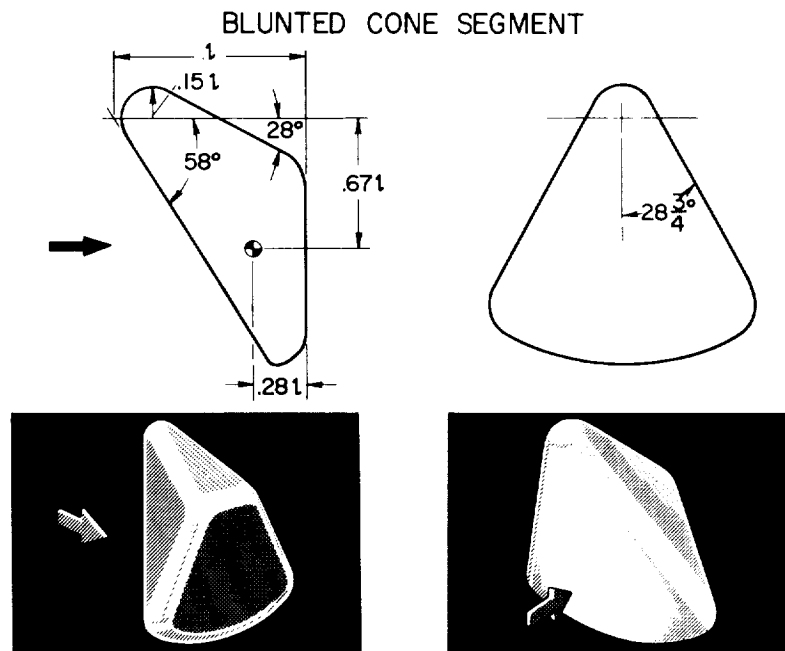


Figure 3

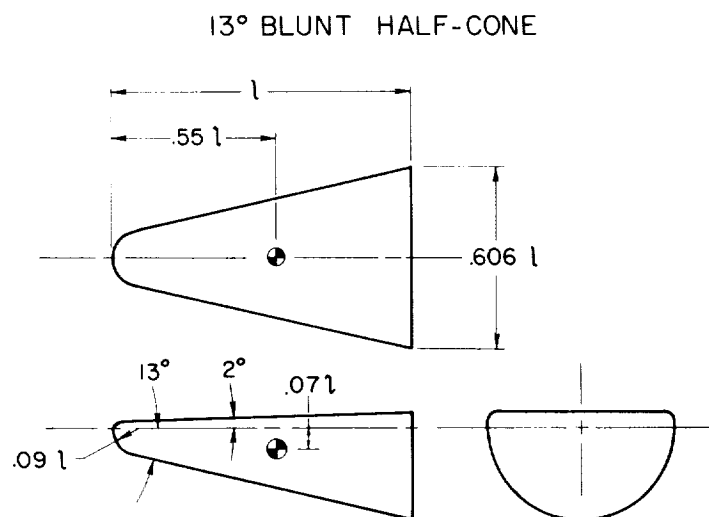


Figure 4

CHARACTERISTICS OF 13° BLUNT-HALF-CONE
AT $M=5$

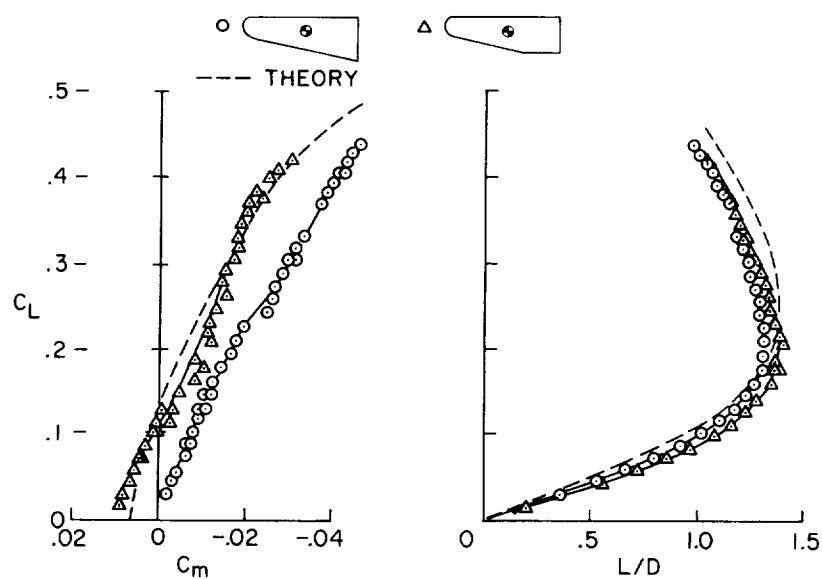


Figure 5

CHARACTERISTICS OF 13° BLUNT HALF-CONE
AT LOW SPEED

$M=0.25$
 $R=25 \times 10^6$

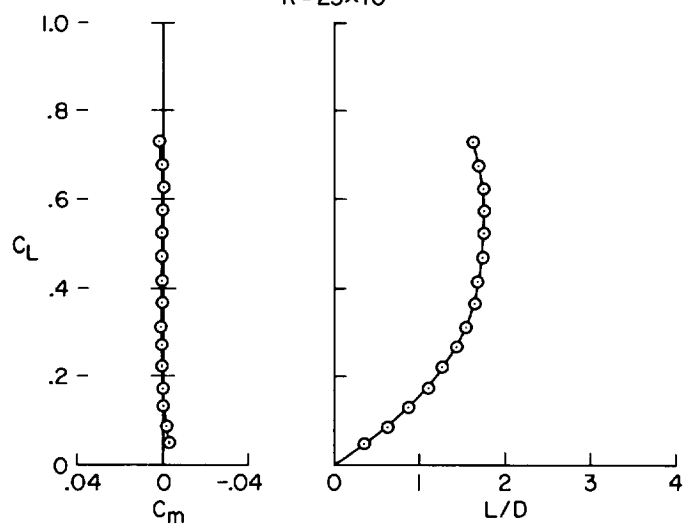


Figure 6

LIFTING BODIES INVESTIGATED

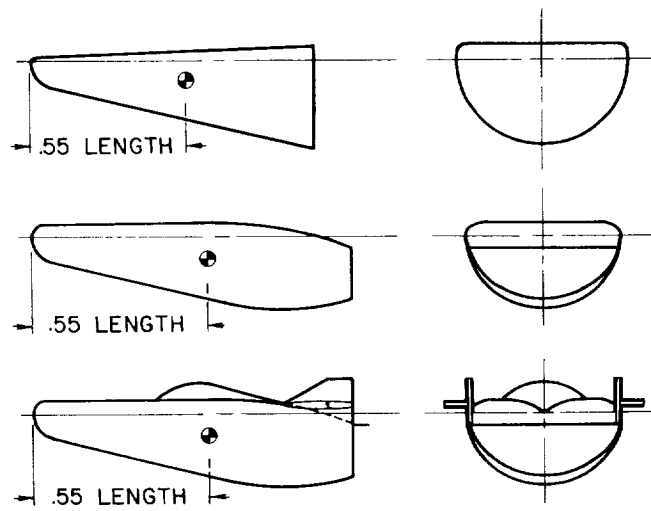


Figure 7

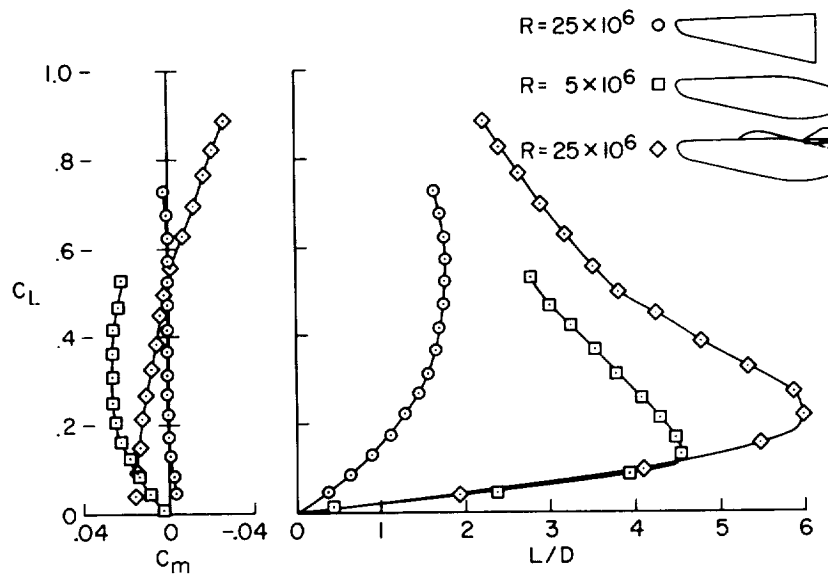
TYPICAL RESULTS AT $M=0.25$ 

Figure 8

MODEL WITH SPHERICAL CANOPY

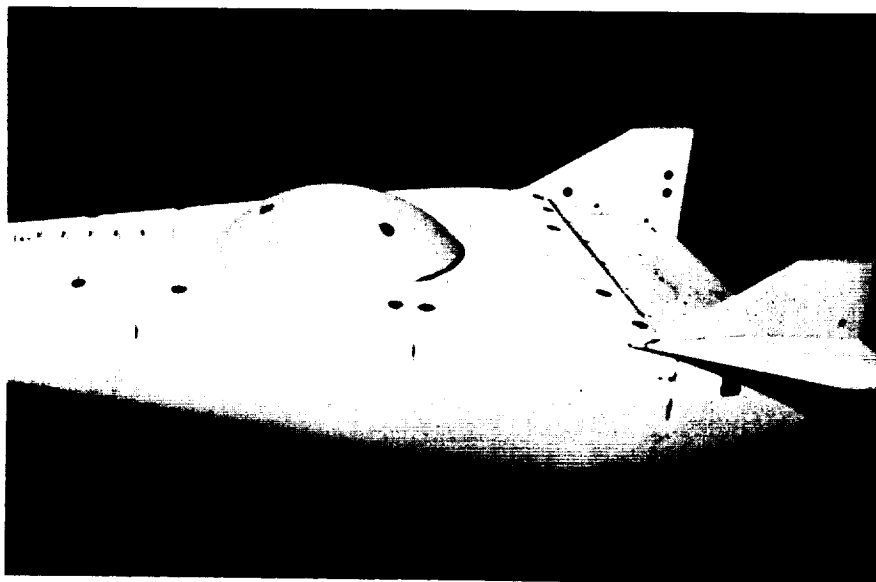


Figure 9

MODEL WITH FAIRED CANOPY

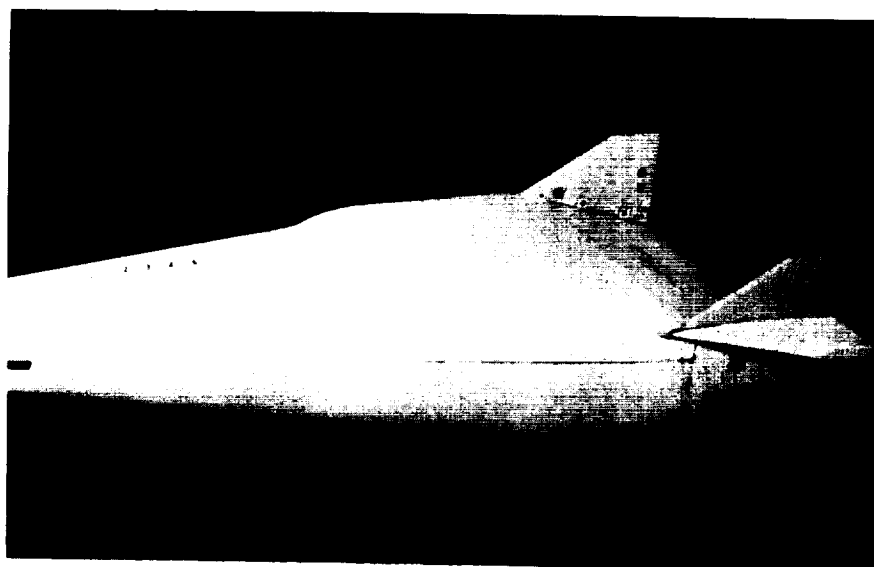


Figure 10

BODY WITH VERTICAL SURFACES AND CANOPY

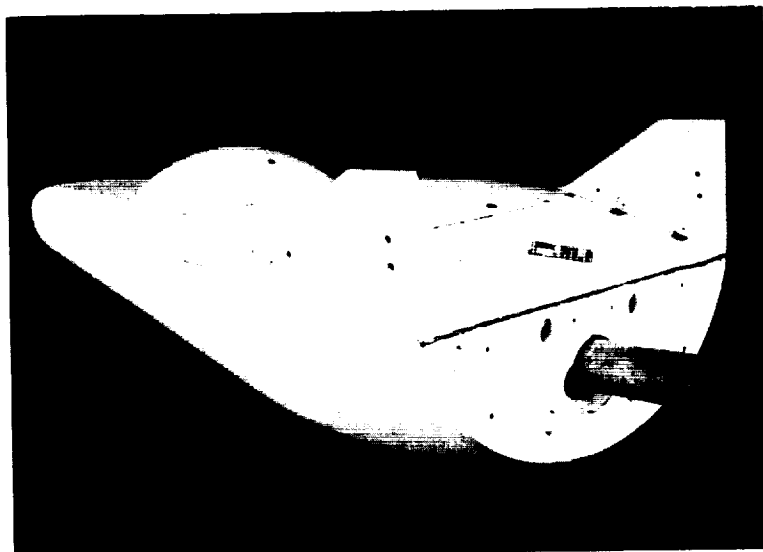


Figure 11

MODIFIED BODY WITH CONTROLS

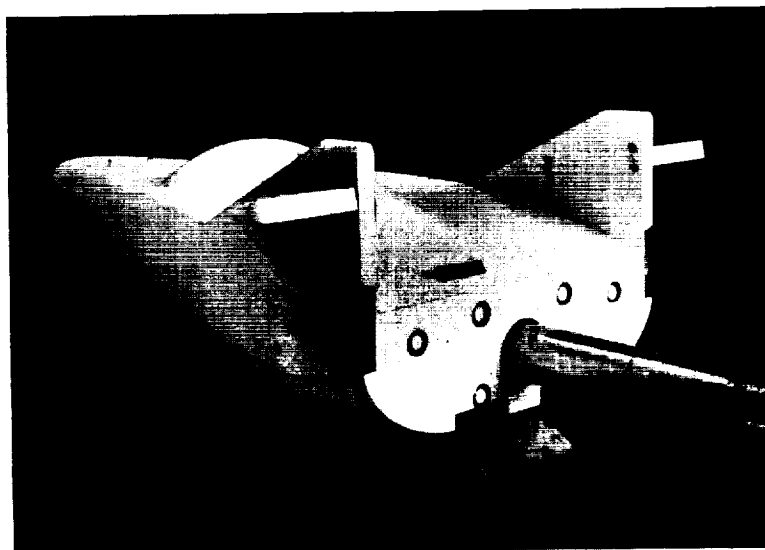


Figure 12

MODEL WITH LANDING GEAR

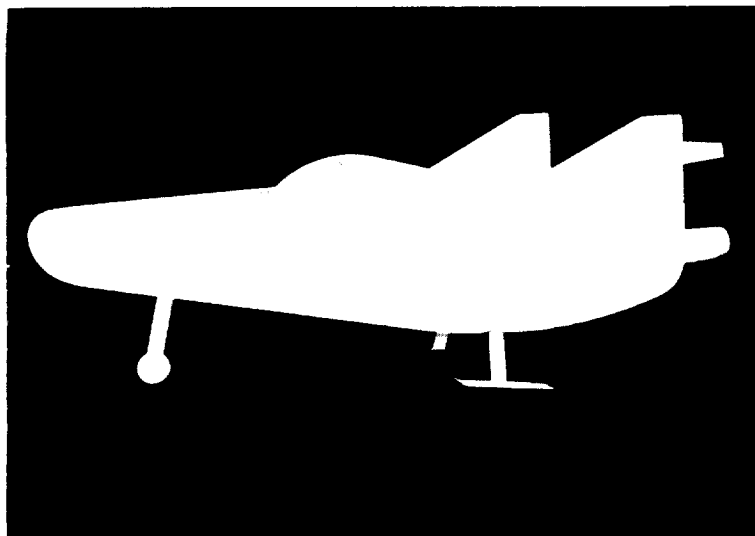


Figure 13

LOW-SPEED CHARACTERISTICS OF LANDING CONFIGURATION

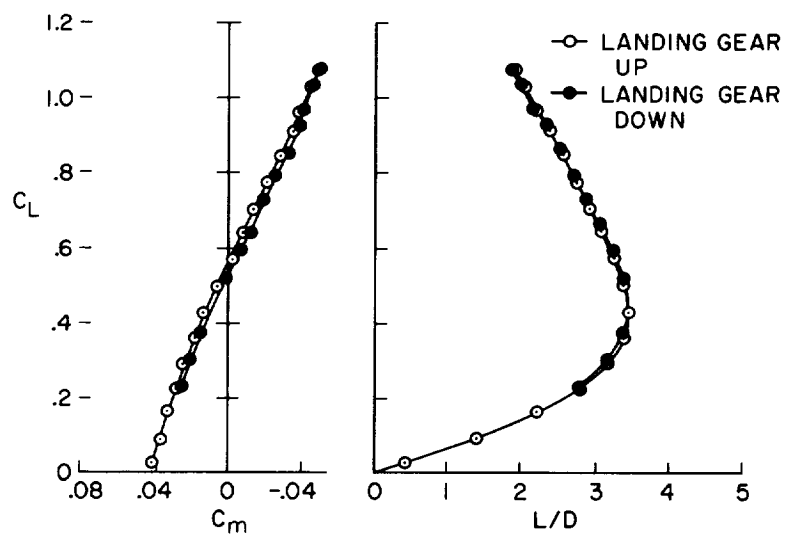
 $M=0.25$
 $R=15 \times 10^6$ 

Figure 14

TYPICAL SUPERSONIC CHARACTERISTICS

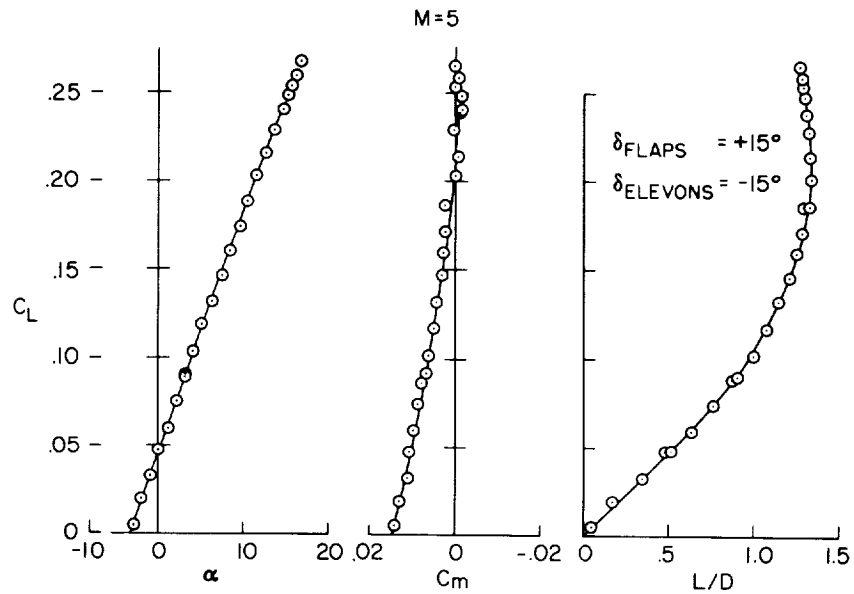


Figure 15

STATIC STABILITY

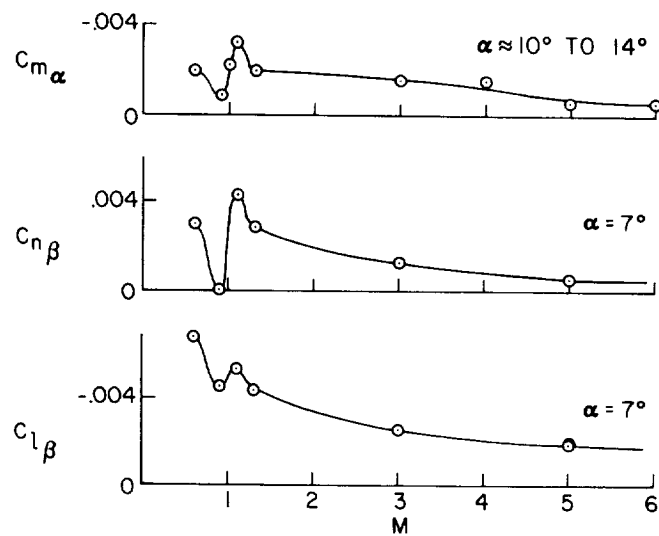


Figure 16

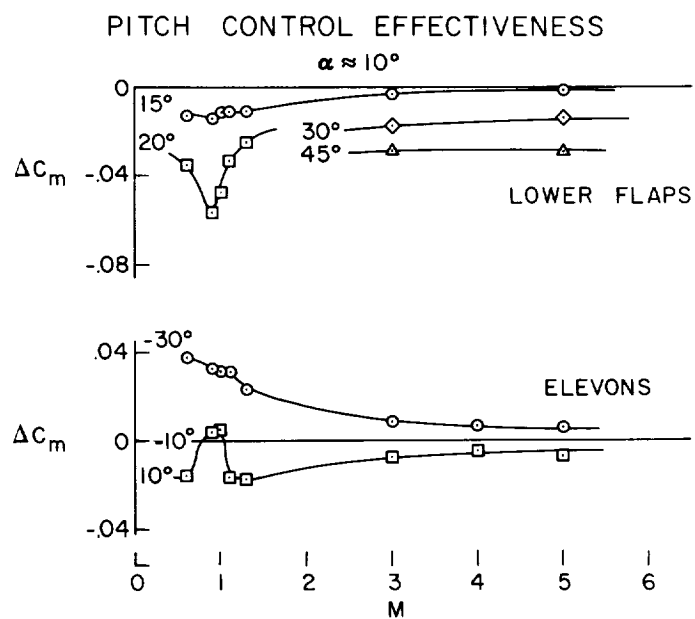


Figure 17

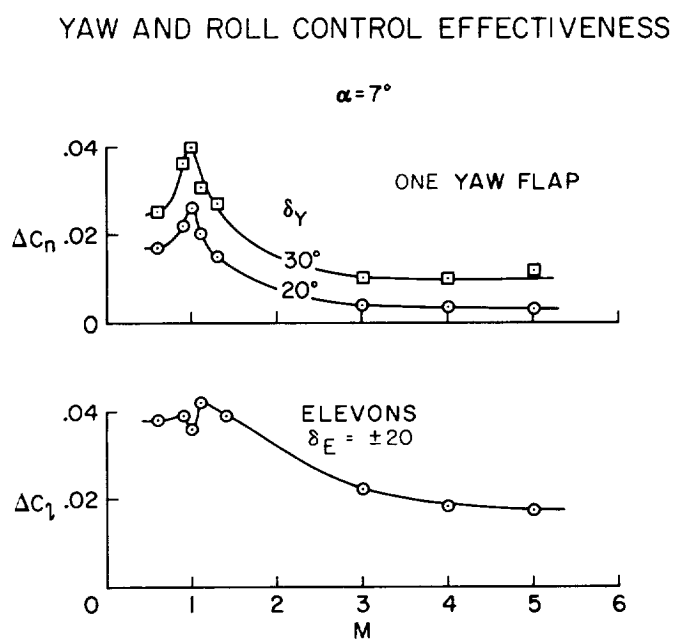


Figure 18

CONVECTIVE HEAT TRANSFER TO A BLUNT LIFTING BODY

By John O. Reller, Jr., and H. Lee Seegmiller
Ames Research Center

SUMMARY

An investigation has been made of the convective heat-transfer characteristics of a blunt lifting shape and of some of the effects of enthalpy level on local heating rates. Measurements in conventional and shock-driven wind tunnels at Mach numbers from 5 to 9 and stagnation enthalpies up to 5,300 Btu/lb are compared with theoretical predictions at Mach numbers and enthalpies characteristic of the high-heating portion of a typical entry trajectory. The distribution of heating rates around a blunt lifting shape is shown to be relatively unaffected by enthalpy level and to compare favorably with theory for equilibrium real-gas flow. It is also shown that control surfaces extending out from the body surface can experience heating rates which exceed those occurring in the body stagnation region. In general, it appears feasible to predict equilibrium convective heat transfer to most body and control surfaces of full-scale blunt lifting shapes during the high-heating portion of an entry trajectory by use of existing theory, along with experimental surveys at relatively low enthalpy levels.

INTRODUCTION

A class of relatively blunt shapes which develop sufficient aerodynamic lift during atmosphere entry to gain some flexibility of operation has been discussed in reference 1. However, these shapes give rise to more complex aerodynamic-heating problems than do simple ballistic vehicles since the shapes themselves are more complicated and since either angle of attack or control-deflection angle may be varied in flight to achieve the desired trajectory. Such changes in flight attitude may cause substantial variations in heating on both body and control surfaces. The purpose of the present investigation is to examine this situation as it relates to a blunt, 30° half-cone shape, introduced in reference 2, and to inquire into methods by which its heating characteristics can be predicted or measured.

SYMBOLS

A	reference area
C_D	drag coefficient
C_p	pressure coefficient
c_p	specific heat at constant pressure
D	drag force
d	maximum body diameter
H	enthalpy
h	heat-transfer coefficient, $\frac{\dot{q} c_{p2}}{(H_{aw} - H_w)A}$ or $\frac{\dot{q}}{(T_{aw} - T_w)A}$
k	thermal conductivity of gas
L	lift force
l	axial distance from nose of body
M	Mach number
N_{St}	Stanton number, $h/\rho U c_p$
N_{Pr}	Prandtl number, $c_p \mu / k$
\dot{q}	heat-transfer rate
R	Reynolds number, $\frac{\rho U (\text{Length})}{\mu}$
S	surface distance from geometric stagnation point, or circumferential surface distance from lower meridian
T	temperature
t	time

U	velocity
W	glide weight
Y	distance normal to body surface
α	angle of flat top surface relative to free-stream direction
δ	control-deflection angle
ρ	density of gas
μ	absolute viscosity

Subscripts:

aw	adiabatic wall
d	referenced to maximum body diameter
r	based on nose radius of curvature
s	stagnation
w	wall, body surface
2	referenced to conditions behind normal shock
TE	trailing edge

RESULTS AND DISCUSSION

Typical Entry Trajectory

The convective-heating-rate history of the blunt, 30° half-cone shape of the present investigation in a typical entry trajectory from a circular orbit is shown in figure 1. The body has a maximum diameter of 10 feet, a value of $W/C_D A$ of 95 lb/sq ft, and develops an L/D ratio of 0.33. Stagnation heating rate \dot{q}_s and enthalpy H_s are shown as a function of time from the initiation of entry to indicate the range of heating conditions encountered. Maximum heating rates are about 70 Btu/(sq ft)(sec), with stagnation enthalpies up to 12,000 Btu/lb. The heating curve has a flat, dished region due to a slow oscillation or "skip" imposed by the requirement (in this trajectory) of a constant L/D glide following the prescribed reverse-thrust phase. At several

locations on the heating-rate curve are shown the flight Mach numbers, while the corresponding Reynolds numbers based on body diameter are presented in a table on the figure. Maximum heating is seen to occur between $M = 26$ and $M = 14$, as R_d increases from 70,000 to just over $1/2$ million. In this relatively low Reynolds number range, it is expected that boundary-layer flow would be essentially laminar.

One additional point must be mentioned with regard to the convective heat-transfer environment. This point has to do with the equilibrium state of the gas. The results of an investigation conducted at Ames Research Center by Paul M. Chung show that, for the range of flight conditions indicated in figure 1, both the inviscid flow and the viscous boundary-layer flow enveloping much of the body can depart substantially from the equilibrium real-gas state because of the time lag in chemical recombination. The resultant effect on local heating rates will not be large, however, if the surface is highly catalytic in the sense that it promotes recombination. In fact, for the case of a relatively cold metallic surface (less than $2,000^\circ \text{R}$) the heating rates should approach those for equilibrium flow as an upper boundary. If the surface is noncatalytic, for example, a plastic or a glass, a considerable reduction in local heating rates can occur because of the lag in recombination at the surface.

From these considerations then, the heating characteristics of this configuration can be studied in conventional wind tunnels, provided the direct effects of enthalpy level can be determined. To determine some of these effects, tests were conducted with the model shown in figure 2. The configuration is essentially one-half of a blunt cone with a semiapex angle of 30° . Flap-type controls extend from the base and are offset from the body center line. Elevon controls were also tested and are shown in a subsequent figure. Reference 1 has presented a few of the aerodynamic force and moment characteristics of this configuration; additional information will be found in reference 3. Tests were conducted in the Ames 10- by 14-inch supersonic wind tunnel at $M = 5$ and at the low value for H_s of 160 Btu/lb and in the Ames 1- by 1-foot hypervelocity shock tunnel at $M \approx 9$ and $H_s \approx 4,000$ Btu/lb. (Note that this latter enthalpy corresponds to a Mach number of about 12 in the flight trajectory of fig. 1.) In both test facilities, thin shell models were used to obtain heating rates by the transient temperature technique. Thermocouple signals were first amplified and then recorded by an oscillograph.

Figure 3 presents two self-illuminated time exposures of one of these models in the shock tunnel. In the vicinity of the body and over both controls can be seen the bright glow of the shock-heated incandescent gas. The outline of the body shock wave can be seen, while in figure 3(b) the rear of the model is illuminated by reflected light from the support system. The camera shutter was closed at about 100 milliseconds after

the start of flow, at which time the model was still enveloped in the high-enthalpy airstream. Although the stagnation enthalpy for this test condition is only about one-third the maximum value desired for the present study, it is sufficiently high to indicate some of the trends in heat transfer with enthalpy. Reynolds numbers were sufficiently low in both facilities so that boundary-layer flow was apparently laminar in all cases.

Stagnation Heat Transfer

Some of the results obtained in these tests as they relate to stagnation-point heat transfer are shown in figure 4 in which the dimensionless heating parameter $(N_{St})_2 (N_{Pr})_2^{2/3} (R_r)_2^{1/2}$ is shown as a function of stagnation enthalpy. The parameter is referenced to conditions behind the normal shock wave with high-temperature gas properties evaluated from reference 4. The circular test-point symbols on figure 4 are data for the present configuration, and the square test-point symbols represent tests of the Project Mercury capsule configuration at the Ames Research Center both in the 10- by 14-inch supersonic wind tunnel and the 2-inch hypervelocity shock tunnel at stagnation enthalpies between about 5,000 and 5,300 Btu/lb. The data are compared with the theory of Fay and Riddell (ref. 5) which was applied to a wide range of conditions (M from 4 to 26 and H_s from 160 to almost 12,000 Btu/lb) that pertain to the three test facilities and the flight trajectory shown previously. Also shown in figure 4 are the two Mach numbers, 14 and 26, which bracket the high heating portion of the trajectory shown in figure 1; the test data extend into the lower part of this region. The theoretical variation, which shows only a moderate dependence on enthalpy, is represented by the shaded region. This shaded area indicates a spread of ± 5 percent in the theoretical estimates which may, in part, be due to our imperfect knowledge of the real-gas properties. Theory and experiment are in good agreement both at the low enthalpies and at moderate enthalpies from 4,000 to 5,000 Btu/lb. Indeed, the experimental results seem to support the indicated theoretical trend. These results suggest, then, that the estimation of heating rates to the stagnation region of a full-scale vehicle of the blunt ballistic or lifting type during the high heating portion of an entry trajectory should be possible with reasonable accuracy.

Heating-Rate Distribution

Top and bottom body meridian at $\alpha = 0^\circ$. - The distribution of heating rate over the surface of the body was also investigated. Local heating rates at $\alpha = 0^\circ$, referenced to the stagnation value, are presented in figure 5 as a function of normalized surface distance along the top and bottom meridian of the body. Heat-transfer data obtained

in the low-enthalpy airstream (circular test-point symbols) are compared with the theories of Lees (ref. 6) and Van Driest (ref. 7) for a laminar boundary layer. The theoretical results were obtained by using the measured surface pressures of reference 3 and are in general agreement with the measured heating rates. One exception, however, is the point on the small upper radius of the nose, where the measured rate exceeded the stagnation-point value. Now, it should be noted that the low-enthalpy test results were obtained in the form of heat-transfer coefficients. However, by referencing the local coefficient to the stagnation value as the ratio h/h_s and by using the "cold wall" assumption, these data for this blunt shape can be interpreted as the ratio of heating rates \dot{q}/\dot{q}_s . As such, they are comparable, within the experimental accuracy, with the heating-rate ratios obtained in the high-enthalpy tests and from theory.

The square test-point symbols in the figure represent results obtained in the Ames 1- by 1-foot hypervelocity shock tunnel in a stream whose enthalpy was about 4,000 Btu/lb. As can be seen in the figure the agreement between the two sets of data is quite favorable in the stagnation region and on the lower surface. On the upper surface, the high-enthalpy data are substantially lower, a fact which is attributed to the relatively lower pressure level in this region caused by the difference in Mach number as well as in enthalpy level.

Finally, in this figure the dashed lines represent the heating distribution at the conditions of $M = 22$ in the reference trajectory. It will be recalled that $M = 22$ is in the region of maximum convective heating for this trajectory. These results were obtained from the theory of Kemp, Rose, and Detra (ref. 8) with the use of Newtonian pressures, and that of Romig and Dore (ref. 9) for both Newtonian and blast-wave pressures (ref. 10). Substantial agreement with the previous results is apparent although these equilibrium real-gas predictions are somewhat lower on the conical section. On the top surface, the predictions for $M = 22$ bracket the shock tunnel data, and it is difficult to say which is more realistic.

Circumferential direction at $\alpha = 0^\circ$.— The variation of local heating rates in a circumferential direction at several locations on the body is shown in figure 6 for $\alpha = 0^\circ$. The symbol S represents surface distance from the lower body meridian, while S_T is one-half the local circumference. The symbols l and l_T refer to axial distances. The conical region, the top leading edge, and the flat top surface of the body are identified in the figure. Data are shown for both enthalpy levels, $H_s = 160$ and 4,000 Btu/lb, while ideal-gas theory for a laminar boundary layer is presented for the rearward position, $l/l_T = 0.75$. The low-enthalpy data at this location are seen to compare favorably with the theoretical prediction, which is based on measured

pressures. Also at $l/l_T = 0.45$ the high- and low-enthalpy data are in agreement in the conical region. On the leading edge and top surface, the high-enthalpy data fall considerably below the heating-rate level for the low-enthalpy data, a fact which has been noted previously in figure 5. Notice also that the top leading edge of the body does not experience high heating rates, at least at this angle of attack, despite its relatively small radius of curvature. In fact, the heating distribution in this region is similar to that for a yawed cylinder.

Variation with angle of attack.- The variation of local heating rates at several points on the body with angle of attack is presented in figure 7. Angle of attack α is measured relative to the top surface. Figure 7(a) shows the locations and test-point symbols for the data in figure 7(b). The angle-of-attack range from -17° to 7° represents trimmed flight at L/D ratios from 0.2 to 0.5. The top curve shows data for the tangent point of the small upper nose radius, where rates up to 20 percent above the normal stagnation value were measured. The square and triangular test-point symbols represent locations about halfway around the top leading edge; the first, on the meridian line where the leading-edge sweep is 0° , and the second, farther back where the leading-edge sweep is 60° . Despite the small radius of curvature, this region is not a critical heating area. Other curves show the expected trends for the lower conical and upper flat surfaces. The solid diamond test-point symbols at $\alpha = 0^\circ$ and $\alpha = 4^\circ$, which are shock-tunnel data points for the conical surface, should be compared with the dashed curve, which is the low-enthalpy heating level for the same location on the body. High-enthalpy data for the leading edge and top surface are lower than comparable low-enthalpy values because of the combined Mach number and enthalpy effect noted previously. In general, these results show that angle of attack does not have a pronounced effect on heating rates for the blunt body tested.

Summary statement.- On the basis of the results discussed so far, in particular, the stagnation-point correlation, the similarity in heating-rate distribution at several enthalpy levels, and the general agreement between theory and experiment in regions where reliable comparisons can be made, it appears that low-enthalpy heating-rate measurements can be used as a basis from which to predict, with reasonable accuracy, the full-scale equilibrium convective-heat-transfer rates over most of the surfaces of a blunt lifting shape. (It must be recalled, however, that in flight a noncatalytic wall condition may reduce the actual heating rates below these predicted values.) Probable exceptions to this general statement are regions of separated flow, such as at the base of this configuration. Heating rates in this region have, to date, only been measured at the low-enthalpy level. Recorded values were from 1 to 5 percent of the stagnation heating rate. These preliminary results are not conclusive, however, since extrapolation to the enthalpy level

of the full-scale vehicle involves nonequilibrium real-gas effects that are difficult to predict.

Control-Surface Heating

Body pressure field.- Before the heat-transfer characteristics of the flap-type controls are examined, the flow field surrounding the body in which the controls operate will be considered. Some results from a pitot-pressure survey rake located at the base of the body and representative measured control pressures are presented in figure 8. The abscissa in both parts of the figure is a nondimensional distance normal to the body surface. Consider first the pitot-survey-rake data shown in the left part of the figure. At the bottom and side of the body, the low-energy air originating at the normal or nearly normal portion of the body shock wave was apparently confined for the most part to a thin layer at the body surface. In this area, at $Y/d < 0.04$, the pressure coefficient must rise from a value near 1.8 at the edge of the boundary layer to the measured value of 4.8 at the location of the first orifice. This latter value approaches the theoretical limit of about 5.2 for isentropic compression behind the oblique shock wave generated by the conical surface. The measured values decrease as the shock wave is approached since the local Mach number is increasing. The lower limit (dashed line) corresponds to the pitot-pressure coefficient for the Mach number just behind the oblique shock wave. The two outermost orifices were outside of the body shock wave and recorded normal shock pressures.

For the upper pitot survey rake, all four orifices were within the body shock wave and recorded a gradually rising pressure with increasing value of Y . The curve through the data falls into the theoretical value (from Prandtl-Meyer expansion of flow behind normal shock) at the body surface, $Y = 0$. The pattern apparently indicates a mixed flow, downstream of a continuously curving shock wave.

On the right side of figure 8, the range of pressures measured on the flap-type controls is presented in coefficient form. The parameter Y_{TE}/d is the nondimensional distance, normal to the body surface, to the flap trailing edge. The upper and lower solid curves in each set are, respectively, the maximum and minimum pressure curves. The vertical bars and test-point symbols correspond to measured data at control deflection angles of 0° , 30° , 60° , and 90° on the upper control and 0° , 30° , and 60° on the lower, where δ is measured from a normal to the base of the model. The dashed portion of the curves for the lower control is an extrapolation to $\delta = 90^\circ$ based on the two theoretical limits shown in the left part of the figure. In general, the lower control experienced higher pressures. Note that at high deflection angles both the upper and lower controls were subject to pressures in excess of the

normal stagnation value and that large gradients occurred. These results are related to the extension of the controls into the high-energy flow discussed previously, which passes through the oblique portions of the body shock wave. This of course implies that the low-energy layer which originates in the normal shock region at the nose does not protect the controls in the same fashion that it does the body surface. This effect is attributed, in part, to a two-dimensional flow over the controls from the center toward the edges which bleeds off the low-energy layer.

It is somewhat surprising that the upper controls experienced these large pressures since they are not indicated by the pitot survey rake. Note, however, that the controls are offset from the body center line, which is the location of the pitot survey rake. Inspection of the pressure distribution on the controls indicated that a large pressure gradient must exist parallel to the base, which, in combination with the control offset, would explain this difference. In view of these findings, then, it might be expected that both upper and lower control-surface heating rates would also vary widely.

Heat transfer to flap-type controls.- Heat-transfer rates to the flap-type controls, referenced to the body stagnation value, are presented as a function of control-deflection angle δ in figures 9 and 10. The angle δ is defined by the small sketches. In figure 9, experimental data and theory are for the outboard trailing edge of the controls, at the locations indicated by the dots in the sketch at the upper right. Three-dimensional laminar-boundary-layer theory based on wedge and Newtonian impact pressures is used for comparison (solid curves), with local Reynolds numbers referenced to the length from the flap leading edge. The dashed curves are similar heating estimates based on measured control pressures. The experimental low-enthalpy heating rates to the trailing edge of both the upper and lower control (circular test-point symbols) are seen to depart substantially from the Newtonian pressure predictions at values of δ greater than 20° and to follow the estimated trend based on measured pressures. On the lower control, the indicated heating rate exceeded that of the body stagnation point at a value of δ of about 50° . On the upper control, the relatively high measured values at low values of δ are attributed to body cross-flow effects. Two data points from the shock tunnel at $\delta = 45^\circ$ are shown (square test-point symbols). The measured value on the lower control agrees with the low-enthalpy result. On the upper control, however, a considerably higher heating rate was measured, which may be indicative of a change in the body cross-flow pattern at the high-enthalpy test conditions.

In figure 10, the shaded areas represent the range of heating rates encountered on the control surfaces at each deflection angle. The data points are the same as those shown in figure 9. Substantial heating gradients are apparent. The shaded areas indicate that the highest heating rate was usually forward of the trailing edge, although the

location of the point of maximum heating has been found to vary with control-deflection angle. Note that the high-enthalpy data for the upper control at $\delta = 45^\circ$ extend into the low-enthalpy range of measured heating rates. The maximum measured rate for these tests was on the lower control at $\delta = 60^\circ$ and was 80 percent greater than the body stagnation value.

Heating rates to the lower controls are presented as a function of angle of attack in figure 11. Data are shown for deflection angles of 0° , 20° , 30° , 45° , and 60° . The angle-of-attack range is from -14° to 7° . It is seen that the general level of heating remains unchanged with angle of attack, although the pattern is somewhat erratic. A similar erratic behavior has been noticed in the measured heating rates to the upper controls. Additional shock-tunnel tests are now in progress and will provide high-enthalpy data at several control-deflection angles and several body angles of attack. Also, a theoretical study of both control pressures and heating rates is underway to evaluate methods of predicting control heating rates at the flight-enthalpy level.

On the basis of present results, it would seem possible to extrapolate control-heating data to the enthalpy level of the full-scale vehicle, much in the same manner as for the body surfaces.

Heat transfer to elevon controls.- Some representative low-enthalpy elevon-heating data are shown in figure 12, where the ratio \dot{q}/\dot{q}_s is given as a function of angle of attack for an elevon deflection angle of 0° . A two-view sketch of these controls giving linear dimensions is shown at the right. It will be noted that the leading-edge radius is $0.02d$, which is only 10 percent of the body nose radius. The data presented are the average of three values measured at different locations on the leading edge or flat surfaces. On the leading edge of the control there was considerable variation in the measured rates, and in several instances at negative α one of the values was in excess of the body stagnation heating rate; thus the presence of the high-energy airflow discussed previously was indicated. As with the flap-type controls, the behavior of the elevons is somewhat erratic with angle of attack. The lower two curves for the upper and lower control surfaces intersect near $\alpha = 0^\circ$ and appear to vary in a predictable fashion with angle of attack at values from 0.1 to about 0.3 of the reference heating rate. Additional elevon heating data have been obtained at deflection angles from -30° to 30° . Preliminary inspection of these data has revealed upper- and lower-surface heating rates ranging up to about $3/4$ of the reference value. Leading-edge values, on the other hand, were relatively unaffected by variation in deflection angle.

These preliminary elevon-heating results indicate that a control of this type will encounter sizable heating rates on leading-edge and

windward surfaces. Local values can approach or exceed that measured at the stagnation point of the body and would appear to result, as was the case for the flap-type controls, from immersion of the control in the high-energy portion of the body flow field rather than in the flow originating at the normal shock wave at the nose.

CONCLUDING REMARKS

This paper has reported an investigation of the convective heat-transfer characteristics of a blunt lifting shape and has examined some of the effects of enthalpy level on these heating characteristics. Heating rates were measured in conventional and shock-driven wind tunnels at stagnation enthalpies up to 5,300 Btu/lb. Stagnation-heating rates have been correlated with theory in a manner that shows only a moderate dependence on enthalpy level. The distribution of heating rates around a blunt lifting shape has been shown to be relatively unaffected by enthalpy level and to compare favorably with theory for equilibrium real-gas flow. It has further been shown that control surfaces extending into the flow field around a blunt lifting shape will encounter relatively high-energy airflow and can experience heating rates which exceed that occurring at the stagnation point of the body. In summary of these results, it appears feasible to use existing theory, along with experimental surveys at relatively low enthalpy levels, to predict equilibrium convective heat transfer to most body and control surfaces of full-scale blunt lifting shapes during the high-heating portion of an entry trajectory.

REFERENCES

1. Dennis, David H., and Edwards, George G.: The Aerodynamic Characteristics of Some Lifting Bodies. (Prospective NASA paper.)
2. Eggers, Alfred J., Jr., and Wong, Thomas J.: Re-Entry and Recovery of Near-Earth Satellites, With Particular Attention to a Manned Vehicle. NASA MEMO 10-2-58A, 1958.
3. Sarabia, Michael F.: Aerodynamic Performance and Static Stability and Control of a High-Lift, High-Drag, Satellite-Entry Vehicle at Mach Numbers From 3 to 6. (Prospective NASA paper.)
4. Hansen, C. Frederick: Approximations for the Thermodynamic and Transport Properties of High-Temperature Air. NACA TN 4150, 1958.
5. Fay, J. A., and Riddell, F. R.: Theory of Stagnation Point Heat Transfer in Dissociated Air. Jour. Aero. Sci., vol. 25, no. 2, Feb. 1958, pp. 73-85, 121.
6. Lees, Lester: Laminar Heat Transfer Over Blunt-Nosed Bodies at Hypersonic Flight Speeds. Jet Propulsion, vol. 26, no. 4, Apr. 1956, pp. 259-269.
7. Van Driest, E. R.: The Laminar Boundary Layer With Variable Fluid Properties. Rep. No. AL-1866, North American Aviation, Inc., Jan. 19, 1954.
8. Kemp, Nelson H., Rose, Peter H., and Detra, Ralph W.: Laminar Heat Transfer Around Blunt Bodies in Dissociated Air. Res. Rep. 15, AVCO Res. Lab., May 1958.
9. Romig, Mary F., and Dore, F. J.: Solutions of the Compressible Laminar Boundary Layer Including the Case of a Dissociated Free Stream. Rep. ZA-7-012, CONVAIR, Aug. 4, 1954.
10. Lees, Lester, and Kubota, Toshi: Inviscid Hypersonic Flow Over Blunt-Nosed Slender Bodies. Jour. Aero. Sci., vol. 24, no. 3, Mar. 1957, pp. 195-202.

STAGNATION ENTHALPY AND HEATING RATE IN TYPICAL TRAJECTORY

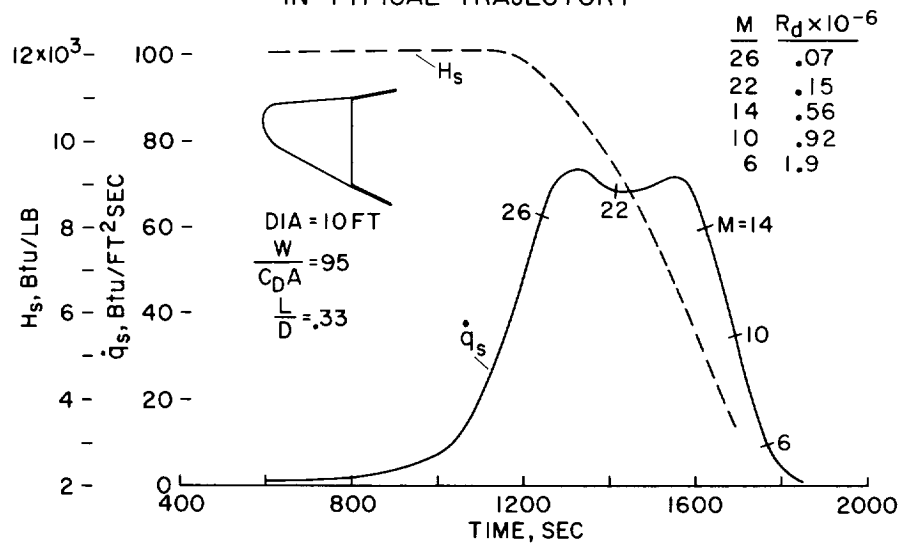


Figure 1

TEST MODEL

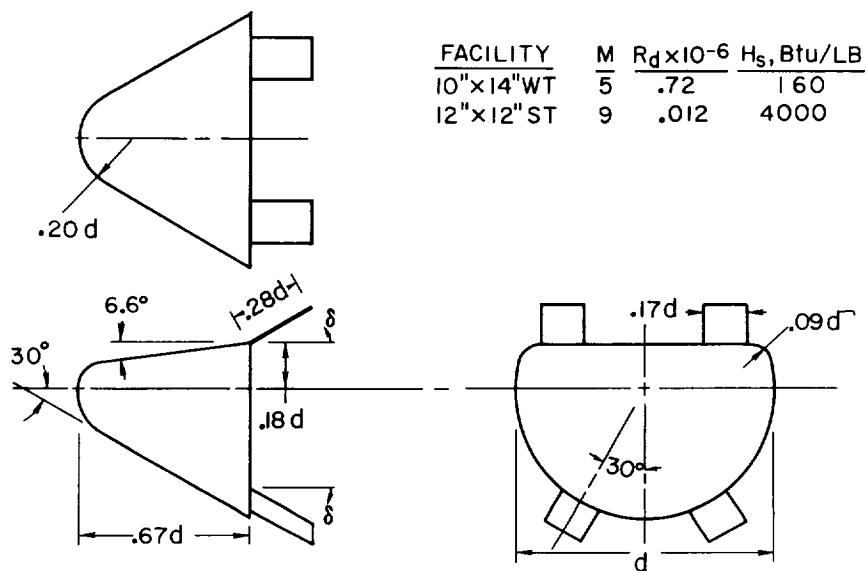


Figure 2

TEST MODEL IN HIGH ENTHALPY AIR STREAM
SIDE VIEW



Figure 3(a)

TEST MODEL IN HIGH ENTHALPY AIR STREAM
REAR VIEW

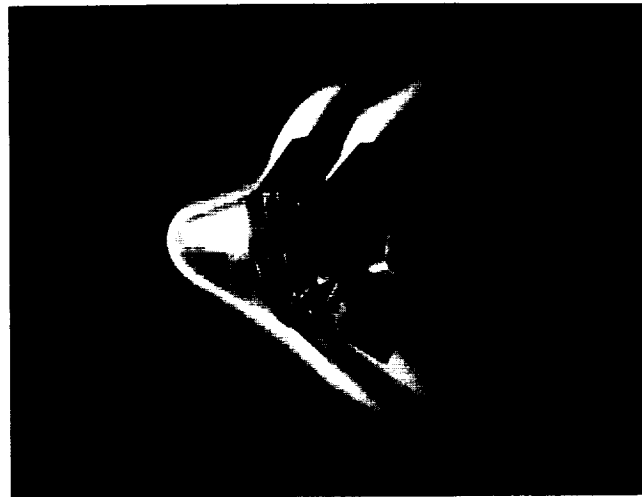


Figure 3(b)

STAGNATION HEATING RATES

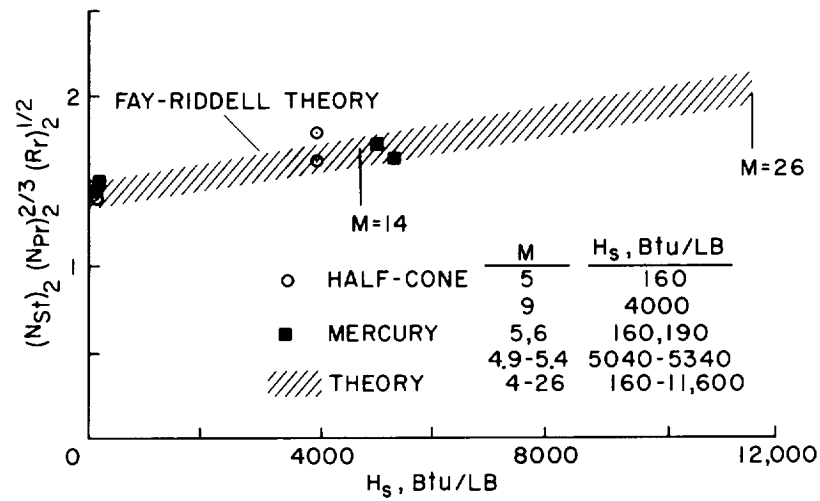


Figure 4

BODY HEATING RATES

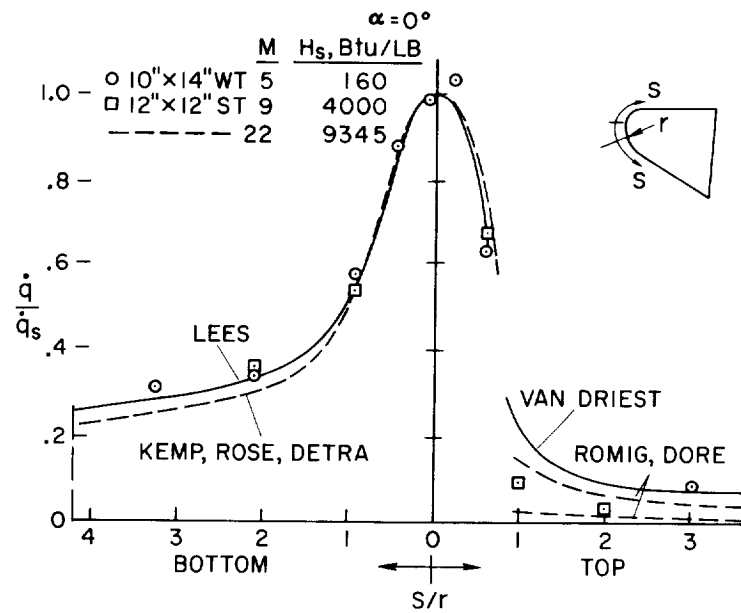


Figure 5

CIRCUMFERENTIAL HEATING RATES $\alpha = 0^\circ$

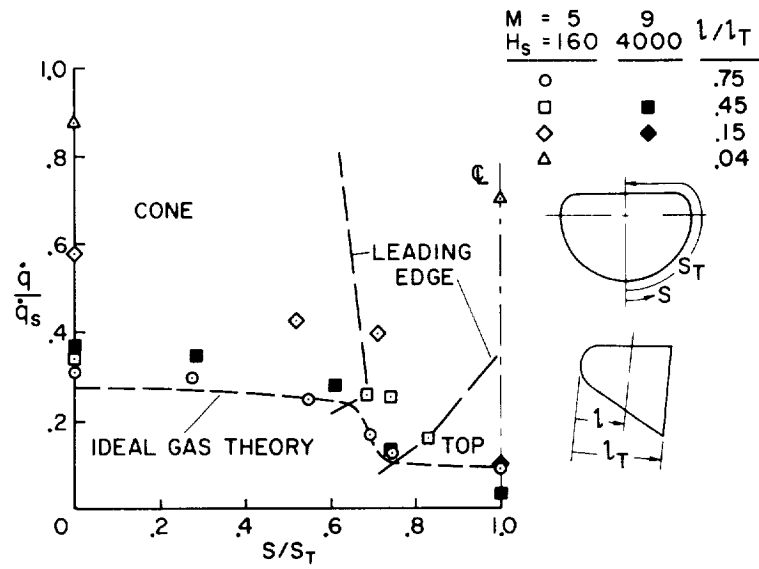


Figure 6

LOCATIONS FOR HEAT-TRANSFER MEASUREMENTS

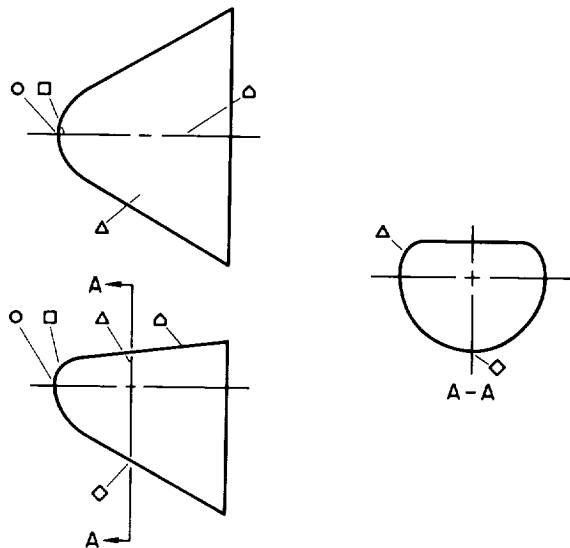


Figure 7(a)

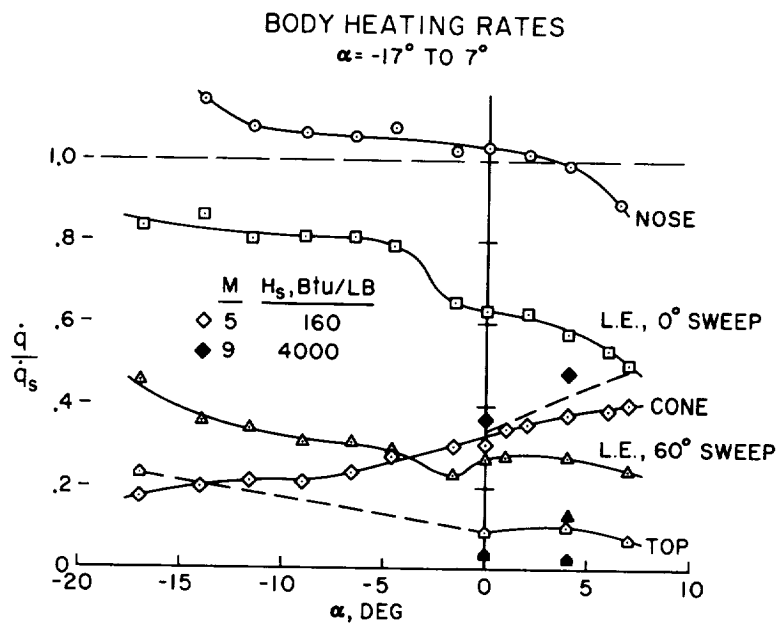


Figure 7(b)

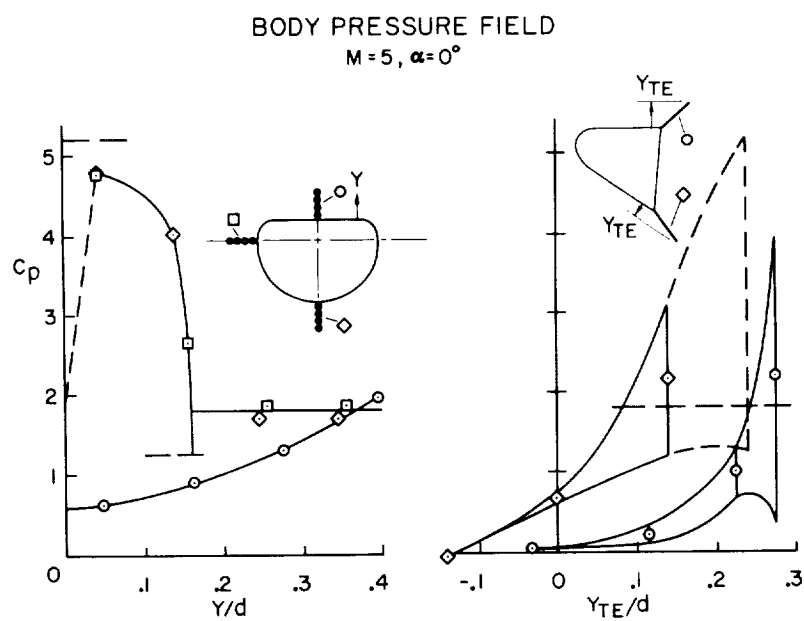


Figure 8

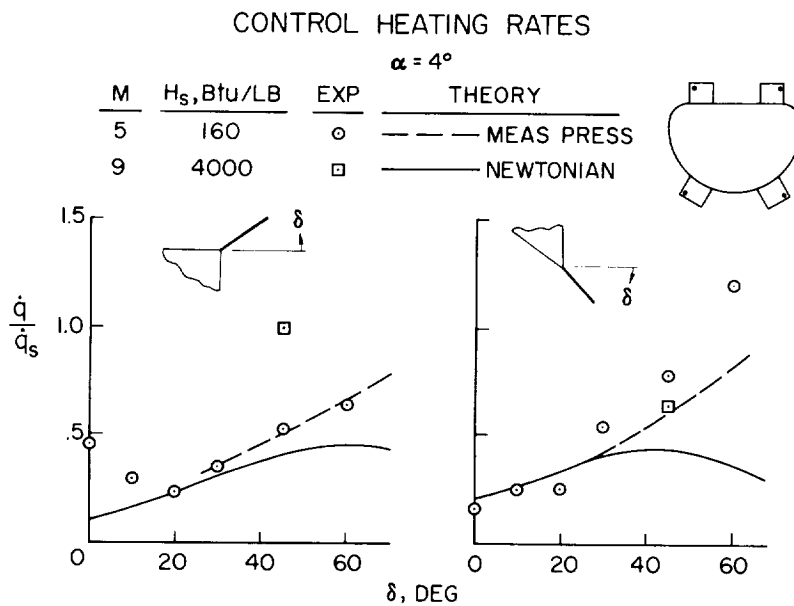


Figure 9

VARIATION OF HEATING RATES ON CONTROL SURFACES

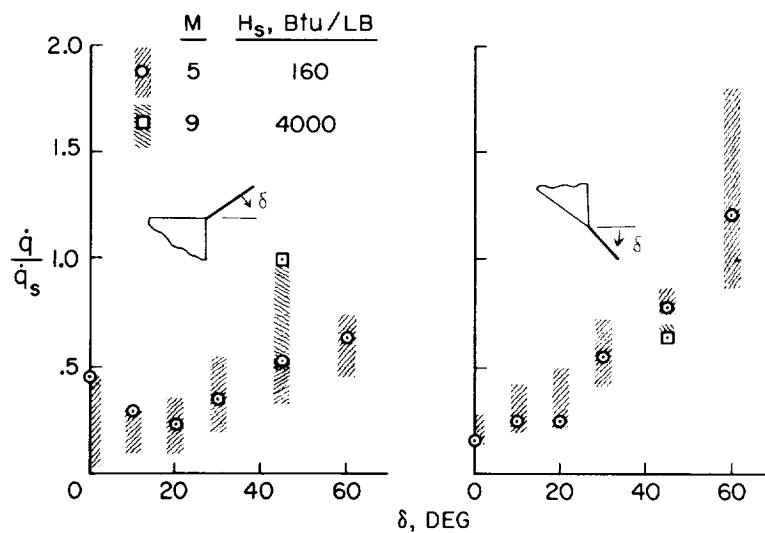


Figure 10

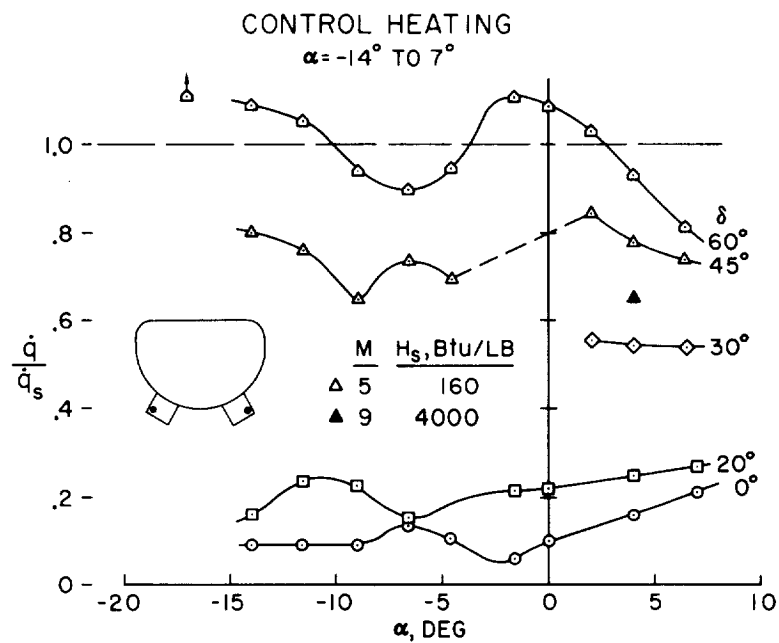


Figure 11

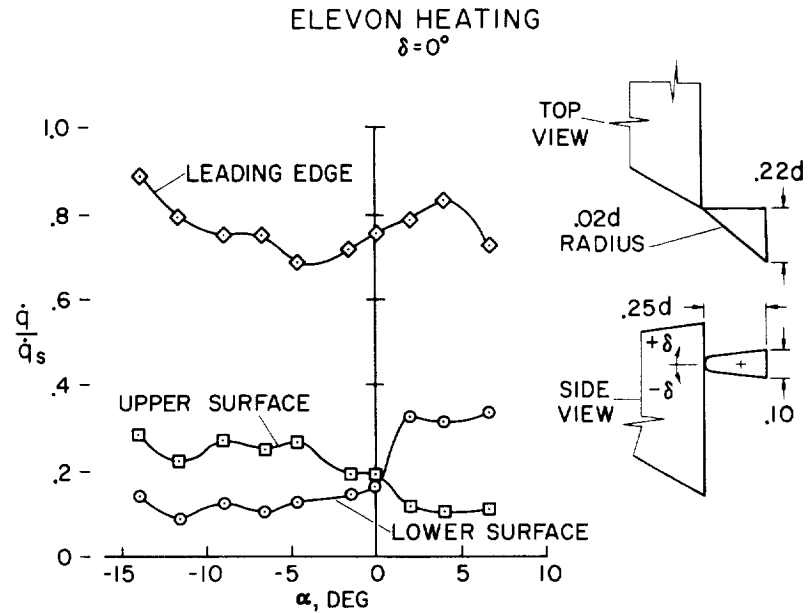


Figure 12

THE AERODYNAMIC-FORCE AND HEAT-TRANSFER CHARACTERISTICS
OF LIFTING REENTRY BODIES

By William O. Armstrong, P. Calvin Stainback,
and Charles H. McLellan
Langley Research Center

SUMMARY

An extensive investigation is in progress to study the aerodynamic-force and heat-transfer characteristics of a large number of lifting-body shapes of varying geometry. This study indicates that in many ways body shape is of secondary importance to other design parameters such as size, weight, planform loading, and lift-drag ratio. Furthermore, for given ratios of lift to drag and weight to base area no specific body shape was found to possess sufficiently superior qualities to exclude consideration of other body shapes. However, the configurations with more nearly flat bottoms appeared to offer some advantages from the standpoint of performance and heat-transfer considerations. Further studies are needed especially to develop more adequate methods of heat-transfer analysis for the more complex configurations.

INTRODUCTION


At the present time, the reentry requirements of space vehicles are not clearly defined and values of maximum lift-drag ratio from 0 to about 2 must be considered. The configurations with high lift-drag ratios provide the largest amount of maneuverability and the greatest reduction in reentry deceleration, while the shapes with low lift-drag ratio have the advantage of a lower total heat load. Since a wide variety of configurations are capable of providing a given lift-drag ratio in the range up to about 2, an extensive investigation is in progress to study the aerodynamic characteristics of a wide variety of generalized lifting-body shapes of varying geometry.

A series of lifting-body configurations shown in figures 1 and 2 have been studied and include full cones, round-bottom half cones and half elliptical cones, flat-bottom half cones of varying types and

amounts of bluntness, and configurations with triangular cross sections. The aerodynamics of all of these configurations have not been examined in detail for the present investigation, but rather a broad view of the overall results has been taken to isolate the significant differences among classes of configurations. If comparisons are restricted to body shapes of the same design maximum lift-drag ratio and the same internal stowage capacity, many of these configurations have rather similar aerodynamic and heat-transfer characteristics. However, a few shape families were found to have important differences in their force and heating characteristics. One shape parameter for which these differences were significant was the curvature of the lifting surface of the vehicle - shown by such configurations as the round- and flat-bottom half-cone body shapes. This paper will discuss at some length the effects of this variation on the force and heat-transfer characteristics of these body shapes. Longitudinal force and stability data, however, have been obtained for all of these configurations, and directional stability and control data were obtained for a few of the more typical configurations.

SYMBOLS


A	maximum body cross-sectional area
a	semiminor axis of ellipse
b	semimajor axis of ellipse
C_D	drag coefficient, Drag/qA
C_L	lift coefficient, Lift/qA
C_{L_α}	lift-curve slope at $\alpha = 0^\circ$, $\partial C_L / \partial \alpha$
C_l	rolling-moment coefficient, Rolling moment/qAD
C_{l_β}	rolling-moment derivative, $\partial C_l / \partial \beta$
C_m	pitching-moment coefficient, Pitching moment/qAD
C_{m_α}	longitudinal-stability derivative, $\partial C_m / \partial \alpha$
C_n	yawing-moment coefficient, Yawing moment/qAD



$C_{n\beta}$	directional-stability derivative, $\partial C_n / \partial \beta$
D	maximum body diameter
h	body height at juncture of nose and afterbody
L/D	lift-drag ratio, C_L / C_D
M	Mach number
N_{Re}	free-stream Reynolds number
q	free-stream dynamic pressure
R	maximum body radius
r	radius of blunted nose cap
S	surface area
s	distance along the body surface
T	temperature
W	weight
W/S	body planform loading
α	angle of attack
β	angle of sideslip
δ	deflection angle
θ	body semiapex angle
ϕ	body radial angle

Subscripts:

f	flaps
MAX	maximum
n	nose
p	planform



DISCUSSION

Force and Moment Study

Most of the test results were obtained at a Mach number of 9.6 in air, but in order to assess the effect of Mach number variation, several configurations were tested for a range of Mach numbers from about 3 to 18. Results for two of these configurations are shown in figure 3 which presents the variation of $(L/D)_{MAX}$, $C_{L\alpha}$, $C_{m\alpha}$, and $C_{n\beta}$ with Mach number for a round-bottom configuration with a spherically blunted nose and a flat-bottom configuration with a canted flat face. All tests were made at a N_{Re} (based on body diameter) of 0.2 million except where noted. This Reynolds number should be representative of flight values for a reasonably sized vehicle at a Mach number of about 20. Data presented for Mach numbers above 10 were obtained in helium.

Newtonian estimates (where pressure ratio is equal to $2 \sin^2 \delta$) were made for the round-bottom configuration, and predictions of $(L/D)_{MAX}$ including skin friction show good agreement with experiment, particularly in the hypersonic Mach number range. Since the drag of this low $(L/D)_{MAX}$ configuration is primarily wave drag, the inviscid $(L/D)_{MAX}$ would be only slightly higher than that shown in figure 3. Predictions of $C_{L\alpha}$ were made by using a somewhat more sophisticated cone-flat-plate theory which combined the effects of the body upper surface estimated by shock-expansion theory with those of the body compression surfaces calculated by using cone data from reference 1 for the conic afterbody and the Newtonian theory for the spherically blunted nose. Figure 3 shows very good agreement between the predicted and experimental values of $C_{L\alpha}$ throughout the Mach number range. Both experiment and theory approach the Newtonian values of $C_{L\alpha}$ at the higher Mach numbers. The predicted values of the stability parameters for the round-bottom configuration also agree fairly well with those shown experimentally, and they exhibit the same trends in the high Mach number range. The moments about the moment-center location selected (centroid of the side-view area) are rather small and the variations in the experimental values of $C_{m\alpha}$ in the hypersonic speed range represent less than a 2-percent change in the body aerodynamic-center position.

The important thing to note from figure 3, however, is that both experimental and predicted results show no appreciable variations in the aerodynamic characteristics of these configurations with Mach number in the higher hypersonic speed range; therefore, data for $M = 9.6$ would be expected to be representative of the aerodynamic characteristics in the high Mach number range for ideal-gas conditions. Unpublished

results from the Langley Research Center indicate that the real-gas effects would be small for bodies of this type.

As previously mentioned, a large variety of lifting bodies are capable of providing a given L/D in the range of interest for reentry. Effects of some of the variations in body configurations shown in the previous figures, such as nose bluntness, are fairly obvious; however, effects of other geometric changes such as varying body cross section may be less apparent. Some of these effects are shown in figure 4 in which $(L/D)_{MAX}$ is plotted against semiapex angle of the bodies.

Experimental results for the round- and flat-bottom shapes are shown by the solid and long-dashed lines, respectively. Newtonian predictions are also included for the sharp round-bottom and flat-bottom half cones. Flagged test-point symbols indicate body shapes having a nose-bluntness ratio h/R equal to 0.4. Figure 4 shows that even the blunter half-body shapes have $(L/D)_{MAX}$ values greater than 0.5. In fact, the half hemisphere has a predicted L/D of 0.5 with the flat surface parallel to the flow and L/D is shown experimentally to be about 0.43. On the other hand, relatively slender bodies are required if values of L/D of 1.5 or greater are desired. As predicted by the Newtonian theory, the flat-bottom half cones have a higher $(L/D)_{MAX}$ than the round-bottom ones. Experimental data also shows the same characteristics for the triangular body sections. However, this effect diminishes with increasing body semiapex angle. Eliminating the high-drag, low-lift sides of the sharp round-bottom half cones, as shown by the $\phi = 45^\circ$ conic segmented body shapes, increases the $(L/D)_{MAX}$ of the configuration; however, this increased $(L/D)_{MAX}$ is accompanied by a reduction in body volume.

For a given design $(L/D)_{MAX}$, the flat-bottom half-cone approach will obviously permit the use of a blunter vehicle which may have some advantages structurally. For example, if an $(L/D)_{MAX}$ of 1.3 is desired, a round-bottom half-cone body with 0.4 bluntness requires a half-cone angle of 10° for this $(L/D)_{MAX}$. However, the half-cone angle can be increased to about 18° for a flat-bottom configuration with the same bluntness and $(L/D)_{MAX}$.

It has been shown that there are differences in the $(L/D)_{MAX}$ of the flat-bottom and round-bottom half-cone configurations; therefore, it would be of interest to examine the longitudinal characteristics of a series of these types of configurations. Figures 5 and 6 present the variation in C_m with angle of attack for a series of round-bottom and flat-bottom cone configurations of varying bluntness. For this study, the moment reference center was arbitrarily chosen as the centroid of

the side-view area. Four bluntness ratios h/R of 0, 0.2, 0.4, and 0.6 and three cone semiapex angles of 10° , 20° , and 40° were tested. Since reentry vehicles will operate primarily in the angle-of-attack range between $(L/D)_{MAX}$ and $C_{L,MAX}$ this angle-of-attack range will be of most interest.

Figure 5 shows that the addition of nose bluntness generates regions of instability in the moment data of the more slender bodies as seen by comparing the sharp 10° half cone with the 0.2 bluntness case. These regions of instability are dissipated by increasing nose bluntness or by increasing the cone semiapex angle. Qualitatively, theory indicates that these unstable regions are due to the interference effects of the blunt nose on the flow field of the body. Methods have not as yet been developed for making a quantitative analysis of the three-dimensional flow fields of these blunted bodies at angles of attack. The existence of these interference effects were clearly seen, however, in schlieren photographs of these tests. Although unstable regions such as these can undoubtedly be handled, they do introduce some additional stability problems which may require a penalty in center-of-gravity position or additional stabilizing surfaces.

Figure 6 shows that essentially the same regions of instability as previously noted for the round-bottom configuration are also found for the flat-bottom case as the configuration is blunted. Here, the nose was blunted by means of a flat canted face having 45° , 60° , and 90° of nose cant. Again, nose bluntness results in regions of instability similar to those shown for the round-bottom case as seen by comparing the sharp configuration with that having a 0.2 bluntness ratio.

These unstable regions are again shown to disappear with increasing nose bluntness. In fact, for the more highly canted faces ($\delta_n = 45^\circ$ and 60°) these unstable regions disappear somewhat more rapidly with increased bluntness than for the round-bottom case. Nose cant provides a sizable pitch-up moment for trimming the configuration at or above $C_{L,MAX}$ so that trailing-edge flaps can be used for trimming at lower angles of attack. The amount of cant required will depend on the actual design and its center-of-gravity location; however, the 60° face cant appears adequate for the center-of-gravity position of the present discussion. It should also be mentioned that variation in cant angle had no appreciable effect on the value of either $(L/D)_{MAX}$ or $C_{L,MAX}$ or the angle of attack at which they occurred for bluntnesses up to about 0.4.

Trim and directional stability coefficients are also important in discussing the aerodynamic characteristics of these lifting-body configurations. While it is impractical to obtain trim and directional data for all of the configurations tested, a few representative models

of both the configurations with relatively low L/D ($L/D \approx 1/2$) and the shapes with relatively high L/D ($L/D \approx 1\frac{1}{2}$) were tested. Figure 7 shows the trim characteristics of three configurations having a value of $(L/D)_{MAX}$ of around 0.6 or 0.7. Similar results for the configurations with higher L/D are shown on figure 8. An arbitrary flap size equal to 10 percent of the body planform area was selected for all configurations. These figures present the variation of C_m with α for the various configurations trimmed at both $(L/D)_{MAX}$ and $C_{L,MAX}$.

The configurations with low $(L/D)_{MAX}$ shown in figure 7 consisted of a blunted flat-bottom, 10° semiapex-angle, half-cone body with a 60° canted flat face and two blunted round-bottom configurations - one having the same canted face as the flat-bottom shape and the other having a spherically blunted nose and a 30° semiapex-angle conic afterbody. The body shapes with higher $(L/D)_{MAX}$ shown in figure 8 consisted of round- and flat-bottom, 10° semiapex angle, half-cone bodies with a 0.3 bluntness ratio and a 60° canted flat face, and a 20° semiapex-angle quarter-conic segmented body with a spherically blunted nose. Again, the body center-of-gravity location was chosen as the centroid of the side-view area except for the case shown in figure 8 of the round-bottom half-cone configuration with a high $(L/D)_{MAX}$. For this body shape, a 1.4-percent rearward shift of the body center of gravity from the side-view area centroid was required in order to trim the configuration at angles of attack up to $C_{L,MAX}$.

Similar trends were observed in the trim characteristics of both the body shapes with low $(L/D)_{MAX}$ ($(L/D)_{MAX} \approx 0.6$ or 0.7 shown in fig. 7) and the configurations with higher $(L/D)_{MAX}$ ($(L/D)_{MAX} \approx 1.5$ shown in fig. 8). From these figures, it can be seen that all these configurations can be trimmed by means of the relatively simple afterbody flap having a flap area equal to 10 percent of the planform area and that they exhibit stable characteristics throughout the angle-of-attack range considered. Predicted moments are shown by the solid and dashed curves and were obtained by adding the incremental flap pitching moments predicted by Newtonian theory to the experimental value of the basic body. Good agreement is shown between these predictions and experimental data. Geometrically, the flat-bottom configuration lends itself to the use of a short, full-span flap and requires relatively low amounts of flap deflection for trim. It might also be mentioned that the trim values for $(L/D)_{MAX}$ and $C_{L,MAX}$ were only slightly different from those obtained for the untrimmed vehicles.

The directional and lateral characteristics of the two round- and flat-bottom half-cone bodies with a flat canted nose are shown in figures 9 and 10. Data for the bodies with low $(L/D)_{MAX}$ are presented in figure 9, and figure 10 presents data for the higher $(L/D)_{MAX}$ shapes.

These figures show the experimental variation in $C_{n\beta}$ and $C_{l\beta}$ with angle of attack and compare these experimental results with predicted values obtained by means of Newtonian theory. It may be seen from figures 9 and 10 that this theory gives reasonable predictions of the lateral and directional characteristics of the body shapes with both low and high $(L/D)_{MAX}$ and provides an excellent indication of the trends of the stability derivatives with angle of attack.

Here, as in the case of the trim characteristics, the configurations with both low and high $(L/D)_{MAX}$ exhibit similar trends in their lateral and directional characteristics. Both flat-bottom configurations are shown to have low positive values of directional stability and virtually no dihedral effects, particularly at the high angles of attack. Since the basic flat-bottom configurations possess a relatively small degree of inherent stability, some modifications would undoubtedly be needed to increase their stability. However, these low values of $C_{n\beta}$ and $C_{l\beta}$ need not necessarily constitute a serious stability problem, since there is a variety of body modifications possible to tailor the stability of the vehicle to the requirements of its particular mission.

An example of one possible modification is shown on figure 9 in which a side flap with span and chord equal to 0.2 of the body diameter was added to both the round- and flat-bottom body shapes of low $(L/D)_{MAX}$. For the flat-bottom case, the flap was rolled out 10° and attached along an extended line of the body surface. The same sized flap was also tested on the round-bottom configuration. In this case, the top of the flap was again rolled out 10° and was attached parallel to the body center line. Results from these tests, indicated by the square symbols on the figure, show that, while these flaps have little effect on the stability derivatives at $\alpha = 0^\circ$, both the lateral and directional stability of the vehicles is increased at angles of attack near 30° - the range of primary interest.

The round-bottom configurations were found to have a large amount of inherent directional stability along with large values of positive dihedral. These large values of roll due to sideslip are usually undesirable from a standpoint of dynamic stability.

Heat-Transfer Study

Thus far, only a discussion of the force and moment characteristics of the configurations considered has been made. However, since the heating characteristics of these bodies are of equal importance, an analysis of these characteristics was made for a few of the configurations. The heat-transfer studies were limited to simple, basic shapes that were amenable to theoretical analysis which should give results with engineering accuracy. Only basic body shapes have been included in the heat-transfer investigation; therefore, the results do not represent the heating characteristics of complete vehicles, which can be altered by the addition of control and stabilizing surfaces. The following analysis will be subdivided into two parts and will consider the total heat absorbed and the peak heating rates encountered during entry.

First to be considered is the effect of body geometry and lift-drag ratio on the total heat load, a parameter of importance for heat sink and ablation shielding. In figure 11, the heat load is presented as a function of the lift-drag ratio for three types of half-body configurations entering the earth's atmosphere from a decaying orbit at zero angle of attack. The method for calculating these heating rates was taken from reference 2. The configurations considered are: (a) half cones of semicircular cross section having bluntness ratios, that is, the ratio of cap radius to base radius, of 0, 0.2, and 0.4, (b) half cones of semicircular cross section having flat nose section with a bluntness ratio h/R of 0.3, and (c) an 80° swept, 45° dihedral configuration.

Along each of the curves for these four configurations (fig. 11), the cone semiapex angle varies from 10° (high L/D) to 40° (low L/D) for the 0 and 0.2 curves and from 20° to 40° for the 0.3 and 0.4 curves.

The ordinate scale is the heat load for the configuration (neglecting the heating rate to the upper surface and the effects of radiation) non-dimensionalized in terms of the heat load of a sphere of the same cross-sectional area and weight entering on a nonlifting trajectory. The heating rates in this figure and in the subsequent ones have been calculated from laminar-boundary-layer theory where possible or by engineering estimates when the shapes were too complex from a theoretical viewpoint. For example, the heat transfer to the blunted cones was calculated from the laminar-boundary-layer theory of reference 3 by assuming that the absence of the upper surface had no influence on the heat-transfer rate to the remainder of the cone. The heat-transfer rate to the cone having a flat nose section was calculated in the same manner by assuming that flow originated at the virtual tip of the blunted cone. The average heat transfer to the flat nose section was assumed to be equal to that of a circular flat face having an area equal to that of the cone face. The average heat-transfer rate for the circular flat face was assumed to be

1.1 times the stagnation-point value. The stagnation-point heat-transfer rate was assumed to be 0.575 of the stagnation-point value of a hemispherically blunted body of equal radius. The heat-transfer rate to the 80° swept, 45° dihedral configuration was estimated by calculating the average heat-transfer rate to an equivalent cone; that is, the cone and dihedral configuration were assumed to have equal surface pressures and lengths. This average heat-transfer rate was assumed to represent the average heating rate to the dihedral configuration; the total heat-transfer rate to this configuration was obtained from the assumed average heat-transfer rate and the area of the dihedral configuration.

Experimental lift-drag ratios, obtained from the force investigation, were used in all cases except for the Newtonian curve. The Newtonian curve was calculated for the hemispherically blunted body assuming inviscid flow and applies for all bluntness ratios from 0 to 1 and semi-apex angles from 10° to 40° .

The major point to note in this comparison is the predominant effect of lift-drag ratio on total heat load. In the region in which Newtonian theory predicted the lift and drag characteristics, the effect of body shape on heat load is important only insofar as the shape changes the value of L/D . Furthermore, in this same region, the assumption of Newtonian flow appears to give a useful, lower asymptotic value of the heat load.

Although figure 11 indicates that the effect of body shape on heat load is, in general, secondary to lift-drag-ratio effects, a somewhat more detailed analysis of the influence of body shape on heat load for a class of bodies previously discussed in the force-study section will be made. A comparison of the heat load for round-bottom and flat-bottom half-circular cones having fixed base areas and weights is presented in figure 12. In this figure, variations in L/D correspond to angle-of-attack changes in the high-drag portion of the lift-drag curve. The two solid curves are for the round-bottom configuration; the dashed curves are for the flat-bottom configuration.

For both configurations, the heat-transfer rate in the range of low L/D (i.e., high angle of attack) was calculated by assuming cross flow to exist over the body. The heat level to the most windward generator of the round-bottom cone was assumed to vary as the sine of the angle of attack of the cone center line as suggested in reference 4. For the flat-bottom cones at low angles of attack, the heat-transfer rate was calculated from strip theory. The two heating rates represented by the circular symbols on the curves for the round-bottom cones are for zero angle of attack and were taken from figure 11. The curves representing the heat load between the limits of these calculations were simply faired, and this faired region is indicated by the dotted section of the curves.

It should be noted that this comparison applies only for simple half-cone bodies, and configuration changes required to obtain vehicles with suitable aerodynamic characteristics must be considered in the final analysis of the total heat load. The heating to the upper surfaces of the configurations has been neglected in computing the heat load. This omission should not be serious, however, since a major portion of the curves for the flat-bottom configuration, where this omission could be serious, was computed for angles of attack equal to or greater than the cone semiapex angle.

Figure 12 indicates that for a given cone angle and L/D , the heat load of the flat-bottom configuration is less than that for the round-bottom configuration. Further, it appears that for low L/D operation, it is preferable, in general, to use a configuration with a low maximum L/D such as a 40° half cone in preference to a high L/D configuration such as a 20° half cone operating at very high angles of attack and, consequently, low values of L/D .

In the previous section, face cant was shown to provide desirable pitch-up moment for trim. The influence of nose-cant blunting on total heat load will be discussed in a limited way. In figure 13 the curve represents the heat load for a 10° flat-bottom sharp half-circular cone. The two vertical lines represent the range of the heating estimate for the cone blunted by means of a flat face having a 60° cant. Bluntness ratios of 0.3 and 0.6 have been considered. The angle of attack of the blunted cone is 30° . The heat load for the blunt cones was calculated by three different procedures which are represented by the solid dots on the vertical line. The upper and lower dots represent the heat load calculated from strip theory. The lower dots represent the heating rate estimate made by assuming flow to start at the virtual tip of the cone; the calculations represented by the upper dots assumed that flow started at the physical leading edge. The middle dots and the curve for the 10° sharp half cone represent the heat estimate made by assuming cross flow. The lower two estimates probably more nearly indicate the change in the heat load due to bluntness while the upper points provide a conservatively high upper limit.

While the results are not conclusive, there appears to be, for these conditions, no significant effect of this type of nose blunting on the heat load for bluntness ratios of 0.3 and only a small penalty at a value of 0.6.

So far, the discussion has dealt only with the total heat loads of these various body shapes. Peak heating rate is an equally important design heating parameter which serves to indicate, to some degree, regions of the body structure requiring heat absorbing material as well as regions where a radiation-cooled structure might be used.

If the round- and flat-bottom body shapes of the same size and weight operating at a fixed L/D are again compared, two factors are found which influence heating rates over these bodies. These two factors are geometry (shape and vehicle attitude) and the difference in C_L at which these bodies operate for a given L/D which results in a difference in flight environment for the two body shapes.

Figures 14 and 15 show the total effect of these two factors, geometry and velocity-altitude differences, on the laminar peak heating rates for equilibrium flight at the body lower meridian or center line of these two vehicles. It should be noted that these heating rates are representative of those occurring over the major portion of the lifting surfaces; however, they do not take into account the edges of either of these bodies which are subjected to higher localized heating. Since in the force investigation bodies in two L/D ranges (about 0.7 and 1.4) have been considered, the distributions presented in figures 14 and 15 are for bodies of these L/D ranges. The peak heating rates in these figures are plotted as a function of distance along the body nondimensionalized in terms of the base radius.

Figure 14 shows that for configurations with both low and high L/D , the flat-bottom shapes, indicated by the dashed line, have a lower heating rate than the round-bottom shapes, shown by the solid curves. For the 40° half-cone shape operating at $L/D = 0.7$, the difference in the heating rate between the round- and flat-bottom configurations is primarily due to difference in body geometry since relatively small differences occurred in the trajectories of the two configurations. However, for the more slender 20° half-cone bodies operating at L/D of 1.4, both geometry and differences in C_L combine to lower the heating rates on the flat-bottom configuration.

Figure 15 shows the effect of nose bluntness on the peak heating rates of both the 40° and approximately 23° round-bottom half-cone shapes at zero angle of attack. Note that for this case the origin of the s/R coordinate is the tangency point of the spherical cap and the conical afterbody. In the case of the 40° cone it can be seen that while bluntness has little effect on the L/D of the configurations, the peak heating rate over the forebody is considerably reduced by increasing nose bluntness, whereas heating rate near the rear of the bodies is essentially unaffected by bluntness. This reduction in heating rate is essentially due to variation in body shape since the trajectories are the same for all configurations. Similar trends due to bluntness are also shown on the right for the more slender configurations with higher values of L/D .

These comparisons of body shape effects on the peak heating rate are independent of vehicle size and weight; however, the actual heating

rates of a configuration are of course strongly dependent upon these parameters. The heating rates shown on these figures are for an assumed weight-to-base-area ratio of 120 lb/sq ft and a base radius of 2.8 feet. This value of 120 lb/sq ft corresponds to a planform loading of about 70 lb/sq ft for a 20° cone and about 160 lb/sq ft for a 40° cone and these values are representative of lifting bodies currently being considered. The temperature scale is for radiation equilibrium and an assumed emissivity of 0.8. This temperature scale serves to indicate the surface temperature level associated with these bodies during equilibrium flight from a decaying orbit.

CONCLUDING REMARKS

This investigation has served to point out some of the relative merits of several simple lifting-body configurations and indicates that in many ways body shape is of secondary importance to other design parameters such as size, weight, planform loading, and lift-drag ratio. Furthermore, for a given lift-drag ratio and weight-to-base-area ratio, no specific body shape was found to possess sufficiently superior qualities to exclude consideration of other body shapes. However, the configurations with more nearly flat bottoms appeared to offer some advantages from the standpoint of performance and heat-transfer considerations. Further studies are needed, especially to develop more adequate methods of heat-transfer analysis for the more complex configurations.

REFERENCES

1. Ames Research Staff: Equations, Tables, and Charts for Compressible Flow. NACA Rep. 1135, 1953. (Supersedes NACA TN 1428.)
2. Chapman, Dean R.: An Approximate Analytical Method for Studying Entry Into Planetary Atmospheres. NASA TR R-11, 1959. (Supersedes NACA TN 4276.)
3. Lees, Lester: Laminar Heat Transfer Over Blunt-Nosed Bodies at Hypersonic Flight Speeds. Jet Propulsion, vol. 26, no. 4, Apr. 1956, pp. 259-269.
4. Reshotko, Eli: Laminar Boundary Layer With Heat Transfer on a Cone at Angle of Attack in a Supersonic Stream. NACA TN 4152, 1957.

LIFTING BODIES

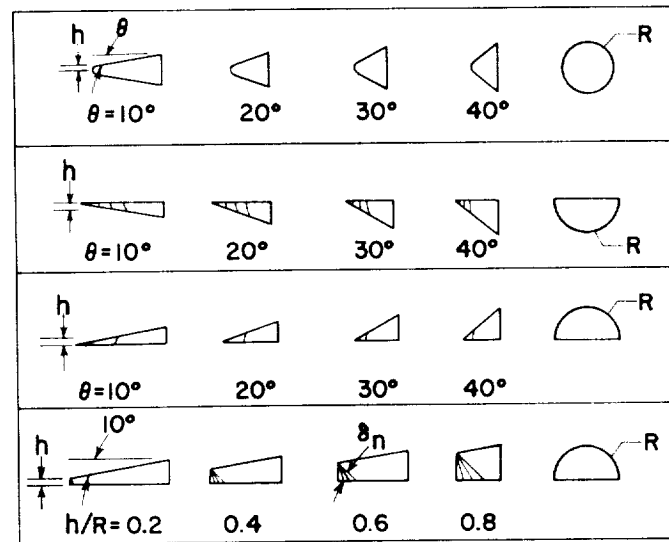


Figure 1

LIFTING BODIES

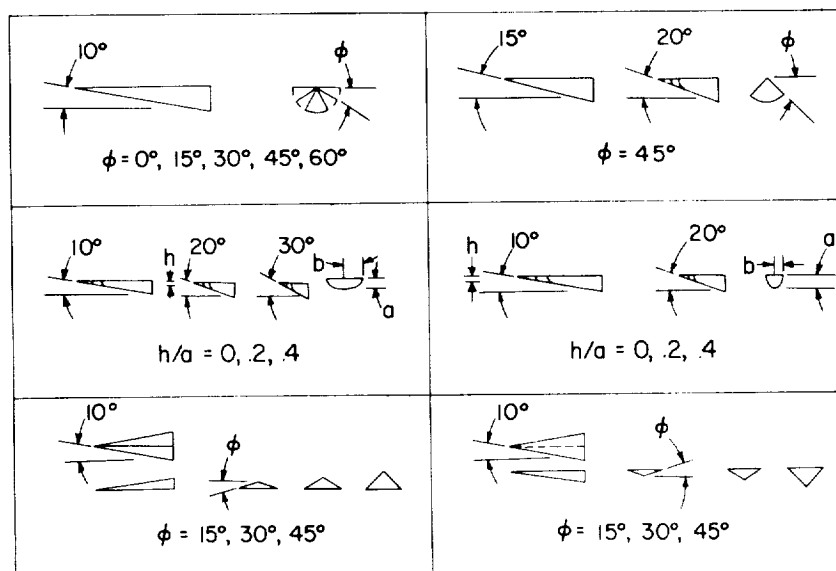


Figure 2

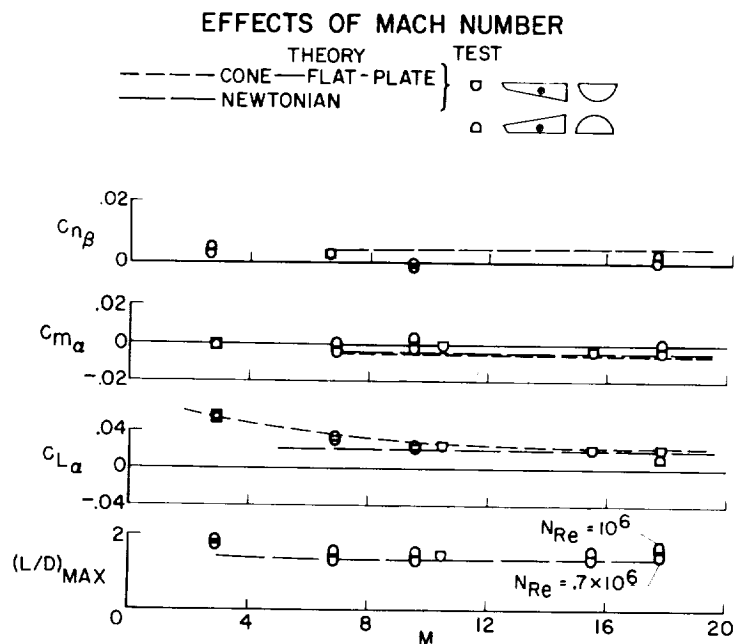


Figure 3

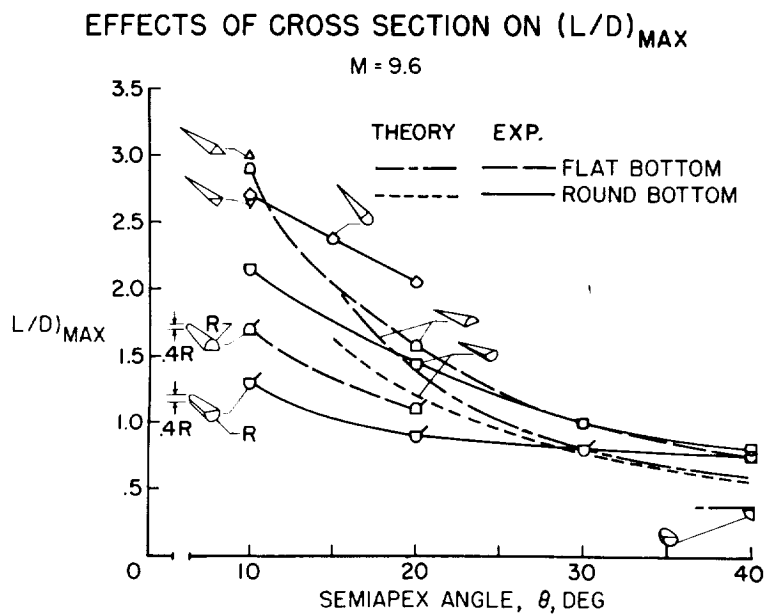


Figure 4

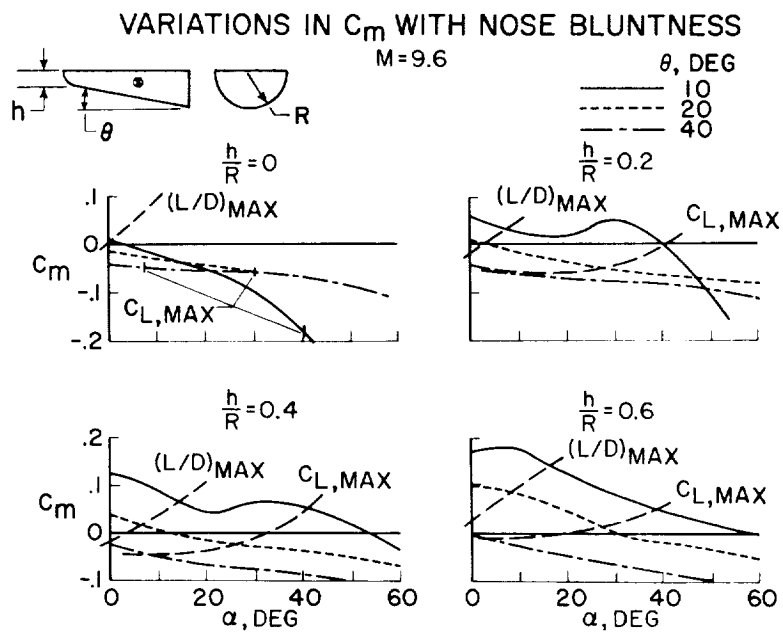


Figure 5

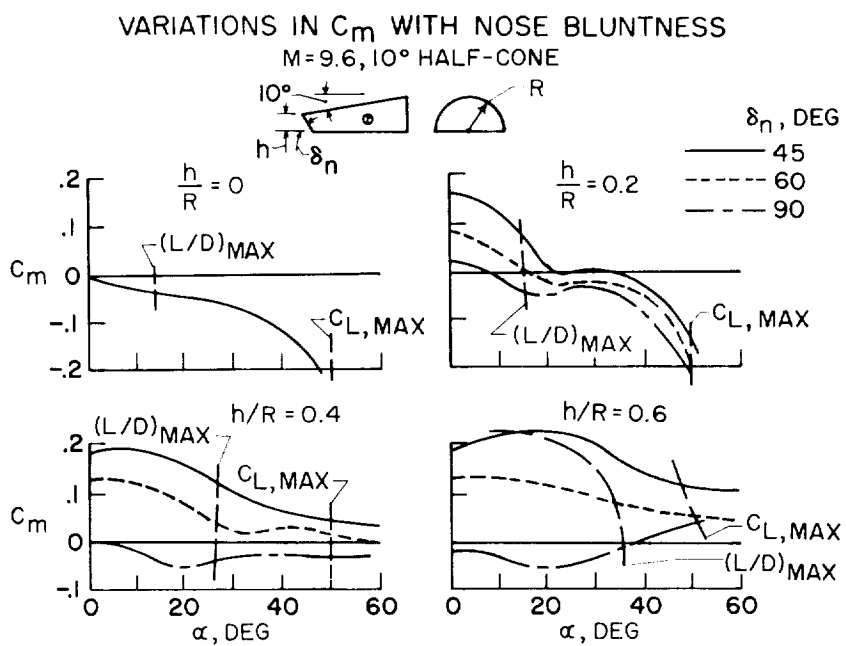


Figure 6

TRIM CHARACTERISTICS

$$\frac{S_f}{S_p} = 0.1; M = 9.6; (L/D)_{MAX} \approx 0.5$$

THEORY TEST
 ———— ○ (L/D)_{MAX}, TRIM
 - - - - - □ (C_L, MAX) TRIM

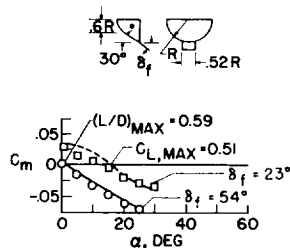
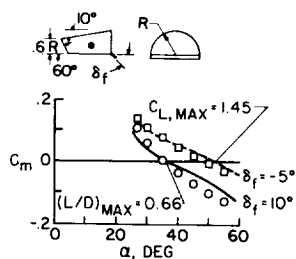
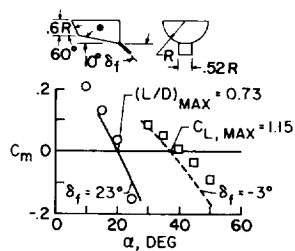


Figure 7

TRIM CHARACTERISTICS

$$\frac{S_f}{S_p} = .1; M = 9.6; (L/D)_{MAX} \approx 1.5$$

THEORY TEST
 ———— ○ (L/D)_{MAX}, TRIM
 - - - - - □ (C_L, MAX) TRIM

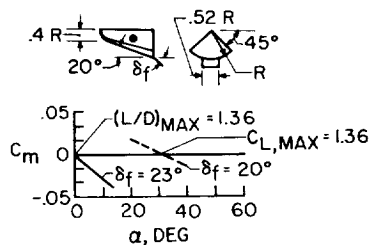
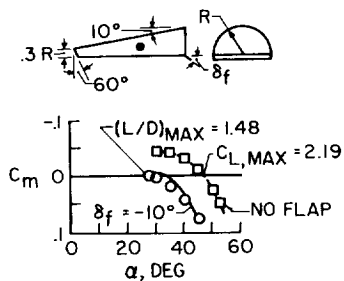
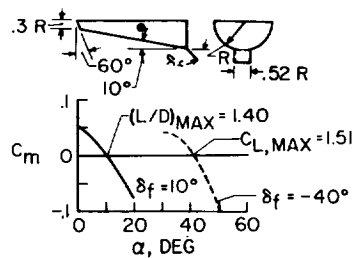


Figure 8

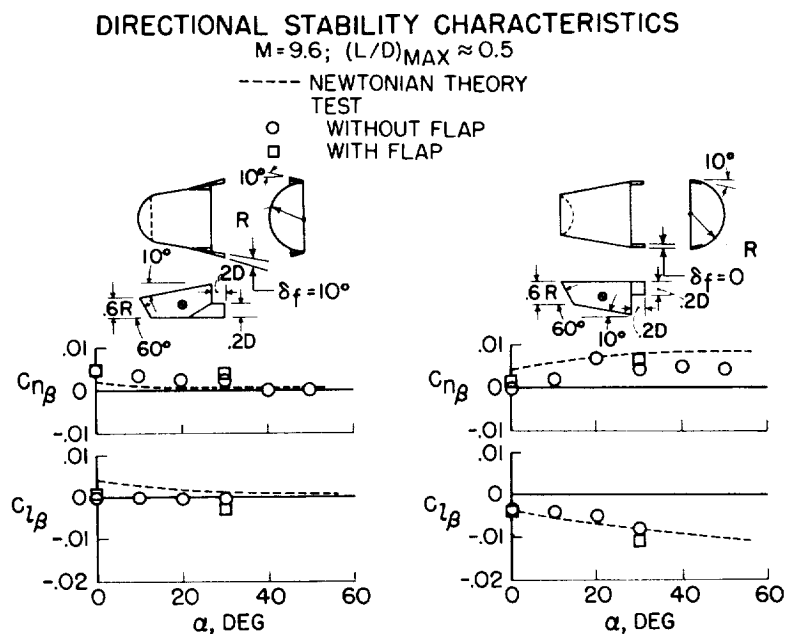


Figure 9

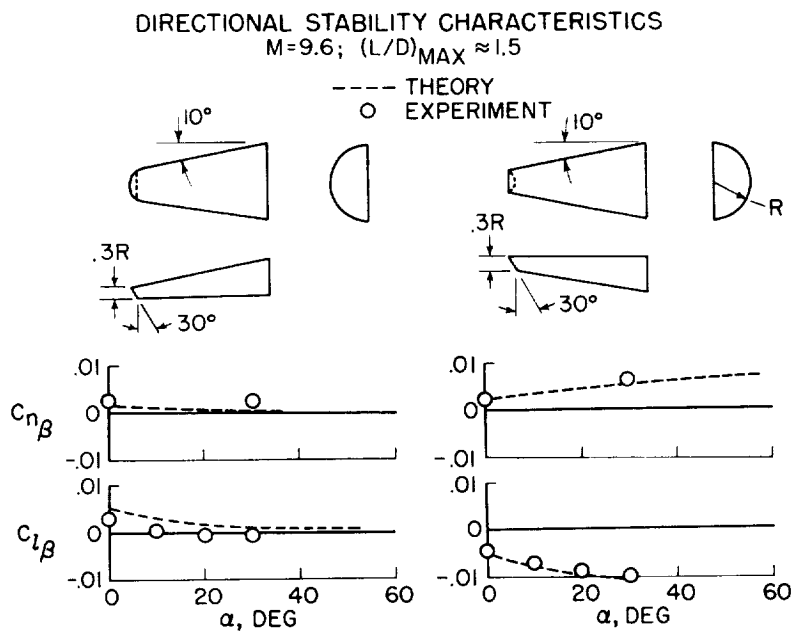


Figure 10

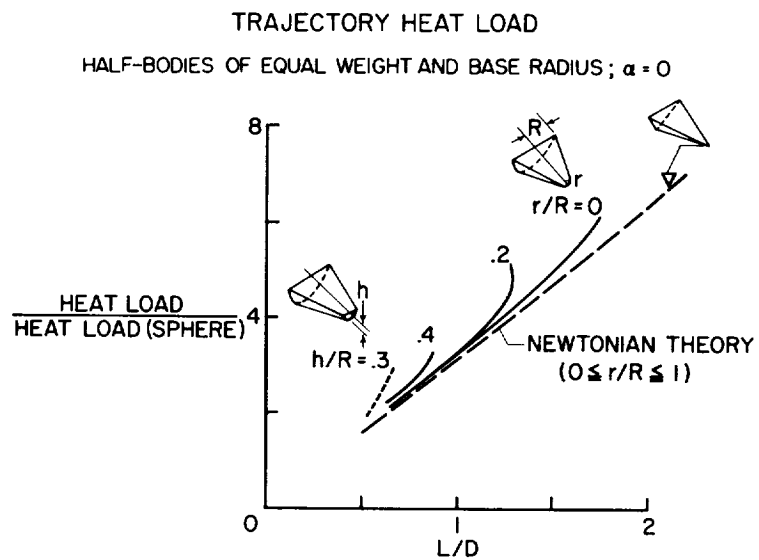


Figure 11

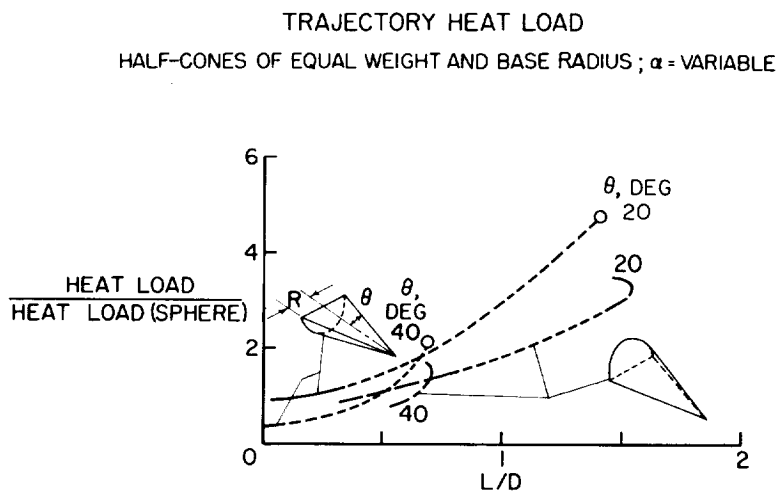


Figure 12

TRAJECTORY HEAT LOAD FOR 10° HALF-CONE
60° CANTED FACE OF VARYING BLUNTNESS; α = VARIABLE

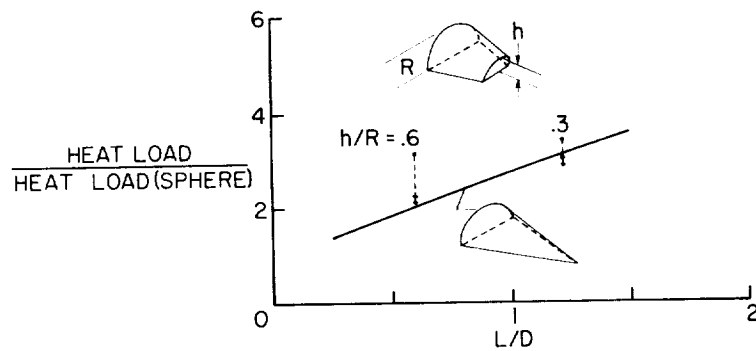


Figure 13

TRAJECTORY PEAK HEATING RATES
ROUND- AND FLAT-BOTTOM HALF-CONES
W/A = 120 LB/SQ FT; R = 2.8 FT

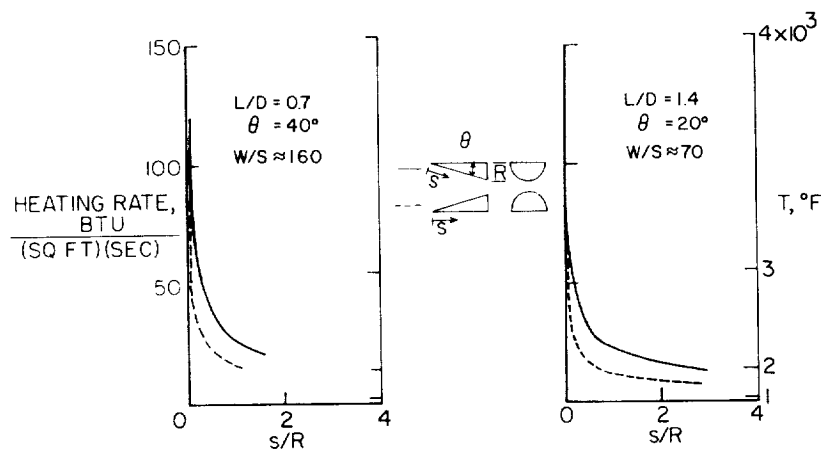


Figure 14

TRAJECTORY PEAK HEATING RATES
 NOSE BLUNTING; $W/A=120$ LB/SQ FT; $R=2.8$ FT; $\alpha = 0$

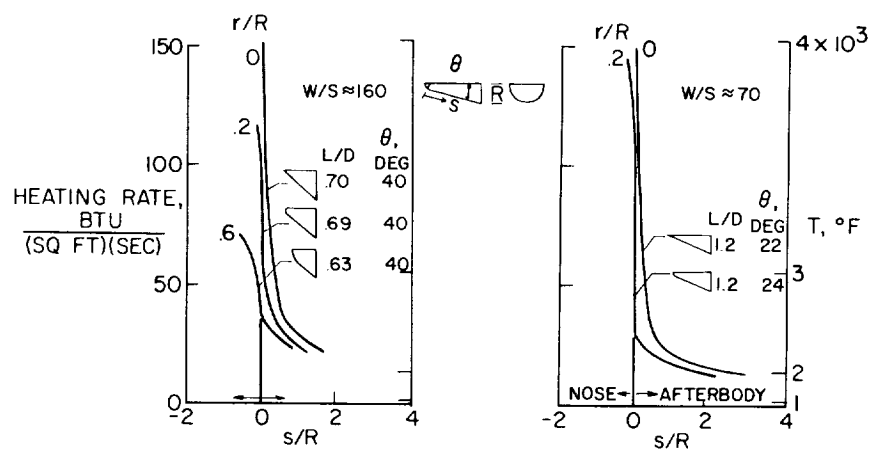


Figure 15



FLOW FIELDS, PRESSURE DISTRIBUTIONS, AND HEAT TRANSFER
FOR DELTA WINGS AT HYPERSONIC SPEEDS

By Mitchel H. Bertram, William V. Feller,
and James C. Dunavant
Langley Research Center

SUMMARY

Successful correlations of pressure on delta-planform wings are shown for both the center-line and spanwise pressure distributions over a range of sweep, Mach number, angle of attack, and dihedral angle. Such correlations allow the application of experimental results to Mach numbers widely different from those at which the data were obtained, thus allowing the prediction of the pressure on the lifting surface of a vehicle such as the Dyna-Soar with confidence. Much of the heat transfer has been found to be amenable to simple approaches which take into account the flow pattern peculiar to the angle-of-attack range under consideration. The leading edge itself has been found to become a trailing edge in the sense of airflow direction at high angles of attack. This is connected with the appearance of conical flow on the delta wing and tends to alleviate the heat transfer to the leading edge.


INTRODUCTION

The delta planform is a type of great interest in hypersonic-glider and lifting-reentry studies. In order to supply the information necessary for the proper evaluation and successful application of this shape an extensive research program has been carried out.

Only a small fraction of the results so far obtained can be treated here; however, it will be the purpose of this paper to give the highlights of the recent research results.

SYMBOLS


a_0 speed of sound, reservoir
 c chord



h	heat-transfer coefficient
h_{MAX}	heat-transfer coefficient on stagnation point of sphere
l	length along leading edge
M	Mach number
N_{St}	Stanton number based on free-stream conditions
p	pressure
p_{MAX}	stagnation pressure behind a normal shock
R	Reynolds number
s	distance along surface from geometric stagnation point of spherical nose
t	thickness
u	velocity
x	chordwise distance
α	angle of attack of plane of leading edges
α_{EFF}	local angle of attack of the wing panel (eq. (1))
β	angle of shock from stream
ζ	surface flow angle measured from center line
θ	ray angle from center line
Γ	dihedral angle
Λ	sweep angle

Subscripts:

c	chord
ϕ	center line
le	leading edge



x chordwise distance from leading edge
 ∞ free stream

Flow Fields and Pressure Distributions

Examples of the models tested are shown in figures 1 and 2. Most of the investigations were concerned with flat or slab delta wings; however, as illustrated in figure 1 a set of models was designed to investigate the effect of dihedral on the underside of the wing.

Models shown in figure 2 are examples of wings with a large amount of blunting which are part of a coordinated delta-wing program. All the models in this program were of this type - that is, a slab with a swept-cylinder leading edge - and many were tested with the two different noses shown here. The length of the wing in terms of diameters varied from facility to facility. For instance, although the models shown in figure 2, which were tested in the Langley 11-inch hypersonic tunnel, are 7 diameters long, the model tested in the Unitary Plan wind tunnel at the Langley Research Center was 20 diameters long.

In figure 3 are presented schlieren photographs of the shock shape on the cylindrical-leading-edge blunt-nose model in top view in order to show the extent of the effect of the blunt nose. In figure 3(a) the model is at zero angle of attack at Mach 6.9 and 9.6 in air and Mach 18.4 in helium. In figure 3(b) the angle of attack ranges from 10° to 30° at Mach 6.9 in air. The bottom wing is 21 diameters long and the top wing corresponds to a 3 times enlargement of that part of the bottom wing ahead of the dashed line. This top wing is only 7 diameters long. At zero angle of attack the Mach 6.9 and 9.6 pictures are very similar, and the shock shape is much the same at Mach 18.4 in helium. If the extent of the nose influence is judged by the inflection in the leading-edge shock, the blunt nose affects less of the wing length as the angle of attack increases. Since the spherical nose has a shock of fixed shape, that is, independent of angle of attack in the range shown here, this change in shock shape is mainly due to changes in the shock around the cylindrical leading edge with angle of attack. Far enough away from the nose, at 0° and 10° angle of attack, the shock is parallel to the leading edge. At 20° and, to a more noticeable extent, at 30° angle of attack the main-stream flow senses the local wing span, and the leading-edge shock shape becomes conical in nature.

Next, the shock is examined in side view. In this case figure 4 presents the shock angle determined from schlieren photographs of the flat wings as a function of angle of attack. Included in this figure but not identified are wings with sharp and blunt noses and leading edges. To avoid data with substantial pressure gradients, data at angles of attack less than about 20° for the blunted wings and within about $1\frac{1}{2}$ diameters of the nose are excluded from this figure. These exclusions are not very limiting because the main interest is in applications of the delta wing in the range of angle of attack from 15° to 50° on reentry vehicles. The location of the wing surface and two-dimensional oblique-shock theory are included in this figure for reference. Note that while for shock angles greater than about 19° the delta-wing shock angles deviate considerably from the two-dimensional theory, the incremental effect of Mach number seems to be given with good accuracy by the theory, and it is expected that with further increases in Mach number there will be an almost negligible change in shock angle. Also noteworthy is the insensitivity of the shock angle to changes in sweep angle and the small shock standoff angle from the wing surface.

As yet there are no adequate theories for predicting the pressures on delta wings with detached shocks. However, this fact does not preclude a correlation of empirical results. Figure 5 shows the wall-to-free-stream static-pressure ratios obtained on the center line of various flat wings. Only data where essentially no longitudinal pressure gradient exists on the center line have been included. The Mach 6.85 and 9.6 data encompass the range of angle of attack up to about 60° . For the flat wings the sweep angles at which pressure data are available are only 70° and 75° ; however, data for delta wings with sweep angles to at least as low as 60° should correlate with the results shown here. The pressure ratio does not appear to vary with leading-edge bluntness, nose shape, or sweep angle. Figure 6 shows the good correlation which results from using the hypersonic similarity parameter $M_\infty \sin \alpha$ suggested by both hypersonic oblique shock theory and Newtonian theory to correlate the wall-to-free-stream static-pressure ratio for the same data. Included in these figures are the results from exact two-dimensional oblique shock theory and Newtonian theory for reference.

The pressure data from wings with dihedral on the underside are shown in figure 7 and these data correlate well with flat-wing data. Data obtained for a 60° swept wing are included here. For these data the angle of attack used in the correlating parameter is the local angle of attack of the wing panel given by the following equation:

$$\tan \alpha_{\text{EFF}} = \tan \left[\alpha + \arctan \left(\tan \theta_{le} \tan \Gamma \right) \right] \frac{\frac{\cos \alpha}{\tan \Gamma}}{\sqrt{1 + \frac{\cos^2 \alpha}{\tan^2 \Gamma}}} \quad (1)$$

With this correlation the center-line pressures on a delta wing may be predicted at Mach numbers considerably different from those of the tests.

Up to now consideration has been given to wings at angles of attack high enough so that no longitudinal pressure gradient exists on the center line of the wing. The question arises as to what extent the center-line pressures are altered in the region of the nose. Figure 8 examines in some detail the center-line pressure distribution on the hemisphere-nose delta wing of 70° sweep. This wing had swept cylinders forming the leading edges, and overall the wing corresponded to the first few feet of an actual hypersonic glider. The data are shown over an extensive range of angle of attack. In this figure the pressure parameter is p/p_{MAX} where p_{MAX} is the stagnation pressure after a normal shock. The distance parameter is distance along the surface on the center of the wing in terms of leading-edge diameters. The origin of the surface distance is always taken at the geometric stagnation point of the spherical nose. On the spherical nose there is a Mach number freeze; that is, p/p_{MAX} is a function only of position on the sphere, not of free-stream Mach number. On the slab portion of the high-pressure side of the wing the pressure gradient induced by the blunt nose, which is so pronounced at zero angle of attack, becomes less severe with increasing angle of attack and virtually disappears at 20° angle of attack and greater. (See ref. 1.)

Thus far only the center line of the wing has been considered. The flow over the wing will now be examined in a more general way. Figure 9 shows tracings of surface flow streamlines formed by flowing lubricating oil impregnated with carbon black on a sharp-leading-edge wing with 75° sweep at Mach 9.6. There is a definite surface flow in toward the center of the wing caused by the pressure gradient induced by the thick boundary layer. However, because of this very gradient, the streamlines external to the boundary layer must be out away from the center of the wing. With increasing angle of attack, as shock-loss effects start to predominate, the flow at the surface also turns out from the center. At 15° angle of attack the flow is away from the wing center line but it still comes in across the leading edge. At 30° angle of attack the flow has turned out to such an extent that in the sense of airflow direction the geometric leading edge has become a trailing edge. An interesting feature of the flow at 30° angle of attack is the appearance of a parting line at about 12° out from the center line of the wing. At 60° angle of attack the flow lines, which for the most part were more or less straight at 15° and 30° angle of attack, appear to be hyperbolic in nature. The parting line referred to at 30° angle of attack has moved into the center of the wing. More detail on these flows is shown in figure 10. Here the surface flow angles measured from these oil flow streaks are shown as a function of ray angle from the apex. This figure shows the movement of the parting line into the center of the wing. A line for perfect radial

flow has been put on the figure for reference. The location of the parting line is given by the point at which the data cross the line for radial flow. Note that the flow lines are very nearly radial in the central region of the wing at 45° angle of attack, and thus at higher angles of attack than this there is no parting line as such, unless one wishes to view the center line of the delta wing as a parting line.

At this point the effect of dihedral on the surface flow angularity will be examined. Shown in figure 11 are results from the 75° swept sharp-leading-edge wing at 30° angle of attack with dihedral angles of 0° and 26° . The angles of the oil-carbon black streaks relative to the center line of the wing are shown as a function of angular measure from the wing center line. The curves, which are fairings of the measurements, have been made exactly parallel to each other. That this can be done indicates that the spanwise pressure distributions should not be a function of dihedral angle. In addition, such an approach as the use of the local angle of attack of the surface in correlating wing pressures is also partially justified.

Figure 12 shows the lateral pressure distributions associated with these flow patterns from 0° to 60° angle of attack. The local pressure in every case has been divided by the pressure on the center line of the wing. Included in this figure are data for two Mach numbers, two sweep angles, and two dihedral angles. Overall one may note the insensitivity of the lateral pressure distributions at angle of attack to variations in any of these parameters. At 30° and 60° angle of attack the flow is conical, as indicated by oil flow tracings, and at the highest angle of attack (60°) the pressure distribution approaches that for a disk at 90° angle of attack to a hypersonic flow, to which it is compared in this figure. At zero angle of attack the pressures are high in the leading-edge region because of boundary-layer displacement effects and the flow is not conical.

Insofar as pressures are concerned successful correlations have been shown for both the center-line and spanwise pressure distributions in which the effect of a modification such as the addition of dihedral to the surface is included. Such correlations allow the application of experimental results to Mach numbers widely different from those at which the data were obtained, thus allowing the prediction of the pressure on the lifting surface of a vehicle such as the Dyna-Soar with confidence.

Heat Transfer

This section will present some of the heat-transfer results from the broad study of delta wings described in part A. Heat-transfer data on some of the configurations were available from $M = 3.5$ to about $M = 18$ from a number of facilities. The lower Mach number tests, however, showed transitional and turbulent flow over much of the surface, and at the highest Mach number the range of angles of attack and configurations studied was less complete. In order to present a clear picture of the overall distribution of heat-transfer rates and their relation to the external flow fields, the present discussion will be based mostly on the fully laminar data at $M = 9.6$ from the Langley 11-inch hypersonic tunnel.

The sharp-leading-edge delta wing will be considered first. It is geometrically simpler, but still indicates the general behavior of the heat transfer to the blunt wing for regions far from the nose and leading edges. Figure 13 shows the trend of heat transfer with angle of attack. The data are for points along the center line of a flat delta wing, presented in the form of the laminar flat-plate correlating parameter N_{St}/R_x based on distance from the nose, with fluid properties evaluated at free-stream conditions.

Up to about 20° the heat transfer increases with angle of attack about as expected for a flat plate, as shown by the solid curve labeled "strip theory." At higher angles of attack, the data depart from the strip-theory trend and approach the dashed curve predicted by cross-flow theory, which regards the wing as a succession of independent spanwise strips in cross flow. For this theory, the component of free-stream velocity normal to the wing shock was used as the cross-flow stream, and the equivalent stagnation-point velocity gradient was calculated from a correlation of experimental pressure distributions measured in circular disks normal to the flow, which will be discussed later in this paper. This assumed pressure distribution does not fit the pressures measured on the delta wing at angles of attack of 30° and less, as was shown in figure 12 but becomes a better approximation at higher angles, and fits very well at $\alpha = 60^\circ$. The cross-flow approach also neglects completely effects of the chordwise component of the flow. A more refined and more nearly correct approach is given by the streamline divergence theory shown by the dot-dashed line. This method, based on the theory of Vaglio-Laurin (ref. 2) involves integrating along streamlines a quantity including local flow conditions and a term expressing the rate of separation or divergence of the streamlines. When the same spanwise component velocities are used as were used in the cross-flow theory to compute the streamlines near the wing center line, the Vaglio-Laurin

theory gives a very good prediction of the heat-transfer rates from about 25° to 60° angle of attack.

The theory of Vaglio-Laurin is actually very general and can be applied whenever the streamlines and flow properties outside the boundary layer are known. Because there is as yet no adequate theoretical method for determining the streamlines over the entire delta wing at all angles of attack, the application of this method will not be discussed further in this paper.

Above about 60° , where the wing shock is curved, the correlation based on the single characteristic length, the distance from the nose, can be expected to break down. The behavior at angles near 90° is discussed further in reference 3. The viscous interaction effects on the wing will be most important near zero angle of attack. Previous studies indicate that the pressure induced by the boundary-layer growth would lead to higher heat-transfer rates than those on a flat plate with constant pressure, but the data near $\alpha = 0^\circ$ are in fact mostly lower. This behavior is examined more closely in figure 14. These data are for points all over the delta wing, plotted against streamwise distance from the leading edges in terms of root chord, and are shown for three Mach numbers. Near the leading edge, the heat transfer is increased by the induced pressure and pressure gradient as expected at the higher Mach numbers, but falls off to values below those predicted for a flat plate without induced pressure, and the decrease is greatest at the highest Mach numbers where the induced pressures are highest.

The explanation is found in the surface flow patterns shown in figure 15. The calculated streamlines outside the boundary layer, shown by the solid lines, are deflected outward and are slightly divergent, which would indicate an increased heat transfer. In the boundary layer near the surface, however, the induced pressure gradients produce a flow toward the center from each leading edge, shown by the dashed lines which are traced from oil streak patterns. This secondary flow piles up low-energy air in the middle of the wing, which thickens the boundary layer there and reduces the heat-transfer rates.

Because the pressure gradients producing this secondary flow decrease with distance from the leading edge, the effect should disappear some distance downstream of the nose of the wing. Available data do not, however, permit an assessment of how far downstream the reduction extends. The effect decreases with angle of attack and is negligible above about 12° at $M = 9.6$.

The spanwise distribution of heat-transfer coefficients on the sharp-leading-edge delta wing is shown in figure 16. Here, the experimental Stanton numbers along each of several spanwise lines are correlated by

taking the ratio of the measured values to the value calculated for the center-line point as though it were part of a flat plate at the same angle of attack as the wing. The curves labeled "strip theory" are included to give a frame of reference. They show the expected effect of the decreasing distance from the leading edge as the point considered moves out spanwise, assuming the streamlines to be straight and parallel, as on a strip of a flat plate.

At zero angle of attack, the heat transfer is high near the leading edge because of the boundary-layer induced pressure. The reduction discussed in figure 15 due to the inward flow near the surface extends over about half the semispan.

At 16° angle of attack, on the lower surface the flow is slightly outward, but the divergence of the streamlines is small and the heat transfer is fairly well predicted by simple strip theory.

At higher angles of attack, shown in figure 17, the pattern changes. The surface flows at $\alpha = 26^\circ$ and 45° on the lower surface show a region with nearly radial streamlines over most of the wing but with an outer region where the flow is outward over the leading edge. For this kind of flow, the uniform parallel flow assumed in the strip theory is clearly inadequate, and in fact the measured heat-transfer distributions resemble more nearly the shapes predicted by the cross-flow theory. The cross-flow pattern is not fully achieved, however, at 45° angle of attack. By $\alpha = 60^\circ$, as shown in figure 9 the central region of nearly radial flow has disappeared, and here the cross-flow theory gives a good prediction of the heat-transfer rates.

In figure 7 it was shown that the pressures on a dihedral wing can be correlated with those for a flat plate by using the local wing panel angle of attack. In figure 18 the heat-transfer rates on three dihedral wings are compared at the same wing panel angle of attack, 26° , and therefore at the same pressure. The flat wing (zero dihedral) data taken from figure 17 are shown by the shaded band. The heat transfer near the center line is considerably increased by the presence of dihedral, by as much as a factor of 2 at 26° dihedral. This is due to the outward component of the flow produced by the dihedral (shown in fig. 11) which thins the boundary layer near the center. The increment in heat transfer due to the dihedral falls off spanwise, and the outer half of the wing panel shows only small differences in heat transfer with dihedral. Thus, for the same lift and planform area a dihedral wing will have a greater heat load than a flat one.

The discussion thus far has dealt with the behavior of sharp-leading-edge delta wings. The nose and leading edges of flight vehicles will necessarily be blunted to some extent. Far from the nose and leading

edges, the trends shown by the sharp wing are generally applicable to the blunt wing also. The heat transfer close to the nose is shown in figure 19. Here, heat-transfer coefficients measured at points along the center line of a spherical-nosed delta wing, expressed as a fraction of the value calculated for the stagnation point of a sphere, are plotted against surface distance from the stagnation point. On the sphere the measured heat-transfer rates agree well with the values calculated by Lees' theory (ref. 4) over the range of angles of attack presented. On the slab, at zero angle of attack figure 8 showed that the pressures induced by the spherical nose extend back over the entire length of this rather short model. The heat-transfer coefficients in figure 19 are also increased but are fairly well predicted by two-dimensional hypersonic similarity theory (ref. 5), which takes into account the pressure and pressure-gradient effects. As the angle of attack increases, the distance over which the induced pressures due to the nose are significant decreases, as was shown in figure 8, and by 21° the heat transfer on the lower surface of the slab is satisfactorily predicted by the constant-pressure strip theory from about 2 or 3 diameters back from the stagnation point.

At higher angles of attack, the flow becomes outward over the leading edge, and the cross-flow type of calculations should be appropriate. At 42° angle of attack, the cross-flow theory in fact gives a good prediction of the center-line heat-transfer rates. The spanwise velocity gradients used for the cross-flow theory calculations were obtained from the velocity distributions shown in figure 20. These were computed from pressure measurements on flat-faced disks normal to the flow, with various corner radii, ranging from the sharp edge to the hemisphere. It was found that the velocity gradients near the center line seemed to vary linearly with the ratio of corner radius to overall diameter, and could be very well represented by the equation:

$$\left. \frac{D}{a_0} \frac{du}{dx} \right|_{x=0} = 0.745 + 3.14 \frac{r}{D}$$

This relation was assumed to be applicable to the delta wing near the center line, with the local span and cylinder radius as D and r , respectively, and using the speed of sound at the fictitious stagnation temperature corresponding to the total energy of the normal component flow.

The cylindrical leading edge of a wing at low angles of attack is usually treated as part of an infinite cylinder. The changes in flow direction of the surface streamlines with angle of attack and the proximity of the blunt nose suggest a limitation to the validity of the isolated-cylinder calculation. This is examined in figure 21.

The maximum heat-transfer coefficients on the cylinder are expressed as a fraction of the value calculated for the stagnation line of an infinite cylinder at zero sweep. Experimental values are shown by faired curves for $M = 9.6$ at three stations, and at $M = 8.1$ from the AEDC B-2 tunnel by the circles. At low angles of attack, up to about 20° , the Mach 9.6 data show a small effect due to the proximity of the nose at the station 1 diameter away from the shoulder, but beyond 3 diameters the heat transfer is independent of distance from the nose within the experimental scatter for both sets of data. Above 20° , however, the $M = 9.6$ data show the development of a distinct trend with distance from the nose.

Up to 20° the data also follow the trend with angle of attack predicted by the infinite-cylinder theory (ref. 6), but depart considerably from this trend at higher angles. In fact, the Mach 8.1 data indicate that the heat transfer actually decreases above about 40° . For angles of attack above 20° , the schlieren photographs of figure 3 show that the shocks are no longer parallel to the cylinder elements, as required for the application of infinite-cylinder theory. For this range, the flow pattern is dependent on the local span as well as on the cylinder diameter, and the "leading edge" must be treated as the round edge of a plate.

A brief overall view of the flow fields and heat transfer to the simple delta wing with laminar flow has been presented. The actual vehicle will, of course, be complicated by fins, controls, and other modifications, which will require detailed study, but the simple-delta-wing results can provide the basis for design of most of the vehicle surface. In spite of the lack of a general theoretical method for computing the flow field and heat transfer for the entire wing at angles of attack, a knowledge of the streamline patterns and pressures allows the prediction of the heat transfer by application of simple methods. Furthermore, these flow fields provide the basis for application of more elaborate theories for turbulent as well as laminar boundary layers.

CONCLUDING REMARKS

In summary, then, insofar as pressures are concerned successful correlations have been shown for both the center-line and spanwise pressure distributions over a range of sweep, Mach number, angle of attack, and dihedral angle. Such correlations allow the application of experimental results to Mach numbers widely different from those at which the data were obtained, thus allowing the prediction of the pressure on the lifting surface of a vehicle such as the Dyna-Soar with confidence. Much of the heat transfer has been found to be amenable to simple approaches which take into account the flow pattern peculiar to the angle-of-attack range under consideration. The leading edge itself has been found to

become a trailing edge in the sense of airflow direction at high angles of attack. This is connected with the appearance of conical flow on the delta wing and tends to alleviate the heat transfer to the leading edge.

REFERENCES

1. Chernyi, G. G.: Effect of a Small Blunting of the Leading Edge of a Profile on Flow Around It at High Supersonic Speeds. Library Translation No. 704, British R.A.E., Nov. 1957. (Available from ASTIA as AD 154789.)
2. Vaglio-Laurin, Roberto: Laminar Heat Transfer on Blunt-Nosed Bodies in Three-Dimensional Hypersonic Flow. WADC Tech. Note 58-147, ASTIA Doc. No. AD 155 588, U.S. Air Force, May 1958.
3. Phillips, William H.: Research on Blunt-Faced Entry Configurations at Angles of Attack Between 60° and 90° . (Prospective NASA paper.)
4. Lees, Lester: Laminar Heat Transfer Over Blunt-Nosed Bodies at Hypersonic Flight Speeds. Jet Propulsion, vol. 26, no. 4, Apr. 1956, pp. 259-269, 274.
5. Bertram, Mitchel H., and Feller, William V.: A Simple Method for Determining Heat Transfer, Skin Friction, and Boundary-Layer Thickness for Hypersonic Laminar Boundary-Layer Flows in a Pressure Gradient. NASA MEMO 5-24-59L, 1959.
6. Beckwith, Ivan E.: Similar Solutions for the Compressible Boundary Layer on a Yawed Cylinder With Transpiration Cooling. NASA TR R-42, 1959. (Supersedes NACA TN 4345.)
7. Lawson, Warren A., McDearmon, R. W., and Rainey, R. W.: Investigation of the Pressure Distributions on Reentry Nose Shapes at a Mach Number of 3.55. NASA TM X-244, 1960.
8. Julius, Jerome D.: Experimental Pressure Distributions Over Blunt Two- and Three-Dimensional Bodies Having Similar Cross Sections at a Mach Number of 4.95. NASA TN D-157, 1959.
9. Cooper, Morton, and Mayo, Edward E.: Measurements of Local Heat Transfer and Pressure on Six 2-Inch-Diameter Blunt Bodies at a Mach Number of 4.95 and at Reynolds Numbers Per Foot Up to 81×10^6 . NASA MEMO 1-3-59L, 1959.

DELTA-WING MODELS

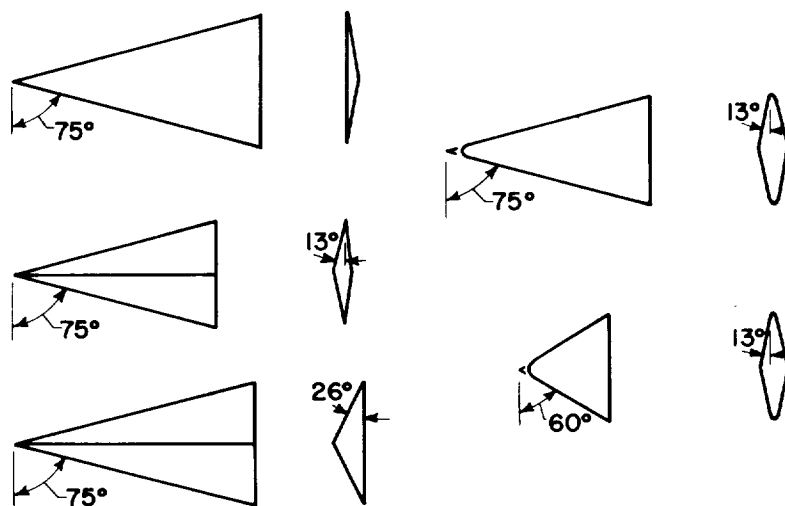


Figure 1

DELTA-WING MODELS

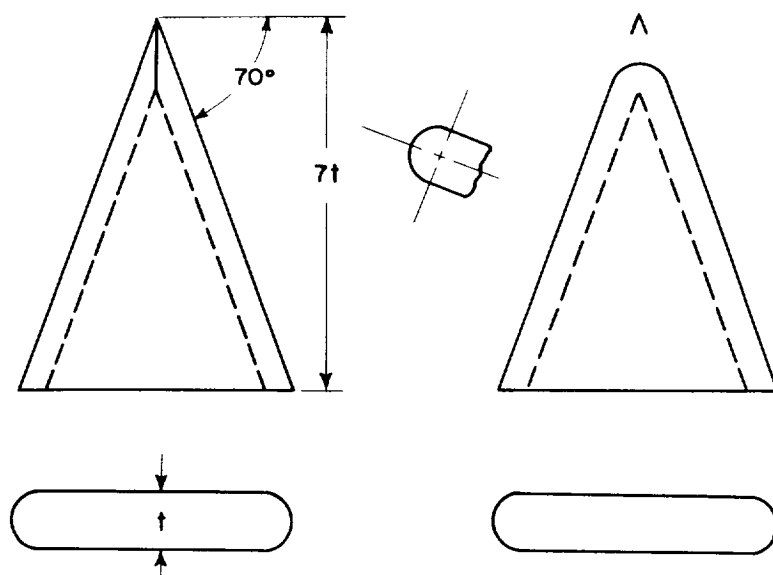


Figure 2

SLAB DELTA WINGS
SCHLIEREN STUDIES AT $\alpha=0^\circ$

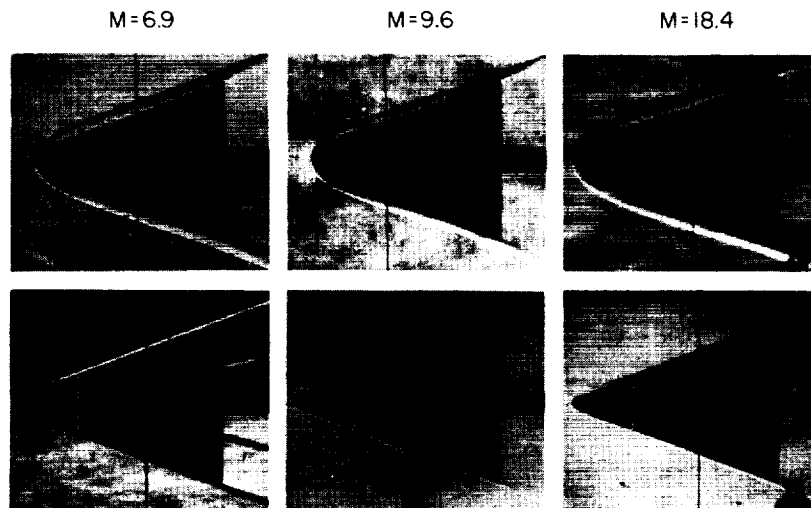


Figure 3(a)

SLAB DELTA WINGS
SCHLIEREN STUDIES AT M=6.9

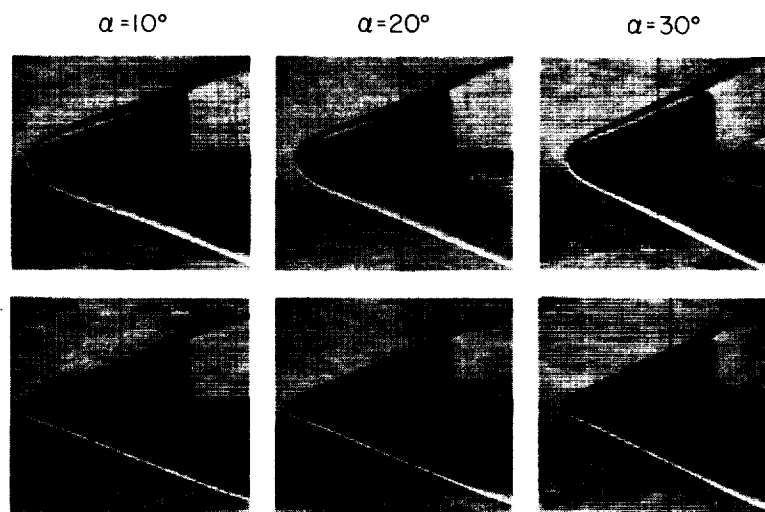


Figure 3(b)

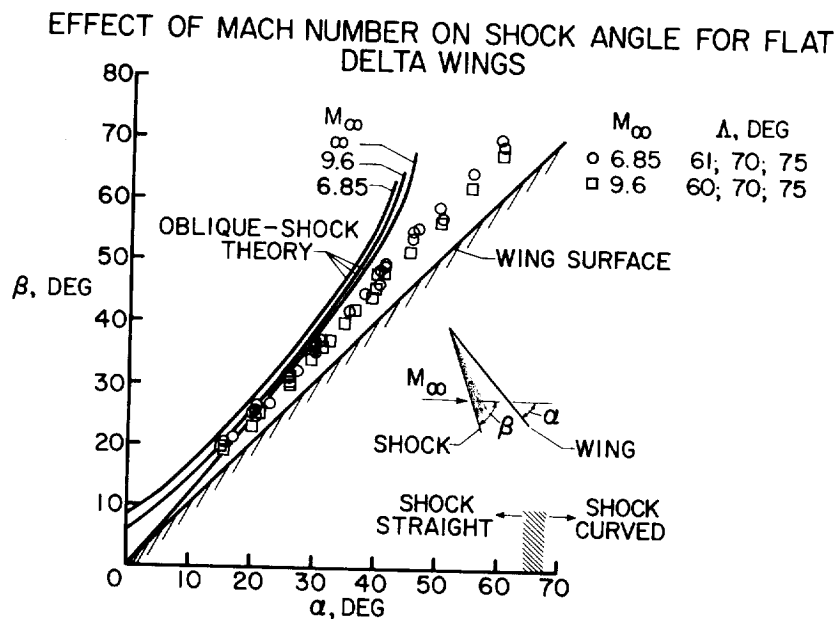


Figure 4

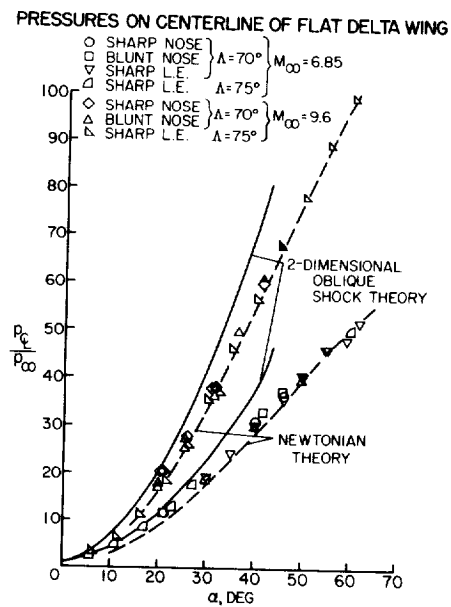


Figure 5

CORRELATION OF PRESSURES ON CENTER LINE OF DELTA WINGS

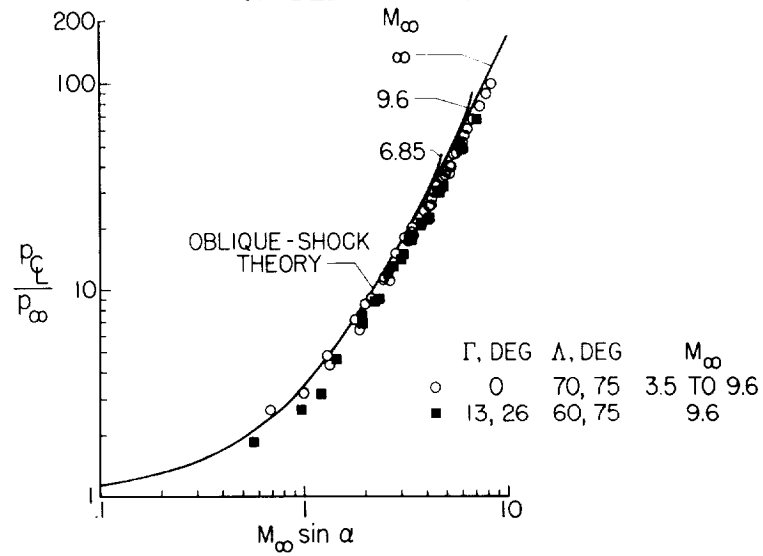


Figure 6

EFFECT OF DIHEDRAL ON SURFACE PRESSURES

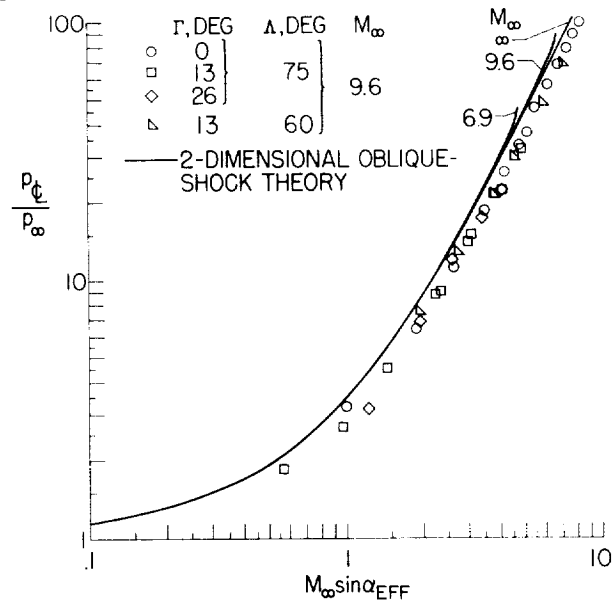


Figure 7

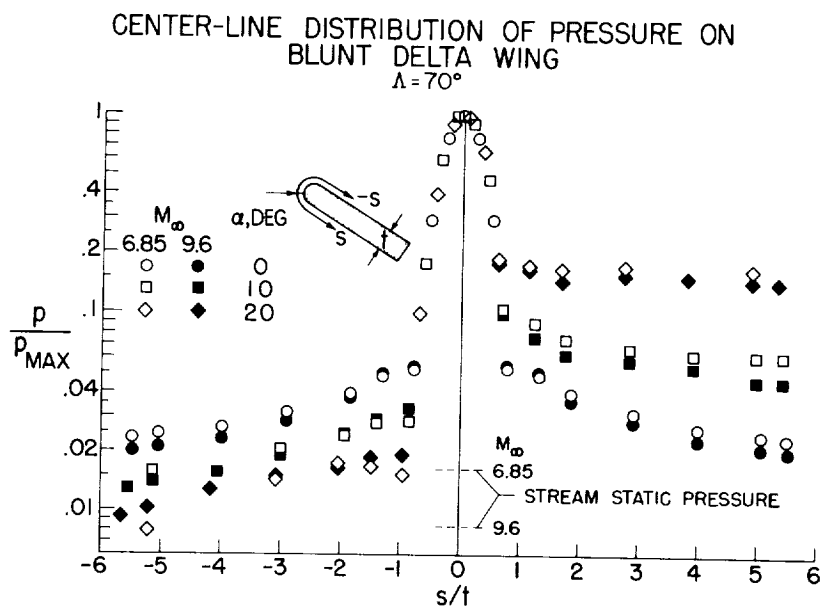


Figure 8

LOWER-SURFACE FLOW PATTERNS ON FLAT DELTA
WINGS
 $M_\infty = 9.6; \Lambda = 75^\circ$

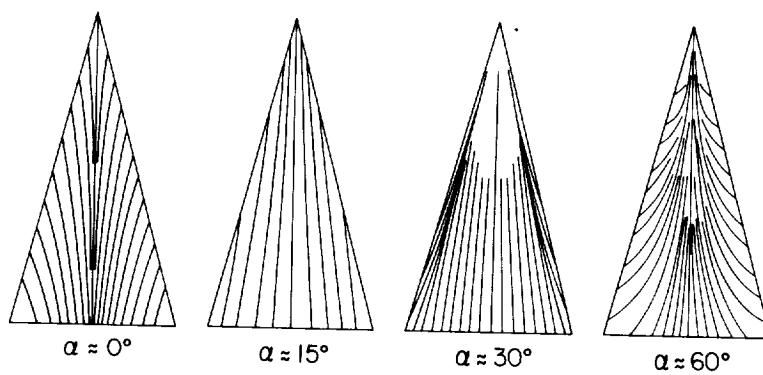


Figure 9

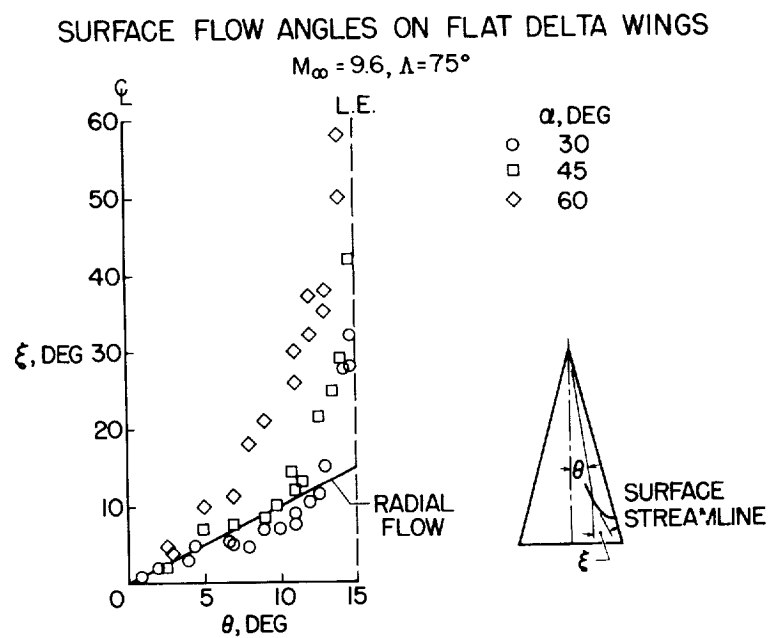


Figure 10

SURFACE FLOW ANGLES ON FLAT AND DIHEDRALED DELTA WINGS

$M_\infty = 9.6; \Lambda = 75^\circ; \alpha = 30^\circ$

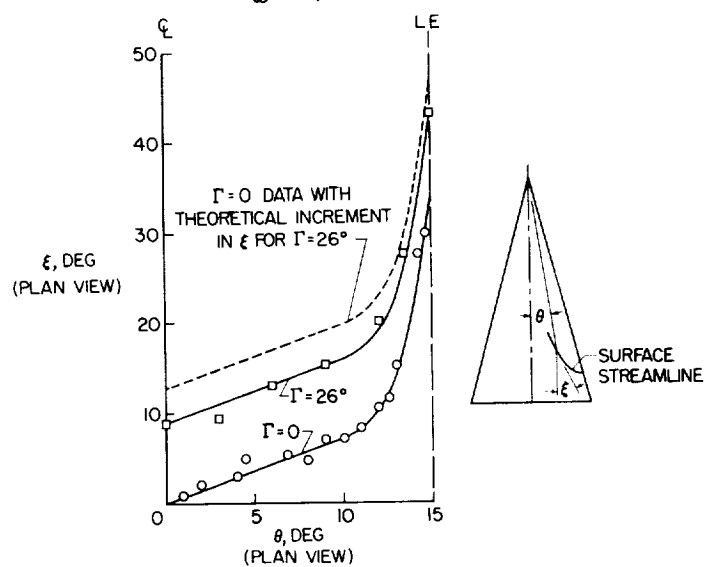


Figure 11

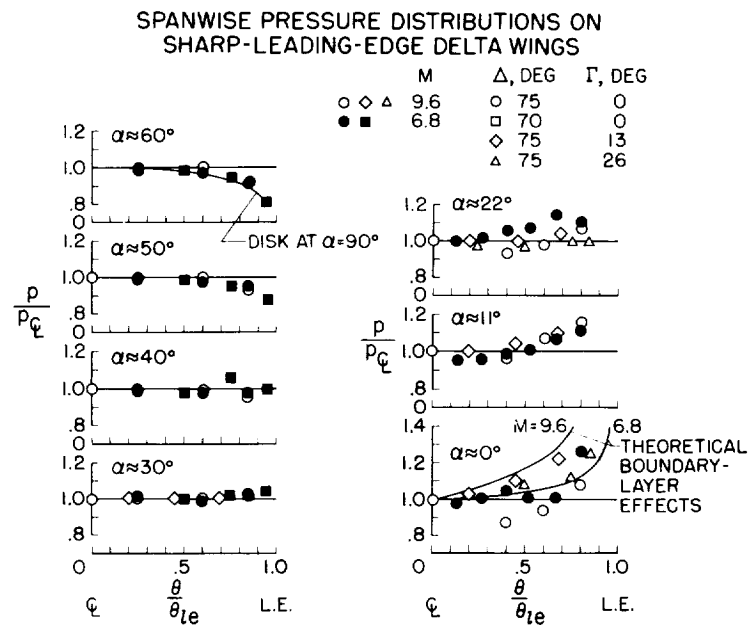


Figure 12

HEAT TRANSFER AT ANGLES OF ATTACK
SHARP LEADING EDGE; $\Delta = 75^\circ$; $\Gamma = 0$; $M_\infty = 9.6$

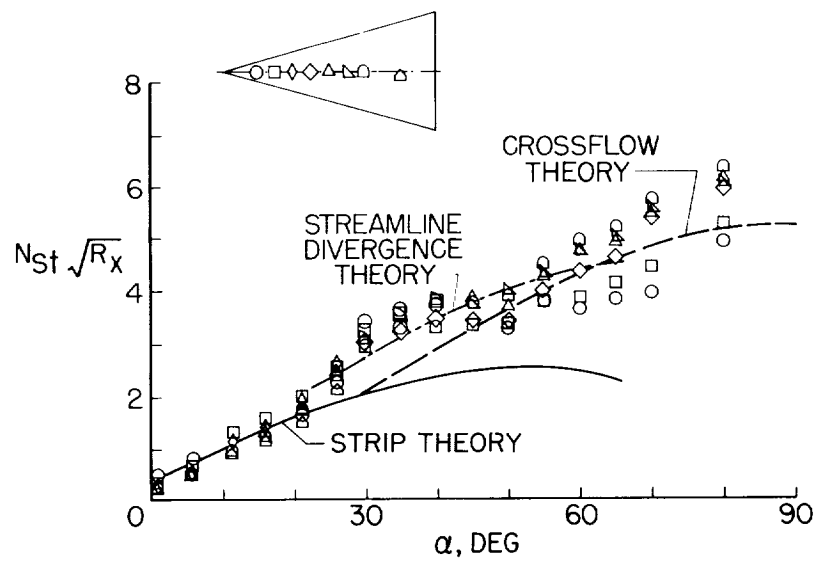


Figure 13

EFFECT OF MACH NUMBER ON HEAT-TRANSFER DISTRIBUTION

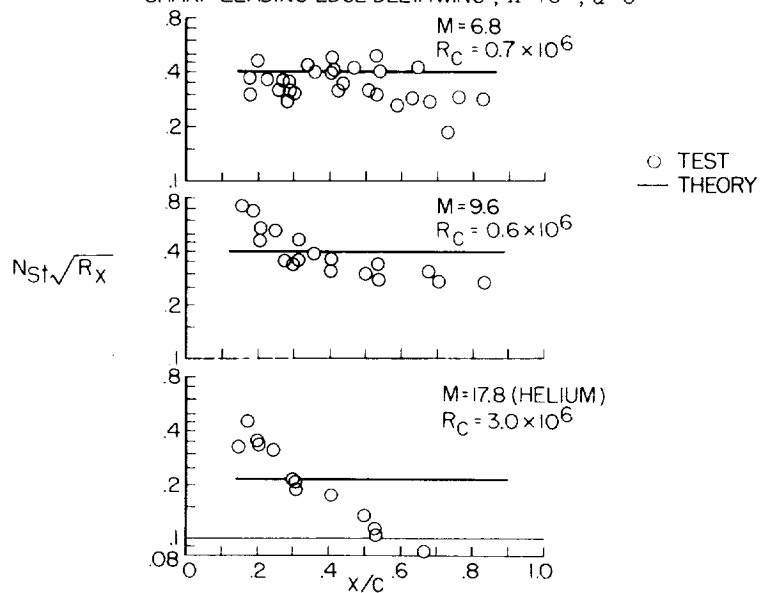
SHARP-LEADING-EDGE DELTAWING ; $\Lambda = 75^\circ$; $\alpha = 0^\circ$ 

Figure 14

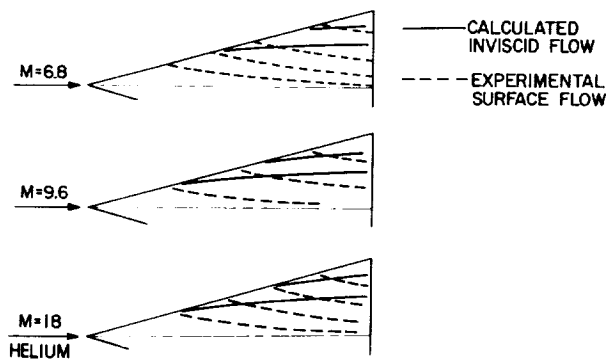
EFFECT OF MACH NUMBER ON FLOW PATTERNS AT $\alpha = 0$ SHARP-LEADING-EDGE DELTA WING ; $\Lambda = 75^\circ$ 

Figure 15

SPANWISE DISTRIBUTION OF HEAT TRANSFER AT ANGLES OF ATTACK
 SHARP-LEADING-EDGE DELTA WING; $\Lambda = 75^\circ$; $M = 9.6$; $R_C = 0.6 \times 10^6$

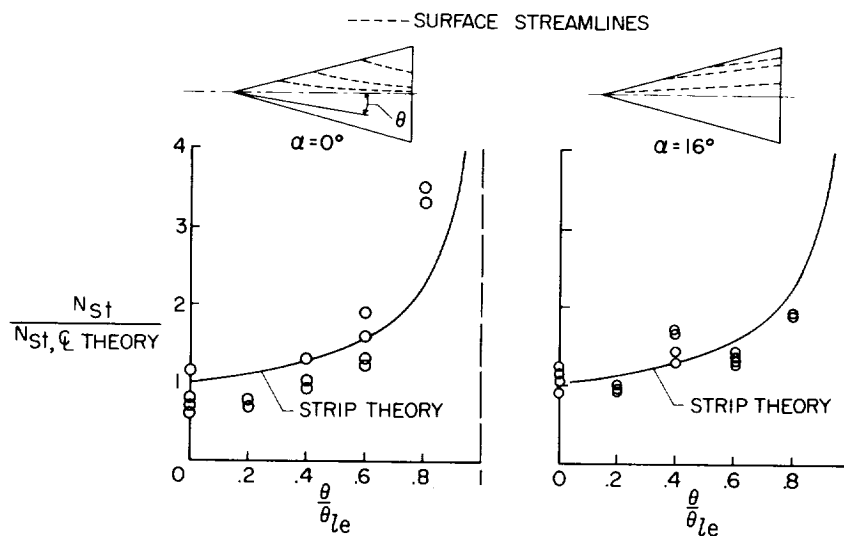


Figure 16

SPANWISE DISTRIBUTION OF HEAT TRANSFER AT ANGLES OF ATTACK
 SHARP-LEADING-EDGE DELTA WING; $\Lambda = 75^\circ$; $M = 9.6$; $R_C = 0.6 \times 10^6$

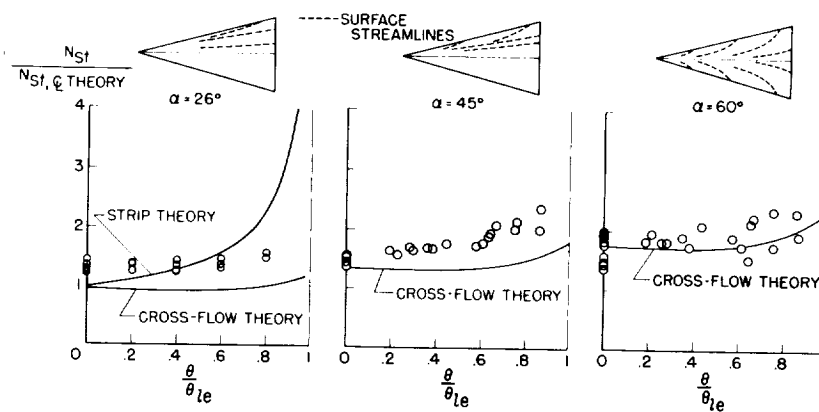


Figure 17

EFFECT OF DIHEDRAL ON HEAT TRANSFER TO DELTA WING
 SHARP LEADING EDGE; $\Lambda=75^\circ$; $M=9.6$; $R_C=0.6 \times 10^6$; $\alpha'_{EFF}=26^\circ$

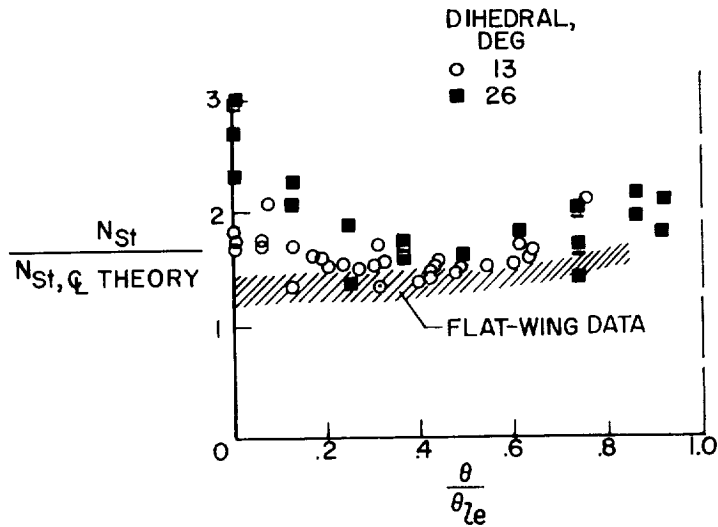


Figure 18

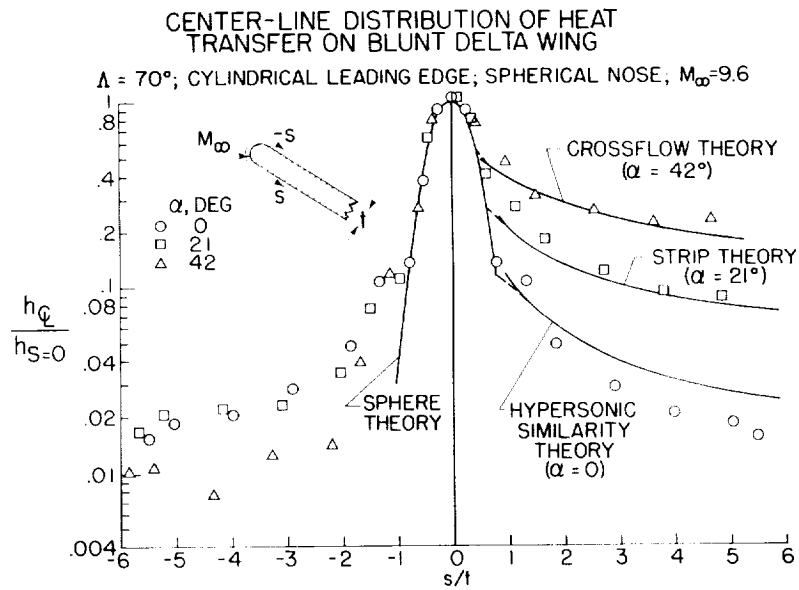


Figure 19

CORRELATION OF VELOCITY DISTRIBUTIONS ON FLAT-NOSED CYLINDERS

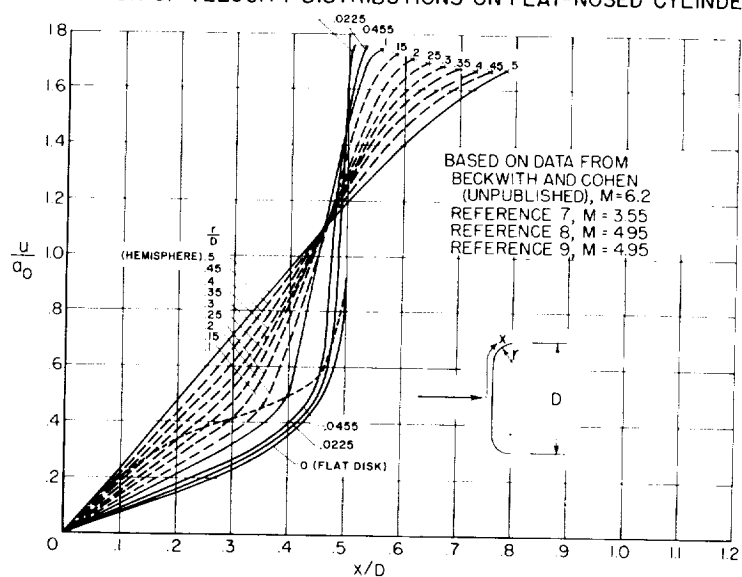


Figure 20

MAXIMUM HEAT TRANSFER ON CYLINDRICAL LEADING EDGE

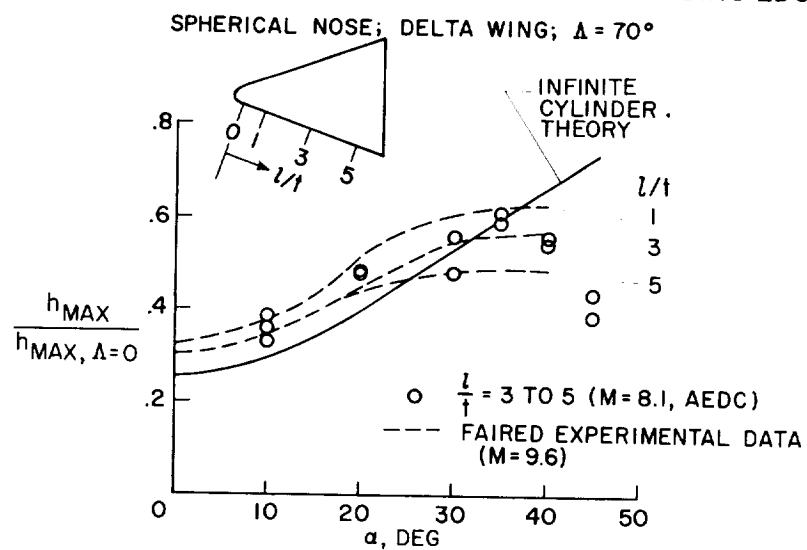


Figure 21

2

4

-

-

-

-

-

v

-

r

|

RESEARCH ON BLUNT-FACED ENTRY CONFIGURATIONS AT
ANGLES OF ATTACK BETWEEN 60° AND 90°

By William H. Phillips
Langley Research Center

SUMMARY

This paper summarizes the aerodynamic characteristics and stability and control of reentry vehicles operating in the angle-of-attack range between 60° and 90° . Both capsule shapes and winged-reentry-type vehicles operating in this high angle-of-attack range are considered. A stable pitching-moment slope exists for the high angles of attack. However, a lack of aerodynamic damping makes stability augmentation necessary. By change in the blunt-face curvature both positive and negative lift-curve slopes can be obtained. Control can be obtained by vane-type flaps deflected to shift the centroid of area. The control effectiveness is good and reasonably linear for control deflections greater than 30° from the stream direction. It appears that at angles of attack near 90° the aerodynamic characteristics, which depend upon pressure forces on the front face, are predictable and independent of Mach number. Heat transfer and flow fields are difficult to predict but some experimental data are presented.

INTRODUCTION

For entries into the atmosphere at small entry angles from low-altitude satellite orbits, blunt-faced nonlifting vehicles, such as that used in Project Mercury, offer advantages of simplicity and minimum time of exposure to high heating conditions. A ballistic capsule, however, suffers from lack of maneuverability. Modification of the capsule design to incorporate provision for control of the angle of attack to produce lift allows reduction of peak deceleration and provides the possibility of control of the landing point. (See refs. 1 and 2.) A winged vehicle may also be designed to enter the atmosphere in the range of angle of attack from 60° to 90° . Some variable-geometry feature may be required to allow the vehicle to pitch down to conventional angles of attack for landing (ref. 3). The present paper summarizes the aerodynamic characteristics and stability and control of vehicles operating in this range.

SYMBOLS

C_D drag coefficient

C_L lift coefficient

$$C_{L_\alpha} = \frac{dC_L}{d\alpha}$$

C_m pitching-moment coefficient

$$C_{mq} = \frac{\partial C_m}{\partial \frac{qc}{2V}}$$

$$C_{m_\alpha} = \frac{dC_m}{d\alpha}$$

C_X axial-force coefficient

$$C_{X_\alpha} = \frac{dC_X}{d\alpha}$$

c chord

\bar{c} mean aerodynamic chord

c_p specific heat of fluid at constant pressure

h heat-transfer coefficient

L/D lift-drag ratio

M Mach number

M_α variation of pitching moment with angle of attack (presented about centroid of area)

M_∞ free-stream Mach number

N_{St} Stanton number, $\frac{h}{\rho V c_p}$

p pressure on wing surface

P_{MAX}	maximum pressure (at stagnation point)
q	dynamic pressure
R	Reynolds number
S	area
V	velocity
α	angle of attack
$\frac{\alpha}{\alpha_0}$	ratio of amplitude of angle of attack to initial amplitude
δ_f	control-flap deflection
ρ	mass density

DISCUSSION

Aerodynamic Characteristics

The variations of lift, drag, and pitching-moment coefficients with angle of attack for a typical delta-wing configuration over the complete range of angle of attack from 0° to 90° are shown in figure 1. This figure indicates the range of conditions with which this paper is concerned and shows the typical variations that may be expected in this range. These data were obtained at a Mach number of 2, but similar trends would be indicated at other Mach numbers. The lift reaches a maximum in the neighborhood of 45° angle of attack and decreases to 0 at close to 90° angle of attack. The lift-curve slopes in the region considered in this paper, therefore, are negative. Simulator studies have shown that a pilot is capable of controlling a lifting vehicle in this region of negative lift-curve slope (refs. 4 and 5). As expected, the drag coefficient reaches its maximum value at 90° angle of attack. Pitching moments are herein presented about the centroid of area which produces a condition of trim at an angle of attack near 90° . For such a center-of-gravity location the vehicle is usually unstable at low angles of attack; however, it should be noted that the pitching-moment coefficient reaches a maximum and that a negative or stable slope exists between about 60° and 90° angle of attack.

Static Longitudinal Stability Characteristics

Basic longitudinal data on wings at an angle of attack of 90° are summarized in figure 2 for a variety of planforms. These results were taken from references 6 to 9 and from unpublished data. These planforms range from circular to a 75° sweptback delta. Planform has little effect on the characteristics provided the face is reasonably flat. The drag coefficient rises through the transonic range and reaches a fairly constant value beyond a Mach number of 2. A test point is given at a Mach number of 6.8 and another from the hot-shot tunnel of the Arnold Engineering Development Center at a Mach number of 18. These points confirm the fact that the drag coefficient does not vary much at hypersonic speeds. The lift-curve slope, when expressed per radian, may be shown to be equal to the negative of the drag coefficient plus the variation of axial-force coefficient with angle of attack. Contributions of the axial-force coefficient, however, are very small for flat wings, generally less than 2 percent of the value of the drag coefficient. For this reason the approximate value of the lift-curve slope per radian may also be read from the curve of drag coefficient by changing the sign. Values of static longitudinal stability C_{m_α} fall within the shaded region shown in figure 2. Most of the scatter is due to experimental error, because of the difficulty of measuring small pitching moments when the model is subjected to a large drag force. In spite of the experimental scatter, however, the variation of longitudinal stability with Mach number is shown to be much less than that usually experienced on conventional airplanes.

The aerodynamic characteristics shown in figure 1 are little affected by any design variation except that of varying the bluntness or curvature of the face. Effects of a wide variation in the face curvature are shown in figure 3. This figure includes data from a systematic series of capsule models tested at a Mach number of 6.8 and a number of winged vehicles. The value of static longitudinal stability C_{m_α} first increases with increased face rounding, and then decreases. These data are for a fixed location of the center of gravity with respect to the break line at the edge of the face. If the center of gravity were moved forward with increasing nose projection, the stability could be maintained. Increasing the curvature of the face first decreases the negative value and then produces a positive value of lift-curve slope. For capsules that are intended to be uncontrolled, a lift-curve slope near zero may be desired to reduce dispersion. For controllable devices, either the region of positive or negative lift-curve slope may be of interest. The values of L/D obtainable in either region of lift-curve slope are adequate for control of range and deceleration. Data for the winged vehicles are too near the origin to allow consistent determination of trends. These results show, however, that

small amounts of curvature may be incorporated in the lower surface of a winged vehicle without greatly affecting its aerodynamic characteristics at angles of attack near 90° .

Static Lateral Stability Characteristics

Lateral stability characteristics follow the same trends as longitudinal stability. The side force due to sideslip corresponds to the lift due to angle of attack, and the rolling moment due to sideslip corresponds to the pitching moment due to angle of attack. Tests have shown that these lateral stability derivatives are approximately constant in the range of angle of attack from 60° to 90° .

Flow Fields

Prediction of the detailed flow patterns on the faces of vehicles in the range approaching an angle of attack of 90° is of interest from the standpoint of aerodynamic heating and load distribution. A technique using small spots of oil on the face of the models has been utilized to trace the flow patterns on several configurations. Two such flow patterns are shown in figure 4, and corresponding schlieren pictures of the flow are shown in figure 5. A theory proposed by Mitchel H. Bertram and James C. Dunavant of the Langley Research Center, based on transformation of the known flow pattern on a circular disk, has been used to predict the streamlines at $\alpha = 90^\circ$. This theory shows good agreement with experiment in the prediction of streamlines and pressure contours. The basis of the theory is shown in figure 6(a). A circle is inscribed in the planform, and three sets of lines parallel to the edges of the planform are drawn, with each set confined to the region between the center of the circle and the corresponding edge. In the regions where the sets of lines do not overlap (indicated by the shaded areas in fig. 6(a)), the velocities that would exist on a circular disk at any distance from the center are assumed to apply along each of the parallel lines passing through this point with the directions normal to the edge of the planform. In the regions where the sets of lines overlap, the velocity components associated with each set of lines are combined vectorially to obtain the resultant velocity at each point. The velocity as a function of radius for a circular disk is shown in figure 6(b).

As the angle of attack changes from 90° to 70° (fig. 5), the stagnation region moves rapidly forward from the centroid of the planform to the nose. Attempts are being made to predict the flow at angles of attack other than 90° , but as yet no good correlation with experiment has been obtained.

The schlieren pictures of figure 5 give an explanation of the static longitudinal stability exhibited by flat-faced configurations.

Newtonian flow theory would predict a constant pressure over the face at a given angle of attack and, therefore, no variation of pitching-moment coefficient with angle of attack would be expected. Actually, however, the curvature of the shock ahead of the wing produces a variation in pressure coefficient. The pressure is greater behind a normal shock than behind an oblique shock. As the angle of attack decreases from 90° to 70° , the shock near the nose becomes normal to the flow, whereas the shock inclination near the trailing edge decreases. Corresponding pressure changes on the face produce a stable variation of pitching-moment coefficient with angle of attack.

Heat Transfer

Measurements of heat transfer to the face of a 75° delta-wing model at a Mach number of 9.6 are shown in figure 7. These data show the variation of Stanton number with distance from the nose along the center line of the planform. Laminar-flow conditions existed in these tests. The spanwise variation of Stanton number is not shown, but, in general, the distribution across the span was fairly constant with a slight increase near the edges.

Simple analysis based on cross-flow theory, and ignoring the three-dimensional nature of the flow, would predict that the Stanton number would vary inversely as the square root of the width of the planform. The experimental data for 90° angle of attack show a much smaller variation than that predicted by this type of theory. Even at lower angles of attack, for which, as shown previously, the stagnation region moves rapidly to the nose, the variation along the center line is less than predicted by this theory. As a result, the heating in the critical region near the nose is reduced. More detailed calculations of the heat transfer at an angle of attack of 90° , based on the three-dimensional flow theory presented previously, have not yet been made, but good agreement with experiment, in the case of laminar flow, would be expected because of the agreement in predicting the flow pattern. Predictions at lower angles of attack are not possible until a suitable flow theory is developed.

Controls

Control of either a winged- or capsule-type vehicle in the high angle-of-attack range may be accomplished by means of vane-type controls hinged along the edges of the vehicle, which may be deflected to shift the centroid of area of the vehicle. Such controls may have their hinge lines located on the upper surface of the wing and set back from the edge to protect them from excessive aerodynamic heating. Typical locations for such controls are illustrated by the delta-wing configuration

in the upper left-hand corner of figure 8. In order to produce control about all three axes, the controls may be deflected in certain combinations. For example, the rear pair of controls on a delta-wing vehicle may be deflected differentially to produce rolling moments. The front pair may be deflected differentially to produce primarily yawing moments. Note that the yawing-moment requirements are small since the vehicle has no restoring moment in yaw in the high angle-of-attack range. The pitching moments may be produced by deflecting the front control alone or by differential deflection of the front and rear controls. The data available on the effect of control surfaces projecting from the edges of delta-wing configurations, capsules, and circular plates are indicated in the plots in figure 8. For controls deflected normal to the airflow, a correlation has been made showing the moment coefficient predicted on the basis of the shift of centroid of area as compared with that measured experimentally. As indicated by this curve these results are in good agreement. The variation of control effectiveness with control deflection has also been predicted by use of Newtonian flow concepts. The variation of control effectiveness with deflection for two controls is shown on the right-hand side of this figure. The results again indicate good prediction of the control effectiveness. Note that the controls produce little moment until they are deflected about 30° from the flow direction. Beyond this point, however, the control effectiveness shows a consistent and fairly linear variation.

Aerodynamic Damping

Aerodynamic damping of vehicles at angles of attack approaching 90° may be either stabilizing or destabilizing and is small in magnitude. Instability of longitudinal or lateral oscillations under conditions of constant dynamic pressure results from the negative lift-curve slope. On this instability is superimposed the well known tendency for the amplitude of oscillations to decrease in the region of increasing dynamic pressure and then to diverge in the region of decreasing dynamic pressure subsequent to the point of peak deceleration. Figure 9 shows this amplitude variation as a function of altitude during the entry. These results were obtained from the theoretical analysis of reference 10. This figure is for an uncontrolled vehicle, and the solid line represents the case with a value of C_{L_α} of -1.27 per radian and zero aerodynamic damping.

The two additional curves indicate the effect of a more negative value of C_{L_α} and also of destabilizing C_{m_q} . Note that in the higher altitude range the aerodynamic characteristics have negligible effect and that the decrease in amplitude results solely from the increasing dynamic pressure. After the point of peak dynamic pressure the aerodynamic damping of an uncontrolled vehicle has a large effect on the amplitudes subsequently reached. The change in amplitude per cycle, however, even

for these rapid divergences, is relatively small. For example, the maximum change in amplitude per cycle in the worst case shown is only about 5 percent. Thus, only a small amount of artificial damping is required to stabilize the motion. Simulator studies of reference 4 have shown that this artificial damping is extremely desirable from the pilots standpoint and, therefore, would probably be provided in any manned vehicle. In the absence of such damping, manual control of the oscillations is possible provided the period is sufficiently long.

CONCLUDING REMARKS

From the data presented, it appears that the aerodynamic characteristics of configurations at angles of attack approaching 90° , which depend on pressure forces on the front face, are predictable and relatively independent of Mach number in the range from zero to the highest Mach number for which test data are available. The static stability characteristics are good and control effectiveness of vane-type controls is linear and predictable. Lack of aerodynamic damping makes the provision of stability augmentation necessary. The three-dimensional nature of the flow makes accurate prediction of flow fields and heat transfer difficult. Experimental data are available, however, which provide a reasonably accurate basis for design. Although most of the available data are confined to the range below a Mach number of 4, the lack of dependence of the results on Reynolds number or on boundary-layer effects allows prediction of hypersonic characteristics with considerable confidence.

REFERENCES

1. Eggleston, John M., and Young, John W.: Trajectory Control for Vehicles Entering the Earth's Atmosphere at Small Flight-Path Angles. NASA MEMO 1-19-59L, 1959.
2. Cheatham, Donald C., Young, John W., and Eggleston, John M.: The Variation and Control of Range Traveled in the Atmosphere by a High-Drag Variable-Lift Entry Vehicle. NASA TN D-230, 1960.
3. Staff of Langley Flight Research Division (Compiled by Donald C. Cheatham): A Concept of a Manned Satellite Reentry Which Is Completed With a Glide Landing. NASA TM X-226, 1959.
4. Eggleston, John M., Baron, Sheldon, and Cheatham, Donald C.: Fixed-Base Simulation Study of a Pilot's Ability To Control a Winged-Satellite Vehicle During High-Drag Variable-Lift Entries. NASA TN D-228, 1960.
5. Assadourian, Arthur, and Cheatham, Donald C.: Longitudinal Range Control During the Atmospheric Phase of a Manned Satellite Reentry. NASA TN D-253, 1960.
6. Spencer, Bernard, Jr.: An Investigation of the Aerodynamic Characteristics at Subsonic Speeds of a Nonlifting-Type Space-Capsule Model Simulating Escape and Reentry Configurations. NASA TM X-228, 1960.
7. Penland, Jim A., and Armstrong, William O.: Static Longitudinal Aerodynamic Characteristics of Several Wing and Blunt-Body Shapes Applicable for Use as Reentry Configurations at a Mach Number of 6.8 and Angles of Attack up to 90° . NASA TM X-65, 1959.
8. Foster, Gerald V.: Exploratory Investigation at Mach Number of 2.01 of the Longitudinal Stability and Control Characteristics of a Winged Reentry Configuration. NASA TM X-178, 1959.
9. Ware, George M.: Low-Subsonic-Speed Static Longitudinal Stability and Control Characteristics of a Winged Reentry-Vehicle Configuration Having Wingtip Panels That Fold up for High-Drag Reentry. NASA TM X-227, 1960.
10. Lichtenstein, Jacob H.: Analytical Investigation of the Dynamic Behavior of a Nonlifting Manned Reentry Vehicle. NASA TN D-416. (Prospective NASA paper.)

LONGITUDINAL CHARACTERISTICS
WINGED VEHICLE

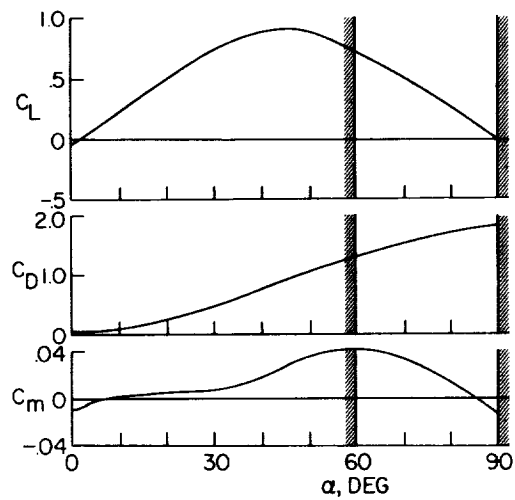


Figure 1

LONGITUDINAL CHARACTERISTICS AT $\alpha = 90^\circ$

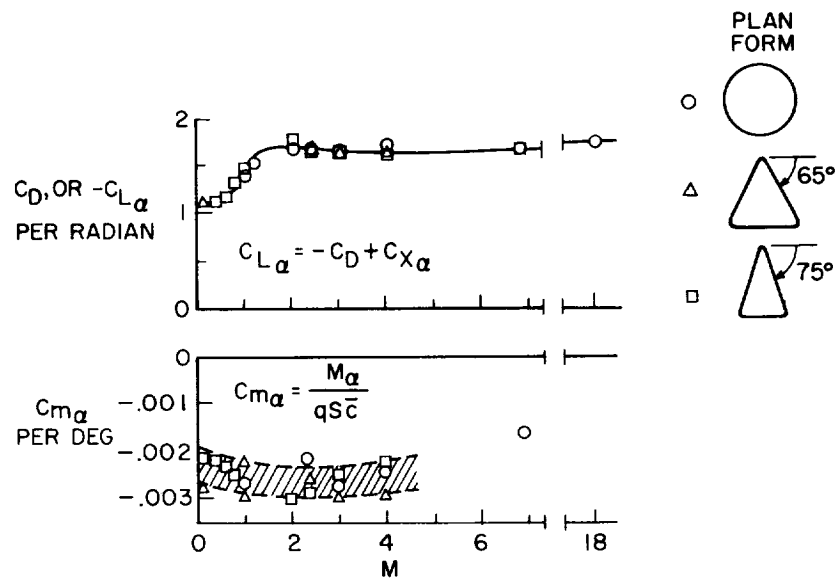


Figure 2

EFFECT OF BLUNTNES OF FACE

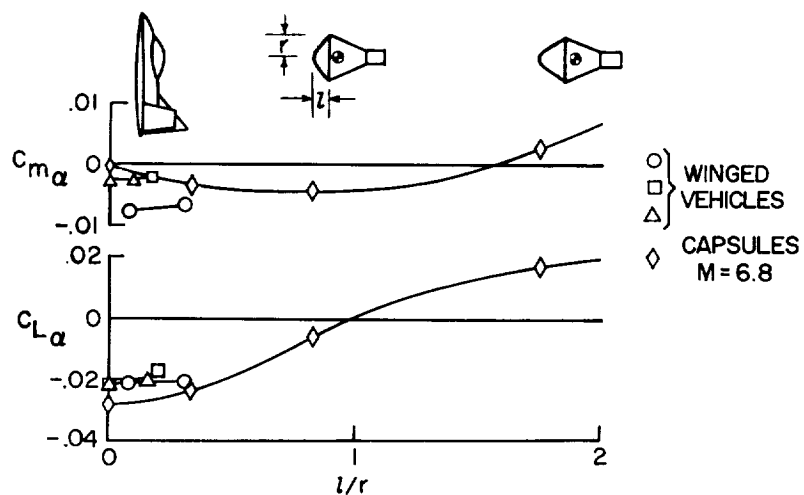


Figure 3

FLOW FIELDS ON DELTA WINGS AT HIGH ANGLE OF ATTACK

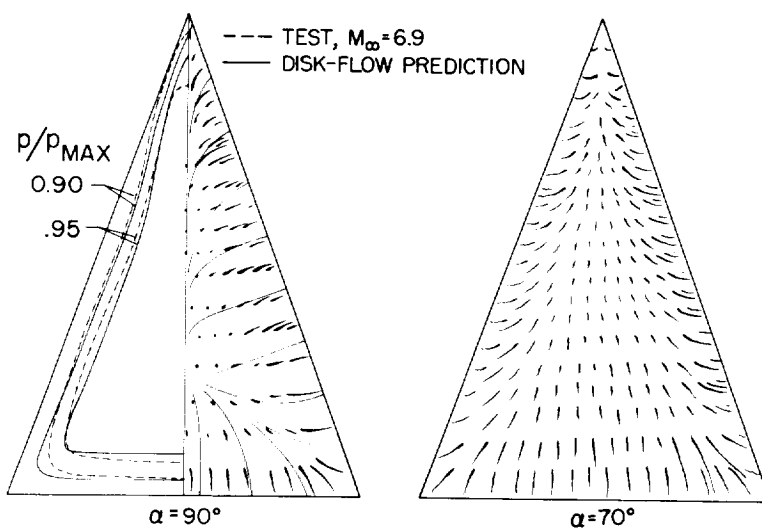


Figure 4

SCHLIEREN PHOTOGRAPHS OF FLOW

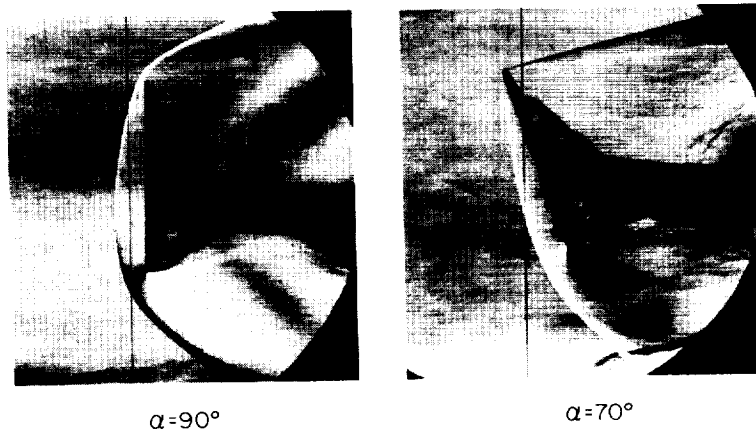


Figure 5

VELOCITY DISTRIBUTION
CALCULATION AT $\alpha = 90^\circ$
FLOW PATTERN CONSTRUCTION

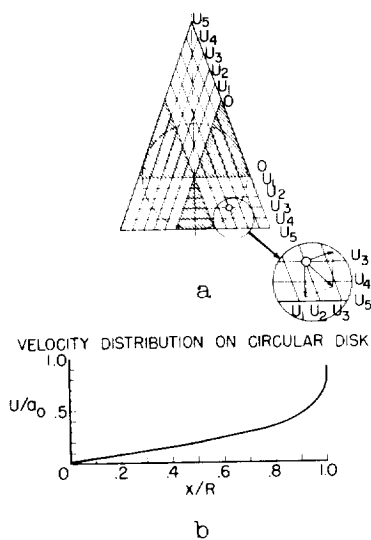


Figure 6

EXPERIMENTAL HEAT TRANSFER TO DELTA WING
 $M=9.6$; $R=450,000$; DATA TAKEN ALONG CENTER LINE

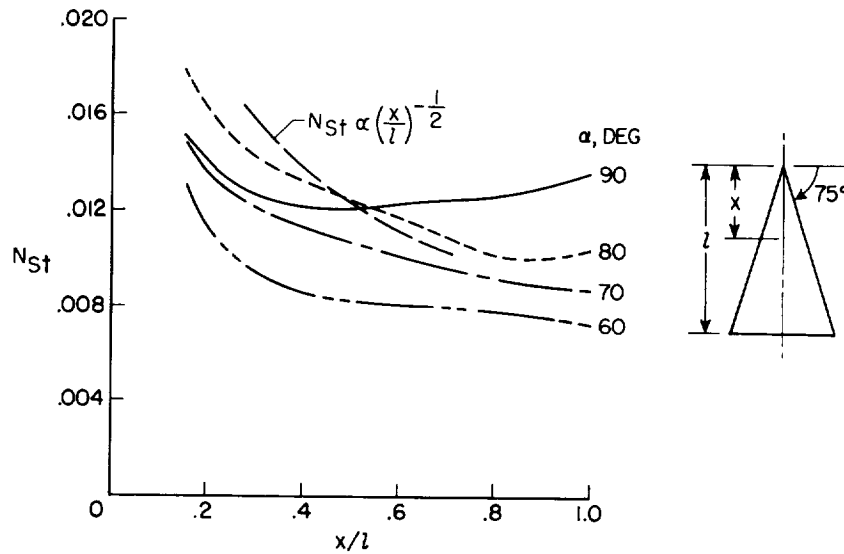


Figure 7

CONTROL-SURFACE EFFECTIVENESS

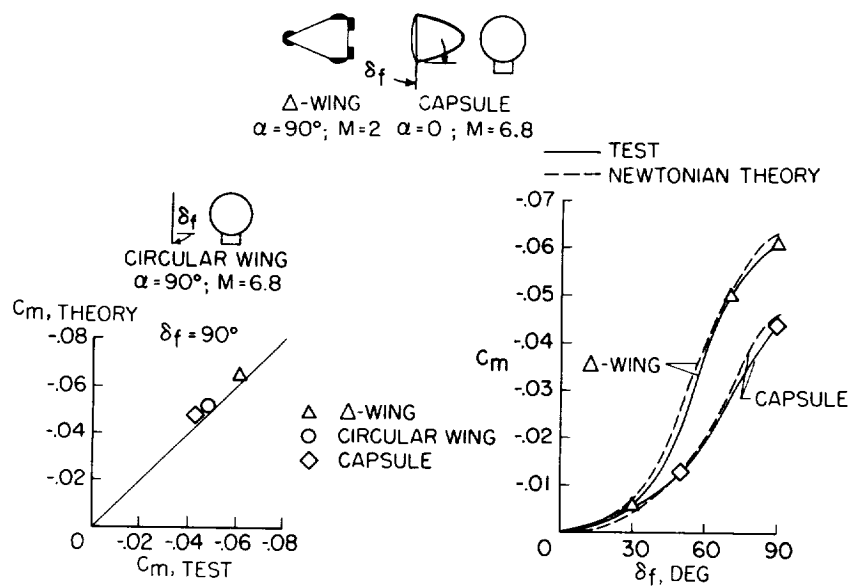


Figure 8

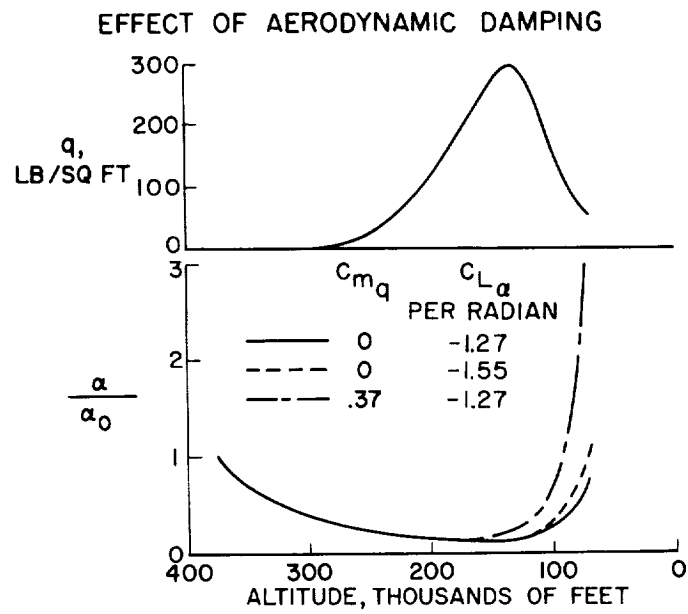


Figure 9

THE EFFECT OF THE BOW SHOCK WAVE ON THE STABILITY
OF BLUNT-NOSED SLENDER BODIES

By Alvin Seiff and Ellis Whiting
Ames Research Center

SUMMARY

Available experimental data on flare-stabilized blunt-nosed bodies of revolution at Mach numbers from 5 to 16 show that the static aerodynamic stability deteriorates with increasing Mach number in this range, and departs increasingly from the Newtonian theoretical estimate with increasing Mach number. The Newtonian estimate may be in error by an order of magnitude at the higher Mach numbers. The reason for this failure of the theory is apparently a failure of the Newtonian flow model to be realized. This model visualizes a bow shock wave closely wrapped about the entire body, confining the disturbed flow field to a thin shock layer. Available flow photographs show that the shock wave does not closely envelop the afterbody, but is forced away by the blast-wave effect of the blunt nose. Thus the blast-wave theory and Newtonian theory come into conflict in the case of blunt-nosed slender bodies, and it appears that Newtonian flow on the afterbodies will not be realized for speeds at least up to satellite speed.

The aerodynamics of the flare on such a body can be analyzed by postulating a Newtonian flow embedded in the main disturbed flow field. This concept leads to theoretical flare pressures about $1/5$ of Newtonian, with a similar loss in normal force and pitching moment of the flare. This result is found to agree with available experiments. The small magnitude of the flare normal force causes the forebody normal force to predominate in determining the overall stability. Since Newtonian theory is inapplicable to the body cylinder, only semiempirical methods are presently available for estimating the forebody forces and moments. One such method is included in this paper and appears to give usefully realistic estimates of the stability.

The phenomena discussed are believed to be of general significance for blunt-nosed slender bodies and bodies involving secondary shock waves on stabilizers and control flaps.

INTRODUCTION

Many examples have occurred in recent years of successful applications of the Newtonian theory to a wide variety of aerodynamic problems. Typically, experimental data have appeared to approach asymptotically the Newtonian estimate at Mach numbers in the order of 5.

The purpose of this paper is to discuss a case in which this behavior is not obtained. The available experimental evidence on the static aerodynamic stability of blunt-nosed flare-stabilized bodies of revolution, some of which is reviewed in this paper, indicates that the Newtonian theory gives a poor estimate of the stability (errors on the order of several hundred percent), at Mach numbers as high as 16, and also appears to disagree increasingly with experiment with increasing Mach number. This raises a very interesting question as to why the theory fails in this case and whether it can be expected to fail similarly in any other cases.

It is the purpose of this paper to discuss this problem, and to determine the theoretical reasons underlying this failure of the Newtonian theory. In addition, a new theoretical concept involving a Newtonian flow field embedded in a disturbed flow field is introduced and applied to the problem. Results are compared with experiment.

SYMBOLS

C_D	drag coefficient based on cylinder cross section
C_m	pitching-moment coefficient about body center of gravity based on cylinder cross section and body length
$C_{m_{\text{FLARE}}}$	flare pitching-moment coefficient
$C_{m_\alpha} = \frac{dC_m}{d\alpha}$	
$C_{m_{\alpha_{\text{EFF}}}}$	effective or equivalent-linear stability coefficient
C_N	normal-force coefficient based on cylinder cross section
C_{N_b}	forebody normal-force coefficient

C_{N_f}	flare normal-force coefficient
$C_{N_{\alpha_i}}$	initial slope of normal-force coefficient
C_{p_l}	pressure coefficient in the stream just ahead of the flare shock wave
C_{p_f}	pressure coefficient on the flare
d_b	diameter of body cylinder
d_f	flare base diameter
l_f	length of flare
M	Mach number
p_l	local static pressure
$p_{B.W.}$	static pressure from blast-wave theory
p_∞	free-stream static pressure
q_l	local dynamic pressure
q_∞	free-stream dynamic pressure
r_b	radius of body cylinder
r_s	radius of cross section of bow shock wave
x	axial distance from stagnation point or shock-wave vertex
$x_{c.p.}$	distance from beginning station of flare to its center of pressure
α	angle of attack
θ_f	half-angle of the flare

DISCUSSION AND ANALYSIS

When the aerodynamic stability characteristics of flare-stabilized blunt-nosed bodies of revolution were first investigated experimentally at hypersonic speeds, beginning about 3 or 4 years ago (ref. 1), some interesting and somewhat unexpected effects were encountered. These are illustrated in figure 1 by some measurements from the Ames supersonic free-flight wind tunnel of the static stability of the Polaris missile configuration. Rather than being practically independent of Mach number in the hypersonic range, as is the case with blunt-nosed low-fineness-ratio bodies, the stability of these bodies deteriorates markedly with increasing Mach number at Mach numbers from 5 to 16. The same characteristic is shown for another configuration in figure 2. In this case, flight data made available through courtesy of the General Electric Corporation, taken together with data from laboratory test facilities, show that supersonically the stability is maximum at about a Mach number of 4 and then falls off by a factor of 16 at a Mach number of 15.

It is also characteristic of these bodies in the hypersonic speed range that the static stability is strongly nonlinear with angle of attack, and this fact has been indicated in the two examples by curves showing effective or equivalent-linear stability coefficients for several amplitudes of pitching oscillation. The apparent upturn in the flight data at Mach numbers above 16 may, in fact, be due to the large amplitudes of pitching which can occur during early stages of the entry into the atmosphere.

The estimate of static stability coefficient by Newtonian theory is shown in figure 2. The actual stability is lower than predicted by an order of magnitude, and, interestingly enough, is diverging from the Newtonian value with increasing Mach number over most of the hypersonic speed range. The Newtonian value appropriate to figure 1 is off the vertical scale at a value of approximately 1.0.

The reason that the Newtonian impact theory fails to predict the stability can be understood from consideration of the shock-wave configurations typical of this class of bodies, as compared with the shock-wave configuration required in Newtonian flow. The Newtonian-shock wave, as indicated in figure 3, is closely wrapped around the body contour and confines the disturbed flow to a thin shock layer. Throughout this shock layer, the flow necessarily proceeds approximately parallel to the body surface, and there is basis for the Newtonian approximation - total loss of the momentum component normal to the body surface and no disturbance to the flow velocity parallel to the surface. In contrast to this, experimental shock waves are shown in figures 4 and 5. The

wave does not closely envelop the afterbody and flare, but is forced away from these surfaces by the explosive introduction of energy into the flow at the blunt nose. The blast-wave theory (ref. 2), in fact, gives a first approximation to the shock-wave shapes that are obtained experimentally, but it does not give a highly accurate description of the waves. A typical comparison is shown in figure 6. This type of comparison has been previously noted in references 3 and 4.

Since the Newtonian theory requires a shock wave which closely envelops the afterbody, and the blast-wave theory indicates that the shock wave is not closely wrapped, it is concluded that the Newtonian theory and the blast-wave theory are in conflict in this case, and that the Newtonian flow will not be realized. One can speculate as to whether there might be some Mach number, sufficiently high to cause the shock wave to become Newtonian, as the ratio of specific heats γ approaches 1 throughout the disturbed flow field. However, this case does not appear to be of immediate concern since tests in air at speeds up to 20,000 ft/sec have indicated that the blast-wave type of shock wave continues to occur.

There still remains the question concerning the loss in static stability with increasing Mach number and its cause. To study this question, attention was fixed on the properties of the local flow field in which the flare operates, and in particular on the dynamic pressure incident on the flare. Historically, local deviations of the dynamic pressure from the free-stream value have repeatedly appeared as a cause of changed effectiveness of stabilizers and control surfaces. The same is true in the case of the flare operating behind a blunt nose at hypersonic speeds, as indicated in figure 7, which shows the dynamic pressure behind a normal shock wave for both a station far downstream, where the static pressure has recovered to free-stream static pressure, and for a station more representative of the flare locations (2.7 diameters behind the nose). In the latter case, the local static pressures were estimated at the higher Mach numbers from Lin's blast-wave theory. It is evident that the dynamic pressure deteriorates in a way very similar to that shown by the static stability of the flared bodies.

For the purposes of calculating the static-pressure distribution on the flare and the stability which it contributes, it can be noted that the Mach numbers on the streamlines approaching the flare are in the low supersonic range ($M = 3$ typically), and that the flare will have associated with it a secondary shock wave. Estimates of the shock-wave angles of the wave generated by the flare indicate that there should be produced a thin shock layer of flow disturbed by the flare. Shadow-graph pictures confirm this. It is therefore feasible to consider an impact type of theory for estimating the characteristics of the flare. The shock layer of the flare is then considered as a Newtonian flow field embedded within the main disturbed flow field.

From such considerations, the pressure coefficient on the flare is found to be

$$C_{p_f} = C_{p_1} + 2 \frac{q_1}{q_\infty} \sin^2 \theta_f \quad (1)$$

and is the sum of the pressure coefficient in the stream just ahead of the flare shock wave, C_{p_1} , and a Newtonian term which, significantly, is multiplied by the ratio of local to free-stream dynamic pressure. Integration of the pressure-distribution equation over the surface of the flare, with the aid of simplifying assumptions appropriate to a small angle of attack, yields an equation for the normal-force coefficient,

$$C_{N_f} = \frac{q_1}{q_\infty} \left[\left(\frac{d_f}{d_b} \right)^2 - 1 \right] (\sin 2\alpha) (\cos^2 \theta_f) \quad (2)$$

which has the initial slope

$$\left(C_{N_{\alpha_1}} \right)_f = 2 \frac{q_1}{q_\infty} \left[\left(\frac{d_f}{d_b} \right)^2 - 1 \right] \cos^2 \theta_f \quad (3)$$

In these equations, the dynamic-pressure ratio again occurs as a factor, but the local static-pressure level in the stream ahead of the flare has dropped out. Finally, the flare center of pressure is given by

$$\frac{x_{c.p.}}{l_f} = \frac{2}{3} \frac{\left(\frac{d_f}{d_b} \right)^3 - 1}{\left(\frac{d_f}{d_b} \right)^2 - 1} \left[\frac{1 + \tan^2 \theta_f}{d_f/d_b - 1} \right] - \frac{1}{d_f/d_b - 1} \quad (4)$$

which is based on the assumption of uniform pressure along rays.

The use of these equations for estimating the stability contributed by the flare in the small-angle range requires that the distribution of dynamic pressures in the nonuniform flow field incident on the flare be

known. In this field, the stagnation pressure is strongly dependent on distance normal to the body axis, due to the highly curved bow shock wave. A simplified technique for calculating the distribution of dynamic pressure over the surface of the flare shock wave has been developed. This technique is not described in detail herein, but it consists in principle of solving the equation of continuity in a step-by-step construction of the flow-field cross section at a station on the flare. The outer boundary condition is the pressure behind the bow shock wave, and the inner boundary pressure, the body pressure, is to be determined. The relative variation of pressure normal to the surface is assumed to be that given by Lin's blast-wave theory. When continuity is satisfied, there will have been determined the distributions of static, dynamic, and stagnation pressures across the field. The procedure gives body surface pressures which agree within 10 or 20 percent with results of exact flow-field solutions. It therefore constitutes a method for obtaining a body pressure distribution from a known shock-wave shape at zero angle of attack. In the examples studied thus far, the calculated variations in dynamic pressure over the flare are not large, but for the purposes of equations (2) and (3), an area-weighted average dynamic pressure is used.

Figure 8 shows a comparison between theory and experiment for the flare of the Polaris missile configuration. Tests were made to determine the nonlinear variations of pitching-moment coefficient with angle of attack for both the complete configuration and the forebody alone. The experimental flare pitching moment shown is the difference between experimental values for the complete configuration and the forebody. The agreement of the theory with these data is satisfactory, although the initial slope has apparently been underestimated by the theory by about 35 percent. The nonlinearity of the experimental data, however, keeps the flare pitching moment relatively close to that predicted out to an angle of attack of 10° .

Of course, an analysis of the flare problem does not constitute a solution to the complete problem of the static stability of the blunt-nosed flared body. There still remains the contribution of the blunt nose and the cylinder to the stability. The blunt-nose contribution can be estimated with engineering accuracy by use of Newtonian theory, but the cylinder problem, a carryover from the lower supersonic speed range, is now complicated by the effects of the blunt nose and the blast-wave type of flow. The estimated relative importance of the body and the flare in determining the overall stability is illustrated in figure 9. (The vectors in the sketch are drawn to scale.) Note that either Newtonian theory or slender-body theory would predict the normal force of the flare to be larger than the normal force of the body. It is because of the upstream bow wave that the flare normal force is small compared with the body normal force. The large body normal force is

near the center of gravity, and small movements of this force will have a sizable effect on the overall stability.

In the example shown, the body stability has been estimated by adjusting the pressure distribution, obtained as described above for zero angle of attack, to correspond to a small angle of attack. This was done by decreasing the local Prandtl-Meyer expansion angles on the windward meridian by the amount of the angle of attack and increasing them by the same amount on the sheltered meridian. This seems to be the same as the method used in reference 5 for estimating body pressures at angle of attack. Integration of the pressures obtained from this assumption, with a cosine distribution around the body, leads to an estimate of the normal force on the body, which, when combined with the theoretical flare normal force, agrees with the experimental total normal force within 10 percent. It was found that an allowance for viscous cross flow, although small, was in the direction to improve agreement with experiment. The limitations of this procedure for estimating body normal force remain to be defined.

The sum of the theoretical flare pitching moments and the estimated body pitching moments is shown in figure 9 compared with experiment. When these calculations are combined, the stability is found to be underestimated. This total estimate is, however, considerably closer than the Newtonian estimate and is in error in a conservative direction. The failure to obtain a closer estimate is probably due largely to the body estimates, where, as noted earlier, a movement of the center of pressure by a few percent of the body length can significantly alter the total stability. Also, there is some indication that the present theory may underestimate the stability contributed by the flare, possibly due to real-gas effects which have not as yet been taken into account. Additional research is therefore needed to clarify the contribution of the body and to evaluate further the flare theory.

CONCLUDING REMARKS

Although there are many remaining questions, the representation of the flow in terms of the present model would appear to be superior to the Newtonian model, and the comparisons with experiment appear to substantiate this. Other cases may occur in which the flow is similar in nature to that described above. One case has, in fact, already been noted - the configuration discussed by Reller (ref. 6), which is a capsule with flap controls for manned entry into the atmosphere. The pressures on the flaps can be estimated by use of equation (1), and the level and trends of variation of the pressure are correctly given. It is expected from these considerations that the flap effectiveness will diminish with increasing Mach number.

Furthermore, it would appear necessary in general to consider carefully the hypersonic stability of blunt-nosed slender bodies. Two causes of appreciable variation in stability with Mach number are (1) the interaction of downstream aerodynamic elements with the bow shock wave or, more precisely, with its wake, and (2) the occurrence at high Mach numbers of a pressure distribution on a slender afterbody which differs from that normally encountered in wind-tunnel tests by approaching a pressure coefficient of zero from above rather than from below. The general understanding of these effects will require much additional study.

REFERENCES

1. Carros, Robert J.: Free-Flight Investigation of Static Stability and Drag of Models of the Second and Third Stages of the Hemisphere-Nosed X-17 at Mach Numbers From 4 to 10. NASA TM X-158, 1960.
2. Lin, Shao-Chi: Cylindrical Shock Waves Produced by Instantaneous Energy Release. Jour. Appl. Phys., vol. 25, no. 1, Jan. 1954, pp. 54-57.
3. Vas, I. E., Bogdonoff, S. M., and Hammitt, A. G.: An Experimental Investigation of the Flow Over Simple Two-Dimensional and Axial Symmetric Bodies at Hypersonic Speeds. Rep. No. 382 (WADC TN 57-246), Dept. Aero. Eng., Princeton Univ., June 1957.
4. Lees, Lester, and Kubota, Toshi: Inviscid Hypersonic Flow Over Blunt-Nosed Slender Bodies. Jour. Aero. Sci., vol. 24, no. 3, Mar. 1957, pp. 195-202.
5. Vas, I. E., and Bogdonoff, S. M.: An Exploratory Study at $M = 14$ of the Flow About a Hemisphere Cylinder at Angle of Attack. Rep. No. 438 (WADC TN 58-331, AD 205 461), Dept. Aero. Eng., Princeton Univ., Sept. 1958.
6. Reller, John O., and Seegmiller, H. L.: Convective Heat Transfer to Some Lifting Bodies. (Prospective NASA paper.)

STATIC STABILITY OF THE POLARIS MISSILE

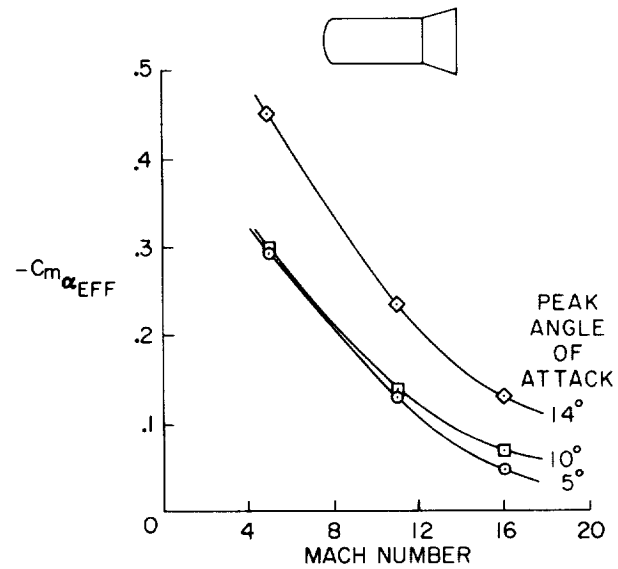


Figure 1

STATIC STABILITY OF THE RVX-1 TEST MODEL

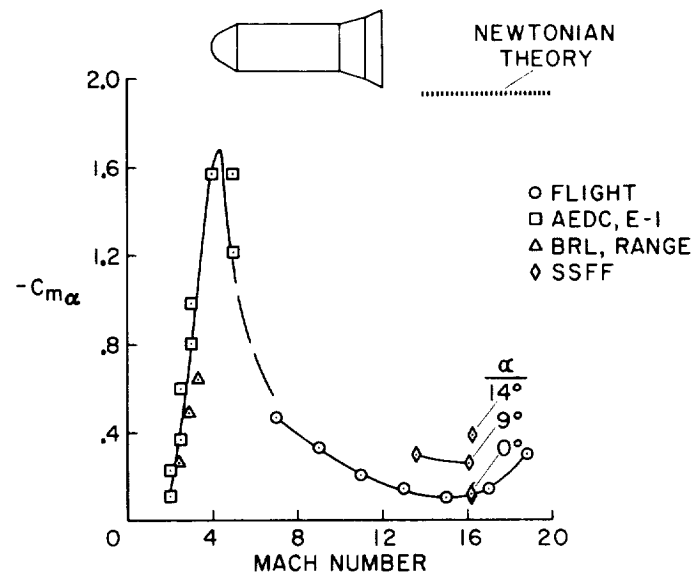


Figure 2

NEWTONIAN SHOCK WAVE

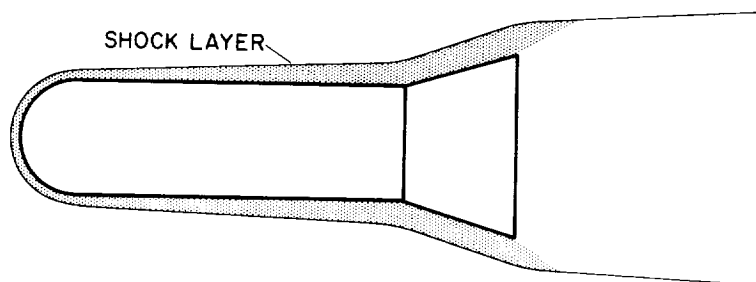


Figure 3

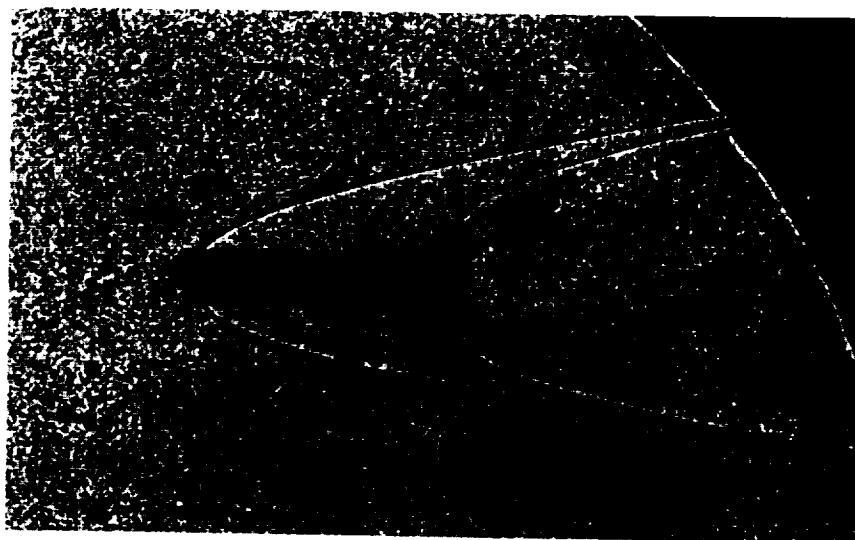
EXPERIMENTAL SHOCK WAVE ON HEMISPHERICAL-
NOSED FLARED BODY
 $M=13.1$ 

Figure 4

EXPERIMENTAL SHOCK WAVE FROM A NEARLY
FLAT-NOSED BODY
M=15

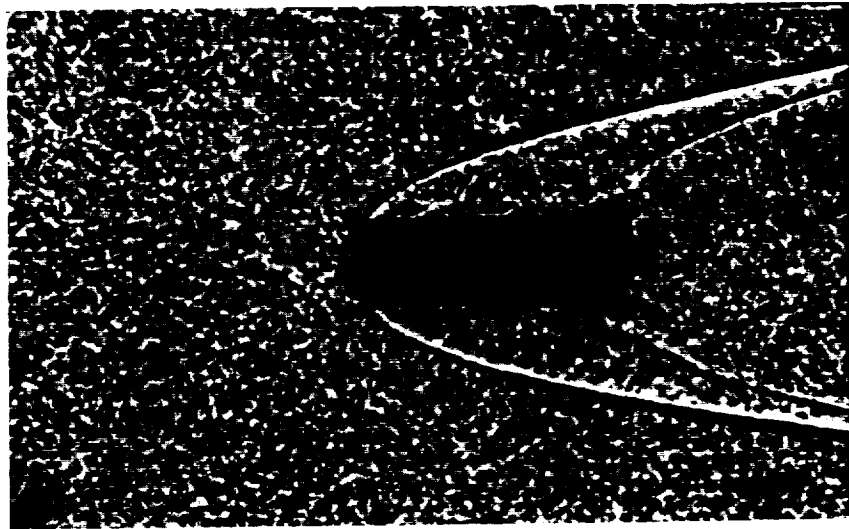


Figure 5

SHOCK WAVE OF A HEMISPHERE-CYLINDER

M=10

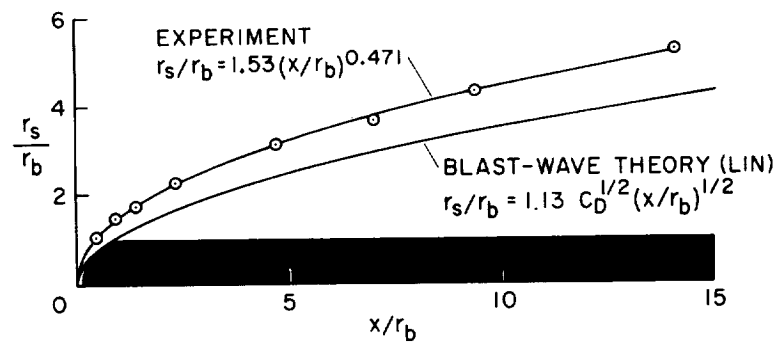


Figure 6

DYNAMIC PRESSURE DOWNSTREAM OF A NORMAL SHOCK WAVE

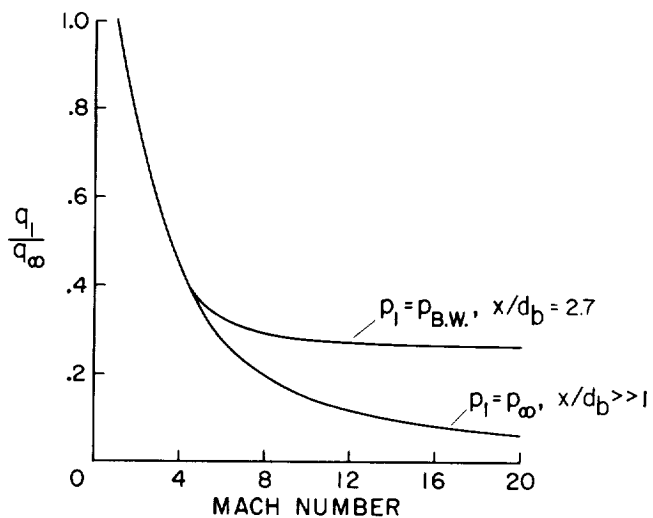


Figure 7

PITCHING MOMENT OF POLARIS FLARE

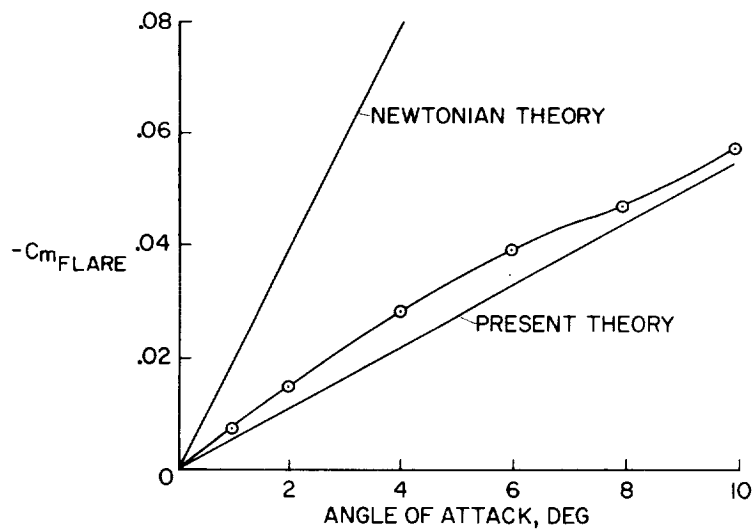
 $M = 11.6$ 

Figure 8

CONTRIBUTIONS OF BODY AND FLARE
TO THE STATIC STABILITY

M=15

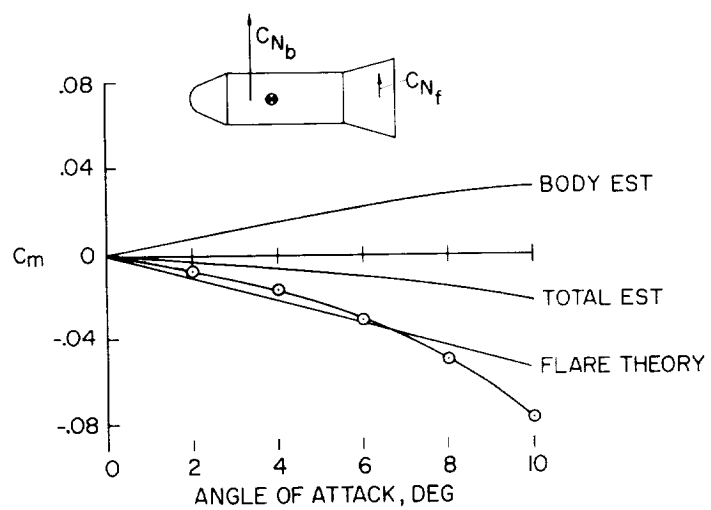


Figure 9

FLEXIBLE GLIDERS

By Robert T. Taylor, Joseph H. Judd, and Donald E. Hewes
Langley Research Center

13

INTRODUCTION

Interest has been expressed in flexible gliders with extremely low wing loading to be used for entry into the earth's atmosphere and for the terminal glide and landing of lifting and nonlifting capsules. Such vehicles appear to offer some very definite advantages both during the atmospheric entry and during the final recovery maneuver. One such vehicle is considered later in this paper, but for the present some of the characteristics of low wing loading during the satellite recovery maneuver are considered.

DISCUSSION

With a low wing loading the reentry vehicle slows down at high altitude where the air density is very low. A typical altitude velocity path is shown in figure 1 for a vehicle with a wing loading W/S of 1.0 pound per square foot entering with circular velocity and whose initial angle of entry γ is -1° . The vehicle was considered to have a constant ratio of lift to drag L/D equal to 0.57. The maximum aerodynamic heat transfer occurs at about 22,000 feet per second where the altitude is about 300,000 feet. When the vehicle has reached an altitude of 200,000 feet, the reentry maneuver has been completed. The expected critical temperature on the vehicle leading edges is shown in figure 2. For the range of wing loading of 0.5 to about 3 pounds per square foot, the temperatures are below 1,500° F and therefore within the capability of available material.

The magnitude of the glide velocities of a lightly loaded glider during the low-speed recovery phase of orbital return are shown in figure 3. The vehicle assumed here was considered to be typical of the lightly loaded configurations with a wing loading of 1 pound per square foot. Trim lift coefficient C_L ranged from about 0.1 to 0.65. The lower line on the figure corresponds to $C_L = 0.10$ whereas the upper line corresponds to $C_L = 0.65$. The vehicle will operate in the shaded area between. The vehicle has a horizontal velocity which ranges from 350 ft/sec to 950 ft/sec at an altitude of 100,000 feet. From this altitude the vehicle would be capable of gliding about 100 miles in

still air in any direction. However, because of the inherently low gliding velocities the lightly loaded vehicles can be greatly affected by winds. An indication of this effect is shown by the dashed line which represents a severe wind velocity distribution over Washington, D.C., which has a 20-percent expectancy. The vehicle velocities at zero altitude, or the landing speed, may vary from about 35 feet per second to about 75 feet per second. Because of these low landing speeds the vehicle could be accommodated by a very small landing area and, if the desired landing area is unattainable, a landing probably could be made without injury.

Estimates of loads due to gusts acting on lightly loaded vehicles have been calculated. For wing loadings of about 1 pound per square foot, the maximum expected loads for average turbulence conditions would be small. It should be noted, however, that large displacements of such vehicles would be likely in turbulence.

The vehicle under consideration, shown in figure 4, is collapsible in order to reduce the destabilizing influence on the booster during launch. The glider is characterized by a flexible membrane which carries the loads in tension during flight. This membrane is attached to the stiffened leading edges and keel, beneath which the load is suspended on shroud lines. Control of such a machine is accomplished by changing the position of the suspended load with respect to the canopy; for example, shifting the load to the left or right of center effects a turn in that direction, and a rearward shift of the load increases the angle of attack.

Many flights have been made of gliders similar to the one shown in figure 4. To date, about 100 experiments have been conducted by using a helicopter to carry the models to altitudes ranging from 200 feet to 2,000 feet. The models varied in construction details and fabric materials, and some were equipped with radio controls. These models varied in wing area from 17 square feet to about 100 square feet. In general, these tests showed the gliders to be stable and controllable. Furthermore, the gliders were observed to have rather flat glide angles. Four rocket-launched tests were conducted from the NASA Wallops Station where the gliders were tracked with both camera and radar. These tests were at altitudes of 1,500 feet and 200,000 feet and at Mach numbers near zero and 3.0, respectively.

Some fairly representative data on such a configuration are shown in figure 5. These data are experimental wind-tunnel determinations of the subsonic lift, drag, and pitching-moment characteristics and are shown here as pitching moment C_m and lift-drag ratio L/D against lift coefficient. The two curves showing highest L/D were obtained with models made of 0.016-inch aluminum sheet with the developed planforms shown. The data thus far obtained on models with fabric membranes have shown lower values of lift-drag ratio. It is felt that proper

"tailoring" of the fabric membrane and other details should improve these lift-drag ratios. The pitching moments thus far obtained on these models have been relatively linear. Furthermore, lift coefficients as high as 1.4 have been obtained.

The static lateral stability parameters $C_{n\beta}$ and $C_{l\beta}$ on a typical configuration plotted against angle of attack α are shown in figure 6. As would be expected from observation of the free glides, the measured longitudinal and lateral data indicate a stable configuration subsonically. Preliminary canopy flutter tests have been made in wind tunnels through the transonic flow regime and at a Mach number of about 1.9; these tests show that the canopy can be flutter free in this region.

The aerodynamic characteristics of the glider have also been studied in the supersonic flight regime with rocket-launched models and in wind-tunnel tests. The rocket tests were conducted at the NASA Wallops Station with a 17-square-foot model launched and tracked at Mach numbers M varying from 3 to 1.3 at altitudes of 150,000 to 200,000 feet. The data were obtained by differentiating the radar flight path of the model.

Tests at Mach numbers from 2.4 to 2.9 were made at the Langley Unitary Plan wind tunnel. These tests were made with the model semi-restrained; that is, the canopy was deployed and flown from the wind-tunnel balance after the tunnel had been brought up to speed. Angle of attack was varied during these runs by means of changing the longitudinal rigging of the wing during the run. The results are shown in figure 7 where the lift-drag ratio is plotted against the lift coefficient. The solid curve is the rocket-launch data ($M \approx 2.0$) and the dashed curve is the wind-tunnel data ($M = 2.65$). The differences shown are not surprising in view of the great differences in models and test conditions. Because these tests were exploratory in nature and primarily aimed at checking out the testing techniques, the ratios of trimmed $(L/D)_{\max}$ shown, about 1.5, are not considered to be the best obtainable in this speed range. However, from the data obtained, flexible gliders are expected to have supersonic and hypersonic performance sufficient to provide low accelerations and good lateral and longitudinal range control.

Because of the low wing loading, the vehicle under consideration operates in flow regimes which are not readily available to the experimenter. The Reynolds number per foot of a vehicle with a wing loading of 1 pound per square foot is on the order of 100 during peak heating. This means that the vehicle (depending upon the characteristic dimension of interest) is probably operating somewhere within the slip-flow regime. (See ref. 1.) In fact, the thin shroud lines of the flexible glider actually operate in the region of free-molecule flow. Figure 8 shows the expected temperatures at peak heating on these lines as a function

of suspension-line sweep. These estimates were made by using free-molecule heat-transfer rates. The upper curve represents the stagnation-point temperature of a line with perfect insulating characteristics, whereas the lower curve represents the surface temperature of a line with perfect conductivity. The temperature of suspension lines of various materials and construction should fall between these two limit curves. For example, a wire shroud of small diameter will probably fall close to the lower curve whereas a shroud line of multistrand cable construction may exhibit somewhat higher temperature on its leading edge and, depending upon the material from which it is constructed, may approach the upper curve in the stagnation region. Positive deployment of such a glider in a space environment may dictate the use of one or more inflatable shroud lines. If this were the case, temperatures of the order of $1,400^{\circ}$ F on these members during reentry might be expected, provided they are about 2 feet in diameter. (See ref. 2.) The calculations used under these conditions are those which correspond to the continuum-flow regime because of the relatively large diameter of the shroud.

CONCLUDING REMARKS

In view of the potential advantages of flexible gliders for the reentry and landing of space vehicles as indicated by the results so far obtained, the concept appears to have merit. Investigations leading to these and other applications are being continued.

REFERENCES

1. Probstein, Ronald F.: Continuum Theory and Rarefied Hypersonic Aerodynamics. WADC TN 58-145, ASTIA Doc. No. AD-155587, U.S. Air Force, July 1958.
2. Romig, Mary F.: Stagnation Point Heat Transfer for Hypersonic Flow. Jet Propulsion (Technical Notes), vol. 26, no. 12, Dec. 1956, pp. 1098-1101.

VELOCITY PROFILES DURING REENTRY

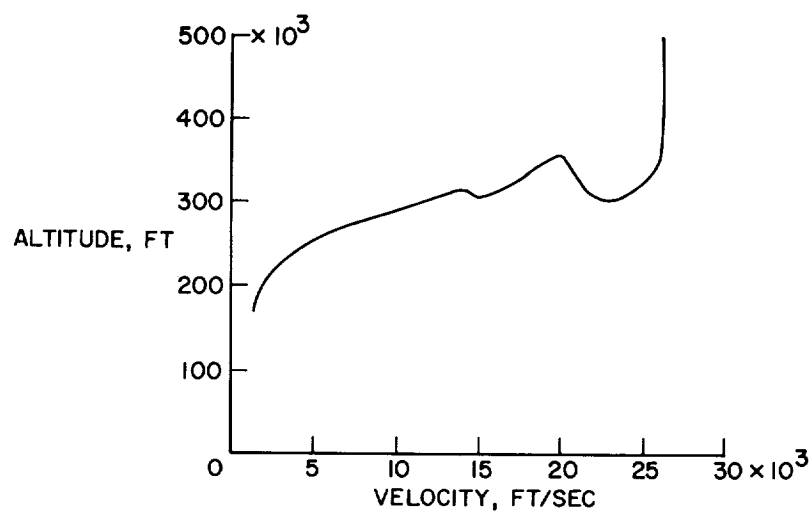
 $\gamma = -1^\circ$; $L/D = 0.57$; $W/S = 1.0$ 

Figure 1

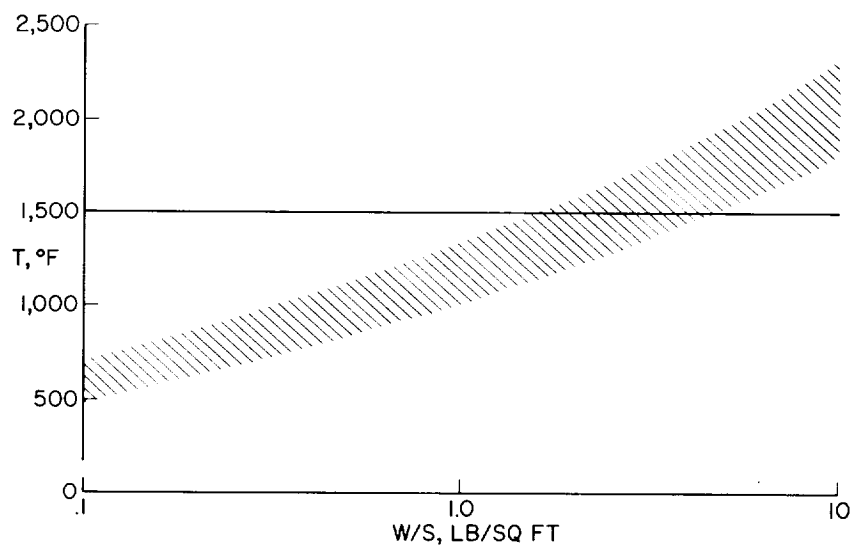
TYPICAL VALUES OF CRITICAL TEMPERATURE
SATELLITE REENTRY AT $C_{L,MAX}$ AND γ OF -1° 

Figure 2

LOW-SPEED GLIDE CAPABILITY

$W/S = 1 \text{ LB/SQ FT}$

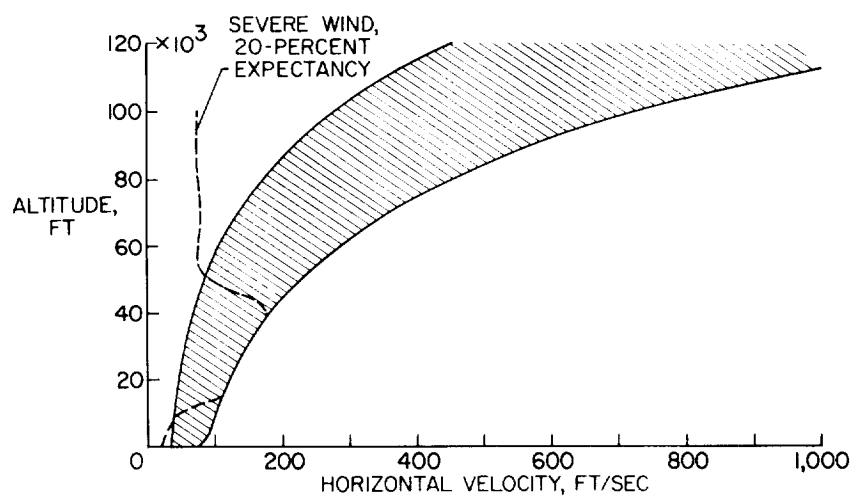


Figure 3

FLEXIBLE GLIDER

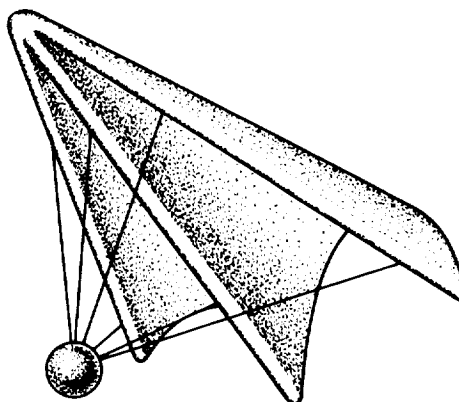


Figure 4

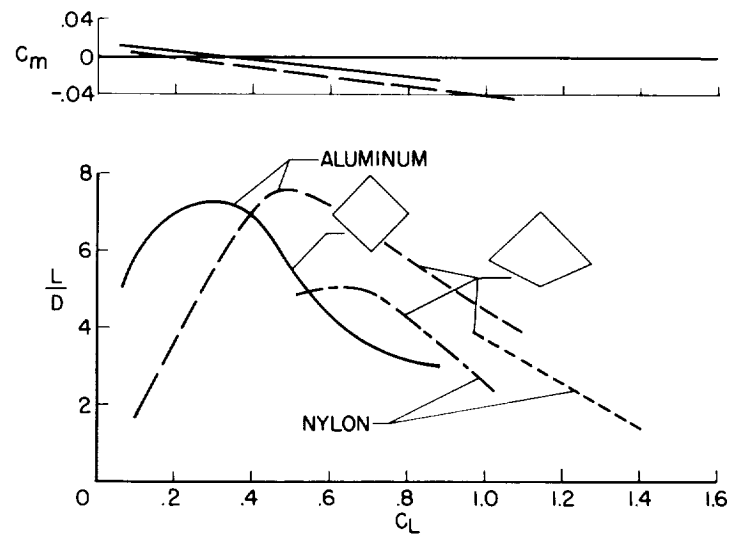
MEASURED VARIATIONS IN L/D AND C_m 

Figure 5

LATERAL CHARACTERISTICS OF ALUMINUM MODEL

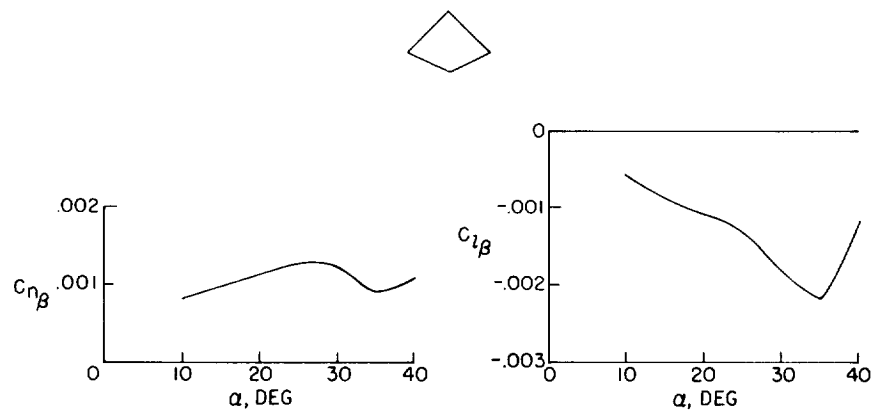


Figure 6

SUPERSONIC AERODYNAMIC CHARACTERISTICS

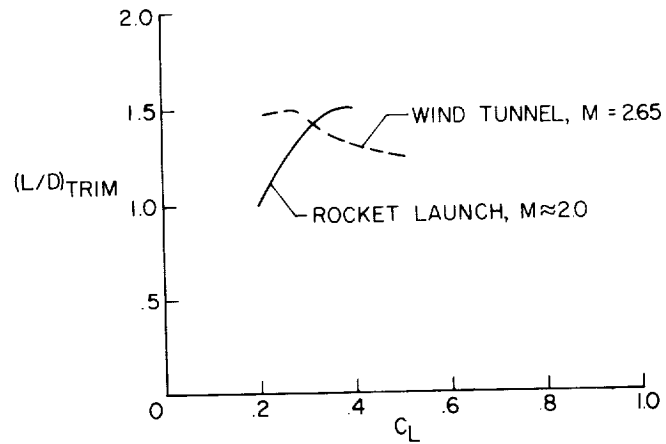


Figure 7

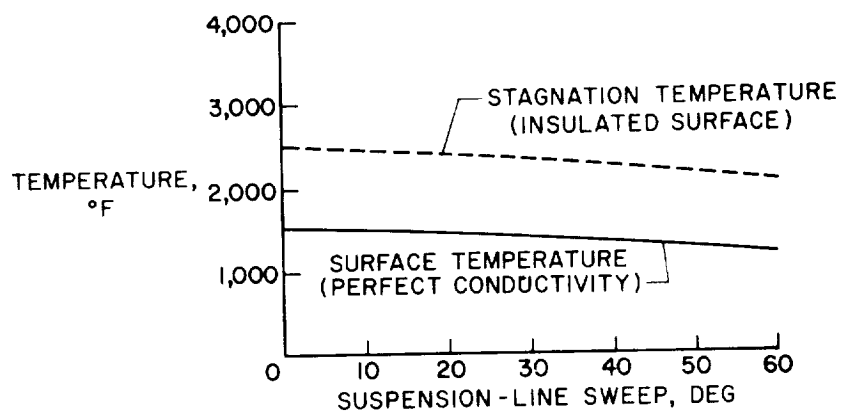
RADIATION-EQUILIBRIUM SUSPENSION -
LINE TEMPERATUREDIAMETER < MEAN FREE PATH
 $W/S = 1$ 

Figure 8

A GUIDANCE TECHNIQUE FOR THE APPROACH
TO AN ATMOSPHERIC REENTRY

By Alan L. Friedlander and David P. Harry III
Lewis Research Center

INTRODUCTION

The current literature contains many reports on the subject of interplanetary and lunar missions with relation to guidance requirements. Studies have been made of the accuracy requirements at cutoff during the initial launch phase (ref. 1), and it is generally accepted that if most mission objectives are to be attained a space vehicle must be equipped with a guidance system allowing trajectory corrections en route. The function of midcourse guidance is to assure a successful rendezvous with the target body at the proper time and place. However, if close tolerance maneuvers (such as atmospheric decelerations) are called for, some form of terminal or approach-phase guidance becomes necessary.

This paper discusses a guidance system that can be used for the approach to an atmospheric reentry. Acceptable values of corridor width for both lifting and nonlifting vehicles have been indicated by Chapman (ref. 2) and also by Frederick C. Grant and by Thomas J. Wong, Glen Goodwin, and Robert Slye in previous papers of this conference. The purpose of this study is to show the feasibility of guiding to within these relatively narrow corridors (on the order of tens of miles). In addition, some of the requirements of the control propulsion devices and measurement accuracies will be discussed. Results are to be presented for a reentry at Earth.

ANALYSIS

Figure 1 shows schematically the portion of the problem considered. It is convenient to divide the guidance problem into the midcourse and approach phases. This study will consider only the approach phase, which is defined here as the region from the Earth's sphere of influence down to the upper atmosphere. Thus, guidance is arbitrarily begun at about 100 Earth radii out. Two-body conic trajectories are assumed.

Residual errors from the midcourse phase are the initial errors for the approach phase. These errors are statistically distributed and values will be shown later.

The conic perigee distance is the parameter used in control. Longitude, latitude, and time of perigee passage are not considered; however, a direction of rotation around the Earth is specified. This definition of the problem leads to a two-dimensional analysis. In establishing ground rules for the guidance problem, it is stressed that the vehicle must be guided to within a desired corridor with a probability of success approaching 100 percent. With this in mind, it is then desirable to perform this task with minimum ΔV , or propellant requirement.

The functional requirements of the guidance system are the following: It must determine the trajectory being flown by taking appropriate measurements and if an apparent error exists, decide what action to take. It must then compute the ΔV necessary and control the execution of the correction.

The measurement scheme of this analysis is schematically shown in figure 2. It includes a clock to measure time increments and passive optical or infrared telescopic devices to measure angles. The system hypothesized is thought of as being completely self-contained. A given set of measurements is made at two positions along the trajectory. Range is determined from the Earth's apparent diameter by the angle ω . The change in the Earth's relative position measured against a star background yields the angular rotation of the vehicle $\Delta\theta$. These measurements are sufficient to determine the trajectory from the "two-position, time of flight" calculation. This is one of many possible schemes; however, investigation has shown this to be a desirable one. A particular advantage is that the requirements on the attitude control system are considerably relaxed. It is only necessary to have the Earth and stars in the same field of view during the instantaneous measurement. The same stars, of course, must be used in the two successive readings.

Errors in the measurement of angles and time are assumed to be random and normally distributed. The size of the error distributions will be described by their standard deviations.

Before continuing the description of the guidance system, consider the effectiveness of making a single-trajectory correction. This is illustrated in figure 3. Assume an initial perigee error of 400 miles, and angular measurement errors of 40 seconds of arc (rms). The ΔV required to make this correction is plotted on the left-hand ordinate as a function of the range from the Earth at which thrust is applied.

The right-hand ordinate shows the maximum corridor width remaining after one correction. It is plotted as a function of the range at which the second measurement is made. The first measurement is taken at 100 Earth radii, and ΔV is applied at the range of the second measurement. Thrust is applied in a direction perpendicular to the range vector. This type of correction has been shown to approximate closely the minimum ΔV cost (ref. 3).

The conflicting requirements of guidance accuracy and propulsion are apparent. To correct the trajectory in the vicinity of 80 Earth radii requires only about 50 ft/sec; however, the corridor width remaining may be as much as 2,500 miles. If the correction is delayed to a range of 1.5 radii, corridor widths of 60 miles can be achieved but at the expense of about 4,000 ft/sec. Although not shown, 20-mile corridors may be achieved at a distance of 80 radii, but instruments must be good to about 0.3 second of arc.

The conclusion to be drawn is this: If only a single correction is to be made, either extremely accurate instrumentation or very large ΔV 's are required to get small corridors. For this reason, a multiple correction guidance scheme is used in this analysis.

The guidance scheme hypothesized has several important aspects. First, the spacing between two successive measurements is proportional to the range of the first measurement. This sequence, however, is modified far from the Earth by a maximum spacing and close to the Earth by a minimum time increment. Such modifications are necessary to provide a more efficient scheduling of trajectory corrections.

Once the basic measurements are made, the vehicle computer reduces the data and determines the trajectory. The method of data reduction used in this analysis includes knowledge of the past history of the vehicle's trajectory. Based on instrument calibration data, statistical estimates of expected trajectory parameters are combined with new information by "least-squares" adjustment. This leads to a better trajectory determination.

Any apparent deviation from a desired corridor width may in part be due to an actual deviation and in part due to measurement errors. The decision as to how to act on apparent deviations is formulated by guidance logic. In principle, corrective action is warranted only if the apparent deviation is significant relative to the uncertainties. The guidance logic tends to prevent both unneeded corrections and over-correction, and thus avoids wasting fuel.

Before presenting results, the following table shows the standard deviations of the errors assumed in calculation:

<u>Quantity</u>	<u>Standard deviation</u>
Basic angular measurements	{ 40 sec arc 120 sec arc
Clocking	0.01 percent (9 sec/day)
Initial perigee	{ 400 miles 8,000 miles
ΔV control:	
Magnitude	0.1 percent
Direction	{ 80 sec arc 240 sec arc

In some cases, more than one error is shown and the effect of that parameter on results will be indicated. Basic angular measurements are accurate to 40 seconds of arc or 120 seconds of arc. It is expected that instruments to provide this rather relaxed accuracy can be easily obtained. Time is measured to an accuracy of about 9 seconds per day.

The 400-mile initial perigee error was chosen arbitrarily to represent good midcourse guidance, while the 8,000-mile error is the result of poor guidance. In calculation, the initial perigee error is assumed to be statistically distributed according to a normal bivariate law. This is a distribution of "hits" resulting from aiming at a bullseye. The control of ΔV is assumed to be accurate to one-tenth percent in magnitude and 80 seconds of arc or 240 seconds of arc in direction. In regard to the error in ΔV control, a parametric study has shown that results are rather insensitive to magnitude errors up to a few percent, and directional errors up to a degree or so.

RESULTS

A simulated approach to atmospheric entry was run on an IBM 704 computer. Statistical results were developed from 100 random trajectory runs generated by "Monte Carlo" techniques. In meeting the ground rules of the problem, all vehicles were guided to within the desired corridor.

Figure 4 illustrates the effect of corridor width, initial perigee error, and instrument accuracy on the corrective velocity requirements. For this example, entry into the atmosphere occurs at a velocity of twice circular ($\bar{V} = 2.0$). Each point plotted represents the maximum total ΔV requirement obtained from the statistical sample.

There are several points to be made from this figure:

(1) The amount of ΔV varies little with corridor width. For example, consider the 400-mile error and the 40 seconds of arc instrument accuracy. A 60-mile corridor can be obtained for 100 ft/sec, while the 8-mile corridor is possible with only an additional 80 ft/sec.

(2) There is a minimum corridor width that can be achieved with a given instrument accuracy. This is indicated by the cutoff of the curves on the left. For 120 seconds of arc, about 20 miles appears to be the limit.

(3) The order of the ΔV required depends mainly on the initial perigee error. Note the break in the ordinate scale. To get some idea of the control propellant weight, assume a specific impulse of about 400 seconds. Then, the amount of propellant ratioed to vehicle gross weight is about 1 or 2 percent for the 400-mile error, and 25 percent for the 8,000-mile error.

(4) One final point that may be of interest is the number of corrections made during the guidance maneuver. To exemplify this, consider the result for the 20-mile corridor. It was possible for the vehicle to make 15 corrections; however, it chose to use thrust only four times on the average. Similarly, an average of five corrections was made to achieve the 8-mile corridor.

CONCLUSIONS

In conclusion, the present analysis has described one approach to the guidance problem. Results have shown that narrow corridors on the order of 10 miles can be achieved, and the amount of control propellant required is not excessive provided initial errors are within reasonable limits. Furthermore, the guidance task can be performed without the necessity of extremely accurate instrumentation if a sophisticated guidance scheme is used.

To increase the generality of the results, a parameteric variation of \bar{V} from escape velocity to 2.5 circular velocity was made. The accuracy of guidance remained unchanged. The amount of ΔV required, of course, decreased with lower entry velocities.

REFERENCES

1. Ehricke, Kraft A.: Error Analysis of Keplerian Flights Involving a Single Central Force Field and Transfer Between Two Central Force Fields. Navigation, vol. 6, Spring 1958, pp. 5-23.
2. Chapman, Dean R.: An Analysis of the Corridor and Guidance Requirements for Supercircular Entry Into Planetary Atmospheres. NASA TR R-55, 1960.
3. Friedlander, Alan L., and Harry, David P., III: Requirements of Trajectory Corrective Impulses During the Approach Phase of an Interplanetary Mission. NASA TN D-255, 1960.

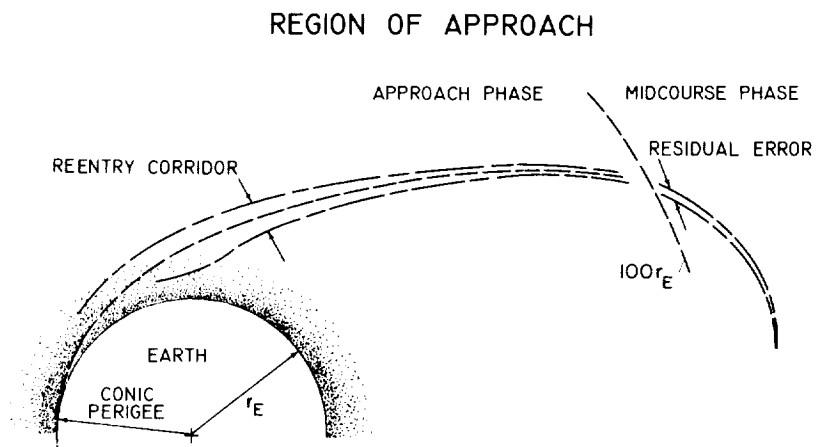


Figure 1

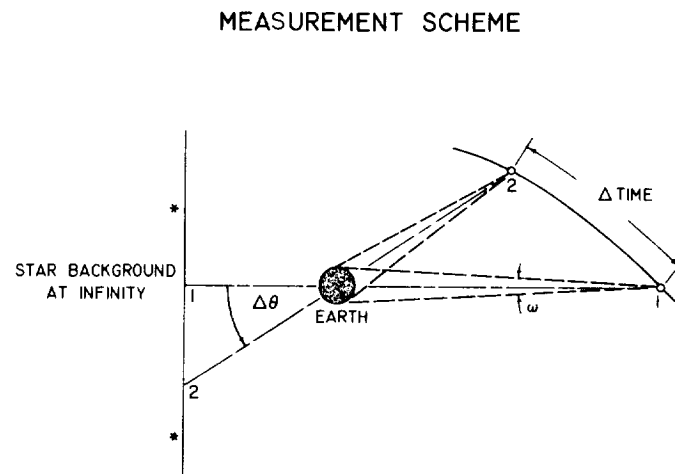


Figure 2

SINGLE-TRAJECTORY CORRECTION

INITIAL PERIGEE ERROR, 400 MILES \bar{v} , 2.0.

INSTRUMENT ACCURACY, 40";

FIRST MEASUREMENT, 100 EARTH RADII

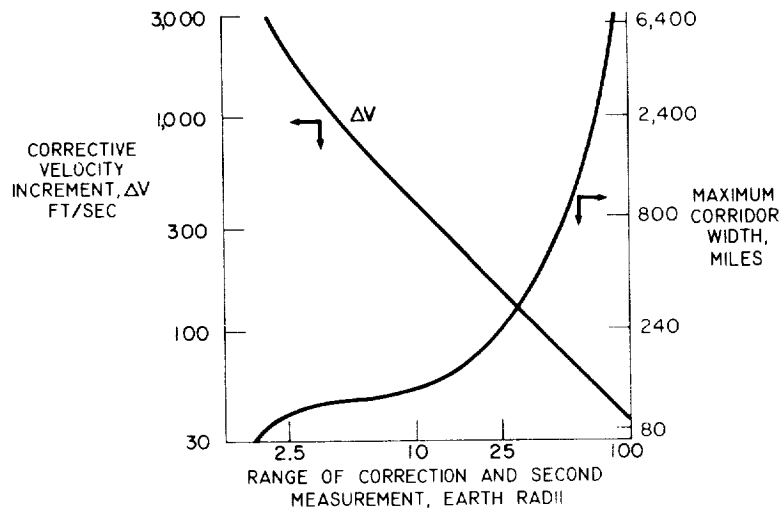


Figure 3

CORRECTIVE VELOCITY REQUIREMENT

$\bar{v} = 2.0$; SUCCESS PROBABILITY, 100 %

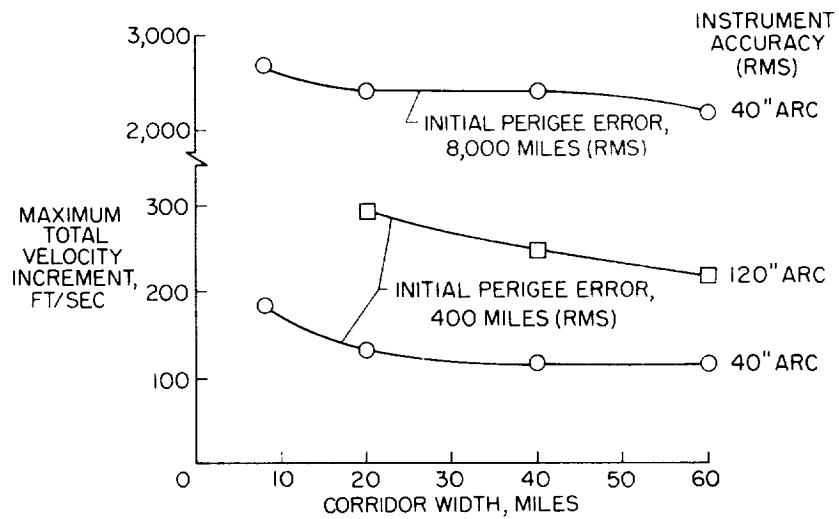


Figure 4

AN EXPLORATORY INVESTIGATION OF SOME MIDCOURSE GUIDANCE
SYSTEMS FOR THE RETURN FROM THE MOON

By G. Allan Smith
Ames Research Center

INTRODUCTION

Chapman (ref. 1) has shown that in order for a vehicle to reenter the earth's atmosphere without exceeding tolerable limits of deceleration or heating, the vehicle trajectory must come within a specified reentry corridor. This corridor is defined by the difference in vacuum perigee radius between two limiting trajectories which would be followed in the absence of the atmosphere. The primary function of the midcourse guidance system is to control the vehicle trajectory so that it will come within the allowable corridor. Wong and Slye (ref. 2) have shown that the width of this corridor depends upon vehicle characteristics and varies from 8 miles for a nonlifting vehicle to 44 miles for a vehicle with lift-drag ratio L/D of 0.5 and to 100 miles for a vehicle with L/D of 0.8.

For the complete lunar circumnavigation mission, it seems probable that the primary guidance system used to predict the future vehicle trajectory will basically integrate the equations of motion for the multi-body problem, using the initial burnout conditions of position and velocity. Subsequent measurements of the vehicle trajectory would be used to refine the initial condition values. However, for the manned mission, the possibility of temporary failure or discontinuity of the primary system must be considered. The necessity of recomputing the trajectory on the basis of measurements obtained from onboard or ground based backup systems is also a possibility. Under such emergency conditions, the use of conic section trajectory calculations appears attractive.

The trajectory considered in this investigation is shown in figure 1. During the midcourse phase, after the vehicle is closer than 190,000 miles to the earth, the gravitational influence of the moon is considered negligible, and it is assumed that the path is an ellipse with one focus at the center of the earth. The perigee radius R_p and range of the vehicle from the earth R are shown.

PRIMARY MEASUREMENTS FOR GUIDANCE SYSTEMS

In figure 2 are illustrated the various measurements that have been considered. From the ground, it is possible to measure range to the vehicle by utilizing a powerful radio transmitter and a transponder aboard the vehicle. This system can also measure the angle of the line of sight to the vehicle ψ with respect to some reference at the antenna. From measurements of Doppler frequency shift, range rate can be determined. Actually, range rate could be classed as either a ground-based or vehicle-based measurement, since it requires only a minimum transponder or precision-frequency source at one station while the main frequency-shift measuring equipment could be at the other station, either on the ground or aboard the vehicle.

From onboard the vehicle, optical sighting angles to the earth and moon can be measured. If an onboard inertial coordinate system referenced to the fixed stars is available, range to the earth can be obtained by triangulation, since the length and direction of the earth-moon line is known as a function of time. That is, the direction of the earth-moon line can be reproduced aboard the vehicle so that the angles A and B can be measured. It is possible to measure the angular rate $\dot{\psi}$ of the range vector with respect to inertial space by optically tracking the earth disk with a telescope mounted on a precessable, gyro-stabilized platform whose angular rate is then measured. Accurate time information should be available both in the vehicle and on the ground.

POSSIBLE GUIDANCE SCHEMES

The primary measurements obtained can be combined in several different ways to compute the elliptical parameters of eccentricity e and perigee radius R_p .

The following table lists some guidance systems which utilize various combinations of primary measurements:

TABLE I

System	Quantities measured	Number of measurement points required
1	R and \dot{R}	2
2	R , \dot{R} , and $\dot{\psi}$	1
3	R and $\Delta\psi$	3
4	R , $\Delta\psi$, and t	2

If, as shown for the first system, measurements are made of range R and range rate \dot{R} , the measurements must be made at two points on the trajectory in order for the elliptical parameters to be computed. The second system requires the measurement of range, range rate, and the angular rate of the range vector $\dot{\psi}$ at only one point on the trajectory. The guidance accuracy achievable with this system depends critically upon the capability of actually mechanizing the measurement of very small angular tracking rates. The third system requires the measurement of range and change in angle $\Delta\psi$ at three points on the trajectory. This system can have excessive errors in trajectory determination even for very high primary-measurement accuracy, because the maximum measurement errors can combine in a very unfavorable manner if they have different signs at the middle observation point compared to the two end points. These procedures require the minimum number of measurements that must be made in each case to determine the orbit from the quantities specified. For instance, in the case of the third system which involves the measurement of only range and angle change, the direction of the major axis of the ellipse is not known, so that only differences in angle can be measured and hence three points on the path are required. The fourth system requires the measurement of range, change in angle, and time t at two points along the trajectory. It has already been discussed in the preceding paper by Alan L. Friedlander and David P. Harry III, whose guidance scheme using these measurements is more sophisticated than that considered here for the three other schemes, since it utilizes the past history of the vehicle trajectory in conjunction with the present measurements and provides a statistical estimate of perigee error. The onboard measurements used in these various guidance procedures could perhaps be carried out completely automatically, or various degrees of pilot participation could be utilized.

PERIGEE ERRORS

An investigation was made of the accuracy with which the perigee radius could be determined by each of the first three methods as a function of the errors in measurement of the primary quantities. Statistical methods were not used in this exploratory investigation; instead, the perigee error was determined by means of maximum measurement errors with the most unfavorable combination of sign for the multiposition measurements. Maximum errors which were thought to be realistic both for the case of currently available components and for improved components which might be available in the next 3 to 5 years were assumed.

Figure 3 presents the results of perigee accuracy calculations for the first system, which involves the measurement of range and range rate. See appendix A. The curves are the envelopes of possible errors in the

calculation of corridor width as a function of range from the earth for two different sets of maximum measurement errors. Corridor width error is considered to be twice as great as perigee error. The upper curve assumed that range was determined by triangulation (appendix B) aboard the vehicle with an error of ± 20 seconds of arc in measurement of angles. (Some type of gyro-stabilization for the optical theodolite is assumed.) This provides range to about 0.01 percent at 200,000 miles with a deterioration to 0.25 percent at 20,000 miles, since the vehicle-earth-moon triangle became quite oblique for an actual trajectory of the lunar return journey which was calculated as a multibody problem on a digital computer to determine a suitable reference ellipse for these calculations. A range-rate error of ± 0.05 percent was assumed. The two points of measurement were taken to differ in range by 20 percent. The lower curve was determined for an assumed future improvement in angular measurement to 5 seconds of arc and in range-rate measurement to 0.01 percent. The maximum measurement errors can either be positive or negative at each of the two measurement points and hence 16 possible sets of trajectory parameters can be calculated at each range. The curves plotted are for the worst possible case, where the range and range-rate errors assume their maximum positive values at the first point and maximum negative values at the second point.

VELOCITY CORRECTIONS FOR R AND \dot{R} SYSTEM

A guidance scheme which would utilize this navigation data in making trajectory corrections was considered. It was assumed that an initial error of 400 miles in perigee existed when the vehicle was 190,000 miles from the earth and that it was desired to hit a 40-mile reentry corridor. Figure 4 shows the change in velocity ΔV required as a function of the number of corrections used by the guidance scheme. It was assumed that the velocity increment was applied perpendicular to the radius vector in order to utilize the minimum velocity increment for a specified perigee correction, as discussed in reference 2. The formula $\Delta V = \frac{V_p}{2R} \Delta R_p$ was used to compute the amount of velocity correction ΔV required at range R for a specified perigee correction ΔR_p on a trajectory with perigee velocity V_p . The indicated perigee error was assumed equal to the true perigee error but velocity corrections were made only to within the measurement accuracy at any particular range as indicated in figure 3. Point A in figure 4 indicates the minimum possible ΔV of 37 feet per second if a single perfect correction could be made at 190,000 miles. Point B indicates a ΔV of 700 feet per second required for the measurement accuracies indicated by the upper curve of figure 3 if only one correction can be made and it must be delayed until 10,000 miles when the maximum error in calculating perigee is less than

half the desired corridor. If two corrections are made, one at 190,000 miles to within the accuracy of the corridor measurement at that point and a final correction at 10,000 miles, the total ΔV is only 285 feet per second. The total ΔV required reduces to 145 feet per second if three additional corrections are used. If the ΔV corrections are accomplished by using fuel with a specific impulse of 300, the fuel weight required is about $1\frac{1}{2}$ percent of total vehicle weight for the five-correction guidance scheme.

It is interesting to note that comparable values were found by Freidlander and Harry in the preceding paper for a system with poorer basic measurement accuracies but a more sophisticated guidance scheme.

PERIGEE ERRORS FOR $R, \dot{R}, \dot{\psi}$ AND $R, \Delta\psi$ SYSTEMS

Figure 5 shows the variation of corridor width for the second system as a function of range when measurements of range R , range rate \dot{R} , and angular rate of the vehicle-earth line of sight $\dot{\psi}$ are made at a single point on the trajectory. This case can be treated entirely analytically and has been considered in several publications (for example, ref. 2). The error coefficients were derived and are presented in appendix C in a particularly useful form which includes range as the only variable. The measurement accuracies used to compute curve 1 are felt to be consistent with current-equipment performance. Current ground-based radio tracking assumed for curve 1 is believed to be as good as 0.005 percent for range and 0.05 percent for range rate. Gyro drift rates of 0.01° per hour are claimed for available airborne components. Curve 2 was computed on the assumption that range was determined by onboard triangulation with an error of 20 seconds of arc in angular measurement and shows the effect of poor range by triangulation at short ranges. Curve 3 assumes range by triangulation and improved angular rate accuracy to 0.001° per hour. Although gyro drift rates this low or lower may be obtained in the zero g environment, it may be more difficult to develop an automatic optical disk tracker to track the earth smoothly enough to realize this overall accuracy. However, this measurement could almost certainly be smoothed for several minutes.

Figure 6 presents results for the case where range and angle measurements are available at three points (taken to be 10 percent different in range between adjacent points). The error equations presented in appendix D were taken from unpublished notes by Dr. W. A. Mersman of Ames Research Center which also show that measurements of range and angle at three points from the ground are sufficient to determine the inclination and orientation of the orbital plane. Azimuth and elevation angles of the vehicle with respect to some reference at the ground site can

therefore be used to determine angle differences in the orbit plane between the range vectors at the three points.

For this case, there are three ranges and two differences in angle to be considered so that 32 sets of elliptical parameters can be computed at each range (again taken to be the range of the farthest point). The maximum error, which is plotted in figure 6, occurs when the range errors are positive at the first and last point and negative for the middle point while the first angle-difference error is negative and the second is positive. For this case as well as for the previous cases, a reference ellipse was assumed with a major axis of 250,000 miles and a perigee radius of 4,000 miles. This trajectory closely approximated an actual multibody trajectory which had been computed. Measured values of range and angle to use in the error equations were taken from this reference ellipse and then increased or decreased by the amount of assumed measurement error.

Ground-based measurement of angle by radio tracking is currently reported at about 1 milliradian or 206 seconds of arc. Improvement to one tenth of this error is generally expected. Even so, the perigee errors attainable by this method appear excessive, with angle measurement being critical. This procedure might be more attractive if optical tracking could be utilized from the ground with a bright light on the vehicle to give a telescopic accuracy of a second or so.

INSTRUMENTATION

Some consideration was given to the onboard instrumentation required for the various guidance systems previously suggested. It appeared that the equipment weight penalty aboard the vehicle to provide guidance data simultaneously from each of these guidance system would be quite small if the pilot were utilized to make the selection of guidance information and to operate some of the equipment. The redundancy provided by this arrangement not only serves in the emergency mode but can greatly improve the reliability of the normal-trajectory correction system. Direct manual operation or semiautomatic operation of the vehicle-contained equipment would greatly reduce the system complexity required as compared with completely automatic operation, particularly if the system had to be designed to cope with temporary component failures and malfunctions or loss of stellar reference sights.

Figure 7 is a block diagram illustrating the instruments that would be required aboard a space vehicle to make primary guidance measurements. A gyro-stabilized platform would serve as an inertially fixed mount for a theodolite used to determine angles. Integrating accelerometers would

also be mounted on the platform to determine the magnitude and inertial direction of the velocity increment resulting from corrective thrust. Since even the most accurate inertial gyros can be expected to show some drift rate, a telescopic star tracker would be mounted on the platform and used periodically to realine it with respect to the fixed stars. A semiautomatic disk tracker mounted on the platform and pointed toward the earth would be used in the second guidance mode to drive the platform at line-of-sight rate $\dot{\psi}$. These vehicle-based measurements would be supplied to an onboard digital computer which would also accept ground-based measurements to form a composite guidance system capable of operating in any of the systems that have been considered.

APPENDIX A

PERIGEE RADIUS COMPUTED FROM MEASUREMENTS OF RANGE AND

RANGE RATE AT TWO POINTS ON THE TRAJECTORY

Starting with the equations for the ellipse at two points defined by $R_1\theta_1$ and $R_2\theta_2$ permits expressions for R_1 and R_2 to be written as follows:

$$R_1 = \frac{P}{1 + e \cos(\theta_1 - \alpha)}$$

$$R_2 = \frac{P}{1 + e \cos(\theta_2 - \alpha)}$$

The angle α is an unknown angle between the major axis of the ellipse and the measurement reference line. Since a measurement of \dot{R} is also available, two other equations to be used are

$$\dot{R}_1 = \frac{e\sqrt{\mu} \sin(\theta_1 - \alpha)}{\sqrt{P}}$$

$$\dot{R}_2 = \frac{e\sqrt{\mu} \sin(\theta_2 - \alpha)}{\sqrt{P}}$$

These equations can be combined to yield an expression for eccentricity

$$e^2 = \frac{P^2 - 2PR_1 + R_1^2}{R_1^2} + \frac{\dot{R}_1^2 P}{\mu}$$

and semilatus rectum

$$P = \frac{R_1^2 R_2^2 (\dot{R}_2^2 - \dot{R}_1^2) - 2\mu R_1 R_2 (R_1 - R_2)}{\mu (R_2^2 - R_1^2)}$$

Figure 3 is a plot of the error in calculating corridor width for various assumed errors in measuring R and \dot{R} . Note that corridor width is considered to be twice perigee error.

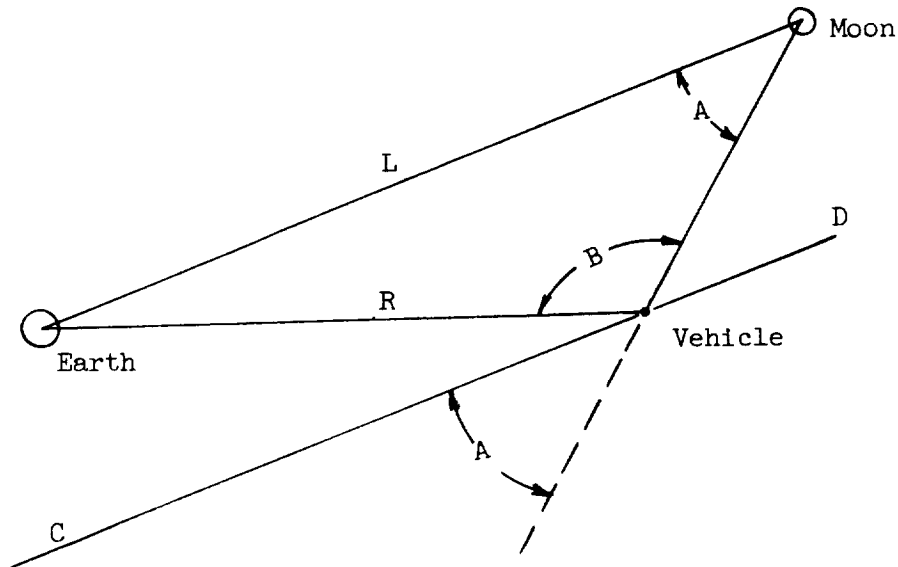
Since errors in measuring the four quantities R_1 , R_2 , \dot{R}_1 , and \dot{R}_2 may be either positive or negative, there are 16 values of R_p to be calculated at each point on the trajectory. Calculations were actually carried out at 10 points along the trajectory between 10,000 and 190,000 miles from the earth. For each point on the trajectory at which a calculation was made, the value of R_1 and \dot{R}_1 were taken to be those at the point in question. The value of R_2 was taken to be 20 percent less than R_1 .

These calculations were carried out on a digital computer. Other runs at 10 percent difference in range between R_1 and R_2 showed slightly more than twice as much error in R_p .

APPENDIX B

RANGE FROM A LUNAR VEHICLE TO THE EARTH BY TRIANGULATION

The vehicle, earth, and moon will form a plane triangle as shown in the following sketch (this plane does not necessarily coincide with the plane of the vehicle orbit):



By the law of sines,

$$R = \frac{L \sin A}{\sin B}$$

The line CD is a line through the vehicle parallel to the earth-moon line L. The error in computing R due to errors in measurement of the angles A and B may be expressed as

$$\Delta R = \frac{\partial R}{\partial A} \Delta A + \frac{\partial R}{\partial B} \Delta B$$

Partial differentiation of the expression for R, yields

$$\frac{\partial R}{\partial A} = \frac{L \cos A}{\sin B}$$

$$\frac{\partial R}{\partial B} = - \frac{L \sin A \cos B}{\sin^2 B}$$

For an actual lunar return the partial derivatives as calculated for various range values are shown in table II. For a constant error in determining angle, the percentage error in determining range increases sharply at the shorter ranges.

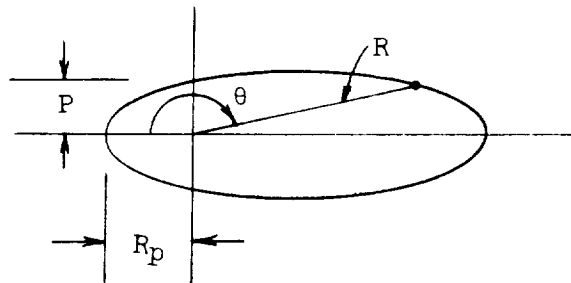
TABLE II

Range, miles	Error coefficients, miles per radian		Range error, for $\Delta A = \Delta B = 20''$
	$\frac{\partial R}{\partial A}$	$\frac{\partial R}{\partial B}$	
12,000	22.60×10^5	1.140×10^5	237.5
24,000	7.22	.708	79.3
47,500	3.72	.621	43.4
70,800	2.97	.630	36.0
96,000	2.53	.616	31.5
120,000	2.27	.589	28.6
142,000	1.99	.535	25.3
166,500	1.57	.392	19.6
190,000	1.27	.344	16.1

APPENDIX C

PERIGEE RADIUS COMPUTED FROM A SINGLE MEASUREMENT OF RANGE,
RANGE RATE, AND ANGULAR RATE

The normal polar equation of an ellipse with one focus at the origin is $R = \frac{P}{1 + e \cos \theta}$ where P is the semilatus rectum and e is eccentricity (see sketch).



The perigee radius is $R_p = \frac{P}{1 + e}$. This equation may be expressed in terms of R , \dot{R} , and $\dot{\theta}$ at any point on the trajectory as

$$R_p = \frac{\frac{R^4 \dot{\theta}^2}{\mu}}{1 + \sqrt{1 + \frac{R^4 \dot{\theta}^2}{\mu} \left(\frac{R^2 \dot{\theta}^2}{\mu} + \frac{\dot{R}^2}{\mu} - \frac{2}{R} \right)}}$$

where $\mu = 1.4077 \times 10^{16} \text{ ft}^3/\text{sec}^2$. The error in computing R_p due to errors in measuring R , \dot{R} , or $\dot{\theta}$ can then be expressed as

$$\Delta R_p = \frac{\partial R_p}{\partial R} \Delta R + \frac{\partial R_p}{\partial \dot{R}} \Delta \dot{R} + \frac{\partial R_p}{\partial \dot{\theta}} \Delta \dot{\theta}$$

where ΔR , $\Delta \dot{R}$, and $\Delta \dot{\theta}$ are measurement errors and ΔR_p is the resulting error in computing R_p .

After some algebraic manipulation, the partial derivative can be expressed as

$$\frac{\partial R_p}{\partial R} = 2 \left(\frac{1+e}{e} \right) \left(\frac{R_p}{R} \right) - \frac{1}{e} \left(\frac{R_p}{R} \right)^2 - \left(\frac{1+e}{e} \right) \left(\frac{R_p}{R} \right)^3$$

$$\frac{\partial R_p}{\partial \dot{R}} = \frac{R_p^{3/2}}{e \sqrt{\mu}} \sqrt{(e-1) + 2 \left(\frac{R_p}{R} \right) - (1+e) \left(\frac{R_p}{R} \right)^2}$$

$$\frac{\partial R_p}{\partial \dot{\theta}} = \frac{1}{e} \sqrt{\frac{R_p(1+e)}{\mu}} (R^2 - R_p^2)$$

Note that R_p and e are the true values for the reference ellipse, which was assumed to have a major axis of 250,000 miles, and that $R_p = 4,000$ miles, which yields $e = 0.968$.

Figure 5 is a plot of the error in computing corridor width as a function of R for various assumed values of error ΔR , $\Delta \dot{R}$, and $\Delta \dot{\theta}$. Note that $\dot{\theta}$ as used in this appendix is equivalent to $\dot{\psi}$ as shown in figure 5.

APPENDIX D

PERIGEE RADIUS COMPUTED FROM MEASUREMENTS OF RANGE AND
ANGLE AT THREE POINTS ON THE TRAJECTORY

The equations which follow were taken from unpublished notes of Dr. W. A. Mersman of the Ames Research Center.

The usual polar equation of an ellipse can be rearranged as

$$R \cos(\theta - \alpha) - P = -R$$

or

$$R \cos \theta \cos \alpha + R \sin \theta \sin \alpha - P = -R$$

if three such equations are written using R_1 , R_2 , R_3 and θ_1 , θ_2 , θ_3 , respectively, they can be solved simultaneously to yield the expressions

$$P = \frac{R_1 R_2 R_3 [\sin(\theta_1 - \theta_2) + \sin(\theta_2 - \theta_3) + \sin(\theta_3 - \theta_1)]}{D}$$

where

$$D = R_1 R_2 \sin(\theta_1 - \theta_2) + R_2 R_3 \sin(\theta_2 - \theta_3) + R_3 R_1 \sin(\theta_3 - \theta_1)$$

and

$$\begin{aligned} D^2 e^2 = & 2R_1^2 R_2^2 [1 - \cos(\theta_1 - \theta_2)] + 2R_2^2 R_3^2 [1 - \cos(\theta_2 - \theta_3)] \\ & + 2R_1^2 R_3^2 [1 - \cos(\theta_1 - \theta_3)] - 2R_1 R_2^2 R_3 [1 - \cos(\theta_2 - \theta_3) \\ & + \cos(\theta_1 - \theta_3) - \cos(\theta_1 - \theta_2)] - 2R_1^2 R_2 R_3 [1 - \cos(\theta_1 - \theta_2) \\ & + \cos(\theta_2 - \theta_3) - \cos(\theta_1 - \theta_3)] - 2R_1 R_2 R_3^2 [1 - \cos(\theta_1 - \theta_3) \\ & + \cos(\theta_1 - \theta_2) - \cos(\theta_2 - \theta_3)] \end{aligned}$$

Figure 6 is a plot of corridor width as a function of range for various values of errors in measuring range and angle. At each point on the trajectory where a calculation was carried out, there are five measured quantities to be considered as having measurement errors, R_1 , R_2 , R_3 , $(\theta_1 - \theta_2)$, and $(\theta_2 - \theta_3)$. The value of $\theta_1 - \theta_3$ was taken as the sum of the two preceding angles. Since the error in each of these five quantities could be either positive or negative, 32 sets of elliptical parameters were calculated at each point. At each point, the values of R_2 and R_3 were taken to be, respectively, 10 and 20 percent less than R_1 .

REFERENCES

1. Chapman, Dean R.: An Analysis of the Corridor and Guidance Requirements for Supercircular Entry Into Planetary Atmospheres. NASA TR R-55, 1960.
2. Wong, Thomas J., and Slye, Robert E.: Effect of Lift on Entry Corridor Width and Guidance Requirements for the Return Lunar Flight. (Prospective NASA paper.)

LUNAR MISSION RETURN TRAJECTORY

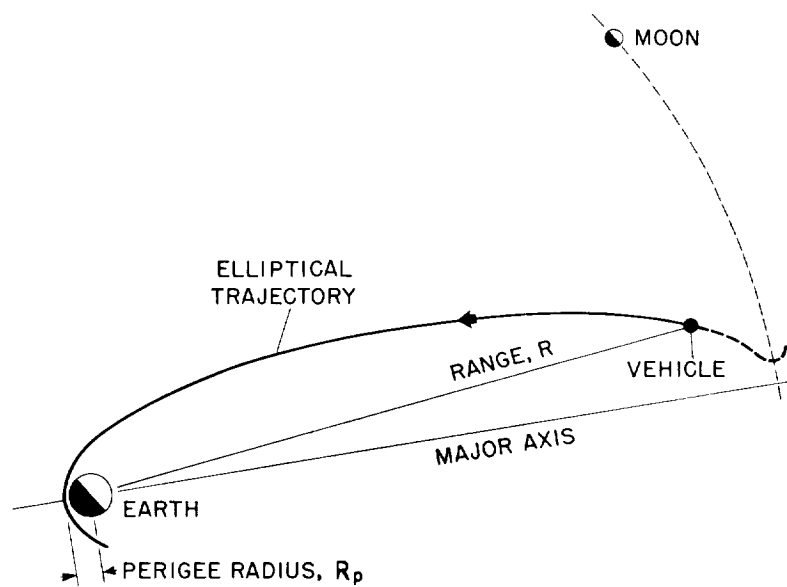


Figure 1

LUNAR MISSION RETURN TRAJECTORY

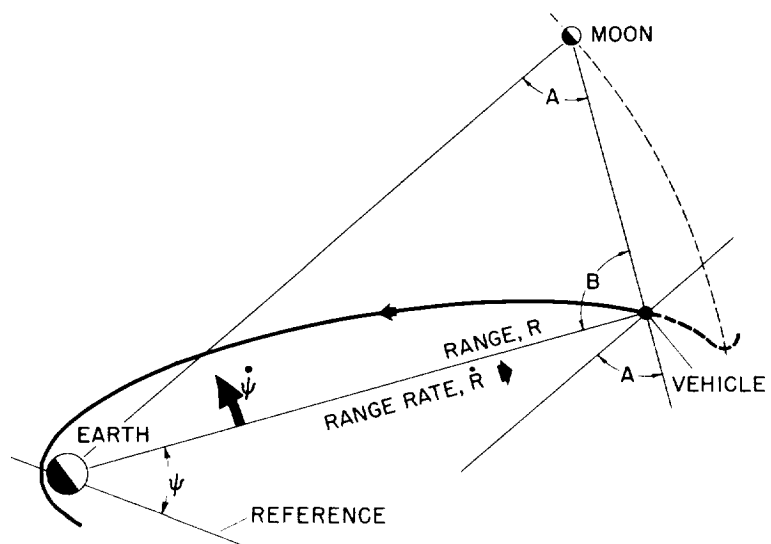


Figure 2

MAXIMUM CORRIDOR WIDTH MEASUREMENT ERROR RANGE AND RANGE RATE AT TWO POINTS, 20% APART

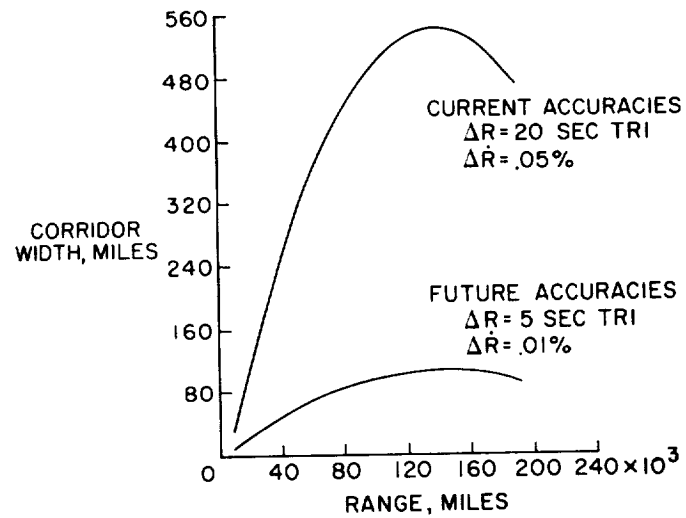


Figure 3

CORRECTIVE-VELOCITY REQUIREMENTS

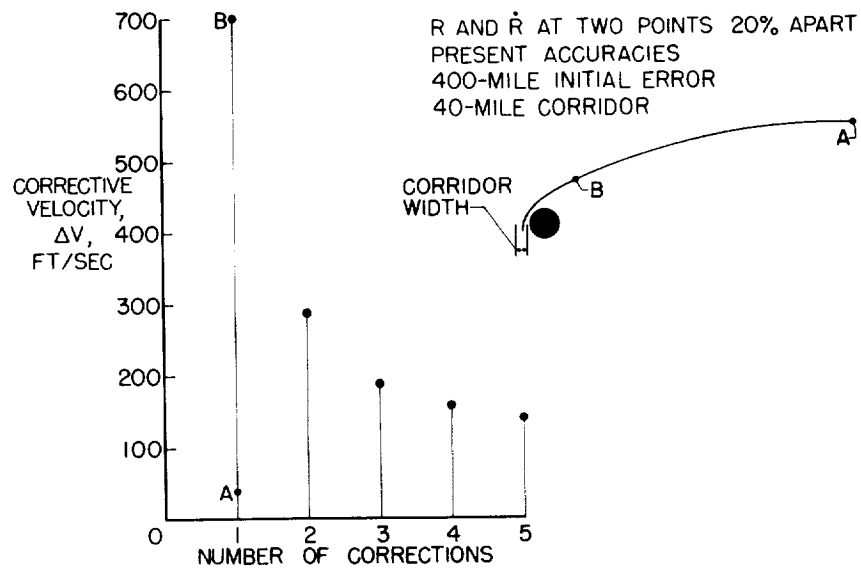


Figure 4

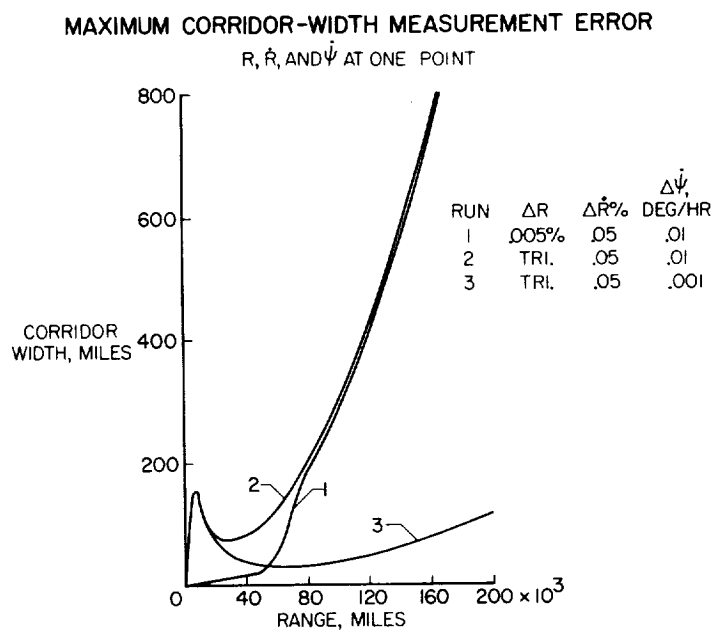


Figure 5

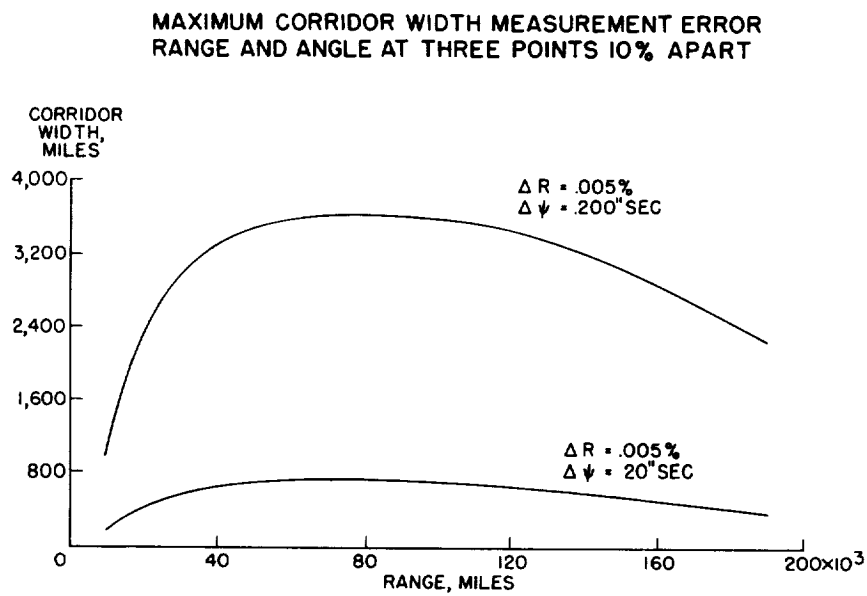


Figure 6

VEHICLE-CONTAINED INSTRUMENTATION

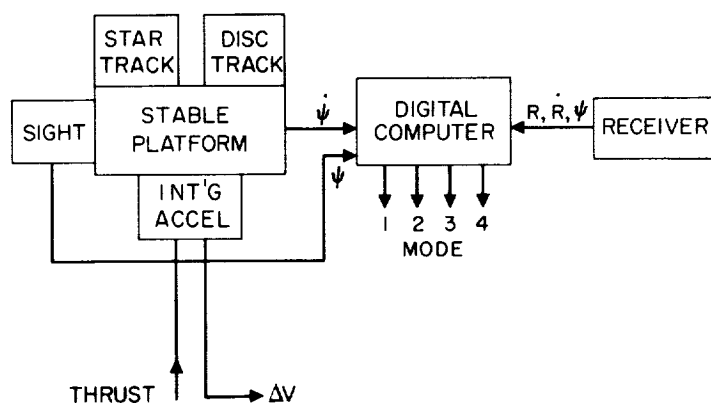


Figure 7

NAVIGATION AND GUIDANCE DURING SATELLITE ENTRY


By John M. Eggleston
Langley Research Center

INTRODUCTION

Whether a vehicle is returning from a near-earth orbit or is returning from a planetary mission, the primary consideration is the desire to land at a specific place on the surface of the earth. The preceding paper has discussed some of the guidance accuracies associated with achieving a desired perigee altitude when returning from planetary missions. For the return from near-earth orbits, the accuracies should be even better. However desirable it may be to assume that such errors are small, it is precisely these inaccuracies that determine how much guidance and how elaborate a navigational procedure is going to be required during the atmospheric portion of the entry. This paper will cover some of the general considerations applicable to entry navigation and the results of experimental and analytical studies on guidance techniques during simulated entries.

SYMBOLS

C_L	lift coefficient
K_1, K_2	gains for automatic control
L/D	lift-drag ratio
V	velocity
α	angle of attack, deg
α_{TRIM}	trim angle of attack, deg
β	angle of sideslip
γ	entry angle




ΔR	range error
$\dot{\Delta R}$	time rate of change in range error
θ	range angle
ρ	density
Subscripts:	
AV	average
MAX	maximum
o	initial
STD	standard

PRELIMINARY CONSIDERATIONS

There appears to be three preliminary considerations: First, gross range requirements should be met by waiting in orbit (either around the earth or another planet) for a favorable return time, by properly programing the thrust for the transfer trajectory, and by small midcourse guidance corrections while on the transfer trajectory.

The second consideration is that of choosing entry conditions most favorable to accurate atmospheric navigation and guidance. This aspect is illustrated in figure 1 where the return from a near-earth orbit is used as the example. This figure shows the effect of velocity on the entry angle and point of entry. If an entry is attempted at a very small entry angle, then an error of 10 ft/sec in retrovelocity can cause extreme errors in the distance covered to the point of entry and thereby put a tremendous burden on the atmospheric guidance system. However, if the entry can be made at a larger entry angle of say 2° then even an error of 10 ft/sec in retrovelocity has very little effect on the point of entry and the atmospheric navigation problem is not so difficult as before. The heating aspect of these larger entry angles has been covered in several preceding papers such as the one by Eugene S. Love.

Once the cumulative maximum expected errors are established, the third consideration is that of having aerodynamic performance capable of correcting those errors. The lift-drag ratio and turning capabilities of the vehicle must be large enough to compensate for the anticipated errors in entry conditions.



In order to keep this paper general, it is assumed that the return trajectory was initiated so as to place the vehicle at the edge of the atmosphere within a corridor defined by the atmospheric range capabilities of the vehicle. How the vehicle may then be guided to a position over the desired landing area is considered.

METHODS OF ENTRY NAVIGATION

At the start of the entry, the vehicle is at its maximum velocity and atmospheric altitude and, therefore, the ability to maneuver is a maximum. However, the uncertainty of which path to follow is also a maximum, since errors in velocity, altitude, atmospheric density, and the lift, drag, and heat-transfer characteristics of the vehicle will be integrated over the entire time to descend. With a reduction in altitude and velocity, the proper path becomes more defined but the ability to make corrections onto that path continually decline. This is the paradox of entry navigation.

In order to solve this navigational paradox, two methods of defining the proper entry path have been studied by industry and by the NASA. The first of these two methods of energy management are illustrated in figure 2. The maneuver-corridor method is to define a velocity corridor emanating from the desired landing site. The corridor is defined by the trajectory which could be flown at the maximum lift-drag ratio of the vehicle and the trajectory which could be flown at the maximum lift coefficient of the vehicle. The two trajectories which define the corridor are derived in terms of the known characteristics of the vehicle and the expected entry conditions. The method involves a display of the instantaneous position of the vehicle relative to the corridor. The attitude of the vehicle is to be controlled so as to keep the vehicle within the corridor at all times. A typical trajectory is shown in figure 2 by a dashed line. The dashes do not always follow the center line since this method is employed primarily for vehicles which are subjected to long periods of heating and occasional changes in angle of attack are required from heating rather than navigational considerations. The accelerations associated with this type of entry are usually low. For the sake of simplicity, the lateral variations of the trajectory are not shown in this figure but will be covered subsequently.

The second method, illustrated in figure 3, is similar to the first but it involves defining a single reference trajectory emanating from the desired landing site. This trajectory is based on the average capabilities of the vehicle and is generated as a function of the measured entry conditions. The pilot regulates the lift of the vehicle

so as to correct any error between his trajectory and the computed reference. If his trajectory is below the reference, the lift is increased; if his trajectory is above the reference, lift is decreased. A typical controlled trajectory, shown in the figure by a dashed line, illustrates the characteristic overshoot and convergence associated with this method of guidance. Because this method has generally been studied in connection with vehicles flying at a high-drag condition the entire entry takes place relatively close to the landing site. Hence, the range indicated in this figure is very short even though the entry conditions for both methods are essentially the same. It should be noted here that for these high-drag short-duration entries it has been found that the guidance maneuvers do not seriously increase the heat input to the vehicle. The trajectories are restricted more by acceleration than by heating.

These two methods of displaying the navigational data are very similar in principle. The maneuver-corridor method has been developed for vehicles whose trajectories are characterized by very long glide periods under slowly changing conditions and, hence, this method requires a high degree of accuracy but also allows for maneuvering if the aerodynamics of the vehicle requires it. Most of the work on this method has been performed by the Dyna-Soar contractors (see ref. 1) and will be discussed in subsequent papers. The second method, that of using an average reference trajectory, has been studied extensively by NASA for vehicles whose trajectories are characterized by high drag and short glide times. Because of the short glide times, the method is not too sensitive to errors in the measured flight conditions or in the composition of the atmosphere. Some of the NASA results (see refs. 2 and 3) obtained with this second method of guidance will be covered in this paper.

GUIDANCE RESULTS

Figure 4 shows some of the range and entry errors that can be compensated for by using the reference-trajectory method. For this study a cockpit simulator was set up complete with pilot controls and an appropriate instrument display. An entry vehicle was simulated with six degrees of freedom so that the pilot had to control both the trajectory and the angular motions of the vehicle. The pilot was presented with a display which showed the reference trajectory which was generated as a function of the measured entry angle. The progress of the actual trajectory was then displayed and the pilot would change the angle of attack commensurate with the indicated error in range, as well as indicated accelerations and stability of the vehicle. From the standpoint of accelerations and guidance, it was found better to undershoot - that is, come in below the reference trajectory - than to overshoot.

In practice, all the information displayed to the pilot would come from onboard equipment. For example, an inertial navigation system could be employed to determine the position and velocity of the vehicle. In addition it would be extremely desirable to establish a radio data link to a ground tracking station just prior to entry. This would allow the pilot to obtain a positional fix for his airborne equipment at a time when accuracy is most critical.

Two other methods of guidance control have been studied and can be illustrated by figure 4. One method was to replace most of the pilot's guidance functions with an automatic angle-of-attack control. Once the pilot has chosen a desirable and aerodynamically feasible landing site, the control of the vehicle is turned over to an automatic controller. The angle of attack is then controlled as a function of the range error and the time rate of change of range error as shown by the following equation:

$$\alpha = \alpha_{\text{TRIM}} + K_1 \Delta R + K_2 \dot{\Delta R}$$

Such a control, with gains K_1 and K_2 properly chosen according to the latitude and inclination of the desired landing site has proven very successful (ref. 2).

The third method has been studied in an effort to eliminate some of the onboard equipment. If, during most of the entry, radio communication can be established through the ionized sheath surrounding the vehicle, then it has been found that a Ground Control Approach (GCA) can be very effective (ref. 3). The ground radar gives the altitude-range information to the GCA personnel who then radio the proper angle-of-attack setting to the pilot. To do this the GCA operator must be experienced in the performance characteristics of the vehicle, and such training can be obtained with simulators. Tests with this type of guidance control have shown good results even with the effect of very large-scale radar noise being included in the simulation.

All of these methods usually led to errors of less than 10 miles when an altitude of 100,000 feet was reached. Some practical cases were also simulated where everything turns out wrong. Figure 5 shows an entry where, unknown to the pilot and the computer which generated the reference trajectory, the atmospheric density was doubled. Also the radar or altitude-range measuring device was subject to large random errors and the stability of the vehicle was reduced to a very marginal level. Even under these adverse conditions the pilots could reduce the range errors to within 40 miles by the time an altitude of 100,000 feet was reached. This is within the glide capabilities of most vehicles considered.

LATERAL-LONGITUDINAL RANGE

Up to this point the discussion of the guidance problem has been limited to range variations only along the flight path, that is, longitudinal range. Figure 6 illustrates the importance of the lateral range of the vehicle both on the atmospheric guidance problem and on the overall design philosophy. This figure shows the intersection of the orbital track of a near-earth satellite with contours drawn around the United States at 500-, 1,000-, 1,500-, and 2,000-mile intervals. For this illustration, the satellite was assumed to follow the Project Mercury range and have a period of 1.5 hours. It can be seen that it is not the distance traveled along the trajectory that determines the wait time in orbit. Rather, it is the lateral deviation off the trajectory, obtained by producing a component of the aerodynamic force normal to the flight path. If a vehicle can achieve 500 miles of lateral range then it may return to the Continental United States from any orbital pass which intersects the 500-mile contour. This figure shows that each 500 miles of lateral-range capability reduces the wait time by one orbit or increases the number of favorable orbits by 2. If on a certain pass a vehicle cannot meet this lateral-range requirement due to L/D or heating or stability limitations, it must make another orbital pass regardless of its longitudinal-range capability.

The final consideration is that of making both the lateral- and the longitudinal-range corrections simultaneously. Figure 7 illustrates how this can be accomplished. In this figure the lateral- and the longitudinal-range capabilities of the vehicle at the start of the entry are displayed. Changes in the longitudinal range, obtained by varying the lift-drag ratio of the vehicle are shown along the abscissa. Changes in the lateral range, obtained by varying the ratio of side force to drag are shown along the ordinate. During the entry, most winged vehicles obtained this sideslip by banking the vehicle but it should be noted that sideslip is a function of angle of attack as well as roll angle. The numbers used in this figure for illustrative purposes are again for vehicles of relatively high drag and a maximum value of L/D of about 0.5. It should be noted that this plot was obtained for a delta-winged vehicle flying at angles of attack greater than that required for maximum lift ($60^\circ \leq \alpha \leq 90^\circ$). In a previous paper, Eugene S. Love showed a similar plot for vehicles at angles of attack of less than 60° . As shown in the figure, landing site 1 is well within the lateral- and longitudinal-range capabilities of the vehicle if these were treated separately. However, considered jointly, this landing site cannot be reached because the longitudinal range from the point of entry to that landing site is too short to allow the vehicle to achieve the necessary lateral range. When the point of entry is close enough to the desired conditions so that one or more of the acceptable landing sites, such as 2 and 3, lie within the joint lateral- and

longitudinal-range capabilities of the vehicle, then the proper angle of sideslip and angle of attack can be established and the entry navigation can be a relatively straightforward procedure by using one of the methods outlined in this paper. For vehicles with low L/D a good procedure for making lateral corrections is to establish a larger than necessary bank angle and hold it until the heading error is zero. For vehicles with high L/D , the longitudinal range is more strongly dependent on bank angle, and the angles of bank, sideslip, and attack must be closely regulated. In so doing the rotation of the earth during the remainder of the entry must be compensated for.

CONCLUDING REMARKS

Studies, which have been summarized herein, have shown the feasibility of range control during the atmospheric entry of manned satellites. The indication is that good accuracies are possible.

REFERENCES

1. DS-I Aerodynamics Group: DS-I Aerodynamics Report - Glider Performance and Aerothermodynamics. Doc. No. D5-4399-1 (Contract No. AF 33(600)-37706), Boeing Airplane Co., 1959.
2. Cheatham, Donald C., Young, John W., and Eggleston, John M.: The Variation and Control of Range Traveled in the Atmosphere by a High-Drag Variable-Lift Entry Vehicle. NASA TN D-230, 1960.
3. Assadourian, Arthur, and Cheatham, Donald C.: Longitudinal Range Control During the Atmospheric Phase of a Manned Satellite Reentry. NASA TN D-253, 1960.

NAVIGATIONAL ERRORS AT REENTRY

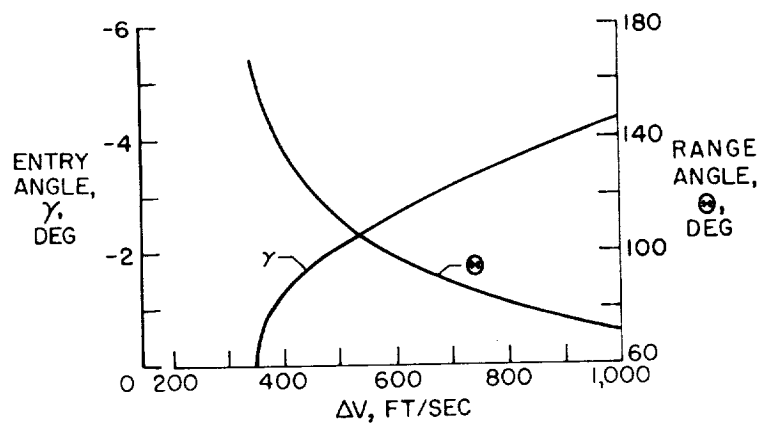
300-MILE ORBIT,
60-MILE ENTRY

Figure 1

MANEUVER CORRIDOR

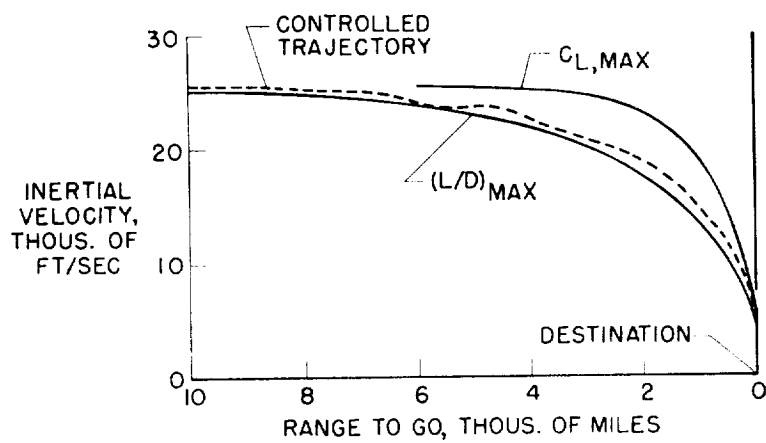


Figure 2

REFERENCE TRAJECTORY

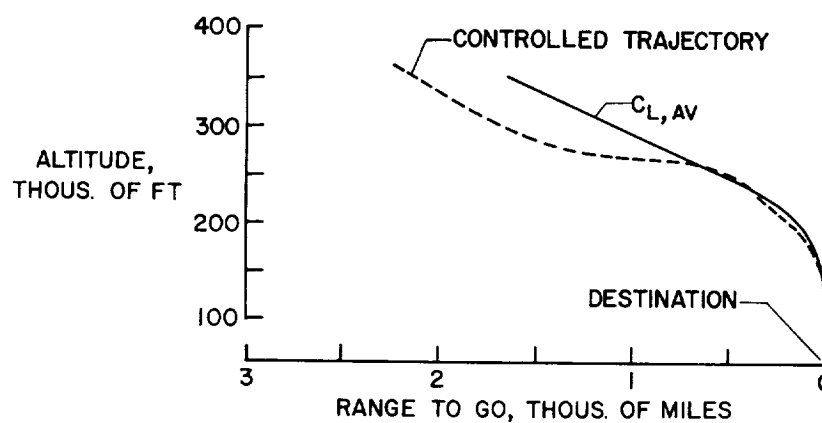


Figure 3

VARIATION IN REENTRY CONDITIONS

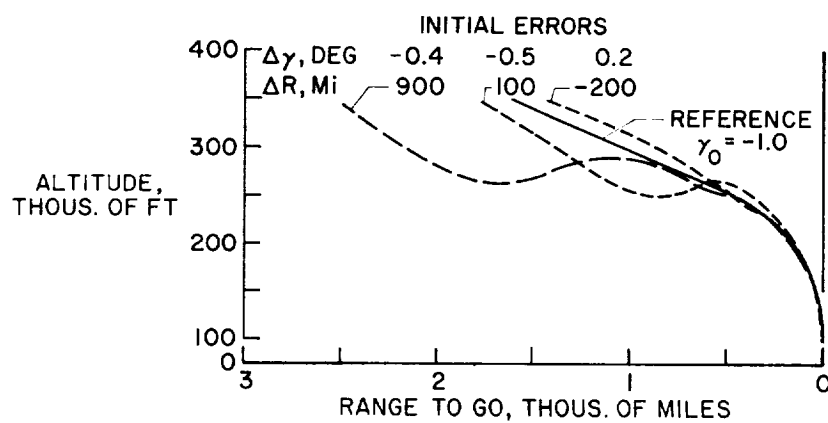


Figure 4

ENTRY GUIDANCE WITH COMPLICATIONS

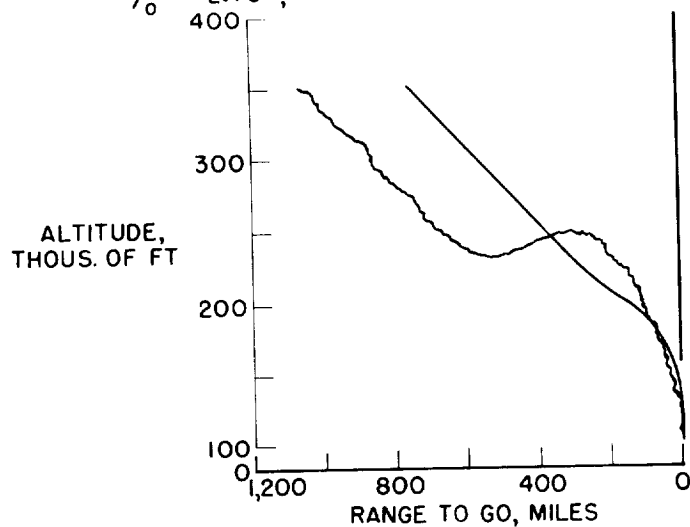
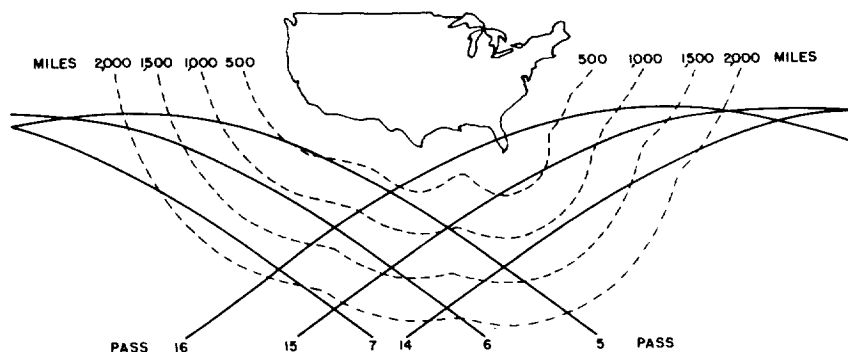
 $\rho = 2\rho_{STD}$; MARGINAL DYNAMIC STABILITY; $\gamma_0 = -2.75^\circ$; RADAR NOISE PRESENT

Figure 5

ENTRY RANGE REQUIREMENTS



LATERAL RANGE, MILES	PASS																MAX. WAIT TIME, HOURS
	WITHIN				WITHOUT								WITHIN				
500	1	2	3	4	5	6	7	8	9	10	11	12	13	14	15	16	13.5 TO 16.5
1,000	1	2	3	4	5	6	7	8	9	10	11	12	13	14	15	16	13.5 TO 14
1,500	1	2	3	4	5	6	7	8	9	10	11	12	13	14	15	16	10.5 TO 11
2,000	1	2	3	4	5	6	7	8	9	10	11	12	13	14	15	16	7.5 TO 8

Figure 6

LATERAL-LONGITUDINAL RANGE COORDINATION

$$\gamma_0 = 1^\circ; V_0 = 25,700 \text{ FT/SEC}$$

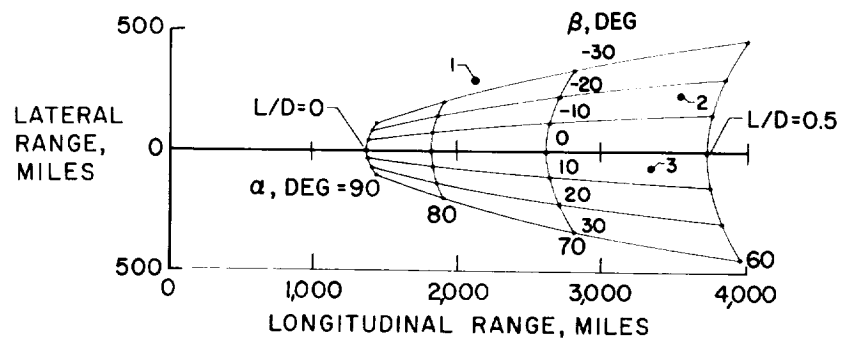


Figure 7

AN INVESTIGATION OF THE ERRORS OF AN INERTIAL
GUIDANCE SYSTEM DURING SATELLITE REENTRY

By John S. White
Ames Research Center

INTRODUCTION


The pilot of a manned satellite vehicle reentering the earth's atmosphere will desire to land at a particular spot on the earth. In order to do this, he must have continuous knowledge of his present position, velocity, and attitude. This information can be obtained either from onboard sources or, in the case of position and velocity, from ground-based radars with telemetry to the vehicle.

However, during the actual reentry, the vehicle will be surrounded by a layer of hot ionized gas, and, at altitudes between 350,000 feet and 150,000 feet, the pilot may not be able to communicate with the ground by radio or radar. Accordingly, a self-contained onboard source of position information may be required. At present, airplanes are using inertial guidance systems as a self-contained means to determine position and attitude with, however, an auxiliary measurement of altitude either from a radar or barometer. These systems have very high accuracies.

Since these auxiliary measurements of altitude probably could not be made in the reentry vehicle, the inertial guidance system must compute altitude from vertical acceleration measurements. The equation for determining altitude solely from acceleration has, at suborbital speeds, an unstable solution, that is, one in which any incorrect initial condition or error in acceleration measurement will cause an error in altitude indication which will grow exponentially with time. The time constant of the solution is considerably less than the satellite reentry time. For this reason, it seemed imperative to make an investigation of the errors that may occur in an inertial guidance system during reentry. This paper presents the results of such an investigation.

SYMBOLS

A area
C_D drag coefficient




D	drag
f	measured acceleration
G_r	gravitational acceleration at surface of earth
h	altitude
L	lift
R_r	radius of earth
t	time
U	uncertainty in acceleration measurement
ΔV	velocity increment produced by retrothrust
W	weight
w	gyro drift rate
γ	flight-path angle
θ	range angle

Subscripts:

i	indicated
o	initial
REF	reference
x	initial horizontal
z	initial vertical
ϵ	error

Dots over symbols indicate derivatives with respect to time.



ANALYSIS

The principal equations used are:

Vehicle position equations:

$$\ddot{h} - (R_r + h)\dot{\theta}^2 = -\frac{G_r R_r^2}{(R_r + h)^2} + L \cos \gamma - D \sin \gamma$$

$$(R_r + h)\ddot{\theta} + 2\dot{h}\dot{\theta} = -L \sin \gamma - D \cos \gamma$$

Computed position equations:

$$\ddot{h}_i - (R_r + h_i)\dot{\theta}_i^2 = -\frac{G_r R_r^2}{(R_r + h_i)^2} - (f_z + U_z) \cos \theta_i + (f_x + U_x) \sin \theta_i$$

$$(R_r + h_i)\ddot{\theta}_i + 2\dot{h}_i\dot{\theta}_i = (f_x + U_x) \cos \theta_i + (f_z + U_z) \sin \theta_i$$

where $(f + U)$ is measured acceleration and U is the measurement error. The vehicle position equations define the altitude h and range angle θ of the vehicle in response to the forces due to gravity (a spherical earth being assumed), lift L , and drag D , the latter two being resolved through the flight-path angle γ . Drag was computed from air density, velocity (including wind velocity due to earth's rotation), and an assumed vehicle $W/C_D A$ of 60. It was assumed that the vehicle attitude was controlled in such a way that the lift-drag ratio was maintained constant at 0.5. The normal initial altitude was 677,000 feet (128 miles). The initial velocity was established by adding to the orbital velocity a ΔV of 250 feet per second in a direction down and to the rear. Such an entry has reasonable acceleration and heating rates.

The computed position equations are the equations which were used by the inertial navigation system to compute indicated altitude h_i and indicated range angle θ_i from indicated gravity and measured accelerations. It was assumed that the accelerometers were inertially fixed;

thus, their output had to be resolved through the indicated range angle θ_i . Since there would be errors in measuring acceleration, there was included an uncertainty U . For simplicity, a steady-state U corresponding to the worst possible case was chosen.

These equations were solved on an IBM 704 electronic data processing machine. The indicated and true quantities were compared to determine the various errors. The computation was ended when the true altitude became 100,000 feet since it was assumed that at this altitude telemetered ground information, radar altimeter, or barometric pressure would be available to correct further indication errors.

The errors were studied as functions of initial condition errors, gyro drift, and accelerometer bias, both singly and collectively. The effect of having the accelerometers switched out for various periods during reentry was also ascertained. Various values of initial conditions and equipment errors were used and the resulting altitude error was studied. Also, the various errors were applied singly and collectively. This study indicated that, over the range considered, the overall altitude error was linearly proportional to the magnitude of the error source and that linear superposition could be used to determine the effects of various error sources applied simultaneously.

Since this is true, significant results can be noted by studying the altitude errors resulting from error sources applied singly. Realistic values were chosen for these error sources so that the resulting altitude errors can be roughly compared.

RESULTS

The results of the calculations are presented as time histories of the system altitude error caused by a single initial condition error or equipment bias with the assumption that no additional information is received aboard the vehicle after retrothrust. The range-angle error and the velocity errors are not so significant since they tend to have a stable solution, if accurate altitude information is given.

Figure 1 shows the altitude error resulting from errors in the various initial conditions. The initial condition errors used are: an altitude error of +500 feet, a vertical velocity error of +1 foot per second, a range-angle error of 10^{-4} radian (about 2,000 feet), a range-angular-velocity error of $5(10)^{-8}$ radian per second, and a much larger range-angle error of $2.2(10)^{-3}$ radian, which is equivalent to an attitude reference error resulting from a gyro drift rate of 0.04° per hour for 3 hours

(or two orbits). Note that the largest source of error is from the attitude reference; this condition implies that such initial attitude errors cannot be tolerated and must be eliminated by means of very much better gyros or by stellar monitoring. The next largest error sources are altitude and range-rate errors, but, for many applications, these errors of about 5,500 feet can be tolerated.

Figure 2 repeats the curve from the previous figure with incorrect initial altitude, and a corresponding curve for the same vehicle starting from an orbiting altitude of 900,000 feet. The latter run lasts considerably longer; therefore, the total altitude error is about 8,000 feet as opposed to the 5,500 feet for the shorter run which starts from the lower altitude. Furthermore, it can be seen that, for both of these curves, the error is building up very rapidly during the last minute or two. About 20 percent of the error occurs during the interval from 150,000 to 100,000 feet. Thus, the altitude error can be considerably reduced if the run can be made somewhat shorter, that is, if the altitude can be monitored from external sources somewhat sooner.

Figure 3 shows the altitude error plotted against time for two reentries starting at different initial altitudes, during which there was a gyro drift of $2(10)^{-7}$ radian per second or 0.04° per hour. The effect of gyro drift is to rotate the accelerometers incorrectly. Since the accelerometer output is very small until after the vehicle has reached an altitude of about 300,000 feet, there will be no significant error until this altitude is reached. Accordingly, the time at this altitude was chosen as a reference and the time scale is shown as time after this reference time $t - t_{REF}$. There is no significant altitude error due to gyro drift until about 5 minutes after t_{REF} . The buildup of the altitude error due to gyro drift is a function of time of drift and the magnitude of the acceleration. For the 900,000-foot-altitude case, the acceleration level was, in general, considerably lower than that for the 677,000-foot case; therefore, the error, at any time after t_{REF} , is less. However, the entry was considerably longer; thus, the final error was much larger.

For $h_0 = 677,000$ feet, the final error is less than the error resulting from the incorrect initial altitude and range-angular-velocity errors shown in figure 1.

Figure 4 shows the altitude error caused by accelerometer biases, the last few minutes of the run not being shown. The uncertainties U_x and U_z are bias errors on the x- and z-accelerometers, respectively. At the beginning of the entry, the x-accelerometer has its sensitive axis along the flight path, and the z-accelerometer has its sensitive

axis along the vertical. Bias errors were assumed in order to avoid statistical methods, on the basis that the assumed steady errors would represent the worst possible case. Thus, for a run with an x-accelerometer bias of 10^{-4} g, the curve shown, along with its image, represents the envelope of possible errors from an accelerometer with 10^{-4} g accuracy.

However, with a z-accelerometer bias, the picture is not as simple. For this case, the bias initially causes a negative altitude error. However, the resolution of this bias through the range angle and the intercoupling of the range and vertical equations cause the error to change direction and eventually become positive. Therefore, constant bias on the z-accelerometer does not represent the worst possible case throughout the entire run. However, until the range angle approaches 90° , the constant bias is the worst possible case, and the curve in figure 4, with its image, represents the envelope of errors out to a range angle of 90° . This angle is marked on this figure and also on figure 5.

Since, at orbital altitudes, the drag is less than the accelerometer accuracy, it would seem that the position computed by assuming zero acceleration would be more accurate than that using the accelerometer output. Figure 5 shows the result of such runs, together with the curves from figure 4. For this case, the accelerometers were switched on at the optimum time of $12\frac{1}{2}$ minutes, as shown.

As can be seen from figure 5, the error due to accelerometer bias is considerably less with the accelerometers off than it is with the accelerometers on, except for the end of the accelerometer bias run where error cancellation occurs. The actual value of final error with the accelerometers off, 7,000 feet, is only slightly larger than the final error caused by incorrect initial conditions.

Data were also obtained from reentries for different vehicles, different initial altitudes, and different values of ΔV . The results of these studies are presented in reference 1. In every case, the errors are less if the accelerometers are left off for a period of time during the early portion of the reentry.

CONCLUDING REMARKS

These results indicate several means by which the altitude error of an inertial navigation system can be reduced during a reentry. They are as follows:

1. Assume zero acceleration until the accelerometer output is comparable to its accuracy.
2. Use reentry trajectories which last only a short time; this condition implies the use of a high velocity increment ΔV , low-lift vehicles, low orbiting altitudes, and early reestablishment of radio contact.
3. Provide correction to the position indication during the initial portions of the reentry; this method is equivalent to lowering the initial altitude.
4. And, of course, use the brute-force technique of improving the initial condition accuracies and using better gyros and accelerometers.

In particular, if 10^{-5} g accelerometers are used instead of 10^{-4} g accelerometers, the errors due to accelerometer bias, even with their outputs used all the time, will be significantly less than the errors caused by poor initial conditions; therefore the latter would be the dominant error sources.

It is of interest to estimate what the actual total error might be for this vehicle entering under these conditions. Since one would not expect all errors to be maximum simultaneously, and since the errors are linear functions of the error sources, the total error was computed by summing all the individual errors on a root-mean-square basis. At 100,000 feet the magnitude of the total altitude error was 10,000 feet with the accelerometers switched out and 16,000 feet with them left on all the time. The corresponding range errors were $1\frac{1}{2}$ miles with accelerometers off and 2 miles with accelerometers on. These errors would result in an erroneous position of the vehicle; however, the glide capabilities of most vehicles are such that these position errors could be corrected during the final glide.

Thus, an inertial navigation system can be used to supply the vehicle with an adequate indication of position and altitude during reentry, in spite of the unstable solution for altitude.

REFERENCE

1. White, John S.: Investigation of the Errors of an Inertial Guidance System During Satellite Reentry. (Prospective NASA Paper.)

ALTITUDE ERROR RESULTING FROM VARIOUS INITIAL CONDITION ERRORS

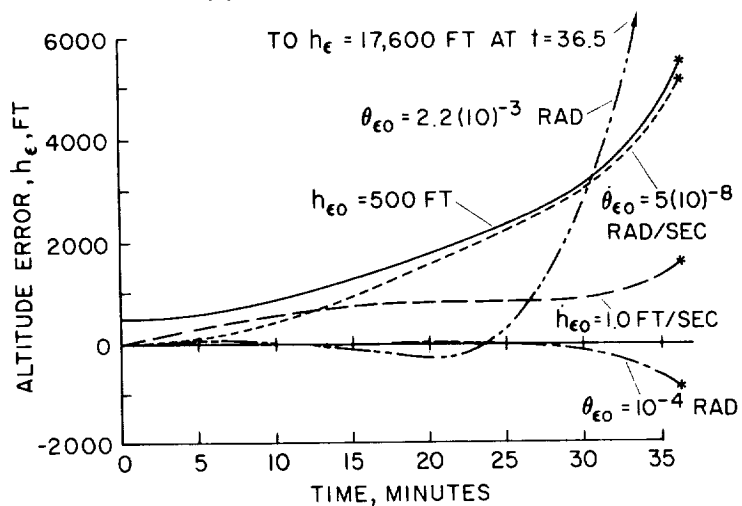


Figure 1

ALTITUDE ERROR FOR TWO INITIAL ALTITUDES RESULTING FROM AN INITIAL ALTITUDE ERROR OF 500 FEET

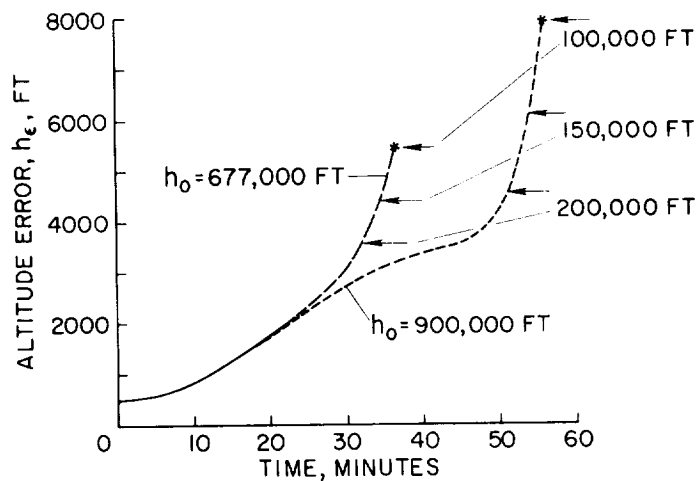


Figure 2

EFFECT OF GYRO DRIFT ON ALTITUDE ERRORS FOR STANDARD VEHICLE

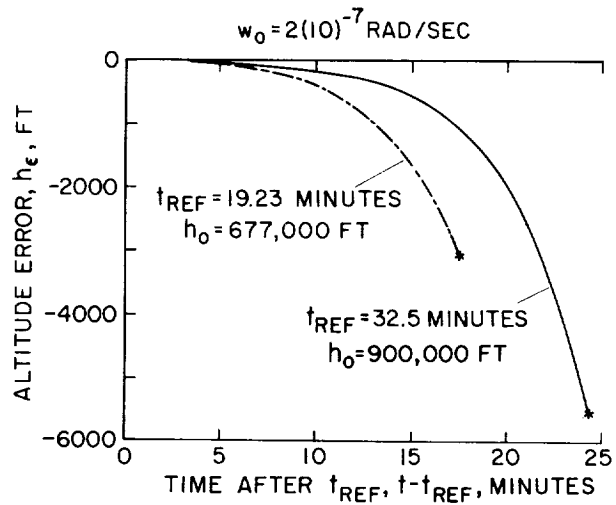


Figure 3

ALTITUDE ERRORS FROM ACCELEROMETER BIASES

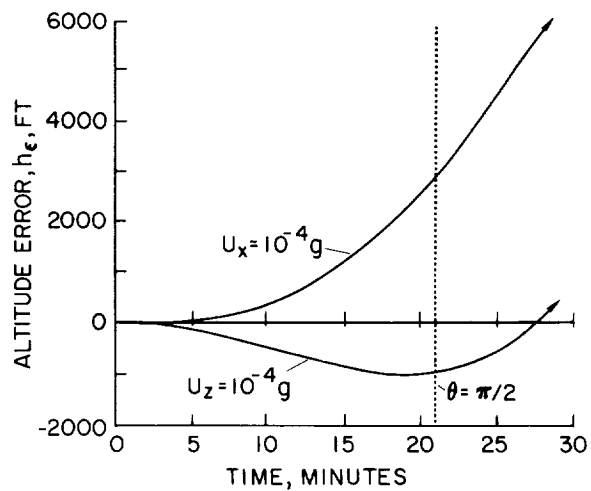


Figure 4

EFFECT OF TURNING OFF ACCELEROMETERS

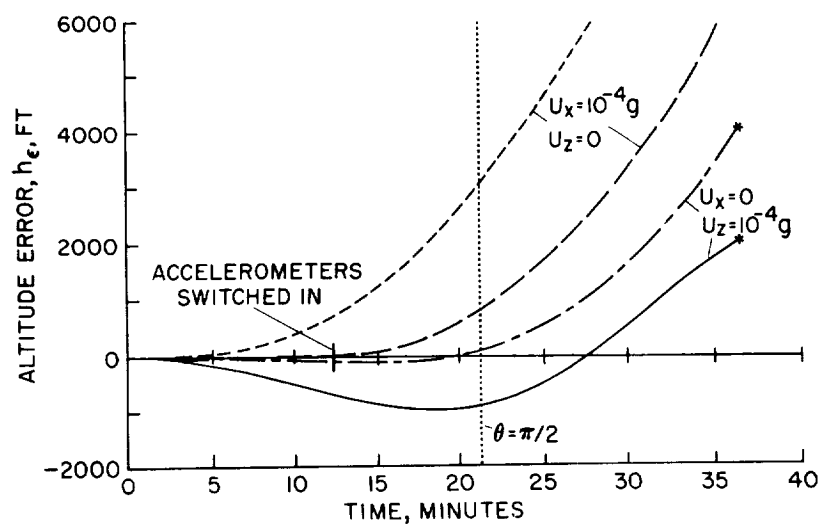


Figure 5

CENTRIFUGE STUDY OF PILOT TOLERANCE TO ACCELERATION AND
THE EFFECTS OF ACCELERATION ON PILOT PERFORMANCE

By Brent Y. Creer, Capt. Harald A. Smedal, USN (MC),
and Rodney C. Wingrove
Ames Research Center

INTRODUCTION

The centrifuge located in the Aviation Medical Acceleration Laboratory at the U.S. Naval Air Development Center, Johnsville, Pa., was used in an investigation conducted by the Ames Research Center. The flight simulator experimental setup utilized the centrifuge in the control loop. The subject pilots were seated in the gondola of the centrifuge and were confronted with a fairly complex task which involved flying a simulated orbital vehicle. This study was split into three phases. The objectives of each phase were as follows:

(1) To obtain information on the combined effects of magnitude and direction of the applied acceleration force and of control task complexity on the pilot's performance.

(2) To establish some meaningful tolerance-to-acceleration times for the direction of acceleration fields encountered by a pilot in a forward-facing position flying along an atmosphere-entry trajectory. A special anterior restraint system was developed in an attempt to increase human tolerance to longitudinal decelerations. Time tolerance to acceleration runs were also made for other directions of acceleration fields.

(3) A preliminary centrifuge investigation was conducted wherein several side-arm controllers were evaluated. One objective was to compare three-axis controllers with the two-axis, toe-pedal-type airplane controls. The toe-pedal-type control used was designed to minimize the effects of acceleration on the pilot's yaw control inputs.

This study was brief and of an exploratory nature. Nevertheless, it is believed that the results will be of value to the orbital-vehicle design engineer. In this paper, the vernacular of the test pilot has been used to describe the direction of the applied acceleration force. The terms "eyeballs in," "eyeballs out," and "eyeballs down" correspond to acceleration fields n_x , $-n_x$, and $-n_z$, respectively, where n_x , $-n_x$, and $-n_z$ refer to the direction of acceleration forces measured in the conventional airplane body-axis coordinate system.

APPARATUS AND TEST PROCEDURES

With regard to apparatus used in this test, the centrifuge located at Johnsville, Pa., has received extensive coverage in the nation's magazines and technical journals and it will be assumed that everyone is generally familiar with this device.

The pilot's restraint system used in the centrifuge tests is shown in figure 1. For protection against eyeballs-in accelerations it was felt that a pilot's couch similar to the type used in the Project Mercury capsule would be adequate for this study. Individual molds were made for each pilot. In figure 1, the pilot was essentially in a sitting position, with his upper body and head held at an angle of 85° to 90° with reference to the thigh position. The lower end of the leg mold in the vicinity of the ankles and the feet was cut off to permit the installation of the toe pedals for yaw control. The pilot's feet were restrained by strapping them in the toe-pedal devices. It might be noted that the toe pedals were actuated by differential rotation of the feet about the ankle joint. Thus, no movement of the leg was required and the entire leg could be firmly restrained. The head restraint, which is a critical item for eyeballs-out accelerations, was incorporated in the helmet system. The helmet was secured into the mold by nylon straps which were attached on each side of the helmet. Face pieces, which were used to restrain the head in the helmet, were individually molded from plaster cast impressions made of each pilot's face. They were designed so that the major portion of the load would be taken over the prominences of the malar bones of the face. The chin cup was included in this restraint system, but only as a minor component since the chin is an unstable support point and its tolerance to large loadings is poor. The face plates were attached to the helmet by adjustable nylon straps fitted into a standard oxygen mask assembly.

The upper half of the torso was restrained by a bib fabricated of straps crossed over the upper portion of the chest so that most of the loading was taken over the upper rib cage. The rather snug fitting bib restricted the expansion of the upper chest. Therefore, the frontal area over the abdomen and lower chest was left essentially unsupported to allow excursion of the diaphragm and movement of the lower rib cage during the normal breathing process. Another separate component was fabricated for the pelvis. This consisted of two slightly crossed straps which were positioned to carry the loading over the pelvic bones and the upper thighs.

The limb restraints were constructed of nylon netting. All anterior restraints were extended through the mold and secured to the structure which supported the styrofoam couches. A more detailed description

of the pilot's restraint system is given in reference 1. It should be noted that anti-g suits were worn by all test subjects.

With regard to test conditions and procedures, the pilot flew the centrifuge as a closed-loop system; that is, for acceleration fields greater than 1 g, the centrifuge was driven in response to the pilot control inputs in such a fashion that the impressed linear accelerations varied in the same manner as the linear accelerations computed from the aircraft equations of motion. A detailed description of the closed-loop centrifuge operation is given in reference 2. In this experiment, the aircraft equations of motion described five degrees of freedom with the vehicle forward velocity assumed constant.

EFFECTS OF ACCELERATION AND CONTROL TASK ON PILOT PERFORMANCE

In this phase of the experiment, six different acceleration fields were investigated. The maximum accelerations investigated were 6g in an eyeballs-in direction, 6g in an eyeballs-down direction, and 7g in an eyeballs-out direction. A number of runs were made in each acceleration field with the complexity of the control task as the variable. The complexity of the control task was varied by changing the damping and frequency of the vehicle longitudinal short-period oscillation. The dynamic characteristics of the roll and yaw modes of airframe motion were held constant.

A qualitative measure of pilot performance was obtained by having the pilot give a numerical rating on the controllability of the simulated vehicle by using the pilot opinion rating schedule presented in table I. This pilot opinion schedule is essentially that presented in reference 3. In order to obtain a quantitative measure of the pilot's performance, a tracking task was utilized. A detailed description of this tracking task is presented in reference 4. A cathode ray tube in the instrument panel was used to display the randomly driven doughnut-shaped target. The pilot's instrument display is shown in figure 2. The vehicle roll and pitch attitude were also displayed on the oscilloscope in the same fashion as they appear on a normal gyro-horizon indicator. The length of the centrifuge runs was $2\frac{1}{2}$ minutes. Approximately $1\frac{1}{2}$ minutes were devoted to the pilot's assessing the controllability of the system, the last minute being devoted to the tracking task.

Figure 3 presents the tracking scores obtained from these tests for one of the subject pilots. This particular pilot was experienced in riding the centrifuge and was thoroughly familiar with the tracking task, and the data obtained from his test runs were believed to be representative of a well-trained pilot preconditioned to the effects

of acceleration forces. The tracking score, which was the quantitative index of pilot performance, is plotted against the magnitude of the g-force. (See ref. 4 for definition of pilot tracking score.) Data for the eyeballs-down, eyeballs-out, and eyeballs-in accelerations are given for well-damped vehicle motions and for lightly damped vehicle motions. The well-damped case corresponds to a fairly easy control task and the lightly damped case corresponds to a fairly difficult control task. Certain tentative conclusions may be drawn from these data. To a first approximation, it appears that any decrement in pilot's tracking score is independent of the direction of the applied acceleration investigated in this program. Pilot's tracking score deteriorated markedly at accelerations greater than about $4g$ for the lightly damped dynamic situation. Finally, it appears that the more difficult control task greatly magnifies any deficiencies in the pilot's performance.

The results of the pilot's ratings on the longitudinal handling qualities of the vehicle obtained from these same performance runs are shown in figure 4. Pilot opinion boundaries which define satisfactory, unsatisfactory, and unacceptable regions of controllability of an entry vehicle are shown in terms of the period and damping ratio of the longitudinal oscillatory mode of motion. The solid-line boundaries to the left of the shaded regions were derived from a moving cockpit flight simulator investigation (see ref. 5), wherein the pilots were exposed to the earth's constant gravitational field. The dashed-line boundaries to the right of the shaded regions were obtained from the centrifuge tests wherein the pilots were immersed in acceleration fields of approximately $6g$ to $7g$. Thus, an increase in the acceleration field results in a corresponding shift in the pilot-opinion boundaries. This shift is from the solid-line boundary toward the dashed-line boundary. The tentative conclusion is reached that regardless of the region of airframe dynamics involved, the pilot feels that in order to have the same level of control over the vehicle an increase in the longitudinal dynamic stability, as shown by the shaded area, is required with increases in the magnitudes of the acceleration impressed upon the pilot. There is some logic to the above results. The pilots often noted that more physical effort was required to control the simulated vehicle under the higher g loadings; consequently, they applied control very cautiously. It is well known that a reduction in manual dexterity and visual acuity may result with increases in the accelerations impressed upon the pilot.

TIME TOLERANCE TO ACCELERATION

In the study to establish some meaningful tolerance-to-acceleration times, a single set of airframe dynamics was used. The pilot was faced

[REDACTED]

with a fairly difficult task when controlling this set of dynamics. The magnitudes of the accelerations investigated ranged from 6g to $8\frac{1}{2}$ g and the directions of the accelerations investigated were eyeballs in, eyeballs down, and eyeballs out; a diagonal acceleration vector was also investigated which consisted of a combination eyeballs-out and eyeballs-down direction.

During the tolerance runs the pilot was required to fly the simulated airplane and, to the best of his ability, track the randomly driven target. He was instructed to terminate the run if bodily pain became excessive, if he became so fatigued that he could no longer continue the run, if his vision markedly deteriorated, or if anything else of an untoward nature occurred. The project medical doctor monitored the pilot's electrocardiogram and respiratory recordings and terminated the run at his discretion. The project engineer monitored the tracings of pilot tracking score and terminated the run if the pilot's tracking score deteriorated markedly. A time history of a typical eyeballs-out endurance run is presented in figure 5. Only the most pertinent traces are presented in this figure; namely, the pilot's tracking score, the pilot's elevator deflection, and a recording of the acceleration trace. The beginning point for measuring tolerance time was taken when the acceleration value was within about 90 percent of that desired. It can be seen from figure 5 that after the initial starting transients in tracking score have subsided, the pilot's tracking efficiency remained essentially constant during the remainder of the run. This characteristic was typical of nearly all test runs. These results were somewhat surprising in view of the fact that the pilot became more fatigued and his vision deteriorated as the run progressed.

A brief survey of existing data on time tolerance to sustained accelerations was made. These data were then amalgamated with the results of the present investigation in an attempt to arrive at tolerance to acceleration boundaries which are meaningful to the orbital vehicle design engineer. Figure 6 presents the available time tolerance to sustained acceleration data for the eyeballs-out case.

Perhaps the most consistent and complete tests on tolerance to eyeballs-out acceleration were conducted by Clarke and Bondurant (ref. 6). The boundary obtained from this investigation is shown by the dashed line in figure 6. In these tests the subjects were in an essentially normal seated position. The anterior torso and extremity restraint system was somewhat similar to the restraint system used in the Ames tests. The head-restraint system for the Clarke tests, however, was arranged so that most of the weight of the head was taken across the subject's forehead. It should be noted that nonpilot subjects were used in this test.

[REDACTED]

[REDACTED]

The data obtained from the tests conducted by the Ames Research Center are plotted as circular test points in figure 6. In a comparison of the tolerance time to acceleration values for the Ames and Clarke tests, it can be seen that a roughly sixfold increase in tolerance times to 7g eyeballs-out acceleration fields was demonstrated in the Ames tests. The Clarke data show a tolerance time of about 0.6 minute at 7g whereas the subjects in the Ames data show a tolerance time of 4 to 5 minutes at 7g. This increase in tolerance is attributed mainly to an improved restraint system and the use of highly motivated test pilots as centrifuge subjects.

The work by Ballinger and Dempsey (ref. 7) is shown by the triangular test points. In these tests the restraint system consisted of a semiprone nylon-net bed. The restraint system, although not designed for operational use in an airborne vehicle, appeared to afford protection to eyeballs-out accelerations nearly comparable to that offered by the system used in the Ames studies. It might be noted that nonpilot subjects were used in the Ballinger tests; however, only a small percentage of the centrifuge test group subjects completed the runs shown. The subjects completing the runs were, of course, those who were most highly motivated and who were physically able to tolerate the fatigue and pain associated with the endurance test trials.

The work conducted by Duane and others (ref. 8) showed that a pilot in a seated position can tolerate backward accelerations up to and including 15g for 5 seconds. Duane employed a restraint system of padded barriers in the front of the lower face, chest, and legs. Here again, nonpilot subjects were used, and only the hardest of subjects apparently completed the 15g run.

A 12g run for one minute was conducted by Ruff (ref. 9). In this case the subject was in the prone position. The original report by Ruff was not available; however, references to his work by other investigators would lead one to believe the subject was uninjured.

The single data point shown in the impact acceleration region was the much publicized run of Stapp (ref. 10) wherein he endured 25g eyeballs-out force for about 1 second. It has been included in figure 6 to show the voluntary endpoint of human exposure to eyeballs-out accelerations. Stapp was injured in this run; however, his injuries were apparently reversible in nature. It should be noted that Stapp's head was not restrained during this run. From a pure tolerance to acceleration standpoint, it would appear that a healthy, highly motivated male, as exemplified by a test pilot, can withstand acceleration fields for the times indicated by the solid-line boundary in figure 6, provided he is suitably restrained.

[REDACTED]

There is a paucity of data from which to draw conclusions on man's ability to perform a control task when he is immersed in an elevated acceleration field. From an extrapolation of the results of the Ames tests and the results of other tests, it would appear that the pilot's ability to perform a manual control task has markedly deteriorated when he is exposed to eyeballs-out accelerations greater than 12g. It has been stated by Duane and others (ref. 8) that, between 12g and 15g, the pilot is capable of simple manual switching operations using the hands and fingers, and the study by Clark and others (ref. 11) has indicated that forearm, hand, finger, and ankle movements were not impaired at 12g. Above 15g there is the possibility of injury to the subject and less possibility that the pilot could assume primary control of the vehicle after removal of the acceleration stresses.

A procedure similar to the one just outlined for the eyeballs-out case was also made for the eyeballs-in and the eyeballs-down accelerations. A summary plot showing the derived time tolerance to acceleration boundaries is shown in figure 7. It is well known that the pilot cannot tolerate g-forces applied in the normal direction as well as he can tolerate g-forces applied in the transverse direction. It had been speculated by several investigators (refs. 6 and 12) that man's tolerance to eyeballs-out acceleration was equal to his tolerance of eyeballs-in accelerations. The results shown in figure 7 would tend to confirm these speculations. The tolerance boundaries to eyeballs-in and eyeballs-out accelerations are shown as being one and the same. One of the major physiological problems encountered by a person immersed in a high acceleration field is his inability to obtain proper respiration (ref. 7). With the pilot positioned for optimum tolerance to the applied acceleration force, indications are that breathing is considerably easier for eyeballs-out acceleration than for eyeballs-in acceleration. A word of caution should be inserted here regarding the use of the derived tolerance boundaries. The pilot of an orbital vehicle will be in a weightless state for extended periods of time before the entry phase of the mission. It is speculated these extended periods of weightlessness may alter the pilot tolerance to high accelerations.

The dashed curve in figure 7 labeled "Entry from parabolic velocity" was computed for a drag-modulated vehicle flying along a ballistic entry trajectory with the vehicle initial velocity taken as parabolic. Each point of the curve represents a different atmosphere-entry trajectory starting from a different initial entry angle. The curve shows, for example, that by proper drag modulation the maximum acceleration which the vehicle would encounter during an entry could be 8g and this level of acceleration must be endured for about $1\frac{2}{3}$ minutes. It has been presumed that structures are currently available which will withstand the heating dictated by the entry conditions making up this curve. On the return from a lunar mission, the depth of the entry

corridor, which must be acquired in order to effect a landing on the earth, increases as the allowable entry accelerations increase (ref. 13). Thus it is desirable to enter at the high g portion of this curve, since this reduces the accuracy demanded of the midcourse navigation and guidance system. The conclusion is reached that for the reentering manned lunar vehicle, man is still the weakest link in the chain. The presence of man would probably prevent the vehicle from flying at the sustained accelerations for which it can be made structurally safe and which would allow an attendant reduction in the accuracies demanded of the navigation system.

The curve for the entry from circular velocities is presented in figure 7 to show the maximum acceleration and length of time which must be endured by an occupant of a drag-modulated ballistic vehicle entering the earth's atmosphere from a circular orbit. Each point of the curve represents a different atmosphere-entry trajectory; however, each point of the curve is computed for an entry angle of -5° . This curve shows the severest acceleration stress which man would probably be required to endure on a controlled, drag-modulated, ballistic reentry from a circular orbit. As can be seen from the figure, man, if properly restrained, is apparently capable of withstanding these stresses.

The ability of the pilot to fly simulated orbital vehicles along representative atmosphere-entry trajectories is discussed in reference 14. In that investigation a centrifuge was used in the flight simulator setup so that the computed time-varying accelerations were actually impressed upon the pilot. A comparison was made of the data for pilot tolerance time for varying accelerations, obtained from reference 14, with the tolerance times obtained from the steady g field tests. In this comparison, the acceleration level used from the atmosphere-entry time histories was the mean of the plateau of the acceleration trace. The initial rate of g rise in these simulated entry flights was comparable to that of the steady g field tests.

A comparison of the data indicated that for the more severe atmosphere entry trajectories, the pilot tolerated average levels of eyeballs-down accelerations for periods of time approaching those determined from the steady g field tests. During these more severe simulated entries, the pilots' vision was greying-out and they were continually on the verge of blackout. Thus, indications were, that in these runs, the pilots were approaching the limit of their tolerance to acceleration.

EVALUATION OF SIDE-ARM CONTROLLERS

An additional item which can strongly influence the performance and efficiency with which a pilot can fly a vehicle in an elevated g field is the design of the pilot's side-arm controller. In an attempt to negate the effects of acceleration forces on the ability of a pilot to control a vehicle, various side-arm controllers have been proposed. It appears, as of the present time, that three-axis side-arm controllers are receiving the most serious consideration. With this type of controller, the pilot's legs can be firmly restrained and they are not used to make control inputs. An alternate class of controller is the two-axis side-arm controller. This class is similar to the three-axis class, except the yaw control is obtained through movement of the feet or legs. The argument as to which class of controller is better hinges (1) upon whether the high acceleration forces would render the legs useless for making control inputs, and (2) upon the ability of the pilot to blend and apply three (instead of two) different control inputs with one hand. An additional objective of the side-arm-controller study was to determine the best side-arm controller from configurations which represent the present state of the art.

The procedure for evaluating the side-arm controllers was very similar to that used in the rest of the study. To each test controller the pilot assigned numerical ratings on vehicle controllability. After each run, the pilot was thoroughly interrogated on the desirability of certain controller characteristics, such as breakout force, force gradients, and axes of control rotations.

Each controller was tested in the earth's gravitational field (static run) and in two elevated acceleration fields, and two to three different sets of airframe dynamics were utilized. The two elevated test accelerations were as follows:

$$n_x = 6g, n_z = 0g \quad \text{and} \quad n_x = -2g, n_z = -4g$$

These accelerations were chosen as typical of those which might be encountered during the launch and entry phases of an orbital mission. The vehicle longitudinal and lateral-directional airframe dynamic characteristics, which are shown in table II, ranged from a well-damped system with moderate control-moment cross coupling (i.e., application of the ailerons produced both rolling and yawing moments) to a lightly damped system with heavy control-moment cross coupling. The parameter $100C_{l\beta}C_{n\delta_a}/C_{n\beta}C_{l\delta_a}$, which is discussed in reference 5, was used as a

measure of the control-moment cross coupling. It was believed that the lightly damped heavily cross-coupled dynamic situation would emphasize existing deficiencies in the various controller configurations.

Figure 8 shows the input axes of rotations for the various test controllers in this investigation. The axis running parallel to the forearm should be regarded as being essentially the center line of the forearm. Sketch F is intended to show that the toe pedals were actuated by differential rotation of the feet about the ankle joint. Photographs of the various test controllers and a photograph showing the lower-leg restraints and the toe-pedal installation is presented as figure 9. The controllers were designated A, B, C, D, E, and toe pedals. Controllers A and B were in the three-axis class. Controllers C, D, and E were in the two-axis class. Note that controller E is held by the fingers (fig. 8).

Figure 10 is a summary plot obtained by averaging each pilot's ratings on vehicle controllability for all the acceleration fields of this investigation and then averaging this average rating for all the pilots (for a given set of airframe dynamics and for a specified controller). Pilot comments from these tests indicated a unanimous preference for a two-axis controller, toe-pedal combination. The difficulty in blending and applying three control inputs through one hand was repeatedly pointed out by the evaluation pilots; this difficulty, however, was not reflected in the pilots' numerical ratings when they used a controller to fly the well-damped configuration. The preference for the two-axis controllers was much stronger for controlling the lightly damped configuration than for controlling the well-damped dynamic one. This was verified by the pilots' numerical rating on vehicle controllability presented in figure 10. An approximately $1\frac{3}{4}$ rating point preference of the two-axis class of controllers is indicated for controlling the lightly damped, heavily cross-coupled vehicle.

Quantitative data as well as subjective pilot comments obtained during the tests did not indicate a clear-cut superiority of any particular two-axis controller over the others. At a roundtable discussion following the tests, participants expressed a general preference for controller E; however, this preference was not a strong one. Arguments in favor of the finger-held controller were as follows: There were some indications that for short-period oscillations the pilot could control a lower level of airframe damping with this type of controller as opposed to the heavier hand-grip type of two-axis controllers. Because the finger-held controller differed from the conventional center stick (i.e., held with fingers, inertia very low, light-force gradients, etc.), some pilots noted that they had less tendency to handle it like a conventional center stick and this reduced their tendency to revert back to center-stick control patterns when faced with a "clutch" situation. The pilots noted that with the

heavier controllers and in the higher g fields, there was an apparent increase in the inertia of the controller and hand. As a result more effort was required to deflect the controller, and the pilots' control inputs were smaller and were made very cautiously; this effort was apparently reduced to some extent when the light pencil controller was used. Arguments not in favor of the finger-held controller were that positioning of the hand on the controller was critical, and as a result, fore-and-aft displacement of the hand and arm relative to the stick, due to high tn_x accelerations, caused some downgrading of the controller in the opinion of the pilots. Pilots also indicated a vague feeling of the controller being somewhat feathery, being tender to use, requiring no work, etc.

As for the axes of control rotations for the hand-grip controllers, the pilots expressed a unanimous preference for the roll axis of rotation to be below and to run essentially parallel to the longitudinal axis of the lower arm, and for the pitch axis of rotation to be perpendicular to the roll axis and to pass through the nominal wrist pivot point. Side-arm controllers B and D exemplify the desired positioning of the roll and pitch axes of rotation. Agreement on the desirable positioning of the yaw axes of rotation for the three-axis controllers was not reached.

The toe pedals, used in conjunction with the two-axis controllers, were considered quite usable. The majority of pilots who used them stated there was no tendency toward inadvertent inputs, and good coordination of the yaw input with the roll input was possible after some practice. No marked reduction in their usefulness was noted for the pure eyeballs-out or eyeballs-in acceleration (maximum values of $n_x = -7g$ and $n_x = 6g$ were tested for periods as long as 5 minutes).

For the combination eyeballs-out and eyeballs-down accelerations ($n_x = -5g$, $n_z = -5g$ and $n_x = -6g$, $n_z = -6g$), the usefulness of the toe pedals was diminished. Blood pooling in the lower extremities caused numbness and pain which precluded precise yaw control inputs with the rudder pedals. Indications were that the acceleration fields in which the toe pedals could be successfully used could be extended appreciably if an improved lower-leg g protection system were used and if the lower leg were positioned so that its long or tibial axis was always perpendicular to the applied acceleration vector.

Interrogation of the pilots after each centrifuge run indicated that for nearly all controllers tested there was an apparent change in friction levels, stick-force gradients, breakout forces, etc., with different levels of the impressed acceleration field. According to pilot opinion, these stick-force changes were usually to the detriment of the controller. It appeared that the variation in stick-force

characteristics with impressed accelerations was partly due to mass unbalance of the controllers and, in part, to deflections in the structure of the stick, which tend to bend the movable parts with an increase in the friction levels, etc. It is recognized that these changes may also be partly imagined as a result of physiological or psychological effects of the impressed accelerations on the pilot. It seemed that the controllers exhibiting the largest changes in force characteristics were of the high inertia, high weight, bulky type which required considerable design effort to attain some semblance of mass balance. It would seem from the experience gained in these tests that a prime consideration in the design of controllers should be to keep them light in weight with low inertia about the control axes.

CONCLUDING REMARKS

The centrifuge study showed there could be marked decreases in pilot tracking performance with increases in the magnitude of the impressed accelerations. Pilot comments indicated that in order to have the same level of control over the vehicle, an increase in the vehicle dynamic stability is required with increases in the magnitude of the acceleration impressed on the pilot. It appears that a great deal of additional research work is warranted in investigating the effects of sustained accelerations on the pilot performance.

The study indicated quite clearly the improvement in tolerance-to-acceleration times which can be realized through relatively minor improvements in the pilot's restraint system. It would appear that with a suitable restraint, the pilot's tolerance to eyeballs-out accelerations can be made equal to his tolerance to eyeballs-in accelerations. It is suggested in this study, that more meaningful tolerance-to-acceleration times may be obtained by using highly trained and highly motivated test subjects, as exemplified by the test pilot.

Finally, pilot comments indicated a unanimous preference for the two-axis class of side controller over the three-axis class. The pedal controls used in this study resulted in effective yaw control for most acceleration fields of this investigation.

~~CONFIDENTIAL~~

REFERENCES

1. Smedal, Harald A., Stinnett, Glen W., and Innis, Robert C.: A Restraint System Enabling Pilot Control Under Moderately High Acceleration in a Varied Acceleration Field. NASA TN D-91, 1960.
2. Woodling, C. H., and Clark, Carl C.: Studies of Pilot Control During Launching and Reentry of Space Vehicles, Utilizing the Human Centrifuge. Report No. 59-39, Inst. Aero. Sci., Jan. 26-29, 1959.
3. Cooper, George E.: Understanding and Interpreting Pilot Opinion. Aero. Eng. Rev., vol. 16, no. 3, Mar. 1957, pp. 47-51, 56.
4. Sadoff, Melvin: The Effects of Longitudinal Control-System Dynamics on Pilot Opinion and Response Characteristics as Determined From Flight Tests and From Ground Simulator Studies. NASA MEMO 10-1-58A, 1958.
5. Creer, Brent Y., Heinle, Donovan R., and Wingrove, Rodney C.: Study of Stability and Control Characteristics of Atmosphere-Entry Type Aircraft Through Use of Piloted Flight Simulators. Paper No. 59-129, Inst. Aero. Sci., Oct. 5-7, 1959.
6. Clarke, Neville P., and Bondurant, Stuart: Human Tolerance to Prolonged Forward and Backward Acceleration. WADC Tech. Rep. 58-267, ASTIA Doc. No. AD 155749, U.S. Air Force, July 1958.
7. Ballinger, E. R., and Dempsey, C. A.: The Effects of Prolonged Acceleration on the Human Body in the Prone and Supine Positions. WADC Tech. Rep. 52-250, U.S. Air Force, July 1952.
8. Duane, T. D., Beckman, Edw. L., Ziegler, J. E., and Hunter, H. N.: Some Observations on Human Tolerance to Accelerative Stress. III. Human Studies of Fifteen Transverse G. Jour. Aviation Medicine, vol. 26, no. 4, Aug. 1955, pp. 298-303.
9. Ruff, Siegfried: Brief Acceleration: Less Than One Second. Vol. II of German Aviation Medicine World War II, ch. VI-C, Dept. of the [U.S.] Air Force, pp. 584-597.
10. Stapp, John P.: Effects of Mechanical Force on Living Tissue. I. Abrupt Deceleration and Windblast. Jour. Aviation Medicine, vol. 26, no. 4, Aug. 1955, pp. 268-288.
11. Clark, W. C., Henry, J. P., Greeley, P. C., and Drury, D. R.: Studies on Flying in the Prone Position. Committee on Aviation Med. Rep. 466, Nat. Res. Council, 1945.



- 
12. Bondurant, Stuart, Clarke, Neville P., et al.: Human Tolerance to Some of the Accelerations Anticipated in Space Flight. WADC Tech. Rep. 58-156, ASTIA Doc. No. AD 151172, U.S. Air Force, Apr. 1958.
 13. Chapman, Dean R.: An Analysis of the Corridor and Guidance Requirements for Supercircular Entry Into Planetary Atmospheres. NASA TR R-55, 1960.
 14. Eggleston, John M., and Cheatham, Donald C.: Piloted Entries Into the Earth's Atmosphere. Paper No. 59-98, Inst. Aero. Sci., June 16-19, 1959.
- 

TABLE I
PILOT OPINION RATING SYSTEM FOR UNIVERSAL USE

	ADJECTIVE RATING	NUMERICAL RATING	DESCRIPTION	PRIMARY MISSION ACCOMPLISHED*	CAN BE LANDED
NORMAL OPERATION	Satisfactory	1	Excellent, includes optimum	Yes	Yes
		2	Good, pleasant to fly	Yes	Yes
		3	Satisfactory, but with some mildly unpleasant characteristics	Yes	Yes
EMERGENCY OPERATION	Unsatisfactory	4	Acceptable, but with unpleasant characteristics	Yes	Yes
		5	Unacceptable for normal operation	Doubtful	Yes
		6	Acceptable for emergency condition only*	Doubtful	Yes
NO OPERATION	Unacceptable	7	Unacceptable even for emergency condition *	No	Doubtful
		8	Unacceptable - dangerous	No	No
		9	Unacceptable - uncontrollable	No	No
	Catastrophic	10	Motions possibly violent enough to prevent pilot escape	No	No

*(Failure of a stability augments)

TABLE II

VEHICLE DYNAMIC CHARACTERISTICS

Vehicle dynamic parameters	Lightly damped, heavily cross- coupled vehicle	Intermediately damped, intermediately cross- coupled vehicle	Well-damped, moderately cross- coupled vehicle
Dutch roll damping ratio	0.11	0.344	0.344
Dutch roll period, sec	2	2	2
Roll time constant, sec	2	1	1
Cross-coupling parameter, $\frac{100C_{\beta} C_{n\delta a}}{C_{n\beta} C_{l\delta a}}$, percent	75	50	25
Longitudinal damping ratio	0.11	0.344	0.5
Longitudinal period, sec	2	2	2

PILOT'S RESTRAINT SYSTEM



Figure 1

PILOT'S INSTRUMENT DISPLAY

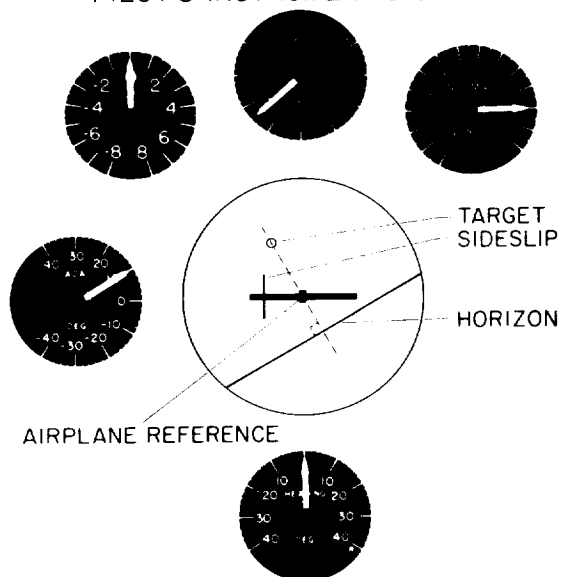


Figure 2

EFFECT OF ACCELERATION ON PILOT PERFORMANCE

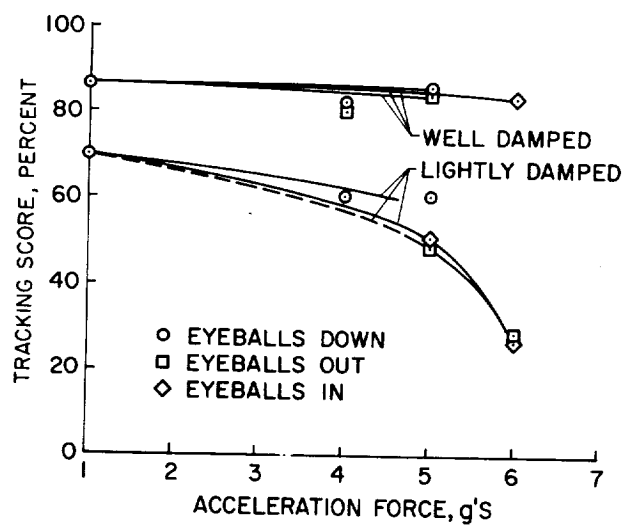


Figure 3

EFFECT OF ACCELERATION ON PILOT-OPINION BOUNDARIES OF LONGITUDINAL HANDLING QUALITIES

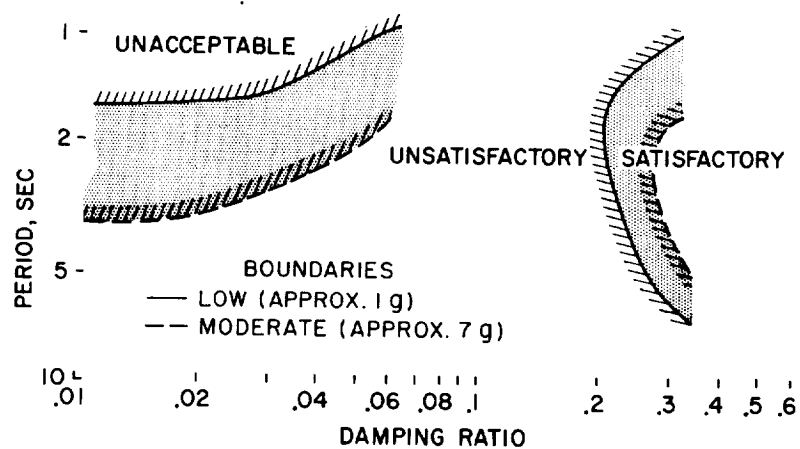


Figure 4

TIME HISTORY OF TOLERANCE RUN

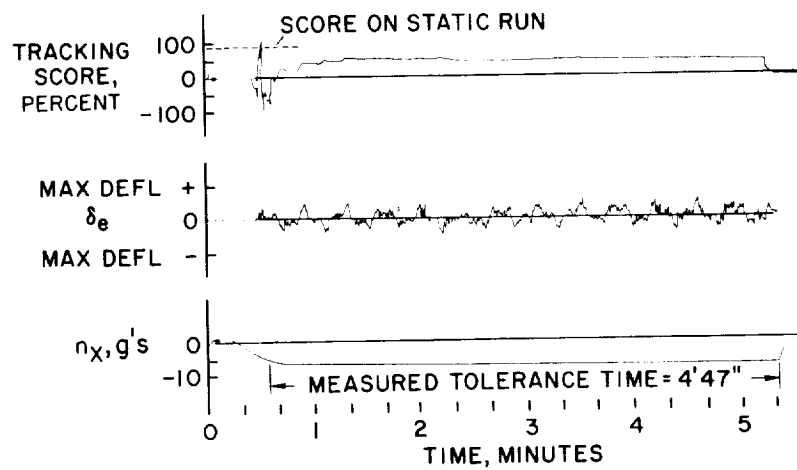


Figure 5

SUMMARY ON TOLERANCE TO EYEBALLS-OUT ACCELERATION

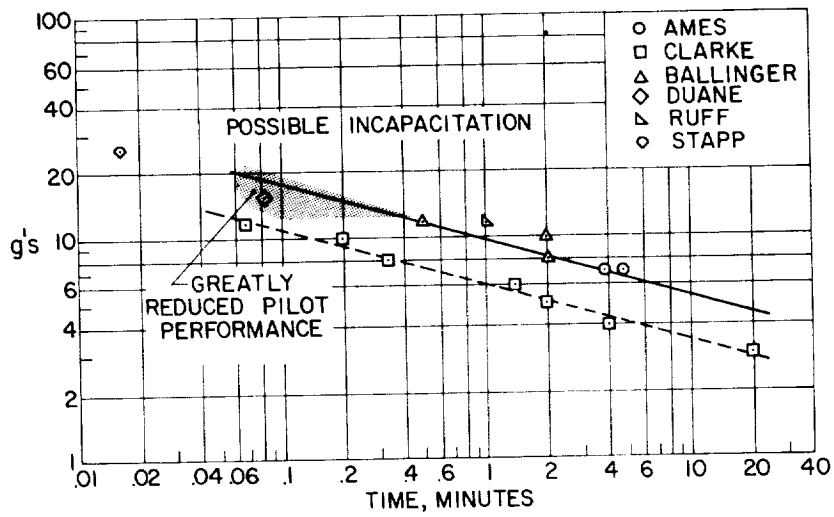


Figure 6

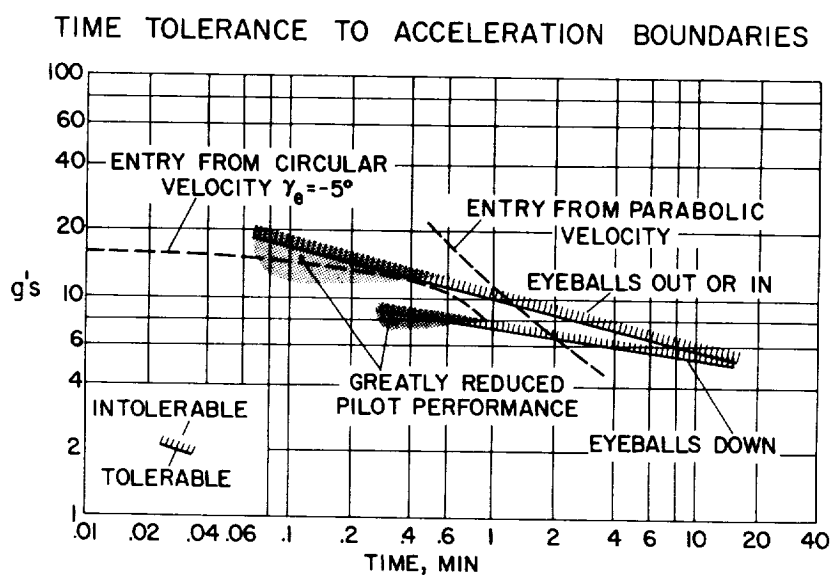


Figure 7

AXES OF ROTATION FOR TEST CONTROLLERS

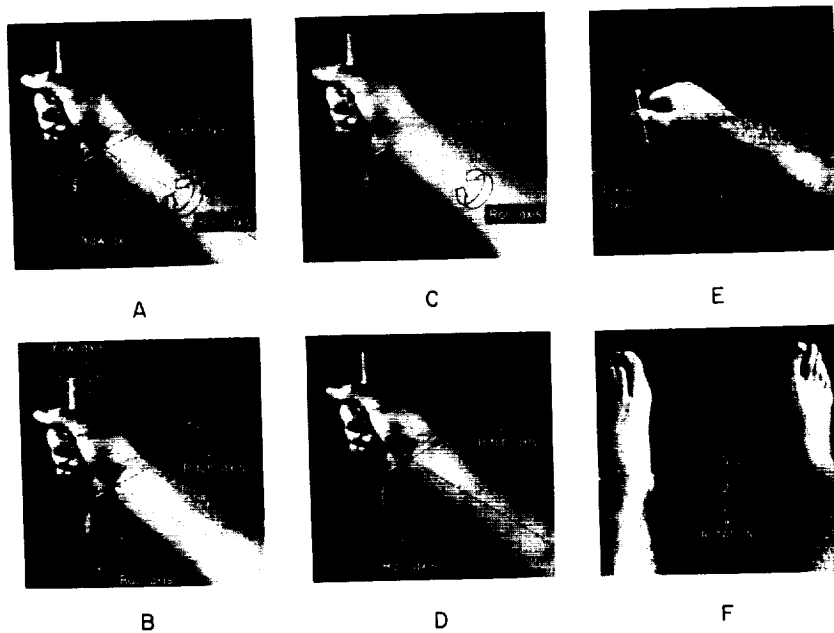


Figure 8

TEST CONTROLLERS

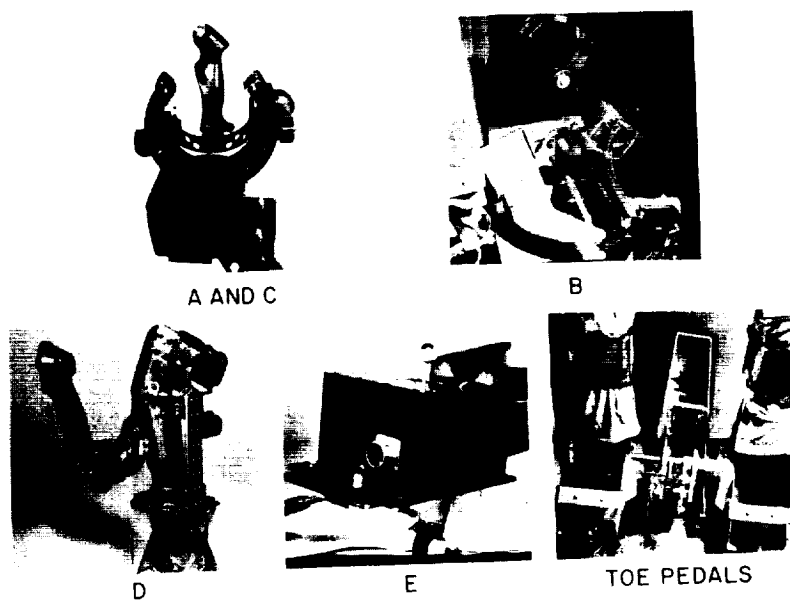


Figure 9

PILOT RATING ON VEHICLE CONTROLLABILITY USING
TEST CONTROLLERS

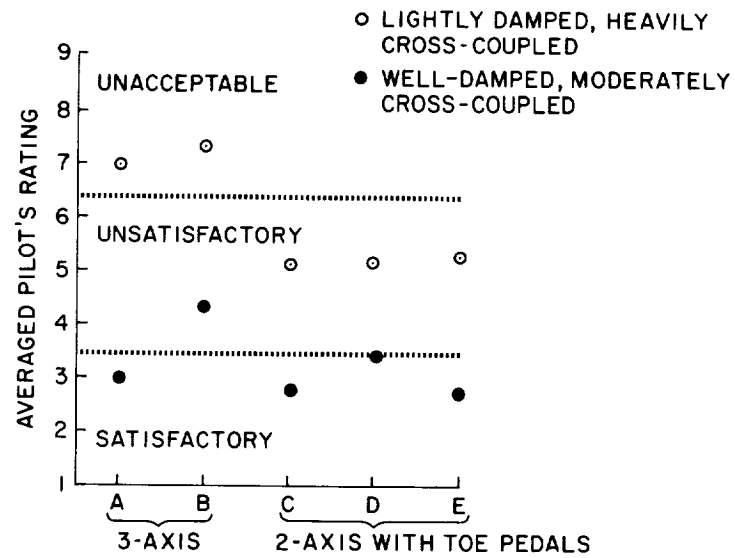


Figure 10

A STUDY OF LONGITUDINAL CONTROL PROBLEMS AT LOW
AND NEGATIVE DAMPING AND STABILITY, WITH
EMPHASIS ON EFFECTS OF MOTION CUES

By Melvin Sadoff, Norman M. McFadden,
and Donovan R. Heinle
Ames Research Center

INTRODUCTION

A number of flight and simulator studies have investigated the range of vehicle dynamics which the pilots consider desirable and the range they can cope with in the event of stability-augmenter failure (e.g., refs. 1 to 11). However, investigations have not been made to determine the accuracy with which simulator studies of longitudinal control problems can be extrapolated to flight. As part of a general study of this problem, a cooperative NASA-AMAL program was conducted on the centrifuge at Johnsville, Pa., to determine the effects of centrifuge motions on pilots' opinions of a wide range of vehicle longitudinal short-period dynamics. The test parameters and measurements duplicated those of earlier studies made at Ames Research Center with a variable stability airplane and with a pitch-roll chair simulator.

This study has three main objectives: First, the centrifuge flight-simulator evaluations are used to identify major longitudinal-control problem areas in terms of vehicle dynamics and to define the minimum damping and stability the pilots will accept in the event of failure of the stability augmenter. Second, the effects of incomplete or spurious motion cues (of the seat-of-the-pants or of the vestibular variety) on control problem simulation are shown by comparing centrifuge, pitch-chair, and fixed-cockpit results with flight-test results. Third, simulator results with a linear analog model replacing the human pilot are analyzed to determine whether pilot-response characteristics, derived by this method, can be related to pilot opinion, thereby making it feasible to predict flight control problems analytically.

SYMBOLS

F_s	pilot stick force, lb
K_p	pilot gain, lb/deg
s	Laplace transform variable
T_I	pilot first-order lag or smoothing term, sec
T_L	pilot first-order lead term, sec
T_N	first-order term which approximates the human actuator lag, sec
δ_{STAB}	stabilizer deflection, deg
ϵ	tracking error, deg
ζ	vehicle damping ratio
θ	vehicle pitch attitude, deg
θ_i	target motion, deg
τ	pilot reaction time, sec
ω_n	vehicle undamped short-period natural frequency in pitch, radians/sec

TESTS AND PROCEDURE

Brief mention might be made of the centrifuge simulator setup and the evaluation procedure used. The centrifuge was operated in conventional closed-loop fashion by tying it electrically to an analog computer which was used to mechanize the aircraft short-period dynamics and the tracking task. (A detailed discussion of the centrifuge operation and capabilities is provided in refs. 12 to 15.) The centrifuge cab included a contoured seat with restraint for the pilot, a force-command center stick similar to that used in the flight study, and a display presenting conventional pitch-attitude information to the pilot, as well as simulated target motion. The pilot-restraint

system was not very critical for this study, since the accelerations encountered were in the relatively low range of 2g to 4g. The system used was a portion of that described in detail in reference 16.

The test conditions corresponded to those covered in previous flight and pitch-chair investigations, which were conducted over a wide range of stable dynamics for constant stick force per g and for a range of unstable dynamics for constant control-system gain.

These test conditions were evaluated by six experienced test pilots, including four from NASA and one each from the Naval and Air Force Flight Test Centers. The pilots began by "feeling out" the pitch-attitude and normal-acceleration responses to stick-force commands. When the pilot considered himself familiar with the vehicle characteristics being simulated, he was given a tracking task of 1 minute's duration from which his quantitative performance was established. The pilot was then asked to evaluate the overall controllability and tracking characteristics of the simulated vehicle.

RESULTS AND DISCUSSION

Pilots' Evaluations of Vehicle Longitudinal

Dynamics With Centrifuge

Stable dynamics.— The results of pilots' evaluations of stable longitudinal short-period dynamics from the centrifuge tests are presented in figure 1. These results represent the average evaluations for the six participating test pilots and they are presented for a constant stick force per g. Shown are regions of satisfactory, unsatisfactory, and unacceptable dynamics expressed in terms of the square of the vehicle aerodynamic natural frequency ω_n^2 and the aerodynamic damping parameter $2\zeta\omega_n$. For those not familiar with this notation, ω_n^2 represents the aerodynamic stiffness or spring constant in pitch and, for a given aircraft, is proportional to the degree of stability or to the maneuver margin. The damping parameter $2\zeta\omega_n$ is inversely proportional to the subsidence time to one-half amplitude of the short-period oscillation. These parameters are those of the characteristic second-order equation used to describe the vehicle motions. For positive ω_n^2 , the motion is either oscillatory or pure subsidence. For the negative ω_n^2 case, to be considered shortly, the vehicle motion is a pure divergence.

It may be seen that the pilots are sensitive primarily to the amount of damping. The minimum damping the pilots considered acceptable for emergency operation (e.g., failure of a pitch damper) corresponds to subsidence times to one-half amplitude of about 2 to 4 seconds.

The region identified by I was considered by the pilots to be the most acceptable area, while regions II, III, and IV were considered by the pilots to be major problem areas. Region II was characterized by a control sensitivity problem; that is, the pilots felt that the stick forces required to maneuver near trim and to track were extremely light, and they found it difficult to avoid inducing continual oscillations. Problem area III was characterized both by moderately sensitive control response and a tendency to overcontrol and exceed the desired response considerably. In region IV, large stick forces were required to maneuver near trim and to track, and an overcontrol tendency was noted.

Unstable dynamics.— Figure 2 presents the results of pilots' evaluations of short-period dynamics extending well into the unstable region. In this case, the control-system gain was held constant, since it is obviously not possible to maintain constant stick force per g as stability decreases through zero. These evaluations show the powerful effects of pitch damping on the degree of instability the pilots would tolerate. For damping less than 1, any instability was considered unacceptable, while for values of damping of about 6, instability corresponding to a negative maneuver margin of about 6 percent was considered acceptable for emergency operation (e.g., failure of a stability augmentor). The line representing the unacceptable boundary in the unstable region corresponds to essentially a constant value of divergence time to double amplitude of about 1 second. This suggests that pilot opinion is related to divergence time rather than to the degree of instability.

Effects of Incomplete or Spurious Motion

Cues on Control-Problem Simulation

The previous section of this paper identified some of the major longitudinal-control problem areas. In this section corresponding data from three different simulators are compared with flight-test results to study the effects of the various incomplete or spurious motion inputs or cues supplied to the pilot. Two of the problem areas just cited will be considered first since this is where the selection of simulators for research will be the most critical.

In figure 3, the flight-test results are compared with three stages of motion simulation. The particular centrifuge used has three degrees

of freedom - two angular rotations and a linear translation in a circle. The desired linear normal accelerations were matched with flight, but this had to be done at the expense of exaggerated angular accelerations in pitch and spurious fore-and-aft accelerations. The pitch-roll chair has two rotational degrees of freedom to match the angular accelerations in flight, but no linear motion. The fixed cockpit, of course, furnishes no motion inputs and the pilot has only the visual instrument display.

The left-hand part of figure 3 compares the four sets of pilot-opinion data as a function of damping at high short-period frequency or stability. The numerical scale used for pilot opinion is one which has been in use at the Ames Research Center for several years. It is described in detail in table I and in reference 17. The first thing to be noted is that all of the curves show fairly good general agreement. However, at low damping where the pilot has difficulty, the centrifuge and fixed-cockpit simulator become somewhat more difficult to control and are rated worse than flight or the pitch-roll chair. This result was unexpected since it was felt that motion inputs would generally have an adverse effect on pilots' ability to control a lightly damped vehicle. Apparently, the correct angular accelerations provided by the pitch-roll chair and flight are beneficial, while the correct normal and spurious angular and longitudinal linear accelerations provided by the centrifuge are less significant in this particular flight problem.

The right-hand part of figure 3 shows, for moderate damping, the comparisons of pilots' ratings of stability from various simulators. Again the curves are in general agreement, but the angular acceleration cues in flight and on the pitch-roll chair appear to be beneficial for moderately unstable dynamics. In the region of low positive stability, the simulator results appear somewhat optimistic.

Figure 4 presents a broad-brush treatment of the overall correspondence between simulator and flight results over the complete range of dynamics covered in this study. Shown are the comparisons between centrifuge and pitch-chair pilot ratings and the corresponding flight-test evaluations. (Fixed-cockpit simulator results fall somewhere between these two sets of data.) The correlation shown is fairly good, indicating that the results of all three modes of simulation extrapolate reasonably well to the flight case. However, a closer look shows somewhat more scatter for the centrifuge correlation, and for extremely poor dynamics (the higher pilot ratings), the centrifuge simulation tends to amplify the flight control problem. This point was considered in detail in figure 3. It would appear, for the particular control problems studied, that angular acceleration cues are more important than linear accelerations for accurate simulator evaluations of flight control problems. However, it must be emphasized that pilots with considerable

experience in centrifuge, pitch-chair, and fixed-cockpit simulators preferred the centrifuge because they considered it more realistic; that is, they felt the control technique in the centrifuge more closely approximated that which they used in flight and they were more appreciative and respectful of the major problem areas.

Analog-Pilot Studies

The final section of this paper is concerned with studies of a mathematical model of the human pilot. The human pilot is of course a remarkably adaptive controller who constantly changes his response characteristics in order to maintain good performance as his task or dynamics problem becomes more difficult. The pilot's changes can be represented mathematically by the terms of an equation expressing his output or control force as a function of his input, the tracking error signal. If the terms of the equation, or analog pilot, can be related to the dynamics of the airplane and its controls and to the pilot opinions of the dynamics just presented, then it should be possible to use the analog pilot to predict adverse pilot opinions or control problem areas on a purely analytical basis.

Analog-pilot model.- With this in mind, figure 5 shows the simulator setup with the analog pilot replacing the human pilot. The expression for the analog pilot contains five parameters; a gain K_p , a reaction time τ , a first-order lead term T_L , and two first-order lag terms, T_N , which approximates the human actuator lag, and T_I , a smoothing term. Of these, the reaction time τ and the actuator lag T_N are relatively unalterable by the human pilot and were fixed at 0.2 and 0.1 second as shown. The other parameters then are presumed to be those that express the changes in the pilot behavior as he copes with changes in the vehicle dynamics, task, and so forth. In this particular study, it was found that the human pilot could be approximated fairly well by changing only the gain and the lead terms; therefore, the smoothing term T_I was fixed at 0.1 second.

Analysis of pilot-response characteristics.- The procedure was to present the analog pilot with the same tracking task given the human pilots during the simulator studies. The two variables, the gain and the lead, were then adjusted on the analog computer until the tracking performance matched that of the human pilot. The procedure is illustrated in figure 6, which presents two typical variations of analog-pilot tracking performance with gain, at constant values of the lead term. Plots are shown for region I, the best dynamics tested, and one problem area (region II, high stability and low damping). For the good

set of dynamics there is a broad range of gain where fairly good tracking is obtained and the human pilots' performance can be matched with a gain of 5 pounds' control force per degree of tracking error and no lead at all. In contrast, for the poor region where the human pilots complained of control sensitivity, the gain must be reduced to about 1 pound per degree, which is only 2 percent of the total control available. The gain adjustment must be fairly precise if either unstable operation of the controls or poor tracking scores are to be avoided. Also, a small increase in lead still further reduces the allowable gain variation and the tracking score. The latter result is characteristic of configurations with control-sensitivity problems and is fairly indicative of the information provided by this method of analysis.

The above procedure was applied to the complete range of dynamics covered in the first part of this paper and the results are summarized in figure 7. The range of gain and the lead required to match the human-pilot tracking scores are shown with boundaries to indicate the corresponding human-pilot opinion of the vehicle dynamics. The major control problem areas are identified as in figure 1; that is, region I, good dynamics; region II, high frequency, low damping; region III, low frequency, low damping; and region IV, low frequency, moderate damping. It can be seen that a reasonable general correlation is established between pilots' opinions of satisfactory, unsatisfactory, and unacceptable dynamics and the values of pilot gain and lead required to cope with these dynamics. Therefore, it appears feasible to predict control-problem areas analytically before extensive pilot-operated simulator studies are available. It may be pertinent to point out that the work reported on in reference 18 also deals with the problem of correlating pilot-response data with conventional handling-qualities research results, typified by the data presented in the first section of this paper. In general, the results of the present study and those presented in reference 18 show substantial areas of agreement.

Example control-problem analysis.- As an example illustrating possible application of the analog-pilot results for predicting flight control problems, a longitudinal-control problem recently encountered during the landing approach of a high-performance airplane is examined. For this particular flight, the pitch damper was inoperative and the problem encountered was one of large, apparently pilot-induced, pitch oscillations just prior to touchdown. With the short-period dynamics adjusted to those of the airplane, the tracking performance of the analog pilot was examined with the results shown in figure 8. Results are shown both for the actual problem with pitch damper inoperative and for the case with pitch damper on. The human pilots' averaged tracking scores from fixed-cockpit simulator evaluations are again included for reference. In this case, the human pilots' tracking scores cannot be utilized to predict the gains and leads required.

However, use can be made of the fact that the human pilots' tracking performance was found to correspond roughly to the maximum performance of the analog pilot. In the present example, this maximum performance is approximately that shown, that is, about 70 and 85 percent. For the case with the pitch damper off, these results would indicate that the pilots would be required to develop very low gains (of the order of 0.5 pound of control force per degree of tracking error) and considerable lead (of the order of 0.8 second) to attain the predicted level of performance. With the pitch damper operative, the allowable gain is increased to about 2 pounds per degree and the required lead reduced to about 0.2 second, both favorable changes. These results are identified in figure 7 as regions A and B. The predicted pilots' ratings (from fig. 7) would be about 6 and 4.5, respectively. Figure 9 presents actual results of pilots' evaluations and tracking performances in a fixed-cockpit simulator for the example control problem. It can be seen that the predicted ratings of about 6 and 4.5 agree reasonably well with the actual ratings of about 5.5 for the pitch damper off and 4 for the pitch damper operative. In addition to the obvious advantage of keeping the pitch damper operative, the results in figure 7 suggest that further improvement could be obtained by reducing the control-system gain. For example, halving the control gain (which is roughly equivalent to doubling the allowable pilot gain) would move configuration B into the satisfactory region and configuration A would improve slightly to a rating of about 5.

CONCLUDING REMARKS

Results of centrifuge flight-simulator evaluations over a wide range of aircraft longitudinal dynamics were used to identify major control problem areas and to define the minimum damping and stability the pilots will accept in the event of stability-augmenter malfunction.

Comparisons of centrifuge, pitch-chair, and fixed-cockpit results with flight-test results indicated:

1. The effects of incomplete or spurious motion cues, of the seat-of-the-pants or vestibular type, on control-problem simulation were found to be important only for problem areas involving high-frequency, lightly damped dynamics or moderately damped, unstable dynamics.
2. Of the three modes of simulation studied, the pitch-chair simulation, which provided accurate angular acceleration cues to the pilot, compared most favorably with flight. The fixed-cockpit simulation and the centrifuge simulation, which supplied accurate normal accelerations

[REDACTED]

at the expense of introducing spurious pitching and longitudinal accelerations, resulted in a deterioration of pilot's evaluations relative to flight-test results in the two problem areas cited.

3. Over all, however, it was shown that all three modes of simulation could be extrapolated to flight with a fair degree of accuracy.

Results of simulator studies with an analog pilot replacing the human pilot were presented illustrating the adaptive capability of human pilots in coping with the wide range of dynamics and the major problem areas covered in this study. It was shown that pilot's response characteristics derived by this method could be related to pilot's opinions, thereby making it feasible to predict flight control problems analytically.

[REDACTED]

REFERENCES

1. Harper, Robert P., Jr.: Flight Evaluations of Various Longitudinal Handling Qualities in a Variable-Stability Jet Fighter. WADC Tech. Rep. 55-299, U.S. Air Force, July 1955.
2. Chalk, Charles R.: Additional Flight Evaluations of Various Longitudinal Handling Qualities in a Variable-Stability Jet Fighter. WADC Tech. Rep. 57-719 Part II (ASTIA Doc. No. AD 206071), U.S. Air Force, July 1958.
3. Hall, Ian A. M.: Effects of Controlled Element on the Human Pilot. WADC Tech. Rep. 57-509 (ASTIA Doc. No. AD 130979), U.S. Air Force, Aug. 1958.
4. Brissenden, Roy F., Alford, William L., and Mallick, Donald L.: Flight Investigation of Pilot's Ability to Control an Airplane Having Positive and Negative Static Longitudinal Stability Coupled With Various Effective Lift-Curve Slopes. NASA TN D-211, 1960.
5. McFadden, Norman M., Pauli, Frank A., and Heinle, Donovan R.: A Flight Study of Longitudinal-Control-System Dynamic Characteristics by the Use of a Variable-Control System Airplane. NACA RM A57L10, 1958.
6. Moul, Martin T., and Brown, Lawrence W.: Effect of Artificial Pitch Damping on the Longitudinal and Rolling Stability of Aircraft With Negative Static Margins. NASA MEMO 5-5-59L, 1959.
7. Brown, B. Porter, and Johnson, Harold I.: Moving-Cockpit Simulator Investigation of the Minimum Tolerable Longitudinal Maneuvering Stability. NASA TN D-26, 1959.
8. Rathert, George A., Jr., Creer, Brent Y., and Douvillier, Joseph G., Jr.: Use of Flight Simulators for Pilot-Control Problems. NASA MEMO 3-6-59A, 1959.
9. Creer, Brent Y., Stewart, John D., Merrick, Robert B., and Drinkwater, Fred J., III: A Pilot Opinion Study of Lateral Control Requirements for Fighter-Type Aircraft. NASA MEMO 1-29-59A, 1959.
10. Douvillier, Joseph G., Jr., Turner, Howard L., McLean, John D., and Heinle, Donovan R.: Effects of Flight Simulator Motion on Pilots' Performance of Tracking Tasks. NASA TN D-143, 1960.

11. Sadoff, Melvin: The Effects of Longitudinal Control-System Dynamics on Pilot Opinion and Response Characteristics as Determined From Flight Tests and From Ground Simulator Studies. NASA MEMO 10-1-58A, 1958.
12. Woodling, C. H., and Clark, Carl C.: Studies of Pilot Control During Launching and Reentry of Space Vehicles, Utilizing the Human Centrifuge. Rep. No. 59-39, Inst. Aero, Sci., Jan. 26-29, 1959.
13. Crosbie, Richard J.: Utilization of a System of Gimbals on the Human Centrifuge for the Control of Direction of Acceleration With Respect to the Subject. Rep. No. 4, Project NM 001 100 303, Aviation Medical Acceleration Lab., U.S. Naval Air Dev. Center (Johnsville, Pa.), Aug. 2, 1956.
14. Clark, Carl, and Crosbie, Richard J.: Centrifuge Simulation of Flight Accelerations. Project TED ADC AE-1410 (NM 11 02 12.6), Aviation Medical Acceleration Lab., U.S. Naval Air Dev. Center (Johnsville, Pa.), Sept. 17, 1957.
15. Anon.: Description of the Human Centrifuge at the Aviation Medical Acceleration Laboratory. Prepared for Armed Forces-NRC Committee on Bio-Astronautics, Acceleration Panel, Woods Hole, Mass., July 16-24, 1959.
16. Smedal, H. A., Stinnett, Glen W., and Innis, Robert C.: A Restraint System Enabling Pilot Control While Under Moderately High Acceleration in a Varied Acceleration Field. NASA TN D-91, 1960. (Prospective NASA paper.)
17. Cooper, George E.: Understanding and Interpreting Pilot Opinion. Aero. Eng. Rev., vol. 16, no. 3, Mar. 1957, pp. 47-51, 56.
18. McRuer, Duane T., Ashkenas, Irving L., and Guerre, C. L.: A Systems Analysis View of Longitudinal Flying Qualities. Rep. TR-6, Systems Technology, Inc., Sept. 30, 1959.

TABLE I

PILOT OPINION RATING SYSTEM FOR UNIVERSAL USE

	ADJECTIVE RATING	NUMERICAL RATING	DESCRIPTION	PRIMARY MISSION ACCOMPLISHED	CAN BE LANDED
NORMAL OPERATION	Satisfactory	1	Excellent, includes optimum	Yes	Yes
		2	Good, pleasant to fly	Yes	Yes
		3	Satisfactory, but with some mildly unpleasant characteristics	Yes	Yes
EMERGENCY OPERATION	Unsatisfactory	4	Acceptable, but with unpleasant characteristics	Yes	Yes
		5	Unacceptable for normal operation	Doubtful	Yes
		6	Acceptable for emergency condition only*	Doubtful	Yes
NO OPERATION	Unacceptable	7	Unacceptable even for emergency condition *	No	Doubtful
		8	Unacceptable - dangerous	No	No
		9	Unacceptable - uncontrollable	No	No
	Catastrophic	10	Motions possibly violent enough to prevent pilot escape	No	No

*(Failure of a stability augmenter)

EVALUATIONS OF STABLE DYNAMICS WITH CENTRIFUGE CONSTANT STICK FORCE PER G

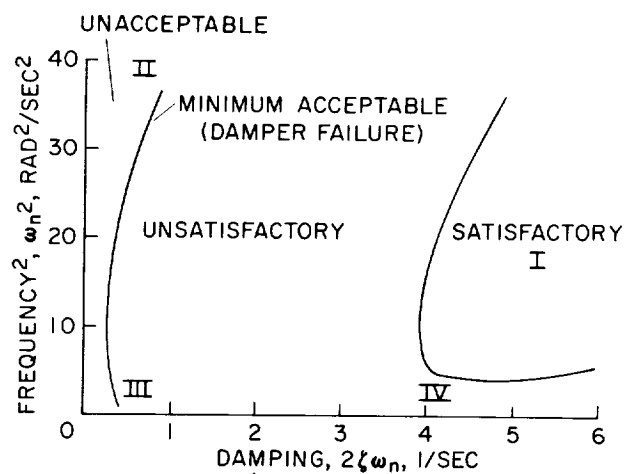


Figure 1

EVALUATIONS OF UNSTABLE DYNAMICS WITH CENTRIFUGE CONSTANT CONTROL SYSTEM GAIN

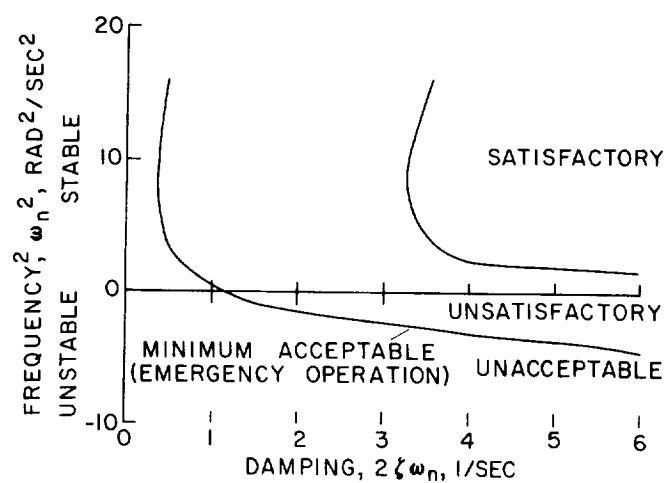


Figure 2

EFFECTS OF INCOMPLETE OR SPURIOUS MOTION CUES

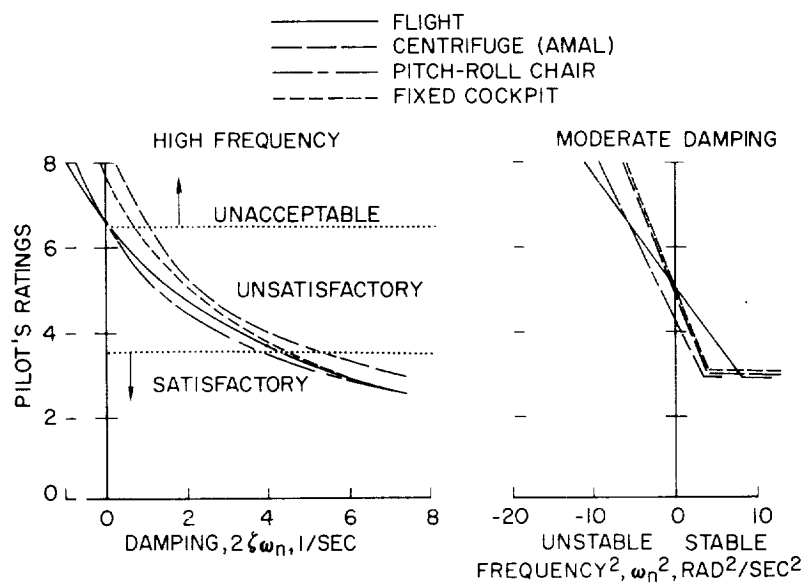


Figure 3

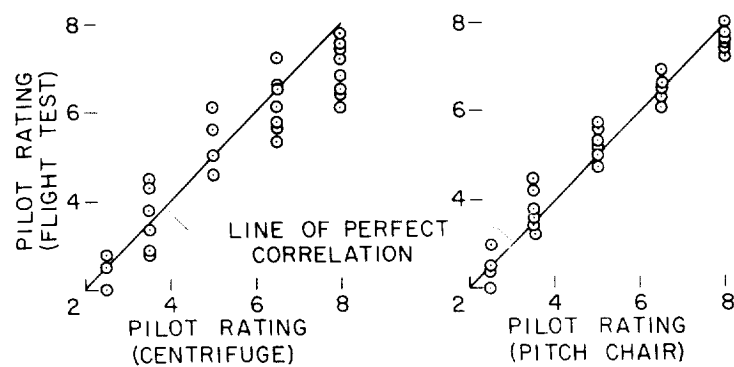
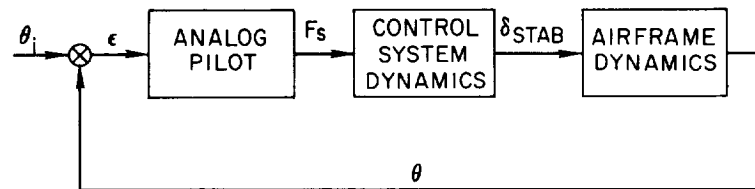
CORRELATION BETWEEN CENTRIFUGE,
PITCH CHAIR, AND FLIGHT EVALUATIONS

Figure 4

SIMULATOR WITH ANALOG PILOT



$$\frac{F_s}{\epsilon} = \frac{K_p e^{-\tau s} (1 + T_L s)}{(1 + T_I s)(1 + T_N s)} = \frac{K_p e^{-2s} (1 + T_L s)}{(1 + .1s)(1 + .1s)}$$

Figure 5

TYPICAL EFFECTS OF DYNAMICS ON PILOT ANALOG

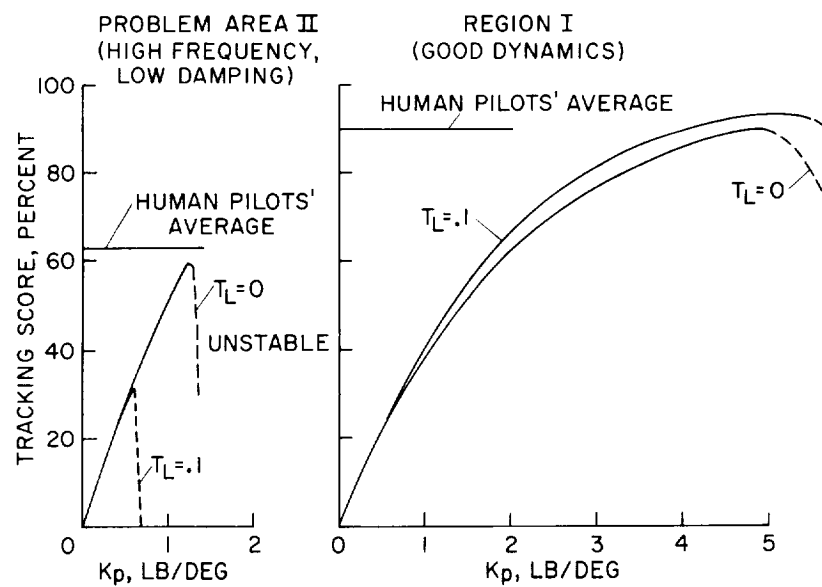


Figure 6

DESIRED HUMAN RESPONSE DEFINED BY USE OF ANALOG PILOT

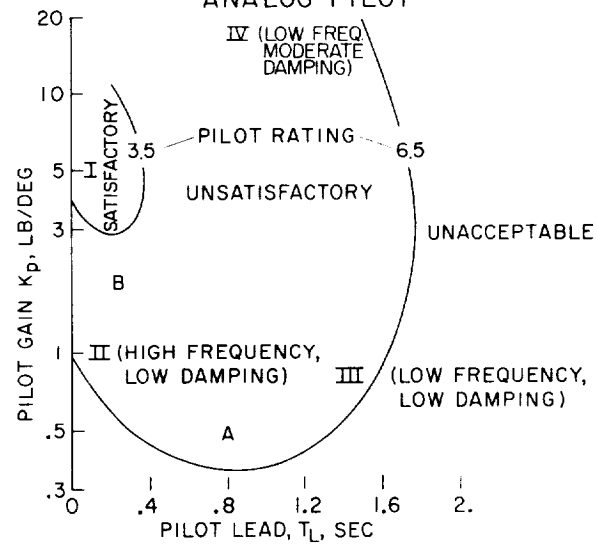


Figure 7

ANALOG PILOT TRACKING CHARACTERISTICS FOR EXAMPLE CONTROL PROBLEM

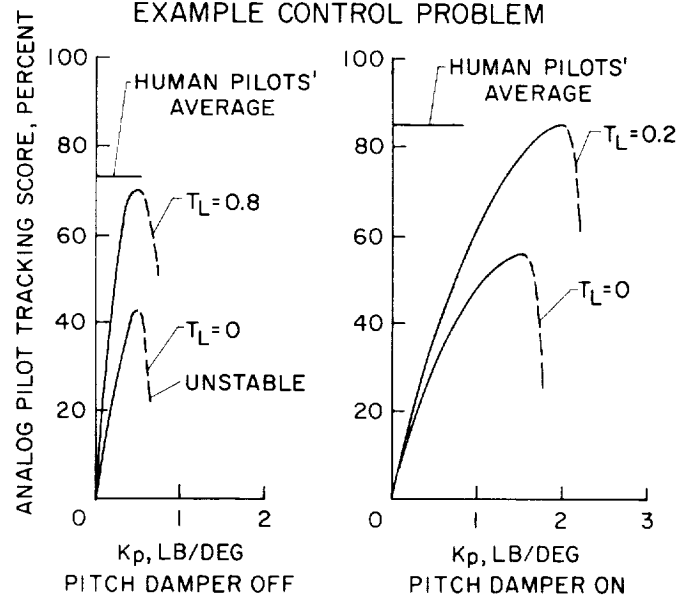


Figure 8

EXAMPLE CONTROL PROBLEM EVALUATION BY
HUMAN PILOTS

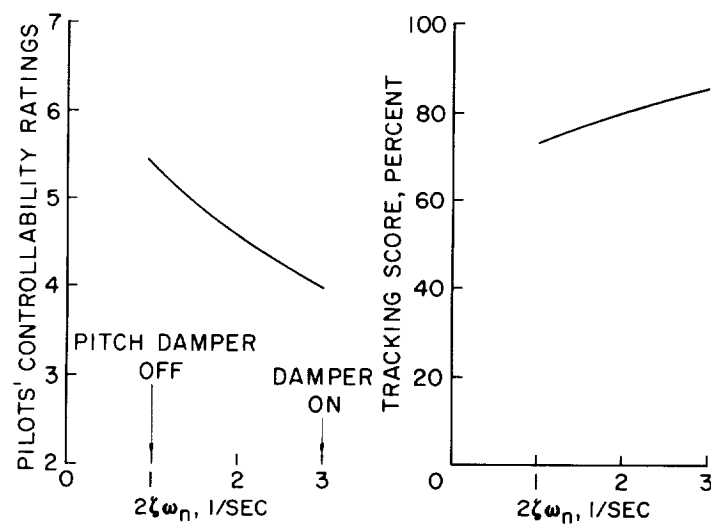


Figure 9

1

REVIEW OF TECHNIQUES APPLICABLE TO THE RECOVERY
OF LIFTING HYPERVELOCITY VEHICLES

By Joseph Weil and Gene J. Matranga
Flight Research Center

SUMMARY

A general review of piloting problems concerned with the recovery phase of lifting hypervelocity vehicles is presented. A short discussion is offered pertinent to the maneuvering capabilities and piloting techniques applicable to the initial approach phase of gliders with low lift-drag ratios. The principal emphasis concerns factors affecting the final approach and landing operation of these gliders. The results of general flight studies as well as recent experience obtained in the approach and landing of the X-15 research airplane are reviewed. Finally, a definition of the limits of piloted flared landings is developed.

In regard to the final approach and landing phase, the more conventional circular pattern and the straight-in approach each had merits that were appreciated by the pilots. The conventional pattern afforded somewhat more flexibility of operation in space positioning prior to the flare, whereas the straight-in approach had the advantage of alleviating pilot-judgment requirements during the flare.

Although there have been a number of problems encountered in X-15 landing operations, the present procedure of a relatively high-speed, circular approach with gear and flap extension delayed until completion of the flare is providing entirely satisfactory landings.

Flight experience has been obtained with vehicles that should have landing characteristics similar to many of the possible future winged reentry vehicles. In general, a usable lift-drag ratio of 3.5 or higher should provide the pilot with fair-to-good landing characteristics and allow a speed flexibility that lends itself to a choice of techniques.

There is strong reason to believe that, regardless of technique, a lift-drag ratio in the flare of approximately 2.5 may represent a practical lower limit for piloted flared landings.

INTRODUCTION

Piloting problems concerned with the recovery phase of lifting hypervelocity vehicles as defined in figure 1 are considered in this paper. The reentry is assumed to be completed at a Mach number of 5 and at 100,000 feet.

A brief discussion is presented relative to the maneuvering capabilities and piloting techniques applicable to the initial approach phase of gliders with low lift-drag ratios. The principal emphasis of this paper, however, is on the final approach and landing operation of such vehicles. The results of general flight studies as well as recent experience obtained in the approach and landing of the X-15 research airplane are reviewed. Finally, a definition of the limits of piloted flared landings is presented.

It should be noted from the outset that, although the use of advanced energy management and automatic landing systems may have an important role in future operations of advanced vehicles, such devices are not considered in this paper, inasmuch as the primary interest was in establishing base line piloting capabilities obtainable with a minimum of guidance aids.

SYMBOLS

g	acceleration due to gravity, ft/sec^2
h	altitude, ft
L/D	lift-drag ratio
$(L/D)_{\text{max}}$	maximum lift-drag ratio
M	Mach number
n	normal-load factor based on weight of 14,000 pounds
t^*	time between completion of flare and minimum touchdown speed, sec
V_i	indicated airspeed, knots
$(V_i)_{\text{TD}}$	indicated airspeed at touchdown, knots

V_v	vertical velocity, ft/sec
W/S	wing loading, lb/sq ft
α	angle of attack, deg
γ	flight-path angle, deg
γ_0	flight-path angle at flare initiation, deg
δ_h	horizontal-stabilizer deflection, deg

Subscripts:

I,III phase of landing technique

INITIAL APPROACH

Figure 2 shows the maneuverability envelope during the initial-approach phase of a reentry vehicle as determined from simulator tests. Data are presented for the X-15 configuration, which has an average maximum lift-drag ratio $(L/D)_{\max}$ of 2.5 in the lower supersonic speed range. The initial conditions are assumed to be a Mach number of 5 at an altitude of 100,000 feet. The maneuverability limits defined were obtained by performing constant bank-angle turns until a desired heading was obtained and then flying near $(L/D)_{\max}$ until a point 30,000 feet over the landing site was reached. For maximum-range considerations the optimum bank angle is a function of the required heading change. It is seen that the lateral-maneuverability potential is slightly greater than 100 nautical miles and the longitudinal range is somewhat over 200 nautical miles. To obtain some appreciation for the ranging problems and to define optimum techniques, simulated visual-flight-rule (VFR) and ground-controlled-approach (GCA) runs were made to representative landing sites at various locations within the envelope. The least difficult navigational problems occurred in the unshaded region A. In this area, range control could be easily obtained by speed-brake modulation. Speed brakes were found to be more effective and desirable than use of S-turns or decrease in lift-drag ratio through high angle-of-attack flight. In region B the navigational problem was somewhat less routine because of the greater requirements for turning flight; however, particularly with ground vectoring the pilot could successfully complete the initial approach without too much difficulty. Considerably more difficulty was experienced in arriving over a landing site in region C

because there is little range margin to compensate for pilot error or for uncertain wind effects.

A number of techniques will be relied on for X-15 navigation during the glide to the base. In normal operations the pilots will be able to complete the mission satisfactorily by following planned procedures with visual cues. The flight operation will be made at a maximum lift-drag ratio ($\alpha = 80^\circ$) until the vicinity of the landing site is reached, at which time excess energy will be dissipated through use of speed brakes and circling flight. For emergency operations ground-vectoring techniques may be used to guide the X-15 to high key. In all instances a pilot will be available on the ground to give the required commands. Because of large variations in effective lift-drag ratio due to deceleration and turning flight, ground monitoring of altitude and velocity in addition to X-Y position will be required. Various techniques are currently being evaluated on the simulator and in flight with the F-104A airplane to develop procedures for different flight regimes and situations. In addition, experience will be obtained during X-15 buildup flights which should serve to improve the ground-vectoring methods.

GENERAL FINAL-APPROACH AND LANDING STUDIES

During the past several years a number of programs have been conducted at the NASA Flight Research Center to study various facets of the approach and landing problems at low lift-drag ratio. The landings were made on a concrete runway. Figure 3 shows representative landing patterns of two low-lift-drag-ratio test beds. By suitable scheduling of thrust- and drag-producing devices a value of $(L/D)_{\max}$ as low as 2.8 was obtained with the F-104A airplane at a wing loading of about 75 pounds per square foot (ref. 1). A similar procedure enabled investigation of a maximum lift-drag ratio as low as 3.8 with the F-102A at a wing loading of about 35 pounds (ref. 2). In both investigations circular landing patterns were used by the pilots. A 270° approach over the touchdown point was generally preferred by the pilots, inasmuch as this enabled them to establish a desired initial orientation prior to turning. In the case of the F-104A, after several buildup flights, landings made at a lift-drag ratio above 3.5 were straightforward and not particularly demanding on piloting technique. In figure 3 for the landing in which $(L/D)_{\max} = 2.8$, although the pattern was steep and tight, arriving at the desired touchdown point presented no particular problems. The main problem was that of judging the factors controlling the flare to achieve acceptable vertical velocity at touchdown. Although this velocity was always less than 2 feet per second, it was believed that the flare with $(L/D)_{\max} = 2.8$ was too demanding for flare technique to be left completely to pilot discretion.

Even at the lowest lift-drag ratio attained in the F-102A, pilot comments indicated that the entire operation including the flare was acceptable. The pilots believed that the lower speeds associated with the lower wing loading of the F-102A made the landing approach easier than did a similar lift-drag ratio with the F-104A.

More recently, another landing technique applicable to gliders with low lift-drag ratios has been developed and demonstrated in flight tests at the Ames Research Center (ref. 3). The technique was designed to simplify the landing procedure of gliders with low lift-drag ratios by explicitly defining the approach flight path required to position precisely the aircraft at the approach end of the runway and by specifying a procedure for programming the flare. Figure 4 shows the various phases of the straight-in approach and flare technique. The initial phase (phase I) of the pattern is a constant-attitude, high-speed dive from altitude aimed at a ground reference point short of the runway threshold. At a specified altitude and speed, a constant g pullout (phase II) is made to a shallow flight path (phase III) along which the airplane decelerates to the touchdown point.

During much of the investigation of reference 3, an F-104A airplane was used as the test bed. Phase I of this landing pattern was entered from an indicated airspeed corresponding to the maximum lift-drag ratio (about 240 knots) at altitudes between 15,000 and 25,000 feet. The pilot then increased the airspeed to that desired at the pull-out. Speeds from 340 to 450 knots and corresponding rates of sink from 150 to 300 feet per second were successfully used in phase I for a configuration having a value of $(L/D)_{\max}$ of 4.0, and a speed of about 300 knots was used for a high-drag configuration having a value of $(L/D)_{\max}$ of 2.8. Forty-five approaches at low values of L/D were made to an 8,000-foot runway, with reported touchdown-point and airspeed variations of ± 600 feet and ± 10 knots, respectively.

In order to provide an optimum landing technique for the X-15 and also to obtain information applicable to other reentry vehicles, a program was conducted at the NASA Flight Research Center with several F-104A airplanes to evaluate circular and straight-in approach procedures under simulated X-15 mission conditions. Six of the eight NASA, Air Force, and Navy pilots participating in the program were designated X-15 pilots. For both the circular and straight-in approach techniques the initial heading of the airplane was usually 90° to the runway. Prior to entering the pattern, the pilot set idle power and used full speed brakes; this procedure produced a value of $(L/D)_{\max}$ of approximately 4. For the straight-in approach a speed of 350 knots was required at the flare-initiation altitude of 2,200 feet with an aim point 10,000 feet from touchdown. The programmed normal acceleration during the flare was 1.4. Flaps and gear were put down after completion of

the flare. For comparative purposes, the pilots also performed conventional 270° patterns at indicated airspeeds from 275 to 300 knots with the same configuration sequence as that for the straight-in approach. During most of the tests, the pilot attempted to touch down as close as possible to a prescribed line on the runway at a speed between 180 to 190 knots and with low vertical velocity.

The experienced test pilots liked the flexibility of the circular pattern, in that it allowed them to exercise judgment by taking advantage of pattern variable geometry. This enabled the pilots to continually monitor and correct for unknowns, such as variable winds, and, thus, provide the desired flare-initiation conditions.

The pilots were well aware of the apparent simplicity of the straight-in approach, but they did encounter situations in maneuvering from arbitrary initial conditions of altitude and heading that they felt might be less conducive to corrective action than was afforded by the conventional 270° pattern. Pilots were particularly apprehensive about effects of wind and errors in judgment that would lead to landing short of the intended touchdown point. The pilots were all favorably impressed, however, by the control of the flare provided by the straight-in procedure. Since the pattern is composed of straight-line elements, it is particularly compatible with practical schemes of electronic guidance or automatic control. It should be pointed out that speed brakes were not used to control flight-path angle and that the use of partial speed brakes as a modulating base would afford an effective way of compensating for some of the aforementioned factors that might impede space positioning during a straight-in approach.

In regard to final control of touchdown conditions, there seemed to be little difference between the two landing techniques and, in either case, winds could cause the desired touchdown point to be off 2,500 feet or more. Although successive landings enabled the pilot to partially compensate for wind by variations in technique, it is thought that $\pm 1,000$ feet might be a realistic figure for control of the touchdown point under favorable practical operating conditions.

In general, most pilots thought that each technique had features that might prove desirable in the recovery operations of reentry gliders, but no pronounced preference of one technique over the other existed. More important, it appears that a good background of methods and experience are available from which to determine the optimum final approach and landing procedure of reentry vehicles, depending on specific mission requirements and vehicle characteristics. As a result of this program, pilots will probably use a composite technique for the X-15 which they feel combines the best features of both methods. This composite technique will involve a circular approach made slightly in excess of

300 knots and flown so that the pilot will have maximum altitude in the final straight-in leg to follow predetermined flare-control procedures.

X-15 APPROACH AND LANDING EXPERIENCE

General flight studies of test beds with low lift-drag ratios, such as those previously discussed, have made possible assessments of low L/D approach and landing problems. It should be remembered, however, that such studies are still only a form of simulation, in that the pilot at his discretion can apply power and wave-off. Landings for the X-15, on the other hand, are made for the first time in an L/D range from 3 to 4 under actual operational conditions. Figure 5 shows a comparison of the landing lift-drag ratio used in previous research gliders with that of the X-15. In the X-15 operations the pilot delays putting the flap and gear down until he is rather close to the ground. In this manner, the flare is essentially completed in an L/D range similar to that of the X-1E airplane.

Thus far, the X-15 landings have incorporated a 360° or 270° pattern over the touchdown point or a modified S-pattern. The patterns have been generally comfortable and there has been no indication of difficulty due to space positioning.

Figure 6 summarizes the X-15 touchdown conditions in terms of vertical velocity and angle of attack for the first 11 flights. The skid and nose landing-gear combination imposed a rather severe angle-of-attack restriction in the initial flights. This has been somewhat relaxed by landing-gear modifications. The dashed lines represent the present approximate design limits. The four open symbols represent conditions obtained with the original landing-gear configuration; the solid symbols represent landings performed after the gear modifications were made. The touchdown conditions of the first three landings paralleled the original design curve. The fourth landing, however, considerably exceeded the design limits and the airplane suffered major structural damage. The solid symbols indicate that the most recent experience is well within the modified design limits. It is interesting to note that the average X-15 touchdown vertical velocity is of the order of 5 to 6 feet per second as compared with a maximum sink speed at touchdown of $4\frac{1}{2}$ feet per second in all previous research-airplane operations.

The reason for this difference is not completely understood but might be due in part to impaired visibility and pilot location relative to the ground prior to touchdown.

Figure 7 presents comparative time histories of the first and fifth landings. In both instances the pitch damper was inoperative. The data

presented are angle of attack, stabilizer deflection, indicated airspeed, vertical velocity, and altitude. In the first landing the approach was made at an indicated airspeed of about 270 knots and the flare was started at about 1,200 feet above the terrain. Shortly after the flap deflection was initiated, a severe pitch oscillation is evident; this was probably triggered by the flap trim change. Possibly because he was hindered by this pitch oscillation, the pilot leveled out about 60 feet in the air. The speed continued to bleed off and the mean angle of attack increased to about 10° . The pilot was indeed fortunate to land the vehicle at the bottom of an oscillation and thus avoid major structural damage on the first flight. The control problem on the first flight was undoubtedly the result of a number of factors. The psychological effect of a first flight coupled with a sensitive side-arm controller, lack of pitch-damper augmentation, and control rate limiting all contributed to the control problem. In the fifth landing the pitch damper was also out, but the pilot was more experienced and had been instructed to use the center stick for landing. Flap deflection was initiated at an altitude of only 250 feet, and the landing gear dropped at 20 feet above the ground. This delay in attaining the landing configuration was partially responsible for maintaining a considerably higher forward speed at touchdown than in landing 1. Although the touchdown vertical velocity was about 5 feet per second, the marked reduction in oscillations and angle of attack clearly indicated that landing 5 was a much more desirable landing.

The importance of technique is shown in figure 8. For each of the landings, the center stick was used and the pitch damper was operative. In landing 4 the approach was made at an indicated airspeed of 255 knots, whereas in landing 7 the approach was made at an indicated airspeed of 305 knots. In landing 4 the low speed and gradual flare resulted in an angle of attack of about 11° at touchdown, with a terminal sink speed of 9 feet per second. As stated previously, major structural damage resulted. In landing 7 the pilot performed the flare more abruptly and completed the flare prior to gear and flap deflection. This technique provided 20 seconds of flight below an altitude of 40 feet. The angle of attack at touchdown was about 8° , and final sink speed was only 3 feet per second, well within the design limits.

Landing 7 was considered by the pilots to be one of the best X-15 landings and illustrates the fact that most experienced test pilots appreciate the importance of excess speed near the ground, even though this technique produced significantly higher sink speeds at altitudes above 100 feet.

At present, it is thought that adherence to the NASA recommendation proposed in 1958 of maintaining an approach speed of about 300 knots with flap and gear extension delayed to as low an altitude as possible

is providing acceptable X-15 landing characteristics. Furthermore, X-15 pilots believe that use of the F-104A provides an effective means of training for X-15 landing operations.

DEVELOPMENT OF LOW-LIFT-DRAG-RATIO CRITERION

Many interrelated factors must be considered in the development of a practical low-lift-drag-ratio landing criterion. For example, the final approach speed should be subsonic to avoid transonic reduction in lift-drag ratio and to minimize problems of acceleration from best lift-drag-ratio cruise speed. Also, the higher the speed and flight-path angle, the more difficult entry into the pattern is likely to become. Such characteristics also produce larger speed loss during the flare maneuver; therefore, the excess speed available following such high-speed flares is not nearly as large as might be expected. The flare normal acceleration should not exceed $3g$ and preferably should not be much greater than $2g$. A reasonable time should be available after flare completion to make final flight-path corrections prior to touchdown. Finally, the minimum landing speed may well be determined by angle-of-attack restrictions imposed by landing-gear design or vehicle control characteristics.

Systematic studies have been made with representative reentry configurations to study the relative importance of the various factors controlling piloted landings at low lift-drag ratios. Figure 9 presents the results of one such analysis. Calculations were made for a series of 60° to 70° delta-wing configurations having a wing loading of 35 pounds per square foot. A $1.5g$ to $2g$ flare was assumed for all conditions.

A landing analysis was made for configurations having values of $(L/D)_{\max}$ shown. For each configuration, landing calculations were made for a range of approach or flare-initiation speeds. It was assumed that an angle-of-attack restriction of 13° existed. This angle-of-attack restriction limited the landing speed to greater than 140 knots. The lines on the right side of the figure define flight-path angle as a function of approach speed for the several configurations. The curved lines on the left represent time remaining to decelerate to minimum landing speed following the completion of the flare. The conditions from which acceptable piloted landings might be made were estimated on the basis of the interrelated factors previously mentioned. The area for acceptable flare-initiation speed is bounded on the high-speed side by $\gamma_0 = -35^\circ$ to -45° and is defined on the low-speed side by a minimum time of approximately 5 seconds to terminate the landing following completion of the flare. Although figure 9 is not exactly applicable, note

that there are flight tests for the F-102A at a value of $(L/D)_{\max}$ of 3.8 at speeds near 200 knots, and the pilots rated the overall characteristics good. Also, based on previous flight studies, this good region should exist for a considerable range of speed. It is at once apparent that a combination of relatively low wing loading and high drag severely limits the attainable approach speeds. For the configurations shown, it is estimated that the lowest value of $(L/D)_{\max}$ at flare initiation from which a piloted landing would be feasible is of the order of 2.5.

As has been previously pointed out, pilots prefer vehicles having lower wing loadings for general landing operations at moderately low L/D . However, it has been found from similar studies that the lower marginal level is relatively unaffected by changes in wing loading.

CONCLUDING REMARKS

The range capabilities have been defined and techniques applicable during the initial approach phase of the recovery of lifting hypervelocity vehicles have been described.

In regard to the final approach and landing phase, the more conventional circular pattern and the straight-in approach both have merits that are appreciated by the pilots. The conventional pattern affords somewhat more flexibility of operation in space positioning prior to the flare, whereas the straight-in approach has the advantage of alleviating pilot-judgment requirements during the flare.

Although there have been a number of problems encountered in X-15 landing operations, the present procedure of a relatively high-speed, circular approach with gear and flap extension delayed until completion of the flare is providing entirely satisfactory landings.

Vehicles that should have landing characteristics similar to many of the possible future lifting reentry vehicles have been flight tested. In general, a usable lift-drag ratio of 3.5 or higher should provide the pilot with fair-to-good landing characteristics and allow a speed flexibility that lends itself to a choice of techniques.

There is reason to believe that, regardless of technique, a lift-drag ratio of approximately 2.5 in the flare may represent a practical lower limit for piloted flared landings.

REFERENCES

1. Matranga, Gene J., and Armstrong, Neil A.: Approach and Landing Investigation at Lift-Drag Ratios of 2 to 4 Utilizing a Straight-Wing Fighter Airplane. NASA TM X-31, 1959.
2. Matranga, Gene J., and Menard, Joseph A.: Approach and Landing Investigation at Lift-Drag Ratios of 3 to 4 Utilizing a Delta-Wing Interceptor Airplane. NASA TM X-125, 1959.
3. Bray, Richard S., Drinkwater, Fred J., III, and White, Maurice D.: A Flight Study of a Power-Off Landing Technique Applicable to Re-Entry Vehicles. (Prospective NASA paper.)

ILLUSTRATION OF RECOVERY PROBLEM

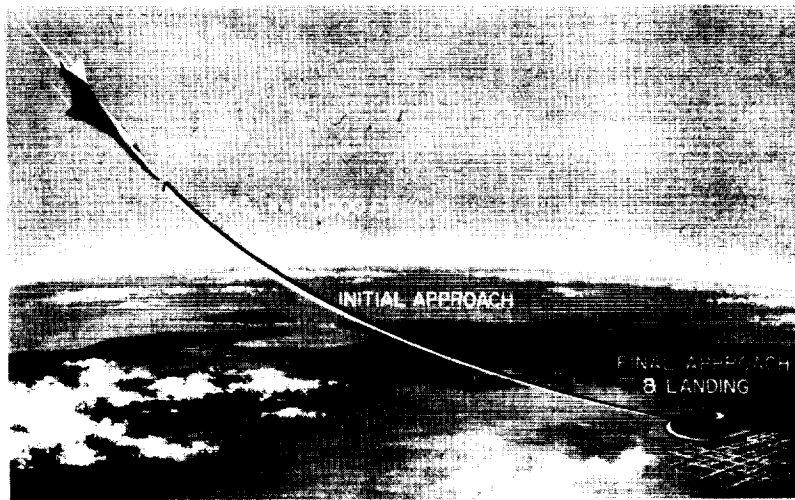


Figure 1

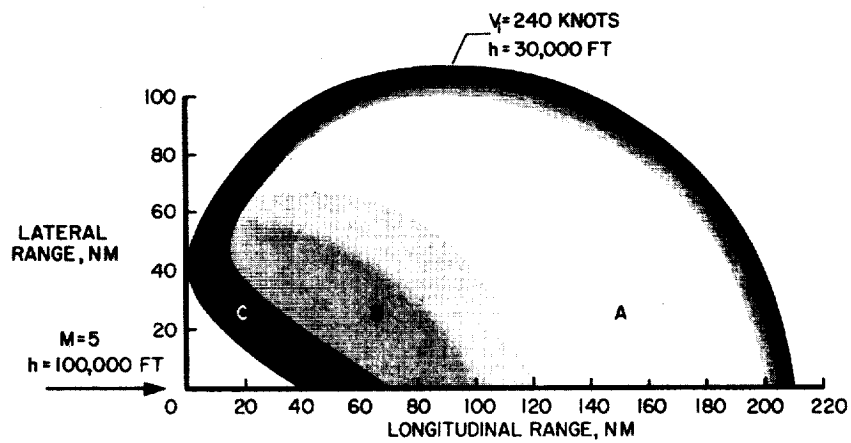
ENTRY VEHICLE MANEUVERABILITY ENVELOPE
DURING INITIAL APPROACH
 $(L/D)_{\max} \approx 2.5$ 

Figure 2

TYPICAL LOW L/D CIRCULAR LANDING PATTERNS

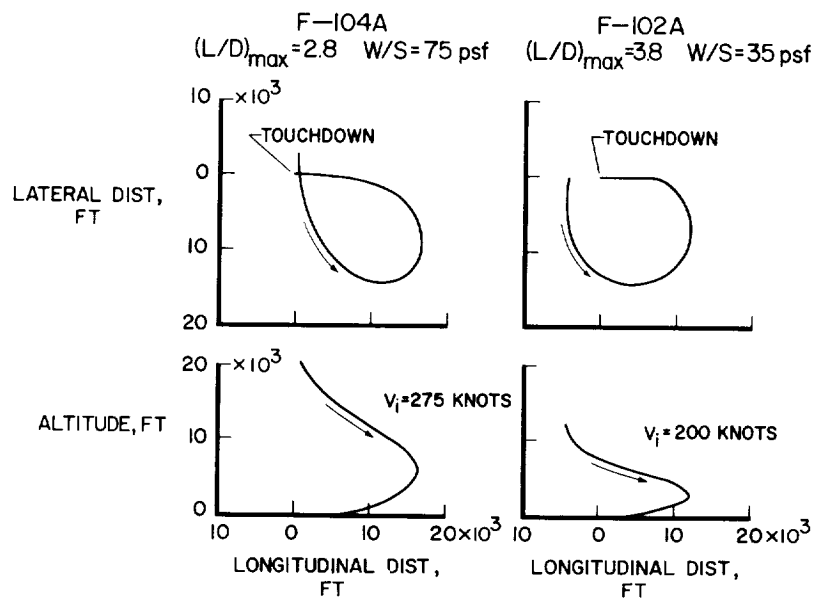


Figure 3

STRAIGHT-IN APPROACH AND FLARE TECHNIQUE

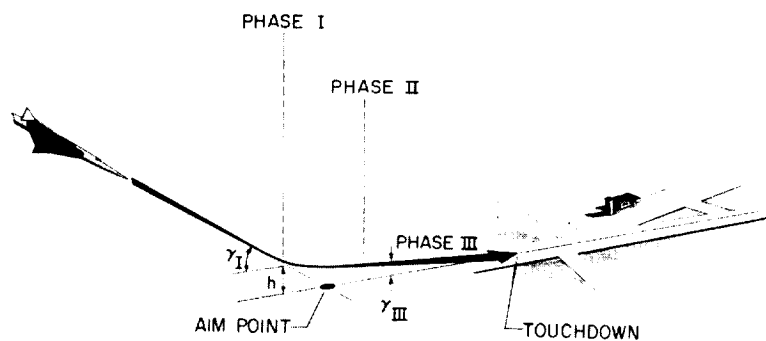


Figure 4

ROCKET AIRPLANE L/D COMPARISON

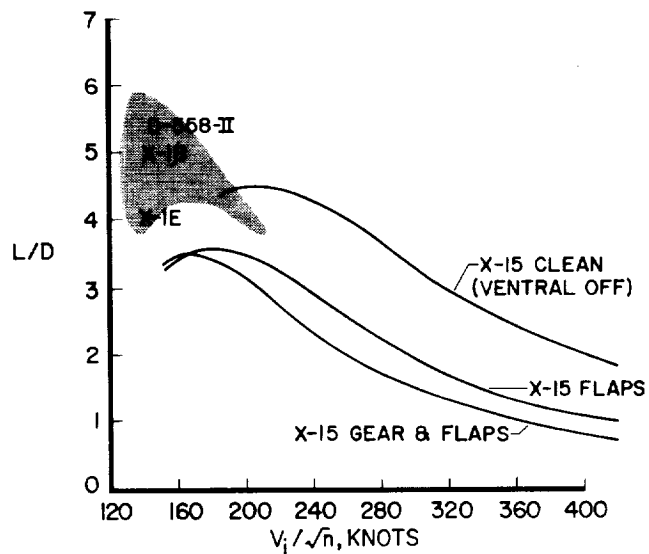


Figure 5

SUMMARY OF X-15 TOUCHDOWN CONDITIONS

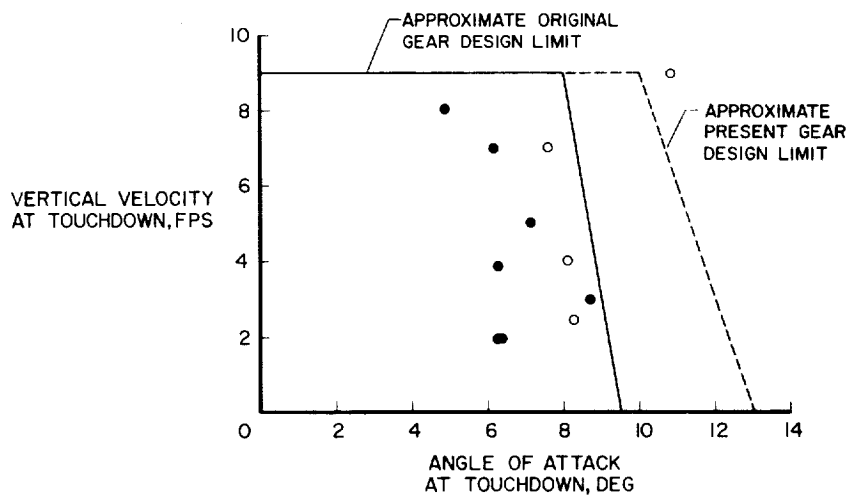


Figure 6

X-15 LANDING CHARACTERISTICS-PITCH DAMPER OFF

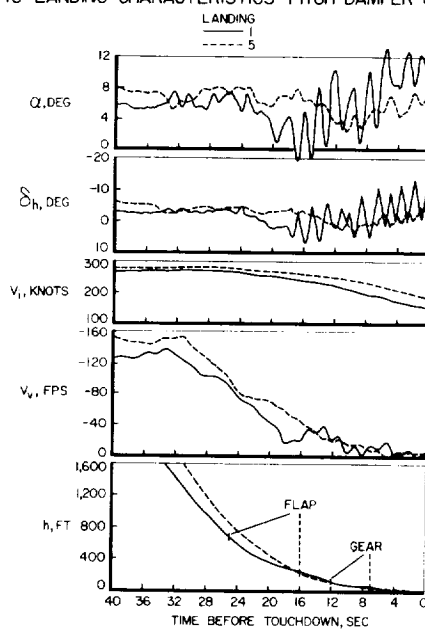


Figure 7

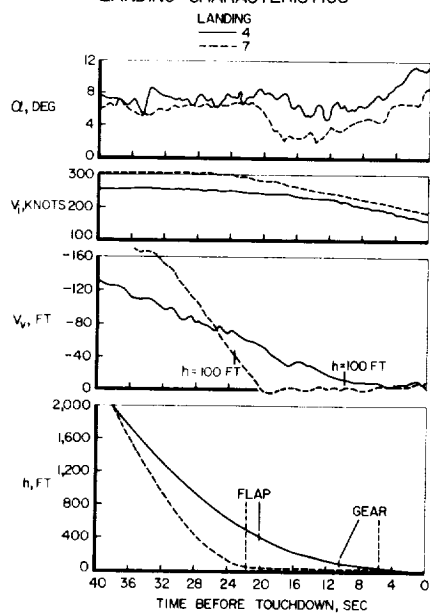
EFFECT OF TECHNIQUE ON X-15
LANDING CHARACTERISTICS

Figure 8

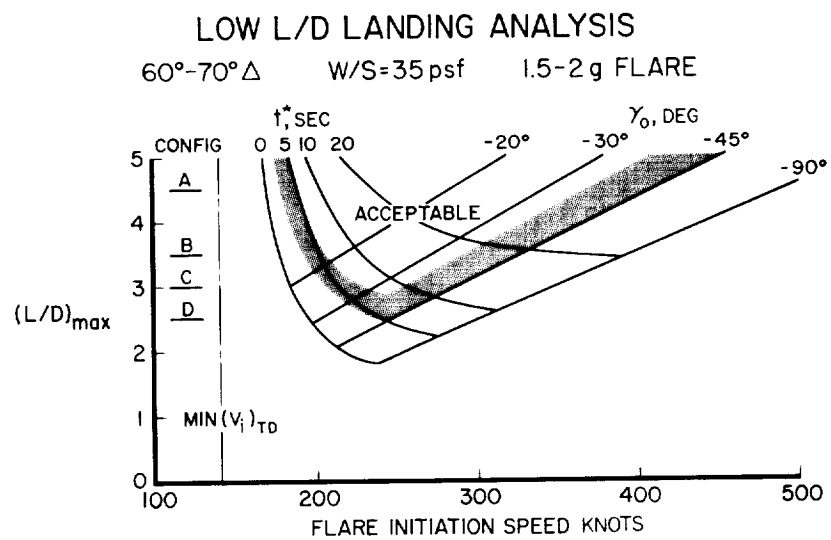


Figure 9

LOW-SPEED FLIGHT CHARACTERISTICS OF REENTRY VEHICLES
OF THE GLIDE-LANDING TYPE

By John W. Paulson, Robert E. Shanks,
and Joseph L. Johnson
Langley Research Center

SUMMARY

A low-speed investigation has been made to determine the flight characteristics of a number of reentry vehicles of the glide-landing type. The investigation consisted of model flight tests, static and dynamic force tests, and analytical studies of the dynamic lateral behavior over an angle-of-attack range from 0° to 40° .

The longitudinal characteristics for glide landings should be satisfactory with the lift-drag ratios and wing loadings now being considered for reentry configurations. The lateral stability characteristics should also be satisfactory except that many of the reentry vehicles are likely to require a roll damper for satisfactory Dutch-roll damping at moderate and high angles of attack. Some configurations with wing-tip vertical tails may have control problems in the form of large adverse aileron yawing moments and low rudder effectiveness.

INTRODUCTION

Reference 1 covers some of the factors involved in the final approach and landing of reentry vehicles. The present paper gives additional information on this subject which includes data obtained from force tests and flight tests of models of a number of specific reentry configurations. The first part of the paper covers longitudinal characteristics, including lift-drag ratio, aerodynamic-center location, and the effect of center-of-gravity location on longitudinal behavior. The second part consists of a discussion of lateral stability and control. Although it is anticipated that the reentry vehicles considered in this paper would not normally be operated at angles of attack greater than about 15° or 20° in the glide approach and landing, the characteristics over a much larger angle-of-attack range are covered to provide information that would be of interest in cases where higher angles of attack are reached inadvertently.

SYMBOLS

b	wing span, ft
\bar{c}	mean aerodynamic chord, ft
C_L	lift coefficient, $\frac{\text{Lift}}{qS}$
C_l	rolling-moment coefficient, $\frac{\text{Rolling moment}}{qSb}$
C_m	pitching-moment coefficient, $\frac{\text{Pitching moment}}{qS\bar{c}}$
C_n	yawing-moment coefficient, $\frac{\text{Yawing moment}}{qSb}$
D	drag, lb
g	acceleration due to gravity, ft/sec ²
I_X	moment of inertia about X-axis, slug-ft ²
I_Z	moment of inertia about Z-axis, slug-ft ²
L	lift, lb
p	rolling velocity, radians/sec
q	dynamic pressure, lb/sq ft; pitching velocity, radians/sec
r	yawing velocity, radians/sec
S	wing area, sq ft
$T_{1/2}$	time to damp to one-half amplitude, sec
V	free-stream velocity, ft/sec
W	weight, lb
α	angle of attack, deg

β angle of sideslip, deg

$$\dot{\beta} = \frac{\partial \beta}{\partial t}$$

δ_a aileron deflection, deg

δ_r rudder deflection, deg

ω angular velocity, radians/sec

$$C_{n\beta} = \frac{\partial C_n}{\partial \beta}$$

$$C_{l\beta} = \frac{\partial C_l}{\partial \beta}$$

$$C_{n\delta_a} = \frac{\partial C_n}{\partial \delta_a}$$

$$C_{l\delta_a} = \frac{\partial C_l}{\partial \delta_a}$$

$$C_{n\delta_r} = \frac{\partial C_n}{\partial \delta_r}$$

$$C_{n_r} = \frac{\partial C_n}{\partial \frac{rb}{2V}}$$

$$C_{l\dot{\beta}} = \frac{\partial C_l}{\partial \frac{\dot{\beta}b}{2V}}$$

$$C_{l_p} = \frac{\partial C_l}{\partial \frac{pb}{2V}}$$

$$C_{n_p} = \frac{\partial C_n}{\partial \frac{pb}{2V}}$$

$$C_{m_q} = \frac{\partial C_m}{\partial \frac{q\bar{c}}{2V}}$$

Subscripts:

MAX maximum

DYN dynamic

RESULTS AND DISCUSSION

Longitudinal Characteristics

Presented in figure 1 is the approximate range of the low-speed maximum trimmed lift-drag ratio as a function of lift coefficient for various reentry vehicles of the glide-landing type currently under

consideration. The figure shows that some reentry vehicles can have fairly high values of L/D , and the maximum L/D values occur at relatively low lift coefficients of 0.2 to 0.3.

One of the reasons for the large spread in L/D values is shown in figure 2 where maximum L/D is plotted as a function of a nondimensional volume parameter (volume to the two-thirds power divided by wing area). In this figure the nose of each model corresponds to its test point. The results shown are for trimmed conditions and a small amount of longitudinal stability. This figure shows that the higher values of L/D are associated with the winged glide-landing configurations and the lower values of L/D are associated with the lifting-body configurations which would have to be landed with a parachute. The data of figure 2 were obtained at low Reynolds numbers; a few tests at higher Reynolds numbers have indicated that L/D values for the corresponding full-scale reentry vehicle may be as much as 0.5 to 1.0 greater than these values. The configurations illustrated in figure 2 were all designed for the hypersonic condition and for the most part have rather low L/D values at subsonic speeds.

Figure 3 shows that substantial increases in subsonic L/D values can be attained when some effort is also made to design the vehicle for the low-speed case. The shaded area represents the region in which the maximum L/D values for the configurations of figure 2 were located. Boattailing the base of the half-cone and pyramid-shaped vehicles increased the L/D values from about 1.5 to 3.8 and from about 3 to 5, respectively. Adding control surfaces to the half-cone vehicle resulted in a further increase to about 4.5. In the case of the winged reentry configuration with the volume ratio of 0.25, an L/D of about 6 was obtained when the model was modified to achieve high L/D at low speeds. With these modifications, the model had a thick, highly cambered wing and teardrop fuselage with a low base area. The hypersonic L/D of this model was reduced by these changes, but the hypersonic L/D values for the half-cone and pyramid-shaped vehicles were relatively unaffected by boattailing. Another method for obtaining good L/D for landing is the use of a variable-geometry vehicle such as the one at the top of figure 3. This configuration has wing tips that are folded up to protect them from high heating rates during reentry at high angles of attack. For landing, the surfaces are folded down and L/D values of about 7 are obtained.

In order to compare the L/D of some of these configurations with those of the research airplanes discussed in reference 1, figure 4 is presented. In this figure the values of L/D for the variable-geometry configuration, the modified half-cone vehicle, and a winged reentry vehicle are given along with values of L/D for the X-15 airplane and for the modified F-102A airplane with landing gear and speed brakes

extended. Data are shown for the low-wing-loading and high-wing-loading cases. The modified F-102A airplane with a maximum L/D of about 3.7 and a wing loading of 35 was satisfactory in the landing approach (ref. 1). It would appear then that the two low-wing-loading reentry configurations would be satisfactory since they have higher values of L/D , particularly at the lower lift coefficients, and also somewhat lower wing loadings than the modified F-102A airplane. These low wing loadings (in the range of 20 to 30) are typical for winged reentry vehicles. A reentry vehicle that is essentially a lifting body, such as the half-cone configuration, will have a much higher wing loading than a winged vehicle having the same volume. For the higher wing-loading case, a comparison is made with the X-15 airplane which was found to have acceptable landing characteristics. The X-15 airplane performs the approach and landing in the low-lift-coefficient range (about 0.2 to 0.4). It would appear that the half-cone configuration, which has a higher L/D in the 0.2 to 0.4 lift-coefficient range and a slightly lower wing loading than the X-15 airplane, would also have satisfactory landing characteristics.

Another low-speed characteristic of interest to the designer of a hypersonic vehicle is the aerodynamic-center location which must, of course, be aft of the center of gravity for longitudinal stability. Shown in figure 5 is the variation of the aerodynamic-center location with leading-edge sweep for thin-flat-plate delta wings. It is seen that there is a systematic variation in aerodynamic-center position with sweep approaching the theoretical value of 50 percent at 90° sweep. Also shown are the aerodynamic-center locations for several reentry vehicles as given by symbols showing their cross-sectional views. These data indicate that a rearward (or stabilizing) shift in aerodynamic center generally results when the wing is very thick, when a large fuselage is added, or when wing-tip vertical tails are used.

Longitudinal flight characteristics obtained with a highly swept delta-wing flying model, which is considered to be generally representative of highly swept reentry vehicles, is presented in figure 6. Plotted in this figure are flight ratings, as shown by the shaded areas, for various combinations of damping in pitch C_{mq} and static longitudinal stability. The vertical line is the boundary between the statically stable condition and the unstable condition, and the diagonal line represents the calculated stick-fixed maneuver point. The maneuver point is that center-of-gravity position where the elevator deflection per g is zero. The maneuver-point line has a slope because the maneuver point is a function of damping in pitch and moves rearward as pitch damping is increased. The lower curve represents the model without pitch damper. These studies showed that for all statically stable conditions the model was easy to fly. As pitch damping was added, good flight behavior could also be obtained with statically unstable conditions. As the maneuver point was approached for any condition of pitch

damping, the model became more difficult to fly and finally became unflyable. The flight tests also showed that when reduced elevator deflection was used, the model could not be flown with as much instability as shown in figure 6; this effect indicated that, to some extent at least, the amount of instability which could be tolerated was a function of the total pitching moment used for control.

These model flight results are in general agreement with analog studies (ref. 2) and with flight studies made with conventional airplanes (ref. 3).

Lateral Characteristics

Presented in figure 7 is the variation with sweep angle of the effective-dihedral parameter $C_{l\beta}$, the steady-state damping-in-roll parameter C_{lp} , the directional-stability parameters $C_{n\beta}$ and $(C_{n\beta})_{DYN}$, and the ratio of the yawing inertia to the rolling inertia I_Z/I_X . These data are for thin delta wings at a lift coefficient of 0.6, but the trends shown are considered to be generally representative of highly swept reentry configurations for a fairly wide lift-coefficient range. The low values of C_{lp} in the region of sweep angles of about 75° and above, accompanied by large negative values of $C_{l\beta}$, tend to produce poor damping of the lateral or Dutch-roll oscillation; and the high ratio of the yawing to rolling inertia means that the Dutch-roll oscillation becomes practically a pure rolling motion about the body X-axis.

The directional-stability data show that $C_{n\beta}$ is low and becomes negative at the higher angles of sweep. The dynamic directional-stability parameter $(C_{n\beta})_{DYN}$, which is defined as $C_{n\beta} - C_{l\beta} \frac{I_Z}{I_X} \sin \alpha$, increases rapidly to large positive values at high sweep angles because of the large positive increases in I_Z/I_X and negative increases in $C_{l\beta}$. It has generally been found that the $(C_{n\beta})_{DYN}$ parameter is a better criterion for directional divergence than the static stability parameter $C_{n\beta}$. For example, it has been found possible to fly models with large negative values of $C_{n\beta}$ as long as $(C_{n\beta})_{DYN}$ remains positive. (See ref. 4.) In general, the information obtained from figure 7 indicates that Dutch-roll stability problems with highly swept configurations might be expected, but a directional-stability problem would probably not occur.

A comparison of directional stability characteristics for four highly swept glide-landing-type reentry configurations is shown in figures 8 and 9. Figure 8 shows $C_{n\beta}$ and $(C_{n\beta})_{DYN}$ for a delta-wing configuration having a relatively small fuselage and for a right-triangular-pyramid configuration. Both of these configurations have positive values of $C_{n\beta}$ over the angle-of-attack range and very large positive values of $(C_{n\beta})_{DYN}$. Such configurations should have no directional-stability problems. Figure 9 shows data for two reentry configurations of another type - that is, flat-bottom configurations having a large fuselage on top of the wing. This type of configuration generally has static directional instability at high angles of attack but $(C_{n\beta})_{DYN}$ remains positive. Flight tests of these models showed that they could be flown without any apparent divergent tendency at angles of attack at which $C_{n\beta}$ is negative, indicating that $(C_{n\beta})_{DYN}$ is the significant parameter in these cases.

These directional-stability parameters, however, are not the only factors affecting the directional characteristics. Lateral-control parameters can also be important, as shown by the data of figure 10. The upper part of the figure shows the ratio of yawing moment to rolling moment produced by aileron deflection $C_{n\delta_a}/C_{l\delta_a}$ for the two flat-bottom configurations having a large fuselage on top of the wing. One configuration has wing-tip vertical tails and the other configuration has a single center vertical tail. The data show that aileron deflection produced small favorable yawing moments over most of the angle-of-attack range for the model with the center tail but produced large adverse yawing moments for the model with the wing-tip tails. The large adverse aileron yawing moments are associated with the large induced loads produced on the vertical-tail surfaces by differential deflection of the ailerons. The plot at the bottom of the figure shows that the rudder effectiveness $C_{n\delta_r}$ remained about constant with angle of attack for the center-tail model, but $C_{n\delta_r}$ decreased rapidly with increasing angle of attack for the model with the wing-tip tails and became practically zero in the higher angle-of-attack range. At the lower angles of attack the adverse aileron yawing moments of the model with the wing-tip tails could be counteracted by rudder control, but at the higher angles of attack at which the rudder effectiveness dropped to zero, the adverse yawing moments produced large yawing motions and the model became uncontrollable. In order to make flights at these high angles of attack for research purposes, additional yawing control was provided in the form of an air jet located at the tail of the model.

The damping-in-roll parameters for four reentry configurations are shown in figure 11. These parameters were measured in forced-oscillation

tests about the body axis so that the parameter is in the form $C_{l_p} + C_{l_{\beta}} \sin \alpha$. The data were obtained for a value of the reduced frequency parameter $\omega b/2V$ of 0.1 and for an amplitude of $\pm 5^\circ$. The damping in roll for the thin delta wing with small fuselage on top decreases with increasing angle of attack and becomes unstable. This variation is similar to that of a wing alone. The damping in roll for the other three configurations remains stable with increasing angle of attack.

The calculated Dutch-roll stability for the configurations of figure 11 is presented in figure 12. The reciprocal of the time to damp to one-half amplitude is plotted against angle of attack. The configuration with the thin delta wing has negative Dutch-roll damping in the higher angle-of-attack range while the other three configurations remain stable over the angle-of-attack range. In model flight tests of these configurations, only the variable-geometry configuration was found to have satisfactory Dutch-roll stability without artificial stabilization over the angle-of-attack test range. For the other three configurations the damping was satisfactory at low angles of attack but decreased to unsatisfactory values as the angle of attack increased. At the higher angles of attack, the thin-delta-wing model was found to be unstable as predicted by the calculations. The flat-bottom configuration having a large fuselage on top of the wing was found to be slightly unstable rather than stable. Artificial stabilization was required at angles of attack above 15° for the thin-delta-wing model and above 25° for the other two models.

In order to provide artificial stabilization in the model flight tests, a roll damper has been used in most cases. Figure 13 shows the relative effect of roll and yaw dampers for reentry configurations of the type illustrated in the figure. The reciprocal of the calculated time to damp to one-half amplitude is plotted against values of the damping-in-roll derivative C_{l_p} , the damping-in-yaw derivative C_{n_r} , and the cross derivative C_{n_p} , yawing moment due to rolling velocity. These results show that an increase in $-C_{l_p}$ produced a large increase in the damping of the Dutch-roll oscillation whereas an increase in $-C_{n_r}$ produced only a very small increment of damping. Another point of interest here is that the derivative C_{n_p} also has a large effect on the damping. This effect can be significant in cases where the ailerons used for roll damping produce large yawing moments. In such cases the damper will produce C_{n_p} as well as C_{l_p} , and the C_{n_p} contribution will be stabilizing when the yawing moments are adverse and destabilizing when the yawing moments are favorable.

CONCLUDING REMARKS

It appears that on the basis of the lift-drag ratios and wing loadings now being considered for reentry configurations, the longitudinal characteristics for glide landings should be satisfactory. As for lateral stability, it appears that there should be no directional divergence problems for the reentry types now under study, but many of the configurations are likely to require a roll damper for satisfactory Dutch-roll damping at moderate and high angles of attack. Some configurations with wing-tip vertical tails may have control problems in the form of large adverse aileron yawing moments and low rudder effectiveness.

Although all of the reentry configurations studied to date have low-speed stability and control problems, most of the configurations could probably be developed into reentry vehicles capable of performing satisfactory glide landings.

REFERENCES

1. Weil, Joseph, and Matranga, Gene J.: Review of Techniques Applicable to the Recovery of Lifting Hypervelocity Vehicles. (Prospective NASA paper.)
2. Moul, Martin T., and Brown, Lawrence W.: Effect of Artificial Pitch Damping on the Longitudinal and Rolling Stability of Aircraft With Negative Static Margins. NASA MEMO 5-5-59L, 1959.
3. Brissenden, Roy F., Alford, William L., and Mallick, Donald L.: Flight Investigation of Pilot's Ability to Control an Airplane Having Positive and Negative Static Longitudinal Stability Coupled With Various Effective Lift-Curve Slopes. NASA TN D-211, 1960.
4. Johnson, Joseph L., Jr.: Wind-Tunnel Investigation of Low-Subsonic Flight Characteristics of a Model of a Canard Airplane Designed for Supersonic Cruise Flight. NASA TM X-229, 1960.

LIFT-DRAG RATIO FOR REENTRY VEHICLES
TRIMMED CONDITIONS

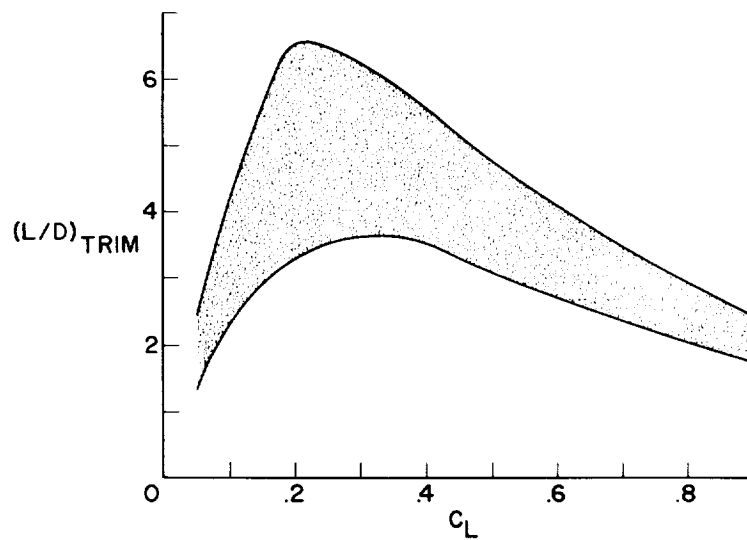


Figure 1

MAXIMUM LIFT-DRAG RATIO
TRIMMED CONDITIONS

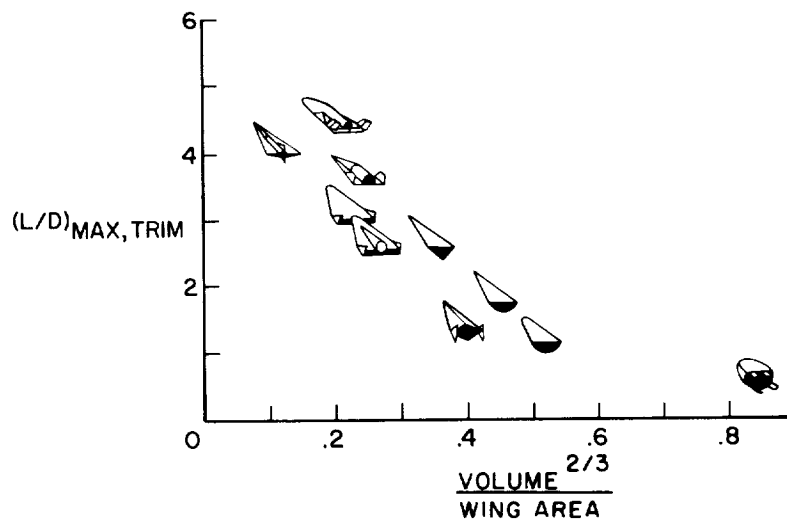


Figure 2

CONFIGURATIONS DESIGNED FOR HIGHER LIFT-DRAG RATIO TRIMMED CONDITIONS

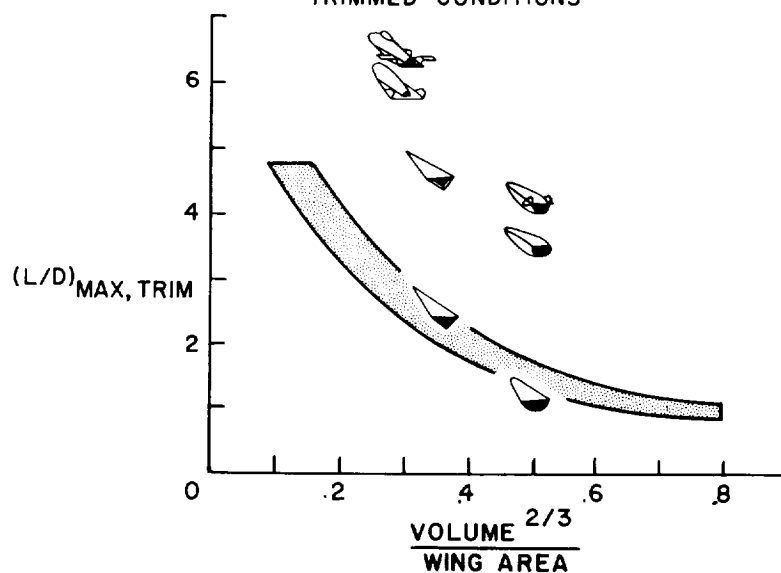


Figure 3

COMPARISON OF L/D FOR REENTRY VEHICLES AND RESEARCH AIRPLANES TRIMMED CONDITIONS

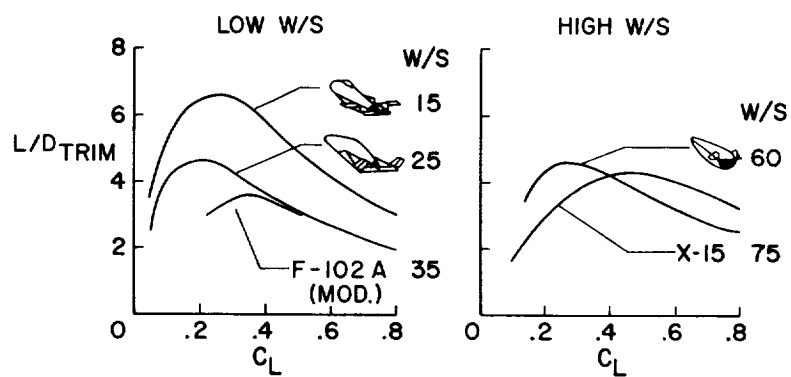


Figure 4

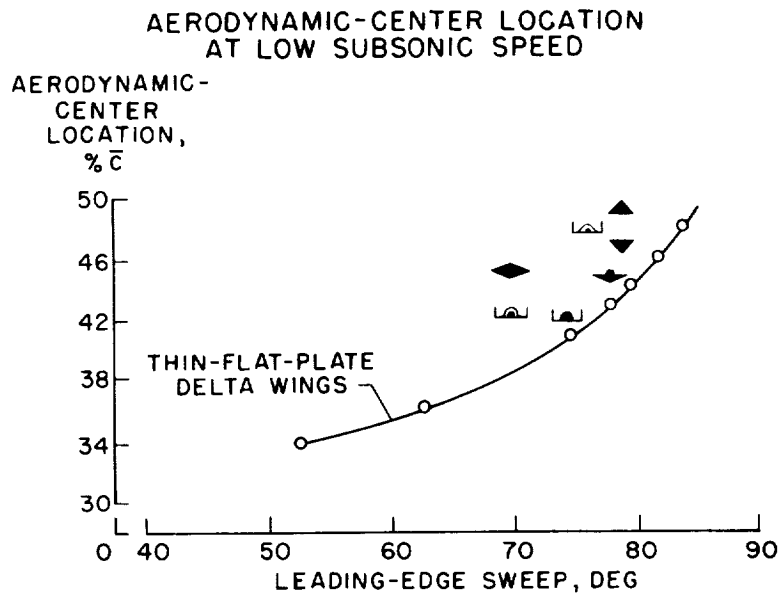


Figure 5

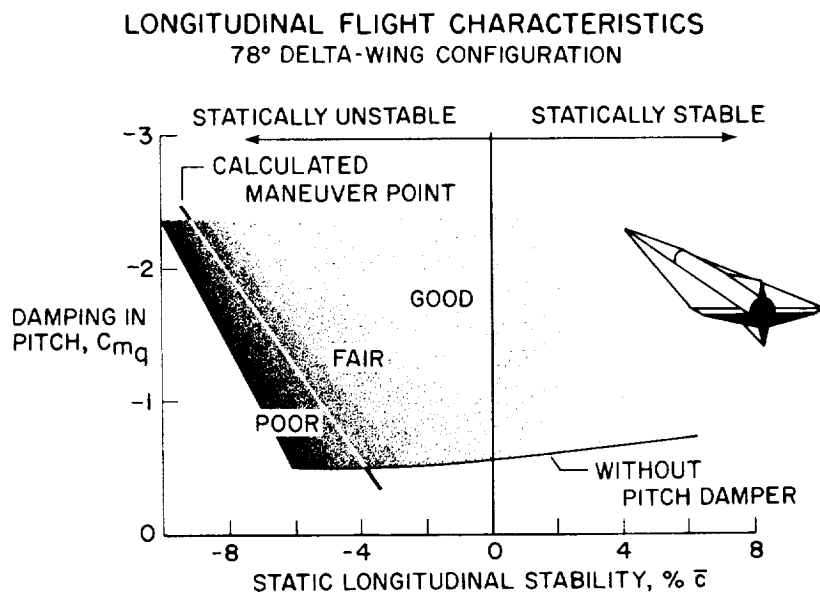


Figure 6

AERODYNAMIC AND INERTIA PARAMETERS OF THIN DELTA WINGS

$C_L = 0.60$

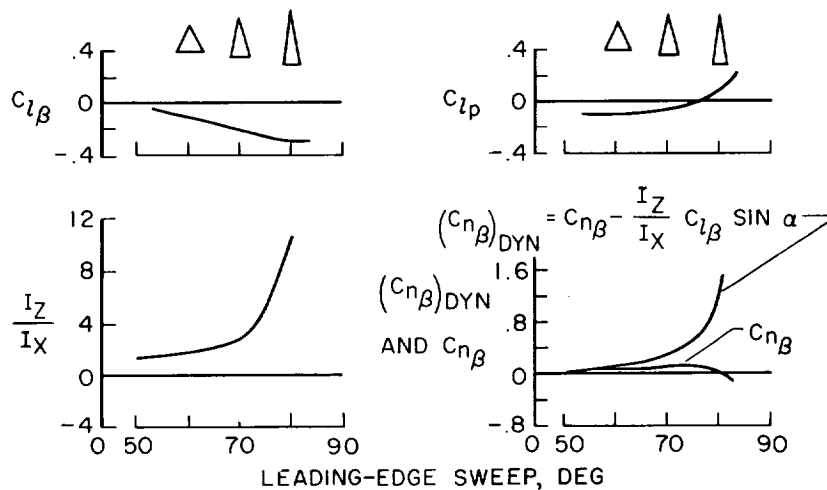


Figure 7

DIRECTIONAL-STABILITY PARAMETERS

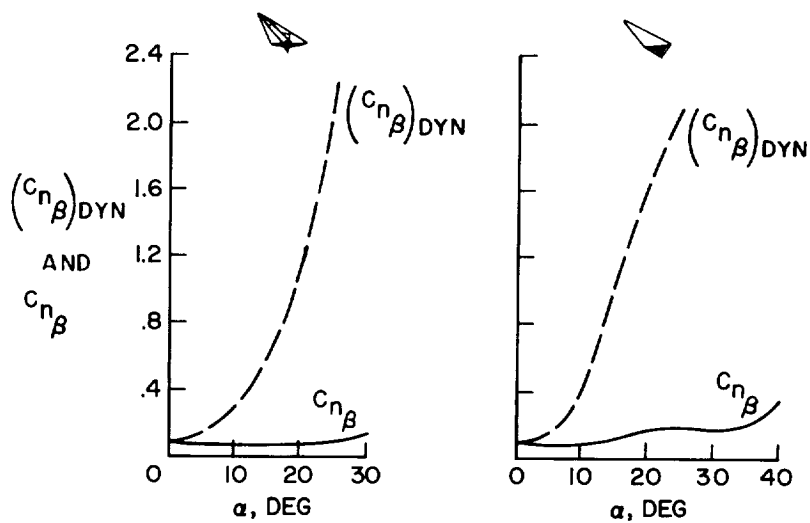


Figure 8

DIRECTIONAL-STABILITY PARAMETERS

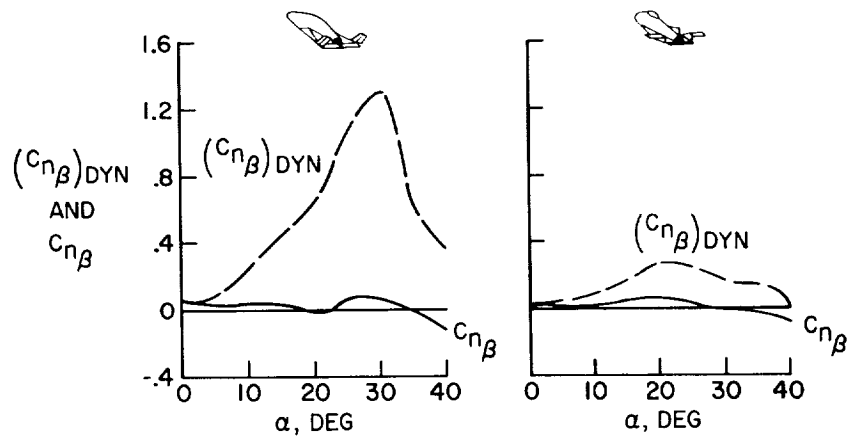


Figure 9

LATERAL-CONTROL PARAMETERS

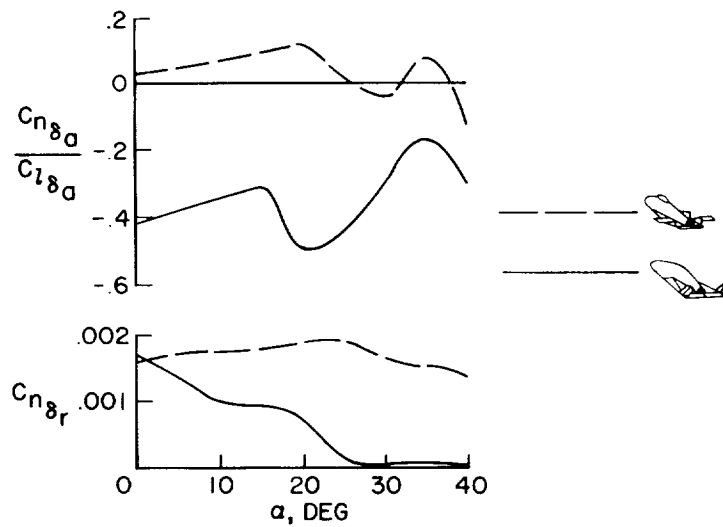


Figure 10

DAMPING-IN-ROLL PARAMETER

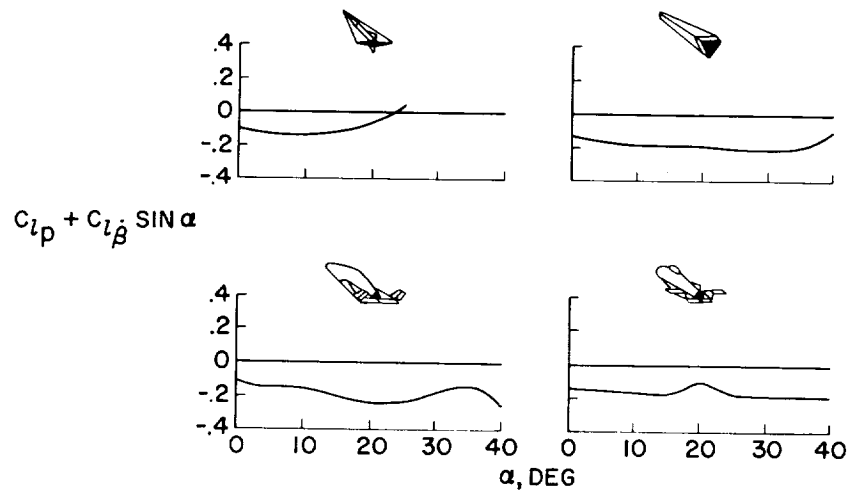


Figure 11

CALCULATED DUTCH-ROLL STABILITY

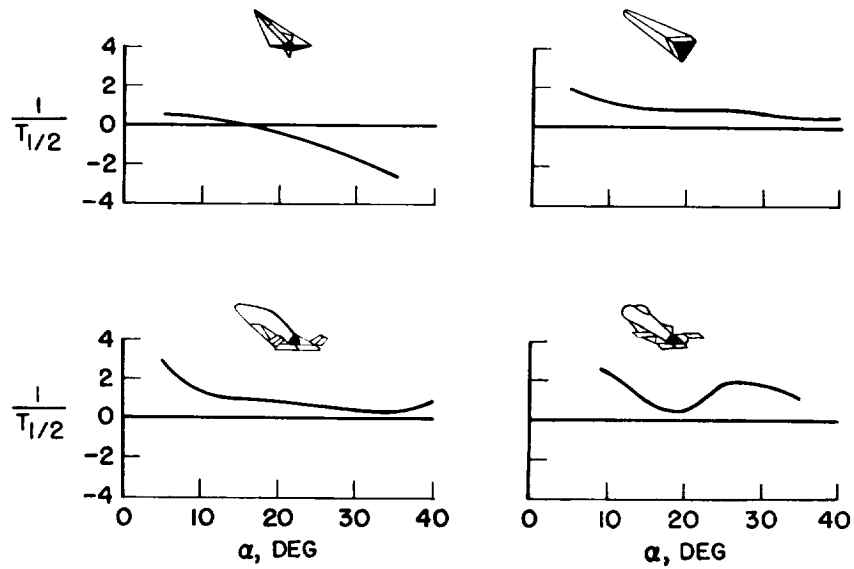


Figure 12

EFFECT OF C_{l_p} , C_{n_p} , AND C_{n_r} ON
CALCULATED DUTCH-ROLL STABILITY

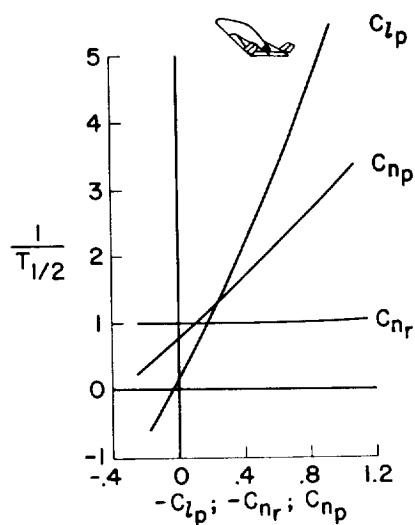


Figure 13

RADIO TRANSMISSION THROUGH THE PLASMA SHEATH
AROUND A LIFTING REENTRY VEHICLE

By Macon C. Ellis, Jr., and Paul W. Huber
Langley Research Center

SUMMARY

A review is made of the general concepts of radio-signal attenuation related to the plasma sheath around a hypersonic reentry vehicle. Plasma-attenuation experiments are described in which telemetry and microwave signals are transmitted through a plasma closely simulating that on a lifting hypersonic reentry vehicle.

Computations are made of the plasma conditions about simple-shaped bodies for the case of real-air, hypersonic, viscous flow. The peak plasma frequency occurs in the shock layer just outside the boundary layer for all cases except for sharp-nose bodies at low angle of attack. The magnitude of the peak plasma frequency at a given aft location is strongly dependent upon the bluntness of the body, and is dependent to a lesser extent on the location along the body. The variation of peak plasma frequency in the shock layer at an aft location for various lifting reentry trajectories is presented to show effects of lift coefficient, wing loading, altitude, and velocity. Plasma collision frequency is also shown to be much less than the plasma frequency during the critical (or peak plasma frequency) part of the flight. It is concluded that signal frequencies of the order of 10 kmc are required to avoid sudden loss of communications during the critical part of a lifting reentry hypersonic vehicle flight.

A brief discussion is given of the areas of research needed in order to understand the plasma-attenuation problem better as well as to indicate the methods of alleviating this problem.

INTRODUCTION

The problem of transmitting radio-frequency signals to and from a high-altitude hypersonic vehicle can be divided into three parts if those

components of the system within the vehicle and on the ground are excluded from consideration. These parts are:

1. Propagation of electromagnetic waves through the atmosphere.
2. Propagation of electromagnetic waves through the ionized gas or plasma surrounding the vehicle.
3. Radiation problems connected with the antenna coupling with the conducting gas.


The present paper is confined to part 2, the plasma-sheath problem, as simply shown in figure 1. The plasma sheath is depicted in the figure as the shaded region enclosed by the shock wave about the vehicle, and a transmitting antenna is indicated at a rearward station on the lower surface. The plasma-sheath problem can be further divided into two parts, namely, the determination of plasma conditions about the vehicle for given flight conditions and the determination of the effects of this plasma on the transmitted signal. The ability to analyze the second of these - the effect of the plasma on the signal - is in much better shape than the ability to specify the given plasma conditions, so that the prime problems at the present time appear to be aerodynamic and thermodynamic ones. However, first a review is given of the simplest theoretical approach in studying the effects of the plasma on the transmitted signal. The electromagnetic-radiation theory utilized is for plane-wave, linearly polarized, monochromatic radiation, and this radiation is assumed to interact with a homogeneous plasma in thermodynamic equilibrium. The primary parameters in this problem are shown in the lower part of the figure, where, first, the signal frequency is obviously the independent variable. Even though the plasma has no net charge outside some minimum distance (the Debye length) within the plasma, it contains free electrons and there exists a natural oscillation of an average free electron at the so-called plasma frequency. The concentration of these free electrons in the gas determines the plasma frequency f_p ; it is proportional to the square root of the electron density. The electron-collision frequency f_c is roughly the average number of times an average electron collides elastically with a heavier particle (ion or neutral). It is emphasized that these quantities are obtained from the state properties of the gas only - for example, temperature and density - and once these properties are known for the flow conditions about the given vehicle, then f_p and f_c are known. The last parameter shown in the lower part of figure 1 is simply the plasma thickness which the wave has to negotiate.

Various aspects of the factors in the plasma-sheath problem have been discussed in some detail in references 1 to 9. After first reviewing

the application of the simple plane-wave theory to transmission through a plasma, the present paper gives results from experiments designed to check this theory. Finally, results of calculations of the plasma conditions about lifting reentry vehicles are presented and estimates made of the transmission frequency required.

SYMBOLS

A	signal attenuation measured in decibels
C_L	lift coefficient, $\frac{L}{\frac{1}{2}\rho V^2 S}$
f	transmitted signal frequency, kmc
f_c	plasma electron-collision frequency, $\nu/2\pi$, kmc
f_p	plasma resonant frequency, kmc
$f_{p,MAX}$	maximum plasma resonant frequency attained during trajectory, kmc
h	altitude, ft
L	lift, lb
M	Mach number
p	absolute pressure, atm
r/R	radial distance from center line of body in terms of body radius
S	wing surface area, sq ft
T	temperature, °K
t	plasma thickness, ft
V	velocity, ft/sec
W/S	wing loading, lb/sq ft
x,y	distances along X- and Y-axes, respectively, ft



x/R	longitudinal distance from nose of body in terms of body radius
α	angle of attack, deg
λ	wavelength, cm
ν	electron-collision frequency (collisions per second), kmc
ρ	mass density, slugs/cu ft
ψ_1	streamline identification (fig. 7)


ATTENUATION CONCEPTS RELATED TO HYPERSONIC REENTRY

Plane-Wave Theory

The solution of the plane-wave attenuation equations for the transmitted portion of the incident signal is shown in figure 2 in the form of attenuation per unit plasma thickness, normalized to the plasma frequency, as a function of signal frequency and collision frequency, nondimensionalized to the plasma frequency. For the collision-frequency parameter f_c/f_p , low values may be regarded as corresponding to high altitudes and high values, to low altitudes. The curve for $f_c/f_p = 0.01$ (high altitude) shows a steep or sudden decrease in attenuation as the value of $f/f_p = 1$ is exceeded so that for values of f/f_p just greater than 1, attenuation is negligible. For intermediate values of f_c/f_p , no such sharp decrease in attenuation is indicated and attenuation values are moderately high over a large range of f/f_p which includes values on both sides of $f/f_p = 1$. For high values of f_c/f_p (low altitudes), low attenuation is seen for a still broader range of f/f_p . Lastly, it is to be noted that not only does attenuation decrease at high values of f/f_p , but also it decreases toward low values of f/f_p ; however, in this very low frequency range, atmospheric noise is a problem and large antennas may be required.

Attenuation Trajectories

Figure 3 shows attenuation trajectories of a possible lifting vehicle reentering from satellite velocity for one flight path and two fixed-frequency transmitters. In understanding this figure, one simple



fact needs to be known first - the fact that the plasma frequency at a point on a vehicle during reentry rises from low values at very high altitudes to a maximum at intermediate altitudes and then decreases again to low values during the latter part of the reentry. The change of attenuation during reentry is seen by following the arrows. The trajectory conditions are as follows: $W/S = 27 \text{ lb/sq ft}$, $C_L = 0.12$, and $f_{p,MAX} = 8 \text{ kmc}$. Estimates of plasma conditions throughout the trajectory have been made for an aft location where the antenna is assumed to be located. For the 3-kmc case, the signal frequency greatly exceeds the plasma frequency for the initial part of the reentry, becomes equal (at $f/f_p = 1$) at some point as the gas temperature around the vehicle increases and f_p increases, and becomes less than the maximum value of f_p of 8 kmc at some lower altitude of the reentry. For this case, attenuation is very high near the loop in the curve. As the reentry vehicle proceeds to still lower altitudes and the plasma sheath becomes cooler, f is still less than f_p , but collision frequencies, that is, f_c/f_p , increase at the lower altitudes; thus, the signal strength is regained more slowly than it was cut off. For the 10-kmc case, signal frequency is always higher than the plasma frequency and thus low attenuations are seen throughout the reentry. This latter case corresponds to the lower, right portion of figure 2, where other generalized attenuation curves for intermediate values of f_c/f_p would also lie.

PLASMA-ATTENUATION EXPERIMENTS

Plasma Production and Diagnosis

The question at this point is the applicability of the plane-wave theory to the plasma-sheath problem. For many years, physicists have used microwave techniques in plasma diagnostics; however, most of their cases have been highly specialized and the phenomena were fairly well known from other observations (refs. 10 to 13). Also, much effort has been spent in diagnosing plasma conditions in rocket-exhaust flames. In most of these cases, however, nonequilibrium effects leading to so-called "chemi-ionization" have been present to confuse the picture. (See ref. 14 which also contains an excellent review and bibliography.) In the Langley Gas Dynamics Branch, a fairly large flame has been developed in which nonequilibrium ionization effects are absent. This flame has been used as the plasma source for studying the electromagnetic-wave-plasma interaction problem in a joint program involving also the Langley Instrument Research Division. (See ref. 15.) In this system, cyanogen and oxygen are burned to produce the primary combustion products of carbon monoxide and nitrogen at a temperature over $4,000^\circ \text{K}$ after

cooling losses. In this flame, a significant ionization of these and small quantities of other products occurs, and this flame plasma closely simulates certain lifting reentry plasma conditions. Apparatus and methods have also been established which allow introduction and mixing into the flame of vaporized potassium, yielding ionization levels even higher than those for gas conditions at the nose of an ICBM. Results to be discussed here are only for the flame without potassium seeding. Earlier work on the combustion of cyanogen and oxygen and the thermodynamic properties of cyanogen are given in references 16 to 26.

Attenuation Results With Cyanogen Flame

Figure 4 shows, at the right, cross sections of the burner chamber and nozzle of the apparatus. (The nozzle is 7.5 cm in diameter.) The theoretical curve is from the generalized attenuation calculations in figure 2, where the value of f_c/f_p , for this case, is 1.5 and was determined from independent flame temperature measurements. The experiments cover a range of frequencies from 0.2 to 20 kmc. With regard to the 20-kmc result ($\lambda = 1.5$ cm) where the microwave beam is transverse to the flame as shown in the bottom sketch, the space resolution should be good since for this case the receiving horn "views" a small section of the flame. The check of the theory is good, within the experimental scatter. For the 8-kmc case ($\lambda = 3.75$ cm), however, the space resolution with this transverse beam is not as good and edge effects would be expected; these results consequently show poorer agreement with theory. For the 9.4-kmc case ($\lambda = 3.2$ cm), but for a different test configuration as shown by the middle sketch, the agreement is again satisfactory as might be expected since, for this case, the waveguide radiator transmits through a nearly flat plasma sheet and edge effects should be minimized. For the 0.2-kmc case ($\lambda = 137$ cm), it might be expected that near-field effects would invalidate the plane-wave theory; however, a surprisingly good check is noted. For this last case, the radiator is an axisymmetric dipole immersed in the flame as shown by the top sketch.

The flame has been used for a direct check of the theory for the results shown in figure 4; however, its principal use is to aid in the study of as many other related problems as possible - for example, antenna details, power loading, radiation patterns, harmonics, polarization, phase shift, and so forth. The result at 9.4 kmc is, as a matter of fact, for a peak power of about 40 kilowatts; thus, it is indicated that power loading up to this value has not affected the plasma which is at a possible flight condition. This last point should be taken as a preliminary result since calculations in progress by other staff members in the Gas Dynamics Branch are indicating possibilities of significant changes from the assumed equilibrium plasma model for short, high-power pulses.

PLASMA CONDITIONS FOR LIFTING REENTRY

Although the general applicability of plane-wave theory has certainly not been proved with finality, it can be applied to flight cases with some confidence. The relative magnitudes of plasma frequencies for several reentry flight cases are shown in figure 5. The plasma frequency is shown as a function of velocity for actual trajectories representing two flow extremes. For the illustrative ICBM case, plasma conditions have been calculated as those behind a normal shock. Normal-shock flow is certainly not typical for actual transmission conditions but this case is presented to show a most extreme case. The maximum value of f_p is seen to be so high that no transmitter is available to just exceed this frequency and thus to avoid intolerable attenuation. The plasma-frequency variation for a glide trajectory for normal-shock plasma conditions falls in a different range of f_p values from that for the ICBM but is pessimistically high. Also, if the overly optimistic assumption of flat-plate oblique-shock conditions for the glider is made, a too low bracketing number will be gotten. Thus, it can be seen that if the transmission frequency is to exceed the plasma frequency, signal frequencies somewhere between 1.0 and 60 kmc will be required. The problem is to determine where in this broad frequency range a realistic case will lie.

Oblique-Shock Plasma Conditions

For the actual vehicle, it is obviously not possible to calculate accurately the flow field pertinent to the transmission problem. The approach in the present paper is to consider the boundary-layer effects first, with the initial assumption of oblique-shock conditions at some typical station on the lower surface of the lifting hypersonic vehicle as those flow conditions just outside the boundary layer. There appears some justification of this simplified flow model, since the surface pressures for this case (at sufficiently high angles of attack) are about the same as those obtained by using modified Newtonian theory. With some prejudgment of critical flight conditions, a Mach number of 20 and an altitude of 200,000 feet is selected for the estimate of plasma conditions as shown in figure 6. Real-gas conditions for thermodynamic equilibrium have been used in calculating the flow; then, this flow was used as external conditions for the boundary-layer calculation. Real-gas oblique-shock conditions were calculated with the use of references 27 to 32. The laminar-boundary-layer calculations are similar, compressible solutions made on the IBM 704 electronic data processing machine by a program developed by Ivan E. Beckwith and Nathaniel B. Cohen of the Langley Research Center for a real gas using the correlation formula for density and transport properties of equilibrium dissociated

air presented in reference 33. All the calculations made for the present study were for zero pressure gradient. A wall temperature of $2,000^{\circ}\text{R}$ was used in the calculation; however, the peak plasma conditions were found to be insensitive to variations in wall temperature. The results, shown in figure 6 in the form of plasma frequencies as a function of y and α , indicate that peak plasma frequencies at low values of α are the result of heating due to large dissipation at the low external stream enthalpies but that at the highest values of α peak plasma frequencies occur in the outer shock layer.

Nose Bluntness Effects

In the simplified flow model just presented, constant conditions in the shock layer have been assumed, and no effects of thickness or bluntness were taken into account. The effects of bluntness are extremely important and must be recognized since the nose must be blunt in order to keep aerodynamic heating rates to acceptable values. Figure 7 shows a result from reference 34 of flow-field calculations for a spherical nose-cylinder body made by using a characteristics solution with real air in thermodynamic equilibrium. The most important basic fact to note is that, as shown by the streamlines in the sketch at the top of the figure, a large fraction of the flow in the shock layer has been processed by the normal or nearly normal shock at the nose. This means that a thick region of high-entropy air (highest at the body) envelopes the body and that this must be properly taken into account in calculating the flow. In the lower part of figure 7, the pressures p and temperatures T at two downstream stations are shown in the small plots merely to indicate the qualitative variations. To be noted is the large temperature increase in moving from the shock to the surface of the body. For a two-dimensional body with the same cross section, it is obvious that the shock is displaced outward and that the absolute thickness of the high-entropy layer will be even thicker. Thus, for a thick-wing three-dimensional flight configuration, the entropy layer will be proportionately thicker than shown here. It should be mentioned that two-dimensional perfect-gas characteristics solutions made for bodies with "sonic-wedge" noses also exhibit the increase in temperature near the surface, but include no real-gas effects. In figure 8, one of these two-dimensional solutions has been used and certain assumptions have been made to estimate a real-gas case. In the case shown in the figure, all the real-gas characteristics solutions available have been used (including unpublished results obtained from Avco Corp. and General Electric Co.) and, together with estimates from the perfect-gas solutions, estimates made of the entropy distribution between the shock and surface, where the surface value is that behind a normal shock. The pressures have been assumed to be unaffected by the other errors. The final result to be seen from figure 8 is that the maximum plasma frequency is about 10 kmc. The viscous boundary

layer is only about $1/3$ foot in thickness. Figure 9 shows also the distribution of the collision frequency in the shock layer. It is seen that at the peak value of f_p , f_c/f_p is a small value. This fact implies sharp signal cutoff when the signal frequency drops below the plasma frequency.

Estimates of Plasma Conditions for

Lifting Reentry Trajectories

Possible trajectories have been calculated and corresponding peak plasma frequencies estimated for a wing loading of 50 lb/sq ft and for the C_L values shown in figures 10 and 11. For these estimates, oblique-shock pressures and normal-shock entropies have been used. It is noted first that the somewhat more elegant estimate of figures 8 and 9 for 20,000 ft/sec ($M \approx 20$) checks the f_p values shown in figure 11 for $C_L = 0.12$, that is, about 10 kmc. The ticks on the f_p curves indicate that at velocities higher than these, the value of the collision-frequency parameter f_c/f_p is less than 0.1; thus, the plasma frequency can be regarded as the value of transmitted-signal frequency for sharp cutoff. The primary result to be noted is that a maximum exists and that its value increases with increasing lift coefficient for a given wing loading. The radar bands at the right show that even X-band radar (3.2 cm) will be cut off for a range of velocities around the maximum for the higher value of C_L . Figures 12 and 13 show similar results for a lower wing loading of 27 lb/sq ft. In figure 13, the maximum values are lower than those in figure 11, and for these cases it is seen that X-band frequencies will be transmitted since they are higher. In all the cases calculated, peak plasma frequencies were external to the boundary layer.

At this point, an estimate can be made of the signal frequency required for a critical flight condition. Figure 14 shows signal attenuation in decibels as a function of signal frequency. In this figure are shown curves for the combined attenuation effects of water vapor and oxygen which are integrated values through the atmosphere for the critical flight condition estimated by using reference 35. For the constant plasma frequency of 10 kmc, two plasma thicknesses are shown to allow for the uncertainty in estimation of the thickness of this peak plasma frequency region. In both cases, the signal frequency required to avoid both plasma attenuation and water-vapor absorption is seen to be between 11 and 13 kmc.

~~CONFIDENTIAL~~

CONCLUDING REMARKS

Engineering estimates have been made for certain requirements for radio-frequency transmission through the plasma sheath surrounding a lifting reentry hypersonic vehicle. First, it appears that the frequencies required to transmit downward and forward from the vehicle are of the order of 10 kmc. For such transmission, sharp leading edges would alleviate the magnitude of frequency required but their use is obviously precluded from heating considerations. Lastly, it appears that rearward locations of the antenna are most favorable.

In regard to more refined estimates of the transmission problem, it appears that increasing knowledge of gas characteristics, both equilibrium and nonequilibrium, makes feasible the effort to improve electromagnetic-wave-plasma interaction calculations utilizing more complete theory than the plane-wave model; however, inability to specify the plasma conditions accurately remains a deterrent. Although no serious doubts exist as to ability to select a frequency that will penetrate a given plasma, many detail problems still need study for the complete system - that is, high-power microwave-plasma interaction effects (where nonequilibrium plasma effects may be relieving factors), antenna breakdown, antenna patterns, acquisition, and so forth.

It must not be overlooked that other possibilities exist which may alleviate or even eliminate parts of the transmission problem. Placement of the antenna on the upper surface or rear of the configuration deserves serious consideration. For example, it appears possible that an antenna for a low-frequency system could be placed on the top surface near the rear of the vehicle so that it "looked" at a receiver obliquely through the wake. At some aft location in the wake, the plasma conditions would allow for transmission of the signal frequency through the wake. Much work is being done at the present time to estimate wake plasma conditions in regard to the radar cross section of wakes of high-speed objects. (See Avco-Everett Research Report 82.)

Consideration of the fact that the downward or forward direction of transmission of electromagnetic radiation may be a requirement for lifting vehicles, continuing investigations appear necessary for better solutions to the problem (other than the use of extreme frequencies). Such investigations should include (1) study of methods of quenching ionization or increasing electron collisions, (2) study of use of magnetic fields across the plasma, (3) study of possible systems utilizing the plasma as the radiator, and (4) study of use of ablating or consumable antennas.

~~CONFIDENTIAL~~

REFERENCES

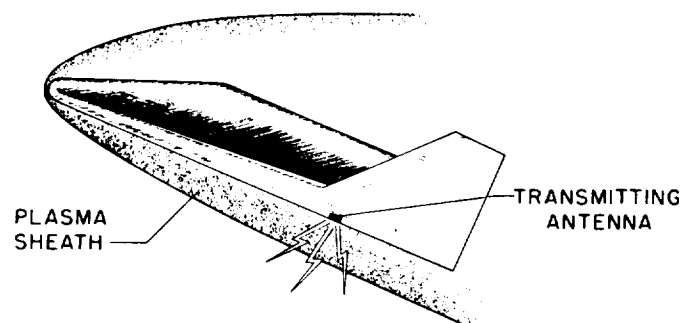
1. Goldberg, P. A.: Electrical Properties of Hypersonic Shock Waves and Their Effect on Aircraft Radio and Radar. Doc. No. D2-1997, Boeing Airplane Co., June 10, 1957.
2. Homic, Stephen G., and Phillips, Richard L.: Communicating With the Hypersonic Vehicle. Astronautics, vol. 4, no. 3, Mar. 1959, pp. 36-37, 92-98.
3. Sisco, W., and Fiskin, J. M.: Shock Ionization Changes EM Propagation Characteristics. Space/Aero., vol. 31, no. 3, Mar. 1959, pp. 66-70.
4. White, J. R.: Communication During Re-Entry Blackout. [Preprint] 963-59, presented at the Am. Rocket Soc. 14th Annual Meeting (Washington, D. C.), Nov. 1959.
5. Bleviss, Z. O.: Transmission of Electromagnetic Waves Through Ionized Air Surrounding Hypersonic Aircraft. Rep. No. SM-22965, Douglas Aircraft Co., Inc., Oct. 1957.
6. MacMurrough, Kilburn: Attenuation of Radio Waves as a Result of Boundary Layer Heating in Missiles Traveling at Supersonic Speeds. NAVORD Rep. 5816, Rev. 1 (NOTS TP 2163), U.S. Naval Ord. Test Station (China Lake, Calif.), Jan. 15, 1959.
7. Tischer, F. J.: Wave Propagation Through Ionized Gas in Space Communications. Rep. No. 59-34, Inst. Aero. Sci., Jan. 1959.
8. Lin, S. C.: A Rough Estimate of the Attenuation of Telemetering Signals Through the Ionized Gas Envelope Around a Typical Re-Entry Missile. Res. Rep. 74 (Contract No. AF04(645)-18), Avco-Everett Res. Lab., Feb. 1956.
9. Feldman, Saul: Trails of Axi-Symmetric Hypersonic Blunt Bodies Flying Through the Atmosphere. Res. Rep. 82 (Contract No. DA-19-020-ORD-4765), Avco-Everett Res. Lab., Dec. 1959.
10. Rudlin, Leonard: Preliminary Results of a Determination of Temperatures of Flames by Means of K-Band Microwave Attenuation. NACA RM E51G20, 1951.
11. Page, F. M., and Sugden, T. M.: A Note on Phase Shift of Microwaves in Flames Containing Free Electrons. GW/Atten/40, Univ. of Cambridge, 1958.

12. Schultz, D. L.: Research at the National Physical Laboratory on the Ionization Properties of Gases at High Temperatures. NPL/Aero/378, British A.R.C., June 1957.
13. Shuler, Kurt E.: A Microwave Investigation of the Ionization of Hydrogen-Oxygen and Acetylene-Oxygen Flames. Jour. Chem. Phys., vol. 22, no. 3, Mar. 1954, pp. 491-502.
14. Balwanz, W. W.: Ionization in Rocket Exhausts - A Survey. NRL Rep. 5193, U.S. Naval Res. Lab., Aug. 25, 1958.
15. Huber, Paul W., and Gooderum, Paul B. (With Appendix A by Theo E. Sims and Duncan E. McIver, Jr., and Appendix B by Joseph Burlock and William L. Grantham): Experiments With Plasmas Produced by Potassium-Seeded Cyanogen-Oxygen Flames for Study of Radio Transmission at Simulated Reentry Vehicle Plasma Conditions. (Prospective NASA paper.)
16. Conway, J. B., Wilson, R. H., Jr., and Grosse, A. V.: The Temperature of the Cyanogen-Oxygen Flame. Jour. American Chem. Soc. (Communications to Ed.), vol. 75, no. 2, Jan. 20, 1953, p. 499.
17. Conway, J. B., Smith, W. F. R., Liddell, W. J., and Grosse, A. V.: The Production of a Flame Temperature of 5000° K. Jour. American Chem. Soc. (Communications to Ed.), vol. 77, no. 7, Apr. 5, 1955, pp. 2026-2027.
18. Conway, J. B., and Grosse, A. V.: The Cyanogen-Oxygen Flame Under Pressure. Jour. American Chem. Soc., vol. 80, no. 12, June 20, 1958, pp. 2972-2976.
19. Doyle, William L.: High Temperature Propellant Systems Using the Liquids: Fluorine, Oxygen, Cyanogen and Hydrogen Cyanide. [Preprint] 736-58, presented at the Am. Rocket Soc. 13th Annual Meeting (New York), Nov. 1958.
20. Hord, Richard A., and Pennington, J. Byron: Temperature and Composition of a Plasma Obtained by Seeding a Cyanogen-Oxygen Flame With Cesium. NASA TN D-380, 1960.
21. Stevenson, D. P.: The Thermodynamic Functions of Cyanogen and the Cyanogen Halides. Jour. Chem. Phys., vol. 7, no. 3, Mar. 1939, pp. 171-174.
22. Thompson, H. W.: The Free Energy of Methyl Cyanide, and Equilibrium Constants of Some Related Reactions. Trans. Faraday Soc., vol. 37, no. 7, July 1941, pp. 344-352.

23. Thomas, N., Gaydon, A. G., and Brewer, L.: Cyanogen Flames and the Dissociation Energy of N_2 . Jour. Chem. Phys., vol. 20, no. 3, Mar. 1952, pp. 369-374.
24. Vallee, Bart L., and Bartholomay, Anthony F.: Cyanogen-Oxygen Flame. Analytical Chem., vol. 28, no. 11, Nov. 1956, pp. 1753-1755.
25. Welcher, Richard P., Berets, Donald J., and Sentz, Lemuel E.: Stability of Cyanogen. Ind. and Eng. Chem., vol. 49, no. 10, Oct. 1957, pp. 1755-1758.
26. Grosse, A. V., and Stokes, C. S.: Study of Ultra High Temperatures. AFOSR-TR-59-168, Res. Inst. of Temple Univ., Apr. 30, 1959.
27. Huber, Paul W.: Tables and Graphs of Normal-Shock Parameters at Hypersonic Mach Numbers and Selected Altitudes. NACA TN 4352, 1958.
28. Feldman, Saul: Hypersonic Gas Dynamic Charts for Equilibrium Air. AVCO Res. Lab., Jan. 1957.
29. Logan, J. G., Jr., and Treanor, C. E.: Tables of Thermodynamic Properties of Air From 3000° K to 10,000° K at Intervals of 100° K. Rep. No. BE-1007-A-3, Cornell Aero. Lab., Inc., Jan. 1957.
30. Fiskin, J. M., Roberts, C. A., and Sisco, W. B.: Equilibrium Composition of Air Below 3,000 Degrees Kelvin Including Electron Densities. Eng. Rep. No. LB-30078, Douglas Aircraft Co., Inc., Apr. 6, 1959.
31. Anon.: Normal and Oblique Shock Characteristics at Hypersonic Speeds. Eng. Rep. No. LB-25599 (ARDC TR-57-184, AD 116202), Douglas Aircraft Co., Inc., Dec. 31, 1957.
32. Trimpi, Robert L., and Jones, Robert A.: A Method of Solution With Tabulated Results for the Attached Oblique Shock-Wave System for Surfaces at Various Angles of Attack, Sweep, and Dihedral in an Equilibrium Real Gas Including the Atmosphere. NASA TR R-63, 1960.
33. Cohen, Nathaniel B.: Correlation Formulas and Tables of Density and Some Transport Properties of Equilibrium Dissociating Air for Use in Solutions of the Boundary-Layer Equations. NASA TN D-194, 1960.
34. Feldman, Saul: A Numerical Comparison Between Exact and Approximate Theories of Hypersonic Inviscid Flow Past Slender Blunt-Nosed Bodies. Res. Rep. 71, Avco-Everett Res. Lab., June 1959.

35. Wilcox, Charles H.: Effects of Atmospheric Attenuation on Reconnaissance Antenna Design. Sci. Rep. No. 1 (AFCRC-TN-57-197, Contract AF19(604)-1708) Res. Labs., Hughes Aircraft Co., Feb. 20, 1957. (Available from ASTIA as Doc. No. AD 117038.)

RADIO TRANSMISSION FROM HYPERSONIC VEHICLE



PLASMA TRANSMISSIBILITY PARAMETERS

- f SIGNAL FREQUENCY, KMC
- f_p PLASMA FREQUENCY, KMC
- f_c PLASMA ELECTRON-COLLISION FREQUENCY, KMC
- t PLASMA THICKNESS, FT

Figure 1

PLASMA ATTENUATION OF RADIO SIGNAL

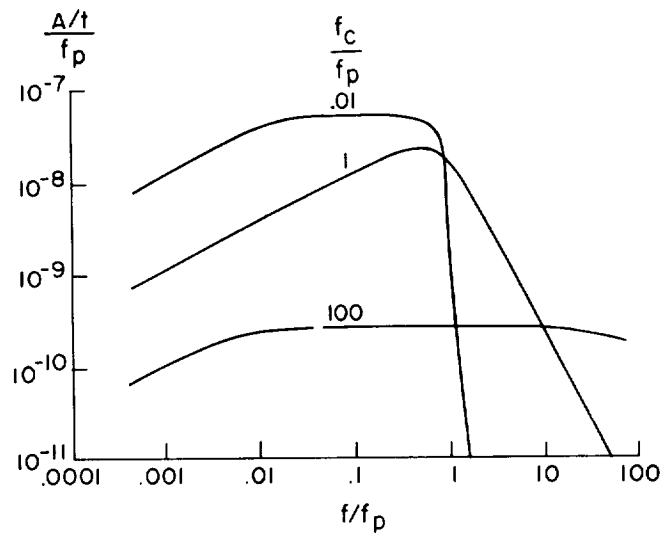


Figure 2

ATTENUATION TRAJECTORY FOR TWO SIGNAL FREQUENCIES

$$\frac{W}{S} = 27; C_L = 0.12; f_{p,MAX} = 8$$

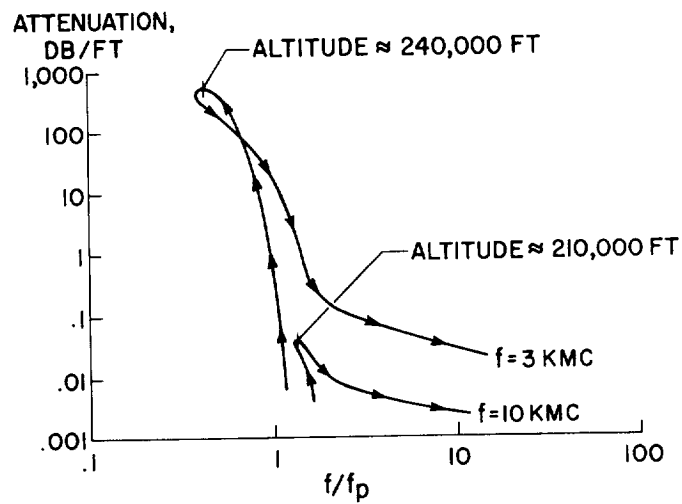


Figure 3

EXPERIMENTAL TRANSMISSION THROUGH CYANOGEN-FLAME PLASMA

$$f_p = 6.3 \text{ KMC}; \frac{f_c}{f_p} = 1.5; T_{\text{FLAME}} = 4150^\circ \text{K}$$

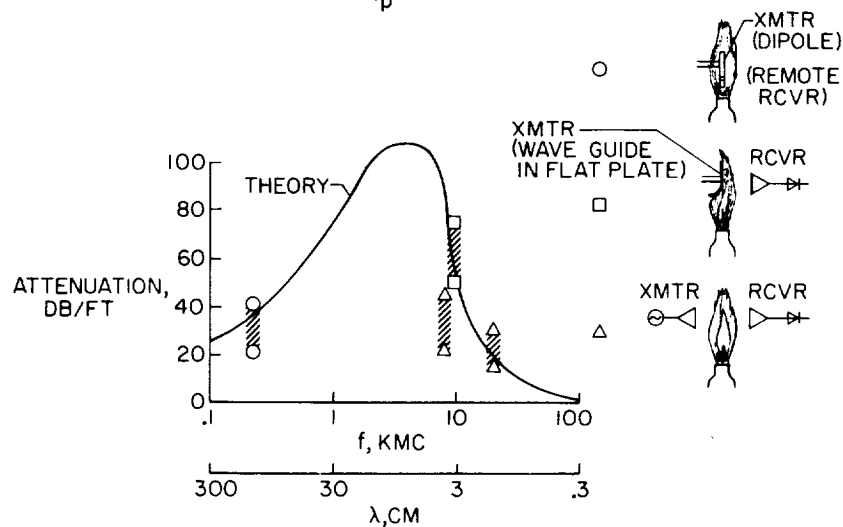


Figure 4

PLASMA-FREQUENCY VARIATION FOR SOME TYPICAL REENTRIES

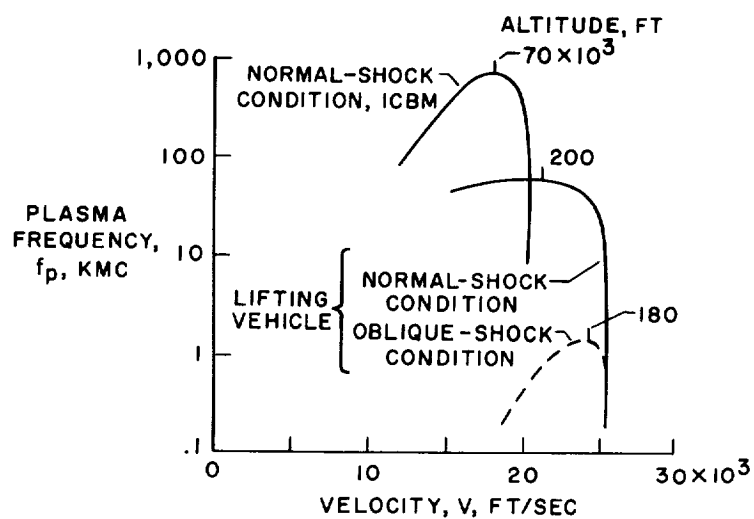


Figure 5

PLASMA FREQUENCIES IN REAL SHOCK LAYER FOR OBLIQUE SHOCK

REAL-GAS FLOW; $x = 25$ FT; $M = 20$; $h = 200,000$ FT

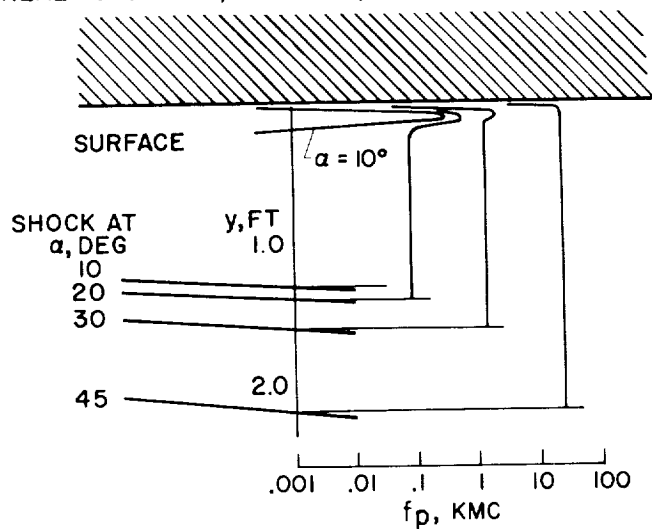


Figure 6

AXISYMMETRIC REAL-GAS CHARACTERISTICS SOLUTION FROM AVCO RESEARCH REPORT 71

$V = 17,500$ FT/SEC; $h = 60,000$ FT

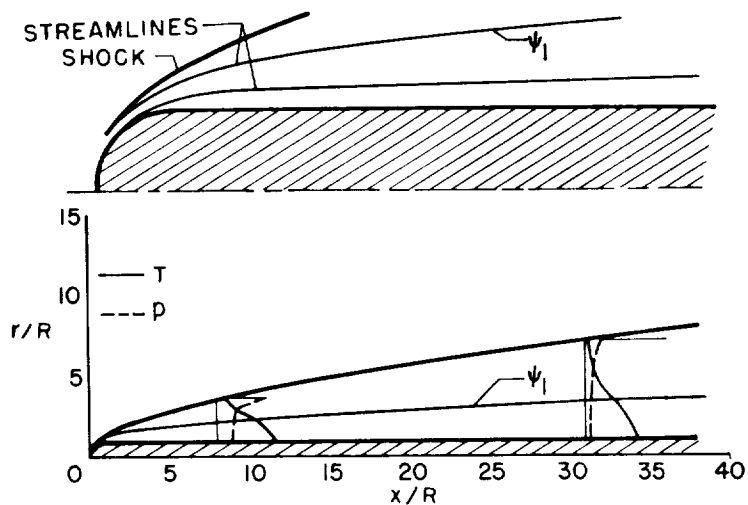


Figure 7

SHOCK-LAYER GAS CONDITIONS FOR LOWER SURFACE OF TWO-DIMENSIONAL SLAB

$M=20$; $\alpha=13^\circ$; $h=200,000$ FT; $x=25$ FT

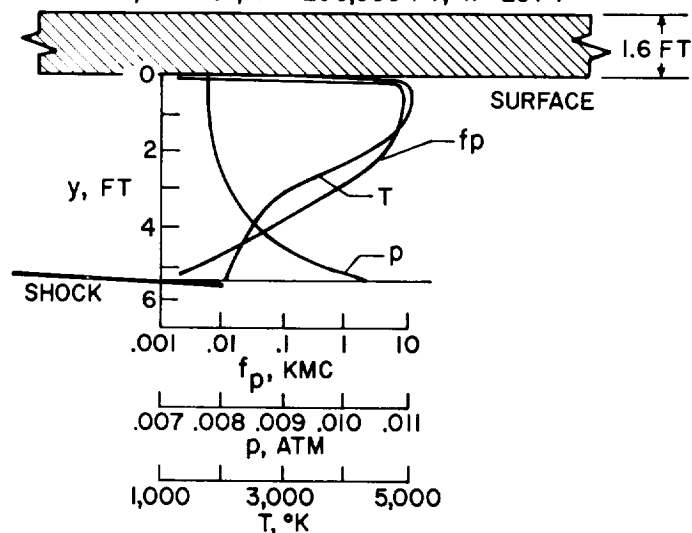


Figure 8

SHOCK-LAYER PLASMA CONDITIONS FOR LOWER SURFACE OF TWO-DIMENSIONAL SLAB

$M=20$; $\alpha=13^\circ$; $h=200,000$ FT; $x=25$ FT

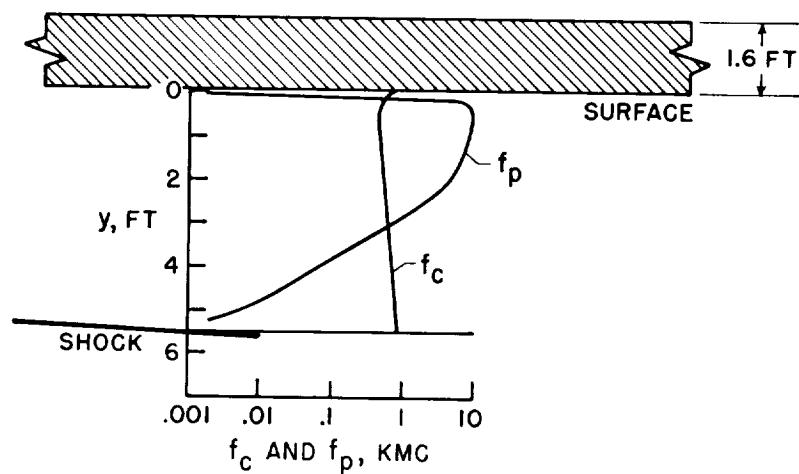


Figure 9

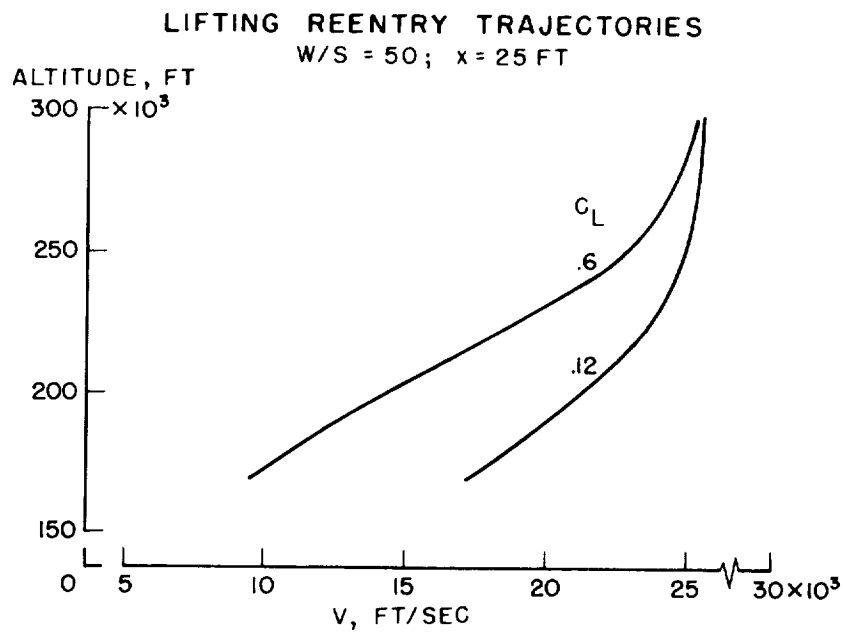


Figure 10

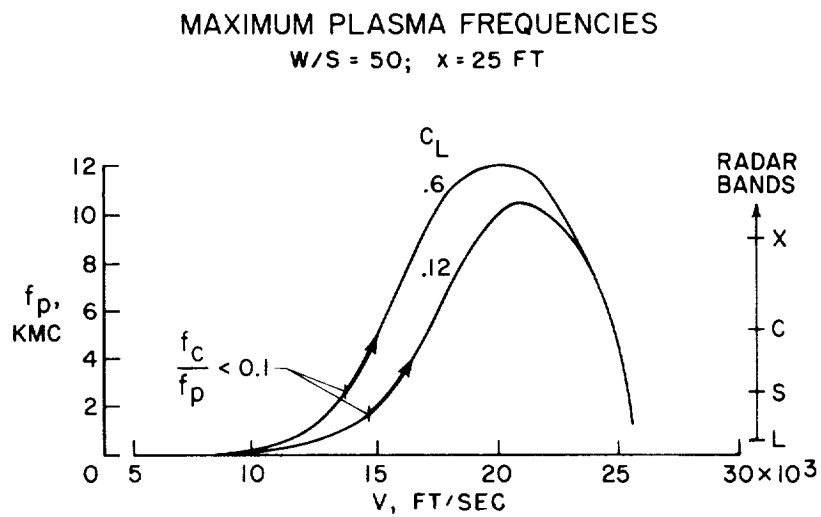


Figure 11

LIFTING REENTRY TRAJECTORIES

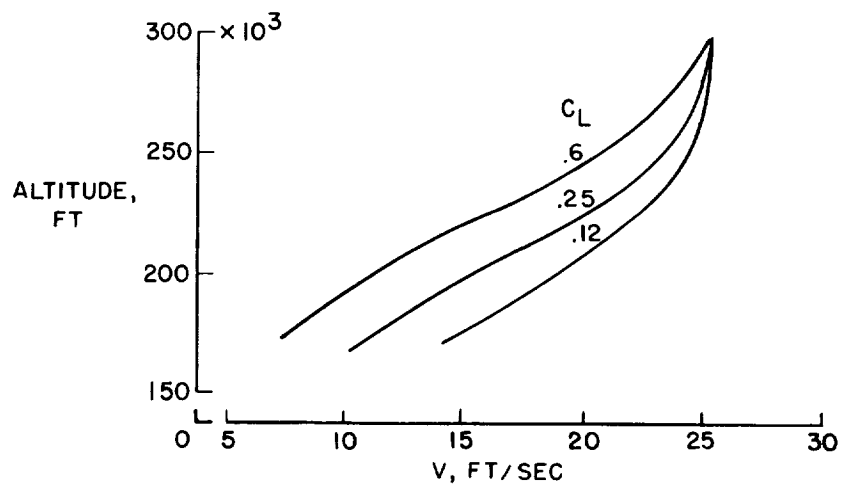
 $W/S = 27$; $x = 25$ FT

Figure 12

MAXIMUM PLASMA FREQUENCIES

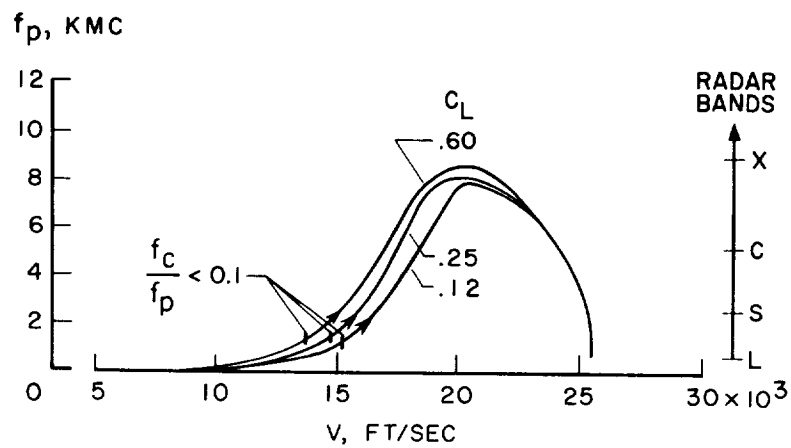
 $W/S = 27$; $x = 25$ FT

Figure 13

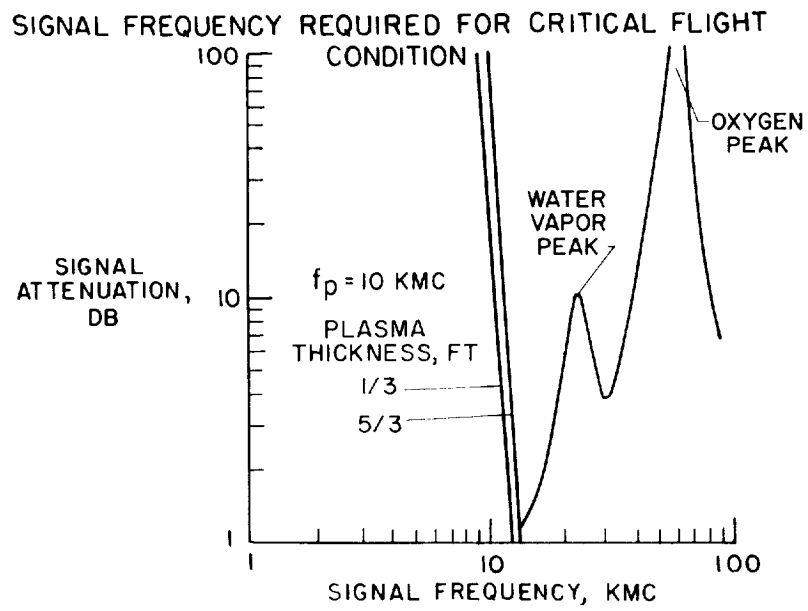


Figure 14

AEROELASTIC RESEARCH AT HIGH SPEEDS

By A. Gerald Rainey
Langley Research Center

23

SUMMARY

Some of the influence of a few configuration variables on various aeroelastic phenomena at low supersonic and hypersonic speeds has been indicated. It has been shown that a need still exists for a better definition of the limits of applicability of various aerodynamic theories. In addition, there are indications that flutter margins for Dyna-Soar-type vehicles will have to be carefully examined at hypersonic speeds as well as in the always troublesome transonic range.

INTRODUCTION

The rigorous requirements imposed on vehicles designed for manned reentry have created aerodynamic and structural conditions which have strained the boundaries of aeroelastic knowledge. New aeroelastic problems have arisen and, unfortunately, not many of the old problems have been abated by these new design requirements. In this paper, some of the current research pertinent to the aerodynamic aspects of these aeroelastic problems is reviewed.

Figure 1 has been prepared to aid in describing some of these problem areas and to delineate the particular aspects discussed in the present paper. The curves drawn in this figure represent typical conditions for a Dyna-Soar-type vehicle in terms of the parameters of most direct interest to the aeroelastician - dynamic pressure and Mach number. Two of the curves represent normal operating conditions - nominal ascent and descent - while the third boundary at higher levels of dynamic pressure represents a design condition for the reentry vehicle which arises from consideration of the requirements for recovering from an off-design trajectory. It is clear that the most severe aeroelastic environment imposed on the reentry vehicle itself is represented by these off-design conditions. The considerations that determine these limit conditions are very interesting. Briefly, at very high velocities these conditions are determined by consideration of the maximum structural

temperatures the vehicle is capable of sustaining, while at lower velocities a relatively arbitrary design limit in dynamic pressure is established. At the intersection of the constant-dynamic-pressure curve and the temperature-limit curve, the combination of maximum dynamic pressure and maximum structural temperatures could create a severe aeroelastic problem area. All along the constant-dynamic-pressure limit, the problems of classical flutter, panel flutter, control effectiveness, and, toward the lower end, transonic flutter must be examined carefully. For the complete booster-vehicle system, the design point for the problems of system stability and atmospheric induced loads occurs in the Mach number range from about 1.0 to 2.0.

The status of the panel flutter problem is discussed in reference 1. A cross section of the literature dealing with the analytical treatment of aeroelastic problems at high speeds is contained in references 2 to 12.

The transonic regime will not be treated at length. This is not to imply that there are no problems here. The critical aeroelastic design conditions may still occur in this speed regime. But in contrast to the other speed regimes, a broad background of experience exists in this area which has provided well-founded procedures for handling these problems (refs. 13 to 15).

This paper consists of two parts. The first part is concerned with some considerations of the structural dynamics problems associated with the boost phase - particularly the aerodynamics involved - and the second part is concerned with the problem of flutter at hypersonic speeds.

SYMBOLS

b	semichord
c	chord
c_n	section normal-force coefficient
E	Young's modulus
EI	bending stiffness
M	Mach number
q_D	dynamic pressure for divergence

t/c	thickness-chord ratio
V	velocity
x/l	distance from nose as a fraction of body length
α_{BASE}	angle of attack of booster at base
Λ	leading-edge sweep angle
μ	mass-ratio parameter
ω_{α}	natural frequency in pitch
ω_h	natural frequency in translation

AERODYNAMIC CONSIDERATIONS OF STRUCTURAL DYNAMICS

PROBLEMS DURING BOOST

Lifting Surfaces

One of the problems associated with the boosting of large winged payloads is the loss in static stability associated with the elastic deformations of the system. This is not a completely new problem in that several failures of transonic aerodynamic research rockets fired at NASA Wallops Station a number of years ago were traced to this phenomenon (ref. 16). Figure 2 illustrates some recent results obtained in a study of this divergence problem for aerodynamically unstable booster-vehicle systems. The curves in the figure are calculated stability boundaries in terms of the dynamic pressure at which the system becomes statically unstable as a function of the control-system effective stiffness. The results were obtained for a model supported in the manner shown schematically in figure 2. The booster is considered to be rigid and is restrained in pitch by a spring whose stiffness simulates the static aspects of a gimbaled engine control system.

The three curves in the figure represent stability boundaries calculated by means of low-aspect-ratio theory (ref. 3) for three different values of the distributed stiffness. The upper radial line represents the boundary along which a completely rigid vehicle would become unstable. The intermediate curve shows the boundary for a vehicle having a representative stiffness typical of Dyna-Soar designs. The lower calculated boundary may be compared with three measured points obtained at transonic speeds for wind-tunnel models whose stiffness was deliberately lowered to facilitate a study of these aeroelastic effects.

The deviation of the curve for the representative stiffness from the rigid boundary indicates that these static aeroelastic effects can intensify the already severe requirements on a control system for these aerodynamically unstable booster-vehicle systems. Some further information concerning this divergence problem is provided by the results contained in figure 3. These results summarize a part of a systematic study of the divergence characteristics of a series of slender delta wings which were supported as cantilever beams from the trailing edge (ref. 17). The results are plotted in terms of a nondimensional divergence parameter which for a given vehicle would simply be proportional to the dynamic pressure. The cantilever restraint corresponds to an infinitely stiff control system - that is, one which does not permit deviations from the guided path. In general, the relieving effects of Mach number associated with the reduction in bending moments about the trailing edge are predicted by the linear theories and by first-order piston theory. In the low supersonic range where this problem is of most direct concern, the lifting-surface theory agrees fairly well with the experiments. Tests on more highly swept delta wings (see ref. 17) indicate that the lifting-surface theory gives good predictions in the low supersonic Mach number range at sweep angles as high as 80° but begins to deviate seriously from the experimental results at a sweep angle of 85° .

Bodies of Revolution

The preceding results are primarily concerned with the aerodynamics associated with deformed lifting surfaces. Methods for handling the aerodynamics arising from elastic deformations of bodies of revolution are also a question of practical concern in the analysis of structural dynamics problems of boosters. Some results of a study of the pressure distributions on deformed and undeformed bodies of revolution are shown in figure 4. The results are presented in the form of the distribution of section normal-force coefficient for a deformed two-stage booster configuration as indicated at the top of the figure. The circular test points are for the deformed booster with its base at zero angle of attack so that the points represent a direct measure of the section normal-force coefficients produced by this particular deformation. As expected, most of this loading occurs on the conical portions of the body.

One commonly used method of incorporating aerodynamic forces in structural dynamics calculations is to measure the pressure changes with angle of attack on a rigid model and reduce these to local section derivatives which are then applied to angle-of-attack changes regardless of how they are produced - that is, whether by rigid-body motions or by deformations. In order to examine the validity of this procedure,

the square test points were predicted from data obtained from measurements on an undeformed body. Comparison of the circles and squares indicates that this commonly used procedure would have given a fair estimate of the loading due to the deformation of this body in all regions except in the region of the transition section where separation effects predominated.

The easily applied momentum theory (ref. 3) gives only a mediocre estimate of the loading due to the deformation of this body and, unfortunately, more accurate aerodynamic theories are not readily applied to deforming arbitrary bodies.

The preceding sections have been concerned with static aeroelastic effects. Of equal interest are the aerodynamics produced by oscillatory motions. Some information pertinent to this problem is contained in the results of a study of the flutter of cones which is briefly summarized in figure 5. This figure shows some flutter boundaries for a cone supported in such a way that it could pitch and translate on the sting-supported springs shown schematically in the figure.

The stability boundaries are plotted in terms of a nondimensional flutter-velocity index which contains the flutter velocity and density and certain properties describing the dynamics and geometry of the model. For a given vehicle this parameter can be thought of as being proportional to the equivalent airspeed or simply the square root of dynamic pressure. In figure 5, these flutter velocities are plotted as functions of the ratio of the translational frequency to the pitch frequency. These frequencies were varied by adjusting the two springs in the simple support system. The two sets of data points shown in the figure refer to experiments at Mach numbers of 2 and 7. It is interesting to note that both the experiments and the calculations indicate that the minimum flutter velocity is essentially independent of Mach number. This is probably due to the fact that the lift and moment characteristics of cones are relatively insensitive to Mach number changes. The flutter boundary is very sensitive to frequency ratio and illustrates once again the undesirable effects of coupled modes approaching each other.

The calculated curves in figure 5 follow the trends of the rather widely scattered experimental points fairly well. The Newtonian theory (refs. 8 and 9) at hypersonic speeds is directly applicable in aeroelastic analysis of deforming arbitrary bodies, but, unfortunately, the adaptation of a low supersonic cone theory by Von Karman (refs. 2, 8, and 9) to this more general case would be very difficult. Simple momentum theory is more amenable to aeroelastic analysis in this low supersonic speed range, but calculations based on this aerodynamic theory gave very poor agreement in this application.

FLUTTER AT HYPERSONIC SPEEDS

Mach Number Trends

In this section some of the recent information obtained in various studies of the flutter characteristics of lifting surfaces at hypersonic speeds will be considered. One fundamental consideration, of course, is the question as to the probability of a given vehicle encountering flutter at hypersonic speeds rather than at some lower Mach number. This question can be discussed with the aid of figure 6 which shows the variation of the flutter-velocity index with Mach number for a few structural and aerodynamic configurations. It may be recalled that the flutter-velocity index for a given vehicle may be thought of as being proportional to the equivalent airspeed. In addition, it should be pointed out that the use of the structural characteristics, such as mass and natural frequency, in this normalized velocity parameter tends to eliminate structural effects from the data so that the aerodynamic effects of configuration changes are more readily apparent.

All the curves exhibit a minimum flutter speed in the transonic range; however, for two of the configurations there is a trend toward low flutter speeds at the higher Mach numbers. The scatter in flutter points for one of the configurations shown is attributed to the ill-behaved structure used which consisted of a thin flat plate of low aspect ratio clamped along its root to the inside of a cylindrical test section. Similar trends toward low flutter speeds have been obtained by the Cornell Aeronautical Laboratory under an Air Force sponsored project.

Trend studies of this nature merely serve as a guide in determining where emphasis should be placed in studying the flutter margins of a vehicle. For a Dyna-Soar-type vehicle, which is required to be flutter free at constant equivalent airspeed over a wide range of Mach number, the flutter characteristics must be examined carefully at hypersonic speeds as well as at transonic speeds.

Aerodynamic Effects of Some Geometric Variables

The uncertainties regarding flutter behavior at hypersonic speeds have provided the motive for a variety of investigations. Figures 7 and 8 summarize different parts of a program designed to provide a better understanding of these hypersonic aeroelastic problems.

Leading-edge-bluntness effects.— Figure 7 illustrates some results obtained in a study of the effects of leading-edge bluntness at a Mach number of 7. The flutter boundaries are presented in the form of the

flutter-velocity index as a function of leading-edge radius for a series of systematically blunted models supported in such a manner as to permit a rigid-body pitch-flapping type of flutter mode. The models were square in planform and the thickness-chord ratio increased with bluntness so that the included angle between the flat sides remained constant at 10° .

The experimental results shown in figure 7 indicate that the effects of blunting the leading edge are slightly beneficial inasmuch as the flutter speed is increased. For the bluntest model, static divergence rather than flutter was encountered. This fact indicates that the effect of the blunting was probably due to a forward shifting of the center of pressure. The piston-theory result is shown for comparison with the experimental results of figure 7 primarily to illustrate one of its limitations, namely, that even the smallest amount of this type of blunting produces serious violations of its assumptions. Attempts at incorporating the more realistic Newtonian theory show some improvement; however, the lack of agreement in trend for the various theories is somewhat disconcerting. The curve labeled "piston-Newtonian theory" was obtained by applying Newtonian theory to the cylindrical leading edge and piston theory over the remainder of the airfoil in the manner described in reference 2. Perhaps an adaptation of blast-wave theory to this problem might provide an improvement.

Sweepback effects.- Another geometrical consideration of practical concern is the effect of sweepback. A study of the hypersonic flutter characteristics of a series of slender delta wings is summarized in figure 8 (ref. 18). These models, varying in leading-edge sweep angle from 60° to 80° , were supported in such a manner that the flutter mode contained rigid-body pitch and flapping motions.

The flutter boundaries are plotted in terms of the flutter-velocity index as a function of leading-edge sweep angle. In this case, the flutter velocities have been adjusted analytically for a systematic variation of frequency ratio which tended to obscure the aerodynamic effects of sweepback. In addition to variations in the sweepback angle, the models tested also varied systematically in the ratio of flapping frequency to pitch frequency. Since this variation in frequency ratio tended to obscure the aerodynamic effects of sweepback, the values of the flutter-velocity index shown in figure 8 have been adjusted analytically so that they would apply to a case of constant frequency ratio. This was accomplished by multiplying the velocity-index values for each model by the ratio of the value calculated for that model at the frequency ratio of the 70° wing to the value calculated for that model at its own frequency ratio. The uncoupled frequency ratio for the 70° wing was 0.592 and varied over the range from 0.488 for the 60° wing to 0.690 for the 80° wing.

Examination of these adjusted experimental points in figure 8 indicates that the aerodynamic effects of sweepback are very small for this case. The piston-theory results show surprisingly good agreement considering its two-dimensional character. The linear theory shows a trend toward increasing flutter velocities with increasing sweep - a trend which is contradictory to the experimental results.

CONCLUDING REMARKS

Some of the influence of a few configuration variables on various aeroelastic phenomena at low supersonic and hypersonic speeds has been indicated. It has been shown that a need still exists for a better definition of the limits of applicability of various aerodynamic theories. In addition, there are indications that flutter margins for Dyna-Soar-type vehicles will have to be carefully examined at hypersonic speeds as well as in the always troublesome transonic range.

REFERENCES

1. Kordes, Eldon E., Tuovila, Weimer J., and Guy, Lawrence D.: Flutter Research on Skin Panels. (Prospective NASA paper.)
2. Morgan, Homer G., Runyan, Harry L., and Huckel, Vera: Theoretical Considerations of Flutter at High Mach Numbers. Jour. Aero. Sci., vol. 25, no. 6, June 1958, pp. 371-381.
3. Bisplinghoff, Raymond L., Ashley, Holt, and Halfman, Robert L.: Aeroelasticity. Addison-Wesley Pub. Co., Inc. (Cambridge, Mass.), c.1955, pp. 418-420.
4. Sauer, Robert: Introduction to Theoretical Gas Dynamics. J. W. Edwards (Ann Arbor, Mich.), 1947, pp. 74-77.
5. Liepmann, H. W., and Roshko, A.: Elements of Gasdynamics. John Wiley & Sons, Inc., c.1957, pp. 233-235.
6. Van Dyke, Milton D.: A Study of Second-Order Supersonic Flow Theory. NACA Rep. 1081, 1952. (Supersedes NACA TN 2200.)
7. Dorrance, William H.: Nonsteady Supersonic Flow About Pointed Bodies of Revolution. Jour. Aero. Sci., vol. 18, no. 8, Aug. 1951, pp. 505-511, 542.
8. Grimminger, G., Williams, E. P., and Young, G. B. W.: Lift on Inclined Bodies of Revolution in Hypersonic Flow. Jour. Aero. Sci., vol. 17, no. 11, Nov. 1950, pp. 675-690.
9. Lees, Lester: Hypersonic Flow. GALCIT Pub. No. 404, 1955.
10. Van Dyke, M. D.: A Study of Hypersonic Small-Disturbance Theory. NACA Rep. 1194, 1954. (Supersedes NACA TN 3173.)
11. Savin, Raymond C.: Application of the Generalized Shock-Expansion Method to Inclined Bodies of Revolution Traveling at High Supersonic Airspeeds. NACA TN 3349, 1955.
12. Zartarian, Garabed, Hsu, Pao Tan, and Ashley, Holt: Dynamic Airloads and Aeroelastic Problems at Entry Mach Numbers. Paper No. 60-32, Inst. Aero. Sci., Jan. 1960.
13. Rainey, A. Gerald: Interpretation and Applicability of Results of Wind-Tunnel Flutter and Control Surface Buzz Investigations. Rep. 219, AGARD, North Atlantic Treaty Organization (Paris), Oct. 1958.

14. Head, A. L., Jr.: A Philosophy of Design for Flutter. Proc. Nat. Specialists Meeting on Dynamics and Aeroelasticity (Fort Worth, Texas), Inst. Aero. Sci., Nov. 1958, pp. 59-65.
15. Mahaffey, P. T.: The Use of Low Speed Flutter Model Tests and Trend Curves To Establish Flutter Boundaries. Proc. Nat. Specialists Meeting on Dynamics and Aeroelasticity (Fort Worth, Texas), Inst. Aero. Sci., Nov. 1958, pp. 66-68.
16. Arbic, Richard G., White, George, and Gillespie, Warren, Jr.: Some Approximate Methods for Estimating the Effects of Aeroelastic Bending of Rocket-Propelled Model-Booster Combinations. NACA RM L53A08, 1953.
17. Woolston, Donald S., Gibson, Frederick W., and Cunningham, Herbert J.: Some Divergence Characteristics of Low-Aspect-Ratio Wings at Transonic and Supersonic Speeds. (Prospective NASA paper.)
18. Miller, Robert W., and Hannah, Margery E.: An Investigation of the Effects of Sweepback on the Flutter of Delta Surfaces at Mach Number 7.0. (Prospective NASA paper.)

BOUNDARIES FOR DISCUSSION OF AEROELASTIC PROBLEM AREAS

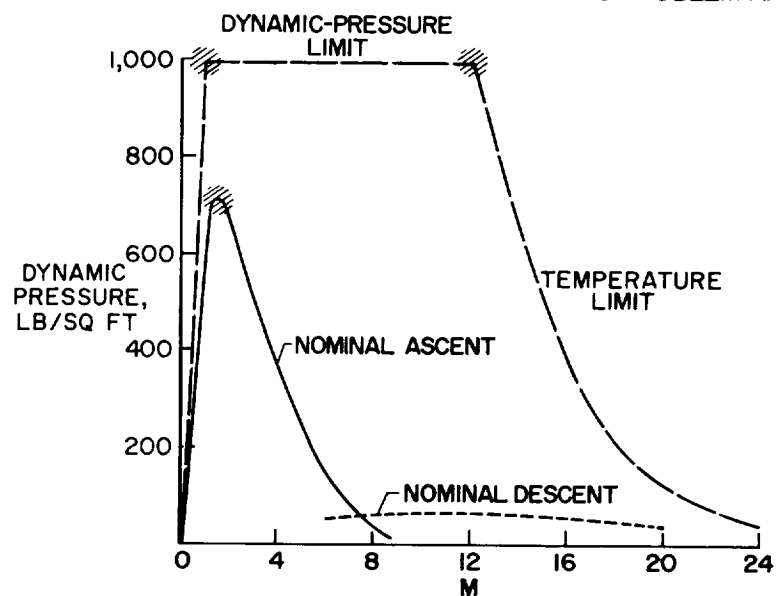


Figure 1

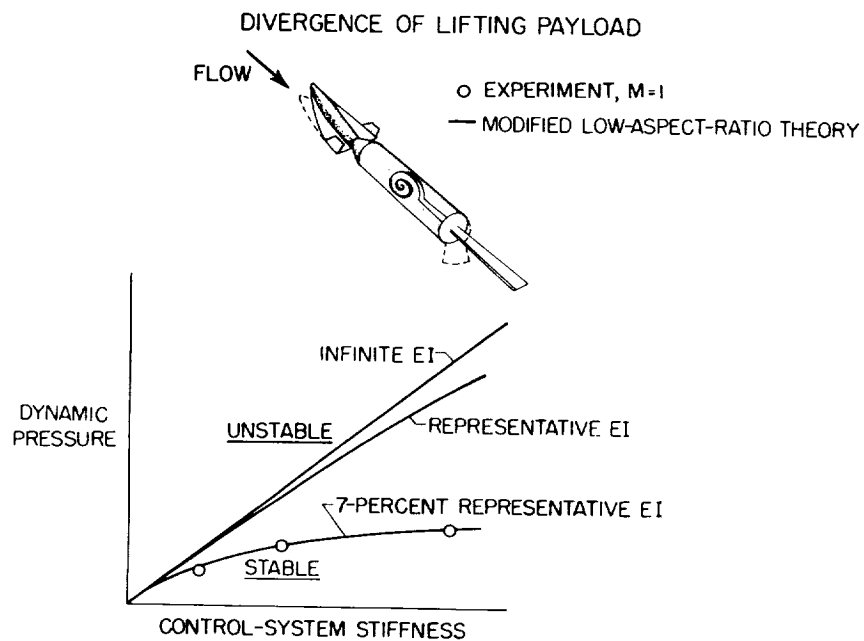


Figure 2

DIVERGENCE OF SLENDER DELTA WINGS $\Lambda = 70^\circ$

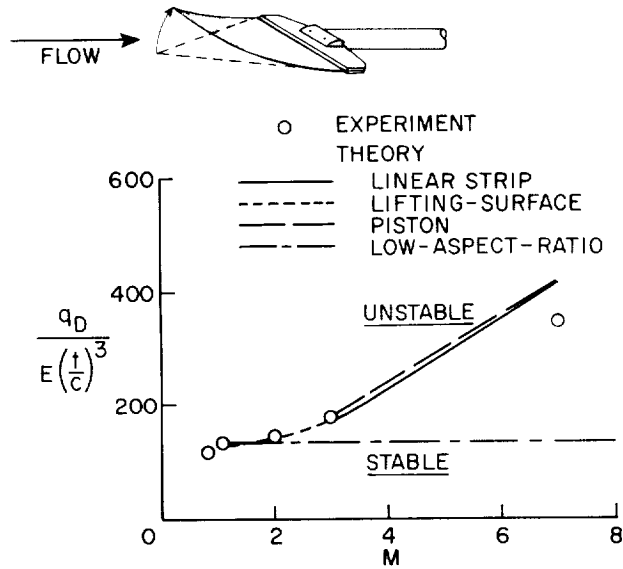


Figure 3

LOADING DUE TO DEFORMATION $M = 1.64$

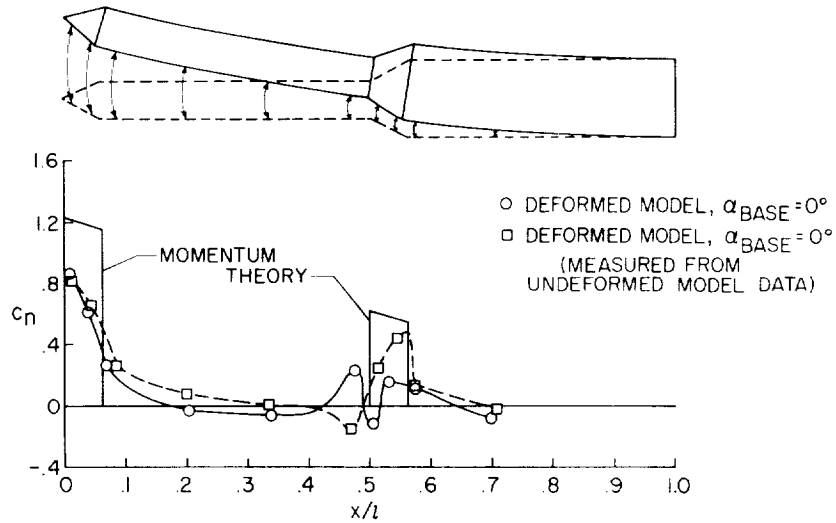


Figure 4

FLUTTER OF CONES

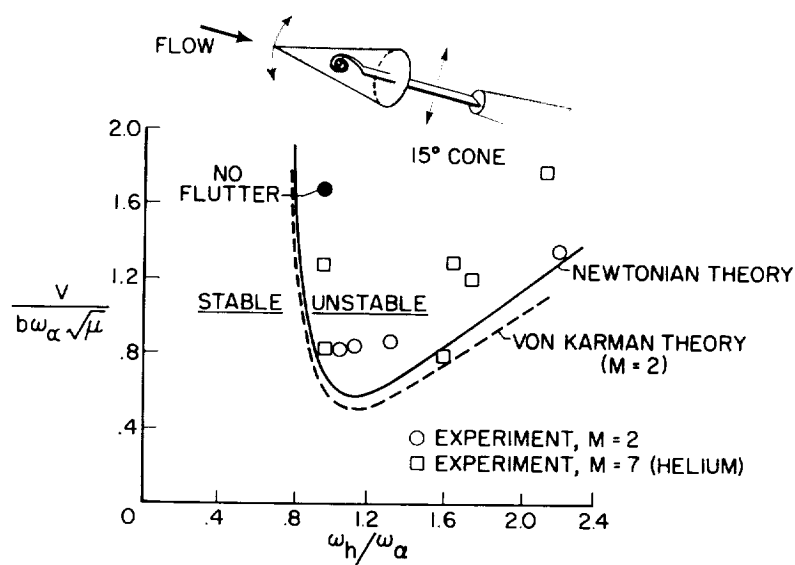


Figure 5

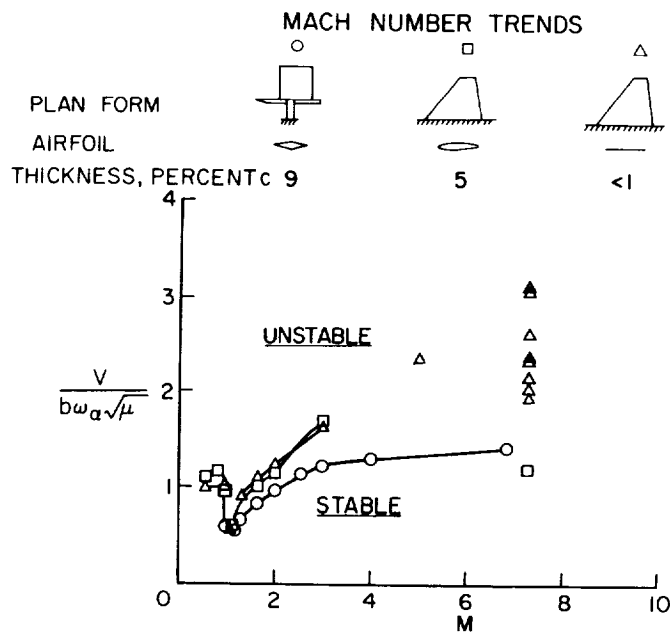


Figure 6

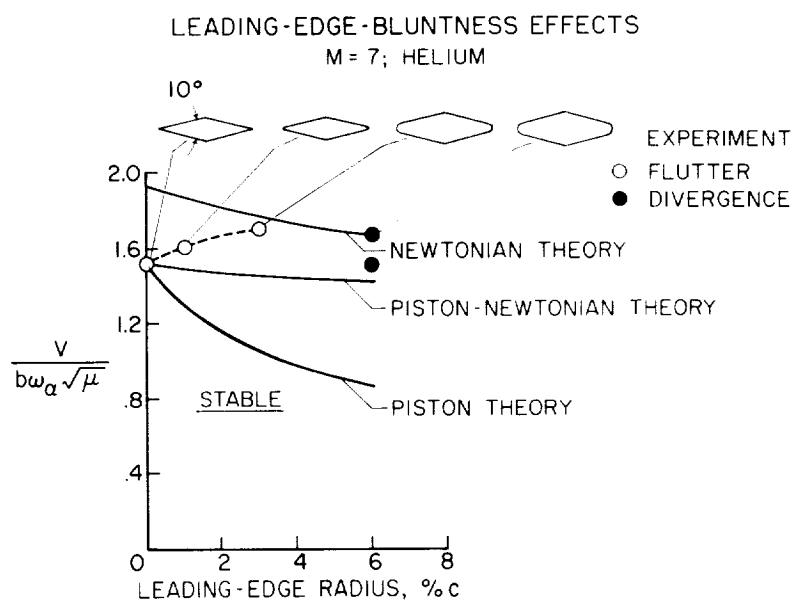


Figure 7

FLUTTER OF SLENDER DELTA WINGS
M = 7; HELIUM; 5% THICK, DOUBLE-WEDGE AIRFOIL

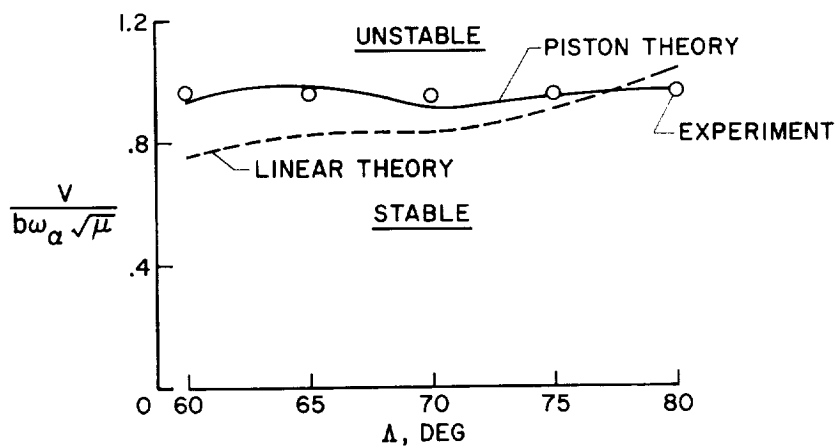


Figure 8

EXPERIMENTAL HYPERSONIC FLUTTER TRENDS
AND PISTON-THEORY COMPARISONS

By Richard P. White, Jr.,
Cornell Aeronautical Laboratory, Inc.

and Dale E. Cooley,
Wright Air Development Division

INTRODUCTION

24

It will soon be necessary to establish flutter prevention design criteria in the hypersonic speed regime, as well as in the lower speed regimes, for hypersonic boost glide and reentry flight vehicles such as the Dyna-Soar. For several years, there have been a number of unsteady-aerodynamic-force theories suitable for use in predicting the flutter characteristics of such lifting surfaces in the supersonic speed regime. In the past few years, however, piston theory, due to its mathematical simplicity, adaptability, and ease of application, has been more widely used than any of the others to calculate the unsteady aerodynamic forces in a supersonic airstream. On the basis of rather limited comparisons with experimental data, flutter results using piston-theory aerodynamics have been generally considered to be adequate above a Mach number of 3.0. The accuracy and applicability of the theory, however, have not been verified conclusively by comparison with a comprehensive and systematic set of experimental results.

The Wright Air Development Division (WADD) recognized the need for such a set of experimental data and in 1958 initiated a series of test programs specifically for this purpose. The programs conducted thus far have used simple, wall-mounted wing models of rectangular planform so that the mass, elastic, and dynamic properties could be easily and accurately defined. The first of these programs was recently completed by the Massachusetts Institute of Technology (M.I.T.) in the Mach number range of 1.5 to 5.0. The results of this program are reported in reference 1. Cornell Aeronautical Laboratory (CAL), in a second program, obtained flutter data with similar models in the Mach number range of 5 to 7. These data were collected during a series of tests in the E-2 hypersonic blowdown tunnel at Arnold Engineering Development Center. This paper will present primarily some of the results obtained by Cornell Aeronautical Laboratory in the latter program.

SYMBOLS

b	model semichord, in.
g_h	structural damping coefficient in the bending degree of freedom (nondimensional)
g_p	structural damping coefficient in the pitch degree of freedom (nondimensional)
g_R	structural damping coefficient in the roll degree of freedom (nondimensional)
g_α	structural damping coefficient in the torsion degree of freedom (nondimensional)
V	velocity, ft/sec
μ	wing-to-air-mass ratio (nondimensional)
ω_F	flutter frequency, radians/sec
ω_R	roll frequency, radians/sec
ω_p	pitch frequency, radians/sec
ω_α	torsional frequency, radians/sec
M	Mach number
N	normalized value
Subscript:	
REF	reference value

DISCUSSION

Figure 1 shows pictures of both the flexible cantilever-type model and the semirigid type used by CAL in the hypersonic speed regime. The cantilever models were used to investigate the effects of Mach number and the semirigid models were used primarily to study the effects on flutter of parameter variations such as elastic axis, center of gravity, frequency ratio, thickness ratio, radius of gyration, and wing-to-air-mass ratio. The basic models, cantilever and semirigid, were of square

planform having a center of gravity at the 50-percent chord and the elastic (or pitch) axis located at the 40-percent chord. The uncoupled bending-torsion (or pitch-roll) frequency ratio was 0.5. A beveled-edge flat-plate profile shape having a thickness ratio of 4 percent was used. Except for the radius of gyration, the basic cantilever models tested by CAL in the Mach number range of 5 to 7 were essentially the same as those tested by M.I.T. in the Mach number range of 1.5 to 5.0.

The cantilever models were rigidly restrained at the root by clamping the spar inboard of the model profile. The semirigid models had a roll axis fixed at the inboard edge of the model by means of the two cross flexures. Spring restraint in the roll degree of freedom was obtained by restraining the deflection of the free end of the roll beam by means of a set of adjustable rollers. The model and the supporting structure for the roll degree of freedom were restrained in pitch by means of a torsion rod. In order that there would be no spring coupling between the roll and pitch degrees of freedom, the axis of the torsion rod was coincident with the undeflected axis of the roll beam and the pitch axis of the model.

Figure 2 presents a plot of the variation of a normalized experimental and theoretical flutter velocity index $\frac{V}{b\omega_{\alpha}\sqrt{\mu}}$ with Mach number

for the basic cantilever model as determined by M.I.T. in the Mach number range of 1.5 to 5.0 and by CAL in the Mach number range of 5 to 7.

The flutter velocity indices $\frac{V}{b\omega_{\alpha}\sqrt{\mu}}$ have been normalized to the exper-

imental value at $M = 1.5$. The experimental data, on which the curve is based, have also been corrected analytically for the small variations which existed between the models. The theoretical curve is based on two-degree-of-freedom piston-theory flutter calculations which include the effects of thickness, the spanwise variation of the mode shapes, but not the effects of structural damping. The results show that the theory is unconservative below a Mach number of approximately 3.5 and conservative between Mach numbers of approximately 3.5 and 6.3. The maximum amount of conservatism, approximately 4 percent, is reached at $M = 5.0$. It is noticed that the rate of increase of the experimental flutter velocity index is continually decreasing with increasing Mach number in the Mach number range of 1.5 to 5.5. At a Mach number of approximately 5.5, the rate of increase becomes zero. Above $M = 5.5$, the slope of the curve changes sign and the flutter velocity index starts to decrease with increasing Mach number. In contrast to this trend, the theoretical results in the Mach number range of 5 to 7 indicate a continually increasing value of the flutter velocity index. Because of

this difference in the trends with Mach number, the theory is approximately 6 percent unconservative at $M = 7$ and the relative trends indicate that the theory may become more unconservative, at an increasing rate, at higher Mach numbers.

In view of the unexpected trend of the experimental flutter data at the higher Mach numbers, corroboratory data were desired and, therefore, a semirigid model, having essentially the same nondimensional profile, mass, and frequency parameters as the cantilever models, was built and tested. A semirigid model was used instead of cantilever models as they were not destroyed at each flutter point and, therefore, flutter data could be obtained throughout the Mach number range with a model having identical parameters rather than with models having nearly identical parameters. Any change in the flutter velocity index with Mach number, therefore, should be due only to a change in aerodynamics. The results of these semirigid model tests are presented in figure 3. The unnormalized cantilever flutter model data obtained by CAL in the Mach number range of 5 to 7 are also presented for purpose of comparison. The results presented in this figure show that the semirigid model experienced approximately the same decrease in the flutter velocity index above $M = 6.0$ as did the cantilever models. It is noted that an identical decrease in the flutter velocity index was obtained in the Mach number range of 6 to 7 during the test of another semirigid model having nearly identical parameters. These results, obtained by independent tests, tend to verify the experimental trend of $\frac{V}{b\omega_{\alpha}\sqrt{\mu}}$ that was obtained with the cantilever models and, in addition, indicate that the cause of the decrease in the value of the flutter velocity index with increasing Mach number must be of aerodynamic origin.

Theoretical analyses were conducted for the semirigid model for which the experimental results are presented in figure 3. The results of these analyses are shown in figure 4. The amount of structural damping included in the uncoupled roll and pitch degrees of freedom, 1 percent and 4 percent, respectively, were the same for all tests and were the values experimentally determined just prior to the flutter tests at each of the three Mach numbers.

Comparison of the experimental variation of the flutter velocity index with Mach number with that which was predicted on the basis of zero structural damping shows that the relative trends are effectively the same as those shown for the cantilever model. It is also noted that the Mach number at which the theoretical results, based on zero structural damping, change from conservative to unconservative ($M = 6.30$) is approximately the same as that determined for the cantilever models. The inclusion of structural damping resulted in a conservative prediction throughout the Mach number range and altered the predicted trend

of the flutter velocity index with Mach number. It is noted, however, that comparison of the experimental results with theoretical results including structural damping still indicates that the decrease in the experimental value of the velocity index above a Mach number of 6 is more rapid with increasing Mach number than that which is predicted theoretically.

Figure 5 presents a comparison of the experimental and theoretical values of the nondimensional flutter frequency $\frac{\omega_F}{\omega_P}$ plotted against Mach number for the basic semirigid model. The results show that inclusion of the measured amounts of structural damping in the theoretical analyses greatly improved the prediction of the flutter frequency. In general, flutter analyses of the semirigid model configurations, including structural damping, predicted the flutter frequency to within 6 percent as compared to within approximately 20 percent when the structural damping was assumed zero.

Since the theoretical analyses now include all known structural, mass, and dynamic effects, which, for the semirigid type of model, can be determined to a relatively high degree of accuracy, it is suggested that the noted differences in the experimental and theoretical trends with Mach number might be caused by Mach number effects which are not correctly predicted by piston theory, or they might be caused by three-dimensional and/or viscous-flow effects which cannot be predicted by piston theory.

The theoretical calculations conducted for both the cantilever and semirigid models indicated that structural damping had a destabilizing effect instead of the usual stabilizing effect. Figure 6 presents the results of analyses that were conducted for the semirigid model in which structural damping was included only in the pitch degree of freedom. The results of these analyses are compared in this figure with those in which the structural damping in both degrees of freedom is assumed to be zero and also with those in which the measured structural damping is included in both the roll and pitch degrees of freedom. Four interesting comments can be made after inspection of the plotted results:

(1) Structural damping is destabilizing in the pitch degree of freedom and stabilizing in the roll degree of freedom.

(2) For a given configuration, the amount of stabilization due to damping in the roll degree of freedom or destabilization due to damping in the pitch degree of freedom increases with Mach number.

(3) The effect of small damping in the roll degree of freedom is more pronounced than that in the pitch degree of freedom.

(4) Structural damping in the pitch degree of freedom caused the greatest change in the predicted flutter frequency.

An extensive examination of the effects of structural damping has not, as yet, been undertaken and, therefore, clarifying comments cannot be made as to the possible mechanism which caused structural damping to have these effects. Inspection of the flutter determinants shows, however, that, because the aerodynamic coupling terms are very large, the phase change caused by the addition of small amounts of structural damping can radically alter the results.

It had been mentioned previously that the noted differences in the experimental and theoretical trends with Mach number might be caused by viscous-flow effects that are not predictable by piston theory. McLellan, Bertram, and Moore (ref. 2) present, for a Mach number of approximately 7.0, some experimental data which give some indications as to the effects of viscosity on the chordwise pressure distribution of a series of airfoils. There appear to be two major viscous effects, in addition to the usual separation near the trailing edge, due to boundary-layer—trailing-edge shock interaction. The first is the effect of the boundary layer at abrupt changes of profile slope. The second is the presence of a pressure peak near the leading edge which is most pronounced at low angles of attack. The results of reference 2 indicate that the agreement between experimental and theoretical pressure distributions can be improved by including the boundary-layer thickness as a profile change.

For a constant Reynolds number, the boundary-layer displacement thickness increases with increasing Mach number. With regards to flutter in the high supersonic and hypersonic flow regimes, the effects of increased airfoil thickness are destabilizing, at least for frequency ratios $\frac{\omega_R}{\omega_P}$ less than 1. It is suggested, therefore, that the thickening of the boundary layer with increasing Mach number could explain, at least in part, the unexpected experimental results obtained with the basic cantilever and semirigid models in the Mach number range of 5 to 7. In addition, since piston theory does not include the effects of viscosity, this might be the reason for the trend toward the unconservative prediction of the flutter velocity index with increasing Mach number.

In addition to the investigation of the effects of Mach number on the flutter characteristics of cantilever and semirigid models, the

effects due to variation of frequency ratio, center-of-gravity location, radius of gyration, mass ratio, elastic-axis location, and thickness ratio were investigated at $M = 6.0$ with semirigid models. By the use of semirigid models and of the special suspension system designed to restrain the models in the pitch and roll degrees of freedom, independent variation of the various parameters could be obtained.

The remaining portion of the paper is devoted to a detailed discussion of the investigations that were conducted at $M = 6.0$ to determine the effects that independent variation of the roll to pitch frequency ratio and center-of-gravity location had on the flutter characteristics of the basic semirigid models. In addition, the results of the investigations conducted to determine the effects due to variation of the wing-to-air-mass ratio, pitch-axis location, thickness, and radius of gyration will be summarized.

Figure 7 compares the experimentally determined and theoretically predicted variation of the flutter velocity index due to changes in the center-of-gravity location. Definitive flutter results could not be determined within the tunnel limits for a center-of-gravity position at the 45-percent chord.

Comparison of the experimental results with theoretical results based on piston-theory aerodynamics shows that the theoretical results did not adequately predict the experimental results for center-of-gravity position forward of the 50-percent chord.

It is believed that the results shown in this figure indicate the reason that the correlation of the experimental and theoretical data is poor for the more forward positions of the center of gravity. It is noted that, theoretically, the flutter velocity index increases very rapidly as the center-of-gravity position approaches that of the center of pressure. If it is assumed that the rapid increase of the experimental results is due to the same reason, then it must be concluded that the actual center of pressure is further aft than that position which is predicted theoretically. Although the inclusion of structural damping did not significantly improve the prediction of the flutter velocity index, it is noted that its inclusion did result in prediction of the flutter frequency to within 6 percent as compared to within 25 percent when structural damping was neglected.

Figure 8 compares the experimentally determined and theoretically predicted change of the flutter velocity index $\frac{V}{b\omega_p\sqrt{\mu}}$ due to variation of the roll to pitch frequency ratio $\frac{\omega_R}{\omega_P}$. These data were obtained with a flutter model having a center of gravity located at approximately the

45-percent chord. The experimental results indicate that the rate of increase of the flutter velocity index becomes progressively larger as the frequency ratio decreases. At a frequency ratio of 0.50, flutter could not be obtained. Although definitive flutter results were not determined for this frequency ratio, the test records indicated that, if flutter could be obtained, it would occur at a much higher value of the flutter velocity index.

Comparison of the experimentally determined variation of the flutter velocity index with that predicted by theoretical analyses using piston-theory aerodynamics shows that the theoretical results did not adequately predict the experimentally determined change below a frequency ratio of approximately 0.60. It is of interest to note from the theoretical results that the stabilizing effects of structural damping decrease as the frequency ratio increases until at a frequency ratio of approximately 0.65 the effects of structural damping tend to become destabilizing. It is noted, in addition, that the inclusion of structural damping in the theoretical analyses greatly improved the prediction of the flutter frequency.

Similar results were obtained with a semirigid model having a center of gravity located at the 50-percent-chord position. The primary difference obtained with this model was that flutter could not be obtained at or below a roll-to-pitch frequency ratio of 0.30.

Since the results obtained for a center-of-gravity variation indicated that the actual center-of-pressure position might be further aft than that which is predicted theoretically, some very approximate analyses were conducted to determine whether a shift of the center-of-pressure position would improve the prediction of the effects due to a frequency-ratio variation. It is noted that the prediction of the experimental results improved as the center-of-pressure position was moved aft from the position predicted by piston theory (39-percent chord). Reasonably good correlation of the experimental results was obtained for an effective center-of-pressure location at the 43-percent chord. Although the results of this crude investigation are not conclusive, they do indicate that an inaccurate prediction of the center-of-pressure location could be the reason that the theoretical results did not predict the variation of the experimental results. It is noted that, for the same shift in the center-of-pressure location, the change in the predicted results was more pronounced for the model having its center of gravity at the 45-percent chord than it was for the model having its center of gravity at the 50-percent-chord position.

In general, the results of the other investigations conducted with semirigid models at $M = 6.0$ permitted the following additional conclusions to be reached. Theoretical results based on piston-theory

~~CONFIDENTIAL~~

aerodynamics did not adequately predict the flutter velocity index for pitch axis locations aft of the 40-percent chord but did adequately predict the effect due to variation of the wing-to-air-mass ratio, radius of gyration, and thickness.

It might be stated that, although the results that have been presented might not decisively prove some of the conclusions that have been postulated, they do indicate that piston-theory aerodynamics might not be as adequate as had been anticipated for the hypersonic speed regime.

If nothing else, the limited results that have been obtained to date indicate that a more extensive investigation of the accuracy and applicability of piston theory should be undertaken. In particular, it is recommended that tests be conducted at Mach numbers greater than 7.0 and that the experimental data be compared with theoretical results based on piston-theory aerodynamics to determine whether the decrease in the flutter velocity index with increasing Mach number continues to be more rapid than that which is predicted. Because of the relative rates of decrease, tests at $M = 8.0$ might be sufficient for this purpose.

CONCLUDING REMARKS

In conclusion, the results which have been presented indicate that, for the simple wing configuration tested, flutter analyses using piston-theory aerodynamics assuming zero structural damping were (1) unconservative below a Mach number of approximately 3.5, (2) conservative between Mach numbers of approximately 3.5 and 6.3, with a maximum conservatism of about 4 percent at a Mach number of 5, and (3) unconservative above a Mach number of 6.3, a maximum unconservative prediction of approximately 6 percent being obtained at a Mach number of 7.0. The inclusion of structural damping in the analyses greatly improved the prediction of the flutter frequency and, in most cases, resulted in a more conservative prediction of the flutter velocity index in the Mach number range of 5 to 7. It should be noted, however, that there was still a more rapid decrease in the experimentally determined flutter velocity index than that which is predicted by theoretical analyses based on piston-theory aerodynamics.

Tests at a Mach number of 6.0 indicate the theoretical analyses based on piston-theory aerodynamics were increasingly conservative for lower frequency ratios and more forward center-of-gravity positions. It appears that the differences between the theoretical and experimental results may be the inadequate prediction by piston theory of important aerodynamic parameters such as center of pressure and lift coefficient.

[REDACTED]

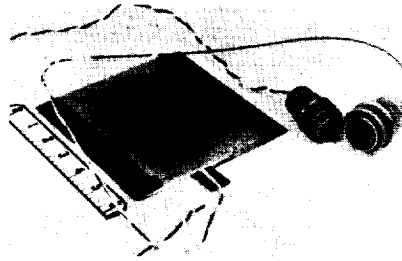
In conducting piston-theory flutter analyses on advanced low-aspect-ratio wing configurations at hypersonic speeds, therefore, it appears advisable, whenever possible, to verify or include corrections to the aerodynamic parameters by the use of experimental wind-tunnel results.

REFERENCES

1. Martuccelli, John R.: Flutter Model Tests at Mach Numbers 1.5-5.0. WADC Tech. Rep. 59-407, U.S. Air Force, Sept. 1959.
2. McLellan, Charles H., Bertram, Mitchell H., and Moore John A.: An Investigation of Four Wings of Square Plan Form at a Mach Number of 6.9 in the Langley 11-Inch Hypersonic Tunnel. NACA Rep. 1310, 1957. (Supersedes NACA RM L51D17.)

[REDACTED]

HYPERSONIC FLUTTER MODELS



CANTILEVER MODEL

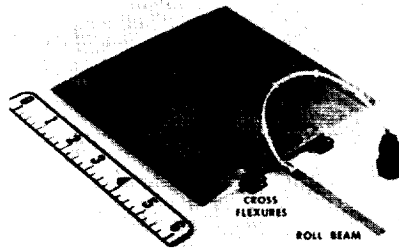
SEMI-RIGID MODEL
HYPERSONIC FLUTTER MODELS

Figure 1

VARIATION OF NORMALIZED FLUTTER VELOCITY INDEX WITH MACH NUMBER

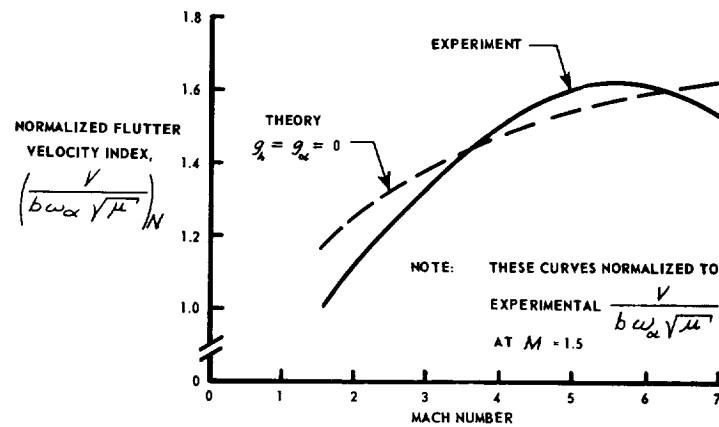


Figure 2

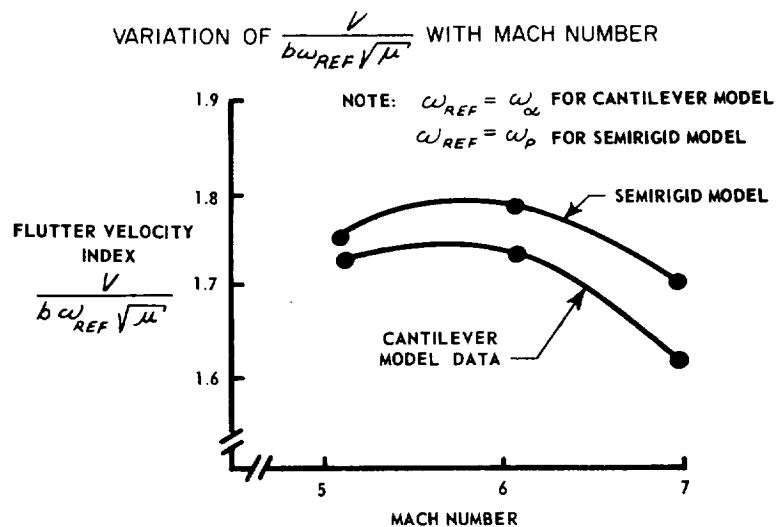


Figure 3

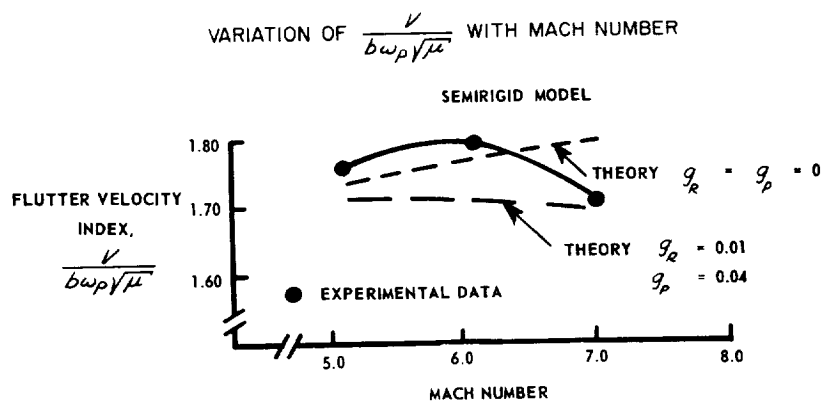


Figure 4

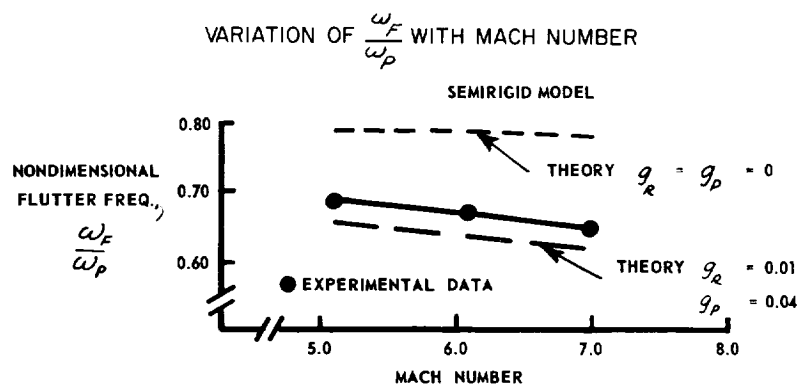


Figure 5

CALCULATED VALUES OF $\frac{V}{b\omega_p\sqrt{\mu}}$ AND $\frac{\omega_F}{\omega_p}$ PLOTTED
AGAINST MACH NUMBER

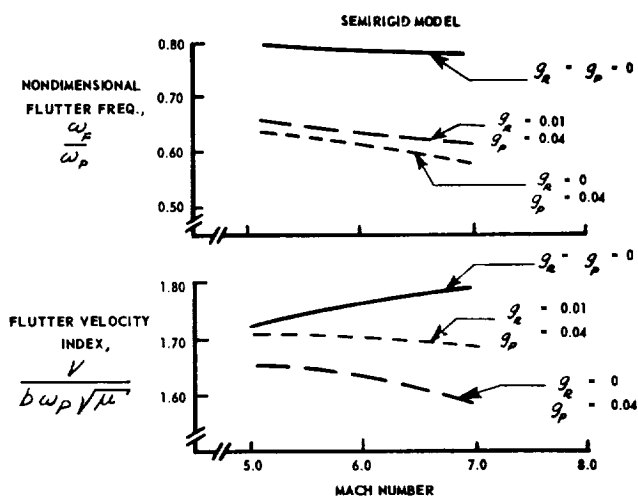


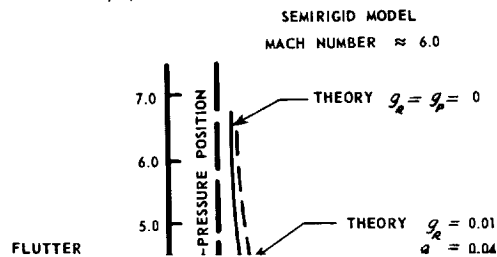
Figure 6

models at full-scale Reynolds numbers.

The investigation of this problem at Ames Research Center began with model tests of the Titan missile which were suggested by Space Technology Laboratories and by the Martin Company. Figure 2 shows the model of the Titan missile connected to calibration equipment in the

[REDACTED]

VARIATION OF $\frac{V}{b\omega_p\sqrt{\mu}}$ WITH CENTER-OF-GRAVITY POSITION



[REDACTED]

The Titan investigation raised many questions, and it became apparent that no general application of the results could be made. Ames Research Center then inaugurated a more general program in which important parameters, such as stiffness, frequency, shape, scale, and damping, could be independently varied and their effects assessed. The program is now in progress. The maximum Reynolds number of the tests up to the present time is 9×10^6 , which corresponds to full-scale velocities of 90 mph on the Titan, or about 40 mph on a vehicle the size of Saturn.

DISCUSSION

The bending stress at the base of the model is used as an indication of model response, although bending stresses or accelerations at other locations on the model can be used almost equally well. A typical response is shown in figure 3. At a given wind speed the transverse stress varies randomly in amplitude but at a constant frequency which is the fundamental bending frequency of the model and support system. The streamwise stress also has an oscillation, but it is usually of smaller amplitude than the transverse oscillations. As indicated in this figure, the oscillating stresses may greatly exceed the average-drag stresses if the damping has the small values typical of present-day missiles, even though the oscillating wind forces are very small. It should be noted that actual data samples are 600 to 1,500 cycles in length. The maximum value of the bending stress in each direction is the quantity that will be presented for various models.

Effects of Nose Shape and Roughness

Two of the more spectacular effects encountered during these wind-tunnel investigations were the interrelated effects of tip shape and of surface roughness of the upper stage. The effects were so large, in fact, that a rather extensive study of them became necessary before the variables of more obvious importance could be intelligently investigated. Figure 4 shows the maximum bending stresses plotted against Reynolds number for the same model with two different noses. (Only the nose portion of the model is shown in this figure.) The Reynolds number is based on the first-stage diameter. The transverse stresses are shown by the solid-line curves, and the streamwise stresses, by the dashed-line curves. It is evident that the transverse stresses were greatly reduced by

tape represented a surface roughness, which, based on model scale, would have a thickness less than $1/32$ of an inch on a missile the size of the Titan.

Considerably different results were obtained when the tape strips were not present, as shown in figure 5. The hemispherical-nose configuration no longer had a large peak in bending stresses at the lower Reynolds numbers, as was the case for the configuration with roughness. The presence of roughness had a much smaller effect with the high-fineness-ratio nose, and a comparison of figures 4 and 5 would show that the tape actually decreased the stresses on this configuration at all of the Reynolds numbers of the tests. Tape strips, of course, represent only one type of roughness. However, similar effects were measured with the addition of grit particles, of conduit-like appendages, and of very small spoilers. Also, there are indications that adjacent structures, in certain positions relative to the model, had the effect of roughness.

The peak in response created by the tape on the hemispherical-nose configuration is typical of the response observed with many different model configurations. The height of the peak and the Reynolds number at which it occurred were affected by such factors as roughness height, position of the roughness with respect to the wind direction, the area covered by the roughness, the fundamental bending frequency of the model, and, of course, nose shape. Figure 6 shows some of the nose shapes investigated. The nose shapes are presented in the approximate order of their effect on model oscillation. The indication is that the blunter noses induce the largest oscillations. This is probably an oversimplification, because the order of merit depends to some extent on whether the configurations had a response peak at Reynolds numbers of interest. The first nose shown in the figure almost always gave the smallest oscillations, but the next three configurations also had a relatively small response at all test and model conditions. The small tip spoiler mounted on configuration 7 to form configuration 3 was only one of several tip additions which reduced the oscillations with the blunted cone nose. Incidentally, spoilers also proved to be helpful at many other locations on the nose or on the upper portion of the upper stage if they were large enough. These latter spoilers were somewhat similar to those already employed on the Vanguard satellite vehicle.

Several difficulties arise in simulating the actual roughness of a full-scale vehicle. There is the obvious difficulty of predicting the height of ice accumulations, weld joints, etc. There are also uncertainties as to the boundary-layer thickness on the model and on the full-scale vehicle. The most useful conclusion from the roughness study thus far is that some nose shapes induce only a small response which is nearly independent of surface roughness. These data should be the most amenable to full-scale extrapolation.

Effects of Oscillation Amplitude

It has long been suspected that there is a coupling between the response of a vehicle and the excitation which induces the response. This possibility was investigated by testing two models of different flexibilities but of the same fundamental bending frequency. Figure 7 shows the results of such tests for two configurations. A computed excitation is used in this figure in preference to bending stresses to eliminate the effects of model dynamics. The excitation can be considered to represent a lift coefficient in the transverse direction. The excitation is computed from the bending-moment response, taking into consideration the mass, stiffness, and measured damping of the models. The method of computation is similar to that used in reference 4. The tip deflections of the flexible models were about 3 times those of the stiff models. The results indicate that model movement at amplitudes representative of full-scale vehicles did not greatly affect the excitation. A similar conclusion was reached in reference 2.

Effects of Frequency

The present tests have also involved changes in model frequency and in air density. Adjustments to these factors provided a means of varying independently the basic simulation parameters, reduced frequency and Reynolds number, and thus of determining how important each of these parameters was to the simulation of a given excitation. It is perhaps obvious that, if either parameter could be ignored, simulation techniques would be simplified. Figure 8 shows the effect of a variation in reduced frequency. Inasmuch as all the data presented were obtained at the same tunnel air density and with the same model diameter, the reduced frequency fD/V is directly proportional to the model frequency f at any one value of Reynolds number R . The effect of frequency was very large for this particular configuration, but this result is typical only of those models which had large response peaks. The same data can be replotted with reduced frequency (or its reciprocal) as the independent variable rather than Reynolds number. This plot is shown in figure 9. In this figure, at any given value of V/fD , the Reynolds number is variable, and a large effect of model frequency still persists.

It can be shown that, if the model diameter is unchanged, a simultaneous duplication of reduced frequency and Reynolds number can be realized by maintaining constant the product of frequency f and density ρ . Data for which this relation was approximately true are presented in figure 10. The results indicate that if $f\rho$ were exactly the same, the measured excitations would be nearly equal even though the range of model frequencies is the same as that presented in figures 8 and 9. It is concluded that, for configurations with large excitations, both reduced frequency and Reynolds number must be duplicated if the

excitation is to be adequately represented. However, it has not yet been shown whether such correlation can be obtained when the model diameter is also varied. In this case it is possible that the boundary-layer thickness might not be correctly scaled to produce the same effects of roughness on models of different sizes.

CONCLUDING REMARKS

The results of the tests, thus far, indicate the following:

1. Very large stresses can be induced on missiles with the blunter noses, particularly if the upper stage is rough.
2. The stresses induced in the models with the high-fineness-ratio noses were generally small.
3. Spoilers, especially when placed at the tip, were effective in reducing the larger oscillations.
4. There is little coupling between the vehicle motion and the aerodynamic excitation.
5. Proper representation of the wind-induced excitation requires the duplication of both reduced frequency and Reynolds number.

Up to now, the tests have been confined to models which have a maximum diameter of approximately 1 foot and which have the basic Titan shape. The investigation is continuing and will extend to other sizes and shapes. In addition, attempts will be made to reveal the aerodynamic mechanism which causes such markedly different responses with seemingly minor changes in model configuration. The final proof of the validity of the wind-tunnel results and application techniques will rest on more complete measurements of the response of full-scale missiles.

REFERENCES

1. Fung, Y. C.: Fluctuating Lift and Drag Acting on a Cylinder in a Flow at Supercritical Reynolds Numbers. GM-TR-0165-00343, Space Tech. Labs., The Ramo-Wooldridge Corp., May 7, 1958.
2. Fung, Y. C.: The Fluctuating Lift Force Acting on a Cylinder Subjected to Forced Oscillations Perpendicular to a Flow at High Reynolds Numbers. GM-TR-0165-00465, Space Tech. Labs., The Ramo-Wooldridge Corp., Sept. 11, 1958.
3. Buell, Donald A., and Kenyon, George C.: The Wind-Induced Loads on a Dynamically Scaled Model of a Large Missile in Launching Position. NASA TM X-109, 1959.
4. Ezra, A. A.: Wind Induced Oscillations of the Titan Missile. Rep. WDD-M-MI-59-7, The Martin Co., Mar. 1959.

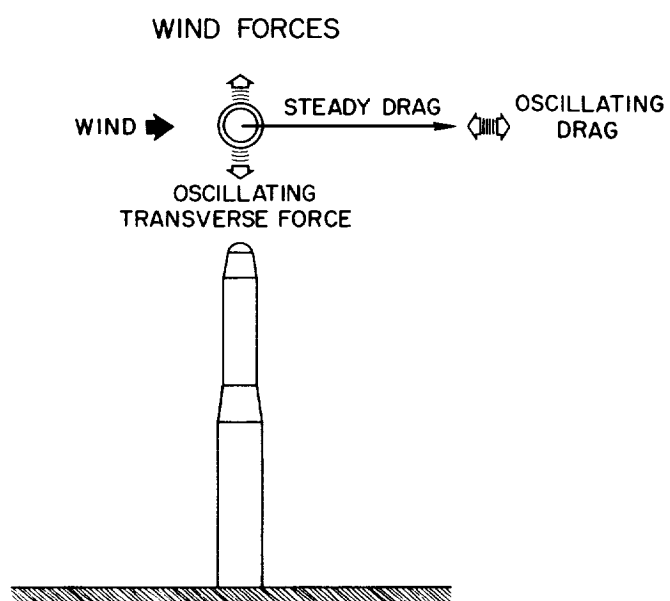


Figure 1

MODEL UNDERGOING CALIBRATION

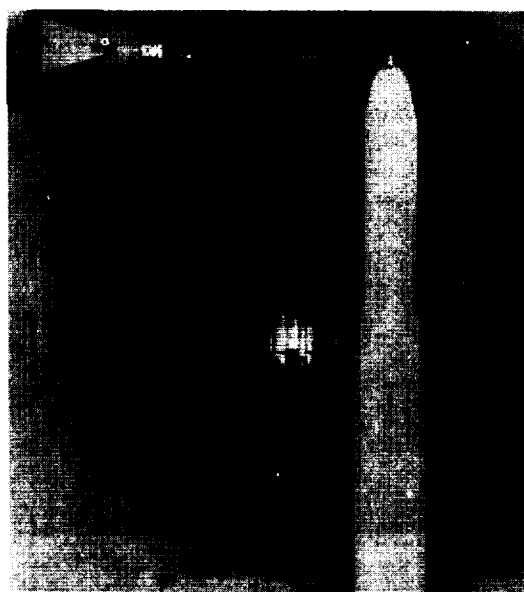


Figure 2

TYPICAL RESPONSE

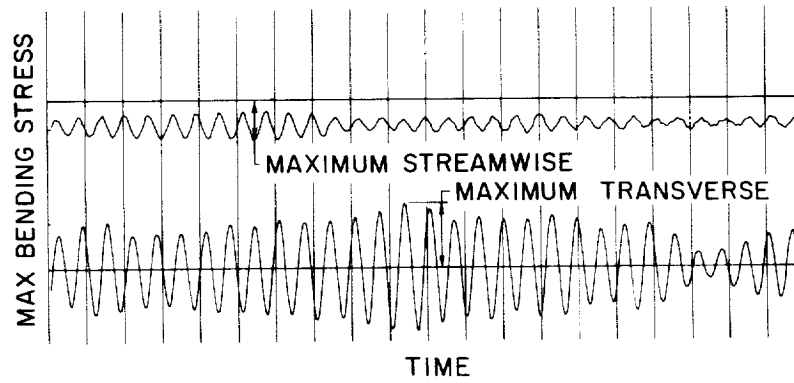


Figure 3

TIP EFFECT WITH ROUGHNESS

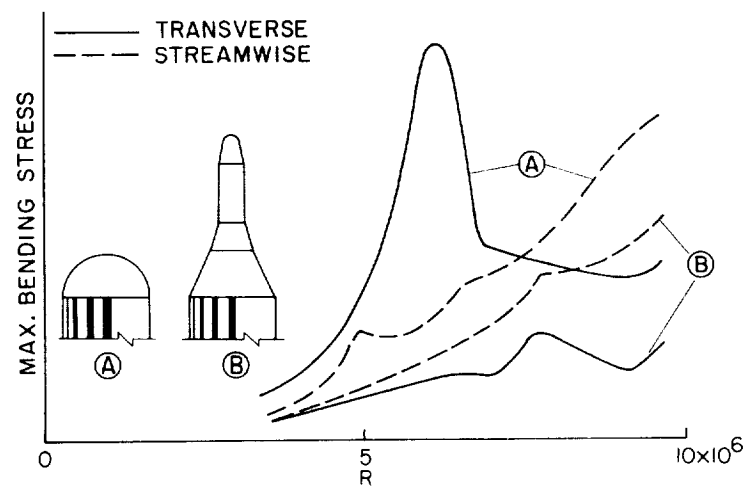


Figure 4

TIP EFFECT WITHOUT ROUGHNESS

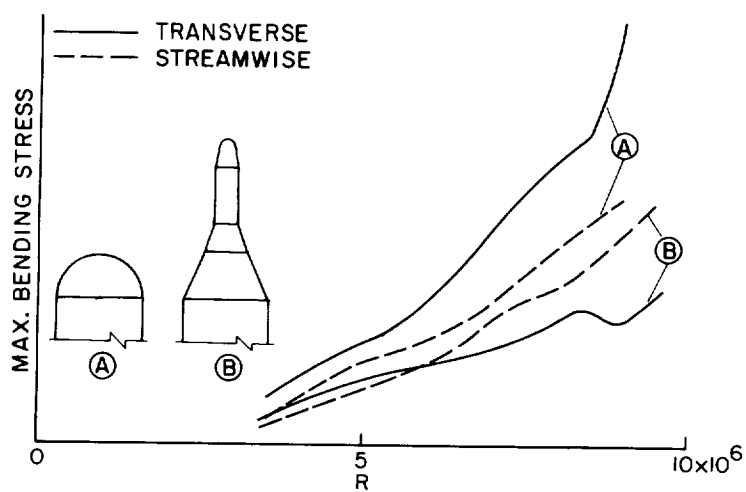


Figure 5

NOSES TESTED

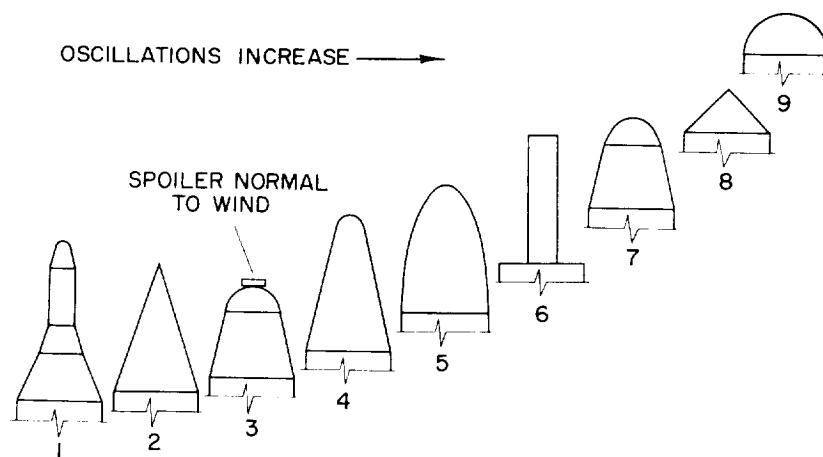


Figure 6

EFFECT OF OSCILLATION AMPLITUDE

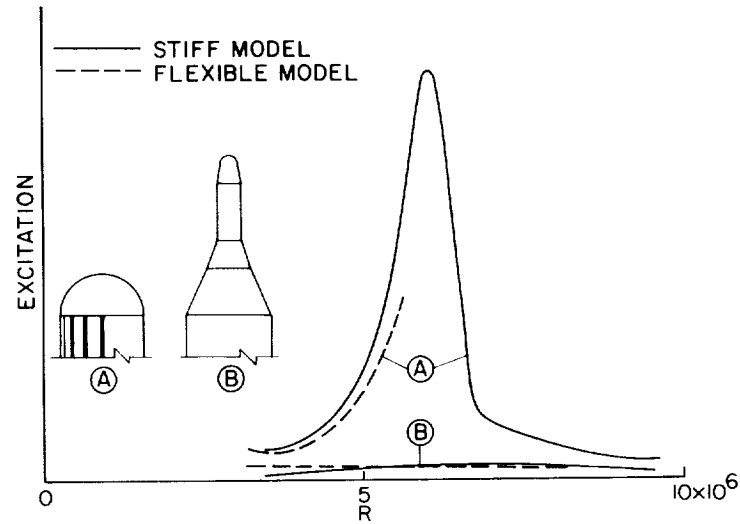


Figure 7

FREQUENCY EFFECT

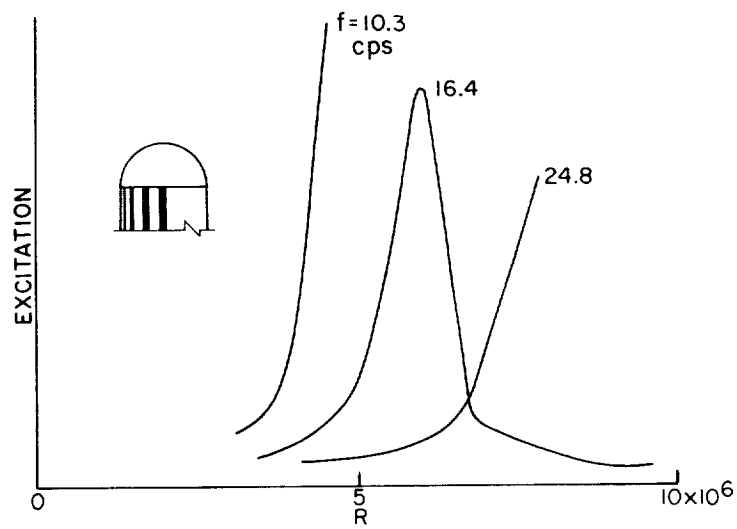


Figure 8

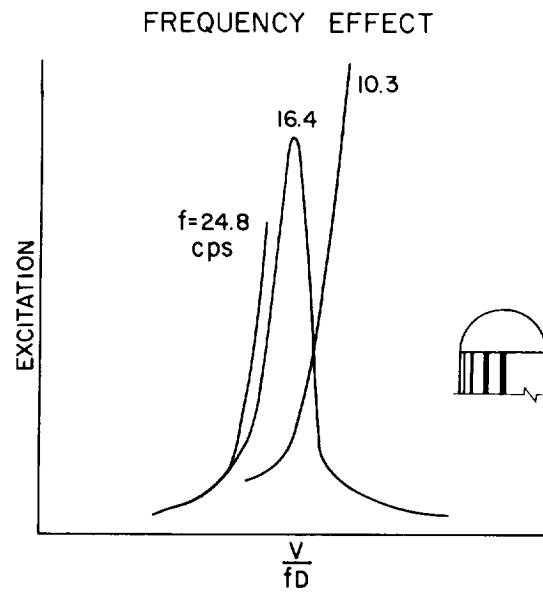
~~CONFIDENTIAL~~

Figure 9

FREQUENCY EFFECT WITH ADJUSTED AIR DENSITY

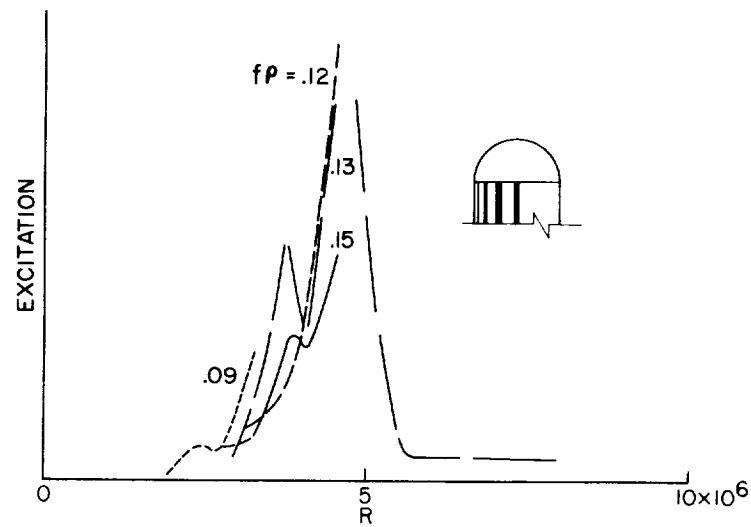


Figure 10

~~CONFIDENTIAL~~

DYNAMIC RESPONSE STUDIES OF LAUNCH VEHICLES

By Harry L. Runyan, Homer G. Morgan,
and H. B. Tolefson
Langley Research Center

INTRODUCTION

This paper is concerned with problems of large boosters and with the dynamic interaction between the missile aerodynamics, the servo system, and the missile flexibility, which may be labeled an aero-servo-elastic problem. Basic equations of motion for the aero-servo-elastic problem have been derived by several authors and are contained in references 1 to 11. Discussed in this paper are a method for obtaining measurements of the aerodynamic inputs (namely, the detailed winds and wind shears), the large influence on the missile loads of types of control systems, and the missile instability problem and how it is influenced by the flexibility of the structure. In order to illustrate the aero-servo-elastic problem and to provide a pictorial representation of the type of instability possible, a short motion picture of a model of a flexible missile has been prepared¹.

The dynamic instability illustrated in the motion picture is only part of the problem; for instance, the dynamic loads problem (response to winds, turbulence, etc.) exists which must be considered along with the stability problem. Even though the system may avoid instability, a small stability margin will significantly affect dynamic loads. There are several critical times during launch in which loads can be produced that can influence the design of certain portions of the missile. For instance, when the missile is still on the launch pad, ground winds may induce severe stresses at the base. Another critical time occurs at launch when the thrust is suddenly applied and can cause bending vibration, longitudinal waves, or even bulging of the tanks. Another critical period is during the time that the missile is in flight and may experience severe winds resulting in large aerodynamic forces; this usually occurs when the vehicle is close to the maximum dynamic-pressure condition. This wind-shear problem will be discussed in the next section.

¹A motion-picture film supplement (L-539) illustrating the aero-servo-elastic problem is available on loan from NASA Headquarters, Code BIV, Washington, D.C.

DETAILED WIND AND WIND-SHEAR MEASUREMENTS

In this section are described some recent developments in the problem of obtaining measurements of the wind shears and turbulence along missile flight paths. Recent work at the Langley Research Center has indicated that detailed data on the shears and turbulence actually traversed by a missile can be obtained by photographing the visible trail left by a rocket. Figure 1 shows a schematic view of the installation at NASA Wallops Station for obtaining these measurements. The distorted exhaust trail is shown a short time after the missile was fired. This trail may be either the actual exhaust trail of the rocket engine or an artificially generated smoke trail produced by a small inexpensive rocket. The trail, of course, is initially a smooth curve tracing the flight path of the missile, but after a short time interval the trail is bent and distorted because of the varying wind velocities at the different altitudes.

Cameras are located at points I and II (fig. 3) and simultaneous photographs are taken every few seconds. A pair of photographs of the exhaust trail taken at one of the Little Joe firings is shown in figure 2. A series of these photographs from the two cameras provides the information on the drift of the trail necessary to deduce the detailed wind structure along the missile flight path. The wind velocities based on two successive photographs are shown in figure 3. The vertical scale is altitude in feet and the horizontal scale is wind velocity in feet per second. This figure shows the north-to-south component of the wind. The velocities were obtained at each 100-foot altitude interval for altitudes from 5,000 to 45,000 feet.

A major point of interest in the smoke-trail data is the irregular and random character of the wind fluctuations experienced by the missile. Many of the fine fluctuations are only 300 or 400 feet thick, and even the more severe velocity changes are confined to relatively thin layers. In one case, for example, the wind varied from about 80 to 15 ft/sec for an altitude of only 2,500 feet. Other measurements which have been taken as part of this program show similar types of fluctuations in the wind profile.

As a matter of interest, balloon wind measurements taken several hours prior to launch for this Little Joe firing are shown in figure 4. The balloon sounding, of course, is an averaged or highly smoothed wind measurement, so that the fine-grain structure does not appear in the profile, although there is an indication of the rather severe shear at the 15,000-foot level.

The presence of the small-scale wind fluctuations, measured by the smoke-trail technique, is evident. Many of the larger missiles pass

through these altitudes at Mach numbers of 1.0 to 1.5. The combination of this flight speed and the spatial distribution of these wind fluctuations can result in input frequencies of the order of 0.5 cps for the large disturbances and as high as 3.0 to 4.0 cps for smaller fluctuations. These input frequencies may coincide with some of the predominant structural frequencies of large missiles and, hence, can result in critical structural loading conditions. Some of these structural frequencies will be discussed in more detail later in this paper. Langley Research Center is continuing to make detailed wind measurements at NASA Wallops Station and plans are under way to obtain additional measurements at Cape Canaveral.

STRUCTURAL FEEDBACK

This section is concerned with the aero-servo-elastic, or structural feedback, problem. The importance of this problem has recently been demonstrated in the selection of the diameter of the upper stages of Saturn. Based wholly on the study of the stiffness of the upper stages for various diameters, it was found that diameters corresponding to the existing missiles could not readily be dynamically stabilized for large payloads and that it was necessary to use a larger diameter upper stage for our future space missions.

Studies of the structural feedback problem have been made on a Saturn-type configuration. The configurations studied are shown on figure 5. Each configuration has 220-inch-diameter second and third stages with 37,000-pound payloads. The two types of payloads considered are 160-inch-diameter cylindrical payload and a 1,000-square-foot winged payload.

Frequency Calculations

One of the primary ingredients of all dynamic-response problems including structural feedback is the vibration modes (and the associated frequencies) of the system and, hence, these modes must be accurately determined. Figure 6 shows the results of frequency calculations for the cylindrical payload case. Based on elementary beam theory, six free-free bending frequencies of the vehicle are shown which range from 1.5 cps for the first mode to 23 cps for the sixth mode. When the theory is modified to include the effect of transverse shear, these frequencies drop considerably, ranging from a decrease of about 6 percent in the first mode and 11 percent in the third to 30 percent in the sixth. However, the addition of a rotary inertia term decreased the frequencies only a slight additional amount, which indicated that, while shear effects

~~CONFIDENTIAL~~

are quite large and must be included, rotary inertia effects can possibly be neglected. The necessity of analyzing these large configurations as accurately as possible is especially significant since it probably will be difficult, if not impossible, to perform a vibration test to check calculations on vehicles such as Saturn. Research on more accurate methods for calculating these modes is currently in progress at Langley and involves both analytical and experimental studies.

Response to Sinusoidal Gust

In this section some specific results of structural feedback studies are considered. These results are the response of a vehicle to sinusoidal gusts, the effect of varying the control system on the loads due to a wind shear input, and the effect of flexibility on the stability of the system. All the results in the remainder of the paper have been obtained on an analog computer. Six degrees of freedom were used in the analysis: rigid-body pitch, translation, gimbaled engine, and three elastic modes. For a practical design analysis of such a flexible booster, probably six elastic modes would have to be used; however, three modes have been used in this study since this number was considered sufficient for trend studies. Fuel sloshing has been neglected by assuming that effective baffling is provided. The vehicle is assumed to be flying at maximum dynamic-pressure conditions with no time-varying parameters for the few seconds of exposure to wind disturbance. In the future this program will be extended to include time-varying parameters and the actual wind structure.

Figure 7 shows the ratio of dynamic-to-static deflection $\frac{z}{z_0}$ at the top of the booster due to a sinusoidal gust for both the cylindrical and winged payload cases. Both curves have been normalized to the static deflection of the winged payload case. This ratio is plotted against the frequency f of the sinusoidal input gust of constant amplitude. The first peak corresponds to the first elastic mode, the second peak to the second mode, and so on. The winged payload case exhibits lightly damped first and second modes, whereas the cylindrical payload exhibits a heavily damped first mode but a lightly damped second mode. Even though the system is stable, very large amplification of the response is obtained as a result of the influence of the control system. Of course, large loads would be experienced at this point under some of the wind-shear conditions mentioned previously. For instance, it was mentioned in the section "Detailed Wind and Wind-Shear Measurements" that there are disturbances which combined with the vehicle speed could result in inputs having frequencies close to the structural frequencies shown in figure 7. Obviously, large dynamic responses could result, with possible damage to the vehicle as it passes through wind turbulence layers.

~~CONFIDENTIAL~~

Effect of Type of Control System on Dynamic Loads

Next the problem of how the dynamic loads on a missile can be reduced by the type of control system is discussed. As a typical input, a rather mild wind-shear input having a slope of 20 ft/sec per 1,000 feet of altitude was selected and this input was continued until the velocity reached 80 ft/sec.

In figure 8 the bending moment at the 65-percent station is plotted against a parameter η , which is defined in the equation on the figure. Here δ_c is the command angle given to the engine, θ_e is the pitch error signal, α is the angle of attack, and $\dot{\theta}$ is the pitch rate of the missile. K_1 and K_2 are the system gains. The pitch error signal and the pitch rate are measured at the top of the first stage, whereas the angle of attack is measured at the top of the vehicle. The quantity η occurs as coefficients of the pitch error signal as $(1 - \eta)$ and of the angle of attack as η . This form of the equation was selected to provide a consistent variation from a control system having pitch and pitch rate only (i.e., for $\eta = 0$) to the case where the engine command signal is obtained from the angle of attack and pitch-rate signals ($\eta = 1$). Examination of figure 8 shows a large reduction in bending moment as η approaches 1. This reduction is due to the fact that the angle-of-attack sensor immediately feels the gust and commands the engine "to gimbal" so that the missile is turned into the wind, thus reducing the angle of attack and, consequently, the loads. For the pitch and pitch-rate control system, the missile must actually respond to the wind before engine corrective action is commanded. In figure 9 results are given for the engine gimbal angle δ for the same case plotted against η . The engine gimbal angle is also reduced as η increases; however, a minimum value is reached at about $\eta = 0.8$. A final choice of η for a given application will depend on some compromise between such factors as strength, control, and reliability requirements.

Based on the same equation for engine control, the effect of placing a winged payload on the vehicle is shown in figure 10. As a reminder, both payloads are 37,000 pounds and the winged payload is a 1,000-square-foot delta wing. Again bending moment at the 65-percent station is plotted against η . For pitch and pitch-rate control only ($\eta = 0$) the winged payload increased the bending moment by a factor of 5 over the value for the cylindrical payload. As the factor η approaches 1, a large decrease in the bending moment occurs for both cases. The bending moment for winged payload case has been reduced to almost the same level as that for the cylindrical payload for pitch and pitch-rate control only ($\eta = 0$). Thus, it is apparent that, for this example, if the control system of the missile had been designed to handle a cylindrical payload with pitch and pitch rate, a winged payload could be accommodated by changing the type of control system to include an angle-of-attack sensor without structural modification.

EFFECT OF MISSILE FLEXIBILITY ON STABILITY

The effect of the flexibility of the missile on the stability of the system is shown in figure 11. By utilizing the winged payload case, the structural frequencies of the missile were reduced while the rigid-body-pitch-engine frequency was held constant. The results are shown in figure 11 where bending moment is plotted against the ratio of first bending frequency f_1 to the rigid-body-pitch-engine frequency f_r .

Results are given for three control systems - pitch and pitch rate ($\eta = 0$), angle of attack and pitch rate ($\eta = 1.0$), and one intermediate ($\eta = 0.465$). Note that in the two upper curves the bending moment actually decreases as the frequency ratio is reduced, whereas there is practically no change with f_1/f_r for angle of attack and pitch-rate control. Each case, however, becomes dynamically unstable when the frequency ratio is reduced to the boundary indicated and, for all three cases, became dynamically unstable in the second bending mode. The minimum frequency ratio at which the system became unstable was about 5 (for the intermediate value of $\eta = 0.465$). These calculations have also been repeated for the cylindrical payload case and a similar result was obtained except that the boundary was not as curved but did occur at a frequency ratio of about 5.

CONCLUDING REMARKS

The problem areas of the aero-servo-elastic system have been discussed and some of the efforts in measuring the inputs to the system have been introduced. For instance, a method has been presented for determining the detailed wind structure by the use of smoke trails and the large velocity fluctuations which are not obtained by the usual balloon measurements. In addition, when considering the missile system in its entirety, it was shown that the type of control system can have a large effect on the dynamic loads and should be considered early in the design.

REFERENCES

1. Barton, Millard V.: Generalized Missile Dynamics Analysis. I - Development and Application. GM-TR-0165-00438, Space Tech. Labs., The Ramo-Wooldridge Corp., Apr. 7, 1958.
2. Young, Dana: Generalized Missile Dynamics Analysis. II - Equations of Motion. GM-TR-0165-00359, Space Tech. Labs., The Ramo-Wooldridge Corp., Apr. 7, 1958.
3. Miles, J. W., and Young, Dana: Generalized Missile Dynamics Analysis. III - Aerodynamics. GM-TR-0165-00360, Space Tech. Labs., The Ramo-Wooldridge Corp., Apr. 7, 1958.
4. Miles, J. W., and Young, Dana: Generalized Missile Dynamics Analysis. IV - Sloshing. GM-TR-0165-00361, Space Tech. Labs., The Ramo-Wooldridge Corp., Apr. 7, 1958.
5. Fowler, J.: Generalized Missile Dynamics Analysis. V - Calculation of Bending Modes. GM-TR-0165-00445, Space Tech. Labs., The Ramo-Wooldridge Corp., Apr. 7, 1958.
6. Martin, Donald C.: Generalized Missile Dynamics Analysis. VI - Control System Equations. GM-TR-0165-00430, Space Tech. Labs., The Ramo-Wooldridge Corp., Apr. 7, 1958.
7. Brooks, John A.: Generalized Missile Dynamics Analysis. VII - Programming. GM-TR-0165-00431, Space Tech. Labs., The Ramo-Wooldridge Corp., Apr. 7, 1958.
8. Kachigan, K.: The General Theory and Analysis of a Flexible Bodied Missile With Autopilot Control. Rep. ZU-7-048 (Contract No. AFO4(645)-4), CONVAIR, Nov. 11, 1955.
9. Edelen, D. G. B., and Bloom, B. H.: Vanguard System Response to Aerodynamic and Internal Excitations (Dynamic Loads). Eng. Rep. No. 8979, The Martin Co., Sept. 1957.
10. Farrell, R.: Flight Controls Data - Mathematical Representation of Missile Dynamics Transfer Functions Used in Control System Analyses. WDD-M-SR-58-31, The Martin Co., Sept. 1958.
11. Brook, A.: Flight Control Data - Structural Vibration Equations and the F-65 Program. WDD-M-SR-59-21, The Martin Co., Apr. 1959.

CAMERA INSTALLATION

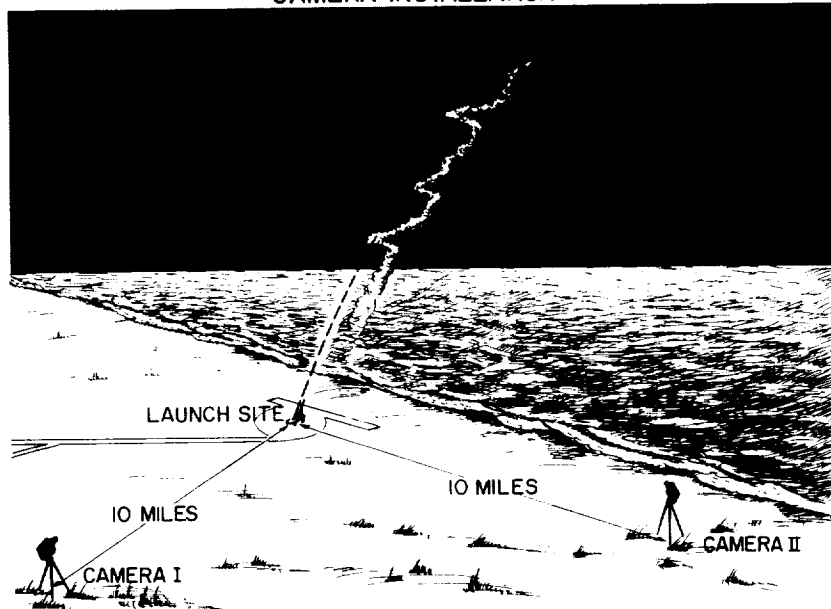


Figure 1

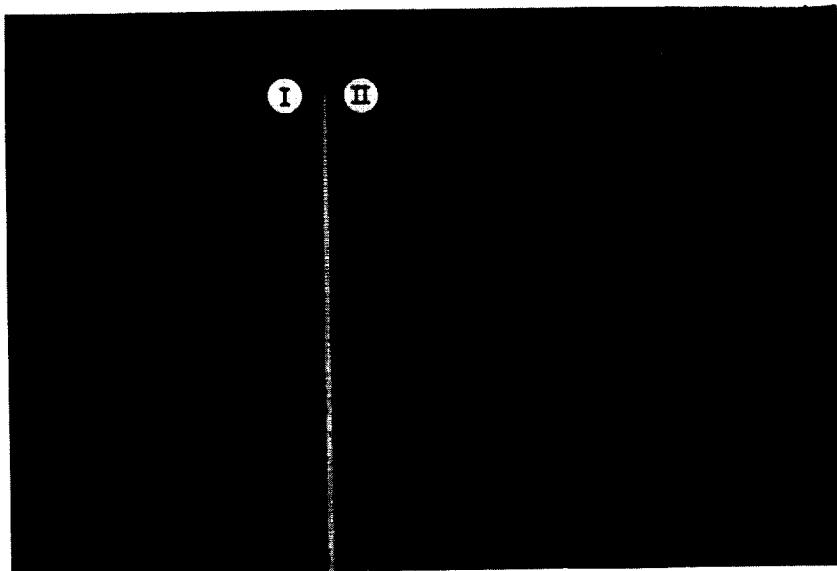


Figure 2

SMOKE-TRAIL WIND MEASUREMENTS

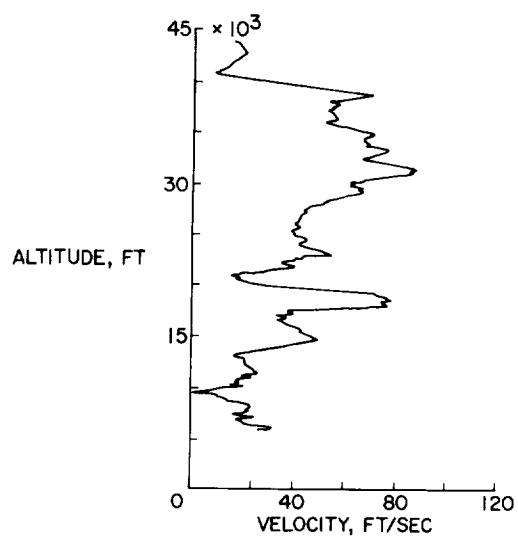


Figure 3

BALLOON WIND MEASUREMENTS

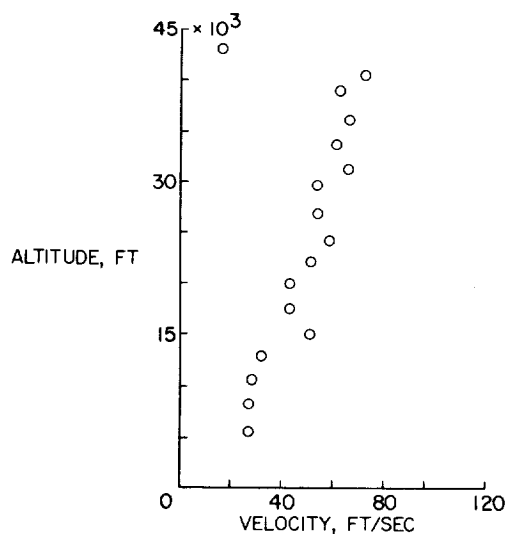


Figure 4

ROOSTER CONFIGURATIONS 37,000-LB PAYLOAD

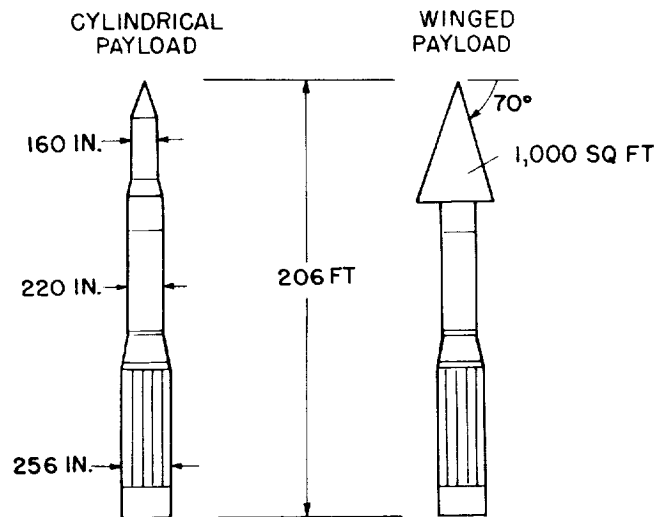


Figure 5

BOOSTER BENDING FREQUENCIES

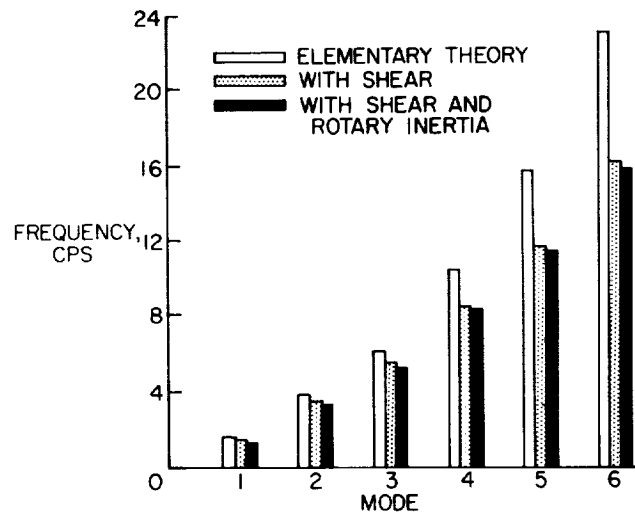


Figure 6

NOSE DEFLECTION DUE TO SINUSOIDAL GUST

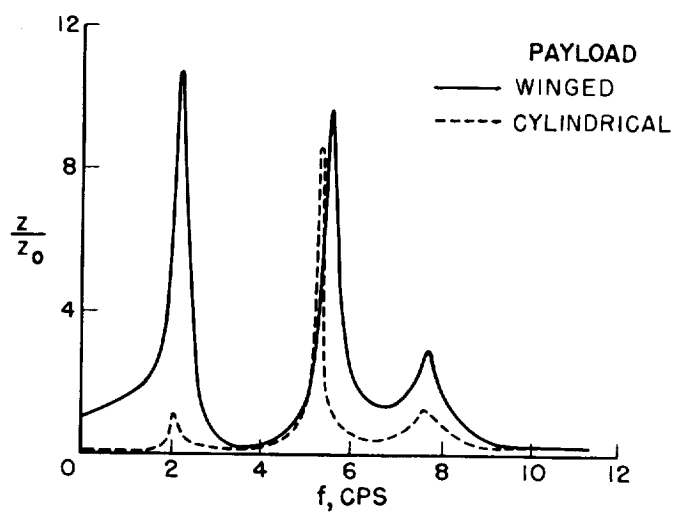


Figure 7

EFFECT OF TYPE OF FEEDBACK

$$\delta_C = K_1 [(1-\eta)\theta_e + \eta a] + K_2 \dot{\theta}$$

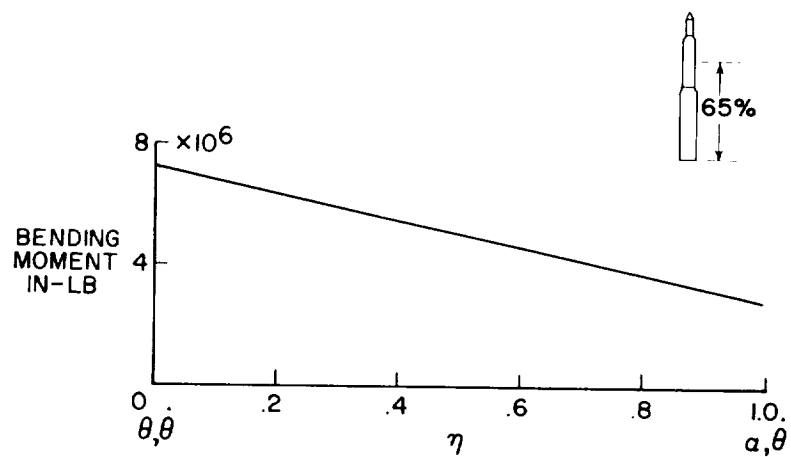


Figure 8

EFFECT OF TYPE OF FEEDBACK

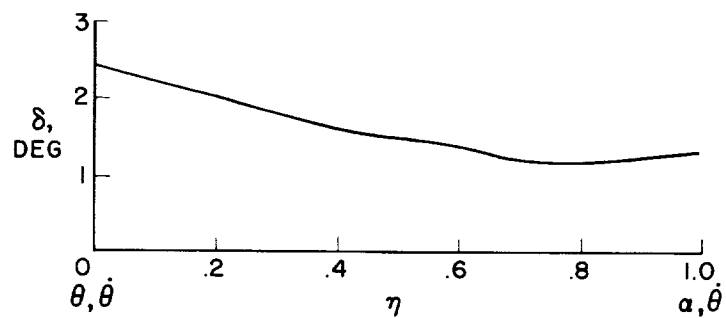


Figure 9

BENDING MOMENT FOR WINGED AND CYLINDRICAL PAYLOADS

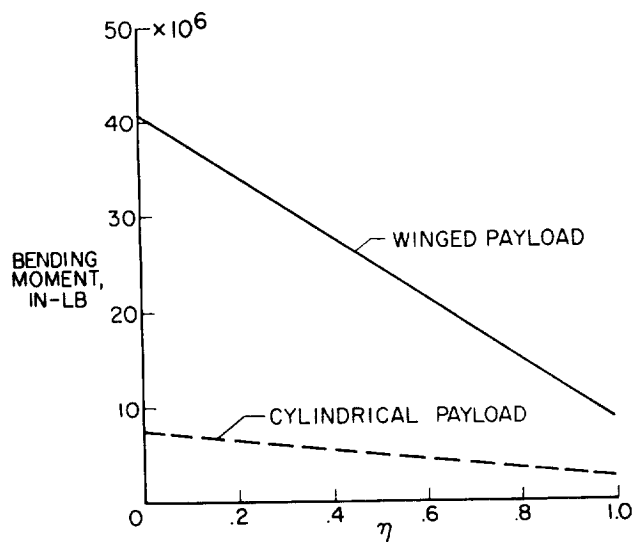


Figure 10

VARIATION OF BENDING MOMENT WITH FREQUENCY
WINGED PAYLOAD

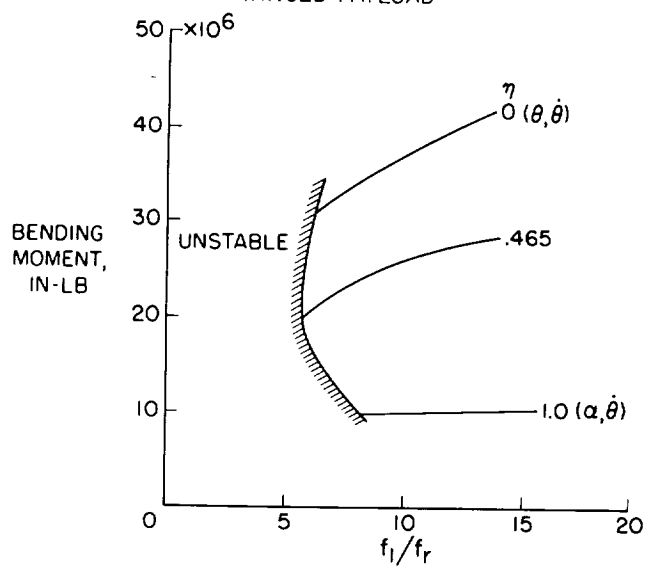


Figure 11

FLUTTER RESEARCH ON SKIN PANELS

By Eldon E. Kordes, Weimer J. Tuovila, and Lawrence D. Guy
Langley Research Center

SUMMARY

Representative experimental results are presented to show the current status of the panel flutter problem. Results are presented for unstiffened rectangular panels and for rectangular panels stiffened by corrugated backing. Flutter boundaries are established for all types of panels when considered on the basis of equivalent isotropic plates. The effects of Mach number, differential pressure, and aerodynamic heating on panel flutter are discussed. A flutter analysis of orthotropic panels is presented in the appendix.

INTRODUCTION

The problem of panel flutter has become critical with the inception of hypersonic and reentry vehicles, particularly when the exposed skin panels are not designed to carry appreciable structural loads. For this type of exposed surfaces, panel flutter becomes the primary weight-establishing design criterion for the exposed skin panels. Some typical skin panels for hypersonic and reentry vehicles are shown in figure 1.

The panel at the upper left of figure 1 is a simple unstiffened flat plate. For a multibay region of the exposed surface which is made up of sheet and stringers, as shown at the upper right of figure 1, the portion of the sheet between stringers is considered to act as an independent panel. For the purpose of this paper these two panel types are referred to as unstiffened panels. The two panel types shown at the bottom of figure 1 are stiffened by corrugations. The corrugation pitch is small and the panel and corrugated backing act as a unit. Both of the corrugation-stiffened panels have a much higher stiffness parallel to the corrugation than in the other direction.

The flutter behavior of these types of panels has been the subject of many theoretical investigations. Comparison of the predictions of theory with experimental flutter data shows marked disagreement for all but the simplest configurations. Therefore, experimentally determined

flutter boundaries must be relied on for design information. Such experimental work is presently in progress and some recent flutter results for rectangular panels are presented in this paper.

SYMBOLS

$$A = R_x - 2n^2\pi^2\left(\frac{l}{w}\right)^2 \frac{D_{xy}}{D_x}$$

$$\bar{A} = \bar{R}_x - 2n^2\left(\frac{l}{w}\right)_{\text{EFF}}^2$$

A_0 enclosed area of torque cell

$$B = k^2 + n^2\pi^2\left(\frac{l}{w}\right)^2 R_y - n^4\pi^4\left(\frac{l}{w}\right)^4 \frac{D_y}{D_x}$$

$$\bar{B} = \bar{k}^2 + n^2\left(\frac{l}{w}\right)_{\text{EFF}}^2 \bar{R}_y - n^4\left(\frac{l}{w}\right)_{\text{EFF}}^4 \frac{D_x D_y}{D_{xy}^2}$$

D_{EFF} flexural rigidity of equivalent isotropic plate

D_x flexural rigidity of orthotropic plate in x-direction

D_y flexural rigidity of orthotropic plate in y-direction

D_{xy} twisting stiffness of orthotropic plate relative to x- and y-directions

E Young's modulus of elasticity

G shear modulus of elasticity

h normalized depth of corrugations

k frequency parameter, $\omega l^2 \sqrt{\frac{\gamma}{D_x}}$


$$\bar{k} = \frac{k}{\pi^2}$$

L lateral aerodynamic loading

l, w dimensions of orthotropic plate (see sketch 1 in appendix)

$l_{\text{EFF}}, w_{\text{EFF}}$ dimensions of equivalent isotropic plate

M	Mach number
N_x, N_y	midplane stresses in x- and y-directions
n	integer
Δp	differential static pressure
q	dynamic pressure, $\rho U^2/2$
$R_x = N_x l^2/D_x$	
$\bar{R}_x = R_x/\pi^2$	
$R_y = N_y l^2/D_x$	
$\bar{R}_y = \frac{R_y}{\pi^2} \frac{D_x}{D_{xy}}$	
Re	real part
T_0	stagnation temperature
t	thickness of material
t_{EFF}	thickness of equivalent isotropic plate
U	velocity of air flow
W	lateral deflection of panel
\bar{W}_n	deflection function (eq. (3))
x, y, z	Cartesian coordinates (see sketch 1)
$x_1 = \frac{x}{l}$	
$\beta = \sqrt{M^2 - 1}$	
γ	mass of plate per unit area
λ	dynamic-pressure parameter, $2ql^3/\beta D_x$




λ_{cr}	critical value of λ
ν	Poisson's ratio
ρ	mass density of air
τ	time
ω	circular frequency

FLUTTER OF UNSTIFFENED PANELS

Effect of Panel Aspect Ratio

Experimental results for the flutter of unstiffened rectangular flat panels are shown in figure 2. In this figure the abscissa is the panel length-width ratio on a log scale and the ordinate is a modified-thickness-ratio parameter which has been shown by theory to be the primary panel-flutter parameter. In this thickness-ratio parameter, t/l is the ratio of panel thickness to panel length, M is the Mach number, q is the dynamic pressure at flutter, and E is the Young's modulus of the material. In figure 2 a vertical bar represents the test results for panels with a given length-width ratio but with varying sizes, materials, Mach number, and temperature. The number by each bar is the number of test points and the length of the bar indicates the scatter of the results. An envelope curve has been drawn to enclose the upper end of the scatter band and hence should be a conservative boundary. The flutter region lies below this curve. Note that many of the panels tested were very long and narrow; such panels are of considerable practical importance and flutter data on them have not been available until recently. Because flutter amplitudes are usually limited by the nonlinear behavior of the panels, panel flutter is considered to be primarily a fatigue problem. The severity of the flutter is therefore of interest. In the tests represented by the results in figure 2, panels with lower length-width ratios usually exhibited relatively large amplitude vibrations and many panels failed before flutter could be stopped. On the other hand, the long, narrow panels exhibited mild flutter. In some cases these flutter vibrations were difficult to distinguish from the background noise without a spectral analysis.

The thickness-ratio parameter used in figure 2 does not contain all the factors that are known to affect the flutter boundaries - hence, the scatter. However, this flutter parameter has proven to be very useful in comparing the results from a wide variety of test conditions.



Effect of Differential Pressure

One of the factors not accounted for in the parameter is the effect of differential pressure. Previous investigators (see, for example, refs. 1 and 2) have shown that small amounts of differential pressure, either positive or negative, reduce the thickness required to prevent flutter. The results presented in figure 2 were obtained by holding the differential pressure as near to zero as possible. This was done for two reasons. First, the design information obtained should be conservative, and second, the influence of other factors can be studied without being masked by scatter caused by varying differential pressures.

Effect of Midplane Stresses

Another important effect on panel flutter is the influence of stresses and buckling caused in the panel by aerodynamic heating and loading. This effect has been recently investigated in detail by means of a series of tests like the one illustrated in figure 3. This figure shows the history of a typical tunnel run at $M = 3$, a stagnation temperature of 500°F , a dynamic pressure of 3,100 psf, and zero differential pressure. During this run the panel temperature varied with time as shown. All other test conditions were held constant. The panel did not flutter until the temperature reached 150° , where flutter started as indicated by the open symbol. When the panel temperature reached 300° the flutter stopped, as indicated by the solid symbol. Theory predicts that as a panel is heated the effects of thermal expansion will develop compressive midplane stresses that increase the susceptibility to flutter. After buckling, the additional temperature rise increases the depth of buckles, thereby stiffening the panel and finally stopping the flutter.

The results of many such runs are shown in figure 4. The thickness-ratio parameter for flutter is shown as a function of the panel temperature rise. These results were obtained on aluminum panels with a length-width ratio of 10 tested at a Mach number of 3. Only panel thickness, stagnation temperature, and dynamic pressure were changed from test to test. Again the open symbols indicate flutter starts and the solid symbols indicate flutter stops. If these results are compared with the results shown in figure 2 it can be seen the maximum value of the thickness-ratio parameter for the start of flutter from figure 4 agrees with the envelope curve in figure 2 for an l/w of 10. Furthermore, the range of scatter of data below the envelope agrees with the range obtained by varying the temperature only. Thus, these results indicate that midplane stress is the primary cause of scatter.

Effect of Mach Number

The effect of Mach number on panel flutter is shown in figure 5, where the thickness-ratio parameter is plotted against Mach number at flutter. The tests were run at zero differential pressure on initially flat panels buckled by heat. The vertical bars represent the range of the test results for each Mach number and the number by each bar represents the number of test points. Any substantial Mach number trend in these data is obscured by the scatter. Again a large part of this scatter is probably due to differences in midplane stress.

FLUTTER OF CORRUGATION-STIFFENED PANELS

Next, consider the flutter of the panels stiffened by corrugations shown in figure 1. Tests have been run on both types of corrugation-stiffened panels shown. The panels were tested both with the flow direction along the corrugations and with the flow across the corrugations. The flutter results for the corrugation-stiffened panels with the flow direction across the corrugations are presented in figure 6. In this figure, the thickness-ratio parameter on the ordinate is based on an effective thickness, and the length-width ratio on the abscissa is based on an effective width. The length l is taken to be the actual length. The effective thickness and width are the dimensions of an equivalent isotropic plate that would have the same important stiffness characteristics as the actual orthotropic, corrugation-stiffened panel. (See the appendix.) The equivalent isotropic plate is found to have a greatly reduced structural width. Hence, almost-square corrugation-stiffened panels have large effective length-width ratios. It should be pointed out that this effective length-width ratio is a structural ratio and that the aerodynamic length-width ratio of the original panel is unchanged.

Using these effective dimensions allows the results for the various types of panels to be compared on the same basis. In figure 6 the solid bars are the flutter results for the corrugation-stiffened panels and the shaded bars are the results for unstiffened panels from figure 2. The envelope curve from figure 2 has been extended to include the present data. This envelope has been drawn as a continuous curve even though the results are for entirely different types of panels. At present there is no experimental verification that the flutter results for corrugation-stiffened panels with effective length-width ratio less than 10 will agree with the results for unstiffened panels. The small variation of the thickness-ratio parameter over a wide range of the length-width ratio indicates that stiffening the panel across the width has very little beneficial effect in preventing flutter. Incidentally, some of the corrugation-stiffened panels tested represented an actual design for a hypersonic vehicle. These panels fluttered at unsatisfactorily low

dynamic pressures. A "fix" was obtained on these panels by welding small strips to the back of the corrugations, and flutter was thereby prevented for dynamic pressures of twice the original flutter value.

Results for stiffened panels with the flow direction along the corrugations do not appear in this figure because no flutter was obtained up to the maximum tunnel conditions, which were about 40 percent greater than the conditions required for flutter of the best corrugation-stiffened panel shown. The panels with corrugations aligned with the flow are very stiff along the length, and on an equivalent basis the value of the thickness-ratio parameter would be very large - well outside the flutter region.

For all the corrugation-stiffened panels that fluttered, the flutter was very sudden and very severe. The panels failed unless flutter was stopped in a few seconds.

PANEL FLUTTER ON X-15 AIRPLANE

The material presented so far summarizes the present understanding of the flutter of flat panels based on theoretical calculations and experimental results. It is of interest to examine these results in terms of a full-scale vehicle. The X-15 was designed as a manned hypersonic and reentry vehicle and the exposed surfaces of this vehicle consist of several of the panel types shown in figure 1. Figure 7 shows the X-15 and some of the regions where unstiffened panels and corrugation-stiffened panels are used. The shaded areas represent fairing panels stiffened by corrugations across the flow direction and the black areas represent unstiffened panels that have a length-width ratio of 10. Wind-tunnel tests on the full-scale vertical tail and on full-scale panels from the side fairings have shown that panel flutter exists in the operating range of the X-15. Severe vibrations that appeared during the early flights were in part traced to flutter of these side-fairing panels.

The flutter data for panels from the X-15 are shown in figure 8 in relation to the flutter boundary established in figure 6. The ordinate is the familiar thickness-ratio parameter based on the panel length and effective thickness and the abscissa is the ratio of the panel length to the effective width. The circle point represents a flutter point for the unstiffened panel on the vertical tail. This was not a boundary point (as indicated by the arrow); it was obtained from wind-tunnel tests for conditions beyond the design range of the vehicle. The square symbol at l/w_{EFF} of 150 was a flutter-boundary point obtained in flight on one of the corrugation-stiffened panels from the side fairing, and the square symbols at l/w_{EFF} at 4 represent flutter-boundary points from

wind-tunnel tests of another fairing panel obtained at two different Mach numbers. These results are gratifying. The results for the panel with $l/w_{EFF} = 4$ are seen to agree with the envelope curve established in figure 2 by the results for unstiffened panels. This agreement indicates that the flutter of corrugation-stiffened and unstiffened panels can be satisfactorily compared on the basis of equivalent isotropic plates. For the panel at $l/w_{EFF} = 4$, a single strap riveted to the back of this panel doubled the dynamic pressure required for flutter; three straps were necessary to prevent flutter within the design range of the vehicle.

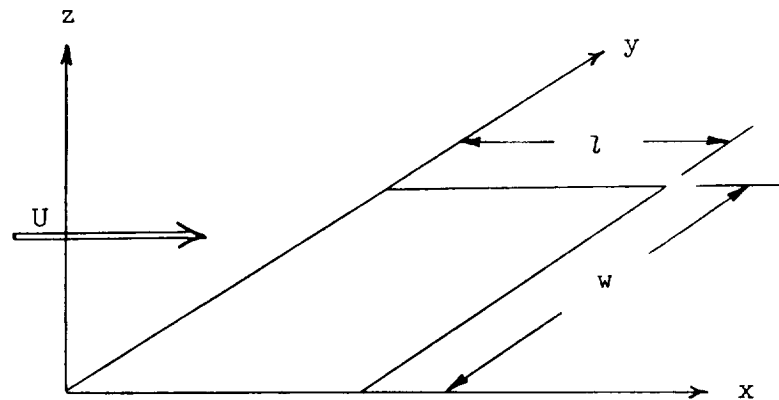
CONCLUDING REMARKS

Experimental flutter results have been presented for panel configurations including long narrow panels and corrugation-stiffened panels for which previously no information was available. Aerodynamic heating was shown to have considerable effect on the flutter results. Flutter boundaries were established for all types of panels when considered on the basis of equivalent isotropic plates. The results of wind-tunnel tests were shown to agree well with flight data obtained from a hypersonic vehicle. Also, the fact has been established that from the standpoint of flutter, corrugation-stiffened panels should be designed so that the flow is along the corrugations in order to obtain the greatest flutter margin.

APPENDIX

FLUTTER ANALYSIS OF ORTHOTROPIC PLATES

The panel configuration to be analyzed herein consists of a simply supported flat plate mounted in a rigid wall with supersonic air flowing over the top surface. The plate has different elastic properties in the flow direction than in the direction across the flow. The plate has a length l in the flow direction and a width w and is subjected to constant midplane forces of intensities N_x and N_y (positive in compression).



Sketch 1

In the analysis, small-deflection thin-plate theory for anisotropic plates (see ref. 3) is assumed to apply. The equilibrium equation and boundary conditions are:

$$\left. \begin{aligned} D_x \frac{\partial^4 W}{\partial x^4} + 2D_{xy} \frac{\partial^4 W}{\partial x^2 \partial y^2} + D_y \frac{\partial^4 W}{\partial y^4} + N_x \frac{\partial^2 W}{\partial x^2} + N_y \frac{\partial^2 W}{\partial y^2} + \gamma \frac{\partial^2 W}{\partial \tau^2} &= L(x, y, \tau) \\ W(0, y, \tau) = W(l, y, \tau) = W(x, 0, \tau) = W(x, w, \tau) &= 0 \\ \frac{\partial^2 W}{\partial x^2}(0, y, \tau) = \frac{\partial^2 W}{\partial x^2}(l, y, \tau) = \frac{\partial^2 W}{\partial y^2}(x, 0, \tau) = \frac{\partial^2 W}{\partial y^2}(x, w, \tau) &= 0 \end{aligned} \right\} \quad (1)$$

where $W(x, y, \tau)$ is the lateral deflection of the plate and $L(x, y, \tau)$ is the lateral load per unit area due to aerodynamic pressure. The flexural rigidities of the plate in the x - and y -directions are D_x

and D_y , respectively, D_{xy} is the twisting stiffness relative to the x - and y -directions, and γ is the density of the plate per unit area.

It is assumed that the air forces yielded by linearized static aerodynamic theory give an adequate approximation. The flutter analysis that follows is based on aerodynamic strip theory and follows the procedure given in reference 4 for the flutter of isotropic plates.

The aerodynamic loading is given by the simple Ackeret value and equation (1) becomes

$$D_x \frac{\partial^4 W}{\partial x^4} + 2D_{xy} \frac{\partial^2 W}{\partial x^2 \partial y^2} + D_y \frac{\partial^4 W}{\partial y^4} + N_x \frac{\partial^2 W}{\partial x^2} + N_y \frac{\partial^2 W}{\partial y^2} + \gamma \frac{\partial^2 W}{\partial \tau^2} + \frac{2q}{\beta} \frac{\partial W}{\partial x} = 0 \quad (2)$$

where q is the dynamic pressure $\rho U^2/2$, $\beta = \sqrt{M^2 - 1}$, and M is the Mach number.

For harmonic motion of the simply supported plate the lateral deflection can be written in the form

$$W = \text{Re} \left[\bar{W}_n(x) \sin \frac{n\pi y}{l} e^{i\omega\tau} \right] \quad (3)$$

where ω is the circular frequency.

Substituting equation (3) into equation (2) yields

$$\begin{aligned} \bar{W}_n^{IV} - 2n^2\pi^2 \left(\frac{l}{w}\right)^2 \frac{D_{xy}}{D_x} \bar{W}_n'' + n^4\pi^4 \left(\frac{l}{w}\right)^4 \frac{D_y}{D_x} \bar{W}_n + R_x \bar{W}_n'' \\ - n^2\pi^2 R_y \left(\frac{l}{w}\right)^2 \bar{W}_n + \lambda \bar{W}_n' - k^2 \bar{W}_n = 0 \end{aligned} \quad (4)$$

and the associated boundary conditions

$$\bar{W}_n(0) = \bar{W}_n''(0) = \bar{W}_n(l) = \bar{W}_n''(l) = 0$$

where the primes denote differentiation with respect to $x_1 = \frac{x}{l}$ and

$$\left. \begin{aligned} R_x &= \frac{N_x l^2}{D_x} & \lambda &= \frac{2ql^3}{\beta D_x} \\ R_y &= \frac{N_y l^2}{D_x} & k^2 &= \frac{\gamma l^4}{D_x} \omega^2 \end{aligned} \right\} \quad (5)$$

Equation (4) can be rewritten:

$$\bar{w}_n^{IV} + A\bar{w}_n'' + \lambda\bar{w}_n' - B\bar{w}_n = 0 \quad (6)$$

where

$$\left. \begin{aligned} A &= R_x - 2n^2\pi^2\left(\frac{l}{w}\right)^2 \frac{D_{xy}}{D_x} \\ B &= k^2 + n^2\pi^2\left(\frac{l}{w}\right)^2 R_y - n^4\pi^4\left(\frac{l}{w}\right)^4 \frac{D_y}{D_x} \end{aligned} \right\} \quad (7)$$

Equations (6) and (7) are now in the same form as equations (7) and (8), respectively, of reference 4, and the solutions presented therein in terms of the parameters A, B, and λ apply to the present problem. The results presented in reference 4 show that the value of λ_{cr} is essentially dependent on the parameter A and that the results for a plate aspect ratio of 1 could be extended to apply to other aspect ratios through the use of this parameter. It was shown also that coupling between the various modes in the y-direction is slight and that λ_{cr} is virtually independent of the value of R_y .

Examination of the parameters of the present problem in equations (5) and (7) shows that the orthotropic plate properties can be replaced by the properties of an equivalent isotropic plate that has the same important stiffness characteristics for flutter. From aerodynamic consideration the equivalent plate must have the same length l and plate stiffness D_x in the flow direction as the orthotropic plate. Since the value of λ_{cr} is essentially dependent on A, the effective structural aspect ratio for the equivalent isotropic plate can be determined from the last term in A by means of the relation

$$\left(\frac{l}{w}\right)_{EFF} = \frac{l}{w} \sqrt{\frac{D_{xy}}{D_x}} \quad (8)$$

where $\left(\frac{l}{w}\right)_{EFF}$ is the effective length-width ratio of the equivalent plate.

Equation (7) can be rewritten:

$$\left. \begin{aligned} \bar{A} &= \bar{R}_x - 2n^2 \left(\frac{l}{w} \right)_{\text{EFF}}^2 \\ \bar{B} &= \bar{k}^2 + n^2 \left(\frac{l}{w} \right)_{\text{EFF}}^2 \bar{R}_y - n^4 \left(\frac{l}{w} \right)_{\text{EFF}}^4 \frac{D_x D_y}{D_{xy}^2} \end{aligned} \right\} \quad (9)$$

where

$$\bar{R}_x = \frac{R_x}{\pi^2}$$

$$\bar{R}_y = \frac{R_y}{\pi^2} \frac{D_x}{D_{xy}}$$

$$\bar{k} = \frac{k}{\pi^2}$$

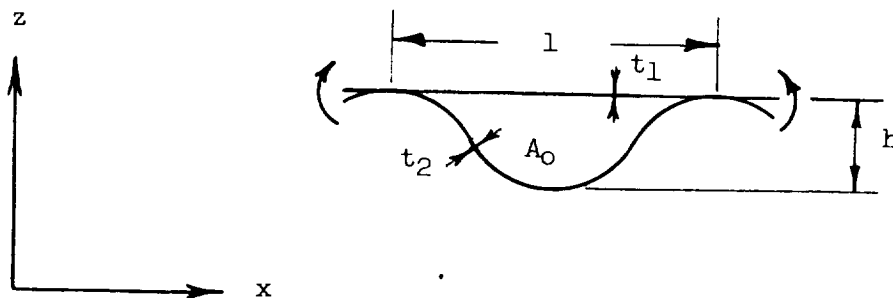
Since λ_{cr} has been shown to be essentially independent of \bar{R}_y , the essential properties of the equivalent isotropic plate are defined by the three quantities l_{EFF} , D_x , and w_{EFF} . The last term in \bar{B} appears as a constant and hence would not alter the value of λ_{cr} for which the values of \bar{B} become complex and the motion becomes unstable.

The properties of the equivalent isotropic plate are as follows:

$$\left. \begin{aligned} l_{\text{EFF}} &= l \\ w_{\text{EFF}} &= w \sqrt{\frac{D_x}{D_{xy}}} \\ D_{\text{EFF}} &= D_x \\ t_{\text{EFF}} &= \left[12(1 - \nu^2) \frac{D_x}{E} \right]^{1/3} \end{aligned} \right\} \quad (10)$$

where D_{EFF} is the plate stiffness of the equivalent plate, t_{EFF} is the thickness, l_{EFF} is the length, w_{EFF} is the width, ν is Poisson's ratio, and E is Young's modulus of elasticity.

For the corrugation-stiffened panels discussed in this paper, the stiffness properties were obtained as follows: The plate stiffness D_x was calculated for a unit element of the panel shown in the following sketch:



Sketch 2

The element consisted of one corrugation and the cover sheet. The stiffness D_x was obtained by analyzing the element as a structural bent. (See, for example, ref. 5.) The stiffness D_{xy} was obtained from the torsional stiffness of the element shown in sketch 2 by means of the relation

$$\frac{D_{xy}}{G} = \frac{4A_0^2}{\oint \frac{ds}{t}} \quad (11)$$

where A_0 is the enclosed area of the torque cell, ds is the length of a differential element of the sheet, t is the sheet thickness, and h is the normalized depth of the corrugation. The properties of the equivalent isotropic plate were obtained from equations (10).

REFERENCES

1. Tuovila, W. J., and Hess, Robert W.: Experimental Investigation of Flutter of Buckled Curved Panels Having Longitudinal Stringers at Transonic and Supersonic Speeds. NASA MEMO 5-18-59L, 1959.
2. Sylvester, Maurice A.: Experimental Studies of Flutter of Buckled Rectangular Panels at Mach Numbers From 1.2 to 3.0 Including Effects of Pressure Differential and of Panel Width-Length Ratio. NACA RM L55I30, 1955.
3. Timoshenko, S.: Theory of Plates and Shells. McGraw-Hill Book Co., Inc., 1940.
4. Hedgepeth, John M.: Flutter of Rectangular Simply Supported Panels at High Supersonic Speeds. Jour. Aero. Sci., vol. 24, no. 8, Aug. 1957, pp. 563-573, 586.
5. Wang, Chu-Kia: Statically Indeterminate Structures. McGraw-Hill Book Co., Inc., 1953.

PANELS FOR HYPERSONIC VEHICLES

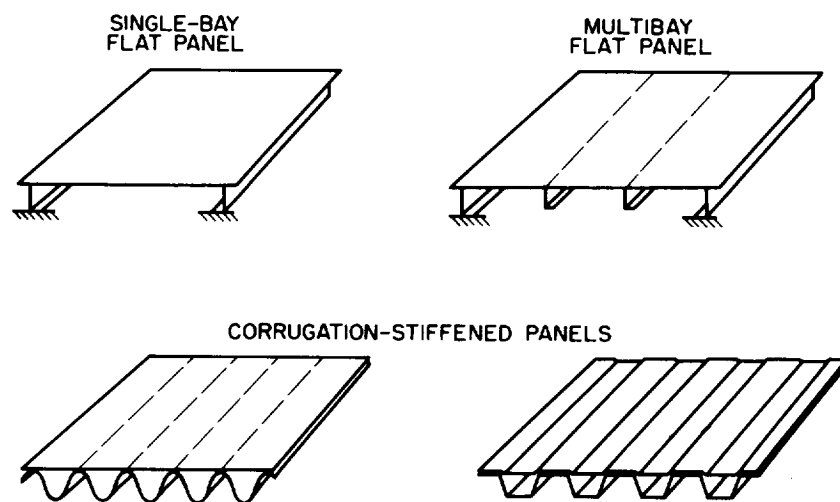


Figure 1

FLUTTER OF UNSTIFFENED PANELS

$$\Delta p \approx 0$$

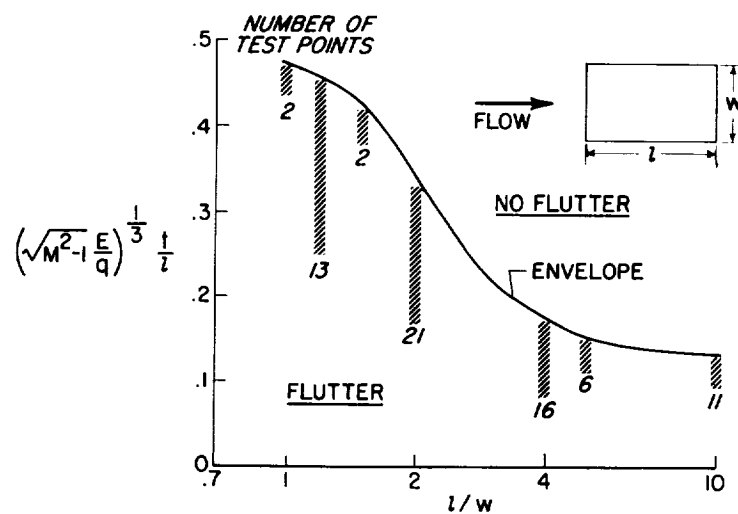


Figure 2

TYPICAL TRANSIENT-HEATING TEST

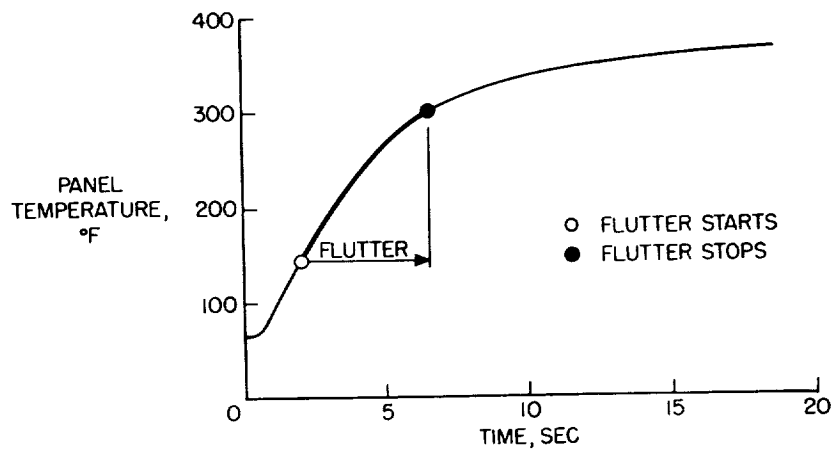
 $M=3.0$; $T_0=500^\circ\text{F}$; $q=3,100$ PSF


Figure 3

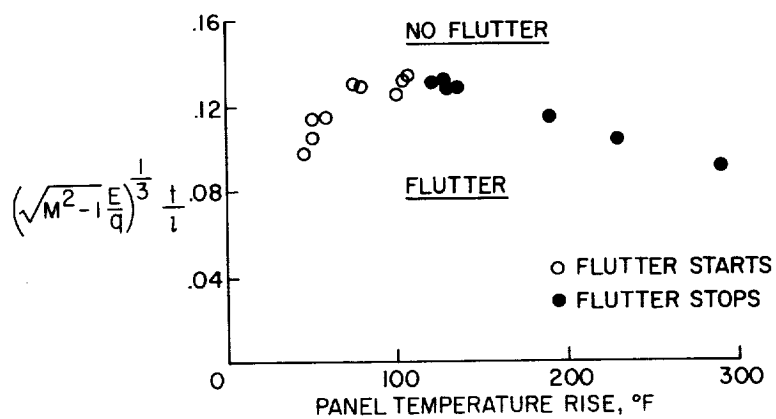
EFFECT OF AERODYNAMIC HEATING ON
FLUTTER OF CLAMPED PANELS
 $M=3$; $l/w=10$; $\Delta p \approx 0$


Figure 4

EFFECTS OF MACH NUMBER PANELS BUCKLED BY HEAT; $\Delta p \approx 0$

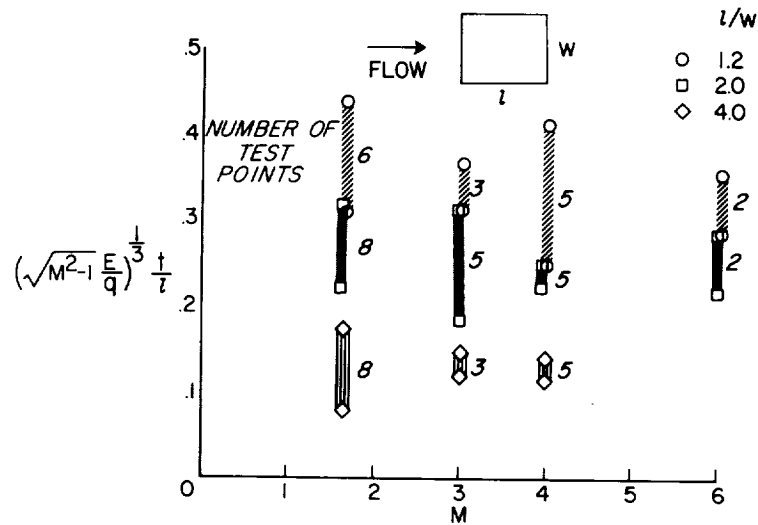


Figure 5

FLUTTER OF CORRUGATION-STIFFENED PANELS $\Delta p \approx 0$

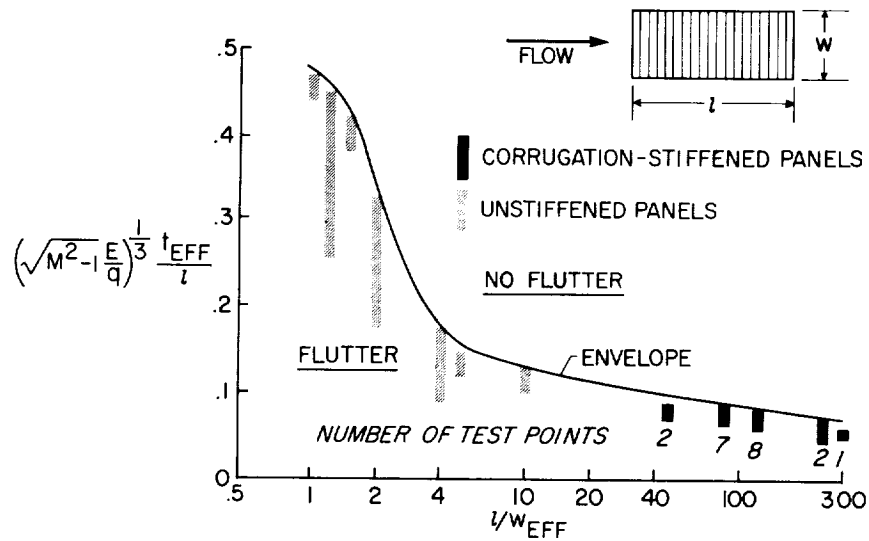


Figure 6

REGIONS OF X-15 RESEARCH AIRCRAFT AFFECTED BY PANEL FLUTTER

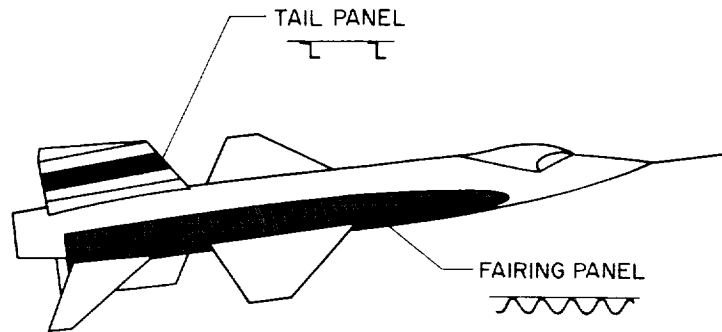


Figure 7

X-15 PANEL-FLUTTER RESULTS

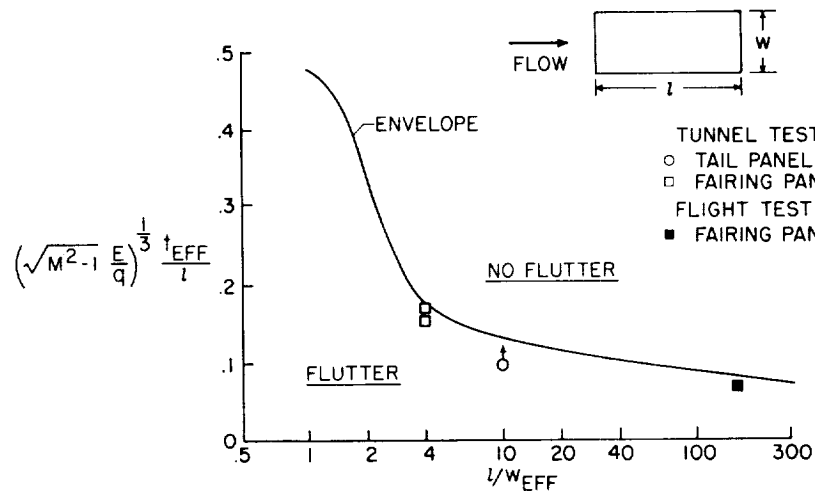


Figure 8

NOISE CONSIDERATIONS FOR MANNED REENTRY VEHICLES

By David A. Hilton, William H. Mayes, and Harvey H. Hubbard
Langley Research Center

SUMMARY

Noise measurements pertaining mainly to the static firing, launch, and exit flight phases are presented for three rocket-powered vehicles in the Project Mercury test program. Both internal and external data from onboard recordings are presented for a range of Mach numbers and dynamic pressures and for different external vehicle shapes.

The main sources of noise are noted to be the rocket engines during static firing and launch and the aerodynamic boundary layer during the high-dynamic-pressure portions of the flight. Rocket-engine noise measurements along the surface of the Mercury Big Joe vehicle were noted to correlate well with data from small models and available data for other large rockets. Measurements have indicated that the aerodynamic noise pressures increase approximately as the dynamic pressure increases and may vary according to the external shape of the vehicle, the highest noise levels being associated with conditions of flow separation. There is also a trend for the aerodynamic noise spectra to peak at higher frequencies as the flight Mach number increases.

INTRODUCTION

Manned space flight operations involve some potentially serious noise environments both inside and outside the space vehicle. (See refs. 1 to 4.) These problems arise for some rather obvious reasons; namely, the use of very powerful engines, the high airspeeds attained within the earth's atmosphere, and the need to save weight in the basic structure in order to accommodate the maximum payload. There is a need for maintaining the integrity of the space vehicle structure and for eliminating malfunction of its sensitive control equipment. There is also a need to control the inside noise environments of the occupied area to insure safety of the occupants, and to allow them to communicate with the ground station and to perform other assigned duties.

Although some analytical studies have been made of the noise environments of ground-launched space vehicles (refs. 1 and 2), very little measured data are generally available, particularly for large vehicles. Recent flight tests of three rocket-powered vehicles in connection with Project Mercury have, however, provided some data of this type for a range of operating conditions. Some of these data are presented and are compared, where possible, with results from other studies. An attempt is also made to generalize these data for use in predicting the noise environments of future space vehicles.

SOURCES OF NOISE

The noise sources that are of concern for manned reentry vehicles are indicated schematically in figure 1. A flight path extends from launch through the exit phase to space flight conditions and reentry. Also indicated on figure 1 are the major sources of noise in each phase of the flights. At lift-off and also during static firing, the main sources of noise are the rocket engines. During the exit phase of the flight, particularly during conditions of high dynamic pressure, the main noise comes from the fluctuating pressures in the aerodynamic boundary layer. Internal equipment such as air conditioners, etc., are expected to be the main source of noise during space flight, whereas during the reentry phase the noise is expected to be of aerodynamic origin. This paper contains information relating mainly to the launch and exit phases of the flight during which time the highest noise levels are encountered.

TEST VEHICLES

Recent noise research studies accomplished in connection with Project Mercury have provided some information for the various noise sources noted in figure 1, by use of the test vehicles schematically shown in figure 2. The test vehicles shown are the Big Joe, which was instrumented by NASA Space Task Group personnel and fired from Cape Canaveral, Florida, and the Little Joe 2 and Little Joe 1B vehicles, which were instrumented by Langley Research Center personnel and fired from Wallops Island, Virginia. The approximate location of both external and internal microphone stations are indicated. The internal microphones were located at the position where the pilot's head would be located, approximately 6 inches from the capsule side wall. The flight data were recorded with the aid of onboard tape recorders which were recovered after the flights. It should be noted that the external geometries of the vehicles differ, and that the Mach number and free-stream dynamic-pressure ranges for these vehicles are also different.


NOISE AT LIFT-OFF

Data relating to the external noise environment of an entire launch vehicle, including the manned compartment and the booster sections, are given in figure 3. Sound pressure levels in decibels (reference level, 0.0002 dyne/cm^2) are plotted for various distances h/d , where h is the distance measured from the nozzle exit plane toward the nose of the vehicle, and d is the equivalent nozzle diameter. For a multiple-nozzle arrangement, d is assumed to be the diameter of a circular nozzle equivalent in area to the sum of the smaller ones. As a matter of interest, the thrust of large booster engines per unit nozzle exit area is nearly a constant. Thus, this quantity d is essentially proportional to the square root of the total thrust of the vehicle.

The locations of the two lines (fig. 3) were based on experimental results from model supersonic jets and small rocket engines. The line on the left represents estimated sound pressure levels along the outside of the vehicle for the case where the rocket-engine exhaust exits straight down and is not deflected. (See refs. 5 and 6.) Such a condition as this might exist when the vehicle is at a high enough altitude to be outside of the ground effects but still at some low flight velocity. It has been found in some unpublished model studies that a turning of the exhaust stream results also in a turning of the noise field and by about the same amount. On this basis the line on the right has been drawn in to indicate the maximum sound pressure levels that would result from a 90° deflection of the exhaust stream.

Plotted on figure 3 also are several data points obtained for rocket engines of various thrust ratings. It will be noted that the data for large rocket engines fall generally between the extreme values of the lines. The only exceptions are the two data points on the extreme right. These apply to an engine having noise spectra which contain large discrete peaks resulting probably from rough burning. It can be seen that the sound pressure levels increase in general for stations closer to the nozzle exit, that is, for smaller values of h/d . Although this is a rather unsophisticated approach to predicting the sound pressure levels along the surface of the vehicle, the fact that data correlate well for a wide range of jet sizes gives confidence that it will be useful for larger thrust vehicles such as the Saturn.

Of particular interest are the data indicated by the blocked-in symbols from unpublished work of William H. Mayes and Phillip M. Edge, which apply directly to the Atlas vehicle of Project Mercury. In addition to the overall sound pressure levels, it is of interest to know the spectra at various stations along the vehicle. As an example of the data obtained for the Atlas vehicle in the region where the manned capsule will be located, spectra for both external and internal measuring




stations are included in figure 4. Sound pressure levels are shown for various octave bands in cps. The spectra measured at other external stations along the vehicle were of higher levels but did not differ appreciably in shape from the external spectra shown in figure 4. A procedure for correlating rocket engine sound spectrum levels in the region of the vehicle is given in reference 7.

The differences in sound pressure level between the external and internal spectra of figure 4 are an indication of the noise transmission loss associated with the capsule structure. Shown for comparison is the internal spectrum as estimated theoretically from pure inertia considerations of the mass law. (See ref. 8.) It may be seen that more noise reduction occurred at the lower frequencies than would be predicted. Other noise transmission studies conducted on this same capsule structure have also confirmed this finding. It is believed that this additional noise reduction at the low frequencies results from stiffness effects due to the characteristic shape of the capsule.

IN-FLIGHT NOISE

As an example of the type of data that have been measured in space vehicles, a time history of the internal capsule noise for the lift-off and subsequent free-flight operation of the Big Joe Mercury vehicle is shown in figure 5. These data from the work of William T. Lauten and David A. Hilton were obtained with the aid of an onboard tape recorder recovered after the flight. Some of the significant events such as launch, maximum dynamic pressure, and approximate reentry, etc., are indicated. The electrical-circuit noise, or so-called "hash level," was about 100 db as noted in figure 4 for the gain settings used in this experiment. It can be noted that the highest sound pressure levels were recorded during the time that the vehicle was operating at its maximum dynamic pressure, and it is believed that this noise is due to the aerodynamic boundary layer. As a result of exploratory communication studies with various types of personal flight equipment, there is some concern for the reliability of two-way voice communications in the presence of aerodynamic sound pressure levels which exceed 120 db.

In addition to the data illustrated in figure 4, similar onboard recordings have been successfully made for two Little Joe Mercury vehicles of the type illustrated in figure 2. The capsules were similar in shape but differed somewhat in their external forebody configurations. Little Joe tests have produced similar results; namely, the internal aerodynamic sound pressure levels were higher than those from the other major sources and persisted for a longer period of time. Thus, because of the relative importance of the aerodynamic noise, it is necessary to understand the



manner in which this noise is related to vehicle geometry and performance in the Mach number and dynamic-pressure ranges of interest.

Consequently, the noise data from two of these tests have been plotted in figure 6 as a function of dynamic pressure q along with a curve of estimated maximum external sound pressure levels based on available wind-tunnel tests (ref. 9), flight tests of Norman J. McLeod and Gareth H. Jordan, and flight and rotating cylinder tests of reference 7. The estimated external sound pressure levels of the figure were calculated as follows:

$$\text{Sound pressure level} = 20 \log_{10} \left(\frac{0.006q}{p_{\text{ref}}} \right) \text{db}$$

where the reference pressure p_{ref} is equal to 4.177×10^{-7} lb/sq ft. The differences between the estimated external and the measured internal sound pressure levels are indications of the noise transmission loss through the structure.

It is noted that the internal noise pressures increase as the dynamic pressure increases, the noise pressures being roughly proportional to the dynamic pressure. The curve of small dashes applies to the Big Joe vehicle and is plotted in such a way that flight Mach numbers 1.0, 2.0, 3.0, and 4.0 are indicated. It will be noted that at any given value of dynamic pressure the lower sound pressure level is associated with the higher Mach number. Data for the Little Joe 2 vehicle, as shown by the solid curve, show similar results for the Mach number range up to nearly 6.0. It is believed that this reduction in internal sound pressure level at the higher Mach numbers may result from differences in the noise spectra.

In order to illustrate these differences, internal noise spectra in the Big Joe vehicle for the same value of dynamic pressure but for two different Mach numbers are shown in figure 7. In this figure, sound pressure level is plotted for various octave bands for both subsonic and supersonic Mach numbers. It is evident from the figure that the spectrum at the higher Mach number peaks at a higher frequency. This shift of the peak of the spectrum toward higher frequencies is believed to result in a greater transmission loss through the structure (ref. 8) and thus to lower inside sound pressure levels. It should be noted that these are internal spectra; the external spectra would be expected also to shift in this same manner and probably by a greater amount.

Another factor which was noted to be of significance with respect to the inside sound pressure levels is the outside geometry of the vehicle. Some of the effects of external geometry on the aerodynamic sound

~~CONFIDENTIAL~~

pressure levels are shown in figure 8. A dimensionless ratio of noise pressure to dynamic pressure is plotted as a function of Mach number for the three test configurations. The lowest noise pressures measured are for the Big Joe Mercury vehicle. In general, it can be seen that, for a given value of local dynamic pressure, the inside noise pressures decrease as the Mach number increases. For the reentry configuration where the blunt base is forward, the aerodynamic noise pressures were noted to be markedly lower than those during the exit phase. The reason for these lower noise pressures in reentry is not fully understood at the present time; however, they are believed to be due in part to the difference in capsule orientation (ref. 10) and also to Mach number effects.

Although some minor differences existed in construction and internal sound treatment, it is believed that the differences in the measured noise pressures between Little Joe 2 and the Big Joe vehicle may be ascribed mainly to differences in external geometry. Of particular interest is a direct comparison of the data for Little Joe 2 with that for Little Joe 1B. In this comparison the only significant difference in the two configurations was the presence of a Marman band spoiler on Little Joe 1B to increase its aerodynamic stability. The resulting internal noise pressures are seen to be markedly higher in this latter case. These noise pressure increases are due possibly to separated flow conditions induced by the spoiler and are of the same order of magnitude as those previously measured in a wind-tunnel model having separated flow and different external contours. (See ref. 11.)

Also of interest with regard to the excitation of the heat shields are the fluctuating external surface pressures due to the presence of the spoiler. These external data are shown in figure 9 where the ratio of sound pressure to dynamic pressure is again shown as a function of Mach number. The horizontal line of small dashes represents the maximum values that would be estimated on the basis of available wind-tunnel and low-speed flight data. (See refs. 7 and 9.) The data measured with a surface pressure pickup on the conical section of the Little Joe 1B vehicle in the sketch are higher at some Mach numbers than the maximum values that would have been predicted for the "no spoiler" case. A distinguishing characteristic of the external noise is the existence of large-amplitude low-frequency disturbances, particularly at the lower Mach numbers. It should be emphasized that these data were measured at a single point on the vehicle and hence may apply directly to only a small area on its surface. Furthermore, the surface-pressure conditions at any point may be a function of Mach number and hence would probably vary as a function of time.

~~CONFIDENTIAL~~

CONCLUDING REMARKS

The main sources of noise for a rocket-powered reentry vehicle are noted to be the engines during static firing and launch and the aerodynamic boundary layer during the high dynamic pressure portions of the flight. Rocket engine noise measurements along the surface of the Mercury Big Joe vehicle were noted to correlate well with data from small models and with available data for other large rockets. Measurements for three different flight vehicles have indicated that the aerodynamic noise pressures increase approximately as the dynamic pressure increases and may vary according to the external shape of the vehicle, the highest sound pressure levels being associated with conditions of flow separation. There is also a trend for the aerodynamic noise spectra to peak at higher frequencies as the Mach number increases.

REFERENCES

1. Von Gierke, H. E.: Vibration and Noise Problems Expected in Manned Space Craft. Noise Control, vol. 5, no. 3, May 1959, pp. 9-16.
2. Nadel, Aaron B.: Auditory Noise and Vibration Problems for Manned Space Vehicles. Res. Memo. RM 59TMP-50, General Electric Co., Oct. 20, 1959.
3. Dyer, I., Franken, P. A., and Ungar, E. E.: Noise Environments of Flight Vehicles. Noise Control, vol. 6, no. 1, Jan.-Feb. 1960, pp. 31-40, 51.
4. Franken, Peter A., Kerwin, Edward M., Jr., and the Staff of Bolt Beranek and Newman, Inc. (Cambridge, Mass.): Methods of Flight Vehicle Noise Prediction. WADC Tech. Rep. 58-343, ASTIA Doc. No. AD 205776, U.S. Air Force, Nov. 1958.
5. Mayes, William H., Lanford, Wade E., and Hubbard, Harvey H.: Near-Field and Far-Field Noise Surveys of Solid-Fuel Rocket Engines for a Range of Nozzle Exit Pressures. NASA TN D-21, 1959.
6. Von Gierke, H. E.: Recent Advances and Problems in Aviation Acoustics. Presented at Third International Congress on Acoustics (Stuttgart, Germany), Sept. 1-8, 1959.
7. Eldred, Ken: Prediction of Sonic Exposure Histories. Proceedings of the Symposium on Fatigue of Aircraft Structures, WADC Tech. Rep. 59-507, U.S. Air Force, Aug. 1959, pp. 396-415.
8. Nichols, R. H., Jr., Sleeper, H. P., Jr., Wallace, R. L., Jr., and Ericson, H. L.: Acoustic Materials and Acoustical Treatments for Aircraft. Jour. Acous. Soc. Am., vol. 19, no. 3, May 1947, pp. 428-443.
9. Willmarth, William W.: Wall Pressure Fluctuations in a Turbulent Boundary Layer. NACA TN 4139, 1958.
10. Callaghan, Edmund E.: An Estimate of the Fluctuating Surface Pressures Encountered in the Reentry of a Ballistic Missile. NACA TN 4315, 1958.
11. Regier, Arthur A.: Noise, Vibration, and Aircraft Structures. Preprint no. 631, S.M.F. Fund Preprint, Inst. Aero. Sci., Jan. 23-26, 1956.

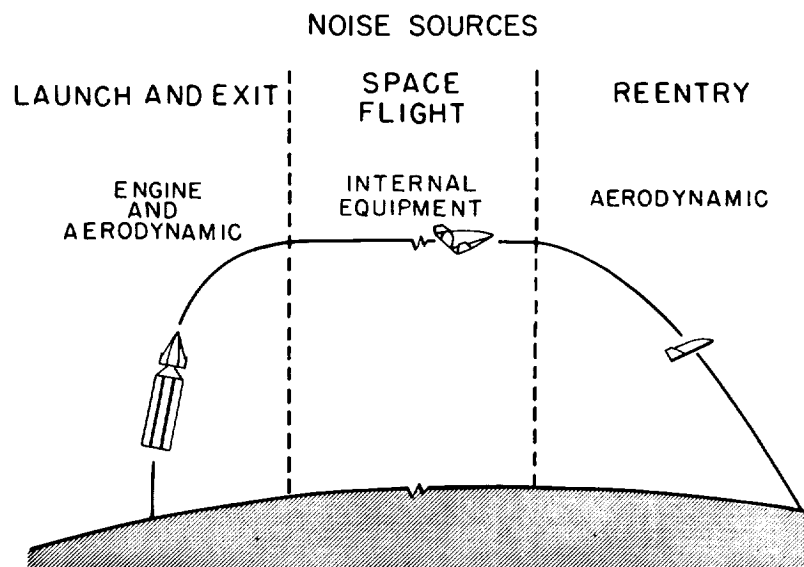


Figure 1

MERCURY TEST VEHICLES

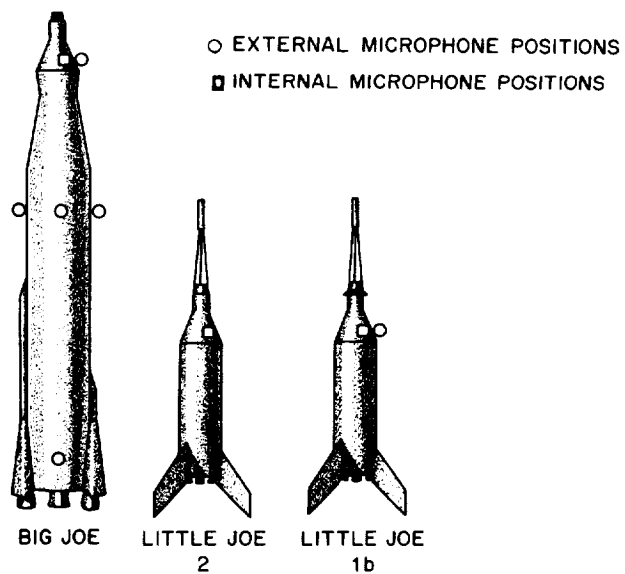


Figure 2

EXTERNAL SOUND PRESSURE LEVELS AT LIFT-OFF

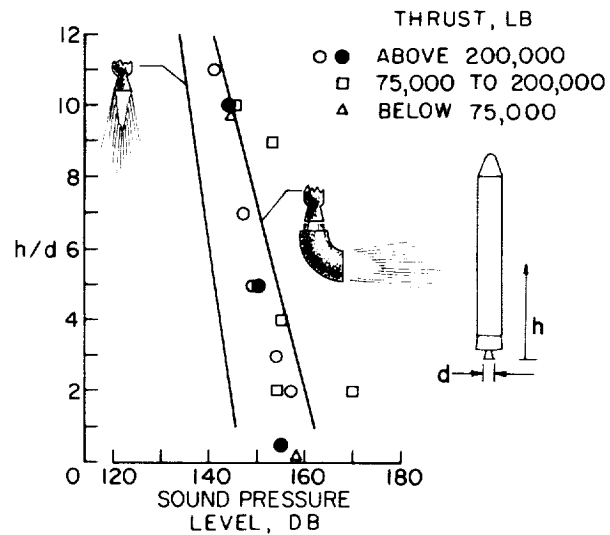


Figure 3

CAPSULE NOISE FROM ROCKET ENGINE

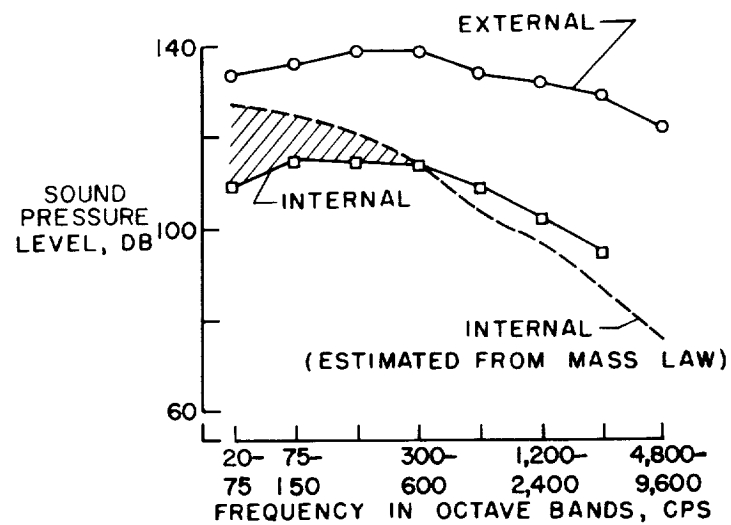


Figure 4

INTERNAL NOISE, BIG JOE

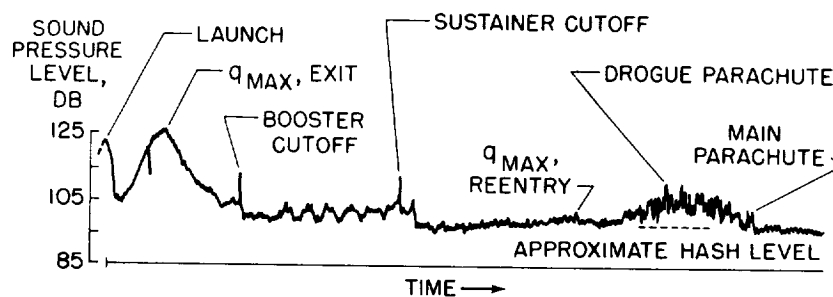


Figure 5

EFFECTS OF DYNAMIC PRESSURE

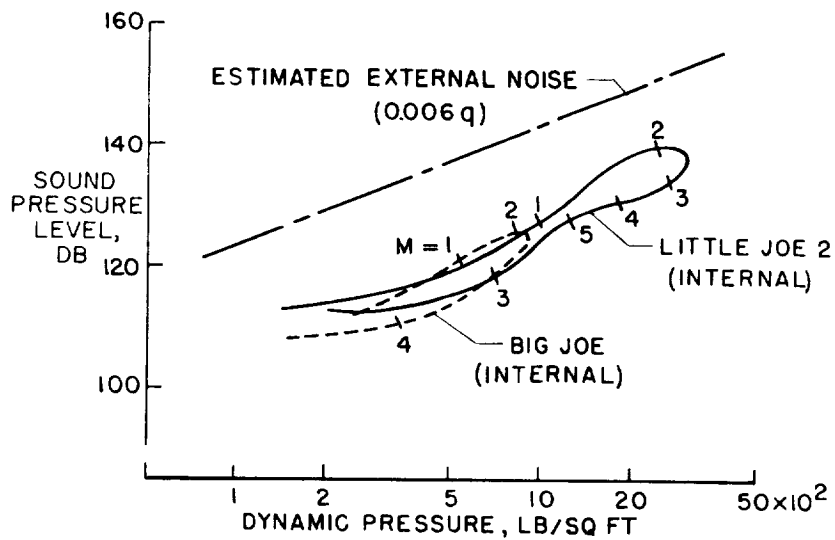


Figure 6

BIG JOE INTERNAL SPECTRA DURING EXIT

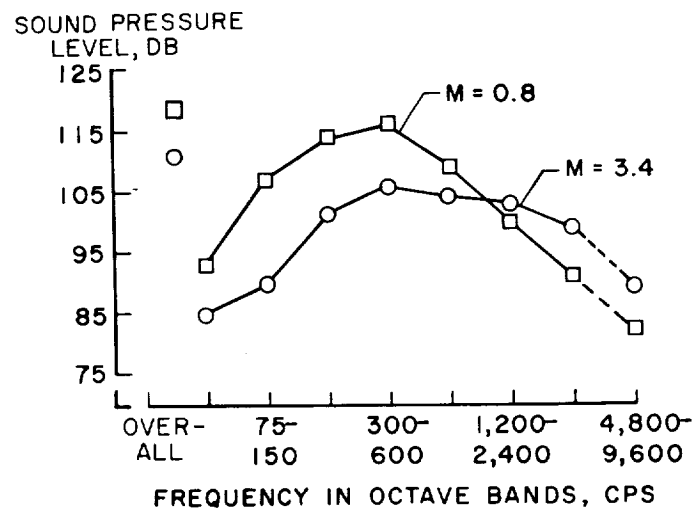


Figure 7

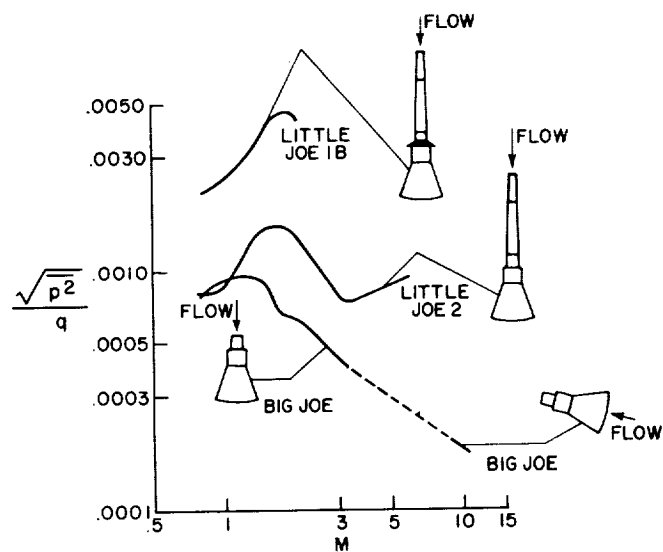
INTERNAL NOISE PRESSURES
EFFECTS OF GEOMETRY

Figure 8

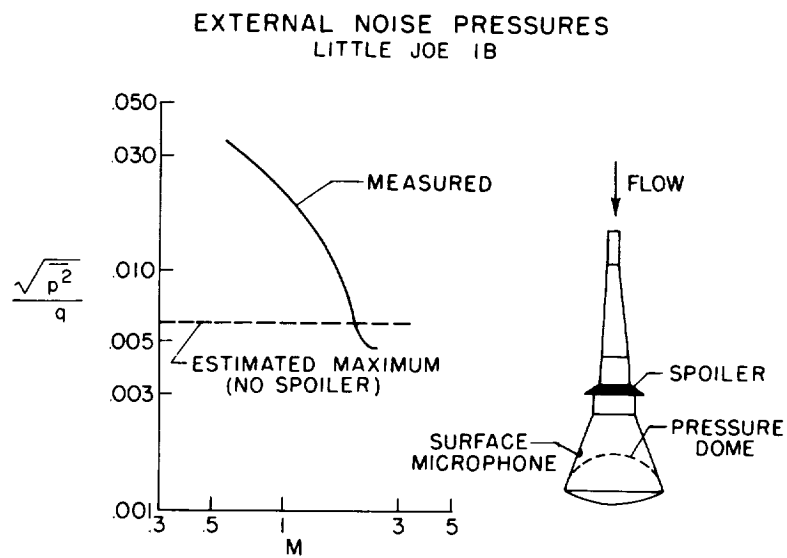


Figure 9

1

SOME LANDING STUDIES PERTINENT TO
GLIDER-REENTRY VEHICLES

By John C. Houbolt and Sidney A. Batterson
Langley Research Center

SUMMARY

Results are presented of some landing studies that may serve as guidelines in the consideration of landing problems of glider-reentry configurations.

The effect of the initial conditions of sinking velocity, angle of attack, and pitch rate on impact severity and the effect of locating the rear gear in various positions are discussed. Some information is included regarding the influence of landing-gear location on effective masses. Preliminary experimental results on the slideout phase of landing include sliding and rolling friction coefficients that have been determined from tests of various skids and all-metal wheels.

INTRODUCTION

Among the problems to be considered for glider-reentry vehicles is that of providing safe landing on return. Studies pertinent to the landing of these configurations have therefore been made, and the purpose of this paper is to present the results. It is convenient to separate the presentation into two parts.

Part I deals analytically with the effect of the initial conditions of sinking velocity, angle of attack, and pitch rate on impact severity, as well as the effect of rear-landing-gear position, including the influence of landing-gear location on the effective masses.

Part II deals with preliminary results of an experimental investigation of landing gears for glider-reentry vehicles. The configurations studied consist of a skid-type main gear and a nose gear equipped with either a skid or an all-metal wheel. This arrangement is reliable and also saves weight since it does not require cooling during reentry. Reentry vehicles of this type are very restricted in a choice of landing sites. The runway available for recovery may under some conditions be as

short as 5,000 feet and may be composed of either a concrete, asphalt, or lakebed surface. During the landing and subsequent slideout, the landing gear must provide adequate directional stability and, in addition, develop a drag load large enough to stop the vehicle before the end of the runway is reached. The problems arising from these conditions were studied at the Langley landing loads track by making simulated landings using a variety of skid configurations and all-metal wheels.

SYMBOLS

e	distance between center of gravity and main (rear) landing gear
e_{cr}	maximum distance between center of gravity and main landing gear for no second impact
e_{cp}	distance between center of gravity and center of percussion
e_n	distance between center of gravity and nose landing gear
e_R	distance between center of gravity and main landing gear at which tail load balances airplane weight
F	force
g	acceleration of gravity
k	radius of gyration in pitch
L_t	tail load
m	total mass
m_1	effective mass at main (rear) landing gear
m_2	effective mass at nose landing gear
n_1	$n_1 = \frac{\ddot{y}_0 + e\ddot{a}_0}{g}$
V	velocity
W	weight

y	vertical displacement
\dot{y}	vertical velocity
\ddot{y}	vertical acceleration
α	angle of attack
$\dot{\alpha}$	angular velocity in pitch
$\ddot{\alpha}$	angular acceleration in pitch
μ	coefficient of friction

Subscripts:

1	refers to main (rear) landing gear
2	refers to nose landing gear
o	initial condition at center of gravity

I - LANDING IMPACT ANALYSIS

The factors to be considered in part I of the present study are indicated in figure 1. First shown are the approach conditions α_o , $\dot{\alpha}_o$, and \dot{y}_o and the distance e between the main landing gear and the center of gravity. Next are indicated the effective masses m_1 and m_2 at the main and the nose landing gear, respectively.

Initial Conditions

The initial conditions which affect the severity of the first impact in landing are shown in figure 2. The vehicle is considered to have a nonrebounding type of landing gear, which has an essentially rectangular force-deflection curve, as would be obtained, for example, by use of a plastic yielding strut. The important result shown in the figure is the fact that the strut deflection can be expressed completely in terms of the initial velocity and acceleration at the landing-gear location, regardless of whether the velocity is due to a vertical translation or a pitch rate or whether the acceleration is due to a translatory acceleration or a pitch acceleration, as would result in the case of a non l g wing lift or an out-of-trim pitching moment. Note that the distance e of the gear aft of the center of gravity enters into the determination of

the velocity and acceleration at the gear. For reentry-type gliders, e generally will be much larger than is used in airplane configurations so as to avoid the tail scrubbing problem that is associated with the necessary high angle-of-attack, low lift-drag-ratio landing approach. Increased e therefore tends to make pitch rate and angular acceleration enter more prominently into the landing problem than heretofore. Conceivably, then, from a design standpoint, it may become necessary to establish realistic values of $\dot{\alpha}_0$ and $\ddot{\alpha}_0$ as well as $\dot{\gamma}_0$ and $\ddot{\gamma}_0$.

Rear-Landing-Gear Location

A more definite consequence of the use of large approach angles of attack and main landing gears placed well to the rear is the fact that increased attention must be focused on impacts which follow the initial impact; the second impact of the rear landing gear may, in fact, be much more severe than the first. An explanation is readily afforded by means of the schematic sketches shown on figure 3. With reference to the top sketch of figure 3, the high angle-of-attack approach and the upward pointing flow vector caused by the sinking speed mean that the stabilizer must have a rather large negative deflection to keep the airplane in trim and may even have to have a download for the situation where the wing center of lift is behind the center of gravity. After initial impact of the rear landing gear and during nose landing-gear impact, the landing condition becomes that shown on the lower sketch of figure 3. The tail has encountered two sizable increases in negative angle of attack, namely, the rotation of the vehicle to horizontal (or even to a slight negative attitude) and a change in the wind-flow direction to nearly horizontal. The download on the tail is now very large. All the loads - the tail load, the weight and download on the wing, and the large upload at the nose - are in directions virtually to drive the tail into the ground. Note that the initial conditions for the second rear impact about to occur in this figure are mainly those of large initial accelerations, the potential-energy type of impact in contrast to the kinetic-energy type of the first impact. Mention may also be made that the use of landing gears with some rebound characteristics would only serve to aggravate the situation. Such gears would feed back a potential energy into the system, which would then have to be taken out again; they should therefore be avoided if possible, especially because of the second rear-impact condition.

The second rear impact occurs only if the gear is located sufficiently aft. For gear location closer to the center of gravity, only one rear impact will occur. The difference in the landing sequences for these two situations is indicated in figure 4. For values of e less than a value which for the present purpose is designated e_{cr} , the vehicle first impacts on the rear gear, then pivots about the rear-gear point,

impacts on the nose gear, and comes to rest. For e greater than e_{cr} the first two phases are the same, but during the nose-gear impact the rear gear deflects further. The nose gear comes to rest, but the rear gear continues to deflect until the final rest position is obtained. Note that for $e > e_{cr}$ three movements of the rear gear occur in contrast to only one for $e < e_{cr}$.

Figure 5 indicates more specifically the effect of rear-gear location on impact severity. A configuration, representative of the X-15 airplane, having a weight of 14,000 pounds, a pitch radius of gyration of 161 inches, and a distance between the center of gravity and the nose gear of 280 inches, was arbitrarily chosen for study, and rear-gear positions covering the range from the center of gravity back to the rear of the fuselage were investigated. Results for energy absorbed and for strut travel are given in terms of the rear-gear location e . The plot at the top of the figure shows the energy absorbed in the first rear impact, the second rear impact, and in the nose gear; and the bottom plot shows rear and nose strut travel. The solid curves apply for an approach angle of attack of 10° , whereas the dashed curves apply to an approach angle of attack of 8° . Two main points are to be made from this figure: first, note the very pronounced increase in rear-strut travel as e is increased from a value of around 135 to 200 inches; at $e = 200$ inches, in fact, the total strut travel is on the order of three times the travel brought about by first impact alone; second, notice the marked decrease in rear-strut travel when the angle of attack is reduced from 10° to 8° . Angle of attack thus appears to be quite important and is discussed in more detail subsequently.

A further comment pertinent to figure 5 is in connection with the three values of e labeled on the abscissa as e_R , e_{cp} , and e_{cr} . If e is less than e_R , then the download at the tail will cause a tail-down rocking of the airplane, and therefore the region of $e < e_R$ is to be avoided. The value e_{cp} designates the location of the center of percussion; it is important from an effective mass consideration and is discussed further subsequently. The value of e_{cr} was mentioned previously in connection with figure 4; it separates the region where no additional rear-strut movement occurs during nose impact from that where some such movement occurs.

Figure 6 shows shock-strut force for a landing of the X-15 airplane (an e of 195 inches). The second rear impact is three to four times as severe as the first. Although the characteristics of the actual X-15 shock strut are somewhat different from those of the assumed idealization, these results furnish a qualitative substantiation of the predictions in figure 5.

In figure 7, additional results pertaining to the location of the rear landing gear are given; again, a nonrebounding type of gear having an essentially rectangular force-deflection curve was assumed. The solid-line curve is the maximum rear-gear force that can be applied in

first impact without exceeding a chosen design acceleration of 2.5g at any point in the vehicle. Thus, for example, a landing gear located 100 inches behind the center of gravity must not develop more than 20,000 pounds of force. The broken-line curves apply for the nose and second rear impact, and follow from two conditions: first, again that an acceleration of 2.5g is nowhere exceeded and second, that during nose impact the airplane simply pivots around the rear gear. For values of e less than about 135 inches, the force F_2 provided by the nose strut is sufficient to absorb completely the energy remaining in the airplane after initial impact. The force F_1 in the rear strut does not exceed that provided so that no further deflection of the rear strut takes place. However, for e greater than about 135 inches, the force F_1 necessary to satisfy the two conditions previously stated on acceleration and pivoting exceeds that provided. The rear strut therefore has to move farther, and the extent of this additional travel is governed by the distance by which the dashed curves for F_1 fall above the solid curve for F_1 . Results are presented for several combinations of airplane weight and download at the tail and indicate that a much greater strut travel is to be expected for the cases of high W and large L_t . It is interesting to note that the additional rear-strut travel in the region of high e can be avoided if desired; thus, if maximum nose-strut load provided is made to follow the lower dot-dash branch on the right of figure 7 instead of the upper branch, then this lower nose load and the rear-gear load along the solid F_1 line will arrest the airplane without further rear-strut travel, of course at the expense of increased nose-gear deflection.

Approach Angle of Attack

Figure 8 brings out more specifically the influence of approach angle of attack. The left side of the figure shows the total rear-strut deflection that would occur as a function of α_0 for the condition of an initial sinking velocity of 9 fps, and for a rear-strut location e of 195 inches. Note the very abrupt increase in strut deflection in the neighborhood of α_0 of 10° to 12° . From a design standpoint the strut travel must, of course, be limited; if, for example, a value of 1.5 feet is chosen, then the approach angle of attack must not be greater than 9.4° . This angle and the chosen design sinking speed of 9 fps thus fix the upper right-hand corner of the illustrative design-limit envelope shown on the right-hand side of the figure. Choosing lower sinking velocities yields different limiting values of α_0 , which then fix the right edge of the limit envelope. Approach angle of attack is thus an important consideration in the design of reentry gliders for landing.

Further results on angle of attack are given in figure 9, where the vertical velocity of the nose gear is given in terms of approach angle of attack for two different values of e . Initially, the airplane is assumed to be sinking at 9 fps. After initial rear impact the nose velocity has increased to the values shown by the solid lines. In the interval between the end of this first impact and just before nose touchdown, the vertical velocity increases to the dotted-line values. Notice that no strong dependence of nose-gear vertical velocity on angle of attack is indicated; an increase in severity of second rear-gear impact with increased approach angle of attack cannot therefore be attributed to a marked increase in nose-gear-impact severity. The main reason for increased severity of second impacts with large α_0 is associated with the download at the tail. Increasing α_0 means that the tail has to be deflected downward more; this increased deflection leads to a larger tail load, which then not only accelerates the tail into the ground more severely, but also causes an increase in the static load that must be supported by the main gear.

Effective Masses

Results which pertain to effective masses are next considered briefly. Effective masses are of interest because of the role they play in the drop-test development of the landing struts where, for example, concentrated masses are used. Figure 10 shows the effective mass on the nose strut and the effective mass on the rear strut (expressed as a ratio to the total mass) as a function of the load ratios F_1/F_2 and F_2/F_1 . These results show that care must be used in the selection of the appropriate effective mass because no unique value exists. The notable exception is for the case of $e = 93$ inches, since for this case the effective masses are independent of the applied loads. The dynamical significance of the 93-inch location might be stated as follows: If a pivot point is located 93 inches behind the center of gravity, then the nose strut will be located at the associated center of percussion. Conversely, if the pivot point is considered to be at the nose strut, then a distance of 93 inches represents the center-of-percussion location for the rear strut. Expressed mathematically, the condition for constant effective masses is established when the product of e and the distance between the nose gear and the center of gravity equals the square of the pitch radius of gyration k . The main point to be made about this figure is that the center-of-percussion location is desirable from the standpoint of choosing "universal" effective masses. Other factors are also favorable for this location; that is, the amount of energy to be absorbed is fairly low and the amount of travel necessary for both the rear and nose struts is also quite low. (See fig. 5.)

II - INVESTIGATION OF SKIDS AND METAL WHEELS FOR REENTRY LANDINGS

Apparatus and Test Procedure

Figure 11(a) shows the installation used for the skid tests. A variety of shoe-type skids of different material were attached to the bottom of a special test fixture which in turn was bolted to the axle of a fighter-airplane nose landing gear. Figure 11(b) is a photograph of two steel wire-brush skids which were also adapted for testing with this fixture. For test of the all-metal wheels, the fixture was removed and the wheels were mounted on the strut axle. The two types of wheels tested are shown in figure 12. The wheel shown in figure 12(a) has a steel-wire brush for a tire. The wheel shown in figure 12(b) has a solid-metal tire supported by a series of leaf springs arranged around the periphery of the wheel. The drop linkage and instrumentation used for this investigation were similar to those described in reference 1. The static vertical load was 2,150 pounds and the tests were made at speeds ranging up to 180 feet per second on concrete, asphalt, and a simulated lakebed surface.

The asphalt runway was made with two different types of surfaces. The first 400 feet had a smooth sand finish whereas the remaining length was considerably rougher, having been surfaced with a mix containing a relatively large stone aggregate.

Reliability of Test Results

Because of the equipment used for these tests it was necessary to make each test over the same section of runway. To investigate the effect of making repeated slideouts over the same portion of runway surface, a steel skid was selected as a control. It was the first skid tested and was retested when inspection of the landing surface indicated significant changes. Figure 13 shows the effect on coefficient of friction obtained during these tests of the steel skid on concrete and on both types of asphalt surface. The numbers by each test point indicate the total number of runs that had been made on each surface when that particular data point was obtained. It can be seen that for all surfaces the earlier runs yielded somewhat higher friction coefficients, but the actual difference is small. Other data indicate that this effect is somewhat greater for skids made of metals softer than steel and less for skids of the harder materials.

Results

Skids on concrete.- The variation of the coefficient of friction with forward speed during slideouts on concrete is shown in figure 14. It can be seen that for operation on a concrete surface, the softer materials and wire-brush skids develop the higher coefficients. For the shoe-type skids, the coefficients of the softer metals decrease with increases in forward speed, whereas the coefficients for the hardest materials appear independent of forward speed. These results suggest that the magnitude of the coefficient of friction for the shoe-type skids depends on the force developed as the concrete plows out some of the metal as well as on the force required to shear the junctions formed at the points of actual contact of the friction pairs. (See ref. 2, ch. 5.) The effect of the plowing term, as would be expected, is most apparent for the results obtained with the softer materials and decreases with increase in speed, since the metal becomes hotter and a reduction in the strength properties of the material occurs.

Skids on asphalt.- The results obtained on the asphalt surfaces are shown in figure 15. The solid lines are the variations obtained on concrete and are included only for reference. It can be seen that again the wire-brush skid and the shoe-type skids made of the softer metals give the higher coefficients of friction. It can also be seen that the coefficients for the shoe-type skids are somewhat higher on the smooth surface asphalt than on the rough surface. This trend, however, is reversed for the wire-brush skid.

Skids on lakebed.- Difficulties encountered in maintaining a stable lakebed runway limited the number of tests made on this surface. The data obtained for the skids are shown in figure 16. It can be seen that the value for copper, which was much higher than that for steel on concrete (fig. 14), is about the same as that for steel on the lakebed. This result suggests that for a shoe-type skid, the coefficient of friction on lakebed is independent of the skid material. It can also be seen that the 3-inch wire-brush skid developed a coefficient of friction of about 0.6, which was the highest obtained during these tests.

Effect of skid temperature.- In order to simulate the skid temperature expected to exist during landings following atmospheric reentry, some tests were made with the skids heated to approximately 800° F. These tests were made on the concrete and asphalt surfaces, and the results indicated that heating the skids to this temperature had no significant effect on the coefficients of friction.

All-metal wheels.- The rolling coefficients of friction developed by the wheels are shown in figure 17. It can be seen that on both concrete and asphalt surfaces, the wheel equipped with a wire-brush tire had

rolling coefficients of friction significantly higher than the wheel equipped with the solid metal tire. Although the differences between the concrete and asphalt surfaces do not appear to affect the rolling coefficient for each wheel, rolling over the lakebed surface does cause a small increase in the coefficient associated with the wire-brush tire. No data were obtained for the solid-metal-tire wheel on the lakebed.

Figure 18 shows a time history of the spin-up drag coefficient of friction obtained on concrete during a landing impact of the wheel equipped with a wire-brush tire. It can be seen that the maximum coefficient which is developed just prior to wheel spin-up approaches a value of 0.6. On the basis of results obtained with rubber pneumatic tires, it is reasonable to believe that if this wheel were equipped with a simple mechanical brake, a maximum coefficient of approximately the same value could be developed during braking.

Discussion of Results

Some workable landing-gear configurations for reentry-type vehicles can be determined from considerations of the landing requirements and the preceding results. The main landing gear must provide the predominant stopping force, since it not only supports the largest part of the vehicle weight but must also develop a significantly higher coefficient of friction than the nose landing gear in order to insure adequate yaw stability during slideout. An idea of the order of friction coefficient necessary to stop the vehicle can be obtained from figure 19. In this figure, slideout distance is shown as a function of horizontal landing velocity for two cases, one in which skids are used on both nose- and rear-landing gears and one in which a nose wheel having no appreciable rolling resistance is used in conjunction with the rear skids. In the first case, in order to obtain positive directional stability, the coefficient of friction developed at the nose μ_2 is selected as equal to $1/2$ of the coefficient developed by the rear skid μ_1 . In the second case μ_2 is taken as zero. Results are shown for two values of e/e_n , the ratio of main-landing-gear and nose-landing-gear distances to the vehicle center of gravity. If a landing velocity of 200 miles per hour and slideout distance of 5,000 feet is chosen as an example, it can be seen that the coefficient for the main skid must lie between approximately 0.30 and 0.45 for the various configurations shown in figure 19.

Use of a shoe-type skid for the main landing gear does not appear to be promising (figs. 14 and 15). Although one made of copper would yield a friction coefficient high enough to stop the vehicle, its melting point is too low to withstand the reentry temperatures. Nickel is a borderline case at the lower forward speeds, but its friction coefficient

drops off too much at the higher velocities. The remaining shoe-type skids tested yield too low a coefficient on the hard-surfaced runways. A wire-brush type of skid, however, does show promise for use on the main landing gear. It develops a coefficient of friction which is apparently large enough to bring the slideout distance down to within reasonable limits. Furthermore, when used with a nose gear equipped with either type of the all-metal wheels tested (fig. 17), the ratio of the coefficients of friction between the main and nose landing gear would be greater than 2, which should provide adequate directional stability during slideout on all types of landing surfaces. The wire-brush type of skid might also be used in combination with a nose gear equipped with a hard cermet or tungsten carbide shoe skid. However, the directional stability of this combination appears to be marginal on both the smooth asphalt and lakebed surfaces. It should be pointed out that the wire-brush skids used for these tests were merely exploratory models and that further research could possibly lead to the development of wire-brush skids capable of developing higher coefficients which would have a larger margin of stability when used with a nose skid.

Since the spin-up data (fig. 18) indicated a maximum friction coefficient of almost 0.6 for the wire-brush wheel, the possibility of using this wheel equipped with manually operated mechanical brakes on the main landing gears is suggested. This type of arrangement would have an added advantage of providing a steering capability during slideout.

CONCLUDING REMARKS

Results pertinent to the impact phase of the landing of reentry-glider vehicles of part I deal mainly with the significance of various approach conditions and the importance of rear-landing-gear location. In the analytical study the nose-landing-gear position was considered fixed, while the position of the rear landing gear was varied. Analogous type results could, of course, be obtained by fixing the rear-gear location and allowing the nose-gear position to vary. Another factor must be kept in mind in such a treatment, however, as follows. As the nose gear is moved rearward, it not only becomes the main energy absorption gear, but also supports more of the static weight of the vehicle during slideout, with a corresponding decrease in the weight to be supported by the rear gear. If directional stability is to be maintained, however, the coefficient of sliding friction on the nose skid must be kept low relative to the rear skids. Because of this required lower skidding coefficient and because of the decreased weight on the rear skids, the total retardation force available for stopping the vehicle would be considerably reduced and larger stopping distances would therefore be required.

The principal results indicated by the experimental investigation presented in part II are as follows:

(a) Wire-brush-type main landing skids, together with either a shoe-type skid or all-metal nose-wheel landing gear appeared feasible for use on manned reentry vehicles.

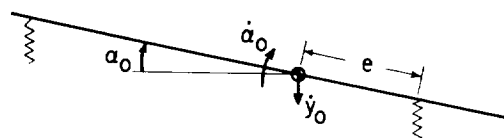
(b) A wire-brush wheel equipped with a brake might also prove practical for the main landing gear.

REFERENCES

1. Dreher, Robert C., and Batterson, Sidney A.: Landing and Taxiing Tests Over Various Types of Runway Lights. NACA RM L58C28a, 1958.
2. Bowden, F. P., and Tabor, D.: The Friction and Lubrication of Solids. The Clarendon Press (Oxford), 1954.

FACTORS STUDIED

APPROACH CONDITIONS AND REAR GEAR LOCATION



EFFECTIVE MASSES



Figure 1

INFLUENCE OF INITIAL CONDITIONS ON LANDING SEVERITY

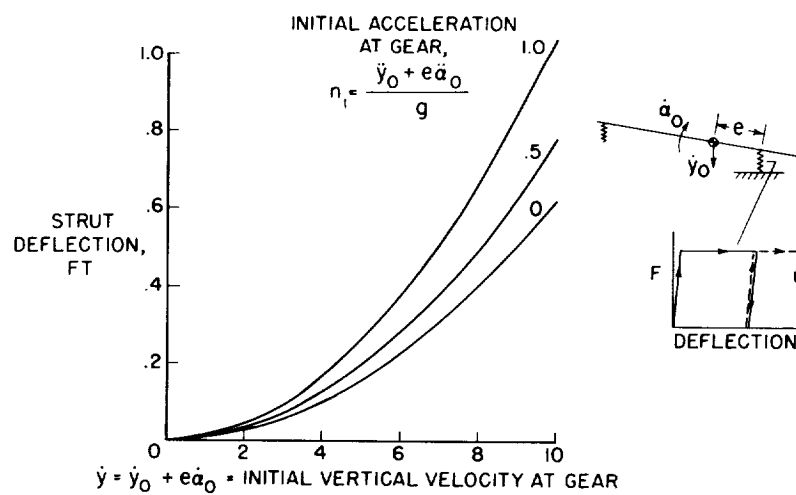


Figure 2

LANDING SEQUENCE SHOWING CONDITIONS LEADING TO SEVERE SECOND IMPACT

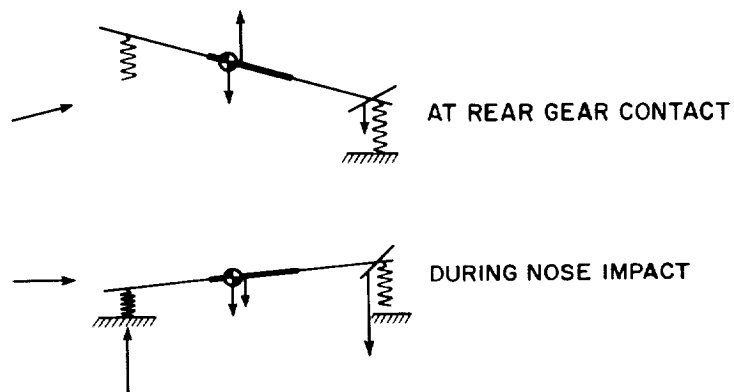


Figure 3

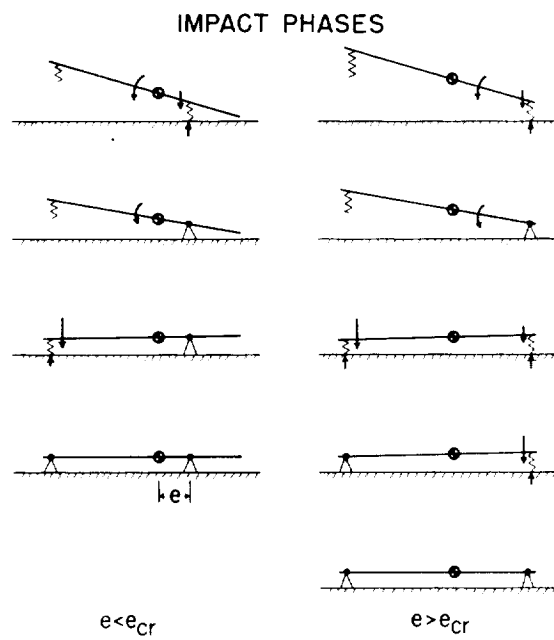


Figure 4

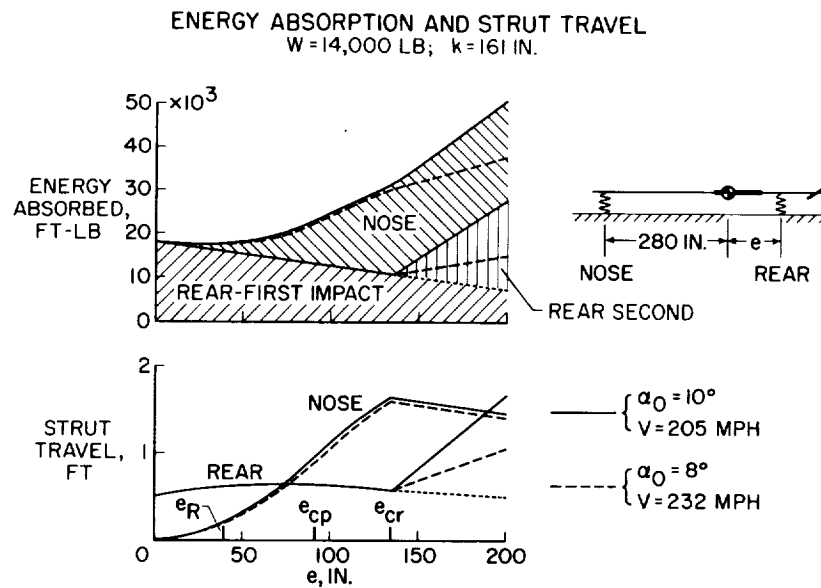


Figure 5

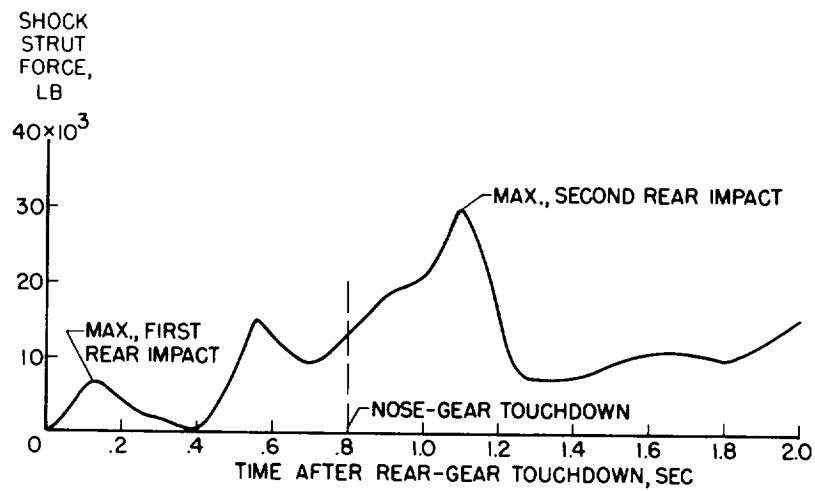
FORCE IN REAR STRUT OF X-15 DURING LANDING

Figure 6

IMPACT FORCES

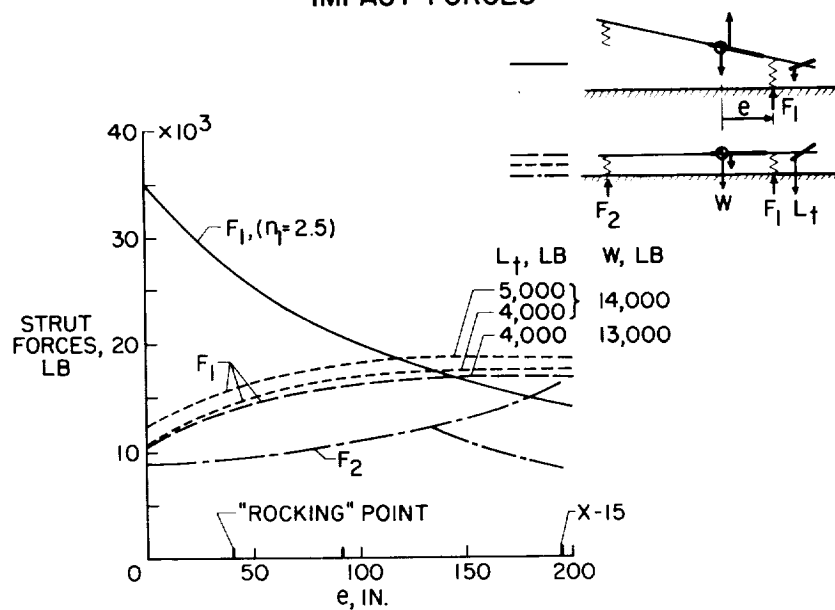


Figure 7

INFLUENCE OF APPROACH ANGLE OF ATTACK

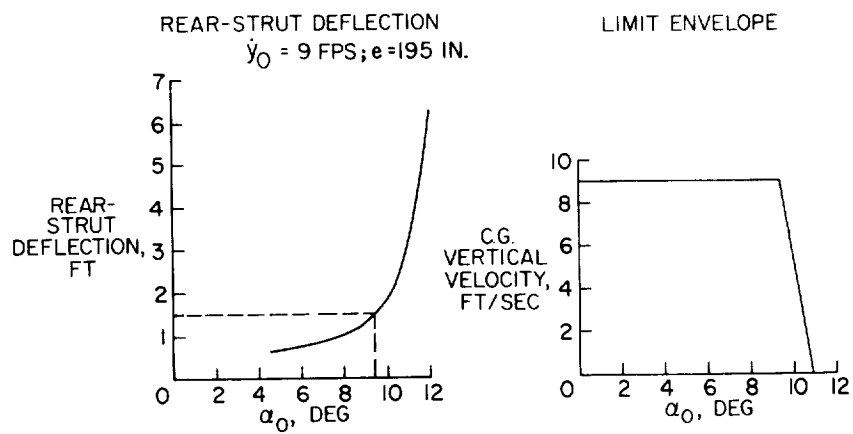


Figure 8

NOSE-GEAR VERTICAL VELOCITIES

$$\dot{y}_0 = 9 \text{ FT/SEC}; \dot{\alpha}_0 = 0^\circ$$

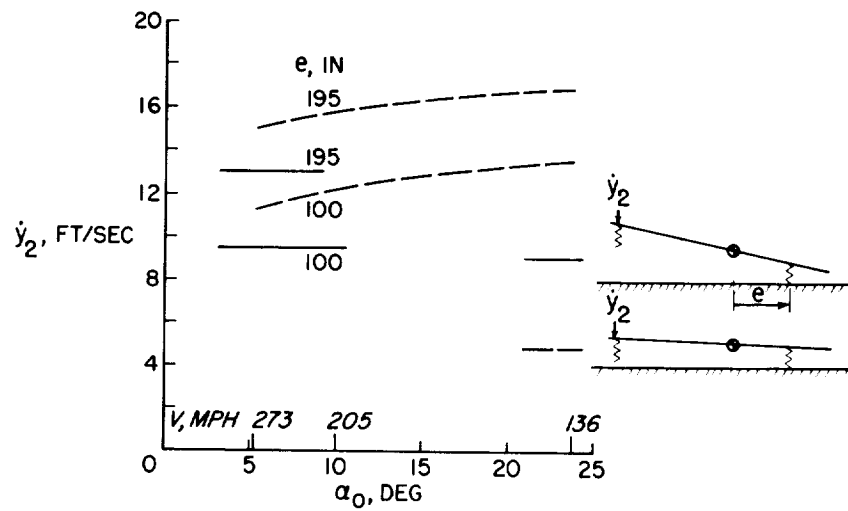


Figure 9

INFLUENCE OF LOADS ON EFFECTIVE MASSES

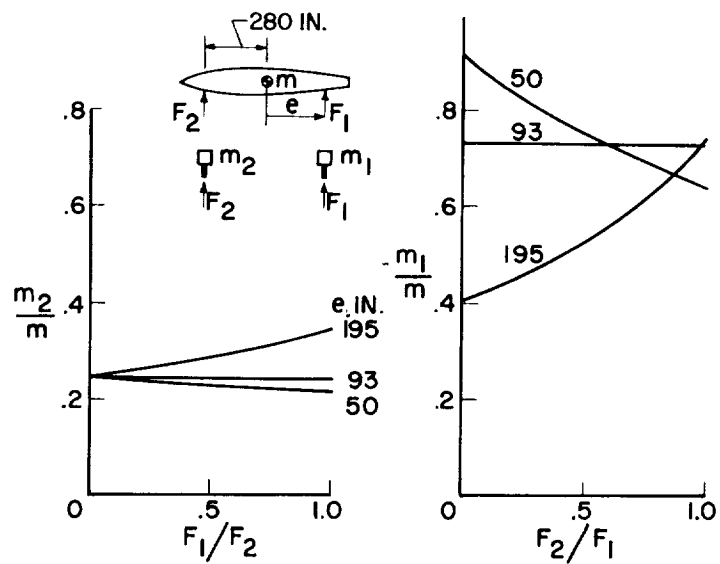


Figure 10

SKID CONFIGURATIONS

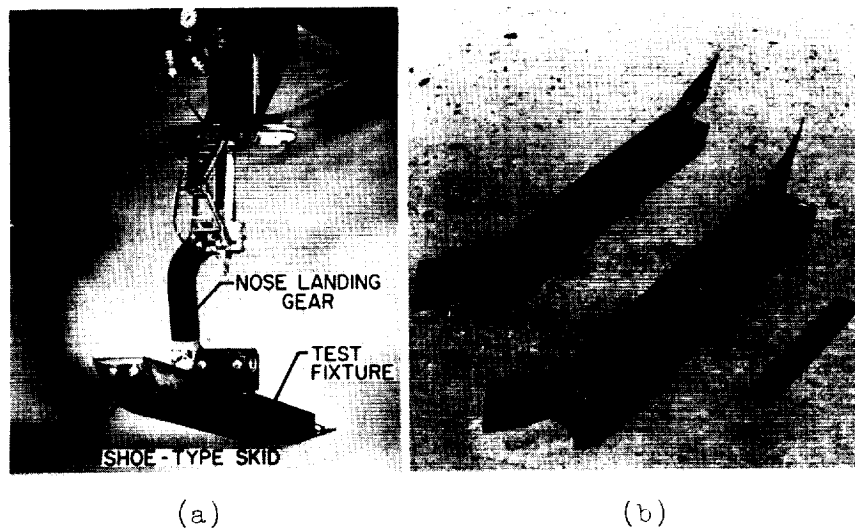


Figure 11

ALL-METAL WHEELS

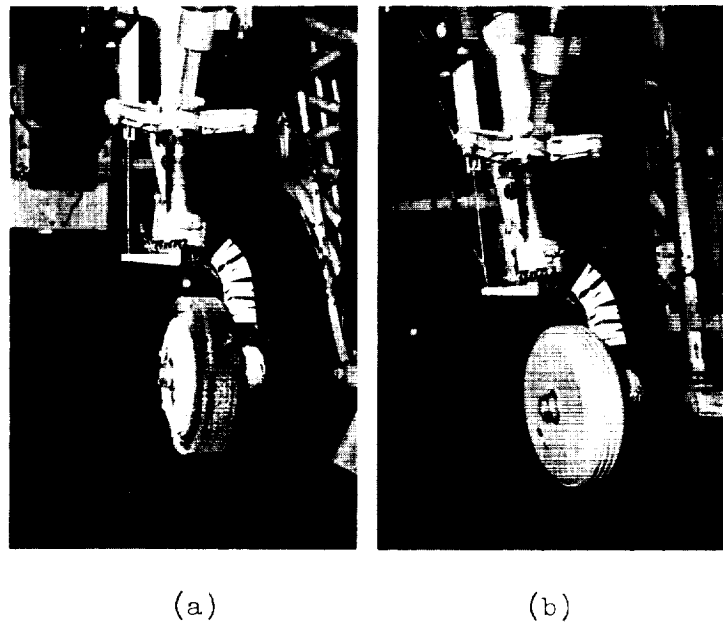


Figure 12

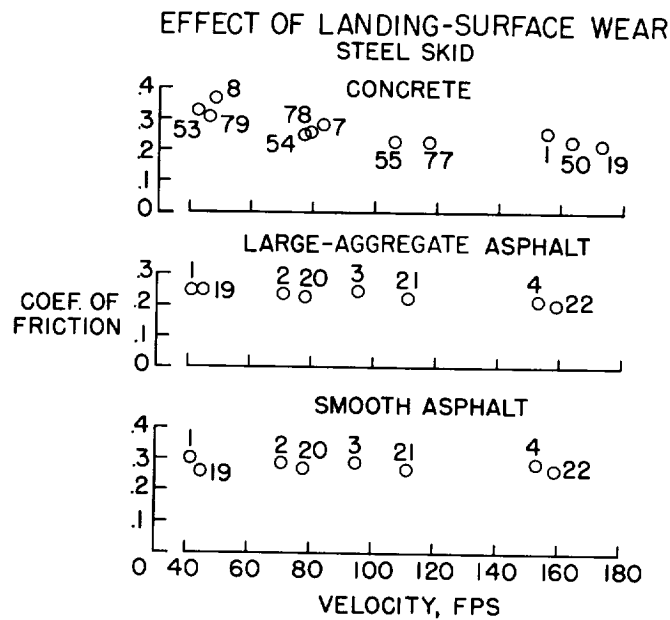


Figure 13

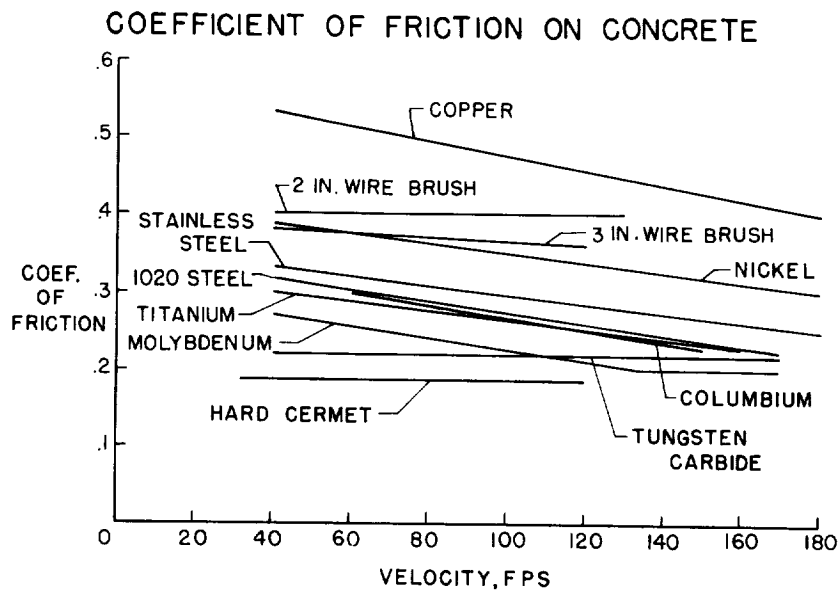


Figure 14

EFFECT OF LANDING SURFACE

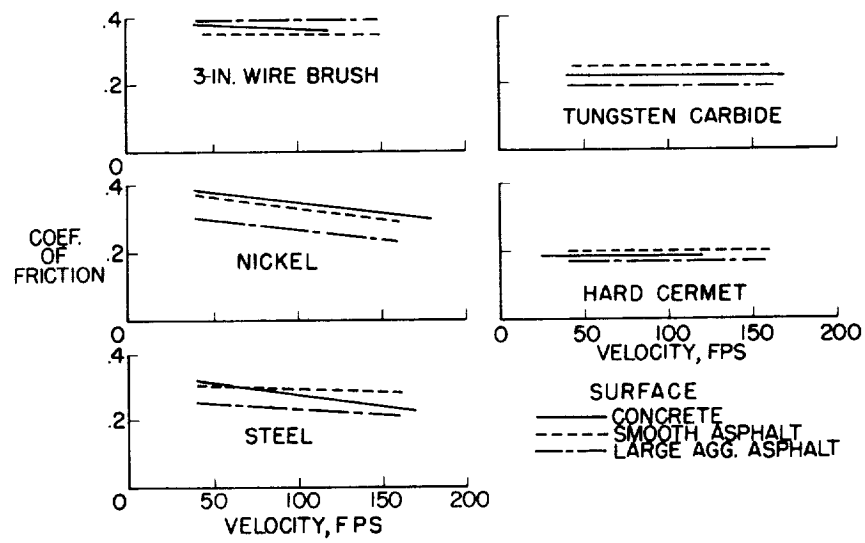


Figure 15

COEFFICIENT OF FRICTION ON LAKE BED

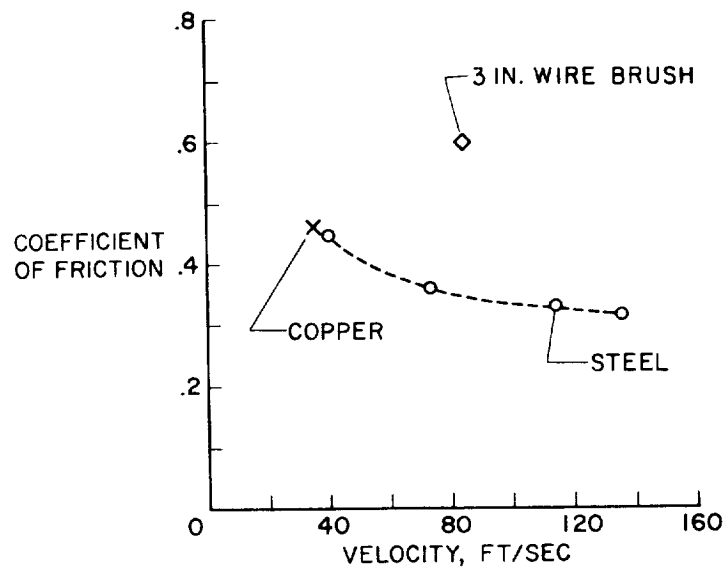


Figure 16

ROLLING FRICTION COEFFICIENTS

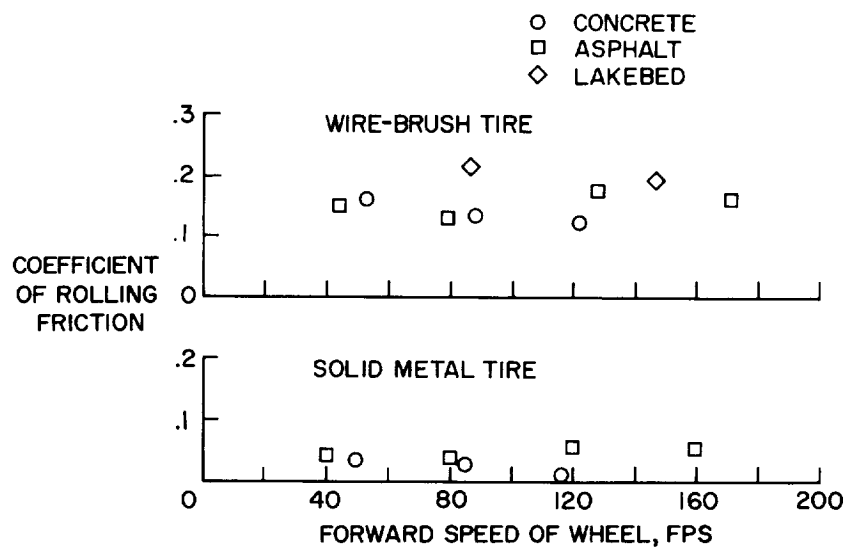


Figure 17

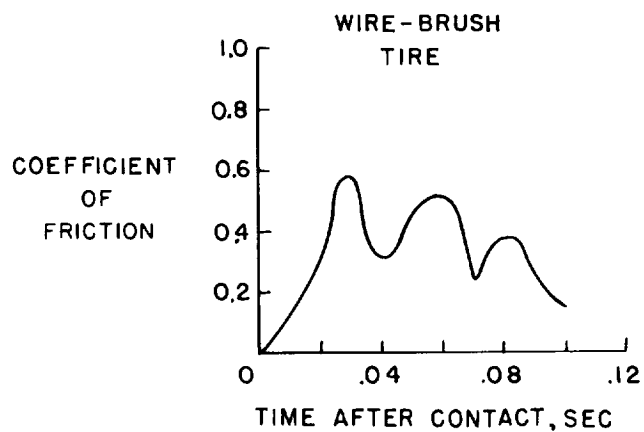
COEFFICIENT OF FRICTION DURING SPIN-UP
ON CONCRETE

Figure 18

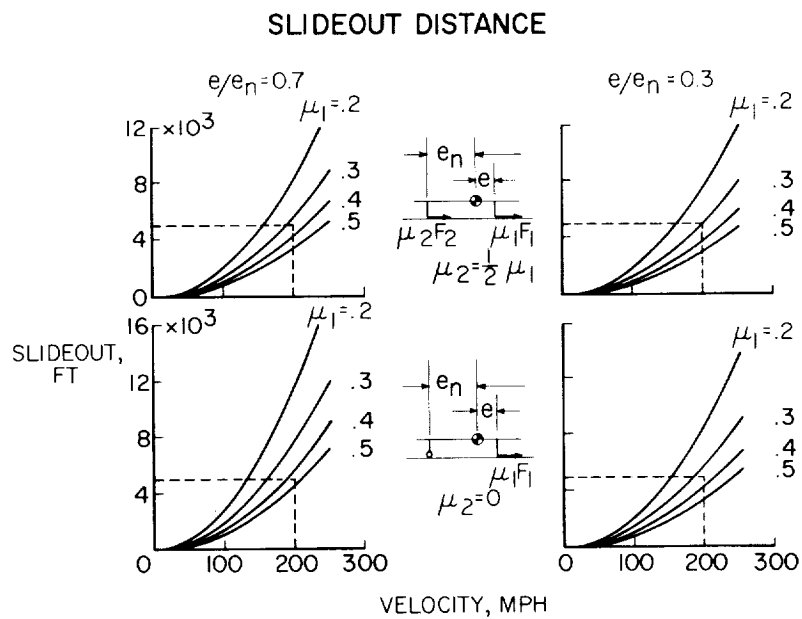


Figure 19

LANDING ENERGY DISSIPATION FOR MANNED REENTRY VEHICLES

By Lloyd J. Fisher, Jr.
Langley Research Center

SUMMARY

Analytical and experimental investigations have been made to determine the landing-energy-dissipation characteristics for several types of landing gear for manned reentry vehicles. The landing vehicles are considered in two categories: those having essentially vertical-descent paths, the parachute-supported vehicles, and those having essentially horizontal paths, the lifting vehicles. The energy-dissipation devices discussed are crushable materials such as foamed plastics and honeycomb for internal application in couch-support systems, yielding metal elements as part of the structure of capsules or as alternates for oleos in landing-gear struts, inflatable bags, braking rockets, and shaped surfaces for water impact.

It appears feasible to readily evaluate landing-gear systems for internal or external application in hard-surface or water landings by using computational procedures and free-body landing techniques with dynamic models. The systems investigated have shown very interesting energy-dissipation characteristics over a considerable range of landing parameters. Acceptable gear can be developed along lines similar to those presented if stroke requirements and human-tolerance limits are considered.

INTRODUCTION

The landing vehicles for manned reentry are considered in two categories: those having essentially vertical-descent paths, the parachute-supported vehicles, and those having essentially horizontal paths, the lifting vehicles. Because of the nature of the operation, numerous maintenance free landings are not required; consequently, one-shot landing gears having replaceable elements are particularly interesting. This paper presents some brief results from analytical and experimental investigations of energy dissipation with such landing gear in order to give a general idea of feasibility.

STATEMENT OF PROBLEM

The major variables of landing energy dissipation are velocity and stopping distance and the quantities to be determined as far as man is concerned are maximum acceleration, duration, and onset rate of acceleration. (See ref. 1.) Possible acceleration time histories for reentry landings are shown in figure 1. For orientation purposes typical accelerations are shown by the broken lines. Maximum acceleration and duration are apparent on a time history but onset rate is not so obvious. For purposes of this paper onset rate is considered as the ratio of plateau acceleration to time for reaching plateau. The plateau value is obtained by approximating the more complicated time histories with a simple trapezoid as shown by the solid line.

Acceleration and onset rate determine man's tolerance to impact and the physical relationship of these parameters shows what compromises can be made between the two for the stopping distances available. These relationships are shown in figure 2 where maximum acceleration in g units is plotted against stopping distance in inches. (See ref. 2.) The data shown are at an impact velocity of 30 ft/sec, a value familiar for parachute-supported vehicles. The lower curve is for an infinite onset rate and the curves for onset rates of 9,000, 1,500, and 400 g/sec are from trapezoidal acceleration time histories. The dashed curve represents a linear buildup to maximum acceleration at maximum time and with the curve for infinite onset rate forms a limit for the given conditions. A frequently quoted tolerance for man with load applied sternumward is shown by this point at 40g, 1,500 g/sec, and about $8\frac{1}{2}$ inches stopping distance. It should be realized that the stopping distances shown in this figure are the absolute minimum for the given conditions.

DISCUSSION

A short motion-picture film supplement illustrating the effects discussed in this paper has been prepared¹.

Various energy-dissipation devices are being considered for manned reentry vehicles. Those receiving most attention presently are yielding metal elements as part of the structure of capsules or as alternates for oleos in landing-gear struts, inflatable bags, crushable materials such as foamed plastics and honeycombs, braking rockets, and shaped surfaces for water impact.

¹This motion-picture film supplement (L-540) is available on loan from NASA Headquarters, Code BIV, Washington, D.C.

Couch Support

The crushable materials are receiving most attention for internal application in couch-support systems. It is difficult to scale such materials; therefore, full-scale testing appears best. Results from drop tests using a combination of semirigid plastic and aluminum honeycomb are given in figure 3. (See ref. 2.) The drop-test model consisted of 4 inches of each material with a metal plate separating the two. The static loading for the test weight was 1 psi. Aluminum honeycomb is an efficient material for impact load alleviation since up to 80 percent of its depth is usable and there is little rebound. However, the stiffness of the material results in high onset rates of acceleration. These may be controlled by reducing the initial area of contact, by precrushing, or by combining with foamed plastic as shown here. Plateau acceleration was about 30g and the onset rate was about 2,500 g/sec for this combination. The initial shape of the acceleration followed the simple one-degree-of-freedom spring constant for springs in series. One of the problems inherent in work of this nature is shown by the sharp peaks in the record indicating that the test weight "virtually" bottomed before the impact velocity had been completely dissipated.

Vertical-Landing Vehicles

It usually is feasible to absorb only part of the landing energy with coach or seat supports; therefore, some external absorption must be provided. The inflatable bag lends itself very well to energy absorption for the vertical-landing vehicle. Included in this category are the emergency escape pods and the reentry ballistic capsules. A number of bag shapes such as a cylinder, sphere, or torus might be used depending on design requirements. (See ref. 3.)

Torus-shaped bag.— A drawing of a model of a torus-shaped landing bag is shown in figure 4. This bag is divided into eight compartments, the partitions of which are shown by dashed lines in the plan view of the torus. The compartments are needed in cocked landings to permit pressure buildup under that part of the capsule impacting first. Each compartment has a blowout patch so that air can escape from the bag to regulate acceleration and prevent rebound. The patches are designed to blow out at scale pressure.

Sequence photographs of landings of the torus-bag model are given in figure 5. Figure 5(a) shows the model in a vertical flight path. The blowout patches (little white disks) can be seen just after blowout in the fourth picture of the sequence. Figure 5(b) shows the model in a 63° flight path. An additional air bag has been used in this

condition to ease turnover impact. Turnover results if horizontal velocity is too great but turnover is a secondary problem which can be solved by the same technique used for the main air bag.

Figure 6 gives full-scale accelerations for torus bag landings at several attitudes in a flight path that would result from a horizontal wind velocity of about 9 knots. The positive and negative attitudes and axes of the capsule are illustrated by the sketches with direction of flight path shown by the arrows. These data are for a vertical impact velocity of 30 ft/sec, a flight-path angle of 60° , a vehicle weight of 1,200 pounds, and a 3.5-foot torus section diameter. The acceleration along the X-axis shows a maximum of about 30g (full scale) at a 0° landing with a decrease in acceleration as attitude is changed. The acceleration along the Z-axis is zero at a 0° landing and increases in magnitude as attitude is changed. Maximum onset rate for this air bag was about 600 g/sec.

Vertical-cylinder bag.- A drawing of a vertical-cylinder landing-bag model is shown in figure 7. The air chamber upper body of the model is used to improve scaling accuracy and is not a part of an actual vehicle. The air bag is installed between the air chamber and a heat shield and is opened from a collapsed position by the weight of the heat shield. There is essentially unrestricted flow between the air bag and air chamber. Orifices which are always open are located around the upper part of the bag. The bag is dimensionally representative of a prototype 6 feet in diameter, 4 feet long, used with a 2,000-pound capsule.

An acceleration time history for this configuration in a landing on concrete at a flight-path angle of 90° (vertical) and a 0° contact attitude is given in figure 8. Computed and experimental results are in good agreement at model scale and scale up to full size as shown here. Comparisons with large-scale model tests also indicate agreement. This bag was designed for low accelerations and results in a maximum value of about 10g. Onset rate was about 200 g/sec. Landings at other flight-path angles and attitudes have shown similarly acceptable acceleration.

Computations of acceleration for the various systems discussed herein have been made at the 0° attitude, vertical flight-path condition only.

Compliant metal legs.- A drawing of a model used to investigate energy dissipation and scaling methods for compliant-metal-leg shock absorbers is shown in figure 9. The model consisted of a steel weight attached to a wooden base by 3003-H14 aluminum-alloy legs and weighed about 30 pounds. The legs were made of rectangular strips bent as shown. This initial bend was used in an attempt to reduce onset rate

and to control the location of bending during impact. A large-scale model similar to this one and weighing about 200 pounds was also tested.

Figure 10 gives an acceleration time history for the compliant-metal-leg models in landings on concrete. The small-scale-model data are shown by the long-dash—short-dash line and the large-scale-model data by the dashed line. The agreement is very good. The computed acceleration time history shown by the solid line uses a value of yield stress about one-fourth greater than the handbook value because of work hardening during fabrication, high strain rates during impact, and plastic flow.

The onset rate of acceleration for these configurations is high, about 10,000 g/sec. Other investigations using tapered legs have given onset rates of about 2,000 g/sec for the same design maximum acceleration. A photograph showing the tapered compliant metal legs installed between a capsule and heat shield is shown as figure 11. The tapered legs are prebent into a modified "S" curve. Typical sequence photographs of a landing on concrete are given in figure 12.

Water impact.— Another method for landing a space capsule is the water landing. (The configurations discussed previously have lower accelerations in water landings than in hard-surface landings.) The water landing provides a way of obtaining long stroke without onboard devices, that is, by shaping the vehicle for water penetration. It is also of interest where accuracy for hitting a landing area is a question. Peak impact accelerations for two capsules landing on water are given in figure 13. (See refs. 4 and 5.) One capsule impacts on a 126-inch spherical radius heat shield and the other on a 53° conical heat shield. Both model and full-scale experimental investigations were made for the 126-inch spherical radius model. The model results are shown by the solid line and full-scale results by the dashed line. Experimental model results for the 53° conical model are shown by the lower solid line. Computed results for both configurations, by using well established procedures, are shown by the circles. Excellent agreement is indicated between model, full scale, and computation. The curves show that configuration shape has a significant influence on landing acceleration. At 0° contact attitude the 126-inch spherical radius model has a blunt shape, water penetration is small, and the peak acceleration is high. Onset rate is about 20,000 g/sec. As contact attitude changes from 0° , the accelerations decrease rapidly and onset rate also decreases to about 800 g/sec at a 30° contact attitude. The difference is due to the more pointed shape of the impacting surface as attitude increases. The 53° conical model has fairly low accelerations, about 10g, and shows little change with change in attitude. Onset rate is about 400 g/sec. The accelerations in the 10g region for both models result from fairly deep water penetration or in other words relatively long strokes.

Braking rocket.- Another long-stroke system for energy dissipation in a capsule landing is the braking rocket. This system employs rocket thrust aligned with the flight path for stopping. If g tolerance for man is greatly reduced by long exposure to zero or very low gravity in space environment, the low landing accelerations possible with the braking rocket could be the answer for returning from such missions. Typical sequence photographs of a landing of a dynamic model using this system are given in figure 14. Only a very few landings have been made with this model but the behavior and control have been very good. A maximum acceleration of about 3g occurred in these tests. A change in landing condition such as an increase in speed would result in higher accelerations or would require more thrust or thrust duration than used in the test. Depending on design requirements, a wide range of acceleration and stroke is possible with the braking rocket.

Horizontal-Landing Vehicle

Each of the systems discussed has special advantages, as an example the compliant metal elements can be more adaptable to space environments than certain other systems, especially as alternates to oleos in shock-absorber struts. An application of the compliant metal principle similar to that already shown for a capsule has been investigated on a dynamic model of a horizontal-landing reentry vehicle. Figure 15 is a photograph of the model. The landing gear consists of a pair of main skids aft and a dual nose wheel with tires forward. Simple yielding metal strips are incorporated into the gear struts and they deform in bending during landing impact. Brief tests were also made with the nose wheel moved aft and with a nose skid replacing the original wheel.

Typical sequence photographs of a landing made with the main-skid nose-wheel landing gear are given in figure 16. The main gear contacts first, then the model trims down, and the nose wheel impacts; thus the shock strut is deformed.

A schematic time history of part of a landing is given in figure 17. Shown in this figure is attitude, accelerations at the nose gear, and accelerations at the main gear. At point 1 the main gear contacts the runway and the model trims down to nose-wheel impact at point 2. The nose-gear shock strut deformed during impact at point 2. At about the same time a reaction acceleration occurred which caused the main-gear struts to yield at point 3. During the nose-wheel impact the force or accelerations built up along an elastic line and upon reaching the yield stress of the strut remained fairly constant through the yield or deformation stroke. In the case of the main gear, the struts yield in the plastic range at a small value of acceleration, but the acceleration builds up again because the gear bottomed. Maximum landing acceleration always occurred at nose-gear impact and was about 5g. Moving the

nose wheel aft or replacing the wheel with the nose skid had little effect on acceleration or stability.

CONCLUDING REMARKS

It appears feasible to readily evaluate landing-gear systems for internal or external application in hard-surface or water landings by computation methods and free-body landing techniques with dynamic models. The systems investigated have shown very interesting landing-energy-dissipation characteristics over a considerable range of landing parameters. Acceptable gear could be developed along lines similar to those presented if stroke requirements and human-tolerance limits are considered.

REFERENCES

1. Eiband, A. Martin: Human Tolerance to Rapidly Applied Accelerations: A Summary of the Literature. NASA MEMO 5-19-59E, 1959.
2. O'Bryan, Thomas C., and Hatch, Howard G., Jr.: Limited Investigation of Crushable Structures for Acceleration Protection of Occupants of Vehicles at Low Impact Speeds. NASA TN D-158, 1959.
3. Esgar, Jack B., and Morgan, William C.: An Analytical Study of Soft Landings on Gas Filled Bags. (Prospective NASA paper.)
4. Vaughan, Victor L., Jr.: Water-Landing Impact Accelerations for Three Models of Reentry Capsules. NASA TN D-145, 1959.
5. McGehee, John R., Hathaway, Melvin E., and Vaughan, Victor L., Jr.: Water-Landing Characteristics of a Reentry Capsule. NASA MEMO 5-23-59L, 1959.

TYPICAL ACCELERATION TIME HISTORIES

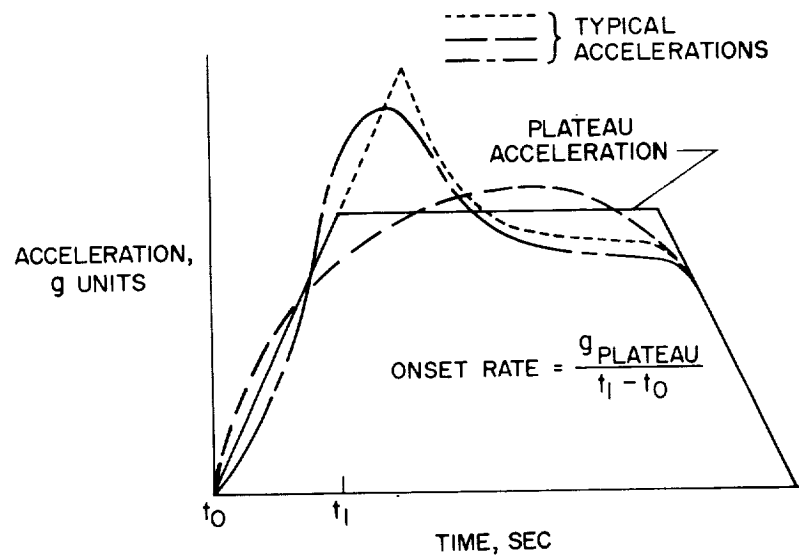


Figure 1

VARIATION OF MAXIMUM ACCELERATION WITH STOPPING DISTANCE
IMPACT VELOCITY = 30 FT/SEC

IMPACT VELOCITY = 30 FT/SEC

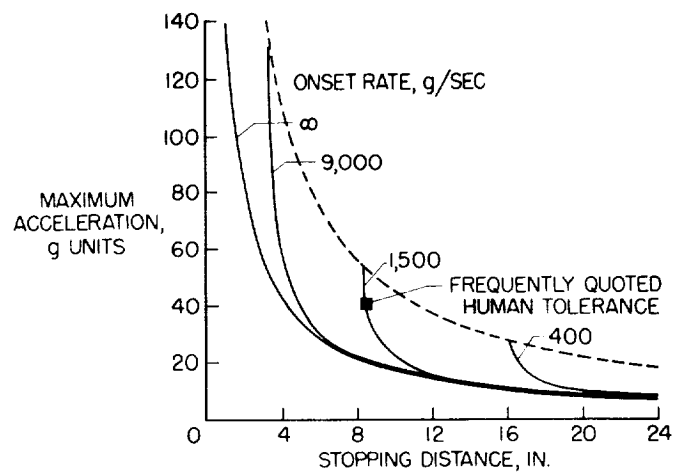


Figure 2

ACCELERATION TIME HISTORY FOR COMBINATION OF
ALUMINUM HONEYCOMB AND FOAMED PLASTIC
VERTICAL IMPACT VELOCITY, 30 FT/SEC; STATIC LOADING, 1 PSI

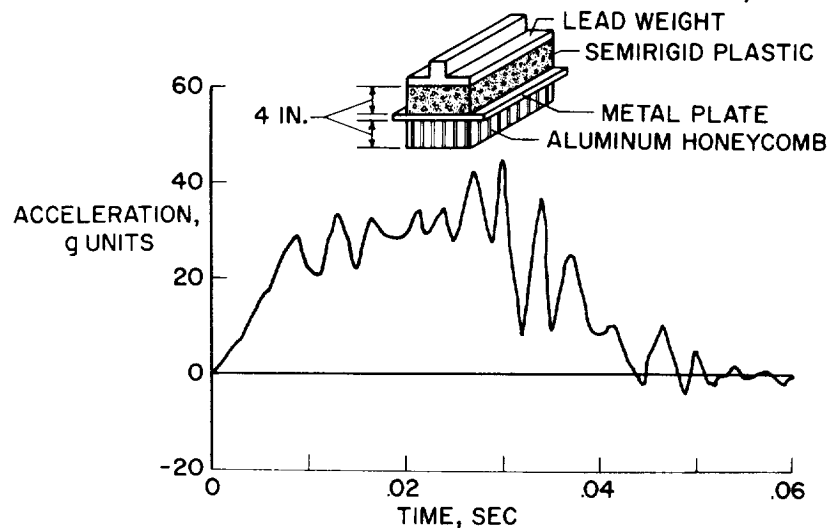


Figure 3

TORUS-SHAPED LANDING-BAG MODEL

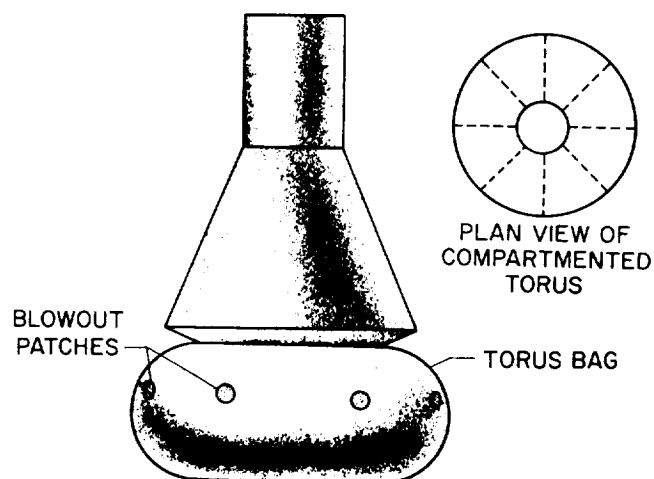


Figure 4

SEQUENCE OF TORUS BAG LANDINGS ON CONCRETE
FLIGHT-PATH ANGLE, 90° ; CONTACT ATTITUDE, 0°

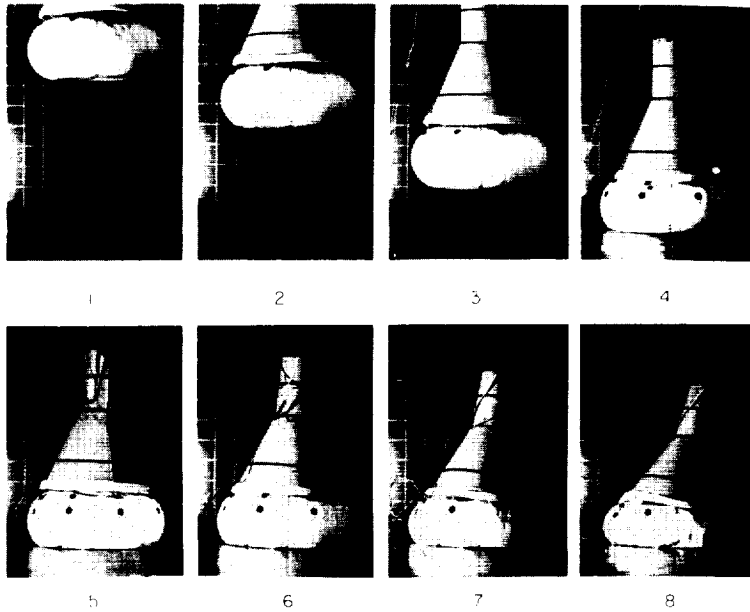


Figure 5(a)

SEQUENCE OF TORUS BAG LANDINGS ON CONCRETE
FLIGHT-PATH ANGLE, 63° ; CONTACT ATTITUDE, -26°

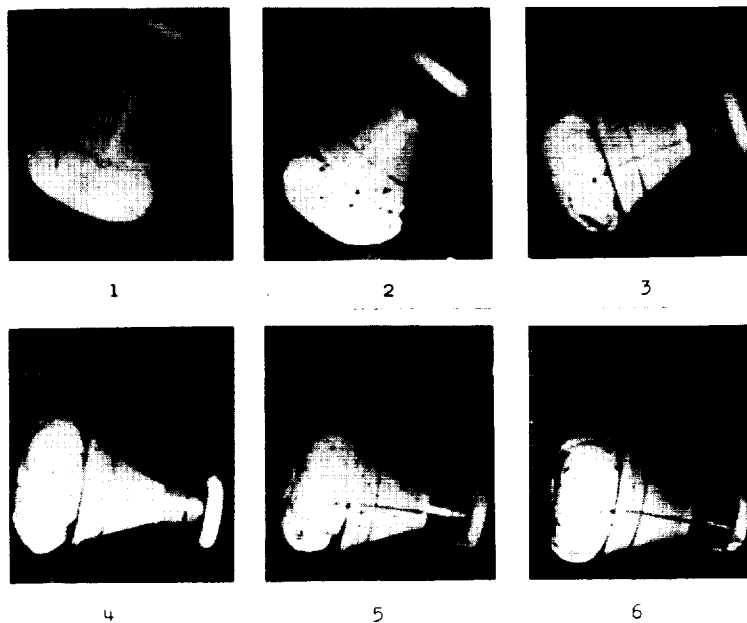


Figure 5(b)

ACCELERATIONS FOR
TORUS AIR BAG LANDINGS ON CONCRETE
VERTICAL IMPACT VELOCITY, 30 FT/SEC; FLIGHT-PATH ANGLE, 60°;
WEIGHT, 1,200 LB; TORUS SECTION DIAMETER, 3.5 FT

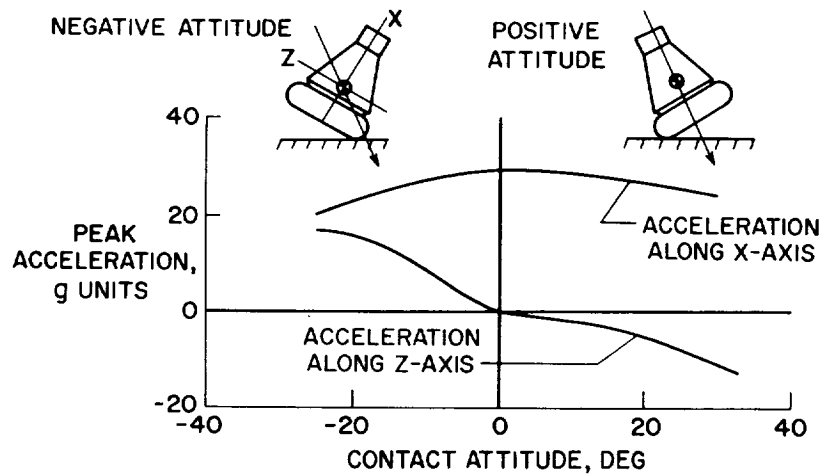


Figure 6

VERTICAL-CYLINDER LANDING-BAG MODEL

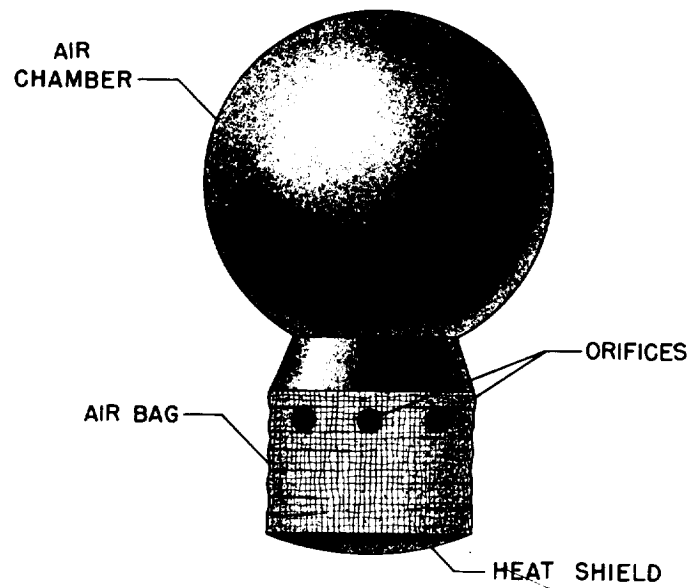


Figure 7

ACCELERATION TIME HISTORY FOR VERTICAL-CYLINDER BAG LANDING ON CONCRETE

IMPACT VELOCITY, 30 FT/SEC; FLIGHT-PATH ANGLE, 90°;
CONTACT ATTITUDE, 0; WEIGHT, 2,000 LB

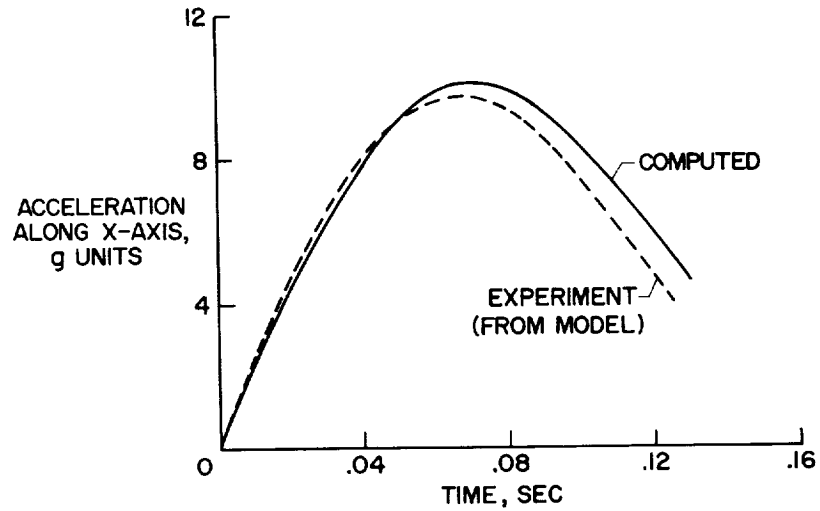


Figure 8

SMALL-SCALE COMPLIABLE-METAL-LEG MODEL

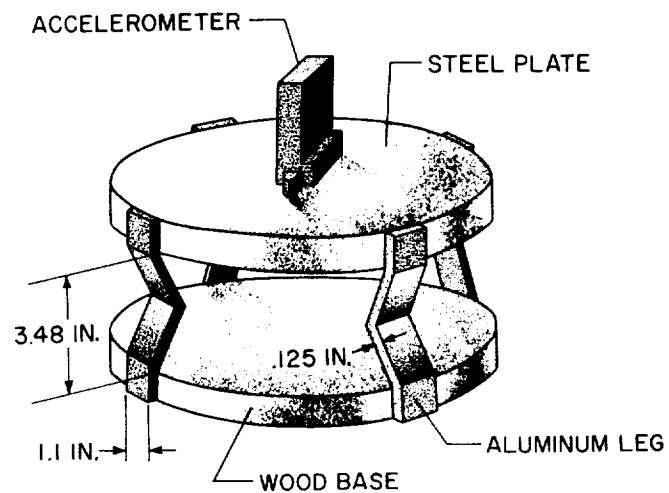


Figure 9

ACCELERATION TIME HISTORY FOR
COMPLIABLE-METAL-LEG MODEL LANDINGS ON CONCRETE
IMPACT VELOCITY (FULL SCALE), 30 FT/SEC
FLIGHT-PATH ANGLE, 90°; CONTACT ATTITUDE, 0

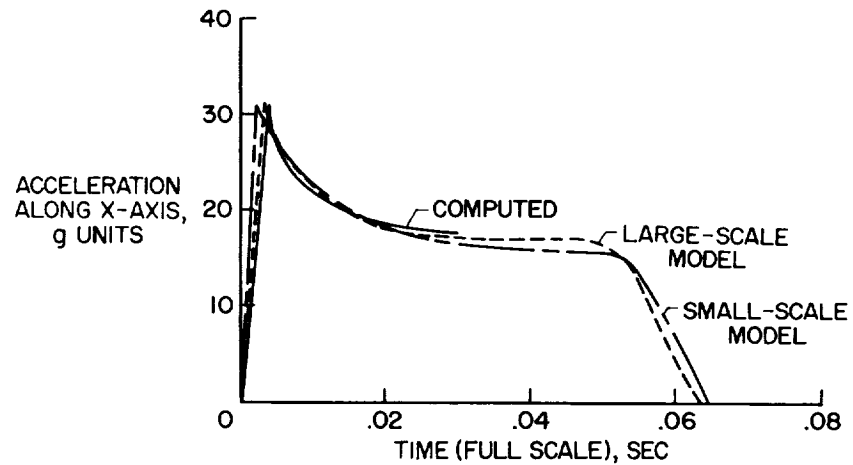


Figure 10

DYNAMIC MODEL WITH COMPLIABLE METAL LEGS
BETWEEN CAPSULE AND HEAT SHIELD

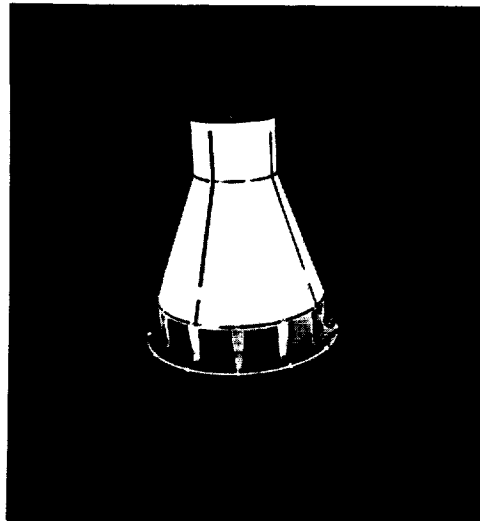


Figure 11

SEQUENCE OF COMPLIABLE-METAL-LEG MODEL
LANDING ON CONCRETE
FLIGHT-PATH ANGLE, 90°; CONTACT ATTITUDE, 30°

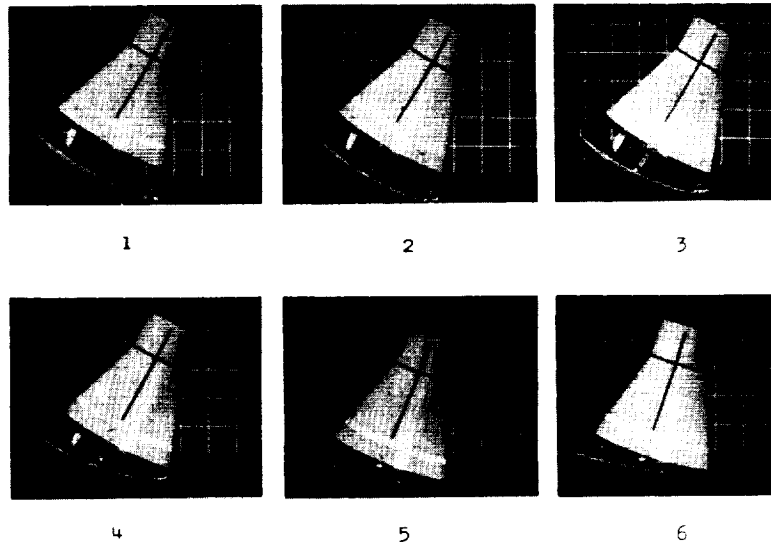


Figure 12

ACCELERATIONS FOR CAPSULES LANDING ON WATER
IMPACT VELOCITY (FULL SCALE), 30 FT/SEC; FLIGHT-PATH ANGLE, 90°;
WEIGHT (FULL SCALE), 2,000 LB

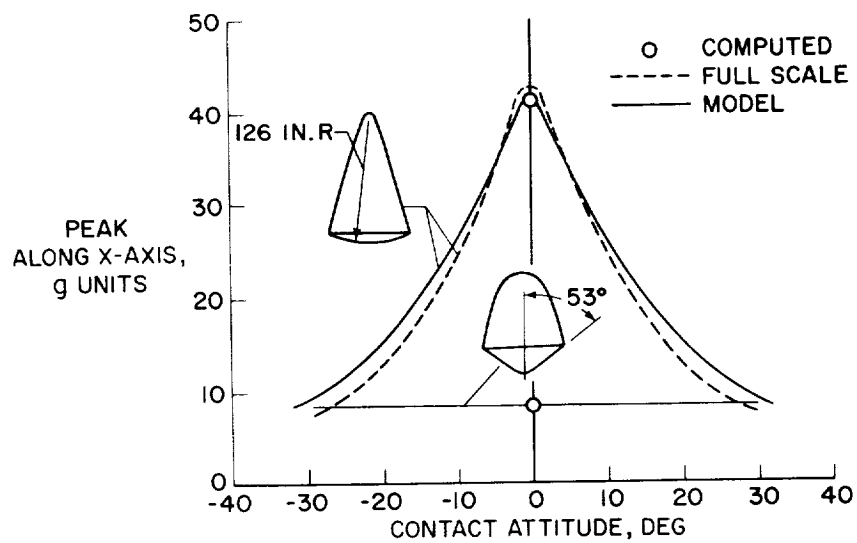


Figure 13

SEQUENCE OF BRAKING-ROCKET MODEL LANDING
ON CONCRETE
FLIGHT-PATH ANGLE, 60°

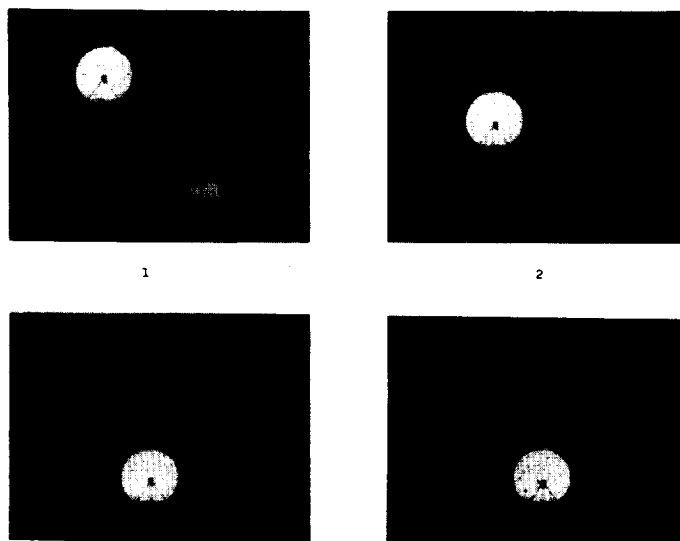


Figure 14

DYNAMIC MODEL OF HORIZONTAL-LANDING REENTRY VEHICLE

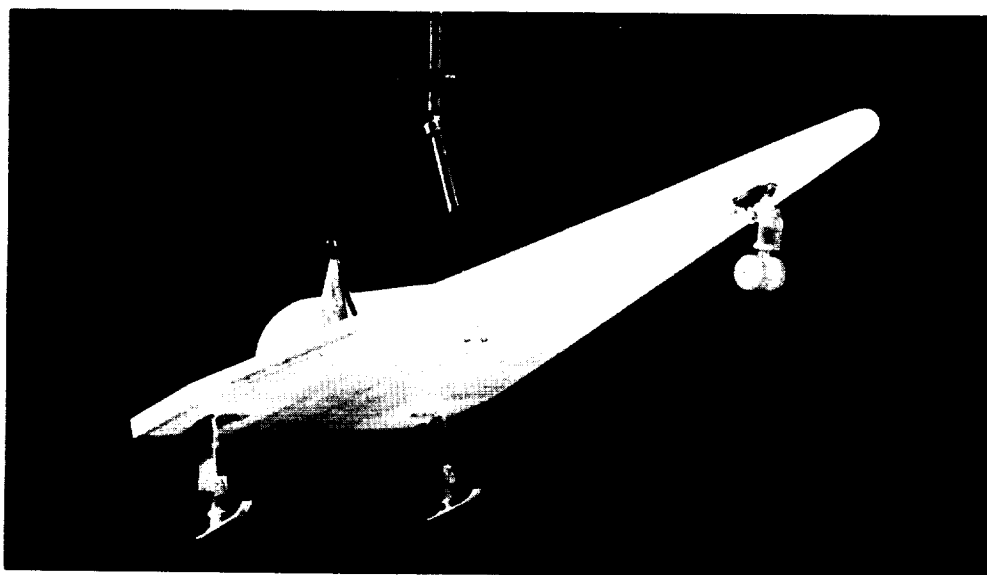


Figure 15

SEQUENCE OF MODEL LANDING WITH MAIN-SKID
NOSE-WHEEL LANDING GEAR

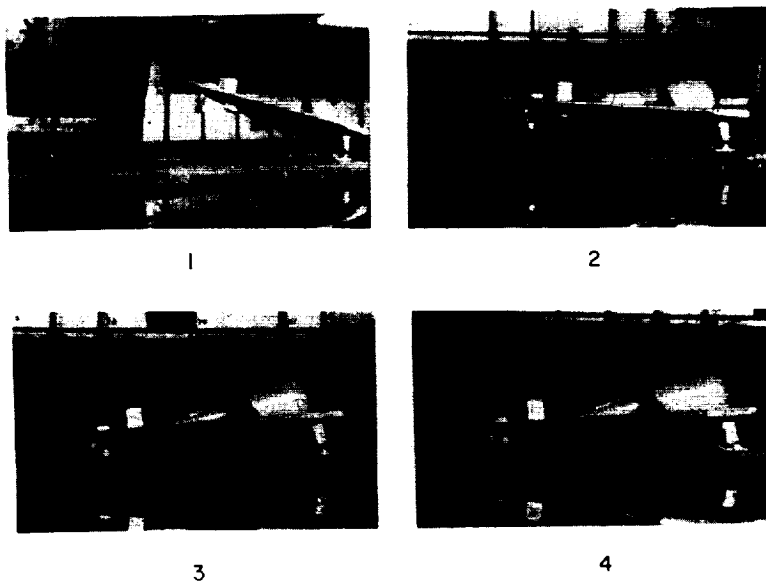


Figure 16

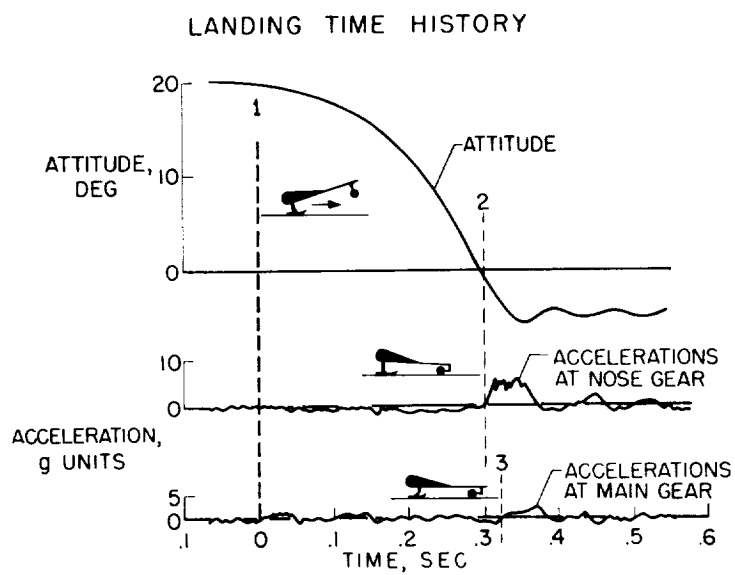


Figure 17

STRUCTURES FOR REENTRY HEATING

By Roger A. Anderson and Robert T. Swann
Langley Research Center

SUMMARY

The basic structural approaches for dealing with reentry heating of manned vehicles are summarized. The weight and development status of both radiative and ablative shields are given and the application of these shields to various vehicles is indicated.


INTRODUCTION

Feasibility for lightweight structure is one of the major considerations in selection of a configuration for a manned vehicle capable of executing an atmospheric entry at orbital speeds. The major uncertainty in structure arises from the severity of the heating environment, which not only demands that familiar methods of construction be exploited to the fullest but that investigation be made of new materials and associated construction methods. Progress is being made in these investigations as may be seen from references 1 and 2.

The purpose of the present investigation is to review in rather broad outline the heating encountered by manned vehicles during reentry and to summarize some of the basic structural approaches for dealing with the problem. Both radiative- and ablative-cooling systems are described and compared. Research and development work has proceeded with these systems to the extent that weight estimates can be given and an appraisal made of the probable application of these systems to certain types of manned vehicles.

SYMBOLS


C	heat capacity, Btu/lb
Δh	heat of vaporization (or other phase change), Btu/lb
H_{eff}	effective heat of ablation, Btu/lb



k	thermal conductivity, Btu/(hr)(ft)(°F)
q	heating rate, Btu/(sq ft)(sec)
Q	total aerodynamic heat input, Btu/sq ft
L/D	lift-drag ratio
S	surface area
t	time during which heating occurs, hr
T	absolute temperature, °R (unless denoted in °F)
V	velocity
W	weight
ΔW	weight of heat-protection system per unit area, lb/sq ft
α	constant of proportionality (eq. (1))
ϵ	emissivity
ρ	density, lb/cu ft
σ	Stefan-Boltzmann constant, Btu/(hr)(sq ft)(°R) ⁴

Subscripts:

A	ablation
B	final value at inner surface
e	radiation-equilibrium value
i	initial value at inner surface
m	mean value
max	maximum
o	outer surface



HEATING ENVIRONMENT

The heating inputs to manned reentry vehicles are shown in figure 1. Maximum heating rate has been plotted against total heat load per unit area and a band of combinations of these two quantities encountered by manned vehicles has been defined. This band is based on an analysis of the heating histories experienced by vehicles having large variations in wing loading and lift-drag ratio. The range of heat rates and heat loads at various points on these vehicles is reflected in the range of the vertical and horizontal scales, whereas heating time is reflected in the width of the "manned-vehicle band." The left edge of the band corresponds to about 4 minutes of heating and the right edge to about 70 minutes. This variation in heating time is associated with changes in average lift-drag ratio during reentry from 0 to about 2.5.

Similarly, the height of the band in figure 1 is associated with changes in wing or area loading and with changes in entry velocity. Very lightly loaded vehicles fall at the lower end of the band, while vehicles of comparable lift-drag ratio but with heavier loadings per unit area are shifted upwards along a constant time line. The most severe heating conditions are encountered by vehicles which combine a high L/D with a high W/S.

Some vehicles with wing or area loadings varying from about 25 to 75 lb/sq ft have been placed on the band in the vicinity of the maximum heat rate and heat load for which an important area of their structure is designed. For example, the Project Mercury capsule is shown near the design point for its front-face heat shield. (See fig. 1.) In actuality, a considerable range in heating conditions is encountered from the front face to the rearward areas of the capsule as indicated by the length of the line extending from the capsule. A similar line drawn through the reentry glider gives the range of heating conditions encountered from the nose stagnation point to the rearward areas. When variations in L/D, W/S, and vehicle shape are considered, it is apparent that structures must be provided to handle heating inputs varying from about 1,000 to over 100,000 Btu/sq ft and to survive heating rates of less than 10 to more than 100 Btu/(sq ft)(sec). Radiation-equilibrium temperatures associated with these heat rates are shown on the scale at the right in figure 1. As noted, they are computed with the assumption that a material emissivity of 0.8 is achieved.

A conservative evaluation of the current status of structural design for this operating environment is indicated in figure 2. Established areas for designs based on radiation and absorption of heat are indicated. As shown, radiative structures can handle large total heat

loads but have temperature or heating-rate limitations. Up to a temperature level of a little over $2,000^{\circ}\text{F}$, a capability for constructing metallic surfaces using nickel and cobalt-base materials has been demonstrated, but at higher temperatures rather serious material problems arise. The arrow at the metallic-surface boundary in figure 2 indicates that current research efforts are devoted to raising this boundary up to about $3,000^{\circ}\text{F}$ through use of the refractory metals.

Although not indicated in figure 2, a capability currently exists for constructing smaller structural components, such as nose caps, for temperatures above $3,000^{\circ}\text{F}$ by using ceramic materials. Similarly, recent work with inflatable structures of metal fabric indicates a capability for use at about the $1,500^{\circ}\text{F}$ level.

In contrast to the area for structures which dissipate heat by radiation, an area for structural design based largely on heat absorption is also shown in figure 2. The absorptive designs include liquid and metal heat sinks and ablative shields. Absorption of heat by ablation of surface material has proven to be an efficient and practical means for achieving self-regulated transpiration cooling for missile nose cones and has recently been extended to the design of the Mercury capsule heat shield. The edge of the absorption area in figure 2 represents an approximate boundary of present test experience with ablative cooling. Use of this cooling concept for longer reentry times and larger heat loads should be possible but poses a challenge in weight reduction which will be discussed later in this paper. The arrow at the ablative surface boundary indicates that present research efforts are devoted to ablative systems which can operate for flight times associated with lifting vehicles and to systems which combine absorption with radiative cooling.

RADIATIVE SYSTEMS

The principal types of radiative structures that have been investigated are indicated in figure 3. They may be classified according to whether the structure and its internal contents are unprotected, partially protected, or fully protected from high temperatures. In each case 95 percent or more of the heating input is dissipated by radiation, with the remainder being absorbed by a temperature rise in the structure or by an internal cooling system.

The unprotected structure applies to lightly loaded vehicles with large lifting or drag surfaces. Small, but structurally important, reductions in operating temperature are achieved by internal radiation of heat from the highly heated surfaces on the windward side of the

component to the surfaces of lesser heating on the leeward side. Special construction techniques which use corrugated metal and expansion joints have been developed; these techniques alleviate thermal stresses and permit use of thin sheet metal in the presence of large temperature gradients as is demonstrated in reference 1. Corresponding weights are in the range of 1 to 3 lb/sq ft of wetted area depending upon vehicle type and external load conditions.

The partially protected structure (fig. 3) is designed to cope with a more severe heating environment. It uses an arrangement of insulating shields to block the inward flow of heat at the highly heated windward surfaces. The temperature of the structure behind the shields is thereby reduced to values which lie close to the radiation-equilibrium value for the leeward side of the component. This means in some cases that a load-bearing structure operates at temperatures that are 60 percent or less of those on the shield surfaces.

The fully protected structure is designed to obtain the degree of internal-temperature control necessary for cargo areas and requires the addition of a cooling system to absorb heat that passes through the insulating shields. Cooling systems using gases and water as expendable coolants have been investigated. When consideration is given to the large storage-volume requirements for gaseous coolants, it becomes clear that water-boiling systems are the most practical choice. They are capable of maintaining desired interior-wall temperatures of 150° F or less by boiling at reduced pressures.

The price to be paid for obtaining a cool interior with a radiation-cooled vehicle can be assessed in terms of weight. In the remaining discussion, therefore, attention is given to the weight of radiation shields with back-surface cooling and to the weight of the alternate device, the ablative shield.

The characteristics of two types of radiative-shield designs undergoing investigation are shown in figure 4. One of these designs uses a metallic wall as the hot radiating surface; the other uses ceramic materials. The corrugated outer wall shown in figure 4 is but one of several lightweight metallic outer walls that have been investigated. This work has indicated that superalloy surfaces can be operated successfully at temperatures up to 2,200° F. Special problems encountered in the design of such surfaces are discussed in reference 2. Through the use of refractory metals in place of superalloys, a potential for operating temperatures up to 3,000° F exists.

The ceramic shield is being investigated for surface temperatures in excess of 3,000° F. The materials required are foamed ceramics of low thermal conductivity which also have enough mechanical integrity to serve as the vehicle surface. With these shields, provision of a

reliable attachment of a thick layer of low-density ceramic to the load-bearing structure is a problem. A possible solution indicated in figure 4 is the use of a corrugated-metallic-honeycomb attachment. The proximity of the water-cooling system confines melting of the honeycomb to a short distance beneath the surface.

At the present time, there is a rather important difference in the insulating capability of these two types of radiative-shield designs which has a large effect on the amount of water required for back-surface cooling. This weight difference is shown in figure 5 where the weight per unit area ΔW of shields and water required to maintain a 150° F environment is plotted as a function of external heat load. The weight ΔW does not include the load-bearing structure.

The lowest curve in figure 5 gives the weight achieved with insulating shields which utilize superalloys for the external surface. The next higher curve is a conservative estimate of the weight penalty involved in substituting a refractory metal surface for the superalloy surface in order to achieve a higher operating temperature. The highest curve applies to the ceramic shield. It is based on the insulating properties of materials such as foamed quartz, aluminum oxide, and zirconia. The derivation of these curves is indicated in the appendix. The comparison shows that the weight penalty associated with higher maximum surface temperatures becomes increasingly severe, particularly for the larger heat loads.

An important characteristic of these radiative-cooling systems is that although weight increases with total heat load, system efficiency is greater at higher heat loads. Thus, the lower curve in figure 5 shows that in the heat-load range of 10,000 to 20,000 Btu/sq ft, corresponding to design values for body areas of vehicles, each pound of system weight handles 6,000 to 7,000 Btu, while at the larger heat loads well over 20,000 Btu can be handled by each pound. Even with the foamed-ceramic shield, a system efficiency of 10,000 Btu/lb and higher can be achieved when the total heat load exceeds 100,000 Btu/sq ft. Heat loads of this magnitude are encountered at the stagnation areas of lifting vehicles. These high weight efficiencies for radiative-cooling systems at large heat loads may be compared with the efficiency of ablative shields, which provide a practical method for handling high heat rates, but which encounter difficulty in maintaining a high weight efficiency as heating time is increased. Two approaches for alleviating this difficulty are discussed in the next section.

ABLATIVE SYSTEMS

Cross sections of two ablative heat shields are shown in figure 6. The shield material may be thought of as being composed of an ablation layer and a self-insulation layer. The latter layer protects the structure by acting as a sink for heat which is conducted from the hot surface. The weight of the self-insulation layer depends on flight time and can become very substantial for lifting vehicles if the temperature rise at the back surface must be restricted. One way to reduce this weight is to find a suitable shield material which ablates at a low temperature and which is also a poor heat conductor. An alternate method, which permits use of presently developed shield materials, is to provide the back surface with a water-cooling system. This method is indicated by the lower sketch in figure 6. The use of water as a back-surface heat sink will reduce the thickness of the insulation layer, and it may be expected that the combined weight of water and insulation will be less than the weight of the self-insulation layer in the shield without a water-cooling system.

Calculations illustrating the effect of a back-surface water-cooling system on the weight of an ablating shield are shown in figure 7. Calculations were performed for a typical heat load of 20,000 Btu/sq ft with the assumption that the ablating material yields an average effective heat of ablation of 4,000 Btu/lb during reentry. Details of these calculations are given in the appendix. The resulting weight ΔW is plotted as a function of the temperature for ablation, or vaporization, of an idealized shield material which does not leave a char residue.

Increases in vaporization temperature mean increased heat conduction toward the back surface as well as increased radiation from the heated face. The interaction of these two trends with increasing surface temperature leads to a weight for uncooled shields that first increases rapidly due to heat conduction toward the back surface and then levels off due to increased radiation cooling at the front face. The weight of uncooled shields for a given total heat load is also seen to be influenced significantly by increases in heating time. In order to obtain a weight of 5 lb/sq ft, which is the minimum that can be achieved with this combination of heat load and H_{eff} , the ablation temperature must approach the allowable temperature for the back surface of the shield. A system efficiency of 4,000 Btu/lb is then approached.

The curves for the water-cooled shield show that the weight of these shields (including water weight) is relatively insensitive to variations in ablation temperature and heating time. (See fig. 7.) Significant weight reductions over that for uncooled shields are achieved even in the temperature range around 1,000° F associated with

a low-temperature ablator such as Teflon. The downward trend of the curves at the higher temperatures indicates that a substantial fraction of the heat load is being dissipated at the surface by radiation. It would appear from this comparison that the use of a back-surface water-cooling system permits the selection of the ablating material on grounds other than its ablating temperature and makes possible the achievement of a weight efficiency for the system equal to or greater than the material H_{eff} , even for long heating times.

RADIATIVE SYSTEMS WITH TRANSIENT ABSORPTION

An entry maneuver which presents a challenge in structural design is that initiated at steep angles with a subsequent pull-up to an equilibrium flight path. The type of heating history encountered is shown in figure 8. During the initial dip into the atmosphere, heating rates and surface temperatures are encountered which are difficult to handle with radiation systems, but the principal part of the heat load occurs at heating rates that are compatible with radiation cooling. Modification of radiation-shield systems to provide transient heat absorption is therefore desirable.

The sketches in figure 8 show how the ceramic-wall and metallic-wall designs described previously (fig. 4) can be modified to provide a transient period of absorption followed by radiation. One modification consists of impregnating the porous-ceramic shield with a vaporizing material which when heated will generate gas for a period of transpiration cooling. Analysis of such a system indicates that materials with decomposition or vaporization temperatures below $1,000^{\circ}\text{F}$ should generate gas at a sufficient rate to reduce surface temperatures to 70 percent or less of the radiation-equilibrium value. Such reductions would permit a surface designed for a temperature of $3,000^{\circ}\text{F}$ to operate under a transient condition that would ordinarily produce a $4,000^{\circ}\text{F}$ temperature at the surface. Calculated weights of vaporizing material required to produce the necessary surface cooling during a steep-angle reentry at orbital velocity are of the order of 1 lb/sq ft. A limited number of hot-gas-jet tests of such systems have been made with porous ceramics impregnated with various organic and inorganic materials.

Possible modifications to an insulating shield with a metallic wall are indicated by the remaining two sketches in figure 8. One possibility is to apply a thin layer of ablating material directly to the external surface of the solid shield. This layer would appear to provide a positive method of temperature control, but the risk is run that a thin layer may be lost during the heating of the boost phase and the subsequent exposure to the vacuum of space. An alternative is

to impregnate the insulating material beneath the shield with a vaporizing material and to substitute a porous metallic shield for the solid one. The degree of temperature reduction of the metallic surface again depends upon the rate of gas generation beneath the surface. Although all of these approaches appear promising, system development is in an early stage, and much experimental work will be required to prove their reliability.

THERMAL-PROTECTION SUMMARY

A summary of the weight of protection systems is given in figures 9 and 10. Radiative systems are shown in figure 9; their weight, in lb/sq ft of vehicle surface, is shown superimposed on the vehicle-heating environment. The weights given are those required to step down from the external environment to a low-temperature interior. With each system, a gradual weight increase occurs as the total heat load increases but, more importantly, step increases in weight take place at certain temperature limits for design of the outer surface.

Of these systems, the superalloy shields may be placed in the category of being well-developed and ready for application to those areas of reentry vehicles where maximum temperatures do not exceed 2,200° F. Vehicle areas exposed to higher temperatures require refractory-metal shields. The construction of such shields is perhaps more art than science at the present time, but current work indicates that present technology should permit design of shields that would be serviceable for at least 2 hours at high temperature. This lifetime should be sufficient for one or more flights before shield replacement.

At higher heat rates the area for application of foamed-ceramic shields is encountered. It is difficult to assess the development status of shields based on these new materials because of the proprietary nature of much of the work. The exploratory tests that have been accomplished, however, indicate that there should be no technical barrier in achieving designs of the weight shown in figure 9.

The ablative-system summary given in figure 10 shows that through the use of a back-surface cooling system, ablative shields of reasonable weight extend well into the manned-vehicle band. Near the low L/D edge of the band, shield weights are encountered in the range 3 to 8 lb/sq ft. Considerable experience has already been accumulated in the design of shields of these weights for ballistic vehicles. Even though these weights are somewhat heavier than those indicated for the ceramic shields in figure 9, they provide a current solution for heavily loaded reentry vehicles of compact design which fall in

[REDACTED]

this area of the band. They also provide the only currently available solution for entries at the higher heating rates associated with return from lunar missions.

CONCLUDING REMARKS

Practical structural approaches are available for a substantial area of the manned-reentry-vehicle band. The choice between radiative and ablative structures is seen to depend mainly on vehicle wing or area loading and lift-drag ratio. Radiative structures appear to be the logical choice for lightly loaded vehicles independent of their lift-drag ratio. Similarly, it appears that the ablative approach could be readily extended to the design of compact vehicles developing a moderate amount of lift during reentry.

[REDACTED]

|

APPENDIX

WEIGHT ANALYSIS OF THERMAL PROTECTION SYSTEMS

Radiative System Weight Analysis

In the weight analysis of radiative systems, the heat capacity of the insulation layer was neglected and the conductivity-density product was assumed to vary with the cube of the mean temperature of the insulation. Thus,

$$k\rho = \alpha T_m^3 \quad (1)$$

where

$$T_m^3 = \frac{1}{T_o - T_i} \int_{T_i}^{T_o} T^3 dT = \frac{(T_o^2 + T_i^2)(T_o + T_i)}{4} \quad (2)$$

The value of α depends upon the type of insulation required for tolerance of the maximum value of T_o during a flight.

With these simplifications the minimum weight of insulation and back-surface coolant can be expressed as

$$\sqrt{\frac{\alpha Q}{\sigma \epsilon_o \Delta h} \left[1 - \left(\frac{T_i}{T_e} \right)^4 \right]} - \frac{\alpha}{4\sigma \epsilon_o}$$

To obtain the weights shown in figure 5, the value of Δh was taken to be 1,000 Btu/lb corresponding to boiling water, and the values of the remaining parameters are given in the following table as a function of the maximum outer-surface temperature:

$(T_o)_{\max}$, °F	Type of insulation	$\frac{(\text{Btu})(\text{lb})}{(\text{ft})^4(\text{hr})(^\circ\text{R})^4}$	Type of outer shield	ϵ_o	Weight of outer shield, lb/sq ft
2,200	Fibrous	0.1×10^{-9}	Superalloy	0.9	1.0
3,000	Fibrous	$.1 \times 10^{-9}$	Refractory metal	.9	1.5
4,000	Foamed- ceramic	1.0×10^{-9}	Foamed- ceramic	.5	---

Ablative Shield Weight Analysis

For the purpose of a weight analysis of ablation shields the initial temperature of the shield outer surface was assumed to be the ablation temperature. The distribution of temperature through the shield thickness was assumed to be linear and the heat conducted to the back surface was assumed to be negligible insofar as its effect on the heat balance at the outer surface was concerned.

For a constant outer-surface heating rate, the weight required for an ablating shield having an initial back-surface temperature T_i and a final back-surface temperature T_B was calculated from the following equation:

$$\frac{\Delta W H_{\text{eff}}}{Q \left[1 - \left(\frac{T_A}{T_e} \right)^4 \right]} = \frac{1}{2} \left(1 + \sqrt{1 + \frac{8k\rho t}{C} \left(\log_e \frac{T_A - T_i}{T_A - T_B} \right)^{-1} \left\{ \frac{H_{\text{eff}}}{Q \left[1 - \left(\frac{T_A}{T_e} \right)^4 \right]} \right\}^2} \right) \quad (3)$$

It may be noted that the value of H_{eff} used in this equation should not include a radiation-cooling contribution, inasmuch as radiation at the outer surface is accounted for by the factor $\left[1 - \left(\frac{T_A}{T_e} \right)^4 \right]$.

The values of $k\rho$ and C used to obtain the weights given in figure 7 were $15 \frac{(\text{Btu})(\text{lb})}{(\text{ft})^4(\text{hr})(^\circ\text{F})}$ and 0.25 Btu/lb , respectively.

For the shield whose back surface is maintained at the initial temperature by a water-cooling system, the optimum weight combination of ablation layer, insulation layer, and coolant can be obtained from the following equation:

$$\begin{aligned}
 \frac{\Delta W H_{\text{eff}}}{Q \left[1 - \left(\frac{T_A}{T_e} \right)^4 \right]} &= \frac{1}{2} \left\{ 1 + \sqrt{1 + \frac{4k\rho t (T_A - T_i) \left(\frac{H_{\text{eff}}}{Q} \right)^2}{\Delta h \left[1 - \left(\frac{T_A}{T_e} \right)^4 \right]^2}} \right\} \\
 &- \frac{k\rho t (T_A - T_i) \left(\frac{H_{\text{eff}}}{Q} \right)^2}{\Delta h \left[1 - \left(\frac{T_A}{T_e} \right)^4 \right]^2} \log_e \left\{ \frac{\sqrt{1 + \frac{4k\rho t (T_A - T_i) \left(\frac{H_{\text{eff}}}{Q} \right)^2}{\Delta h \left[1 - \left(\frac{T_A}{T_e} \right)^4 \right]^2}} - 1}{\sqrt{1 + \frac{4k\rho t (T_A - T_i) \left(\frac{H_{\text{eff}}}{Q} \right)^2}{\Delta h \left[1 - \left(\frac{T_A}{T_e} \right)^4 \right]^2}} + 1} \right\} \quad (4)
 \end{aligned}$$

In order to determine the validity of the constant heating-rate approximation, triangular heat pulses of various shapes but having the same heating time and heat input were investigated. These calculations indicated that the weight for a more realistic heat pulse should not differ from that calculated by equation (4) by more than 5 percent.

A more refined analysis was also made without the restriction of a linear gradient throughout the shield thickness. Numerical results from an IBM type 650 electronic data processing machine indicate that the weight obtained with the linear temperature gradient is conservative by 5 to 10 percent.

REFERENCES

1. Pride, Richard A., Royster, Dick M., and Helms, Bobbie F.: Experimental Study of a Hot Structure for a Reentry Vehicle. (Prospective NASA paper.)
2. Anderson, Melvin S., Trussell, Donald H., and Stroud, C. W.: Research on Radiation Heat Shields for Bodies and Leading Edges. (Prospective NASA paper.)

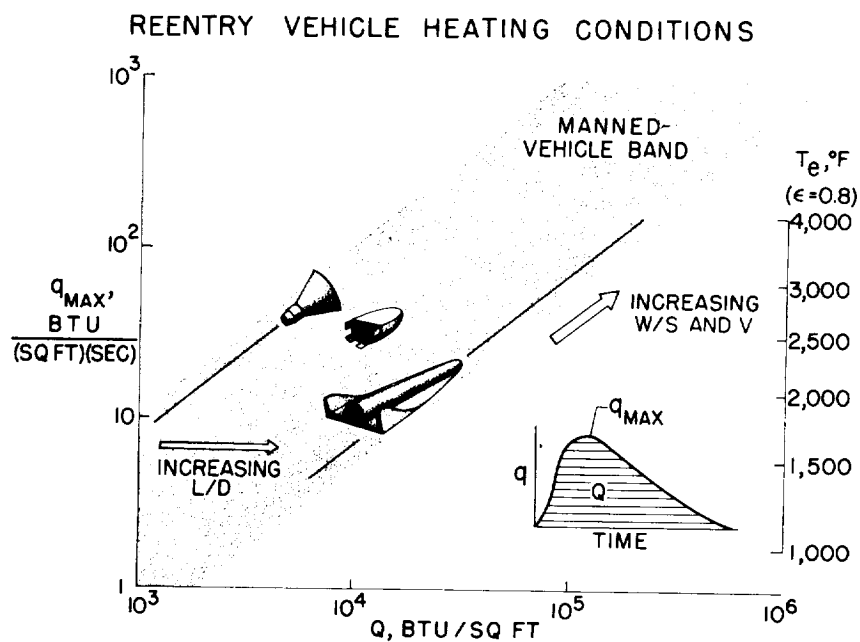


Figure 1

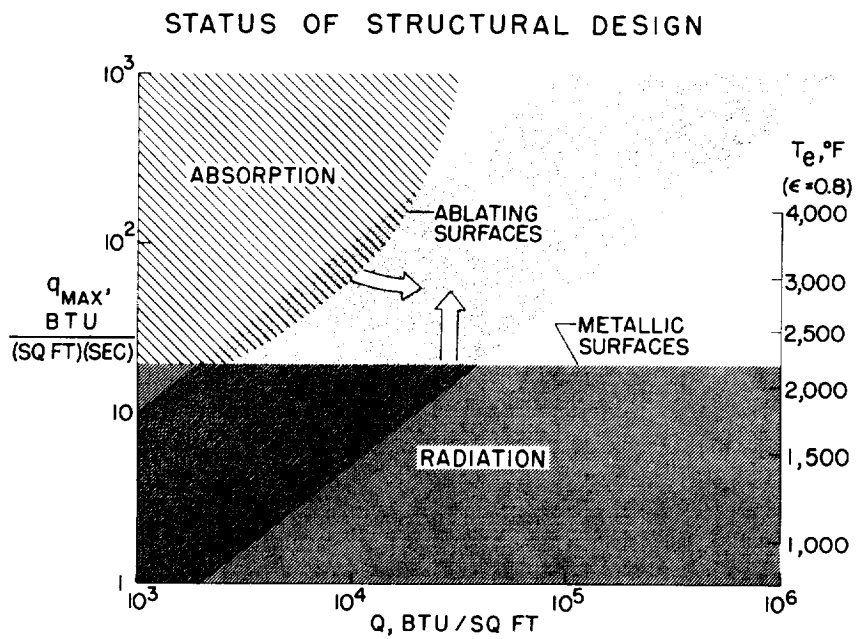
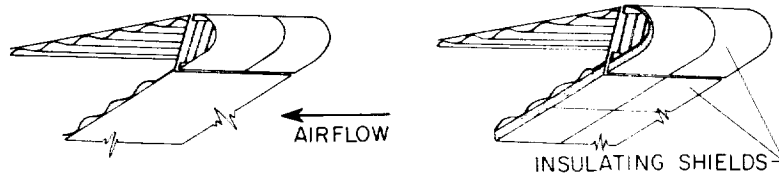


Figure 2

RADIATIVE STRUCTURES

UNPROTECTED
($W=1$ TO 3 LB/SQ FT; WETTED AREA)

PARTIALLY PROTECTED



FULLY PROTECTED

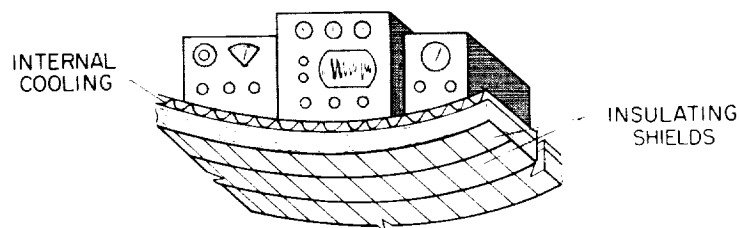


Figure 3

RADIATIVE HEAT SHIELDS

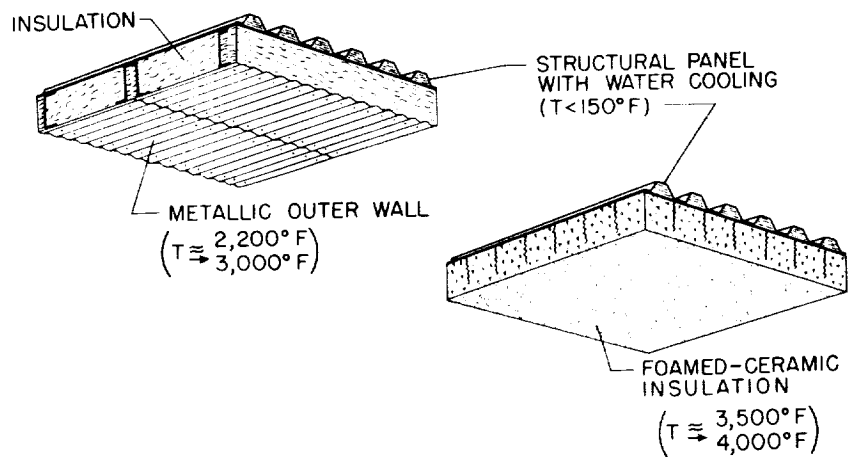


Figure 4

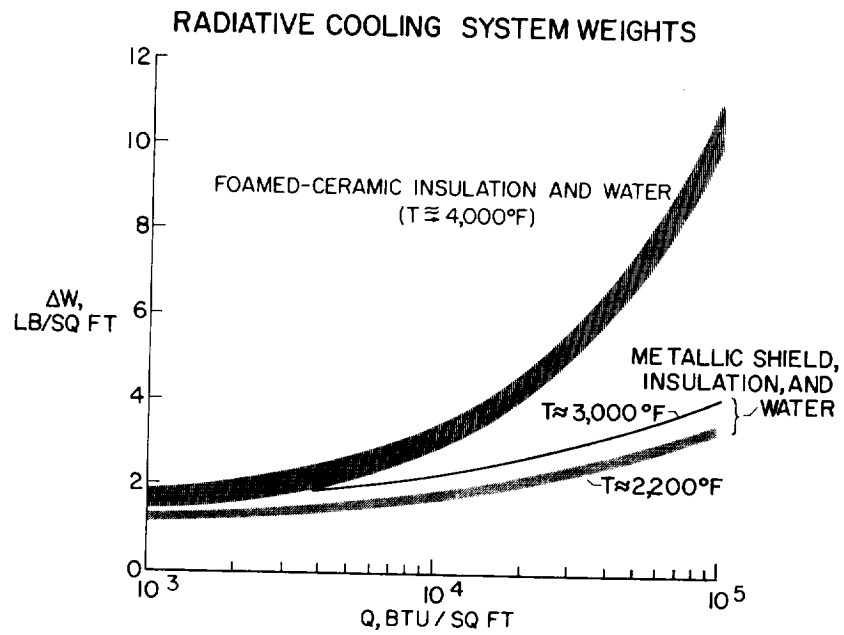


Figure 5

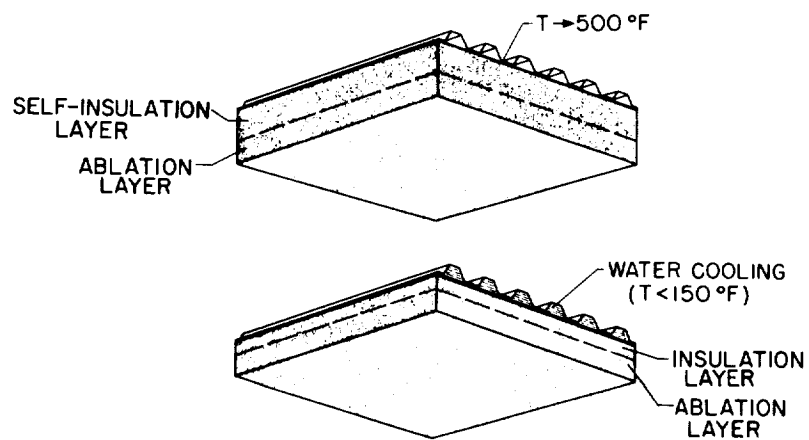
ABLATIVE HEAT SHIELDS

Figure 6

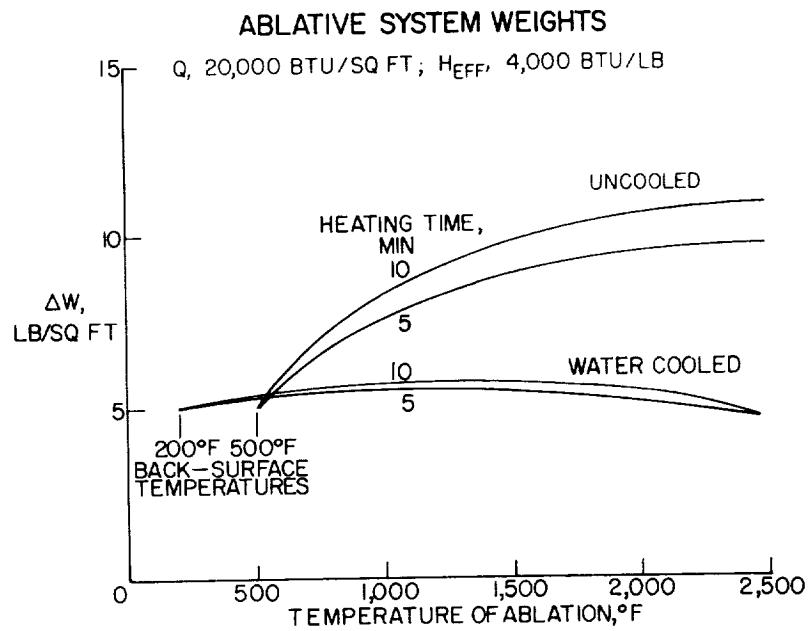


Figure 7.

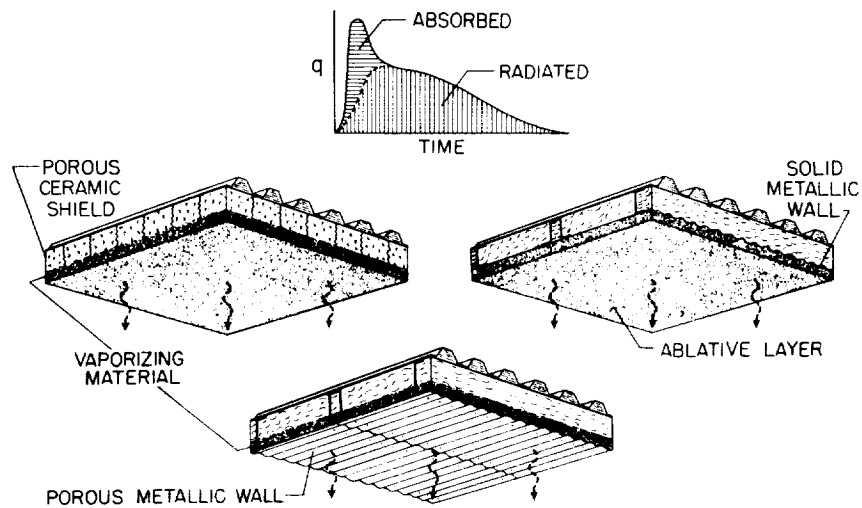
RADIATIVE HEAT SHIELDS WITH TRANSIENT ABSORPTION

Figure 8

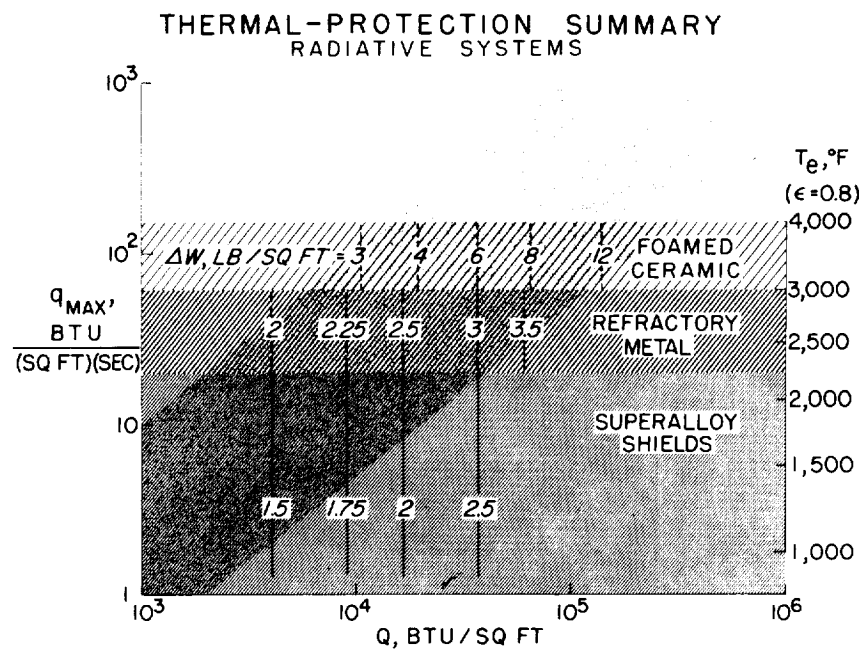


Figure 9

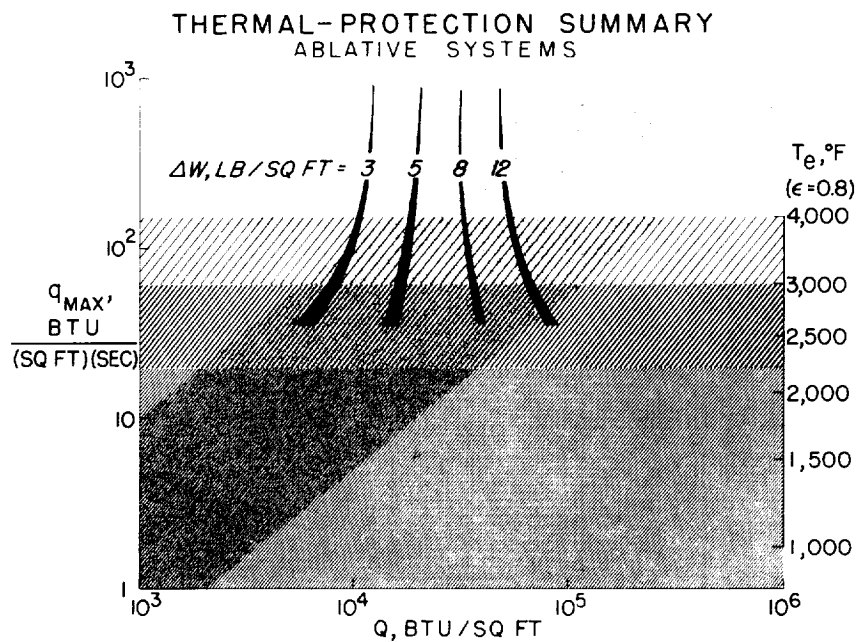


Figure 10

ABLATION FOR MANNED REENTRY VEHICLES

By Leonard Roberts
Langley Research Center

INTRODUCTION


The success of the ablation shield for high-speed ballistic missiles and the successful flight test of the Project Mercury ablation shield suggest that ablation may have more general application to reentry heating problems. Before such a conclusion can be drawn, it is well to take stock of our present understanding of ablation and consider whether its success to date can be expected to continue when applied to vehicles which will have a heating experience of long duration.

The heat protection system for a manned reentry vehicle must satisfy two important requirements; it must dispose of heat efficiently and at the same time maintain the structure of the vehicle at a desirable temperature. Moreover, if the vehicle is to be allowed a wide flight-path corridor, the system must operate efficiently over the long time associated with the glide trajectory and must also be capable of a high rate of heat disposal as required by the reentry of shorter duration.


This paper has as its purpose the clarification of the present ideas as to the most appropriate type of ablation for manned vehicles keeping in mind the importance of versatility as well as efficiency.

SYMBOLS

A	reference area for drag and lift, sq ft
C_D	drag coefficient
c	specific heat, Btu/(lb)(°R)
d	leading-edge diameter, ft
G_{MAX}	maximum deceleration, g units



\bar{H}	dimensionless effective heat of ablation
H_a	heat of ablation, Btu/lb
H_{EFF}	effective heat of ablation, Btu/lb
h_e	stream enthalpy
h_w	wall enthalpy
k	thermal conductivity, Btu/(ft)(°R)(sec)
L/D	lift-drag ratio
m	mass of vehicle, slugs
Q	total convective heat input, Btu/sq ft
q_{MAX}	maximum convective heating rate, Btu/(sq ft)(sec)
R	nose radius, ft
T_a	ablation temperature, °R
T_b	back-surface temperature, °R
T_{MAX}	maximum surface temperature, °R
t	time, sec
W	weight loss due to ablation, lb/sq ft
W'	weight of self-insulation, lb/sq ft
W_{CHAR}	weight of char, lb/sq ft
W_i	weight of insulation, lb/sq ft
W_o	weight loss due to ablation with no radiation or accumulation, lb/sq ft
W_w	weight of water coolant, lb/sq ft
β	fraction of stream enthalpy absorbed by gas products of ablation



ϵ	emissivity
Λ	angle of sweep
ρ	density, lb/cu ft
σ	Boltzmann constant, 0.48×10^{-12} Btu/(sq ft)(sec)($^{\circ}\text{R}^4$)
X_1	radiation parameter
X_2	conduction parameter

ANALYSIS

Aerodynamic Heating

Throughout the paper, consideration is restricted to the heating problems of the nose or leading edge of a vehicle which enters the atmosphere at near-satellite speed; it is also assumed that the vehicle enters the atmosphere at a small angle and operates at a constant lift-drag ratio. This limitation of constant L/D yields trajectories which can be analyzed more easily but still allows a fairly broad comparative picture to be obtained. For these trajectories the laminar heating experience is determined by two parameters as shown by Chapman (ref. 1). The first of these parameters depends on the vehicle design and attitude in flight. This parameter is written, for the nose,

$$\left(\frac{m}{C_{DAR}}\right)^{1/2}$$

or, for the leading edge,

$$\left(\frac{m}{C_{DA\delta}}\right)^{1/2} \cos \Lambda$$

The second parameter depends on the trajectory and is simply the maximum deceleration G_{MAX} experienced by the vehicle during its reentry. Small values of G_{MAX} are associated with reentry of long duration and vice versa.

The maximum heating rate and the total aerodynamic heat input per unit area for the nose may be expressed in terms of $\left(\frac{m}{C_{DAR}}\right)^{1/2}$ and G_{MAX} (following Chapmen in ref. 1) in a very simple way:

$$q_{MAX} \approx 40 \left(\frac{m}{C_{DAR}}\right)^{1/2} (G_{MAX}^2 - 1)^{1/4} \text{ Btu/(sq ft)(sec)} \quad (1)$$

$$Q \approx 4,800 \left(\frac{m}{C_{DAR}}\right)^{1/2} (G_{MAX}^2 - 1)^{-1/4} \text{ Btu/sq ft} \quad (2)$$

For the leading edge, $\left(\frac{m}{C_{DAd}}\right)^{1/2} \cos \Lambda$ should replace $\left(\frac{m}{C_{DAR}}\right)^{1/2}$. In these simplified expressions the relation

$$G_{MAX} = \left(\frac{L}{D}\right)^{-1} \left[1 + \left(\frac{L}{D}\right)^2\right]^{1/2}$$

has been used in conjunction with the expressions for q_{MAX} and Q derived in reference 1. (When $L/D = 0$, the quantity $(G_{MAX}^2 - 1)^{1/4}$ is written more correctly $(G_{MAX})^{1/2}$ but the error is not significant since $G_{MAX} > 8$ for nonlifting vehicles.)

An integrated "time of reentry" may also be calculated from reference 1 to give the approximate relation

$$t = 2,400 (G_{MAX}^2 - 1)^{-1/2} \text{ sec} \quad (3a)$$

It is interesting to note that the heating duration obtained by assuming a triangular heat pulse having q_{MAX} and Q given by equations (1) and (2), respectively, also gives

$$t = \frac{2Q}{q_{MAX}} = 2,400 (G_{MAX}^2 - 1)^{-1/2} \text{ sec} \quad (3b)$$

Also of interest is the expression for the maximum equilibrium radiation temperature attained by the surface of the vehicle during flight; this

is obtained by equating the radiative cooling rate with the aerodynamic heating rate:

$$q_{\text{MAX}} = \sigma \epsilon T_{\text{MAX}}^4$$

which may be written approximately, using equation (1) and the numerical value of σ (0.48×10^{-12} Btu/(sq ft)(sec)($^{\circ}\text{R}^4$)), as

$$\epsilon \left(\frac{T_{\text{MAX}}}{3000} \right)^4 = \left(\frac{m}{C_{\text{DAR}}} \right)^{1/2} (G_{\text{MAX}}^2 - 1)^{1/4} \quad (4)$$

where T_{MAX} is in $^{\circ}\text{R}$.

Present metallic radiation shields are limited by temperature and emissivity to values of $\epsilon \left(\frac{T_{\text{MAX}}}{3000} \right)^4 < 1$. Thus, if the vehicle design and the reentry trajectory are such that

$$\left(\frac{m}{C_{\text{DAR}}} \right)^{1/2} (G_{\text{MAX}}^2 - 1)^{1/4} > 1$$

an ablation-type shield is more appropriate. (See fig. 1.)

Ablation

For the purpose of this paper, ablation materials have been placed in three broad categories; they are

- (1) Low-temperature ablators
- (2) Radiating high-temperature ablators
- (3) Composite charring ablators

The means whereby these materials dispose of energy and their behavior during ablation are presented in table I. Briefly, the total weight of the shield is the sum of that actually lost or charred by ablation and that required as self-insulation so that the back-surface temperature does not exceed its design value.

The low-temperature ablation materials absorb heat in the phase change and in the stream boundary layer; Teflon and nylon are typical.

~~CONFIDENTIAL~~

In a given duration a major part of the heat input is disposed by ablation; this results in a weight loss W (lb/sq ft). In addition, a certain fraction of the heat input is accumulated by the remaining shield, and in order to maintain the structure at a required temperature, say $1,000^\circ \text{R}$, a weight W' (lb/sq ft) is required to insulate against the accumulated heat.

The high-temperature radiating ablation materials dispose of heat primarily by radiation and in the phase change. Because the surface temperature is high, there is relatively little weight loss but a significant amount of accumulation of heat can take place. A large weight W' is required to insulate against this accumulated heat.

Finally, there are composite charring ablators; the fiber glass and phenolic shield proposed for the Project Mercury capsule is typical. Here ablation causes a phase change in the phenolic resin leaving a residual char which is held by the fiber-glass matrix. The low-temperature resin provides back-surface-temperature control while the char radiates at a high temperature. If the heating rate is sufficiently high, the fiber glass also ablates.

In general, then, part of the heat is radiated, part is disposed by ablation, and part is accumulated by the shield.

In any analysis of the behavior of the shield during reentry, these three effects - ablation, radiation, and accumulation - must be represented.

Consider first the simplest case of ablation without radiation or accumulation of heat by the remaining shield. The effective heat capacity of the ablation material may be written in the approximate form

$$H_{\text{EFF}} = H_a + \beta(h_e - h_w)$$

The integrated value over a trajectory at constant L/D as obtained in reference 2 is written

$$H_{\text{EFF}} = \frac{13500}{2} \bar{H} \quad (5)$$

where

$$\bar{H} = \beta \left[1 - \left(\frac{H_a}{H_a + 13500\beta} \right)^{1/2} \right]^{-1}$$

~~CONFIDENTIAL~~

Thus,

$$W_0 = \frac{Q}{H_{EFF}} = \frac{7 \left(\frac{m}{C_{DAR}} \right)^{1/2}}{\bar{H} (G_{MAX}^2 - 1)^{1/4}} \text{ lb/sq ft} \quad (6)$$

which is the total weight per unit area lost from the shield.

When radiation and accumulation are present, the total amount of heat available to cause ablation is reduced to an amount

$$Q(1 - x_1 - x_2)$$

where x_1 is the fractional reduction due to radiation and x_2 is the fractional reduction due to accumulation. More generally then

$$W = W_0(1 - x_1 - x_2) \text{ lb/sq ft} \quad (7)$$

is the total weight loss per unit area. In equation (7) the ratios x_1 and x_2 are written, respectively,

$$x_1 = \frac{\epsilon \left(\frac{T_{MAX}}{3000} \right)^4}{\left(\frac{m}{C_{DAR}} \right)^{1/2} (G_{MAX}^2 - 1)^{1/4}}$$

$$x_2 = \frac{\left(2\rho c \frac{T_{MAX} - T_b}{3000} \right) \left(\frac{k}{\rho c} \right)^{1/2}}{\left(\frac{m}{C_{DAR}} \right)^{1/2}}$$

(using the analysis of ref. 2). In particular it is seen that, if $x_1 + x_2 = 1$, then $W = 0$ and no ablation takes place. The shield then acts as a radiation shield with a certain amount of heat accumulation. If $x_2 = 0$ and $x_1 = 1$, the shield is in radiative equilibrium, and, if $x_1 = 0$ and $x_2 = 1$, the shield acts as a heat sink.

As previously noted, an additional weight W' will be required to ensure that the temperature of the structure is maintained below a

specified design temperature. The self-insulation weight for an allowable 500° R rise in back-surface temperature is

$$W' = \frac{QX_2}{500\rho c} = 32\left(\frac{\rho k}{c}\right)^{1/2} \left(\frac{T_{MAX} - T_b}{500}\right) (G_{MAX}^2 - 1)^{-1/4} \text{ lb/sq ft} \quad (9)$$

Obviously, low values of T_{MAX} and ρk lead to low insulation requirements as shown by equation (9).

For the low-temperature material and the charring material, W' is the amount of virgin material required as self-insulation; for these materials, therefore, T_{MAX} should be replaced by T_a .

Comparison With Flight Test Data

In September 1959 the Space Task Group of the NASA at Langley Field, Va., tested an ablation shield for Project Mercury. The vehicle used was termed "Big Joe" and the successful flight test of its shield gives an indication of the behavior of composite charring materials, in this case fiber glass and phenolic resin. (Fig. 2 shows a simplified picture of the behavior of this material.) The char operates at a high temperature and radiates, while conduction through the char causes ablation of the resin at a temperature of about $1,500^{\circ}$ R. The flight data showed that 2.0 lb/sq ft of char was produced during the flight and the maximum temperature attained was $2,700^{\circ}$ R; the calculated values of 2.05 lb/sq ft of char and $2,750^{\circ}$ R maximum temperature agree extremely well with the flight data. In order to obtain the calculated values, the expressions for W_0 , X_1 , and X_2 were amended to take account of the fact that the entry velocity of the Big Joe capsule differed from circular velocity. A detailed analysis of the charring ablation will appear in a forthcoming NASA publication.

Also shown in figure 2 are the calculated values for the Project Mercury capsule which is scheduled for a maximum acceleration of 8g or 9g. The figure shows that the Mercury capsule will require a total weight between 6 and 8 lb/sq ft for thermal protection, the higher value being associated with the condition of small lift due to asymmetry in flight. More than one-half of this total weight is required as self-insulation (to prevent leakage of heat to the back surface) even though the ablation temperature of $1,500^{\circ}$ R is not very high.

General Considerations

Quite generally the problem of maintaining a desirable back-surface temperature for long periods is handled most efficiently by absorbing the heat leakage at a low temperature near the back surface. For the charring ablators this is done most easily by using a low-temperature phenolic resin. For the high-temperature radiating ablators which do not contain resin or some other form of low-temperature material, additional absorbing material must be supplied. If it is assumed that water is supplied in sufficient amount to absorb the accumulated heat by vaporization, the use of these high-temperature radiating ablators becomes feasible. If water is not supplied, the amount of insulation required to maintain the back surface at a low temperature for the flight duration becomes intolerable.

In order to compare the weight requirements for the three previously discussed ablation materials, the weight of water W_w (for the radiating ablator) and the weight of self-insulation W_i (where now $W' = W_w + W_i$) are found. It is assumed that only a small fraction of the total aerodynamic heat input is absorbed by the water, the major fraction being radiated at the surface. A conservative value of W' is obtained by writing

$$\frac{\rho k (T_{MAX} - 670)}{W_i} t = 1,000 W_w \quad (10)$$

where in equation (10) the water absorbs 1,000 Btu/lb by vaporizing at a temperature of 670° R. The symmetry of equation (10) with respect to W_i and W_w leads to a condition in which

$$W_i = W_w = \left(\rho k t \frac{T_{MAX} - 670}{1000} \right)^{1/2} \quad (11)$$

in order for $W' = W_i + W_w$ to be a minimum. Thus, using equation (3)

$$W' = \frac{170(\rho k)^{1/2} \left(\frac{T_{MAX} - 670}{3000} \right)^{1/2}}{(G_{MAX}^2 - 1)^{1/4}} \quad (12)$$

where, from equation (4),

$$\frac{T_{MAX}}{3000} = \epsilon^{-1/4} \left[\left(\frac{m}{C_{DAR}} \right)^{1/2} (G_{MAX}^2 - 1)^{1/4} \right]^{1/4} \quad (13)$$

For the purpose of the present comparison the simple optimum, wherein the insulation weight and water weight are equal, is used.

When $T_{MAX} > T_a$ ablation does not occur and $W = 0$; when $T_{MAX} < T_a$ limited ablation occurs and $W \neq 0$. A representative value $T_a = 4,000^\circ R$ is used here for the high-temperature ablators. The comparison of weight requirements is made for a range of the vehicle design parameter $\left(\frac{m}{C_{DAR}}\right)^{1/2}$ with $G_{MAX} = 2$ and the results are shown in figure 3. The following material properties were assumed in this comparison:

For low-temperature ablator,

$$H_a = 1,000 \text{ Btu/lb}$$

$$\beta = 1/2$$

$$T_a = 1,000^\circ R$$

For high-temperature ablator,

$$\epsilon = 1/2$$

$$\rho k = 0.005 \frac{\text{Btu}}{(\text{sec})(\text{ft})(^\circ R)} \frac{\text{lb}}{\text{cu ft}}$$

$$T_a = 4,000^\circ R$$

For radiating composite ablator,

Resin:

$$H_a = 1,000 \text{ Btu/lb}$$

$$\rho k = 0.008 \frac{\text{Btu}}{(\text{sec})(^\circ R)(\text{ft})} \frac{\text{lb}}{\text{cu ft}}$$

$$T_a = 1,000^\circ R$$

$$\beta = 1/2$$

Char:

$$\epsilon = 0.8$$

For the composite ablator the fraction of resin was assumed to be 0.4 and that of the gas products to be 0.1.

A more general weight chart is shown in figure 4 where lines of constant weight are drawn on a plot of $\left(\frac{m}{C_{DAR}}\right)^{1/2}$ against G_{MAX} . The circles indicate the points of intersection of the W curves for the low-temperature material and the composite radiating material. The dashed part of the curve denotes the region in which the composite material is most efficient and the solid part of the curve shows where the low-temperature material is most efficient. These regions are apparent in figure 5 where the locus of the circled points has been plotted. It is seen that the line dividing these regions is approximately

$$\left(\frac{m}{C_{DAR}}\right)^{1/2} = 1$$

DISCUSSION

Before the suitability of any one type of ablation shield for a manned vehicle can be discussed, it should be noted that no general conclusion can be drawn concerning the overall weight of such a shield unless the entire design of the vehicle is considered. However it is possible to discuss local hot spots, such as the nose or leading surface, on a separate basis since they are limited regions of major concern.

Presently conceived metallic radiation shields are limited to heating rates below about 35 or 40 Btu/(sq ft)(sec); for heating rates in excess of this range the melting temperature of metals such as molybdenum is approached and the resulting loss in strength prohibits their use. As figure 1 shows, such a limitation places a restriction on the vehicle design and on the maximum deceleration allowed during reentry. If the design parameter $\left(\frac{m}{C_{DAR}}\right)^{1/2}$ (or $\left(\frac{m}{C_{DAd}}\right)^{1/2} \cos \Lambda$) is equal to unity, for example, the vehicle is confined to a maximum deceleration of less than 1.4g; more highly loaded vehicles are even further restricted.

By using an ablation shield, since the heating rate presents no problem, the vehicle is allowed a greater variation both in design and deceleration and therefore greater maneuverability in reentry. The cost of this increased versatility must be assessed in terms of the weight of the ablation shield.

It should also be noted that the quantitative results discussed herein are representative of the classes of material under consideration but do not necessarily represent the minimum weights achievable. Current research, both in low-temperature and radiating ablation materials (charring and noncharring), may well produce refinements which will further increase the efficiency of these materials.

It is evident from the preceding results that under certain conditions (when the design parameter $\left(\frac{m}{C_{DAR}}\right)^{1/2}$ is less than unity in the present comparison) the low-temperature ablators are more efficient and result in less weight, whereas for other conditions, $\left(\frac{m}{C_{DAR}}\right)^{1/2} > 1$, radiating ablators are better. Roughly speaking, in order to use radiation as a primary means of cooling, the surface temperature is high enough to cause a severe insulation problem even at low heating rates and the weight of insulation exceeds that weight which would be required of a low-temperature ablation shield to dispose of the same amount of heat. At higher heating rates the "fourth power law" makes radiation more attractive (providing the material can withstand the high temperature and is a good insulator).

In terms of the parameters $\left(\frac{m}{C_{DAR}}\right)^{1/2}$ and G_{MAX} the weight can be written, very approximately (for the property values used herein), as

$$W = 12(G_{MAX}^2 - 1)^{-1/4} \left[\left(\frac{m}{C_{DAR}}\right)^{1/2} \right]^{1/8} \text{ lb/sq ft}$$

for the composite radiating ablator, whereas

$$W = 12(G_{MAX}^2 - 1)^{-1/4} \left(\frac{m}{C_{DAR}}\right)^{1/2} \text{ lb/sq ft}$$

for the low-temperature ablation material. The appearance of $\left(\frac{m}{C_{DAR}}\right)^{1/2}$ raised to the 1/8 power (reflecting $W \sim T_{MAX}^{1/2}$, $T_{MAX} \sim q_{MAX}^{1/4}$, and $q_{MAX} \sim \left(\frac{m}{C_{DAR}}\right)^{1/2}$) shows immediately that $\left(\frac{m}{C_{DAR}}\right)^{1/2}$ is the crossover

value. It is seen from figure 5 that for $\left(\frac{m}{C_{DAR}}\right)^{1/2} > 1$ the composite radiating ablation material is more efficient, whereas for $\frac{q_{MAX}}{40} < 1$, that is,

$$\left(\frac{m}{C_{DAR}}\right)^{1/2} < (G_{MAX}^2 - 1)^{-1/4}$$

the metallic radiation shield may be used. (The metallic shield used in conjunction with the best available insulating material and cooled by vaporizing water at the back surface is efficient for $q_{MAX} < 40$.) In view of the relatively small region, roughly

$$(G_{MAX}^2 - 1)^{-1/4} < \left(\frac{m}{C_{DAR}}\right)^{1/2} < 1$$

in which the low-temperature ablation materials are most efficient, it appears that the radiating ablation materials are more appropriate for manned-vehicle application especially in the region of low maximum deceleration.

This paper has considered only trajectories which result from an assumption of constant lift-drag ratio. More generally the vehicle may have variable or modulated lift; this allows the vehicle to make a shorter duration reentry with limited deceleration usually at the expense of higher heating rates. In order to use such a maneuver, therefore, the shield may be required to undergo high heating rates during part of the reentry and low heating rates for the remainder. Again the radiating composite shield seems to be the answer.

The final choice of materials will depend on mechanical as well as thermal properties. Low-temperature materials may undergo undesirable changes in shape since a considerable fraction of the shield actually leaves the vehicle; charring materials must have sufficient strength to withstand vibration and shear forces and long-duration tests of these materials are therefore desirable before they can be used with complete confidence.

In view of the potential versatility of ablation materials for manned-flight application, considerable effort is warranted in the development of ablation materials having the appropriate thermal and mechanical behavior.

CONFIDENTIAL
CONCLUDING REMARKS

The use of ablation materials for the nose and leading edges of manned vehicles allows versatility in the design and operation of the vehicle.

A review of the type of ablation materials available shows that the low-temperature ablators may lose a considerable amount of material, especially for the low-deceleration, long-duration reentry; the high-temperature ablators require an additional back-surface cooling device (water cooling, for example). The composite materials have the advantage of radiating at a high temperature but, since ablation takes place within the material at a low temperature, back-surface-temperature control is assured.

The Big Joe test shows that a shield of large dimensions (30 sq ft) can be manufactured and flown successfully, and the agreement between flight and theory indicates that charring ablation is sufficiently well understood that it can be predicted with fair accuracy.

This paper has been concerned only with reentry from satellite speed; when return from orbits of higher energy is considered, the heating problem is increased and the need for a versatile shield is further emphasized. It seems likely, therefore, that the radiating composite ablation materials will play an increasingly important part in the design of manned reentry vehicles.

REFERENCES

1. Chapman, Dean R.: An Analysis of the Corridor and Guidance Requirements for Supercircular Entry Into Planetary Atmospheres. NASA TR R-55, 1960.
2. Roberts, Leonard: An Analysis of Ablation-Shield Requirements for Manned Reentry Vehicles. NASA TR R-62, 1960.

CONFIDENTIAL

TABLE I

CLASSIFICATION OF ABLATION MATERIALS

CLASS	ENERGY DISPOSAL	TYPICAL MATERIALS	BEHAVIOR
LOW-TEMPERATURE ABLATORS	PHASE CHANGE; BOUNDARY LAYER	TEFLON; NYLON	<p>1,500° R 1,000° R</p>
HIGH-TEMPERATURE ABLATORS	RADIATION; PHASE CHANGE	FOAMED QUARTZ; FIBER GLASS	<p>4,000° R 1,000° R</p>
COMPOSITE CHARRING ABLATORS	RADIATION; PHASE CHANGE	FIBER GLASS AND PHENOLIC; NYLON AND PHENOLIC	<p>3,000° R 1,500° R 1,000° R</p>

HEATING ENVIRONMENT PARAMETERS

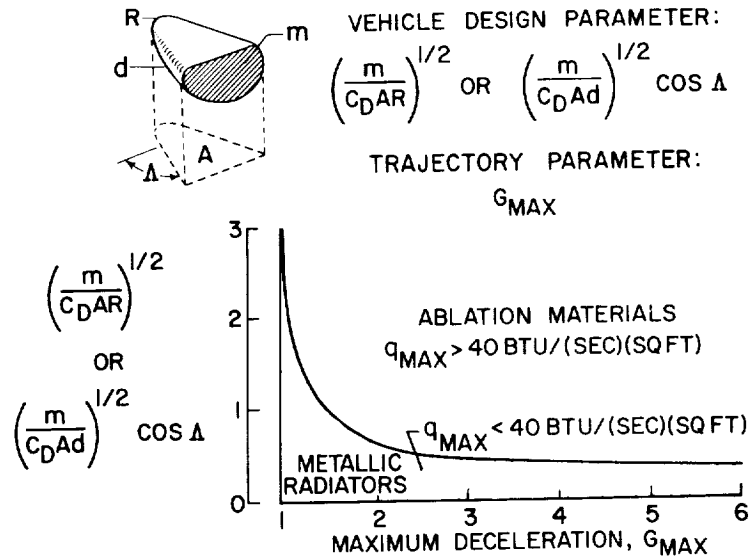


Figure 1

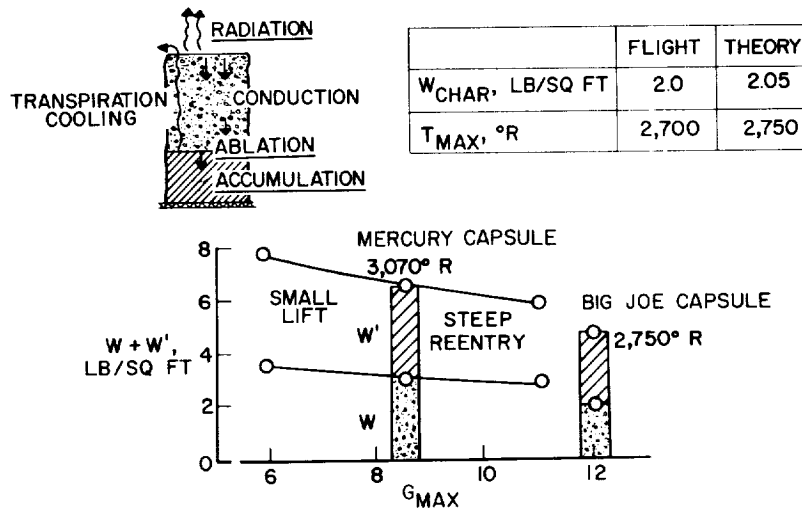
BIG JOE SHIELD
60% FIBER GLASS AND 40% PHENOLIC

Figure 2

ABLATION FOR MANNED VEHICLES

$G_{MAX} = 2$

_____ LOW-TEMPERATURE ABLATORS
 - - - - - HIGH-TEMPERATURE ABLATORS (WATER COOLED)
 - - - - - COMPOSITE CHARRING ABLATORS
 (WITH LOW-TEMPERATURE PHENOLIC)

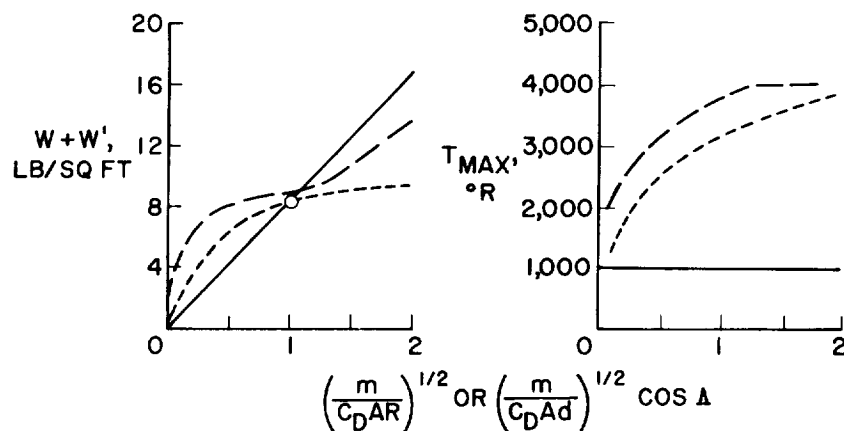


Figure 3

ABLATION-SHIELD WEIGHT REQUIREMENTS

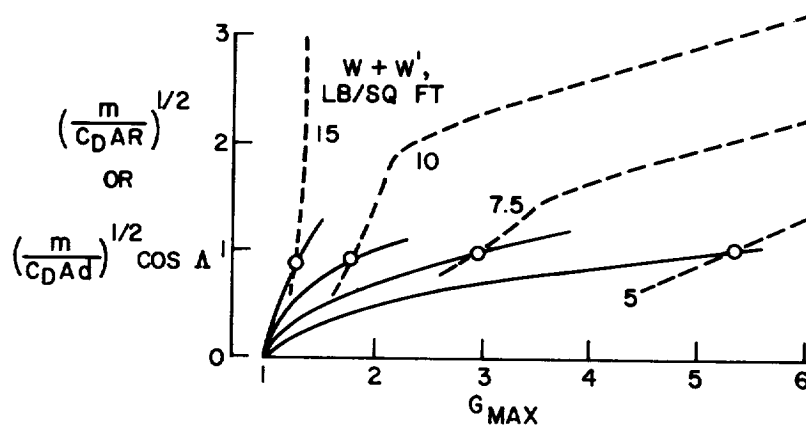


Figure 4

DESIGN CRITERIA

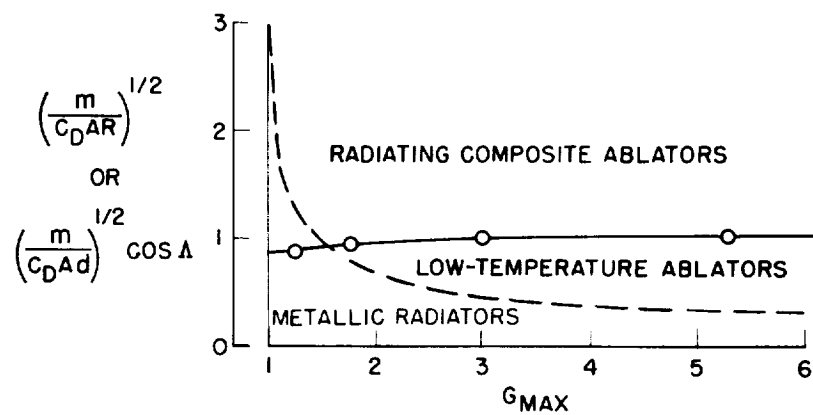


Figure 5

ABLATIVE PROPERTIES OF MATERIALS

By Raymond C. Savin and Hermilo Gloria
Ames Research Center

33

INTRODUCTION

It has already been demonstrated by full-scale flight tests that ablation cooling is an effective means of providing thermal protection for vehicles which encounter a strong, short heat pulse, such as an ICPM. It appears also that this method of thermal protection can be efficiently utilized for vehicles having a relatively weak but long heat pulse, such as those associated with reentry from satellite orbits. The purpose of this paper is to present some results of an investigation in which existing analytical results are employed in combination with experiment to obtain some ablative properties of a group of materials.

SYMBOLS

h_e	enthalpy at edge of boundary layer
h_w	enthalpy at wall
H_A	intrinsic heat capacity
H_{EFF}	effective heat of ablation
m	initial mass of model
\dot{m}	mass rate of ablation
\dot{q}_o	heat-transfer rate to nonablating surface at ablation temperature
η	transpiration factor
η_L	transpiration correlating factor for laminar flow
η_T	transpiration correlating factor for turbulent flow

s surface area
t time
 μ ratio of molecular weights of air to injected vapor

DISCUSSION

A brief review of analytic and experimental results for the ablation characteristics of Teflon is shown in figure 1. The effective heat of ablation H_{EFF} is shown in the figure as a function of the enthalpy difference across the boundary layer. The symbols represent stagnation-point data obtained in arc-jet facilities at AVCO (ref. 1) and at the Langley Research Center. It can be seen that a linear variation of H_{EFF} with enthalpy difference, as indicated by the solid line, represents a reasonable approximation to these data. The intercept of this line with the vertical axis represents the heat absorbed by the solid material in raising the temperature from some initial value up to the vaporization temperature. It also includes the latent heat of vaporization. This quantity, H_A , corresponds then to the material's intrinsic heat capacity. Now H_{EFF} is greater than H_A because of the absorption and shielding effect of the vapor given off. This contribution to effective heat capacity is represented by the term $\eta(h_e - h_w)$ where η is the slope of the line. The effective heat of ablation, then, can be expressed as shown in figure 2.

On the basis that vaporization is analogous to transpiration cooling, references 1, 2, and 3 have shown theoretically that the first expression shown in figure 2 applies to materials which ablate by essentially complete vaporization - that is, for materials such as Teflon which can, for practical purposes, be treated as sublimers. The term η was obtained from the correlation of transpiration results for various mass injections and for various types of boundary-layer flows. For example, for a three-dimensional laminar boundary layer, Hidalgo (ref. 4) empirically derived the second expression in figure 2 for the transpiration factor η where μ is the molecular weight ratio of air to the injected vapor. For turbulent boundary layers, transpiration data on cones from reference 5 were correlated to arrive at the expressions for η shown in figure 2 for local supersonic flow and for local subsonic flow. It is apparent from these equations that, once a value for η is determined from experiment for a particular type of boundary-layer flow, μ can be evaluated. Therefore values of η for other types of boundary layers can be determined.

Recently, these quantities have been determined for a group of thermoplastic materials with the aid of the Ames atmosphere entry simulator. This facility is described in detail in reference 6. By employing small-scale test models, the motion and heating of reentry vehicles can be simulated in this facility. Briefly, this is done by launching a model at full-scale speeds through air which has been expanded through a supersonic nozzle. The nozzle is designed to produce an exponential variation in density with distance corresponding to altitude in the atmosphere. The increment of altitude simulated is approximately 130,000 feet and can be adjusted to simulate that portion of the atmosphere over which the majority of heating occurs. In this manner, local enthalpies, local Reynolds numbers, and the total convective heat per unit mass of a full-scale reentry vehicle can be essentially duplicated.

In the tests of present interest, spherically tipped cone-cylinder models were launched at initial or entry velocities varying from approximately 13,000 to about 22,000 feet per second. Ablation data were obtained from these tests by weighing and measuring the models before launching and after recovery. In this manner, ablation weight losses over the forward faces of the models were obtained for a number of test trajectories.

A typical example of how these weight losses were utilized to obtain the intrinsic heat capacity and transpiration factor for one of the test materials is shown in figure 3. Experimental data obtained in the simulator for polycarbonate plastic are represented by the circular symbols. The data are presented in terms of percentages of the initial mass of the model and are plotted as a function of the stagnation enthalpy corresponding to the entry velocity obtained for each test. The solid line represents calculated mass losses as determined by integrating the local mass rate of ablation \dot{m} over the nose area s and over the trajectory time t . Now \dot{m} is given by the ratio \dot{q}_0/H_{EFF} where \dot{q}_0 is the heating rate to the nonablating surface but at the ablation temperature. Therefore, \dot{q}_0 represents the aerodynamic heat input. In the calculations, local heating rates were determined as suggested by Lees' analysis for turbulent heating. (See ref. 7.) By assuming various combinations of H_A and η_T , various curves of mass loss as a function of entry velocity were obtained and compared with experimental results. The curve which gave the best fit to the experimental data is shown in figure 3. The values of H_A and η_T which define this curve are also shown.

The intrinsic heat capacities and turbulent transpiration factors obtained in the manner just described are shown in table I for each material tested in the simulator. Also shown are the corresponding

laminar transpiration factors which were determined from the laminar and subsonic turbulent expressions for η given in figure 2. With these results for H_A and η , the effective heats of ablation can now be calculated for these materials for either laminar or turbulent flow.

The results of such calculations are presented in figure 4, where H_{EFF} is shown as a function of stagnation enthalpy potential. The simulator results are represented by the solid lines. Also shown are the Teflon data obtained in arc jets, repeated from figure 1. For ease of comparison, the Teflon line is shown slightly heavier than the others. It is interesting to note that three of the materials tested have effective heats of ablation greater than Teflon. In fact, the effective heat of ablation of polyethylene is more than 50 percent higher than that of Teflon. Perhaps the more important thing to note from these results, however, is that, with the exception of ceramic Teflon, all these materials exhibit effective heats of ablation in excess of 4,000 Btu/lb at enthalpy levels corresponding to satellite reentry peak heating, that is, at about 9,000 Btu/lb. It is probable, therefore, that other criteria will be more important in assessing the practicability of these materials for heat protection. For example, an important consideration is the effect of heat absorption when they are exposed to the very low heating rates and relatively long periods of time associated with the initial phase of reentry from satellite orbits.

REFERENCES

1. Georgiev, Steven, Hidalgo, Henry, and Adams, Mac C.: On Ablation for the Recovery of Satellites. Res. Rep. 47 (Contract AF 04(647)-278), AVCO Res. Lab., Mar. 6, 1959.
2. Gross, J. J., Masson, D. J., and Gazely, C., Jr.: General Characteristics of Binary Boundary Layers With Applications to Sublimation Cooling. Rand Rep. 1371, May 8, 1958.
3. Stewart, J. D.: Transpiration Cooling: An Engineering Approach. Doc. No. R59SD338, Missile and Space Vehicle Dept., Gen. Elec. Co., May 1, 1959.
4. Hidalgo, Henry: A Theory of Ablation of Glassy Materials for Laminar and Turbulent Heating. Res. Rep. 62, AVCO Res. Lab., June 1959.
5. Pappas, C. C.: Effect of Injection of Foreign Gases on the Skin Friction and Heat Transfer of the Turbulent Boundary Layer. Rep. No. 59-78, Inst. Aero. Sci., Jan. 26-29, 1959.
6. Hamaker, Frank M.: The Ames Atmosphere Entry Simulator and Its Application to the Investigation of Ethyl Cellulose as an Ablative Material for Ballistic Missiles. (Prospective NASA Paper.)
7. Lees, Lester: Similarity Parameters for Surface Melting of a Blunt Nosed Body in a High Velocity Gas Stream. ARS Jour., vol. 29, no. 5, May 1959, pp. 345-354.

TABLE I

INTRINSIC HEAT CAPACITIES AND TRANSPIRATION FACTORS

TEST MATERIALS	INTRINSIC HEAT CAPACITIES, H_A , BTU/LB	TRANSPIRATION FACTORS	
		TURBULENT, η_T	LAMINAR, η_L
CERAMIC-FILLED TEFLON (FLUOROGREEN T, JOHN DORÉ CO.)	550	0.09	0.27
TEFLON (DUPONT)	750	.21	.40
ETHYL CELLULOSE (BLUE ETHOCEL, DOW CHEMICAL)	1,000	.36	.50
POLYCARBONATE LEXAN, GENERAL ELECTRIC)	1,250	.36	.50
HIGH-DENSITY POLYETHYLENE (FORTIFLEX, CELANESE CORP.)	2,000	.36	.50

HEAT OF ABLATION FOR TEFLON

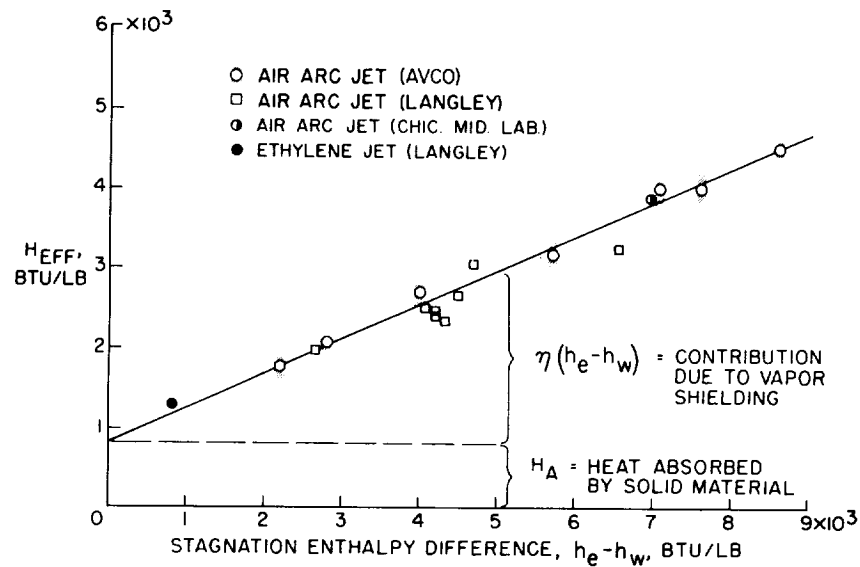


Figure 1

HEAT OF ABLATION FOR SUBLIMATION

$$H_{EFF} = H_A + \eta(h_e - h_w)$$

THREE-DIMENSIONAL LAMINAR BOUNDARY LAYER :

$$\eta_L = \frac{3}{5} \mu^{\frac{1}{4}}$$

THREE-DIMENSIONAL TURBULENT BOUNDARY LAYER :

LOCAL SUPERSONIC FLOW

$$\eta_T = \frac{1}{5} \mu^{\frac{1}{3}}$$

LOCAL SUBSONIC FLOW

$$\eta_T = \frac{3}{5} \mu^{\frac{3}{5}}$$

Figure 2

DETERMINATION OF INTRINSIC HEAT CAPACITY AND TRANSPIRATION FACTOR FOR POLYCARBONATE

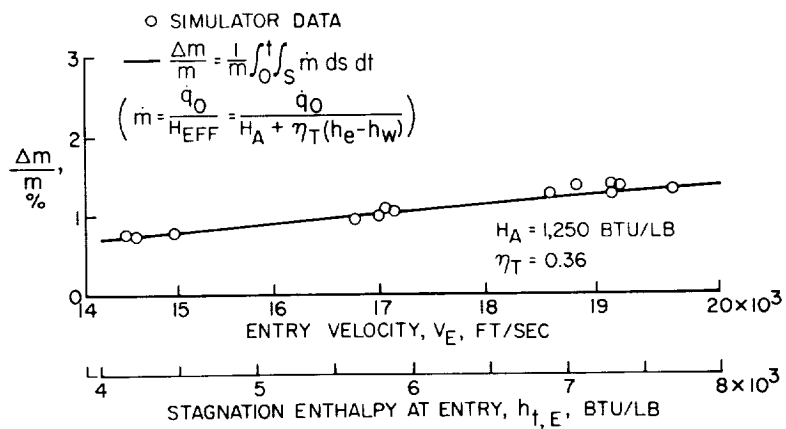


Figure 3

STAGNATION - POINT HEATS OF ABLATION

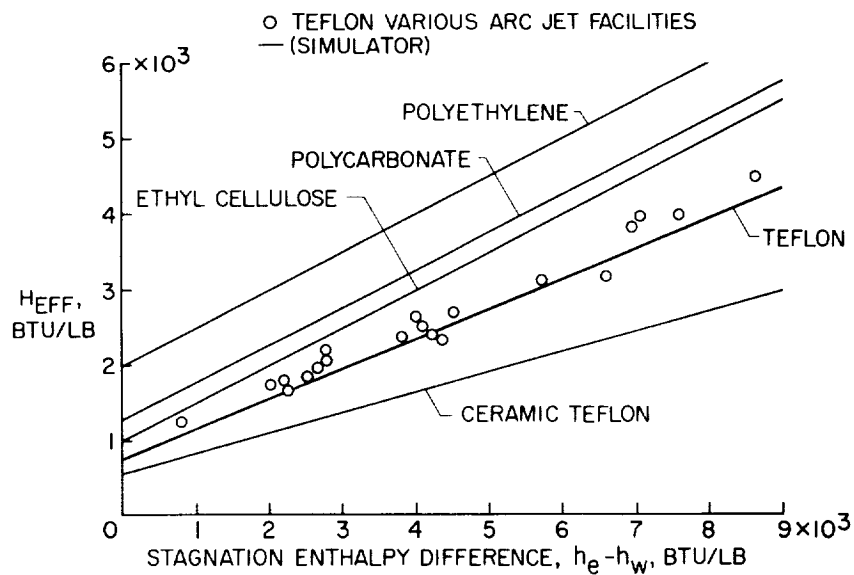


Figure 4

A METHOD OF CORRELATING ABLATING MATERIALS

By Bernard Rashis and Andrew J. Chapman III
Langley Research Center

SUMMARY


An analytical procedure is described for the derivation of effective heat of ablation relationships for any type of boundary layer. The relationships are given in terms of correlation parameters which include the effects of enthalpy potential across the boundary layer, ratios of wall to local-stream temperature, and the thermodynamic properties of the ablating material. Experimental results for several materials as obtained from both ethylene- and arc-heated air jets are presented in terms of the derived parameters. Good agreement was obtained between these values and the corresponding predicted values.

INTRODUCTION

In reference 1, there is given the framework of an excellent theoretical treatment which shows how the similarity parameters of ablation are related to the parameters of transpiration cooling. The analysis of reference 1 does not, however, include the effects of different ratios of wall to stream temperature nor does it include the cases wherein the vaporized material has specific heat values different from those of air. The purpose of this paper is to show how the relations between the ablation parameters and the material and boundary-layer characteristics may be derived for any type of boundary layer simply and directly from transpiration cooling results. The method used will be that which is reported in reference 2.

SYMBOLS

c_p	specific heat, Btu/(lb)(°R)
F	ratio of the coolant mass-flow rate to local air mass-flow rate




f	fraction of ablated material vaporized
h	enthalpy, Btu/lb
H_{EFF}	effective heat of ablation, Btu/lb
\dot{m}	ablation rate, lb/(sq ft)(sec)
n	temperature ratio exponent
N_{ST}	Stanton number
q	heat-transfer rate, Btu/(sq ft)(sec)
q_0	heat-transfer rate to ablating surface, Btu/(sq ft)(sec)
Q_A	material intrinsic heat capacity, Btu/lb
T	temperature, $^{\circ}R$

Subscripts:

aw	adiabatic wall
c	coolant
l	local
o	zero ejection or uncooled case
w	wall
w_{AIR}	air at wall temperature

DESCRIPTION OF CORRELATION METHOD

The method described in reference 2 is based upon the following two concepts. The first is that the heat-shielding capacity of an ablating material over and above what it could absorb prior to vaporization is due to the shielding effect of the vaporized material being ejected into the boundary layer. This vapor-shielding effect is denoted as $H_{EFF} - Q_A$, where H_{EFF} is the overall heat-shielding capacity of the material or what is commonly called the effective heat of ablation.



The quantity Q_A is the heat-absorbing capacity of the material prior to vaporization and hereinafter is referred to as the material intrinsic heat capacity.

Figure 1 shows this vapor-shielding effect for three materials, Teflon, nylon, and the inorganic salt ammonium chloride (NH_4Cl) as a function of the enthalpy potential across the boundary layer $h_{aw} - h_{w,AIR}$. The results shown were derived from tests made with hemispherical and flat nose-shape models and apply only to the three-dimensional laminar stagnation boundary layer. The tests were conducted in both ethylene- and arc-heated air jets, and the jet characteristics are summarized in table 1.

Figure 1 clearly shows that the vapor-shielding effect is different for the three different materials. In order to correlate these differences, a unifying concept is required. The concept that was used in reference 2 is that the vapor-shielding effect is identical to that of foreign-gas transpiration into air boundary layers.

Analysis of a number of transpiration cooling studies, both theoretical and experimental (refs. 3 to 9), revealed that the significant transpiration correlation parameters are those on the left of the following equations:

$$\frac{N_{St,o}}{N_{St}} = \frac{H_{EFF}}{Q_A} \quad (1)$$

$$\frac{\frac{F}{N_{St,o}} \left(\frac{T_l}{T_w} \right)^n \left(\frac{c_{p,c}}{c_{p,l}} \right)}{\frac{N_{St}}{N_{St,o}}} = f \frac{(h_{aw} - h_{w,AIR}) \left(\frac{T_l}{T_w} \right)^n \left(\frac{c_{p,c}}{c_{p,l}} \right)}{Q_A} \quad (2)$$

The ratio $N_{St,o}/N_{St}$ is the zero mass ejection value of the nondimensional heat-transfer coefficient or Stanton number divided by the value of the Stanton number as affected by mass ejection. Since mass ejection reduces the Stanton number, this ratio is greater than one. Denoting the heat-transfer rate to an ablating surface as $q\phi$, an energy balance results in the following expression:

$$q\phi = \dot{m}Q_A$$

where \dot{m} is the ablation rate. Since by definition

$$H_{\text{EFF}} = \frac{q_o}{\dot{m}}$$

where q_o is the heat transfer to a nonablating surface having the same temperature as the ablating surface, there results

$$\frac{q_o}{q_\phi} = \frac{H_{\text{EFF}}}{Q_A}$$

Since $N_{\text{St},o}/N_{\text{St}}$ is analogous to q_o/q_ϕ , equation (1) is obtained.

The parameter that correlates the transpiration flow rates is the term on the left of equation (2). The parameter

$$\frac{\frac{F}{N_{\text{St},o}} \left(\frac{T_l}{T_w} \right)^n}{\frac{N_{\text{St}}}{N_{\text{St},o}}}$$

was established by normalizing theoretical calculations for air-to-air transpiration cooling (refs. 3 and 4), where the exponent n is a constant for any one type boundary layer.

Normalization of theoretical calculations for foreign-gas ejection (refs. 5, 6, and 7) into air boundary layers indicated that the preceding parameter should be multiplied by the specific-heat ratio. The combined parameter

$$\frac{\frac{F}{N_{\text{St},o}} \left(\frac{T_l}{T_w} \right)^n \left(\frac{C_{p,c}}{C_{p,l}} \right)}{\frac{N_{\text{St}}}{N_{\text{St},o}}}$$

when applied to available experimental results (refs. 8 and 9) enabled correlation of the data. The term shown on the right of equation (2) is the transpiration correlation parameter redefined so as to apply to ablating materials.

Thus, once the functional relationship between the transpiration parameters is known, the corresponding functional relationship is known between the ablation parameters by virtue of equations (1) and (2).

The connecting link is the factor f which is the percentage of the ablated material vaporized.

The curves shown in figure 2 were obtained when the correlation procedure was applied to the theoretical calculations of references 3, 4, and 8. With these curves values of the material overall effectiveness are obtained upon substitution of the material property values as denoted by $c_{p,c}$, T_w , Q_A , and the factor f . A discussion of f is given in reference 10. Briefly, for a given material which melts and vaporizes, f increases with flight speed at constant pressure and decreases with increase in pressure at constant flight speed. For any given flight conditions, f increases with the Prandtl number of the melt. The quantities $c_{p,c}$, T_w , and Q_A are determinable from either analysis or laboratory type tests.

COMPARISON OF EXPERIMENTAL DATA AND ANALYSIS

Figure 3 shows the experimental data of figure 1 replotted in terms of the ablation correlation parameters. In the reduction of the data, f was assumed equal to 1 (100-percent vaporization) for all three materials. The values of $c_{p,c}$, T_w , and Q_A used are given in the following table:

	Teflon	Nylon	NH ₄ Cl
Weight, lb/cu ft	130	71	95
T_w , °R	Ref. 10	1,160	1,100
$c_{p,c}$	Ref. 11	0.4	0.33
Q_A	900	500	1,600
f	1.0	1.0	1.0

The $c_{p,l}$ used in the calculations was the average specific heat for the temperature range through the boundary layer.

The solid curve shown in figure 3 is the applicable correlation curve (curve ③ of fig. 2). It should be noted that the data for all the materials and all the test conditions have been successfully correlated. Also, the experimental results are in good agreement with the curve.



CONCLUDING REMARKS

Effective heat-of-ablation relationships for several types of boundary layers were derived simply and directly from transpiration-cooling results.

The predicted effective heats of ablation for a three-dimensional laminar stagnation boundary layer were in agreement with values derived from tests conducted at boundary-layer enthalpy potentials ranging from 800 to approximately 7,000 Btu/lb.



REFERENCES

1. Lees, Lester: Similarity Parameters for Surface Melting of a Blunt-Nosed Body in a High Velocity Gas Stream. Rep. No. GM-TM-184 (Contract No. AF 18(600)-1190), Guided Missile Res. Div., The Ramo-Wooldridge Corp., July 29, 1957.
2. Rashis, Bernard, and Hopko, Russell N.: An Analytical Investigation of Ablation. NASA TM X-300. (Prospective NASA paper.)
3. Brown, W. Byron, and Donoughe, Patrick L.: Tables of Exact Laminar-Boundary-Layer Solutions When the Wall Is Porous and Fluid Properties Are Variable. NACA TN 2479, 1951.
4. Reshotko, Eli, and Cohen, Clarence B.: Heat Transfer at the Forward Stagnation Point of Blunt Bodies. NACA TN 3513, 1955.
5. Hayday, A. A.: Mass Transfer Cooling in a Steady Laminar Boundary Layer Near the Stagnation Point. 1959 Heat Transfer and Fluid Mechanics Institute (Held at Univ. of California), Stanford Univ. Press, June 1959, pp. 156-170.
6. Eckert, E. R. G., Schneider, P. J., and Koehler, F.: Mass Transfer Cooling of a Laminar Air Boundary Layer by Injection of a Light-Weight Gas. Tech. Rep. No. 8 (Contract No. AF-18(600)-1226), Heat Transfer Lab., Univ. Of Minnesota, Apr. 1956.
7. Baron, Judson R.: The Binary-Mixture Boundary Layer Associated With Mass Transfer Cooling at High Speeds. Tech. Rep. 160, Naval Supersonic Lab., M.I.T., May 1956.
8. Leadon, B. M., and Scott, C. J.: Measurement of Recovery Factors and Heat Transfer Coefficients With Transpiration Cooling in a Turbulent Boundary Layer at $M = 3.0$ Using Air and Helium as Coolants. Res. Rep. No. 126 (Contract AF 18 (600)-1226), Inst. Tech., Dept. Aero. Eng., Univ. of Minnesota, Feb. 1956.
9. Rashis, Bernard: Exploratory Investigation of Transpiration Cooling of a 40° Double Wedge Using Nitrogen and Helium as Coolants at Stagnation Temperatures of $1,295^\circ$ to $2,910^\circ$ F. NACA RM L57F11, 1957.
10. Scala, Sinclair M.: A Study of Hypersonic Ablation. Tech. Inf. Series No. R59SD438 (Contract No. AF 04(647)-269), Missile and Space Vehicle Dept., Gen. Elec. Co., Sept. 30, 1959.



- 
11. Siegle, J. C., and Muus, L. T.: Pyrolysis of Polytetrafluoroethylene. Presented at meeting of American Chem. Soc., Sept. 17, 1956.
- 

TABLE I.- JET CHARACTERISTICS

Characteristic	Ethylene-heated jet (NASA)	Arc-heated jet (Chicago Midway Labs.)	Arc-heated jet (NASA)
Mach number	2.0	0.2	2.0
Stagnation temperature, OR	3,760	10,800	6,000 to 11,000
Stagnation enthalpy potential, Btu/lb	1,200	6,000 to 7,000	3,000 to 8,000
Dynamic pressure, lb/sq ft	6,000	50	20,000 to 40,000
Heat source	Ethylene combustion	Electric arc	Electric arc
Stagnation heat flux, Btu/(sq ft)(sec)	100 to 125	110	2,000 to 3,500
Test time duration, sec	20 to 40	120	8 to 15

VARIATION OF SHIELDING EFFECT WITH ENTHALPY POTENTIAL
THREE-DIMENSIONAL LAMINAR STAGNATION

MATERIAL	ETHYLENE-HEATED	ARC-HEATED, NASA	ARC-HEATED, C.M.L.
TEFLON	●	○	⊙
NYLON	▲	△	
NH ₄ Cl		□	

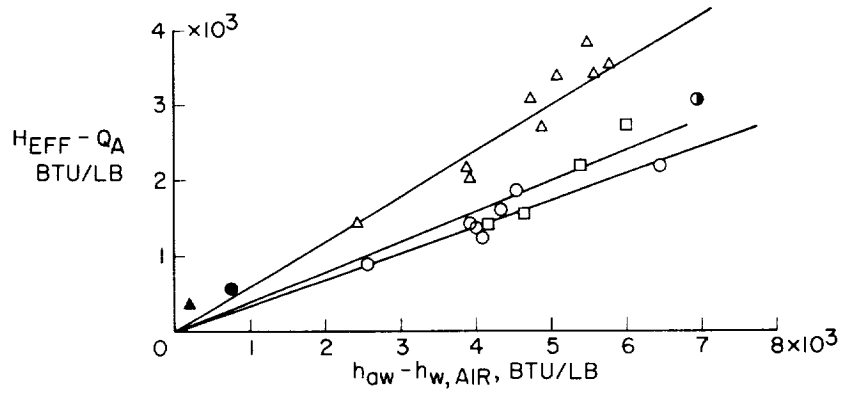


Figure 1

CORRELATION CURVES

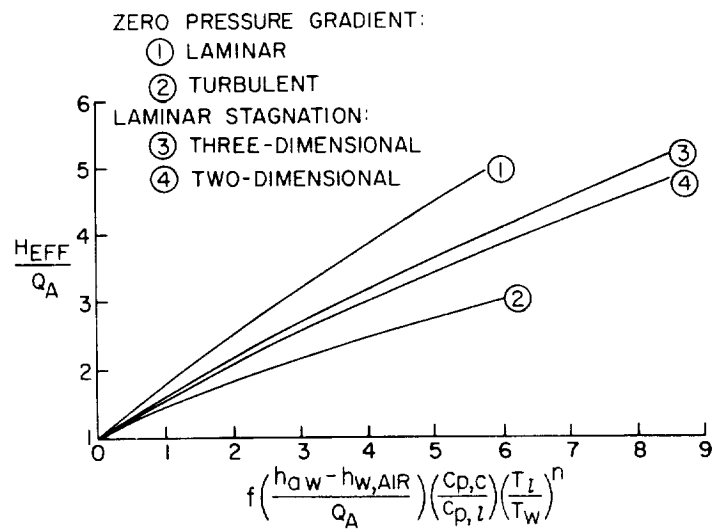


Figure 2

CORRELATION OF ABLATION TEST RESULTS
THREE-DIMENSIONAL LAMINAR STAGNATION

MATERIAL	ETHYLENE- HEATED	ARC-HEATED, NASA	ARC-HEATED, C.M.L.
TEFLON	●	○	●
NYLON	▲	△	
NH ₄ Cl		□	

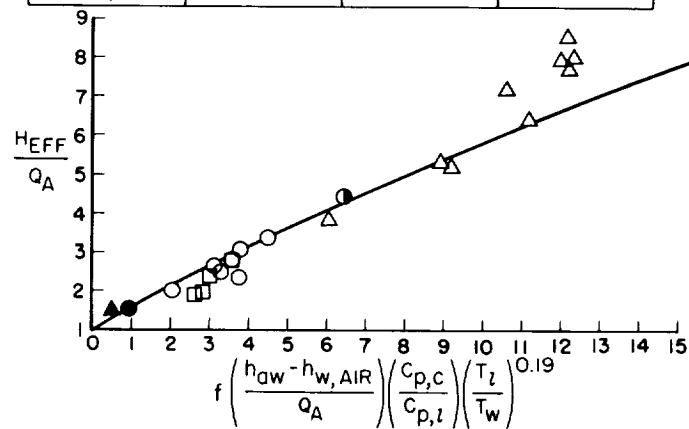


Figure 3

[REDACTED]

[REDACTED]

RESEARCH ON RADIATION HEAT SHIELDS FOR
BODIES AND LEADING EDGES

By Melvin S. Anderson, Donald H. Trussell,
and C. W. Stroud
Langley Research Center

SUMMARY

Two types of radiation heat shields designed for protection of the primary structure of a lifting reentry vehicle are discussed. The shields considered are body heat shields for protection of large areas of the vehicle and leading-edge heat shields for protection of the more severely heated stagnation areas. Results of research on body shields fabricated from super-alloy materials are given, and problems associated with construction of similar shields of refractory metals are indicated. Some preliminary results are presented from arc-jet tests made on leading edges fabricated of graphite and pyrolytic-graphite materials.

35

INTRODUCTION

The discussion of heat protection systems in reference 1 has indicated the need for some form of radiating heat shield for the most severely heated portion of a lifting reentry vehicle. Two types of heat shields are considered for this purpose and might be placed as shown in figure 1: body heat shields to protect a large area of the vehicle and leading-edge and nose shields to protect stagnation areas where the heating is most intense. The heat shield must withstand the reentry environment but is separated from the load-carrying functions of the underlying primary structure. This separation of functions allows the heat shield to be designed to the upper temperature limits of the material and the primary structure to be designed principally to meet the load requirements. For example, a body shield fabricated from one of the superalloys might operate at 2,200° F while protecting a cooled aluminum structure operating at 100° F to 200° F. Heat shields may be considered as secondary structure and as such pose several unique design problems. Because of the differences in heating between the body and the leading edges, the solutions for these problems take on different forms and are discussed separately. Body heat shields are treated first and leading-edge heat shields, second. Particular designs which have reached an

advanced state of development or have undergone preliminary experimental investigation are discussed.

BODY HEAT SHIELDS

Some of the important requirements for a body heat shield are as follows:

- (1) Light weight must be provided.
- (2) High temperatures must be sustained.
- (3) Thermal expansion must be absorbed.

(4) Air loads must be supported and stable conditions maintained in the airstream.

- (5) Construction in refractory metals must be possible.

For the protection of a reentry vehicle, minimum weight is an important criterion. The heat shield must withstand high temperatures and absorb thermal expansion of as much as 1/8 inch per foot without overstressing or distorting the shield or primary structure. The shield must support some air loads and be stable for all conditions of reentry heating and aerodynamic loading. Additionally, construction in refractory metals will be required to withstand temperatures between 2,200° and 3,000° F.

Two types of shields which can meet most of these requirements are shown schematically in figure 2. The first, denoted as a panel shield, consists of stiffened panels such as honeycomb sandwiches, arranged in rectangular arrays and supported by a minimum number of attachments. Thermal expansion is permitted by the spacing between panels. The second shield design consists of a single sheet that can accommodate expansion locally by some device, such as corrugating or dimpling, which reduces the number of expansion joints required. A single-skin design can have a weight advantage over a stiffened panel; however, some loss in insulating efficiency results because of the need for more attachments.

Figure 3 depicts a panel heat shield which has been developed by the Bell Aircraft Corporation. The honeycomb panel is supported by flexible clips at each corner to permit thermal expansion. Shiplap joints between panels allow movement of each panel with respect to the others. Shield weight including supports is about 0.9 lb/sq ft.

The proper accommodation of thermal expansion was a difficult design problem. Panels which were held in place by retaining straps or by screws

in oversized holes had a tendency to bind and not to allow the expansion desired. The panels of the final design are on firm supports yet offer little restraint of expansion to adjacent panels. Extensive work has also been done in minimizing heat paths from shield to structure, which has resulted in a heat shield with high insulating efficiency.

This panel, which is constructed of a cobalt-base alloy (Haynes alloy no. 25), is in an advanced state of development and has successfully withstood the heating tests, wind-tunnel tests, noise tests, and flight tests indicated in the following table:

- | | |
|--|----------------|
| (1) Heating tests: | |
| (a) Maximum temperature, °F | 2,200 |
| (b) Temperature difference between shield and water cooled structure, °F | 2,000 |
| (c) Temperature rate, °F/sec | 50 |
| (2) Wind-tunnel tests: | |
| (a) Mach number range | 0.7 to 4.0 |
| (b) Dynamic pressure, lb/sq ft | 2,000 to 6,000 |
| (3) Noise test: | |
| (a) Noise level for $10\frac{1}{2}$ hr, db | 144 |
| (b) Noise level for additional 1/2 hr, db | 148 |
| (4) Flight tests (several panels mounted and flown on large bomber): | |
| (a) Time at subsonic or transonic speed, hr | 19.5 |
| (b) Time at supersonic speed, hr | 2.5 |
| (c) Total time, hr | 22.0 |

The cobalt-base alloy from which the panel was fabricated can sustain the maximum temperature shown in this table for only short times. The long-time temperature capability is about 2,000° F. Similar temperature capabilities apply to the other superalloys. This temperature limit may be extended by use of refractory metals, although fabrication of a refractory-metal honeycomb panel appears to be rather difficult. An alternate approach would be to fabricate a stiffened panel by resistance welding or mechanical fastenings. Both approaches require further investigation.

In order to obtain a simpler heat shield that might be more amenable to fabrication in refractory metals, a single-corrugated-skin heat shield has been undergoing development and tests at the Langley Research Center. The details of this shield are indicated in figure 4. The slightly corrugated skin allows thermal expansion in one direction. Expansion in the other direction is accomplished by flexure of the supports, which

also serve as stiffeners for the primary structure. At the lap joint, one sheet is fastened to one stiffener and the adjacent sheet fastened to the other stiffener; thus, movement of the two sheets with respect to each other is allowed. The ceramic bushings at the attachments (shown by the darkly hatched areas) help insulate the structure and provide a solid foundation for mounting the shield. The range of dimensions shown was found to give satisfactory performance for the various tests made. This particular shield design with attachments weighs about 0.6 lb/sq ft. Figure 5 is a photograph of such a shield both before and after a series of heating and wind-tunnel tests. The tested panel surface has become oxidized and discolored from the heat but has undergone little distortion.

The environmental tests, which this shield and similar ones have undergone, are listed in the following table:

Heating tests:

(a) Maximum temperature, °F	2,100
(b) Temperature difference between shield and structure:	
Transient conditions, °F	1,600
Steady-state conditions, °F	900
(c) Temperature rate, °F/sec	20

Wind-tunnel tests:

(a) Mach number	3
(b) Dynamic pressure, lb/sq ft	3,000
(c) Stagnation temperature, °F	660

The heating tests and wind-tunnel tests imposed rather severe temperature and aerodynamic conditions on the heat shields. The ability of these heat shields to withstand these severe aerodynamic conditions as well as the high temperature is a strong indication that the heat shields could survive actual reentry. Because of the relative simplicity of construction, the extension of the temperature capabilities of such shields by use of refractory metals may be possible with the present state of knowledge, and this work is currently being pursued.

LEADING-EDGE SHIELDS

In the leading-edge stagnation area, equilibrium temperatures in excess of 3,000° F and maximum heating rates in excess of 100 Btu/ft²-sec are expected. To meet these conditions, numerous leading-edge designs have been proposed and various materials have been suggested. Two configurations currently under investigation are illustrated in figure 6. The first configuration makes use of a large leading-edge radius which

• serves to reduce the maximum heating rate and thereby keeps the temperatures compatible with refractory-metal construction. Fabrication of such leading edges using coated molybdenum appears possible. A second approach utilizes nonmetallic materials which can withstand the more severe temperature and thermal shock conditions associated with smaller leading-edge radii. For this approach, tests by the Bell Aircraft Corporation have shown siliconized graphite to be a promising material. Full-scale leading edges of the nonmetallic type made of AGX graphite are presently undergoing tests at the Langley Research Center, and some preliminary results are presented herein.

The tests performed thus far have been made to determine whether a hardware item of reasonable size and shape can actually withstand the thermal environment expected on reentry. These tests were conducted in an arc-jet facility of the Langley structures research laboratory. Flow is subsonic (about 230 fps) and exhausts through a nozzle having a 2.5-by 12-inch rectangular exit. Temperature of the stream is about 9,000° F with an enthalpy of approximately 5,000 Btu/lb. Heating rates of 180 Btu/ft² and equilibrium temperatures in excess of 3,500° F were obtained on the 1-inch-radius AGX specimens.

Figure 7 shows the particular leading-edge configurations investigated to date. The first type, shown at the top of the figure, was built to determine erosion rates and to determine whether simple graphite shells of 1-, 2-, and 3-inch leading-edge radii could survive the test conditions. The second type, shown at the lower left of figure 7 is representative of a plausible design with provision for attachment to the wing structure. Both designs were tested in 12-inch lengths. Tests have also been made on a 3-inch-long specimen machined from AGX graphite and then coated by vapor depositing pyrolytic graphite on the external surfaces to a thickness of either 1/16 or 1/8 inch (shown at lower right of figure 7). No delamination of the pyrolytic graphite or deleterious separations from the AGX substrate occurred during the tests.

Each type of specimen had a total thickness of 1/4 inch for the leading-edge shell. All specimens survived tests of up to 5 minutes duration without failure other than surface erosion or oxidation.

Figure 8 shows the variation with time of the temperature in back of the stagnation point for a typical test of two leading-edge specimens. One specimen was made entirely of AGX graphite (shown by the solid curve) whereas the other had a 1/8-inch coating of pyrolytic graphite. An equilibrium temperature of about 3,500° F was reached by the AGX graphite leading edge but thermocouple failure at 2 minutes prevented measurement of the equilibrium temperature for the pyrolytic-graphite specimen.

• An unusual characteristic of pyrolytic graphite is that its thermal conductivity is much greater in the direction parallel to its surface

than in the direction normal to its surface. The lower rate of temperature rise indicates that the conductivity of pyrolytic graphite normal to its surface is substantially less than that of AGX graphite.

Considerable erosion occurred during the tests as shown by the thickness loss at the stagnation point for the two specimens. (See fig. 8.) The circular symbols at 1 and 3 minutes were obtained from two other tests of similar AGX graphite leading-edge specimens. Less regression is shown for the pyrolytic graphite than for the AGX graphite leading edge. During many reentry flights peak temperatures on a highly swept leading edge may not exceed $3,000^{\circ}\text{F}$, and erosion rates would be correspondingly smaller than that shown. Moreover, peak temperatures would be sustained for only a part of the flight. Hence it is probably feasible to make a graphite leading edge of sufficient thickness to survive a single reentry. However, it would be desirable to have highly reliable oxidation resistant coatings so that a substantial weight saving could be realized.

CONCLUDING REMARKS

Results have been presented of tests made on shields designed to protect the body or the leading edges of a reentry vehicle. Body heat shields fabricated from the superalloys have been successfully subjected to various environmental conditions produced by heating, noise, and aerodynamic tests. In order to extend the temperature capabilities of such shields, work is in progress in adapting the proven designs to construction in refractory metals. For the stagnation areas, graphite and pyrolytic graphite leading edges have been built and successfully tested in an arc jet. Specimen temperatures of $3,500^{\circ}\text{F}$ were sustained without failure. Surface erosion rates were high, although sufficient thickness could probably be provided to survive a single reentry.

REFERENCE

1. Anderson, Roger A., and Swann, Robert T.: Structures for Reentry Heating. Prospective NASA paper.

HEAT-SHIELDED STRUCTURE

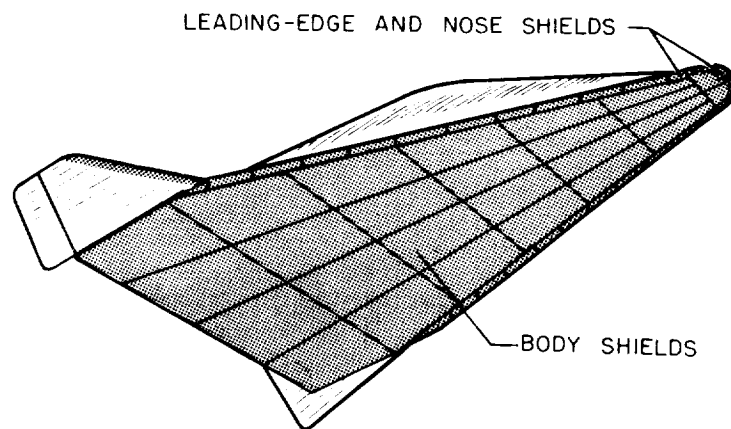


Figure 1

BODY-SHIELD DESIGN

REQUIREMENTS

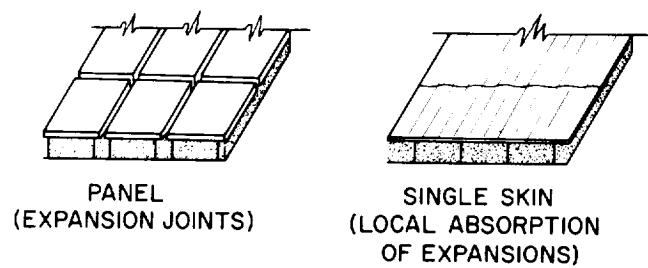


Figure 2

HONEYCOMB-PANEL HEAT SHIELD
SHIELD WEIGHT, 0.9 PSF

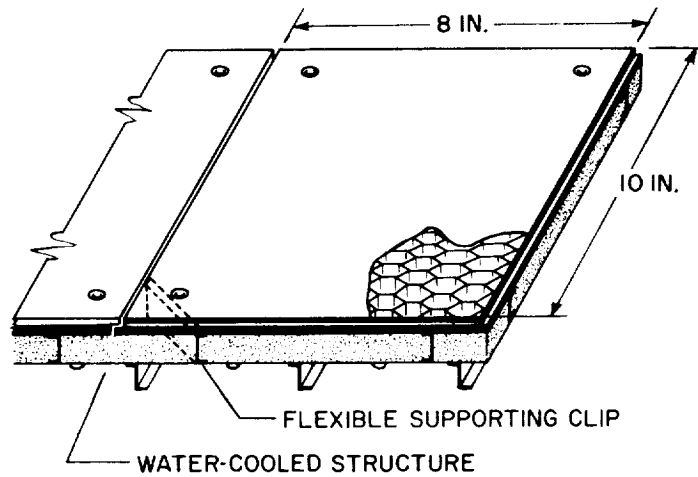


Figure 3

DETAIL OF TYPICAL DESIGN TESTED
SHIELD WEIGHT, 0.6 PSF

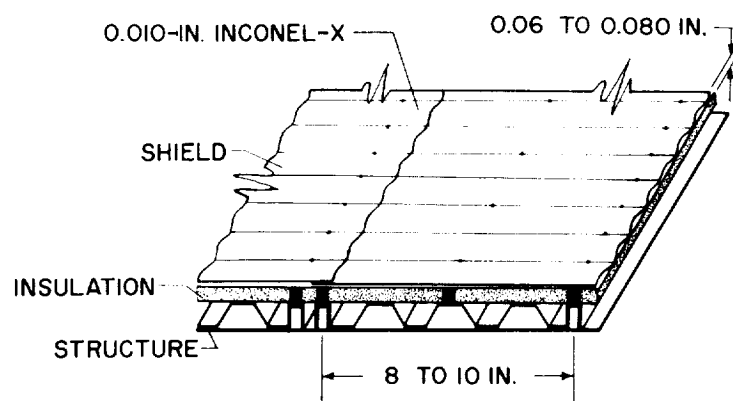


Figure 4

SINGLE-CORRUGATED-SKIN HEAT SHIELD

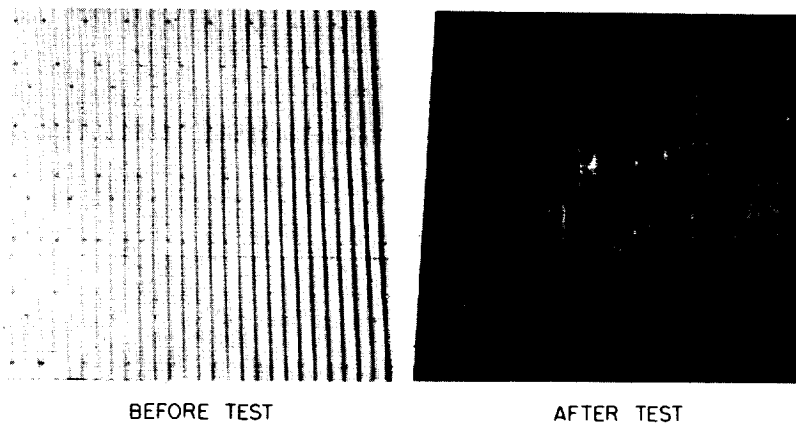


Figure 5

LEADING-EDGE CONCEPTS

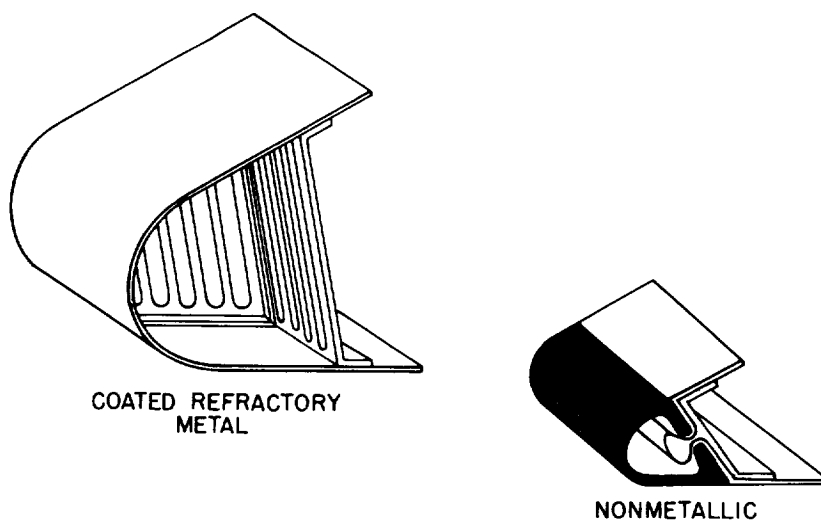


Figure 6

GRAPHITE TEST SPECIMENS

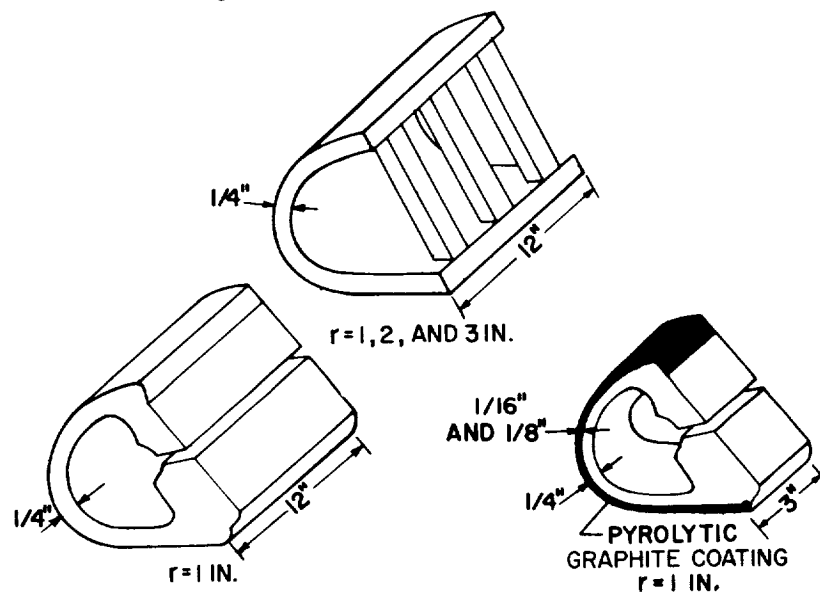


Figure 7

GRAPHITE LEADING EDGE, ARC-JET TEST

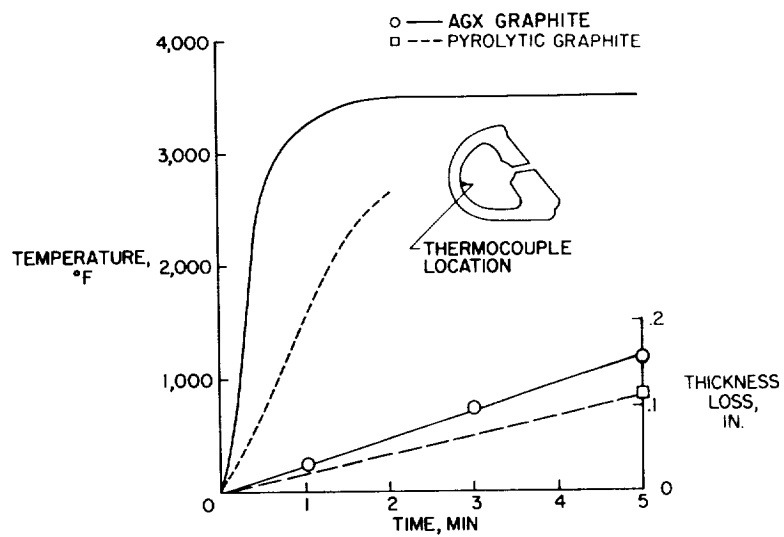


Figure 8

MATERIALS FOR APPLICATION TO MANNED REENTRY VEHICLES

By Eldon E. Mathauser
Langley Research Center

INTRODUCTION

The severe thermal environment associated with manned reentry vehicles has motivated many investigations on materials to determine their potential usefulness for reentry structures. In this paper the status of materials for reentry structures is reviewed briefly, and the results of several studies of materials made by NASA are presented.

The general types of materials for possible use in manned reentry vehicles include the superalloys, the refractory metals with primary emphasis on structural sheet, and various nose and leading-edge materials exemplified by ceramics, cermets, and graphite. Several other types of materials are also applicable to various types of manned reentry vehicles. These include ablation materials that have been discussed in a previous paper by Raymond C. Savin and Hermilio Gloria, fabrics for inflatable reentry vehicles discussed in a succeeding paper by Robert W. Leonard, George W. Brooks, and Harvey G. McComb, Jr., and low-density metals such as aluminum, magnesium, and beryllium that are applicable for structural use at relatively low temperatures. No further discussion of these last three types of materials is given in this paper.

36

STATUS OF SUPERALLOYS

A brief review of the status of superalloys is presented next. At the present time two important types of superalloys are available, namely, the nickel-base alloys of which René 41 is an example, and the cobalt-base alloys of which Haynes Alloy No. 25 is an example. Both types are excellent high-temperature materials that should find extensive use in reentry structures. These alloys are commercially available in structural sizes and quantities, can be fabricated satisfactorily with existing knowledge and available facilities, and also possess important high-temperature properties such as adequate strength and ductility, excellent resistance to oxidation, and high emissivity in the neighborhood of 2,000° F. The status of the superalloys with respect to application in reentry structures may be termed as excellent.

CONFIDENTIAL

STATUS OF REFRACTORY METAL SHEET

Consideration is given next to refractory metal sheet. Several refractory metals that have structural potential have been developed in the past few years although few applications of these metals have been made for several reasons. These reasons include fabrication problems, lack of reliable oxidation-resistant coatings, and limited availability. The availability of refractory metals has a most important bearing on application of these materials to reentry structures, and, for this reason, this problem is discussed next.

Four refractory metals, namely, molybdenum, niobium (also known as columbium), tantalum, and tungsten are considered because of their potentially useful mechanical properties at elevated temperatures and because of expected availability for reentry structures. Alloyed molybdenum sheet is currently available in thicknesses on the order of 0.010 inch. These sheets are generally of marginal structural quality; that is, the sheets may be appropriate for structural heat shields or leading edges but not for primary load-carrying members. A gradual improvement in overall quality of molybdenum sheet is expected as a result of a sheet-rolling program that will be underway soon.

With regard to niobium alloys, considerable effort has been expended recently to develop these alloys for structural use. At the present time only small experimental quantities are available; however, on the basis of present development programs, it appears that sheets of structural size and quality will be commercially available within the next 1 to 2 years.

Tantalum-alloy sheet and pure tungsten sheet are currently available in approximately 6-inch-wide strips. No sheet rolling or extensive development programs on either of these materials exist as far as can be determined. It is believed that neither will be available in sheets of structural size or quality within the next two years unless considerably increased support and emphasis is given to their development.

This review of refractory metals is concerned with the current status of thin sheet. The availability of coatings for oxidation protection also has an important bearing on the potential application of the refractory metals. With regard to molybdenum sheet, commercial coatings are available that show considerable promise for structural applications. One of these coatings will be discussed in greater detail subsequently. Because of the limited availability of the last three refractory metals discussed, relatively little progress had been made in the past to develop coatings for these metals. Present efforts to develop coatings, however, are paralleling developments in the metals. For this reason, it appears that suitable coatings will become available when refractory metal sheet is commercially available.

STATUS OF REFRACTORY MATERIALS

Next, a review of the status of refractory materials that have potential application in the severely heated stagnation areas of the reentry vehicles is presented. NASA has conducted screening tests on many different refractory materials, and the status of these materials for leading-edge or nose applications is discussed in conjunction with the following table:

Refractory material	Status
Coated metals	Performance in ceramic-heated jets satisfactory; adequate oxidation protection provided by several types of coatings including silicides and metal platings
Ceramic	Several types including oxides, nitrides, carbides, and borides survived heated-jet tests satisfactorily
Cermets	Few types tested; none appear promising
Graphite	Oxidation and erosion obtained with uncoated graphite in heated-jet tests; graphite protected with flame-sprayed, vapor-deposited, or multilayer coatings performed satisfactorily

Four types of refractory materials are noted: coated metals, ceramics, cermets, and graphite. The screening tests on these materials were conducted in ceramic-heated jets, electric arc-powered air jets, and an arc-image furnace. Evaluation of the suitability of the materials for high-temperature applications was made on the basis of oxidation, erosion, ablation, thermal shock, and other characteristics. With the exception of the cermets, several materials from each of the types noted performed satisfactorily in the jet tests and appear to be potentially capable of surviving the environment associated with leading edges and noses during reentry. The detailed results from the screening tests are available in several NASA publications (for example, ref. 1) and for this reason no additional discussion is given in this paper.

Although many of the refractory materials displayed capabilities for leading-edge and nose applications, some development efforts would be required to produce satisfactory components from these materials. For

[REDACTED]

the refractory metals, the major effort would probably be devoted to the establishment of a reliable, oxidation-resistant coating. For ceramics and graphite, the major efforts would probably be directed toward the development of appropriate methods of attachment of the relatively brittle components to a flexible metal structure.

EXPERIMENTAL STUDY OF STRUCTURAL APPLICATION OF MOLYBDENUM-ALLOY SHEET

In the remainder of this paper a report on some results that have been obtained from studies of refractory metal sheet is presented. Because of the limited availability of many of the refractory metals, NASA research efforts thus far have been directed primarily at molybdenum sheet and have been restricted to small structural specimens. One type of specimen that was employed in an NASA study is shown in figure 1. The specimen shown is a corrugated-core sandwich that was used to determine the "state of the art" of resistance welding and of protective coatings. The specimen was also suitable for compressive strength testing. The sandwich was fabricated from 0.010-inch-thick sheet of molybdenum alloyed with 0.5-percent titanium. The two face sheets were resistance welded to the corrugated core. The overall thickness of the sandwich was $1/4$ inch, the length in the direction of the corrugations was 2 inches, and the overall width was $2\frac{1}{2}$ inches. The molybdenum sheet used in fabrication of these sandwich specimens was specially reprocessed by cold-rolling and heat-treating operations. This reprocessing improved the overall quality of the sheet as well as the quality of the resistance welds. The reprocessing procedure was applied only to molybdenum strips 2 inches wide and, consequently, this strip size dictated the size of the sandwiches. It may be noted that successful resistance welding of molybdenum sheet is difficult to accomplish and these sandwich specimens, as far as can be determined, display the first example of generally good resistance welds obtained in molybdenum sheet.

These sandwiches were coated after welding with a commercially available coating known as W-2 which is based on molybdenum disilicide. The coating is applied by pack-deposition techniques which produce a chemical reaction between certain coating powders and the molybdenum sheet. Mechanical property tests were made on the molybdenum sheet to determine whether any loss of strength or embrittlement occurred as a result of the coating. Some of these results are given in figure 2. The dark bars indicate room-temperature tensile properties obtained from uncoated reprocessed sheet, and the shaded bars indicate properties from the reprocessed sheet with the W-2 coating. The yield and

[REDACTED]

ultimate strengths were reduced approximately 25 percent as a result of the coating. No significant change in Young's modulus was obtained. Although a change in elongation was obtained, this change is not considered to be particularly significant. The results shown in figure 2 suggest that if molybdenum sheet is of structural quality and is acceptable for structural applications in the uncoated condition, the application of an oxidation-resistant coating will not necessarily embrittle the sheet or otherwise impair its usefulness for structural applications.

The performance of the resistance-welded, W-2 coated sandwiches in compressive strength tests is indicated in figure 3. Compressive strength of the corrugated-core sandwiches is plotted against test temperature. The curve indicates the trend of the test data denoted by the symbols. In these strength tests the sandwiches were heated to test temperature with radiant heating equipment and were exposed in air at the test temperature for 0.1 hour prior to loading. A rather small decrease in strength was obtained with the sandwich specimen up to approximately 2,000° F; whereas, above 2,000° F, the compressive strength decreased very rapidly with increasing temperature. It should be noted that the compressive strength of the sandwiches generally exceeded the tensile yield stress for the coated sheet. In view of these test results it appears that molybdenum sheet joined by resistance welding may find some application in structures at high temperatures.

The thickness of the coating on these sandwiches was approximately 0.001 inch. This coating thickness provided adequate oxidation protection for the duration of the compressive strength tests; however, oxidation tests on the coated sandwiches were required to establish the total time that the sandwiches would be protected by this coating. A view of a sandwich specimen that was subjected to an oxidation test is given in figure 4. This figure shows a sandwich that was tested in a furnace at 2,700° F for 3.2 hours. The view at the left shows the appearance of the specimen upon removal from the furnace. Oxidation damage is visible; however, the full extent of the damage is not evident because the coating remained intact over some of the oxidized areas. The view on the right shows the full extent of the oxidation damage. This result suggests that various techniques other than visual examination will be required to detect oxidation damage in refractory-metal structures after exposure to high temperatures. Examination of the oxidized sandwich indicates that the oxidation damage generally originated at the spot welds. It appears that the weld areas were not adequately coated, possibly because of insufficient cleaning prior to coating. This particular sandwich failed in this test at 2,700° F after exposure for 3.2 hours; however, it should be noted that no evidence of any oxidation damage was obtained in the first 2 hours of exposure. The appearance of the sandwich after 2 hours of exposure is given in figure 1. The fact that no evidence of oxidation was obtained within 2 hours is significant in view of the small thickness of coating. The 0.001-inch-thick coating increased the weight

[REDACTED]

of the sandwich only 4 percent. Furthermore, this sandwich specimen represents the first attempt to coat this type of structural assembly. Considerable improvement in the life of the sandwiches should be obtained with a thicker coating and with recently improved methods of application of the W-2 coating.

An indication of the oxidation protection that can be provided by the W-2 coating is given in figure 5. This figure gives the results of oxidation tests on small coated strips of molybdenum. The temperatures at which the specimens were exposed in a furnace in air are plotted against life of the specimens. Lifetime here is defined as time of exposure at temperature during which no visible evidence of oxidation was detected. These specimens were coated with the W-2 coating to a thickness of 0.002 inch, a thickness that is double the thickness employed on the sandwiches described previously. Above 2,600° F, the life of the coated specimen increases somewhat over the minimum life obtained at 2,600° F. At temperatures above 2,600° F the coating develops a liquid phase which promotes self-healing and increases the life of the specimens. At still higher temperatures the curve is expected to reverse toward zero specimen life. Tests conducted by other investigators (ref. 2) suggest that zero life may be obtained in the 3,300° F to 3,500° F temperature range. The significant results in figure 5 are that rather long life as well as small test scatter were obtained with this 0.002-inch-thick coating. This thickness of coating increased the weight of the 0.010-inch-thick sheet by approximately 7 percent.

These oxidation-test results were obtained from furnace tests in which very slight air movement existed. It is of interest to determine whether thin coatings, such as the W-2, will provide adequate oxidation protection in high-speed airflow, particularly at temperatures at which the coating may contain a liquid phase. The results of one such aerodynamic test (ref. 1) are shown in figure 6. In this figure are shown two molybdenum specimens which are hollow hemispherical-nosed tubes 3 inches long and 1/2 inch in diameter. Both the bare specimen shown in the upper left and the W-2 coated specimen shown in the upper right were subjected to an air flow at a Mach number of 2 and a temperature of nearly 3,000° F for approximately 1 minute in a ceramic-heated jet. The uncoated specimen failed very quickly; whereas, the coated specimen survived the test. Only a slight darkening at the nose indicates that the coated specimen had been subjected to the heated-jet test. On the basis of aerodynamic tests such as these, as well as oxidation tests in a furnace, it is concluded that the W-2 coating does have considerable potential for oxidation protection of molybdenum sheet.

One remaining item regarding the potential usefulness of the W-2 coating is its emissivity. Widely varying values have been obtained for the emissivity of this coating at elevated temperatures. Some very

[REDACTED]

recent results on the emissivity of this coating have been made available to NASA by the Bell Aircraft Corp. and are presented next. These results are included with the emissivity of several other materials in figure 7. Emissivity is plotted against temperature. The symbols on the curve for the W-2 coated molybdenum represent an average of several experimental readings. These emissivity values were obtained from tests in a helium atmosphere. Preoxidation of the coated specimens for several hours at 2,500° F in air followed by tests in a helium atmosphere yielded essentially the same results. Emissivity values obtained from W-2 coated molybdenum by other investigators range up to 0.9 in the neighborhood of 2,000° F. Some of these tests were made in air rather than in an inert atmosphere. It appears that differences in emissivity values for the W-2 coating can be expected between tests conducted in air or in either vacuum or inert gas and between specimens that were preoxidized at high temperatures and specimens that were not oxidized. Further differences would also be expected from variability in the coating and methods of application of the coating. Finally, it appears that standardization of test equipment and test techniques will be needed before general agreement on the emissivity of coated metals is obtained.

CONCLUDING REMARKS

The nickel-base and cobalt-base superalloys are excellent materials of construction that are expected to find wide application in reentry structures for temperatures up to approximately 2,000° F. For higher temperature applications, molybdenum or niobium alloys are the most promising materials at present. Several difficulties will have to be overcome in the use of either material, although none of these difficulties appear insurmountable. It appears that only modest development programs are needed to make structural components, such as heat shields, available in the near future from these materials. Some development efforts are also required to make satisfactory leading-edge and nose components from the refractory materials that include coated metals, ceramics, and coated graphite.

REFERENCES

1. Trout, Otto F., Jr.: Exploratory Investigation of Several Coated and Uncoated Metal, Refractory, and Graphite Models in a 3,800° F Stagnation Temperature Air Jet. NASA TN D-190, 1960.
2. Bartlett, E. S., Ogden, H. R., and Jaffee, R. I.: Coatings for Protecting Molybdenum From Oxidation at Elevated Temperature. DMIC Rep. No. 109 (ASTIA AD 210978), Battelle Memorial Inst., Mar. 6, 1959.

RESISTANCE - WELDED CORRUGATED - CORE
ALLOYED-MOLYBDENUM SANDWICH, W-2 COATED

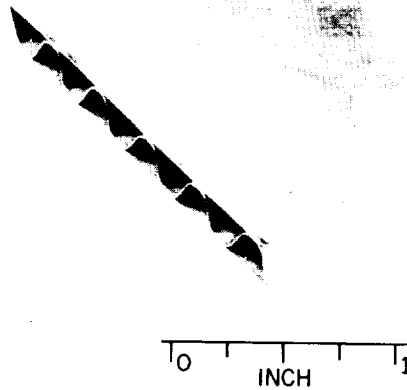


Figure 1

MECHANICAL PROPERTIES OF REPROCESSED MOLYBDENUM
SHEET AT ROOM TEMPERATURE

UNCOATED SHEET (SHEET THICKNESS, 0.010 IN.)
W-2 COATED SHEET (COATING THICKNESS, 0.001 IN.)

YIELD STRESS, KSI	121 87
ULTIMATE STRESS, KSI	136 102
YOUNG'S MODULUS, KSI	42,000 43,000
ELONGATION, PERCENT	3 4

Figure 2

COMPRESSIVE STRENGTH OF RESISTANCE-WELDED
CORRUGATED-CORE SANDWICHES, W-2 COATED

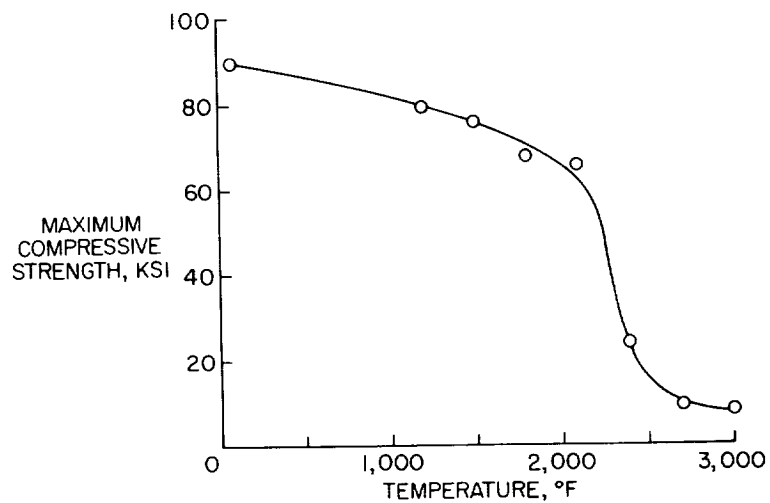


Figure 3

OXIDATION TEST RESULTS FOR COATED
MOLYBDENUM SANDWICH

TEMPERATURE, 2,700° F; EXPOSURE TIME, 3.2 HR

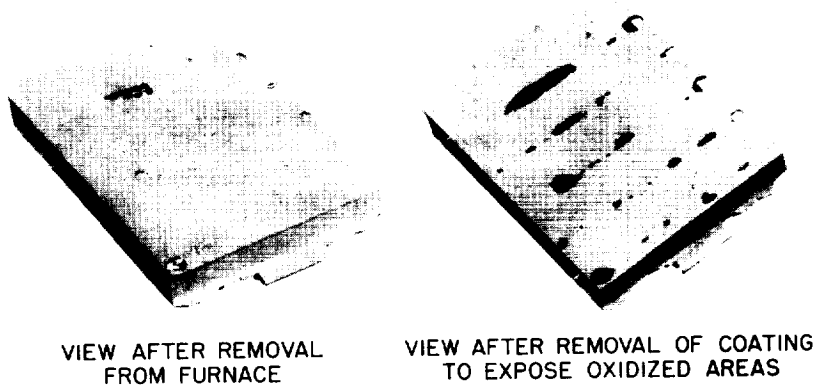


Figure 4

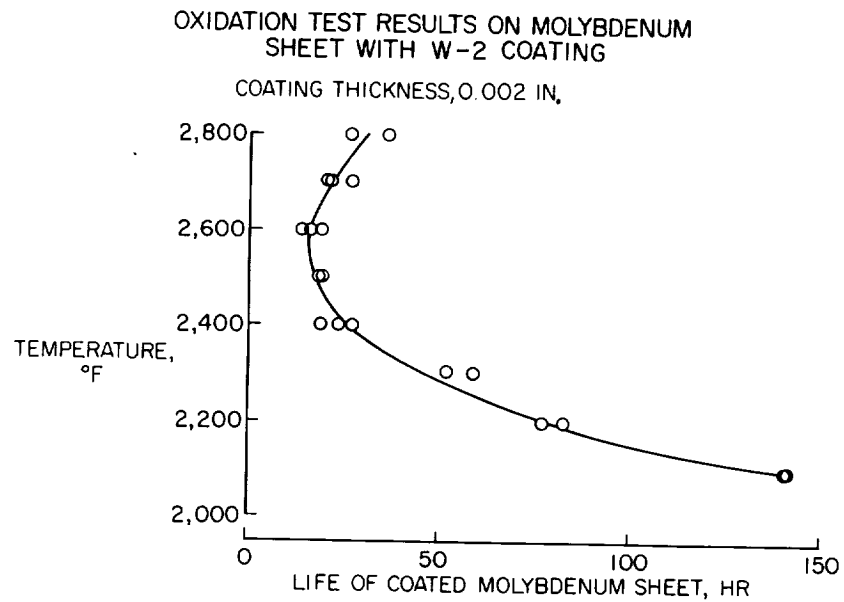


Figure 5

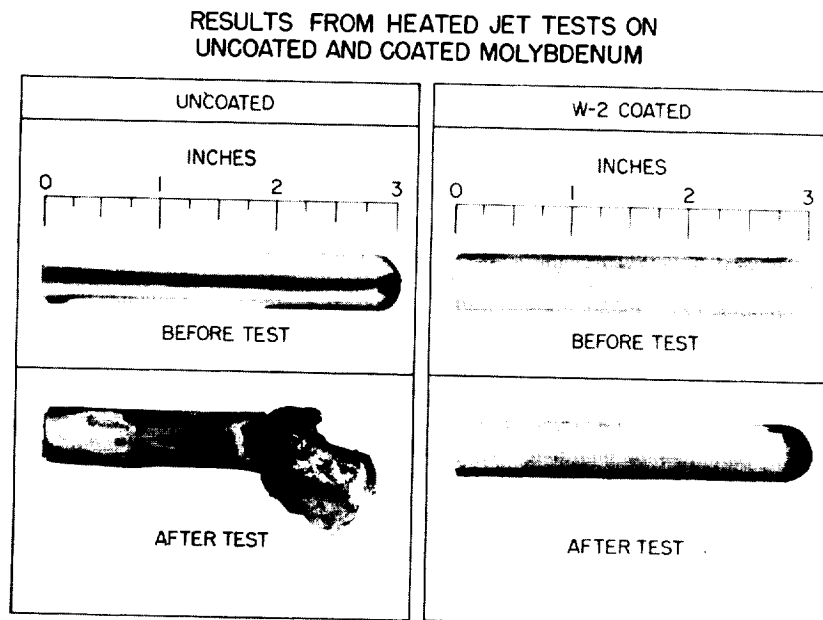


Figure 6

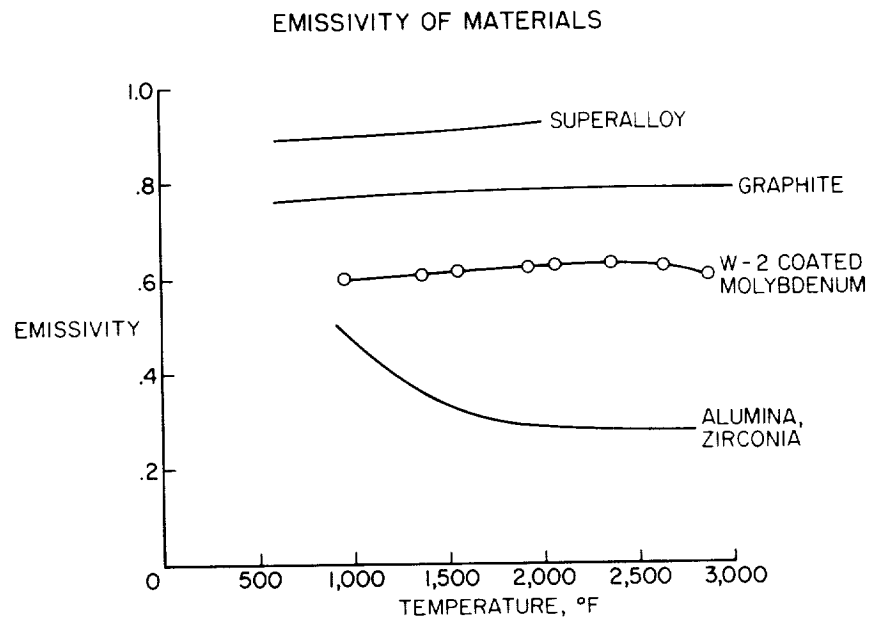


Figure 7

EXPERIMENTAL STUDY OF A HOT STRUCTURE
FOR A REENTRY VEHICLE

By Richard A. Pride, Dick M. Royster,
and Bobbie F. Helms
Langley Research Center

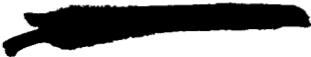
SUMMARY

A large structural model of a reentry vehicle has been built incorporating design concepts applicable to a radiation-cooled vehicle. Thermal-stress alleviating features of the model are discussed. Environmental tests on the model include approximately 100 cycles of loading at room temperature and 33 cycles of combined loading and heating up to temperatures of 1,600° F. Measured temperatures are shown for typical parts of the model. Comparisons are made between experimental and calculated deflections and strains. The structure successfully survived the heating and loading environments.

INTRODUCTION

Reference 1 indicates that the construction of reentry vehicles of low wing loading could be based on radiative-type structure. The load-carrying material of such vehicles would be subjected to high temperatures with large variations in temperature throughout the structure. These conditions present difficult thermal-stress problems in conventional stressed skin design (ref. 2) and have prompted investigation of structural concepts which are more suited to the thermal environment.

This paper describes the available results of a test program on a large sheet metal structure designed to cope with the heating and air loads encountered by a reentry vehicle.


STRUCTURAL DESIGN


The sheet metal structure used in the present investigation is shown in figures 1 and 2. It is triangular in planform and cross section with a length of 12 feet, a width at the back of 7 feet, and a height at the back of $2\frac{3}{4}$ feet. These dimensions provide a planform area of 47 square feet with a sweep angle of 75° . In order to provide the greatest amount of test information, this structural model was designed with one side flat and the other V-shaped. Skin panels and internal structure were symmetrically designed so that the model could be heated and loaded from either side. All parts of the structural model were fabricated from the superalloy, Inconel X.

The exterior of the model is covered with corrugated skin panels with the axis of the corrugations parallel to the flight direction. These skin panels serve a dual purpose; they carry the air loads fore and aft to the supporting internal frames, and they provide torsional stiffness for the model. Expansion joints which extend around the model cross section at 2-foot intervals help to alleviate thermal stresses but prevent the skins from contributing any bending stiffness to the model.

The internal structure is shown in figure 3. It consists of an approximately orthogonal arrangement of transverse frames and longitudinal beams. The skin-panel loads are transmitted to the transverse frames. These frames in turn transmit the loads to the two longitudinal beams. The load-carrying members operate at high temperatures because the heated skin panels radiate heat throughout the internal structure.

Corrugated shear webs are used in both transverse frames and longitudinal beams to carry the shear loads and at the same time to permit differential thermal expansion between top and bottom spar caps without a large buildup of thermal stress. Well-designed corrugated shear webs have efficient load-carrying strength and stiffness values (ref. 3). The average weight of the internal structure in this model is 1.5 lb/sq ft of wetted area, and the average weight of the skin panels is 1.0 lb/sq ft.

A closeup view of the circled region in figure 3 is shown in figure 4. This figure gives a view of an intersection of a transverse frame, longitudinal beam, and skin panels. The longitudinal shear web is a standard 60° corrugation. The spar cap consists of two channels with a cover plate and is spotwelded to the corrugated web on both sides.



The transverse shear web is a specially designed corrugation to provide extreme flexibility normal to the web between the two channels which make up the transverse cap. This flexibility is needed to allow the skin panels to expand or contract freely without large buildup of thermal stress. The transverse shear webs are spliced to the longitudinal webs at their intersection.

The skin panels are attached to the outside flanges of the transverse caps. Skin panels are fabricated by seam welding together two pieces of 0.010-inch-thick sheet. The outer sheet is beaded lightly to stiffen it against local buckling and to preset a pattern which deforms uniformly when thermal expansion across the corrugations is restrained by the underlying transverse channels. The inner sheet is formed to a 60°, 1/2-inch flat corrugation and stops short of the edge of the outer sheet. A Z-stiffener provides the transition from the inner sheet to the outer sheet along the attached edges as shown in figure 5. The skin panels are attached only to the transverse frames and do not come in contact with the longitudinal spar cap. The expansion-joint tie allows the transverse frame channels to move relative to each other as the skin panels expand or contract. The tie also provides continuity between skin panels so that their shear stiffness can be utilized for torsional stiffness of the model. For aerodynamic smoothness, the expansion joint is covered with a strip which is fastened on the upstream side.

In order to help isolate the longitudinal spar caps from the skin panels, the transverse frame channels cross the longitudinal spar cap on the outside. One channel in each frame is rigidly attached to the longitudinal cap but the other channel is freely floating so that the expansion-joint action is not restricted.

A skin sheet thickness of 0.010 inch was selected as minimum gage based on general concepts of noise failures and panel flutter. In order to better define design criteria for these phenomena, noise and flutter tests of this skin panel have been undertaken. Results to date of the noise tests indicate that cracking starts near the rivet line after 20 minutes exposure to 157 decibels of random frequency noise from an air jet. After 2 hours the cracks had lengthened but the panel had not broken up disastrously.

Flutter tests were run in the Langley Unitary Plan wind tunnel on 2-foot-square skin panels. Although the panel with the corrugations parallel to the air flow was more flutter resistant than one with the corrugations perpendicular to the air flow, both orientations withstood a dynamic pressure greater than 2,000 lb/sq ft.

TESTS AND DISCUSSION

In order to study the behavior of the structure when subjected to a simulated reentry environment, the laboratory test setup shown in figure 6 was constructed. The 12-foot-long model is cantilevered from a support at the left in figure 6. The model is mounted with the flat side up for convenience in testing. The testing simulates reentry conditions for a flat-bottom configuration. It should be pointed out that in the figures which follow, whenever top or bottom is mentioned, it refers specifically to the testing orientation of the model; thus the top skin refers to the flat side.

Raised above the model is a large radiator which heats the flat planform area. Planform temperature variations of 250°F are programed into seven control channels, and this variation of heat intensity can be seen in the radiator (fig. 6). Before a test, the radiator is lowered so that it is parallel to and about 4 inches above the flat surface of the model. Programed loading is applied hydraulically by jacks through the whipple-tree system into the underside of the model.

Figure 7 shows a typical programed test environment to which the structural model was exposed. Temperature and load are shown as a function of time up to 20 minutes. Since the model was a research specimen, no attempt was made to duplicate the effects of any specific reentry trajectory. Ramp function inputs were used to simplify the analysis of results. The temperature along the structural leading edge was increased at a rate of 10°F per second up to a maximum for the test series of $1,600^{\circ}\text{F}$, then held constant for about 15 minutes, and finally decreased at a maximum programed rate of 10°F per second. These temperatures are comparable to structural temperatures which would be achieved in a lightly loaded unshielded vehicle or in a more heavily loaded vehicle behind a metallic heat shield. About midway in the test, a load pulse of 150 lb/sq ft was applied which produced maximum stresses of about 30 ksi in the structure.

Prior to the maximum cycle of heat and load at the level shown in figure 7, the model was subjected to about 100 cycles of loading up to 212 lb/sq ft at room temperature and 32 cycles of combined heating and loading at various levels of peak temperature between 400°F and $1,600^{\circ}\text{F}$.

The measured distribution of temperature around the model cross section at a location 9 feet from the nose is given in figure 8. The general trend of the programed temperature variation of 250°F in the flat planform is evident in the top of the figure with the leading edges at about $1,600^{\circ}\text{F}$ and the center at $1,350^{\circ}\text{F}$. The presence of

the two main spar caps lying beneath the heated skin shows up in the two intermediate peaks in the temperature curve. These spar caps are not conductive heat sinks because they are not in contact with the skin; but, since their proximity to the skin blocks the radiation, higher skin temperatures occur above the spars than on either side of the spars. A similar effect is not evident in the bottom skin inasmuch as the temperature levels are lower and radiation heat exchanges are much less. The temperatures shown in figure 8 are for 7 minutes of test time and correspond to approximately steady-state equilibrium for the skin panels.

Variation of temperature with time is shown in figure 9 for selected points on the top and bottom skins and top and bottom spar caps of the longitudinal beams. Temperature is plotted against time in minutes. The top skin shows a response very similar to the programed input (fig. 7) with the exception of the region near the end of the test when natural cooling took place at a slower rate than the maximum programed cooling rate. Heating of the spar caps and bottom skin occurred primarily by radiation from the top skin through the interior of the model. From 5 to 10 minutes elapsed after the top skin reached equilibrium before the other elements essentially reached equilibrium. The maximum temperature difference between the top and bottom spar caps occurs after approximately 7 minutes of test time.

Since the spar caps provide the longitudinal bending stiffness for the model, their temperature differences are reflected in the model deflection as shown in figure 10. Deflection of the model nose δ is plotted against time for the simulated reentry test. The total measured experimental deflection is given by the solid curve. It reaches a peak value of nearly 3 inches due to spar-cap temperature difference at about 7 minutes of test time corresponding to the maximum spar-cap temperature difference shown on the previous figure. Beyond this point, the deflection due to temperature difference decreases even though the absolute spar temperatures are still increasing.

The hump in the deflection curve is produced by the load pulse applied during the heating cycle. Note that deflection due to heating is about three times the deflection due to load. The rapid dropoff in deflection at $17\frac{1}{2}$ minutes corresponds to the time when peak heat input ceased and the entire model began to cool rapidly.

Computed deflections based on beam theory and using the measured temperatures inside the model are shown by the dashed curves in figure 10 for the conditions of heat and load which were superimposed during the test. The agreement between experimental and computed deflections is satisfactory considering the timewise and spacewise temperature variations.

A comparison of experimental and computed strains in the longitudinal compression spar cap is shown in figure 11 for a loading of 212 lb/sq ft on the planform area. Average load strain in the spar-cap cross section is shown as a function of distance from the rear. The solid curve is the computed value of average strain. The circles are average values of room-temperature strain measured with resistance strain gages located in several places on the cross section of the spar cap. The square is a measured load strain for the same applied load during a 1,000° F test. Agreement is shown between theory and experiment.

Figure 12 shows the condition of the structural model at the conclusion of the heating cycles. The only damage observed was a few local buckles in the hottest portions of the back two panels, that is, those with the largest planform temperature differences. Most of the buckles occurred in the two outlined regions and are small and confined to the beaded portion of the outer skin.

CONCLUDING REMARKS

A large structural model has been built incorporating design concepts applicable to a radiation-cooled vehicle. Some of the results of the test experience have been presented. The agreement shown between theory and experiment for deflections and strains indicates that beam bending theory is adequate to describe the average response of the model to applied loads and temperatures. On the basis of these results combined with visual inspection, it is concluded that these design concepts enabled the structure to survive successfully the simulated reentry heating and loading environments.

REFERENCES

1. Anderson, Roger A., and Swann, Robert T.: Structures for Reentry Heating. (Prospective NASA paper; USAF/NASA Conference Paper.)
2. Pride, Richard A., Hall, John B., Jr., and Anderson, Melvin S.: Effects of Rapid Heating on Strength of Airframe Components. NACA TN 4051, 1957.
3. Peterson, James P., and Card, Michael F.: Investigation of the Buckling Strength of Corrugated Webs in Shear. NASA TN D-424, 1960.

STRUCTURAL - MODEL DIMENSIONS

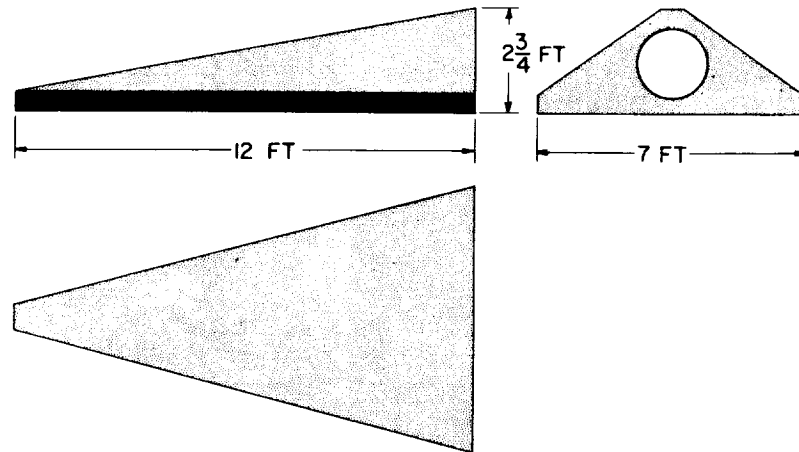


Figure 1

STRUCTURAL-MODEL EXTERIOR

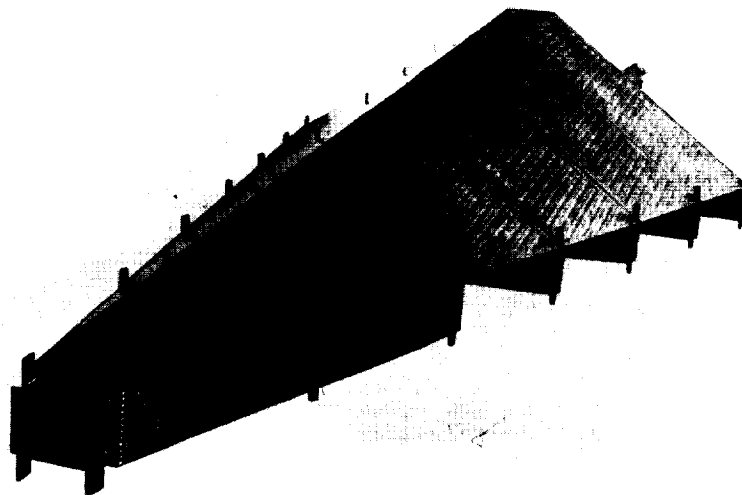


Figure 2

STRUCTURAL-MODEL INTERIOR

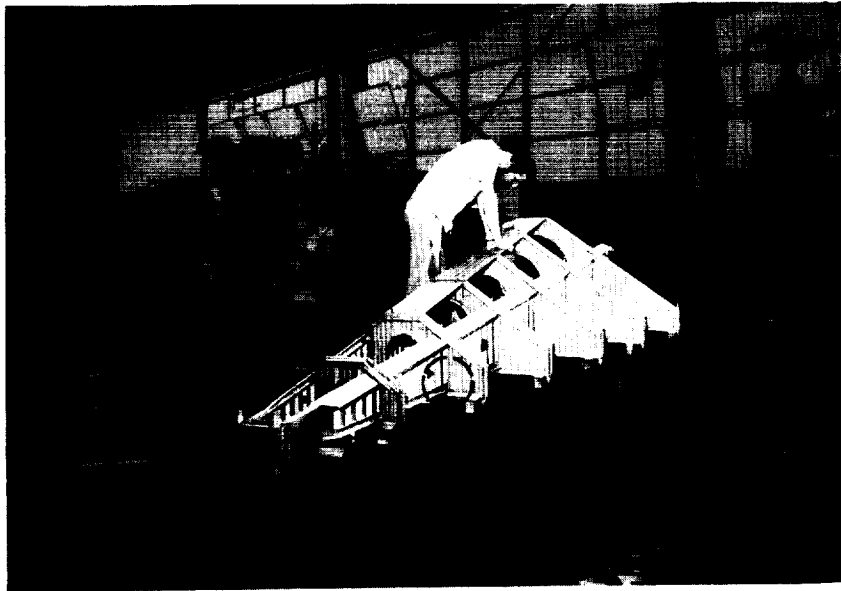


Figure 3

INTERSECTION OF MODEL COMPONENTS

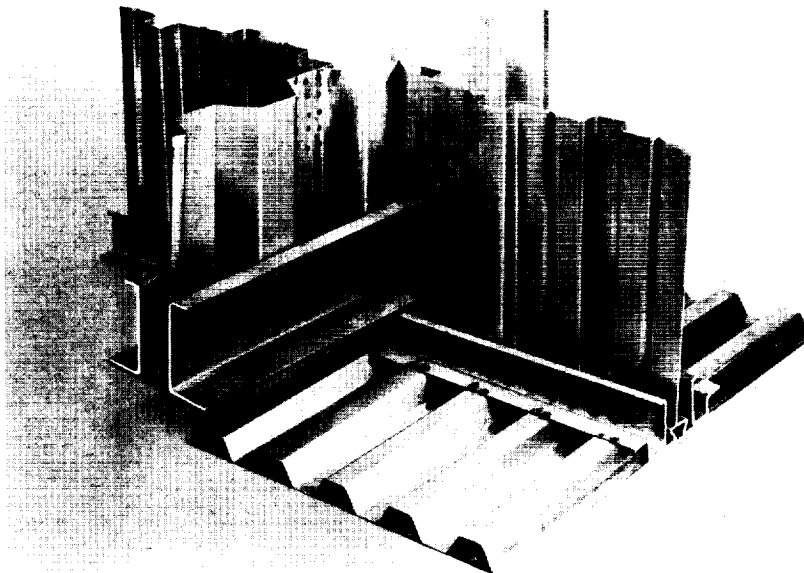


Figure 4

EXPANSION - JOINT DETAIL

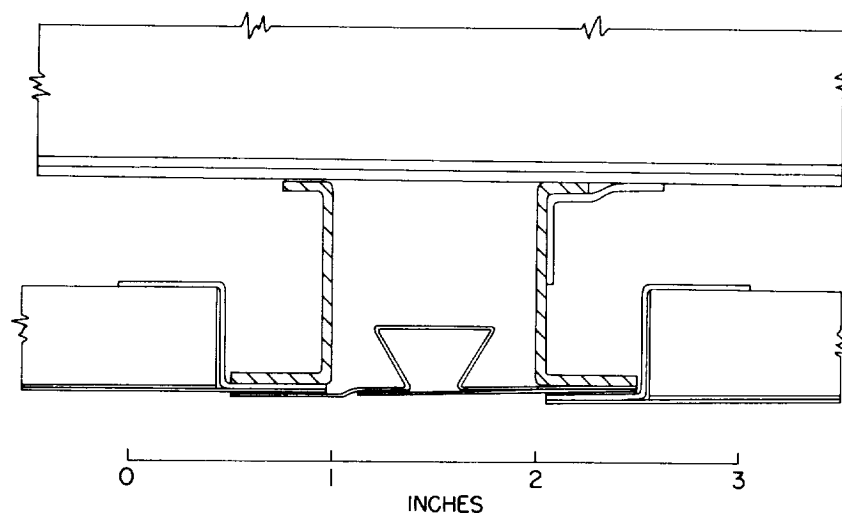


Figure 5

TEST SETUP

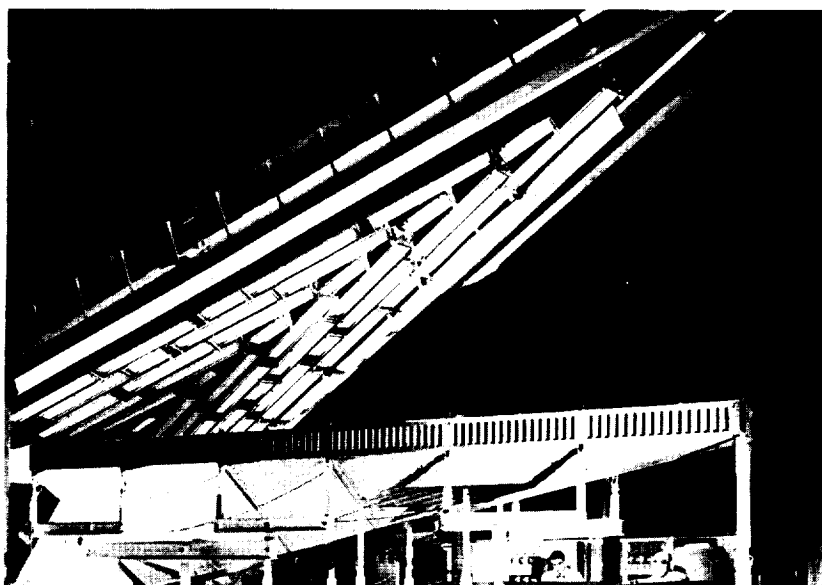


Figure 6

PROGRAMED TEST ENVIRONMENT

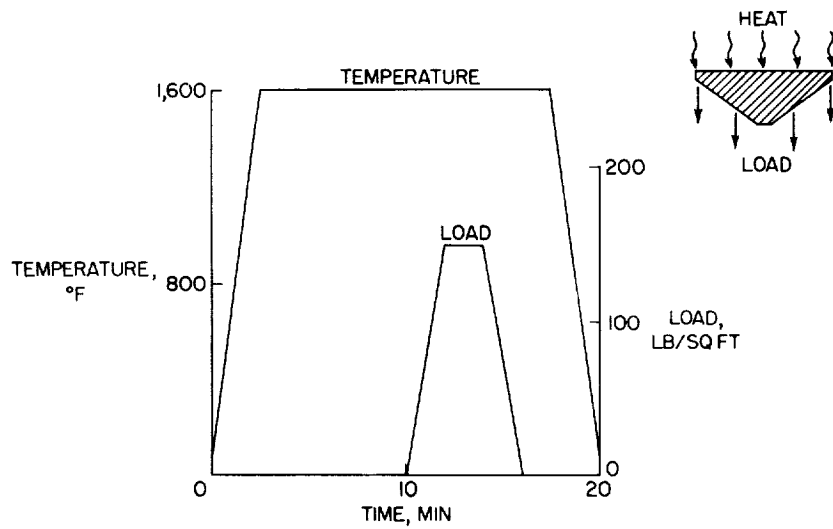


Figure 7

TEMPERATURE VARIATION IN MODEL CROSS SECTION

STATION, 9 FEET FROM NOSE; TEST TIME, 7 MINUTES

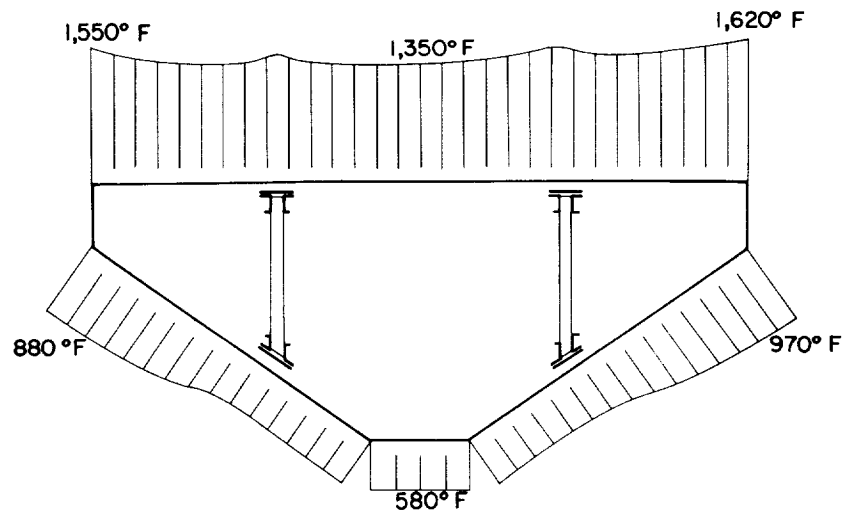


Figure 8

TIME - TEMPERATURE VARIATION IN MODEL CROSS SECTION
STATION, 9 FEET FROM NOSE

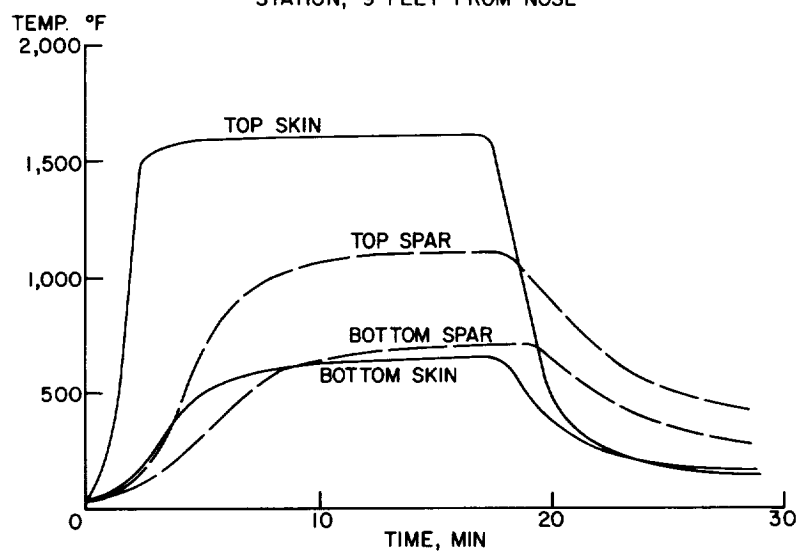


Figure 9

MODEL DEFLECTION DURING SIMULATED REENTRY

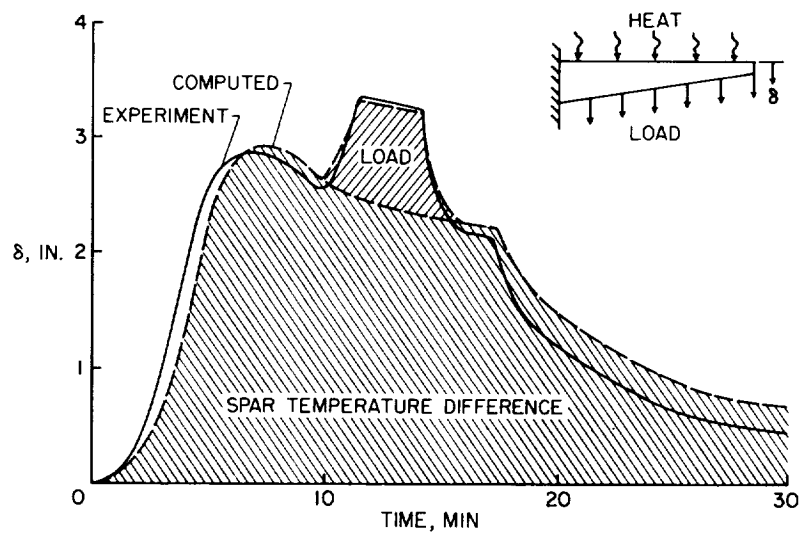


Figure 10

LOAD STRAIN IN COMPRESSION SPAR CAP
LOAD, 212 LB/SQ FT

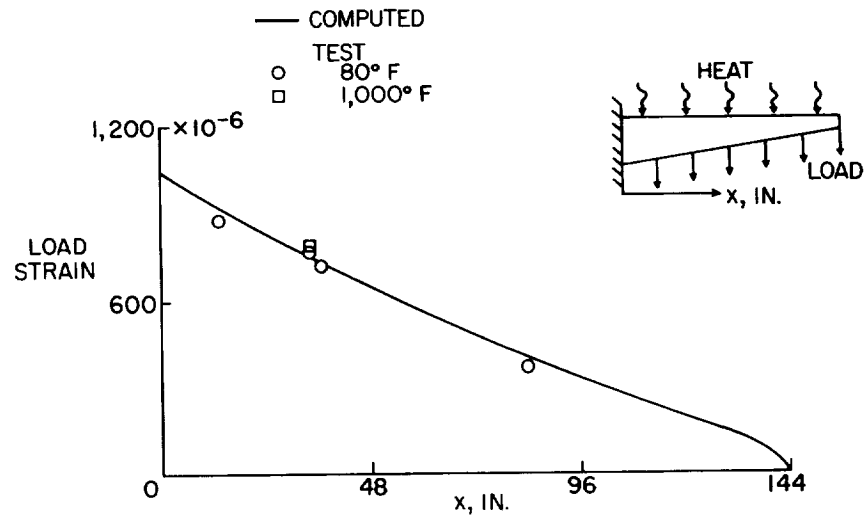


Figure 11

CONDITION AFTER SIMULATED REENTRY



Figure 12

STRUCTURAL CONSIDERATIONS OF INFLATABLE REENTRY VEHICLES

By Robert W. Leonard, George W. Brooks,
and Harvey G. McComb, Jr.
Langley Research Center

SUMMARY

The state of the design art for inflated structures applicable to reentry vehicles is discussed. Included are material properties, calculations of buckling and collapse loads, and calculations of deflections and vibration frequencies. A new theory for the analysis of inflated plates is presented and compared with experiment.

INTRODUCTION

One vehicle which has been proposed as a possible device for achieving manned reentry from orbital flight is the inflatable reentry glider. In this paper some of the problems and properties which must be considered in the design of vehicles of this type are discussed.

It is important to note the state of material availability for application to inflatable reentry vehicles. The expected maximum temperatures on inflated portions of typical proposed vehicles range as high as 1,500° F. This relatively severe temperature environment indicates that an inflatable reentry glider probably must be constructed of woven fabric of high-temperature-resistant metal wire. This fabric must, in turn, be sealed against loss of air pressure by a suitable temperature-resistant coating. At the present time such materials are not available as "off-the-shelf" items. Additional work is needed to improve the quality of woven fabric, to perfect satisfactory joining techniques, and, especially, to improve the properties of available high-temperature-resistant coatings. In spite of these deficiencies, material development for inflatable reentry vehicles is well advanced and this state has been achieved through a modest effort. Thus, with continued or accelerated effort, materials suitable for the construction of an inflatable reentry glider can probably be available in the near future.

SYMBOLS

A	cross-sectional area of inflated structure
c	distance from beam neutral axis to outer fiber
d	distance from cross-sectional center of pressure to outer fiber
F	force
g	structural damping coefficient
h	depth of airmat plate
I	beam cross-sectional moment of inertia
l	length of beam
M	moment
p	internal pressure
q	lateral load intensity
w	lateral deflection of airmat plate
α, β	angles of rotation of airmat drop cords
σ	normal stress
τ	shear stress

PROPERTIES OF INFLATABLE STRUCTURES

Consider now some of the questions of structural configuration and properties which would enter into the design of inflated reentry vehicles. In figure 1 is shown a typical example of such a vehicle. Note that two basic types of structural elements are represented: the inflated circular cylinder which typifies the fuselage construction and the inflated plate which is used for the wings, fins, and control surfaces. Two possible ways of constructing such pneumatic plates are shown in figure 1. At the lower center is shown a plate consisting of an array of tubes, a sort of inflatable equivalent to multiweb construction.

At the right is shown a different arrangement, called "airmat," which was developed by the Goodyear Aircraft Corporation. Airmat consists of two woven covers which are held a fixed distance apart by a regular array of fibers called "drop cords." This arrangement permits an inflatable wing to be tapered in any desired manner. Furthermore, from the standpoint of its strength in bending, airmat is more efficient than the tubular configuration or any similar configuration of the same depth.

Buckling and Collapse Analysis of Inflated Structures

The higher efficiency of airmat plates has been established by simple buckling and collapse analyses. Such analyses are in common use (for example, see ref. 1) and can apparently be applied to any type of inflated structure. The nature and the accuracy of these analyses are illustrated in figure 2 for the case of a load F applied at the tip of an inflated cylindrical cantilever beam of length l . The ordinate of the plot is bending moment at the root, the applied load times the length; the abscissa is the internal pressure in the cylinder. Two calculated curves are shown. The lower curve gives the root bending moment where local buckles, or wrinkles, first appear at the upper extreme fiber. As indicated at the right in figure 2, this is calculated simply as the moment for which the elementary compressive bending stress M_c/I just cancels the tension stress due to pressure. Since this region of zero stress is very localized, the cylinder can carry still more load before collapsing. As the load is increased, the wrinkle progresses around the cross section. Collapse occurs when the wrinkle has progressed all the way to the lower extreme fibers. At this instant, the root cross section takes on the characteristics of a plastic hinge and approximations to the collapse load can be obtained by an application of the theorems of plastic limit analysis. A simple equivalent way of arriving at an approximate collapse load is as follows. Assume that, at collapse, only the extreme lower fibers carry tension to balance the pressure inside the cylinder as indicated at the lower right in figure 2; then, the resisting "plastic hinge" moment is the resultant pressure force pA times the distance d from these extreme fibers to the line of action of the resultant pressure force. Since the cylinder is in equilibrium, this must also be the moment of the applied load at the instant of collapse. The upper curve on the plot in figure 2 has been calculated in this way.

The accuracy of these simple calculations is shown by the experimental points. These data were obtained from cylinders of two different materials, cotton cloth coated with neoprene and fiber-glass cloth coated with latex. Since the cantilever beam is a statically determinate configuration, the buckling and collapse moments do not depend on material properties. Note that the collapse load for a circular cylinder is about twice the buckling load.

Consider now the application of the simple collapse analysis to the 60° inflated delta wing shown in figure 3. This wing is an example of the tubular construction shown in figure 1, with the webs parallel to the root. Again, a concentrated load is applied at the tip. As a result of the tubular construction, collapse occurs simultaneously along each of the webs and at the root according to both experiment and simple theory. The simple criterion for collapse is applied exactly as before, and the resulting moment at the root is plotted in figure 3 against internal pressure. No buckling curve is shown because this configuration is such that there is no discernible difference between buckling and collapse. The experimental points were obtained from a small model made of cotton cloth coated with neoprene. The agreement of these points with the simple collapse theory is seen to be quite good.

The application of the theorems of plastic limit analysis to the collapse of inflated structures leads to the conclusion that this simple theory gives an upper bound on the collapse load. The results shown in figures 2 and 3 indicate that, in many practical cases, this upper bound is quite close to the true collapse load. Thus, the simple collapse criterion appears to be a very useful tool for rough design calculations. It may be applied to any inflated structure, including airmat wing structures.

Deflection Analysis of Inflated Wings

The foregoing results indicate that the determination of collapse loads may be a relatively easy task for the designer of an inflated reentry vehicle. However, the determination of the deformations of the vehicle or the performance of an aeroelastic analysis is quite another matter. Simple beam theories are not adequate for these tasks and material properties must be taken into account; hence, more comprehensive structural theories are needed. Such a theory has been developed for application to plates of the airmat type.

The new airmat-plate theory is a linear "small-deflection" theory based on the following assumptions. It is assumed that the woven material is elastic but orthotropic, that the pressure inside the airmat does not vary with deformation, and that the drop cords are inextensional but they need not remain perpendicular to the covers. (See fig. 4.) This means that transverse shear deformation of the airmat plate is permitted. The theory can be expressed in terms of the deflection w (see fig. 4) and two drop-cord angles α and β . The angle α is shown in figure 4 and β is a similar angle in a plane normal to the figure.

Actually, the airmat-plate theory turns out to be nothing more than a special form of the well-known theory for plates with transverse

shear flexibility. In this case, transverse shear stiffness is the product of the internal pressure p and the depth h of the airmat. In many practical cases this transverse shear stiffness can be expected to be very low so that much of the deflection of the plate is shear deflection not involving deformation of the material in the covers. The theory has been written for the case of constant depth of the airmat plate and inertia forces have been included. These equations are presented in the appendix. Such factors as aerodynamic forces, nonuniform temperature distributions, and depth variations can be inserted if desired.

Some idea of the usefulness of airmat-plate theory is afforded by the comparison with experiment shown in figure 5. A square airmat plate, made of nylon fabric coated with neoprene, was mounted in such a way as to simulate simple support boundary conditions all around. The plate was 18 inches wide with a depth h of 1.125 inches. A uniform external loading q was applied to the surface of the plate at different values of the internal pressure p . Resulting values of the center deflection w , in terms of the depth h of the plate, are plotted in figure 5 against the load q . Data points are shown for three values of internal pressure: 5, 9, and 14 pounds per square inch in excess of the external pressure.

Effective orthotropic elastic constants for the fabric material of the test specimen were obtained from tests of cylinders made from the same material. These constants were used in the new airmat-plate theory (eqs. (A12) to (A14) in the appendix) to calculate deflections of the plate. The calculated values of center deflection, corresponding to each experimental value of internal pressure, are shown by the lines in figure 5. Consider, for a moment, the upper, solid line which gives calculated deflections corresponding to the lowest internal pressure shown on the plot. The importance of transverse shear deformation is shown at the right. It is seen that, for this pressure, approximately three-quarters of the calculated deflection is due to shear alone. Thus, a simple bending analysis which neglects transverse shear flexibility could not be expected to yield even approximately accurate deflections.

In general, the values of deflection calculated with airmat-plate theory are higher than the experimental values. The largest discrepancy is approximately 17 percent at the lowest internal pressure and is believed to be largely due to a peculiarity of the test specimen. The plate specimen used was restrained from shear deformation near its edges by heavy reinforcement which would not be typical of inflated-wing construction. The theory, on the other hand, assumes the plate to be flexible in shear over its whole width, and, hence, can be expected to yield higher deflections especially at the low pressure where shear flexibility is so important. At the highest pressure (the lowest curve), where shear deformation is somewhat less important, the agreement is seen to be quite good.

Material Properties of Fabrics

It is of interest to note in figure 5 that, at each pressure, the experimental points lie approximately on a straight line. This indicates that the behavior of the experimental plate specimen was indeed very nearly linear. Thus, the fabric material of the specimen appears to exhibit linear stress-strain behavior for the range of stress imposed. In spite of this local linear behavior, the stress-strain curve is, on the whole, typically nonlinear. This point is illustrated by the typical stress-strain curves for fabric which are shown in figures 6 and 7.

A single layer of simply woven fabric such as that shown in figure 6 has two sets of perpendicular fibers which are commonly called the warp and the fill fibers. A sheet of such material is thus orthotropic with axes of symmetry in these two perpendicular directions. In the plot in figure 6 is shown a typical stress-strain curve for such a fabric in a state of biaxial tension with stresses σ_{warp} and σ_{fill} in the warp and fill directions. The warp stress is plotted against warp strain for a constant value of the fill stress. Other values of fill stress correspond to different curves as illustrated by the dashed curve for zero fill stress. The initial, curved portion of the stress-strain curve corresponds to the straightening of the warp fibers and bending of the fill fibers as the warp stress is applied; hence, material behavior in this range depends strongly on the tightness of the weave and on the fill stress maintained in the other direction. After this process of straightening and bending of the fibers is nearly complete, the stress-strain behavior depends more on the properties of the material. This curve was based on a linearly elastic fiber material such as metal or fiber glass. Thus, an inflatable reentry structure made from such material might be expected to deform linearly if pressurization has stressed the fabric to this extent.

Note that, in unloading, the curve deviates significantly from the loading path in the lower nonlinear range. This deviation occurs even for fabrics made of linear material. Possible reasons are friction between fibers and exceeding the elastic limit in the fiber straightening process.

In figure 7 is plotted a typical shear stress-strain curve for a simply woven fabric. It is apparent that, at low strains, shear resistance depends strongly on coating characteristics and on friction between the fibers. The friction, in turn, depends strongly on the tension in the fibers. Even for linear fiber material the shear curve is commonly nonlinear and an effective elastic modulus must be assumed for use in a linear elastic theory. As might be expected, the effective shear modulus of simply woven fabrics is generally low; a typical value is one-tenth of the tension modulus as compared with four-tenths for isotropic engineering metals. However, the shear modulus can be raised to nearly

[REDACTED]

this level simply by adding a bias ply, a second layer of fabric oriented at 45° to the first. The upswing at very high shear strains in figure 7 is primarily attributed to bearing pressure between the fibers. For shear of fabrics, it is common for the unloading curve to depart widely from the loading curve as shown, apparently as a result of friction losses.

One more interesting property of fabrics might be mentioned. Poisson's ratio for a woven fabric sheet is largely associated with the stresses in one direction bending the fibers in the other. Thus, Poisson's ratio depends strongly on the weave and the biaxial stress ratio and some rather unusual values can be obtained; in fact, values of Poisson's ratio much higher than 1 are theoretically possible.

It should be pointed out that, as a result of the longstanding interest in balloons and nonrigid airships, there is in existence a fairly large body of literature on fabric properties in general. However, data on metal fabrics are lacking.

Dynamic Behavior of Inflatable Structures

In addition to material properties and static structural behavior, the designer of an inflatable reentry glider must concern himself with such facets of dynamic structural behavior as vibration modes and frequencies, noise response, and flutter. In order to determine the type of dynamic behavior to be expected from inflated structures, vibration tests have been conducted at the Langley Research Center on simple inflated models. Some results of these tests are shown in figure 8.

The upper plot in figure 8 shows typical experimental response curves of a 60° inflated delta-wing model at a given internal pressure. The structure is tapered airmat and the material is silk cloth with a latex coating. Measured amplitude is plotted against vibration frequency with both quantities expressed in terms of values at the first natural frequency. The first mode is found to be a bending mode with the node line at the root. The amplitude is measured at the tip as indicated by the letter A on the small sketch. Note that the peak is relatively sharp with a distinct resonant frequency. The corresponding value of the structural damping coefficient ($g = 0.073$) is only two to four times values found for conventional metal structures. The second mode is a torsion mode with the node line as shown on the sketch. In this case the amplitude was measured at a point along the leading edge. Again the resonant frequency is sharply defined and, in fact, the damping coefficient is 0.045, lower than in the first mode.

Response curves, such as those in the upper plot of figure 8, were obtained for both modes at several values of internal pressure. The

[REDACTED]

[REDACTED]

plot at the bottom shows the increase of resonant frequency with internal pressure for both the first and second modes. The structural damping coefficients maintained the same order of magnitude at all pressures.

The results in figure 8 are evidence that the dynamic behavior of inflated fabric wing structures is much like the dynamic behavior of conventional metal wing structures. Thus, the many dynamic problems which must be considered in the design of conventional structures may also be problems for the designer of inflated structures. For example, flutter analysis probably should be an important part of the design process for inflatable reentry gliders.

The linear airmat-plate theory presented in the appendix may be readily adapted for vibration and flutter analysis. Its use in the calculation of natural vibration frequencies is illustrated in figure 9.

The structure considered is the same square airmat plate of nylon and neoprene discussed previously. The plot in figure 9 gives the lowest three natural frequencies of this plate as a function of internal pressure. An indication of corresponding mode shapes is shown by the small figures in the key. Thus the lowest frequency corresponds to a single half sine wave in both directions and no node line appears. The next two mode shapes differ only in the direction of the single node line. The slight difference in frequency for these two shapes is primarily due to the directional elastic properties of the fabric cover material. The points are measured values of frequency whereas the curves were calculated by the use of airmat-plate theory. The agreement is seen to be reasonably good.

CONCLUDING REMARKS

The state of structural design capability for the inflatable reentry glider can be summarized by the following remarks. In the first place, it must be pointed out that material development for application to inflatable reentry vehicles is not yet complete. In particular, more work is needed on joining techniques and on fabric coatings which will withstand temperatures up to and, perhaps, somewhat beyond 1,500° F. From the standpoint of the structural design process, however, the designer has at his disposal simple, but adequate, procedures for the calculation of buckling and collapse loads on inflatable structures. He also has available a linear theory for the deflection analysis of inflatable wing structures. This linear theory can yield reasonably accurate results in spite of nonlinearities which characterize the mechanical properties of fabric materials. It can also be adapted for

[REDACTED]

vibration and flutter analysis which apparently should be an important part of the design process. Thus, one might conclude that, while there is much work yet to be done, the creation of rational design procedures for inflated reentry vehicles is indeed possible.

APPENDIX

A LINEAR THEORY FOR "AIRMAT" PLATE

INTRODUCTION

This appendix contains a very brief outline of the derivation of the linear differential equations and boundary conditions for a rectangular plate of constant-depth "airmat" construction. The basic assumptions underlying the theory are mentioned in the paper and listed in figure 4. The presence of a bulkhead at the edges of the plate is not explicitly accounted for in the theory. It is assumed, however, that some mechanism exists along the edges of the plate to keep the internal air from escaping.

SYMBOLS

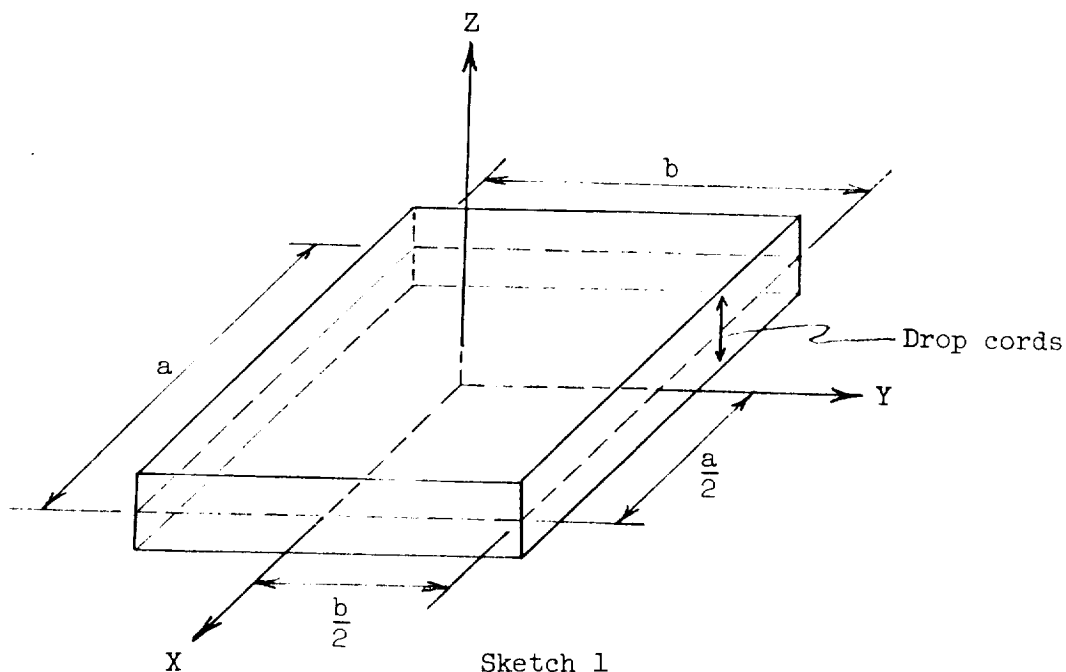
a, b	dimensions of plate in x- and y-directions, respectively
E_W, E_F	Young's modulus in warp direction and fill direction of the covers, respectively
G	modulus of rigidity for cover material
h	depth of plate
M_x, M_y, M_{xy}	plate moments and twist associated with differences between stress resultants in top and bottom covers
m	mass of the plate per unit middle plane area
N_x, N_y, N_{xy}	plate stress resultants associated with sums of stress resultants in top and bottom covers
p	internal pressure
q	external distributed lateral load
t	thickness of each cover
u, v, w	plate displacements, the average of the displacements in the top and bottom covers in x-, y-, and z-directions, respectively

V	volume of plate
W	external work
x, y, z	coordinates
α, β	angles between drop cords and Z-axis in X,Z and Y,Z planes, respectively, associated with differences between displacements in top and bottom covers
μ_{WF}, μ_{FW}	Poisson's ratios, strain in direction of second subscript due to stress in direction of first subscript
Π_C	strain energy in covers
Π_I	work done against internal pressure

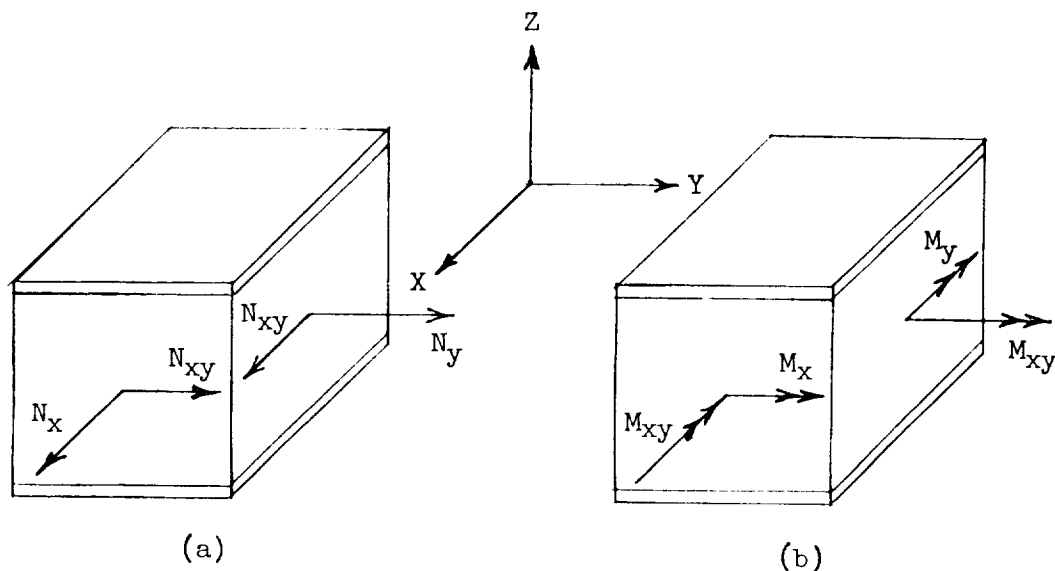
Comma preceding a subscript denotes differentiation with respect to the subscript. Dots over a symbol denote differentiation with respect to time.

ANALYSIS

The coordinate system is chosen so that the middle plane of the plate lies in the X,Y plane as shown in the following sketch:



An element is removed from the plate and shown in the following sketch:



Sketch 2

The plate stress resultants are shown acting on the element in the positive senses in sketch 2(a). In sketch 2(b) the plate moments and twist are shown in the positive senses.

The theory is developed through an application of the calculus of variations by utilizing the principle of virtual work which states

$$\delta(\Pi_C + \Pi_I - W) = 0$$

In this expression Π_C represents the strain energy in the covers, Π_I represents the work done against the internal pressure due to change in volume of the plate, and W represents the potential energy of the external loads. Since a linear theory is sought, in writing expressions for Π_C , Π_I , and W , it is permissible to neglect all terms of order higher than 2 in products of the plate displacements, drop-cord angles, or their derivatives.

The variation of the strain energy in the covers can be written in terms of the plate stress resultants and the plate displacements and drop-cord-angles as follows:

$$\delta \Pi_c = \int_{-b/2}^{b/2} \int_{-a/2}^{a/2} \left[N_x \delta \left(u_{,x} + \frac{1}{2} w_{,x}^2 \right) + N_y \delta \left(v_{,y} + \frac{1}{2} w_{,y}^2 \right) + N_{xy} \delta \left(u_{,y} + v_{,x} + w_{,x} w_{,y} \right) + M_x \delta \alpha_{,x} + M_y \delta \beta_{,y} + M_{xy} \left(\delta \alpha_{,y} + \delta \beta_{,x} \right) \right] dx dy$$

In order to obtain $\delta \Pi_I$, it is necessary to calculate the change in volume of the plate caused by displacements and drop-cord angles u , v , w , α , and β . This change in volume is obtained by calculating the final volume of the plate after an arbitrary displacement and subtracting initial volume. The volume of the deformed plate is calculated from the surface integral (see, for example, ref. 2)

$$V = - \iint_S z dx dy$$

where x , y , and z represent the coordinates of points in the deformed plate surfaces and the surface integral must be evaluated over the six outside surfaces of the plate. The quantity $\delta \Pi_I$ is the negative of the product of the internal pressure and the variation of the increase in volume. The result is

$$\begin{aligned} \delta \Pi_I = & -p \delta \int_{-b/2}^{b/2} \int_{-a/2}^{a/2} h \left[u_{,x} + v_{,y} - \alpha w_{,x} - \beta w_{,y} - \frac{\alpha^2}{2} - \frac{\beta^2}{2} + u_{,x} v_{,y} \right. \\ & \left. - u_{,y} v_{,x} + \frac{h^2}{4} (\alpha_{,x} \beta_{,y} - \alpha_{,y} \beta_{,x}) \right] dx dy + \int_{-b/2}^{b/2} \frac{h^3}{12} (\alpha_{,y} \beta \\ & - \alpha \beta_{,y}) \Big|_{-a/2}^{a/2} dy + \int_{-a/2}^{a/2} \frac{h^3}{12} (\alpha \beta_{,x} - \alpha_{,x} \beta) \Big|_{-b/2}^{b/2} dx \end{aligned}$$

where the symbol $\Big|_{-a/2}^{a/2}$ means that the integrand at $x = \frac{a}{2}$ is subtracted from the integrand at $x = -\frac{a}{2}$, etc.

The external-work term includes inertia contributions. The expression for the variation of the external work is

$$\delta W = \int_{-b/2}^{b/2} \int_{-a/2}^{a/2} \left(q\delta w - m\ddot{w}\delta w - m\ddot{u}\delta u - m\ddot{v}\delta v - \frac{h^2}{4} m\ddot{\alpha}\delta\alpha - \frac{h^2}{4} m\ddot{\beta}\delta\beta \right) dx dy$$

The indicated variational operation is now carried through and certain terms are integrated by parts. There results from this procedure an integral over the area of the middle surface of the plate and integrals along the edges of the plate. Each term in the area integral contains one of the following quantities: δu , δv , δw , $\delta\alpha$, or $\delta\beta$. The coefficients of these five quantities can be set equal to zero independently by the arguments of the calculus of variations. This procedure yields the following partial differential equations of equilibrium for the airmat plate:

$$N_{x,x} + N_{xy,y} = m\ddot{u} \quad (A1)$$

$$N_{y,y} + N_{xy,x} = m\ddot{v} \quad (A2)$$

$$(N_x^w)_{,x} + (N_y^w)_{,y} + (N_{xy}^w)_{,x} + (N_{xy}^w)_{,y} + ph\alpha_{,x} + ph\beta_{,y} + q = m\ddot{w} \quad (A3)$$

$$M_{x,x} + M_{xy,y} - ph(\alpha + w)_{,x} = \frac{h^2}{4} m\ddot{\alpha} \quad (A4)$$

$$M_{y,y} + M_{xy,x} - ph(\beta + w)_{,y} = \frac{h^2}{4} m\ddot{\beta} \quad (A5)$$

Similar arguments applied to the boundary integrals lead to two sets of boundary conditions. Along $x = \pm \frac{a}{2}$

$$\delta u = 0 \quad \text{or} \quad N_x - ph(1 + v_{,y}) = 0$$

$$\delta v = 0 \quad \text{or} \quad N_{xy} + ph u_{,y} = 0$$

$$\delta w = 0 \quad \text{or} \quad N_x^w + N_{xy}^w + ph\alpha = 0$$

$$\delta\alpha = 0 \quad \text{or} \quad M_x - \frac{ph^3}{12} \beta_{,y} = 0$$

$$\delta\beta = 0 \quad \text{or} \quad M_{xy} + \frac{ph^3}{12} \alpha_{,y} = 0$$

Along $y = \pm \frac{b}{2}$ the conditions are the same as those for $x = \pm \frac{a}{2}$ except that u and v , α and β , and x and y are interchanged.

In addition to the differential equations of equilibrium and boundary conditions for the plate, six stress-strain relations are required to specify the problem completely. The form of these stress-strain relations depends on the properties of the cover material. For example, if the covers are a simply woven fabric (fig. 6) with the x and y axes assumed, for simplicity, to lie along the warp and fill directions of the fabric, the linearized stress-strain relations are

$$N_x = 2(A_{11}u_{,x} + A_{12}v_{,y})$$

$$N_y = 2(A_{21}u_{,x} + A_{22}v_{,y})$$

$$N_{xy} = 2A_{33}(u_{,y} + v_{,x})$$

$$M_x = \frac{h^2}{2}(A_{11}\alpha_{,x} + A_{12}\beta_{,y})$$

$$M_y = \frac{h^2}{2}(A_{21}\alpha_{,x} + A_{22}\beta_{,y})$$

$$M_{xy} = \frac{h^2}{2} A_{33}(\alpha_{,y} + \beta_{,x})$$

where

$$A_{11} = \frac{E_W t}{1 - \mu_{WF} \mu_{FW}}$$



$$A_{12} = \frac{\mu_{FW} E_W t}{1 - \mu_{WF} \mu_{FW}}$$

$$A_{21} = \frac{\mu_{FW} E_F t}{1 - \mu_{WF} \mu_{FW}}$$

$$A_{22} = \frac{E_F t}{1 - \mu_{WF} \mu_{FW}}$$

$$A_{33} = Gt$$

When the inertia terms are neglected, the differential equations (eqs. (A1) to (A5)) reduce to

$$N_{x,x} + N_{xy,y} = 0 \quad (A6)$$

$$N_{y,y} + N_{xy,x} = 0 \quad (A7)$$

$$\begin{aligned} N_x w_{,xx} + N_x w_{,x} + N_y w_{,yy} + N_y w_{,y} + N_{xy} w_{,xy} + N_{xy} w_{,y} + N_{xy} w_{,yx} \\ + N_{xy} w_{,x} + ph\alpha_{,x} + ph\beta_{,y} + q = 0 \end{aligned} \quad (A8)$$

$$M_{x,x} + M_{xy,y} - ph(\alpha + w_{,x}) = 0 \quad (A9)$$

$$M_{y,y} + M_{xy,x} - ph(\beta + w_{,y}) = 0 \quad (A10)$$

Use of the equations (A6) and (A7) reduces equation (A8) to

$$N_x w_{,xx} + N_y w_{,yy} + 2N_{xy} w_{,xy} + ph\alpha_{,x} + ph\beta_{,y} + q = 0 \quad (A11)$$



If the plate stresses result from internal pressure alone so that $N_x = N_y = ph$ and $N_{xy} = 0$, the differential equations (A9), (A10), and (A11) become

$$ph(\alpha + w_{,x})_{,x} + ph(\beta + w_{,y})_{,y} + q = 0 \quad (A12)$$

$$M_{x,x} + M_{xy,y} - ph(\alpha + w_{,x}) = 0 \quad (A13)$$

$$M_{y,y} + M_{xy,x} - ph(\beta + w_{,y}) = 0 \quad (A14)$$

These equations are essentially the governing differential equations for plates with transverse shear flexibility taken into account. (See, for example, ref. 3.) The internal pressure p plays the role of the plate transverse shear stiffness.

REFERENCES

1. Topping, A. D.: A Preliminary Study of Methods of Analysis of "Airwall" Structures. GER 5850, Goodyear Aircraft Corp., Feb. 19, 1954.
2. Courant, R.: Differential and Integral Calculus. Vol. II. Interscience Publishers, Inc. (New York), 1952, p. 387.
3. Mindlin, R. D.: Influence of Rotatory Inertia and Shear on Flexural Motions of Isotropic, Elastic Plates. Jour. Appl. Mech., vol. 18, no. 1, Mar. 1951, pp. 31-38.

TYPICAL INFLATABLE REENTRY CONFIGURATION

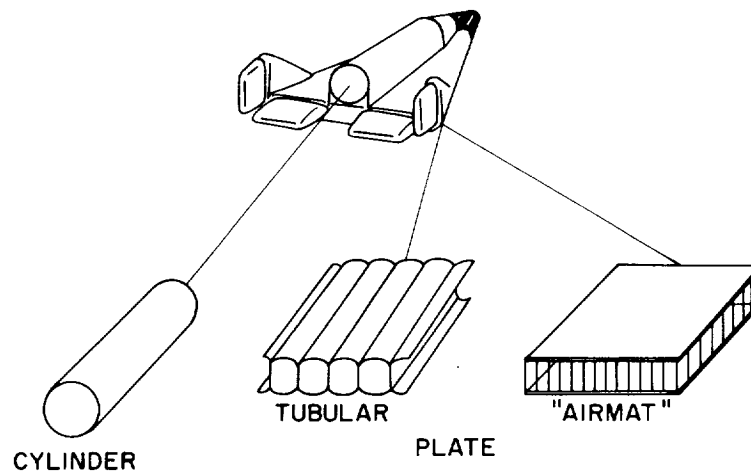


Figure 1

SIMPLE STRENGTH ANALYSIS OF AN INFLATED CYLINDER

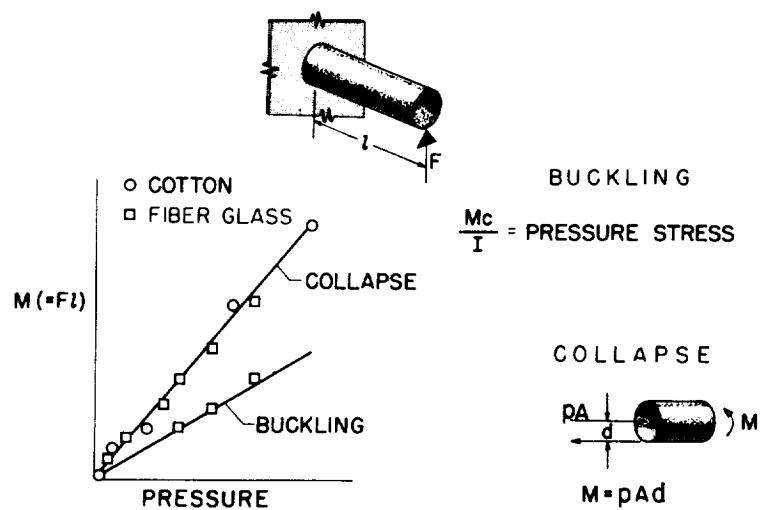


Figure 2

SIMPLE STRENGTH ANALYSIS OF AN INFLATED DELTA WING

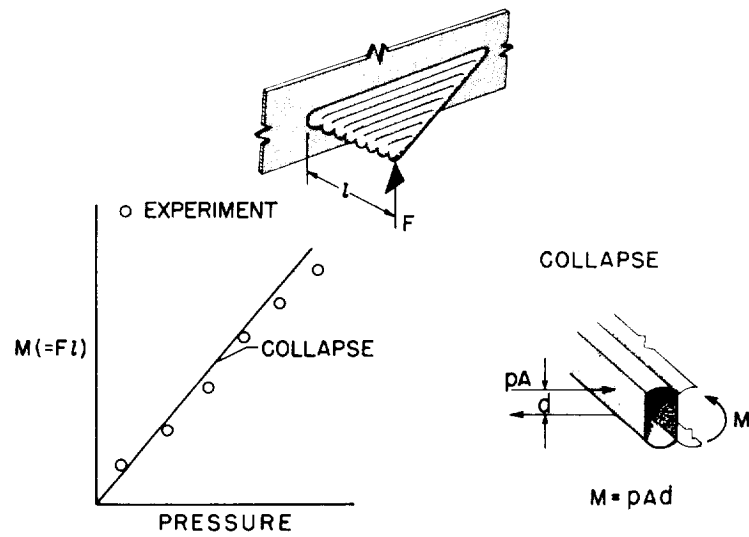
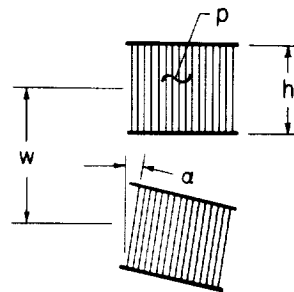


Figure 3

LINEAR AIRMAT PLATE THEORY

ASSUMPTIONS

ELASTIC, ORTHOTROPIC MATERIAL
 CONSTANT PRESSURE
 INEXTENSIONAL DROP CORDS
 TRANSVERSE SHEAR DEFORMATION



$$SHEAR \text{ STIFFNESS} = ph$$

Figure 4

LATERAL DEFLECTION AT CENTER OF SQUARE AIRMAT PLATE

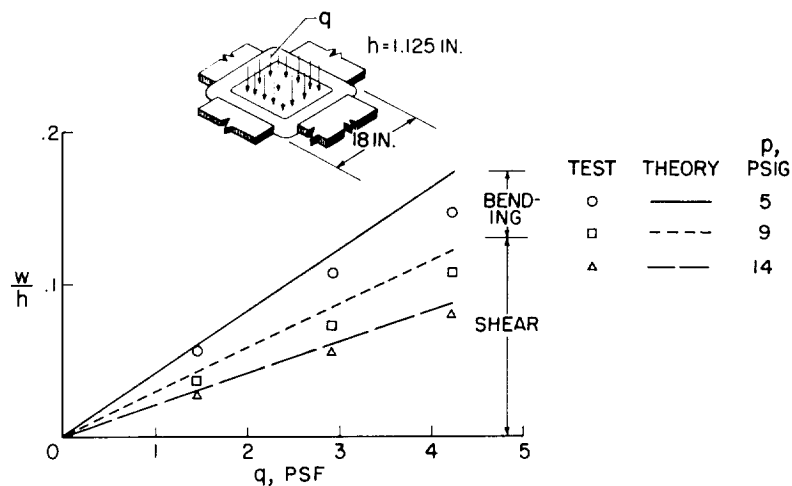


Figure 5

TYPICAL TENSION PROPERTIES OF FABRICS

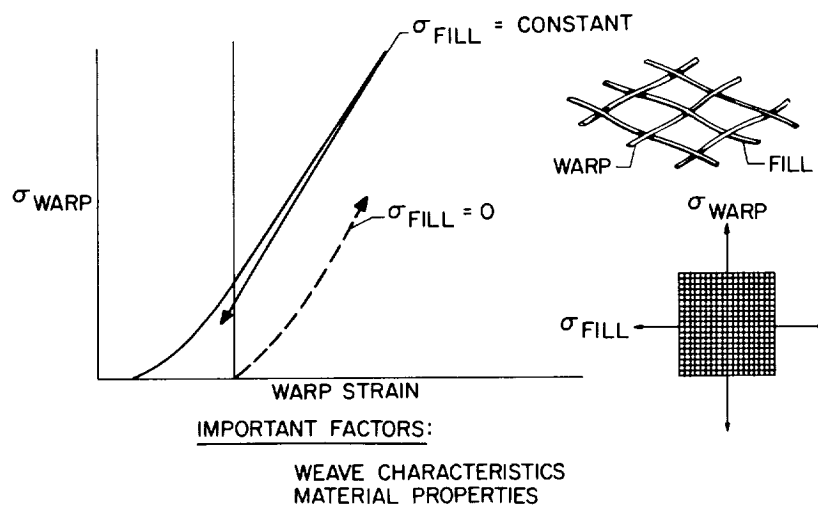
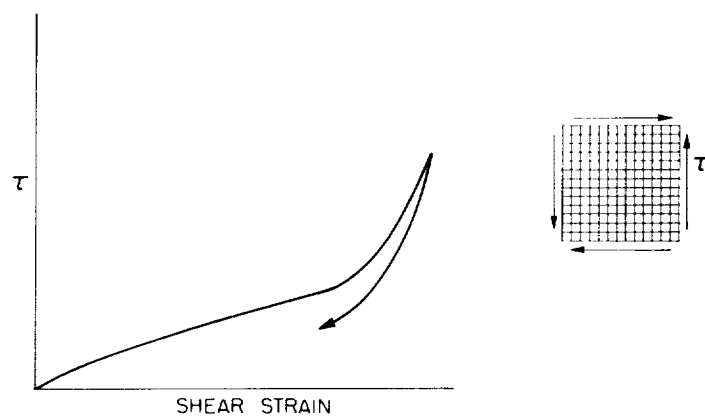


Figure 6

TYPICAL SHEAR PROPERTIES OF FABRICS

IMPORTANT FACTORS:

COATING CHARACTERISTICS
FRICTION (TENSION)

Figure 7

VIBRATION CHARACTERISTICS OF 60° SILK-LATEX DELTA WING

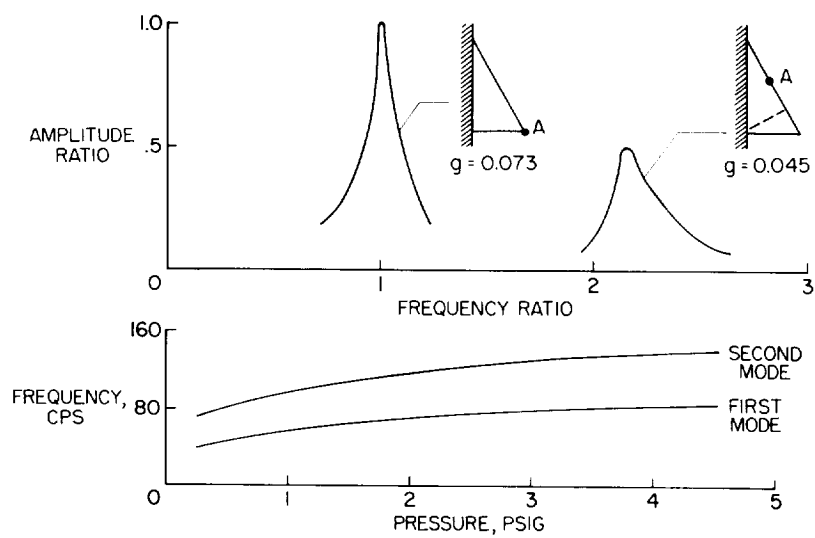


Figure 8

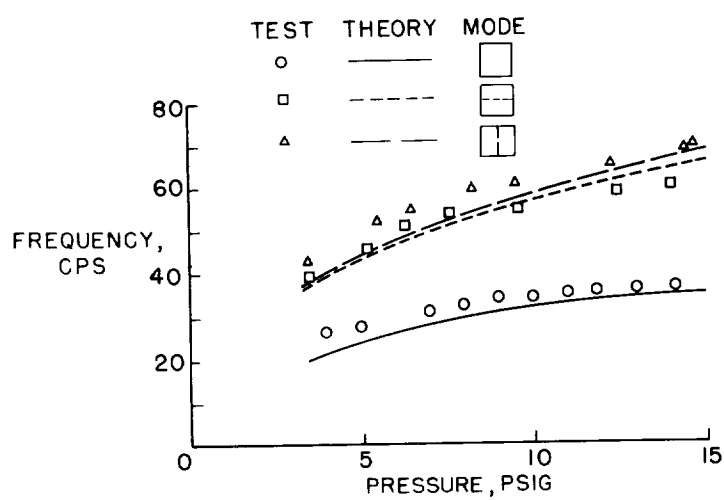
FREQUENCIES OF SQUARE NYLON-NEOPRENE
AIRMAT PLATE

Figure 9